Meshless Method for Slip Flows

Ajit Kumar Mahendra
Enrollment No. PHD/ ENGG01200704012
Bhabha Atomic Research Centre, Mumbai

A thesis submitted to the
Board of studies in Engineering Sciences
In partial fulfillment of the requirements
For the Degree of

DOCTOR OF PHILOSOPHY

of

HOMI BHABHA NATIONAL INSTITUTE

December 2011

HOMI BHABHA NATIONAL INSTITUTE

Recommendations of the Viva Voce Board

As members of the Viva Voce Board, we certify that we have read the dissertation prepared by Ajit Kumar Mahendra, enrollment number *PHD / ENGG01200704012* entitled "Meshless method for slip flows" and recommend that it may be accepted as fulfilling the dissertation requirement for the Degree of Doctor of Philosophy.

Srikumar Banerjee Date: 24 Sept 2013

Chairman Prof. S. Banerjee

Date: 24/09/2013

Guide/Convener Prof. R.K. Singh

Gouthaman Date: 24-9-13.

Technical Adviser Mr. G. Gouthaman

Date: 24/9/13

Member Prof. G.K. Dey

Date:

Member Prof. S.B. Roy

Date: 24.9.13

Member Prof. N.K. Maheshwari

Date: 24/9/13

Examiner Prof. Vishnu D. Sharma 24/9/13

Final approval and acceptance of this dissertation is contingent upon the candidate's submission of the final copies of the dissertation to HBNI.

I hereby certify that I have read this dissertation prepared under my direction and recommend that it may be accepted as fulfilling the dissertation requirement.

24/09/13

Guide : Prof. R.K. Singh

Date: 24/09/2013 Place: BARC Trombay

STATEMENT BY THE AUTHOR

This dissertation has been submitted in partial fulfillment of requirements for an advanced degree at Homi Bhabha National Institute (HBNI) and is deposited in the Library to be made available to borrowers under rules of the HBNI.

Brief quotations from this dissertation are allowable without special permission, provided that accurate acknowledgement of source is made. Requests for permission for extended quotation from or reproduction of this manuscript in whole or in part may be granted by the Competent Authority of HBNI when in his or her judgment the proposed use of the material is in the interests of scholarship. In all other instances, however, permission must be obtained from the author.

Ajit Kumar Mahendra

DECLARATION

I, hereby declare that the investigation presented in the dissertation has been carried out by me. The work is original and has not been submitted earlier as a whole or in part for a degree / diploma at or any other institution / university.

Ajit Kumar Mahendra

Dedicated to my family.

Acknowledgements

In year 2007 Prof. S. Banerjee then Director B.A.R.C. visited our experimental laboratory and encouraged many of us to pursue higher studies and register in Homi Bhabha National Institute. Soon, I had a meeting with my guide Prof. R.K.Singh and my technical adviser Shri. G. Gouthaman and research topic on slip flow was formulated. I thank my guide and technical adviser for guiding me through the rough and choppy sea of research at the same time encouraging me to pursue new research ideas. Prof. R.K. Singh always stressed to look into more fundamental aspects of the subject. Shri. G. Gouthaman encouraged me to venture into unknown territory and difficult terrain of kinetic theory. I express my deep gratitude to my guide Prof. R.K. Singh and my technical adviser Shri. G. Gouthaman for developing insight into practical aspects of computational fluid dynamics.

When I reminisce, I feel very indebted to Shri. B. Bhattacharjee former Director B.A.R.C. who took special interest in laying the foundation of computational fluid dynamics (CFD) laboratory and Prof. S. M. Deshpande who taught me CFD, kinetic flux vector scheme, listened to me patiently and encouraged me. A special thanks goes to Shri. V.D. Puranik who taught me basics of rotating fluid dynamics during my formative years. I am also grateful to staff and faculty of Department of Aerospace Engineering, Indian Institute of Science where I learned gas dynamics.

Thanks are due to Prof. A.K. Suri, Prof. L.M. Gantayet, Prof. P.K. Vijayan, Prof. P.K.Tewari and Prof. G.K. Dey who patiently heard my yearly progress seminars and contributed in enriching my research.

I wish to express my gratitude to Chemical Engineering Group director, Shri. T.K. Bera and Shri. A. Sanyal for providing constant encouragement throughout the course of this research work. I would also thank my colleagues Shri. Mihir Chatterjee and Shri Vinay Kumar for many illuminating discussions in the field of rotating flows and meshless methods and to Shri. G.N. Sashi Kumar for his help in carrying out studies with ant colony optimization method. I am also very thankful to Shri A.K. Kalburgi with whom I had many discussions on experimental aspects of slip flows. I also wish to thank the staff of my laboratory for help in the experimental work.

I am very thankful to Prof. J.C. Mandal and Prof. S.D. Sharma for mentoring and providing encouragement and motivation. Thanks are also due to Dr. C. Praveen with whom I had long sessions of discussions at TIFR-CAM, Bangalore. I also wish to thank Prof. Tatiana G. Elizarova for presenting me her book on Quasi-Gas Dynamic Equations which further ignited my interest in kinetic theory. I am also very thankful to Dr. Chris Greenshields, with whom my chance meeting in Bangalore was god send meaningful coincidence. Interaction with him motivated me towards my research objectives.

It was blessings of my parents and their support which gave me strength at some of the most difficult times. During this period my wife Meeta was posted in United Kingdom and had worked much harder than me while taking care of her busy office schedule as well as the family. I am quite indebted to my wife and understanding children for their unflinching unconditional support, love and patience.

PUBLICATIONS

Publications from present research

Journals and Books

- A.K. Mahendra, R.K.Singh, G. Gouthaman, Meshless kinetic upwind method for compressible, viscous rotating flows. Computers and Fluids 2011; Vol.46 pp.325–332.
  (Research contribution : Development of novel meshless solver SLKNS using split stencil least square method and kinetic scheme.)
- A.K. Mahendra, G. Gouthaman, R.K.Singh, Viscous Compressible Slip Flows. Part 1: Kinetic Flux Vector Splitting and its Variance Reduction form. International Journal of Emerging Multidisciplinary Fluid Sciences, 2011; Vol. 3, pp. 21–47.
  (Research contribution : Development of kinetic flux vector scheme in its variance reduced form.)
- A.K. Mahendra, G. Gouthaman, R.K.Singh,Viscous Compressible Slip Flows. Part 2 : Meshless Solver for Rotating Slip Flows. International Journal of Emerging Multidisciplinary Fluid Sciences, 2011; Vol. 3, pp. 49–83.
  (Research contribution : Development of modified SLKNS.)
- G.N. Sashi Kumar, A.K. Mahendra, G.Gouthaman, Multi-objective shape optimization using ant colony coupled computational fluid dynamics solver. Computers and Fluids 2011; Vol. 46 pp.298–305.

(Research contribution : Multi-objective shape optimization method for ant colony coupled meshless solver SLKNS with adaptive ϵ-dominance strategy.)

- G.N. Sashi Kumar, A.K. Mahendra, A. Sanyal, and G. Gouthaman, A Hybrid Method for Multi-Objective Shape Optimization. Lecture Notes in Computer Science 6457 pp. 563–567, 2010 Springer-Verlag Berlin Heidelberg.
  (Research contribution : Multi-objective shape optimization method with hybrid method based on ant colony optimization and genetic algorithm using meshless solver SLKNS.)

Peer reviewed Symposia and Conferences

- A.K. Mahendra, R.K. Singh, G. Gouthaman, Meshless kinetic upwind method for compressible, viscous rotating flows. Conference on Numerical method for Fluid Dynamics, ICFD 2010, Reading U.K., 12-15 April 2010.
  (Research contribution : Development of novel meshless solver SLKNS using split stencil least square method and kinetic scheme.)
- A.K. Mahendra, R.K. Singh, Meshless kinetic upwind method for rotating slip flows. 12th AeSI Annual CFD Symposium, Bangalore, August 11-12, 2010.
  (Research contribution : Extending the meshless solver SLKNS for slip flows using kinetic theory based method.)
- A.K. Mahendra, R.K. Singh, G. Gouthaman, Shape optimization of stationary body under strongly rotating flows. IUTAM Symposium on Bluff Body Flows, IIT-Kanpur, 12-16 December 2011.
  (Research contribution : Development of multi-objective nonlinear simplex based method using meshless solver SLKNS and Fourier parametrization.)

- G.N. Sashi Kumar, A.K. Mahendra, A. Sanyal, G. Gouthaman, 2D Meshless solver with a better spectral resolution. 13th AeSI Annual CFD Symposium, Bangalore, August 11-12, 2011.
  (Research contribution : Development of meshless solver SLKNS with enhanced spectral properties.)

Research reports

- A.K. Mahendra, Adaptive ϵ-dominance coupled Lp metric strategy for multi objective - multicomponent problems, MDD Internal report, BARC, Trombay, Mumbai, January 2010.
  (Research contribution: Multi-objective methodology using adaptive ϵ-dominance coupled L_p metric strategy.)
- A.K. Mahendra, R.K. Singh, Onsager reciprocity principle for kinetic upwind method, MDD Internal report, BARC, Trombay, Mumbai, December 2010.
  (Research contribution: Development of kinetic model, kinetic scheme following Onsager's reciprocity principle.)
- A.K. Mahendra, R.K. Singh, G. Gouthaman, Kinetic wall and no-slip boundary conditions for continuum flows, MDD Internal report, BARC, Trombay, Mumbai, November 2011.
  (Research contribution: Kinetic theory based wall boundary condition and its comparison with no-slip, Maxwell velocity slip and von Smoluchowski temperature jump for dissipative wall.)

LIST OF CODES

List of codes developed from present research

Table 1: Pre-processing codes

Sr. No.	Code	Description
1.	Cloud-Generator	Generates nodes or cloud of points using elliptic, transfinite interpolation based grid generator.
2.	Cloud-Blanker	Blanks background cloud due to presence of bodies.
3.	Cloud-Merger	Merges sub-clouds around each bodies with the background cloud.
4.	Cloud-Neb-Flag	Generates connectivity, assigns boundary flags and direction cosines for the treatment of boundary points.

Table 2: Flow Solver codes

Sr. No.	Code	Description
1.	SLKNS	SLKNS code for continuum, non-continuum slip flows.
2.	SLKNS-Polar	SLKNS code for axi-symmetric case. The code is three dimensional as it updates azimuthal velocity.

Table 3: Parallelization codes

Sr. No.	Code	Description
1.	Cloud-Graph-Generator	Generates graph based on symmetric connectivity required for partitioning.
2.	Comm-Schedule	Schedules the contention free optimum communication based on number of processor and decomposed domains and prepares a look-up table.
3.	Cloud-Map-G2L	Maps the global data arrays to local data arrays belonging to decomposed domains.
4.	Cloud-Sequencer	Does cloud sequencing from coarse, medium to fine cloud.
5.	Parallel-SLKNS	Parallel version of SLKNS codes for continuum, non-continuum slip flows.
6.	Reconstruct-Cloud	Reconstructs data from all processors and prepares plot files for post-processing.

Table 4: Optimization codes and subroutines

Sr. No.	Code	Description
1.	Cloud-Adapter	Generates cloud after taking input from the optimization code by merging and blanking operations.
2.	Param	Subroutine for parametrization and boundary surface generation.
3.	Multi-Opt	Subroutine for multi-objective optimization based on reference point approach and ϵ dominance strategy. This subroutine plugs into existing Genetic Algorithm (GA), Ant Colony Optimization (ACO), Non-Linear Simplex codes.

Nomenclature

List of some salient variables, constants and symbols.

Greek Symbols

α_g	viscosity coefficient
$\alpha(\sigma_v)$	parameter as a function of tangential momentum coefficient in viscosity relationship
$\alpha^0, \alpha_i^1, \boldsymbol{\alpha}_{ik}^2$	properties of the system in equilibrium
β	thermal speed = $(2RT)^{-1}$
γ	ratio of specific heat
δ	Dirac delta function
δu	statistical fluctuation
δ_o	exponent of the viscosity law of the gas
$\delta(BGK/HS)$	first order slip parameter
δ_{layer}	Ekman and Stewartson boundary layer
ε	Rossby number
ϵ_i	factor used in ϵ-dominance rank
η_i	slope of the connectivity point Pi
κ	thermal conductivity
θ	azimuthal variable
$\vartheta_{\tau,1}$, $\vartheta_{\tau,2}$, $\vartheta_{\tau,3}$	moment closure coefficients associated with the shear stress terms for Burnett equation.
$\vartheta_{q,1}$, $\vartheta_{q,2}$, $\vartheta_{q,3}$	moment closure coefficients associated with the heat flux vector terms for Burnett equation.
λ	mean free path
$\lambda_E^{\pm}$	eigenvalues of the least square matrix C
μ, μ_{num}	physical viscosity and numerical viscosity
ν	collision frequency
$\xi_{1,\tau}$, $\tilde{\xi}_{1,\tau}$	Chapman-Enskog polynomials associated with the shear stress tensor.
$\xi_{1,q}$, $\tilde{\xi}_{1,q}$	Chapman-Enskog polynomials associated with the heat flux vector.

ρ	density
ρ_{sb}	density of particles in side beam
ρ_s	entropy density,
$\rho_{s_{in}}$	entropy density due to internal process
$\rho_{s_{ex}}$	entropy density due to external exchange
ϱ, Θ	scattering angles
σ,σ_i,σ_o, $\sigma_{\vec{t}}$, $\sigma_{\vec{n}}$	accommodation coefficient
σ_v, σ_T	momentum and thermal accommodation coefficient
σ_P, $\sigma(t)$	entropy production and its density
$\sigma(\boldsymbol{X}_i, \boldsymbol{J}_i)$	entropy production density based on flux and force
$\sigma(\boldsymbol{J}_i, \boldsymbol{J}_k)$	entropy production density based in terms of fluxes
ς	macroscopic parameter for Knudsen number
ζ	parameter used in ranking
τ	shear stress tensor
τ_s, τ_f	slow and fast time scale in van Kampen's procedure.
$\phi_X(\boldsymbol{X}_i, \boldsymbol{X}_k)$	dissipation function density
ϕ_o, ϕ_i	variable for determination of derivative at point P_o and P_i
ϕ_{xo}, ϕ_{yo}, ϕ_{zo}	derivative of the variable with respect to *x, y, z.*
φ	dissipation control function
$\boldsymbol{\Phi}_o$	matrix of derivatives ($[\phi_{xo}, \phi_{yo}, \phi_{zo}]^T \in \mathbb{R}^n$)
$\chi, \chi_{avg}, \chi_{ref}$	baroclinic terms
$\bar{\chi}$	dimensionless baroclinic term
ω	angular velocity
$\omega(\vec{v})$	weight function associated with Hermite polynomials.
Δx_i,Δy_i,Δz_i	difference in coordinate distance for the points P_i and P_o
Δbx_i,Δby_i,Δbz_i	deformation for surface points
$\Delta\phi_i$	difference in variable for the points Pi and Po
$\boldsymbol{\Delta\phi}_N$	matrix of observation ($[\Delta\phi_1, \Delta\phi_2, \cdots, \Delta\phi_m]^T \in \mathbb{R}^m$)
Δf,Δf_1	difference in Maxwellian and their Chapman-Enskog term
$\Delta\hat{f}_1$	difference between first order Chapman-Enskog and Maxwellian distribution
$\Delta\bar{f}_1$	difference in first order Chapman-Enskog expansion term for Maxwellian
Δp	pressure drop
Δt	time step
Δt_I, Δt_V, Δt_S	inviscid, viscous and slip time steps
Δu_s	Burnett addition to the slip velocity
Θ_{ij}	function of symmetric tensor
Ξ	linear subspace used in Levermore hierarchy
Φ, Φ_i	perturbation term and its component
Φ_T	perturbation used in trial distribution
Ω_z	axial vorticity vector

$(\Omega_z)_{RB}$	axial vorticity vector for rigid body rotation
Ω_i,$\tilde{\Omega}_i$	decomposed domain and augmented domain
Ω_i^R,Ω_i^S	domain involved in receiving and sending data
$\Omega_i^{R,s}$,$\Omega_i^{R,d}$	domain involved in receiving static and dynamic data
$\Omega_i^{S,s}$,$\Omega_i^{S,d}$	domain involved in sending static and dynamic data
$\bar{\Pi}$	molecular collision cross section
$\overline{\Psi}_{k_1k_2k_3\cdots k_j}(\vec{x},t)$	macroscopic thermodynamic quantity
$\mathbf{\Pi}$	tensor of viscous stresses
$\mathbf{\Lambda}_x, \mathbf{\Lambda}_y, \mathbf{\Lambda}_z$	diagonal matrices
$\bar{\mathbf{\Upsilon}}_j$, $\mathbf{\Upsilon}_j$,$\bar{\mathbf{\Upsilon}}_{jk}$	microscopic tensors
$\mathbf{\Upsilon}_j^{\pm\cdot}$, $\mathbf{\Upsilon}_j^{\cdot\pm}$	microscopic split tensors for 2D geometry.
$\mathbf{\Upsilon}_j^{\pm\cdot\cdot}$, $\mathbf{\Upsilon}_j^{\cdot\pm\cdot}$, $\mathbf{\Upsilon}_j^{\cdot\cdot\pm}$	microscopic split tensors for 3D geometry.
$\mathbf{\Lambda}_j^x, \mathbf{\Lambda}_j^y, \mathbf{\Lambda}_j^z$	macroscopic tensors for x, y, z.
$\mathbf{\Lambda}_j^{\pm\cdot}$, $\mathbf{\Upsilon}_j^{\cdot\pm}$	macroscopic split tensors for 2D geometry.
$\mathbf{\Lambda}_j^{\pm\cdot\cdot}$, $\mathbf{\Upsilon}_j^{\cdot\pm\cdot}$, $\mathbf{\Upsilon}_j^{\cdot\cdot\pm}$	macroscopic split tensors for 3D geometry.
$\mathbf{\Psi}_{m_1m_2\cdots m_k}$,$\mathbf{\Psi}$,$\psi_i$,	moment vectors and its element
$\bar{\mathbf{\Psi}}$	moment function

Roman and Mathematical Symbols

$\vec{a}$	acceleration vector
$\boldsymbol{a}^{(n)}$	expansion coefficient used in Grad moment method.
$a^{(0)}, a_i^{(1)}, a_{ij}^{(2)}$	constants used in Shakhov's model
$A_x^{\pm}$, $A_y^{\pm}$, $A_z^{\pm}$	factors based on error functions.
$A_1^{\pm}$, $A_2^{\pm}$, $A_3^{\pm}$	factors based on error functions.
A_1,A_2	first order and second order velocity slip coefficient associated with shear stress tensor
$A(z), B(z), C(z)$	parameters to calculate the analytical velocity profile
$b_i(x,y)$	basis function
bx, by, bz	Cartesian coordinates of the body
B_x, B_y, B_z	factors based on exponential function.
B_1, B_2, B_3	factors based on exponential function
B_1^T	first order slip coefficient for temperature jump
B_2^T	second order slip coefficient for temperature jump
B_{NS}	breakdown matrix due to moment realizability
Bc	sub-cloud of points lying in non-computing domain
C_l, C_d, C_f	lift, drag and friction coefficients
d_h	hydraulic diameter of the annuli

$d(P_i, P_j)$	Euclidean distance between points P_i and P_j
D	degree of freedom
$D(\sigma_v)$	parameter as a function of tangential momentum coefficient in viscosity relationship
$D(f_g, f_h)$	Symmetric Kullback-Leibler directed divergence for distributions f_g and f_h
ex_i, ey_i, ez_i	scaled error terms for the point P_i
E	total energy
E_{cut}	edge cuts
E_e	set off edges
E_k	Ekman number
Ex_i, Ey_i, Ez_i	error terms for the point P_i
$f(\vec{x}, \vec{v}, \mathbb{I}, t)$	density based velocity distribution function
f_0,f_1	Maxwellian and first order distribution function
$\breve{f}$	number density based distribution function
$f_{1,T}$	trial linearized distribution
$f_1^{\pm}, f_1^{\pm\pm}, f_1^{\pm\pm\pm}$	half range first order distribution function
$f_{1,\Sigma}$	total distribution at the wall
$f_{1,I}$	distribution incident to the wall
$f_{1,R}$	specularly reflected distribution
$f_{0,W}$	Maxwellian distribution at wall condition.
f_{RB}	distribution associated with rigid body rotation.
f_{ref}	reference distribution function.
f_{ES}	ellipsoidal statistical distribution function.
$f^{(H)}$	distribution function at hierarchy H
F_{exp}, F_{num}	experimental and numerical flow rate.
g	magnitude of the relative particle velocity before collision
$g_t(\vec{x})$	trigonometric parametric function
G	undirected weighted graph
G_{mass}, $G_{mass}^{\pm}$	net mass flux and its split form
$\mathcal{G}$	global mapping function
h	distance parameter
H	Boltzmann entropy function
$\bar{H}$	half height of the cylinder
I_τ, I_q	constants used in microscopic tensors.
$\vec{j}_s$	flux of entropy density
$J_B(f, f)$	binary collision term at same position
$J(f, f)$	binary collision term
$J_m(f, f)$	binary collision model
k_B	Boltzmann's constant
$K(f, f, f)$	ternary collision term
Kn, $\mathrm{Kn}_{GL,\zeta}$	Knudsen number and gradient length Knudsen number

$\mathrm{Kn}_\rho, \mathrm{Kn}_T, \mathrm{Kn}_u$	gradient length Knudsen number based on ρ, T and u
Kn_L	Knudsen number based on length scale
$L(f,f,f,f)$	quaternary collision term
L_ρ	characteristic length scale
m_x, m_y, m_z	number of points in the connectivity sub-stencil for x,y,z direction
$\mathcal{L}(\boldsymbol{X},\boldsymbol{J}), \mathcal{L}(\boldsymbol{X},\boldsymbol{J},\lambda)$	Lagrangian in terms of $\boldsymbol{X}$, $\boldsymbol{J}$, and its multiplier.
$\mathcal{L}$	local mapping function
$\dot{m}, \dot{m}_{NS}$	slip and continuum mass flow rate
M	Mach number
M_i	path of message
M_{part}	sub-domain
$\dot{M}_q$,$\dot{M}_\tau$	Mahalanobis speed for thermodynamic force $\boldsymbol{X}_q$, $\boldsymbol{X}_\tau$
$D(f_g\|f_h)$,$D(f_g,f_h)$	Kullback-Leibler directed divergence for distributions f_g and f_h
$n(\vec{x},t)$	number of particles
n, s	subscript denoting the normal and tangential coordinate to the wall
N	sample size used in DSMC
$N(P_o)$	connectivity set for point P_o
$N^{\pm\pm}$, $N^{\pm\pm\pm}$,	split connectivity set for 2-D and 3-D
$N_x^{\pm}(P_o)$	split connectivity sub-stencil for x direction
$N_y^{\pm}(P_o)$	split connectivity sub-stencil for y direction
$N_z^{\pm}(P_o)$	split connectivity sub-stencil for z direction
NS_B,NS_L	breakdown parameter for Navier-Stokes equation
p, $\bar{p}$	pressure and average pressure
$P_k(x,y)$	polynomial in two dimensions.
Pr	Prandtl number
$\vec{q}$	heat flux vector
$\vec{q}^y$,$\vec{q}^*$	goal vectors
rf	relaxation factor
$r_1^k(\vec{x}), r_2^k(\vec{x}), r_3^k(\vec{x})$	3 vertices of simplex r at iteration k
r, r_{wall}	radius and radius of the cylinder
r_i,r_o	inner and outer radius
r_d	dimensionless radius
r_s	radius of the sphere
R	specific gas constant
Re	Reynold's number
Res_2^k	L_2 norm based residue at iteration k
Rp	Reciprocity number
$\mathcal{R}(U^k)$	residue vector

sC	sub-cloud of points
$s_1^k(\vec{x}), s_2^k(\vec{x}), s_3^k(\vec{x})$	3 vertices of simplex s at iteration k
S	surface area
S_p	disjoint sub-sets of vertices
$SN(P_i)$	symmetric connectivity set for point P_i
St	kinetic Strouhal number
t,$\hat{t}$	time and dimensionless time
t_R,$\hat{t}_R$	relaxation time and dimensionless relaxation time
$t_{R,1}$, $t_{R,2}$	relaxation time for momentum transport and energy transport
$t_{R(f)}$, $t_{R(f_0)}$	relaxation time for distribution f and Maxwellian
$t_{R(\tau)}$, $t_{R(q)}$	relaxation time associated with τ and q.
$t_{R(\tau,ii)}$, $t_{R(q,ii)}$	relaxation time due to self collisions of specie i
$t_{R(\tau,jj)}$, $t_{R(q,jj)}$	relaxation time due to self collisions of specie j
$t_{R(\tau,ij)}$, $t_{R(q,ij)}$	relaxation time due to cross collisions of specie i with j
$t_{R(\tau,ji)}$, $t_{R(q,ji)}$	relaxation time due to cross collisions of specie j with i
T, T_o	temperature, average temperature
T_{Max}	Maximum surface temperature
$\bar{T}_M$, T_{ref}	dimensionless and reference temperature
u_z,$u_{z_{\max}}$	axial velocity and its maximum in the annuli
u_B	velocity based on Boltzmann solution.
u_{NS}	velocity based on Navier-Stokes solution.
u_{Kn}	Knudsen contribution to the velocity.
u_s,u_w	slip velocity and wall velocity
u_λ	tangential gas velocity at one mean free path
u_σ	dispersion velocity
$\vec{u}$,$\vec{c}$	macroscopic velocity vector, peculiar velocity
v_{th}	most probable molecular thermal speed
v_z, v_r, v_θ	axial, radial and azimuthal molecular velocity
V	set of vertices
w_v, w_e	set of vertex and edge weights
x_o, y_o, z_o	coordinates of the point P_o
x_i, y_i, z_i	coordinates of the point P_i
$\vec{x}$,$\vec{v}$	position vector and molecular velocity vector
$\hat{\vec{x}}$, $\hat{\vec{v}}$	dimensionless position and velocity vector
X, Y, Q	Parametric, objective and goal space
$\tilde{y}$	y/λ
z	axial variable
$\bar{z}$	element of linear subspace in Levermore hierarchy
$\mathbb{H}^{(n)}$	Hermite or Gram-Charlier polynomials.
$\mathbb{H}(\vec{x}, \vec{v})$	Hamiltonian in 6 dimensional space
$\mathbb{I}$	internal energy variable
$\mathbb{I}_o$	average internal energy parameter

$\mathbb{J}$	linear operator for collision terms
$\mathbb{L}$	Liouville operator
$\mathbb{M}_y$	y directional momentum flux
$\mathbb{O}$	three dimensional rotation operator
$\mathbb{P}(\bar{y})$	collision probability function.
$\mathbb{Q}_y$	y directional energy flux
$\mathbb{S}_{xy}, \mathbb{S}_{yz}, \mathbb{S}_{zx}$	connectivity parameters
$\boldsymbol{G}$, $\boldsymbol{G}^{\pm}$	flux vector and its split form
$\boldsymbol{G}^{\pm}_{m_1 m_2 \cdots m_k}$	spli flux vector in extended thermodynamics
$\boldsymbol{GX}, \boldsymbol{GY}, \boldsymbol{GZ}$	flux vector in x, y, z-direction
$\boldsymbol{GX}^{\pm}_I, \boldsymbol{GY}^{\pm}_I, \boldsymbol{GZ}^{\pm}_I$	inviscid split flux vectors
$\boldsymbol{GX}^{\pm}_V, \boldsymbol{GY}^{\pm}_V, \boldsymbol{GZ}^{\pm}_V$	viscous split flux vectors
$(\boldsymbol{GX}^{\pm}_V)_\Delta, (\boldsymbol{GY}^{\pm}_V)_\Delta$	VRKFVS viscous split flux vectors in x,y-direction
$(\boldsymbol{GZ}^{\pm}_V)_\Delta$	VRKFVS viscous split flux vectors in z-direction
$\boldsymbol{GR}$	radial flux
$\boldsymbol{GR}^{\pm}_I$,$\boldsymbol{GR}^{\pm}_V$	inviscid and viscous radial split flux components
$(\boldsymbol{GR}^{\pm}_I)_{RB}$,$(\boldsymbol{GZ}^{\pm}_I)_{RB}$	r,z split fluxes based on rigid body condition
$(\boldsymbol{GX}^{\pm}_I)_{RB}$,$(\boldsymbol{GY}^{\pm}_I)_{RB}$	x,y split fluxes based on rigid body condition
$\boldsymbol{J}_i$,$\boldsymbol{J}^k_i$	thermodynamic flux
$\boldsymbol{L}_{ij}$,$\boldsymbol{L}^k_{ij}$,$\boldsymbol{L}^{k+1}_{ij}$	Onsager's phenomenological tensor
$\boldsymbol{P}$	Pressure tensor
$\boldsymbol{R}^J_{ik}$,$\boldsymbol{R}^X_{ik}$	symmetric tensor in flux and force space
$\boldsymbol{S}$	source terms
$\boldsymbol{U}$	state update vector, $[\rho, \rho\vec{u}, \rho E]^T$
$\boldsymbol{U}_M$	vector of conserved variable for Maxwellian f_M
$\boldsymbol{U}_{RB}$	state vector based on rigid body condition
$\boldsymbol{U}_{m_1 m_2 \cdots m_k m_{k+1}}$	state vector in extended thermodynamics
$\boldsymbol{X}_i$,$\bar{\boldsymbol{X}}$	thermodynamic force
$\boldsymbol{\mathcal{X}}_{\tau q}$	tensor with components $\{\boldsymbol{X}_\tau, \boldsymbol{X}_q\}$
$\boldsymbol{A}$, $\boldsymbol{A}^{\pm}$	Jacobian matrix and its split form
$\boldsymbol{A}^{\mathcal{T}}$, $\boldsymbol{A}^{\mathcal{A}}$	Jacobian matrix for transport and acoustic flux
$\boldsymbol{A}_M$	adjacency matrix
$\boldsymbol{A}_N$,$\boldsymbol{A}_{N_x}$,$\boldsymbol{A}_{N_y}$,$\boldsymbol{A}_{N_z}$	least square data matrix used in normal equations approach ($\in \mathbb{R}^{n\times m}$) for $N(P_o$, $N_x(P_o$, $N_y(P_o$ and $N_z(P_o$.
$\boldsymbol{\mathcal{A}}$	Matrix due to relaxation of distribution function
$\boldsymbol{c}$,$\boldsymbol{d}$	matrix of coefficients used in radial basis function
$\boldsymbol{C}$	least square cross product matrix
$\boldsymbol{C_M}$,$\tilde{\boldsymbol{C}}_{\boldsymbol{M}}$	communication matrices
$\boldsymbol{H}(\phi_0^{(1),k})$	Hessain matrix after k iteration
$\boldsymbol{I}$	identity invariant tensor / identity matrix
$\boldsymbol{r}$,$\boldsymbol{b}$	vector of radial basis function and polynomial basis
$\boldsymbol{W}$, $\boldsymbol{V}_p$	weight matrix and Vandermonde matrix.

Abbreviations

ACO	Ant colony optimization
AUSM	Advective Upstream splitting method
BBGKY	Bogoliubov, Born, Green, Kirkwood and Yvon
BGK	Bhatnagar-Gross-Krook kinetic model
CIR	Courant, Isaacson and Rees
CLL	Cercignani, Lampis and Lord reflection model
CUSP	Convection upwind and split pressure
DNS	Direct numerical solution
DSMC	Direct Simulation Monte Carlo
DQ	Differential quadrature
EHE	Extended hydrodynamic equations
ES-BGK	Ellipsoidal statistical Bhatnagar-Gross-Krook kinetic model
GA	Genetic algorithm
HS	Hard sphere
ID,OD	Inner diameter, outer diameter
IP	Information preservation
KFVS	Kinetic flux vector splitting
LB	Lattice Boltzmann
m-SLKNS	modified Split stencil least square kinetic upwind method for Navier-Stokes
MACO	Multi-objective ant colony optimization
MD	Molecular dynamics
MEPP	Maximum entropy production principle
MGA	Multi-objective genetic algorithm
MNS	Multi-objective nonlinear simplex
NET	Non-equilibrium thermodynamics
NS	Navier-Stokes
PSO	Particle swarm optimization
PVU	Peculiar velocity upwind
QGD	Quasi gas dynamics
RBF	Radial basis function
RTSM	Relaxation Time Simulation Method
SLKNS	Split stencil least square kinetic upwind method for Navier-Stokes
SSP	Strong stability preserving
TMAC	Tangential momentum accommodation coefficient
VHS	Variable hard sphere
VRKFVS	Variance reduction kinetic flux vector splitting

Synopsis

The thesis deals with the development of meshless method for slip flows based on kinetic scheme incorporating features of non-equilibrium thermodynamics. The subject involves research in the field of kinetic theory, non-equilibrium thermodynamics, kinetic schemes, meshless methods and optimization approaches.

Upwind scheme basically add correct amount of dissipation or entropy so as to satisfy thermodynamics as the state vector is updated. However, most of the upwind schemes fail to ensure the correct distribution of the entropy generation for each thermodynamic force. Hence it is difficult to formulate a single monolithic solver if it is to operate from low speed to hypersonic rarefied flow or from creeping flows to high speed continuum flow. A successful upwind scheme should address two issues: i) the correct amount of dissipation or entropy generation, and ii) distribution of dissipation or entropy generation for each thermodynamic force i.e. in what proportion the thermodynamic forces associated with shear stress tensor and heat flux vector contribute. The kinetic scheme developed in the thesis follows the principle of non-equilibrium thermodynamics and ensures the correct division of entropy generation for each thermodynamic force as the state update moves from one conservation state to another following the path laid down by non-equilibrium thermodynamics. One of the fundamental contributions of the thesis is the development of a new non-equilibrium thermodynamics based kinetic model. Based on this new model, Navier-Stokes equation can be derived with correct Prandtl number. The non-equilibrium part of the distribution function is obtained as full tensor contraction of thermodynamic forces

and its associated microscopic tensors.

It is more rational to incorporate features of non-equilibrium thermodynamics at the microscopic level and apply discretization at the Boltzmann level. A new approach to kinetic flux vector splitting method was formulated guided by the principles of non-equilibrium thermodynamics. Upwind scheme for macroscopic conservation equations in the new approach involves three steps : i) in the first step the Boltzmann equation is rendered into an upwind discretized form, ii) in the second step inviscid fluxes are obtained by taking moments of split Maxwellian distribution, iii) in the third step viscous fluxes are obtained by taking moments and full tensor contraction of split microscopic tensors. The present kinetic upwind scheme can be used to simulate the entire range from rarefied slip flow to continuum flow, creeping flow to flow with shocks as it is derived using kinetic theory incorporating phenomenological theory of non-equilibrium thermodynamics.

There are many approaches for numerical flow modeling of slip and rarefied flows. Most of the slip models in the literature are for simple micro-channel flows with its own geometric specific slip coefficient and range of validity in the Knudsen region. In such a scenario we require a more fundamental approach. One of the motivations of the thesis is to derive a unified wall boundary condition which satisfies non-equilibrium thermodynamics and can simulate both continuum and rarefied slip flow within Navier-Stokes equation in order to avoid extremely costly multi-scale simulation. The thesis presents novel kinetic flux vector splitting based wall boundary which uses Maxwell 's gas-surface interaction model incorporating features of linear non-equilibrium thermodynamics for effective resolution of slip phenomenon.

Recently, shape optimization using numerical methods has made rapid progress. The shape optimization procedure requires repeated grid generation after each iterative step. Most of the industrial problems have many complex components and generation of suitable grid for a

complex multi-body configuration can be very tedious and intensive task and sometimes it becomes the bottleneck. In such a scenario we require a faster, simpler and robust meshless approach. Amongst meshless approaches least square based methods are found to be robust and capable of resolving shocks. Normal equations as well as QR approach used in least square method produces inaccurate results when applied to stretched distribution of points required to resolve boundary layers of a viscous flow problem. The thesis presents a new approach to solve least square problem by generating a non-symmetric cross-product matrix by suitable selection of sub-stencils such that the matrix is diagonally dominant and well conditioned. The thesis describes the novel Split-stencil Least square Kinetic upwind method for Navier-Stokes (SLKNS) solver which makes use of least squares and Kinetic Flux Vector Splitting (KFVS) scheme based on microscopic tensor splitting with kinetic wall boundary condition.

Parallelization of meshless code uses domain decomposition based on graph built on symmetric connectivity. The parallel code uses optimal contention free communication schedule to carry out parallelization. This thesis also uses novel approach for cloud handling by merging the sub-cloud around body undergoing optimization. The multi-objective optimization for meshless method is based on Pareto optimality, ϵ-dominance and reference point approach.

The prime motivation of the thesis is to develop a robust meshless method based on kinetic theory that can carry out multi-objective optimization of stationary bodies under strong rotations and rarefied slip flows. The meshless method described in the thesis is able to resolve slip flow features, supersonic flows and typical features of the strongly rotating flows characterized by steep density gradient and thin boundary layers.

Contents

List of Figures

List of Tables

Chapter 1

Introduction

1.1 Non-continuum slip flow

The presence of rarefied domain around space vehicle or fluid transport in microelectromechanical devices (MEMS) is a typical non-continuum flow feature. Predicting fluid transport for rarefied flows or in micron-sized devices becomes difficult due to breakdown of continuum flow assumption embedded in conventional fluid dynamics. Validity of the Navier-Stokes equation as well as diffusion equation requires sufficient collision of particles and relaxation of the distribution to weak spatial gradients and slow temporal variations. Continuum also breaks down when gradients are substantial relative to the scale of mean free path or temporal changes are relatively rapid compared to mean collision time encountered in astrophysics. For Navier-Stokes equations to remain valid it has also to operate within the framework of Newtonian mechanics following continuum approximation and satisfying constitutive relationships due to collision dominated transport models of shear stress tensor and heat flux vector. Navier-Stokes description for simple fluids breaks down when the characteristic length scale associated with flow approaches the molecular mean free path.[1] As a consequence, the ratio of the mean free path of the molecules to the characteristic dimensions becomes appreciable. This ratio is referred to as the Knudsen number, $\mathrm{Kn} = \frac{\lambda}{L}$, where λ is the mean free path and L is the characteristic length scale. For example L can

[1] Refer Appendix A for determination of mean free path of gas.

also be defined in terms of the macroscopic gradients, e.g., $L = \rho/\frac{\partial \rho}{\partial x}$. Consider a flow in a tube of diameter D as shown in Figure 1.1, in the continuum regime the mean free path λ is small compared to the characteristic length scale i.e. diameter of the tube, D and in such cases collisions are more frequent amongst molecules than they are between molecules and the wall of the container. As a consequence the gas acts like a continuous viscous fluid when Knudsen number, Kn=$\lambda/D < 0.001$ and no-slip condition prevails. When the fluid becomes rarefied as shown in Figure 1.2 the frequency of molecule-molecule collision is less as compared with the molecule-wall collision. In such a case slip exists as fluid properties are no longer continuous and viscosity is undefined as there is no shearing forces between layers of molecules nor is there any momentum exchange. Figure 1.3 shows slip velocity and slip length. Research in slip flows is primarily motivated because of its huge applications in the field of micro devices in engineering, medical and other scientific areas. In micro devices the Knudsen number is large as the characteristic dimension of the micro device is small. In macro level the slip flow is observed for rarefied flow as the mean free path becomes large due to lower pressure.

With the increase of Knudsen number the collision dominated transport models i.e. constitutive relationships of shear stress tensor with deformation tensor becomes invalid due to violation of the inherent assumptions of Navier-Stokes. Classical hydrodynamics fails to describe flow phenomenon observed for rarefied gas with finite Knudsen number. Some of the most significant flow phenomenon for rarefied flow are as follows [267]:

1. Pressure profile observed in Couette and Poiseuille flow is not constant as observed in classical hydrodynamics.

2. Temperature gradient does not drive the heat flux in flow direction as observed in classical hydrodynamics.

3. Observation of Knudsen Paradox.[1]

[1]The mass flow in a Poiseuille flow varies as a function of Knudsen number, showing minimum mass flow in transition regime at Knudsen number of unity.

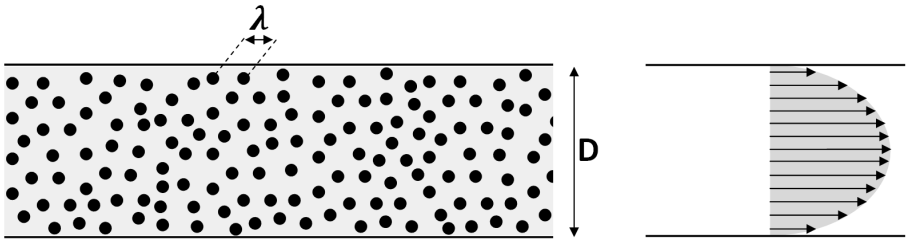

Figure 1.1: Viscous flow given by Kn=λ/D < 0.001, viscous behavior is observed as collisions are more frequent amongst molecules than they are between molecules and the wall of the containing tube, as a consequence no-slip condition prevails.

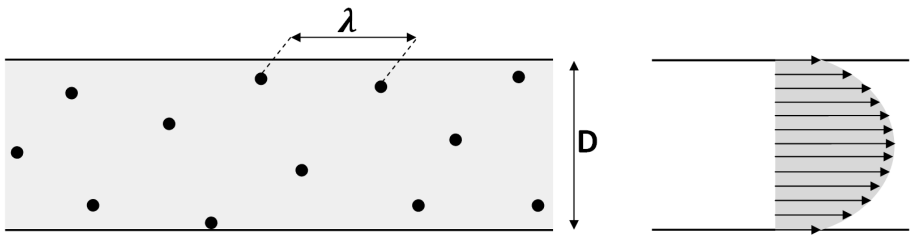

Figure 1.2: Rarefied flow Kn=λ/D∼1.0, viscous behavior is undefined as the frequency of molecule-molecule collision is less as compared with the molecule-wall collision, as a consequence slip exists.

4. Temperature profile in classical hydrodynamics for Poiseuille flow shows variation of fourth-order power law with no dip whereas the temperature profile in rarefied regime shows a dip.[1]

5. Detailed structure of shock, phase speed and attenuation of high frequency sound waves for rarefied flow differs from the classical hydrodynamics.

6. Knudsen boundary layer is observed for all hydrodynamic quantities for rarefied flow.

[1]This can only be described by either super-Burnett equations or higher moment method based regularized Grad like approach.

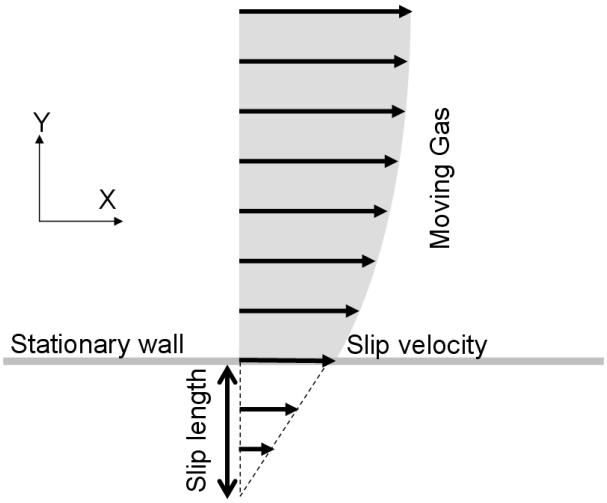

Figure 1.3: Slip Velocity and slip length.

1.1.1 Flow regimes

Based on extent of non-equilibrium effects and rarefaction the flow regime can be broadly classified [114] as

1. No-slip continuum regime : This regime is valid for Kn $<$ 0.001, since continuum and thermodynamic equilibrium prevails hence conventional no-slip is used along with Navier-Stokes equations.

2. Slip-Flow regime: This regime is valid in the range 0.001$<$Kn$<$0.1. The non-equilibrium effects occur in the close proximity of the wall, Navier-Stokes coupled with slip boundary conditions can effectively model velocity slip and temperature jump.

3. Transition regime: In the range 0.1 $<$Kn$<$10 the gas is very rarefied and Navier-Stokes is no longer valid. Flow modelling approach may require molecular or hybrid solvers.

4. Free-molecular flow: The regime is valid beyond Kn$>$10, in this regime collision frequency is very low as the flow is characterized by large mean free path compared to characteristic length scale. This regime can be modeled by collision less form of Boltzmann equation.

Table 1.1: Rarefied flow regime based on different Mach and Reynolds Number

	Reynolds No. $\mathcal{O}(\epsilon)$	Reynolds No. $\mathcal{O}(1)$	Reynolds No. $\mathcal{O}(\frac{1}{\epsilon})$
Mach No. $\mathcal{O}(\epsilon)$	Kn $= \mathcal{O}(1)$ Creeping micro flow	Kn $= \mathcal{O}(\epsilon)$ Moderate micro flow	Kn $= \mathcal{O}(\epsilon^2)$ Low Mach Fanno flow
Mach No. $\mathcal{O}(1)$	Kn $= \mathcal{O}(\frac{1}{\epsilon})$ Transonic free molecular flow	Kn $= \mathcal{O}(1)$ Transonic Micro Flow	Kn $= \mathcal{O}(\epsilon)$ Transonic Fanno Flow
Mach No. $\mathcal{O}(\frac{1}{\epsilon})$	Kn $= \mathcal{O}(\frac{1}{\epsilon^2})$ Hypersonic free molecular flow	Kn $= \mathcal{O}(\frac{1}{\epsilon})$ Hypersonic free molecular flow	Kn $= \mathcal{O}(1)$ Hypersonic Fanno transitional flow

Using kinetic gas theory, we can also express the Knudsen number in terms of Mach number, M and Reynolds number, Re as

$$\mathrm{Kn} = \sqrt{\frac{\pi\gamma}{2}}\frac{\mathrm{M}}{\mathrm{Re}} \tag{1.1}$$

Different $(\mathrm{M}, \mathrm{Re})$ combination will give rise to different types of flow regimes [13]. Perturbation analysis with three orders $\mathcal{O}(\epsilon)$, $\mathcal{O}(1)$ and $\mathcal{O}(\frac{1}{\epsilon})$ of Mach number, M and Reynolds number, Re will lead to nine independent flow regimes based on $(\mathrm{M}, \mathrm{Re})$ matrix. Arkilic *et al.* [13] classified flow regime based on this $(\mathrm{M}, \mathrm{Re})$ matrix as shown in table 1.1. The flow regime characterized by $(\mathrm{M}, \mathrm{Re})$=$\mathcal{O}(\epsilon, \epsilon)$, $\mathcal{O}(1, 1)$ and $\mathcal{O}(\epsilon, 1)$ are classified as micro flows.

1.1.2 Slip boundary condition

The gas surface interaction is also an important aspect, in one of the simplest model called Maxwell model the incident flux of gas molecules hit the wall surface, some molecules undergo specular reflection and some are held by the wall and re-emitted as diffuse reflection. In Maxwell model the tangential momentum accommodation coefficient (TMAC) becomes zero for fully specular and unity for fully diffuse reflection. In rarefied slip flow conditions velocity slip and temperature jump strongly depends on the tangential momentum accommodation

coefficient (TMAC).
Consider a case of rarefied Couette flow confined between concentric inner rotating and outer stationary cylinder, which is one classical fluid dynamics problem. When both the inner and outer walls are diffusive i.e. tangential momentum accommodation coefficient (TMAC) is unity then all the incident flux is re-emitted in a diffuse way in such a case the fluid rotates faster near the rotating inner cylinder as per expectation as shown in Figure 1.4 (a). When both the inner and outer walls are partly diffusive i.e. some part of the incident flux undergoes specular reflection and some part is re-emitted as diffuse reflection, the fluid in such a case shows a presence of minimum tangential speed in between the inner and outer wall as shown in Figure 1.4 (b). When both the inner and outer walls are specular i.e. tangential momentum accommodation coefficient (TMAC) becomes zero then all the incident flux undergo specular reflection, the gas rotates faster near the stationary wall as shown in Figure 1.4 (c). This anomalous behavior is also called ghost effect or flow inversion.
At smaller Knudsen number most of the momentum transfer happens due to molecular collisions. The non-equilibrium effects dominate in the close proximity of the wall, Navier-Stokes coupled with slip boundary conditions defined by gas-surface interaction model can effectively model velocity slip and temperature jump.

1.2 Motivation and objectives of present work

Computation of scramjet technologies, hypersonic re-entry vehicles, aero-assisted orbital transfer vehicle (AOTV), etc involve development of codes which can perform accurate two dimensional, axi-symmetric and three dimensional simulation in continuum as well as non-continuum, non-equilibrium regimes. Most of the non-continuum simulations are based on Direct Simulation Monte Carlo (DSMC) which become prohibitively costly and hence we require development of new upwind method which is fast, accurate with ability to work both in continuum as well as non-continuum regimes.

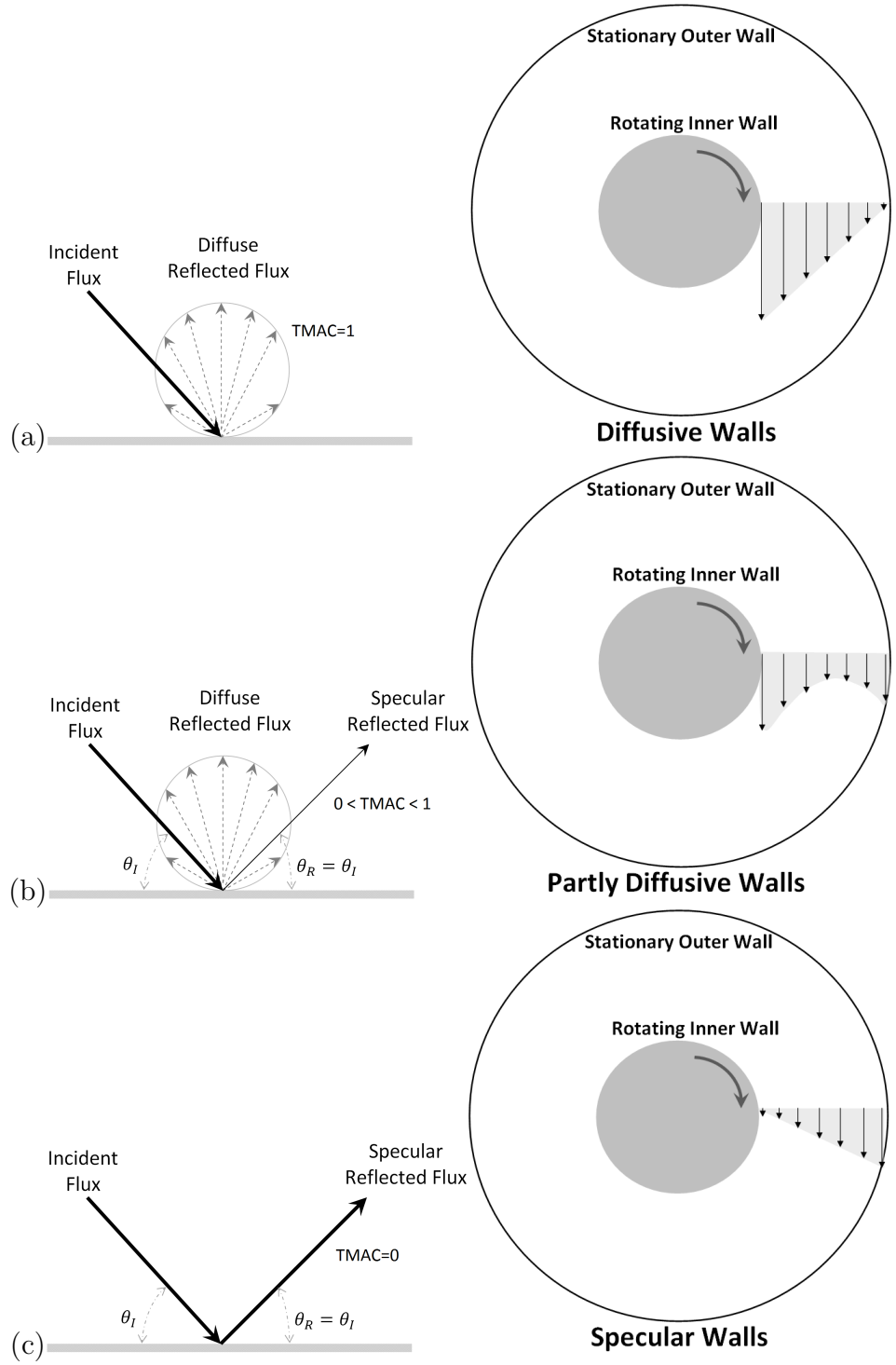

Figure 1.4: Couette rarefied flow for (a) diffusive walls, (b) partly diffusive walls, and (c) specular walls.

1.2.1 Background and application

In order to validate the code we require ground based test facilities which either use free-piston shock tunnel or expansion tubes where high enthalpy slug of test gas is produced for short duration with test times in the range of 0.05-10 ms. Because of short test times there are difficulties associated with process of data acquisition. In such a scenario high speed rotating flow provides hypersonic flows with effective acceleration in the radial direction of the order of few millions g (Earth's gravitational acceleration). For strongly rotating viscous compressible flows confined in a vessel, the gas undergoes rigid-body rotations. The rigid-body rotation is characterized by an exponential density rise in the radial direction towards the periphery with thin boundary layers and a rarefied inner core. In a high speed rotating vessel we get continuum regime towards the periphery, free molecular in the centre region and slip and transition regimes in the intermediate radial regions as shown in Figure 1.5. Thus a rotating high speed wind tunnel provides hypersonic flow conditions under continuum as well as rarefied condition to be analyzed for a longer duration as compared to shock tunnels and expansion tubes. Such a rotating flow is characterized by exponential density rise in the radial direction hence a stationary object placed near the wall might face continuum as well as rarefied slip condition as shown in Figure 1.6. Numerical modeling of such flows is a challenge as regimes change from continuum, slip, transition to non-continuum. A ground based test facility based on rotating vessel provides a unique opportunity to evaluate the research code as continuum to free molecular flow exists within the same domain.

1.2.2 Research objectives

All the research in the development of upwind scheme based on macroscopic theories can be seen in terms of inclusion of physically consistent amount of entropy. In many case, a single solver operating from rarefied flow to hypersonic continuum flow requires corrections and tuning as most of the time it is not known what is the correct amount of entropy generation for a particular regime and the correct distribution of entropy generation for each thermodynamic force. Figure 1.7 shows schematic of entropy generation at two different locations $\vec{x}_1$ and $\vec{x}_2$ in the

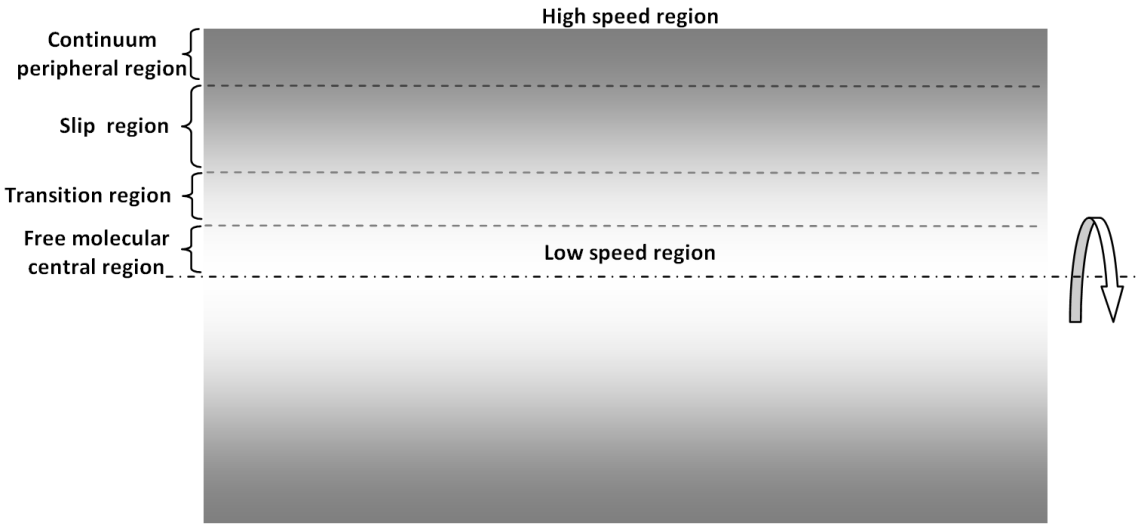

Figure 1.5: Continuum, slip, transition and free molecular flow regimes in a rotating vessel.

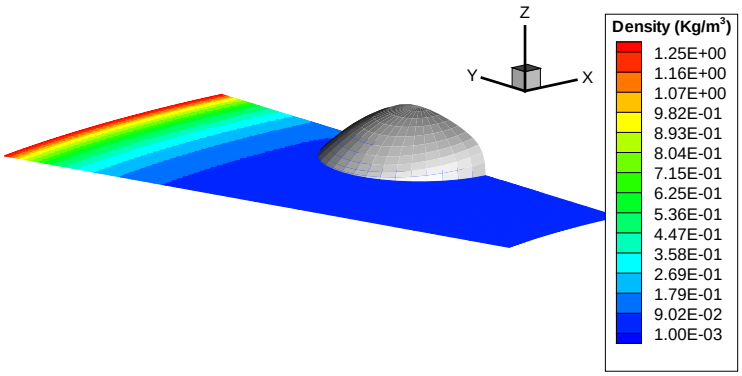

Figure 1.6: Exponential variation of density in a high speed rotating flow field.

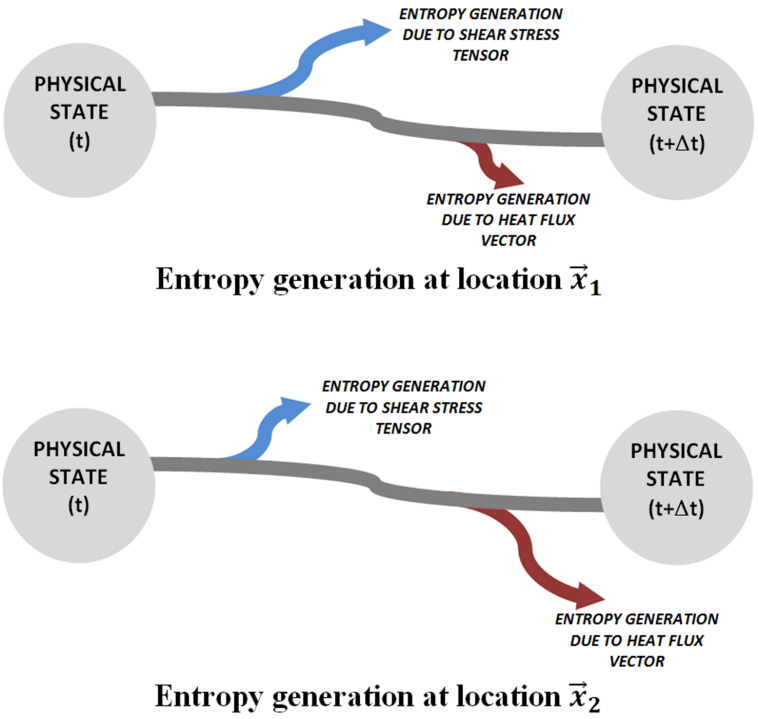

Figure 1.7: Two components of entropy at locations $\vec{x}_1$ and $\vec{x}_2$ as physical state evolves from time t to time $t + \Delta t$.

flow domain as physical state evolves from time t to time $t+\Delta t$. The components of entropy due to thermodynamic forces associated with shear stress tensor and heat flux vector differ in magnitude at two different locations. *Genuine upwind scheme should resolve these different components of entropy generation due to its conjugate thermodynamic force in order to satisfy thermodynamics while the state update happens.* Most of the upwind schemes basically aim to add the correct dissipation or entropy but fail to resolve and ensure the correct distribution of the entropy associated with its conjugate thermodynamic force. If the solver follows and mimics the physics then we can have a single monolithic solver serving the entire range from rarefied flow to continuum flow, creeping flow to flow with shocks.

Figure 1.8 shows different scales involved in the simulation of transport equations for mass, momentum and heat. At the microscopic level Hamilton's equation forms the governing equation for the discrete set of particles described my mass m

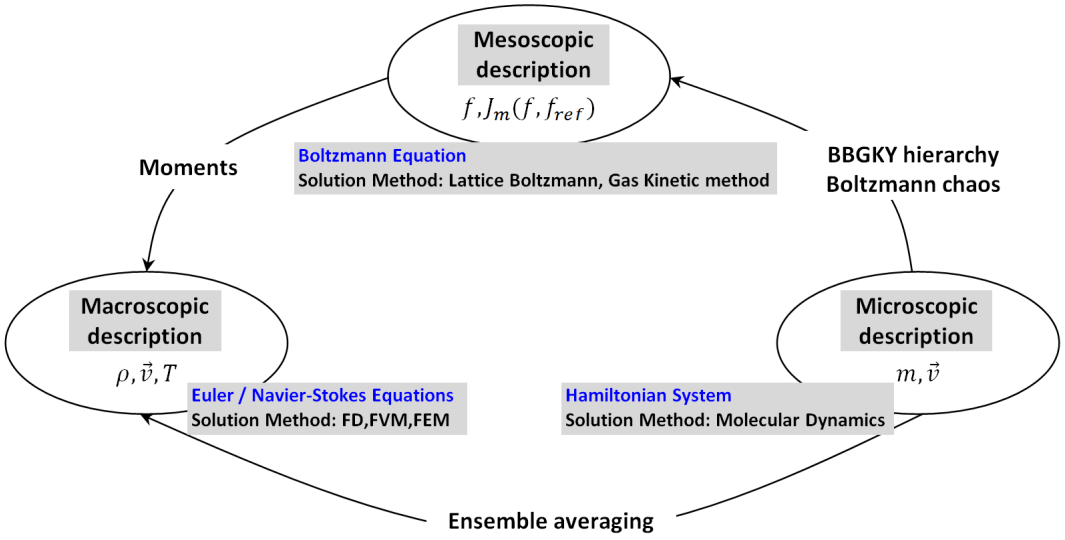

Figure 1.8: Different scales of solution of transport equations.

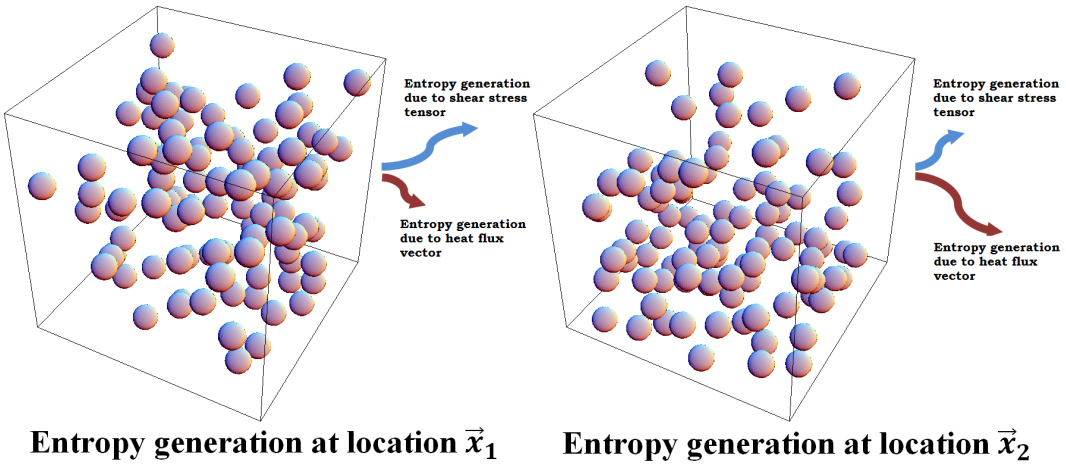

Figure 1.9: Kinetic theory provides molecular description while non-equilibrium thermodynamics provides the relationship between the entropy generation due to thermodynamic forces associated with shear stress tensor and heat flux vector.

and velocity vector $\vec{v}$. Using molecular dynamics this microscopic description can be solved, and averaging the particle ensemble leads to macroscopic description given by density ρ, velocity $\vec{v}$ and temperature T. The macroscopic description is governed by Euler / Navier-Stokes equations that are generally solved by finite difference (FD) or finite volume method (FVM). The mesoscopic description lies in between the macroscopic and microscopic level as it incorporates essential aspects of microscopic processes in order simulate macroscopic behaviour. At the mesoscopic level Boltzmann equation forms the governing equation described by distribution function f and kinetic model $J_m(f, f_{ref})$. Lattice Boltzmann method, gas kinetic method, discrete velocity model, dissipative particle dynamics, etc are used for solving mesoscopic system, and macroscopic description is obtained by taking moments.

Present application involves continuum to rarefied flow within a same domain; mesoscopic theory provides the most practical approach for such a case as macroscopic route becomes physically inconsistent while microscopic methods become computationally expensive. The entropy generation observed at the macroscopic level is a consequence of molecular collisions at the microscopic level. Mesoscopic method based on kinetic theory uses statistical description of a system of molecules and provides model for molecular collisions leading to non-equilibrium phenomena. Non-equilibrium thermodynamics being a phenomenological theory describes this non-equilibrium phenomena and provides linkage with kinetic theory based coefficients of transport and relaxation. Figure 1.9 shows a schematic of entropy generation at two different locations as a physical state evolves in time. The molecular description is provided by the kinetic theory while the relationship between the entropy generation due to thermodynamic forces associated with shear stress tensor and heat flux vector is a feature of non-equilibrium thermodynamics. Kinetic theory and non-equilibrium thermodynamics together become a powerful tool to model non-equilibrium processes of compressible gas.

The most common approach to simulate slip flow is to couple the continuum solver with the slip boundary condition. The slip boundary condition should effectively capture slip flow features under combined effects of adverse pressure gradient, rarefaction and tangential flow gradients. Investigation reveals that there are large numbers of second order slip model existing in the literature each with its

own geometric specific slip coefficient and range of validity in the Knudsen region. Most of the slip models in the literature are for simple micro-channel flows. In such a scenario we require a more fundamental approach based on principles of kinetic theory incorporating phenomenological theory of non-equilibrium thermodynamics to simulate slip flow. However, so far slip flow numerical modeling has not been applied for computation of high speed rotating slip viscous flows as the emphasis has been mostly on micro flows or on aerospace problems arising in external rarefied aerodynamics. One of the motivations of this thesis is to develop a numerical scheme for viscous slip flows with focus on rotating flows. Numerical modeling of such a high speed rotating flows is a challenge as the regime changes from continuum at the periphery to non-continuum free molecular in the central core. Such a flow is also of considerable interest and importance in the field of hydrodynamic bearings, rotating machinery, vacuum pumps and separators.
Shape optimization using numerical methods has made rapid progress. The shape optimization procedure requires repeated grid generation after each iterative step. Most of the industrial problems have many components and generation of suitable grid around them becomes the bottleneck. Generation of suitable grid for a complex multi-body configuration can be very tedious and intensive task. In such a scenario we require a faster, simpler and robust approach. Conventional approach requires grids which include structured multi-block meshes, chimera or overset grids, unstructured grids, Cartesian grids and hybrid grids. Recently meshfree or meshless methods have gained popularity. All meshless numerical methods share a common feature that no mesh is needed and the solver is capable of operating on an arbitrary distribution of points. The objective of the thesis is to simulate rotating, viscous compressible slip flow through kinetic theory route using a meshless method. The objective also includes multi-objective shape optimization of body in high speed rotating flow which will require repeated grid generation and a solver capable of resolving high speed flow features like shocks, weak secondary flow in the axial direction and in slip flow region. The long term goal is to validate developed research codes with rotating high speed wind tunnel for correct aerodynamic properties, understand the high speed flows and extend the solver capabilities for reacting multi-component flows. *The prime motivation of the thesis is to develop a robust meshless method based on kinetic theory and*

non-equilibrium thermodynamics that can carry out multi-objective optimization of stationary bodies under strong rotations and rarefied slip flows. The research requirements and current status in the open literature can be broadly classified as follows :

- Non-equilibrium thermodynamics based approach.
  Literature review reveals that non-equilibrium thermodynamics based approach is still in the realm of physics.

- Kinetic theory and its application to slip flows.
  Literature survey reveals that kinetic scheme based on non-equilibrium thermodynamics has not been extended to slip flow.

- Kinetic theory based method for fine resolution of weak secondary flow.
  Literature reveals that molecular modelling methods use variance reduction approach to simulate low speed weak secondary flows. Thus development of variance reduced form of kinetic scheme may be one of the way to capture weak secondary flow in presence of strong rotating primary flow field.

- Kinetic scheme for axi-symmetric problem.
  Literature reveals that kinetic scheme based on flux vector splitting has not been extended for axi-symmetric flows.

- Least square based meshless method.
  Most of the meshless methods are either based on radial basis functions (RBFs) or they use least square based approach. Literature survey revealed that approach based on least squares as compared to RBFs was found to be significantly better for flow problems with shock. Normal equations as well as QR approach used in least square method produces inaccurate results when applied to ill-conditioned problems. In such a scenario we require a scheme which is computationally faster and provides more stable results than QR.

- Domain decomposition and Parallelization.
  The developed meshless kinetic code requires parallelization to cut down the

simulation time. Research is also required to develop optimal contention free communication schedule.

- Multi-objective shape optimization.
  Literature survey reveals that in most of the multi-objective optimization problems, Pareto optimality forms the basis and gives the set of non-dominated solutions lying on the Pareto front. In such a scenario we require research on suitable method in a meshless framework for obtaining optimum solution from the set of non-dominated solutions.

In the present thesis the development of meshless scheme and slip boundary condition has been accomplished with implementation of the kinetic scheme using first order non-equilibrium thermodynamics based distribution. The thesis describes the novel ***S**plit **L**east square **K**inetic upwind method for **N**avier-**S**tokes equation* (SLKNS) solver which differs from normal equations based least squares method. The new meshless solver, SLKNS avoids ill-conditioning encountered while using highly stretched distribution of points in the boundary layers. Thesis also describes the development of SLKNS solver which requires following steps :

- Development of kinetic scheme:
  - Onsager reciprocity principle based new kinetic model.
  - Distribution function for polyatomic gas based on microscopic tensor and its conjugate thermodynamic force.
  - Microscopic tensor splitting
  - Kinetic slip flow boundary condition.
  - Kinetic theory based approach for slip bordering transition regime.
- Development of meshless method:
  - Development of meshless scheme which can work for highly stretched distribution of points.
  - Parallelization of meshless scheme.
- Development of multi-objective shape optimization:

- Development of tools for pre-processing the geometric shape.
- Development of methodology for multi-objective optimization.

The thesis attempts to give a fresh new look to Navier-Stokes equation from the prism of non-equilibrium thermodynamics and kinetic theory. Present research for the first time adds an additional condition based on the concept of correct distribution of entropy for any upwind scheme to remain valid across different regimes of flow. The scheme developed in the thesis applies discretization at the Boltzmann level and follows the principle of non-equilibrium thermodynamics in order to ensure the correct distribution of entropy generation for each thermodynamic force as the state update moves from one conservation state to another. The present kinetic upwind scheme can be used to simulate the entire range from rarefied flow to continuum flow. The thesis describes the kinetic flux vector splitting scheme for axi-symmetric flows and kinetic flux based slip boundary condition, it also gives the derivations of wall boundary condition for cases with negligible fluid dynamic variations in tangential direction. A novel least square based approach to stretched distribution of points required to resolve viscous boundary layers has been formulated in this thesis.

The focused objectives of the thesis are summarized below:

- Development of kinetic theory based approach to model slip flows.
- Incorporation of phenomenological theory of non-equilibrium thermodynamics.
- Extending the kinetic scheme for resolving weak secondary flow.
- Implementation of the kinetic scheme for axi-symmetric problem.
- Extending the solver for strongly rotating flow field.
- Development of meshless method based on least squares for stretched distribution of points.

- Development of pre-processor for generation of cloud of points and robust meshless scheme to carry out multi-objective optimization of stationary bodies under strong rotations and rarefied slip flows.
- Parallelization of the present meshless code.

1.3 Scope of the thesis

The scope of the present research work covers the development of kinetic theory and non-equilibrium thermodynamics based boundary conditions for slip flow and development of meshless method for highly stretched distribution of points. The scope of work also covers parallelization methodology and investigation of various optimization methods in meshless framework. The scope of the present research work is limited only to the single component compressible gas flows.

1.4 Thesis organization

The thesis is organized into eight chapters and five appendices. Chapter 1 gives the introduction and Chapter 2 gives the description of the research area and its literature review. Chapter 3 to Chapter 7 include original research contributions which are summed up in concluding Chapter 8. Thesis organization is as follows:

- Chapter 1
  The first chapter contains introduction to non-continuum slip flows, challenges in grid generation, motivation for present research, objectives and scope of the thesis and its organization.
- Chapter 2
  The second chapter carries out literature review and identifies potential area of research in the field of slip flow, kinetic theory, non-equilibrium thermodynamics, kinetic scheme, meshless method, parallelization and multi-objective optimization methods.

The present research contribution is described in chapter three to chapter seven, with each chapter focused on the above identified objectives.

- Chapter 3
  The third chapter introduces maximum entropy production principle and investigates its relationship with Onsager's reciprocity principle and Boltzmann equation. The chapter also describes non-equilibrium thermodynamics based new kinetic model and gives distribution function based on it. This is followed by statistical representation of the new kinetic model, establishing relationship between entropy production and Mahalanobis distance, and derivation of Navier-Stokes equations.

- Chapter 4
  The fourth chapter describes the development of a new kinetic upwind method based on split microscopic tensors derived by the author on the principles of non-equilibrium thermodynamics. The chapter also gives the method of derivation for split macroscopic tensors and kinetic split fluxes[1]. Further, it gives linkage of non-equilibrium thermodynamics with the new kinetic method and extended thermodynamics due to split kinetic fluxes.

- Chapter 5
  The fifth chapter describes the kinetic wall boundary conditions using non-equilibrium thermodynamics based distribution function. The chapter derives the gradient based slip flow boundary conditions using half range distribution for cases where tangential variations are negligible. The chapter also derives kinetic flux vector splitting scheme based boundary conditions for cases where tangential variations are dominant. The derived boundary conditions are valid both for continuum as well as non-continuum flows. Further, the chapter gives the treatment of slip flow regime which borders transition flow using collision probability function.

- Chapter 6
  The sixth chapter describes the new least square method using stencil splitting, and development of a meshless solver SLKNS based on kinetic scheme. The chapter gives the implementation of SLKNS and also describes the

[1]Derived expressions of split macroscopic tensors and fluxes are given in Appendix D

meshless pre-processor, parallelization of SLKNS and implementation of multi-objective optimization method.

- Chapter 7
  The chapter seven gives results for test cases used for validating meshless method for stretched distribution of nodes, slip boundary, implementation of KFVS and multi-objective optimization in a strongly rotating flow field.

For each chapter from chapter 2 to chapter 7 sections on "Introduction" and "Summary" are included to introduce and summarize the content of each chapter.

- Chapter 8
  Contributions, present research findings and future recommendations are finally given in this chapter.

Chapter eight is followed by five appendices.

- Appendices A,B,C,D and E
  Five appendices A through E are included in the thesis to describe mean free path of the gas, kinetic theory and fluid flow, treatment of thermally and calorically imperfect gas, expressions for split macroscopic tensors and KFVS fluxes and experimental determination of tangential momentum accommodation coefficient.

Chapter 2

Literature review and potential areas of research

2.1 Introduction

To meet the objectives of thesis, the research requires development of boundary condition which can simulate both continuum and rarefied slip flow within Navier-Stokes equations in order to avoid extremely costly multi-scale simulation. It requires i) suitable upwind scheme which can capture shock, handle strong rotation, weak secondary flow and resolve slip flow features, ii) a meshless scheme which remains well-conditioned in highly stretched grids, resolves features of viscous slip flows and captures shock, iii) parallelization methodology for meshless scheme, iv) multi-objective shape optimization method in a meshless framework, and v) validation of the developed meshless code for slip flow, and demonstration of multi-objective shape optimization capability. Development of such an industrial scale solver for slip flows using meshless method requires research work in wide variety of fields which include i) slip modeling, ii) kinetic theory, iii) non-equilibrium thermodynamics, iv) upwind methods, v) meshless methods, vi) parallelization, and vii) multi-objective shape optimization. This chapter introduces and describes these research fields associated with development of a meshless solver and also carries out literature review and brings out the potential area of research existing in each field. Fig. 2.1 shows the salient research fields associated with the present investigation.

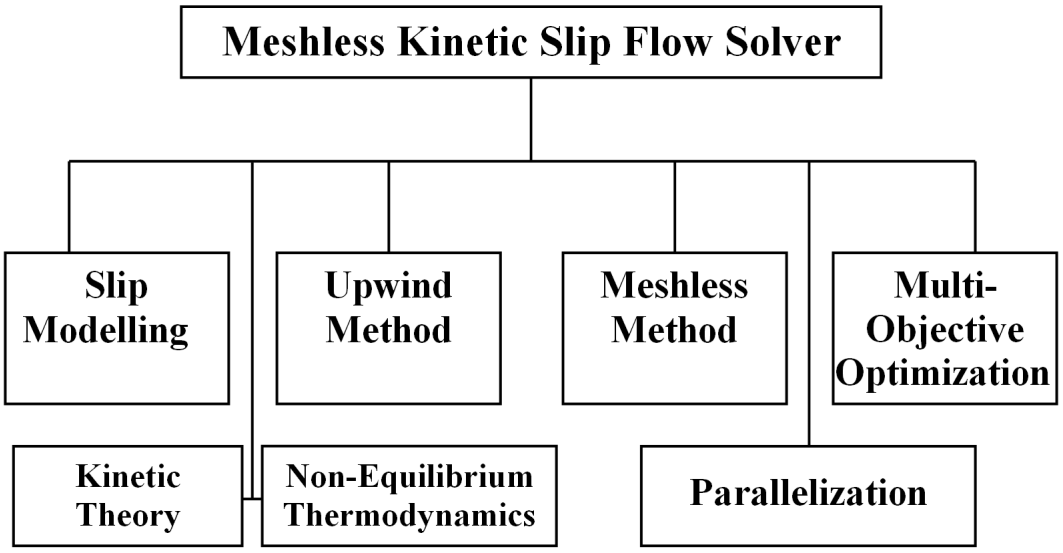

Figure 2.1: Research fields associated with the present investigation.

2.2 Modelling of Slip Flows

As described earlier the presence of rarefied domain around space vehicle or fluid transport in micron-sized devices (MEMS) is a typical non-continuum flow feature[1]. One of the main difficulties in modeling is due to the breakdown of continuum flow assumption as the mean free path of gas molecule is comparable or larger than characteristic dimensions of the flow system. Modelling of slip flow requires i) breakdown determination of Navier-Stokes equation, ii) choice of gas-surface interaction model, and iii) fluid modelling approach.

2.2.1 Breakdown criteria of Navier-Stokes equations

For Navier-Stokes equations to remain valid it should operate within the framework of Newtonian mechanics following continuum approximation and satisfying constitutive relationships due to collision dominated transport models of stress tensor and heat flux vector. Most of the breakdown criteria which are valid for micro flows are not suitable for hypersonic flows. The determination of

[1]The main differences between conventional rarefied flow and fluid transport in MEMS are the operating pressure and extremely low Reynolds number (creeping flow) encountered in the latter.

non-equilibrium and non-continuum regions is generally carried out using a local continuum breakdown parameter called the gradient-length Knudsen number [240, 286] defined as

$$\mathrm{Kn}_{GL,\varsigma} = \frac{\lambda}{\varsigma} |\nabla \varsigma| \tag{2.1}$$

where ς is the parameter of interest, such as density(ρ), bulk velocity magnitude ($|u| = \sqrt{u_x^2 + u_y^2 + u_z^2}$), or temperature (T). λ is the viscosity based mean free path given as

$$\lambda = \mu \sqrt{\frac{\pi}{2\rho p}} \tag{2.2}$$

The actual continuum breakdown parameter is then the maximum of these, that is:

$$\mathrm{Kn}_{GL} = \max(\mathrm{Kn}_{\rho}, \mathrm{Kn}_{|u|}, \mathrm{Kn}_{T}) \tag{2.3}$$

Schwartzentruber and Boyd [240] have recommended values of $\mathrm{Kn}_{GL} > 0.05$ to signify continuum breakdown for representative hypersonic flows. In order to prevent a non-positive distribution function when the Navier Stokes solution is coupled with the Boltzmann solution, Kolobov *et. al.* [143] have used switching criterion which is function of pressure gradient as well as velocity magnitude defined as follows:

$$NS_B = \mathrm{Kn} \sqrt{\left(\frac{\nabla p}{p}\right)^2 + \frac{1}{|u|^2}\left[\left(\frac{\partial u_x}{\partial x}\right)^2 + \left(\frac{\partial u_y}{\partial y}\right)^2 + \left(\frac{\partial u_z}{\partial z}\right)^2\right]} \tag{2.4}$$

Levermore *et al.* [151] have applied the idea of moment realizability to derive criteria for the validity of the Navier-Stokes equation. This criterion is given in terms of the eigenvalues of the non-dimensional 3×3 matrix given as follows

$$B_{NS} = \boldsymbol{I} - \frac{\mu}{p}\left[\nabla \vec{u} + (\nabla \vec{u})^T - \frac{2}{3}\boldsymbol{I}\nabla \cdot \vec{u}\right] - \frac{2}{3}\frac{\rho\kappa}{p^3}\nabla\left(\frac{p}{\rho}\right)\left[\nabla\left(\frac{p}{\rho}\right)\right]^T \tag{2.5}$$

where $\boldsymbol{I}$ is the identity invariant tensor, κ is the thermal conductivity and μ is the viscosity. Significant deviations of the eigenvalues of this breakdown matrix from unity indicate large gradients and significant departure from the equilibrium state. Breakdown criteria can also be formulated based on departure of flow from its equilibrium state. Lockerby *et al.* [164] have suggested breakdown criteria

based on departure relative to near equilibrium or fractional relative departure relative to Navier-Stokes non-equilibrium given as

$$NS_L = \frac{|\int \psi_i (f - f_1) d\vec{v}|}{|\int \psi_i (f_1 - f_0) d\vec{v}|} \tag{2.6}$$

where ψ_i is the moment variable, $\vec{v}$ is the molecular velocity, f is higher order distribution function, f_1 is the first order distribution function corresponding to Navier-Stokes equations and f_0 is the equilibrium distribution.

2.2.2 Gas-surface interaction model

For non-continuum flows, the gas-surface interaction model has a profound influence on the flow parameters e.g. in high altitude hypersonic flights gas-surface interaction plays vital role in the determination of aerodynamic forces and heat transfer. There are several gas-surface interaction models based on treatment of reflected flux e.g. Maxwell model which is the combination of diffuse reflection and specular reflection. Figure 2.2(a) shows the schematic of the Maxwell's gas-surface interaction model. Maxwell model is identified by the tangential accommodation coefficient, $\sigma_{\vec{t}}$, the reflected flux is composed of fraction $(1 - \sigma_{\vec{t}})$ undergoing specular reflection and fraction $(\sigma_{\vec{t}})$ which is re-emitted diffusely as a Maxwellian distribution based on wall condition. Maxwell model is one of the simplest and the most popular model which also satisfies the principle of detailed balance i.e. reciprocity.

Cercignani and Lampis [46] introduced a phenomenological model which was latter on extended by Lords [167]. This model is called CLL (Cercignani, Lampis, Lord) reflection model which is physically more meaningful and satisfies the reciprocity principle. This model is based on normal accommodation coefficient, $\alpha_{\vec{n}}$ as well as tangential accommodation coefficient, $\sigma_{\vec{t}}$. Figure 2.2(b) shows the schematic of the CLL model.

2.2.2.1 Accommodation coefficient for polyatomic gas

Accommodation coefficient basically is a measure of inability of incident molecules to adjust themselves to the body surface. Experiments have revealed that accommodation coefficients are numerically identical for rotational and translational

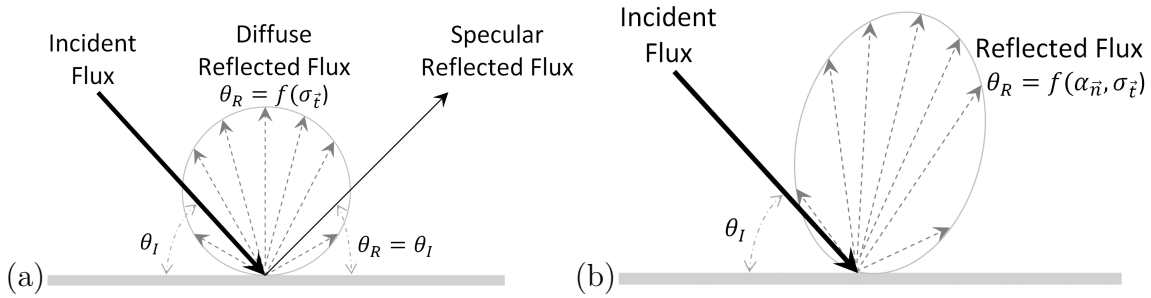

Figure 2.2: Gas-surface interaction models (a) Maxwell specular-diffuse reflection model, (b) CLL (Cercignani, Lampis, Lord) reflection model.

energies. However, vibrational components of the internal energy present in polyatomic gas takes much more time to adjust to new values.

2.2.3 Approaches in slip flow modeling

The fluid modeling can be classified based on three approaches: (i) molecular modeling, (ii) continuum modeling, and (iii) hybrid approach. In the molecular modeling approach [245] the fluid is assumed to be collection of molecules which are to be solved either by deterministic or statistical methods. Direct Simulation Monte Carlo (DSMC) [36] or information preservation (IP) [270] are molecular based methods. One of the main drawbacks of this probabilistic method is the occurrence of statistical noise and inefficient handling near continuum flows and flows with recirculation. Recently, direct numerical simulation (DNS) of Boltzmann transport equation [11, 201] has emerged as a viable alternative to DSMC. Such deterministic methods based on solution of the Boltzmann equation are computationally very expensive due to quadratic cost of the velocity discretization of the collision operator. In the continuum modeling approach the fluid is assumed to be continuous and indivisible. The macroscopic variables like velocity, density, pressure, etc., are defined at every point in space and time. Conservation of mass, energy and momentum based on moment method give rise to extended hydrodynamic equations (EHE) leading to a set of nonlinear partial differential equations like Euler, Navier-Stokes, Burnett, etc. Lattice Boltzmann (LB) method and gas kinetic schemes are also promising approaches as they connect the molecular and continuum descriptions. While hybrid solvers combine the speed of

continuum fluid models and accuracy of kinetic non-continuum models and have also emerged as an important area of research. In the hybrid approach the non-continuum regions are solved using the molecular based methods and interfaced with the continuum regions [11, 42, 143]. The determination of non-equilibrium and continuum regions is generally carried out using a local continuum breakdown parameter. Based on extent of non-equilibrium effects and rarefaction the flow regime can be broadly classified [114]. Table 2.1 shows various flow regimes and corresponding fluid models. Figure 2.3 shows the fluid modeling classification based on molecular, mesoscopic and macroscopic (continuum) approaches. Different approaches in fluid modeling of slip flows can be summarized as :

- Molecular based numerical schemes.
- Direct numerical solution (DNS) of Boltzmann equation.
- Hybrid solver.
- Slip modeling using higher order continuum equations.
- Treatment of slip flow based on slip models and Navier-Stokes equation.
- Treatment of slip flow based on Lattice Boltzmann method.
- Treatment of slip based on Quasi-Gas-Dynamics (QGD) and hydrodynamic theory of Brenner
- Kinetic theory based slip modeling.

2.2.3.1 Molecular based numerical schemes

Molecular based numerical schemes such as direct simulation Monte Carlo (DSMC) becomes a useful tool for rarefied non-continuum flows. The gas-surface interaction in DSMC is implemented using Maxwell as well as CLL (Cercignani, Lampis, Lord) reflection model. In DSMC method microscopic properties are averaged over a small space region to obtain the macroscopic state variables. For low speed rarefied flow the statistical scatter requires a huge sample size. For example, consider the macroscopic velocity of the order $0.1m/s$ with background noise under

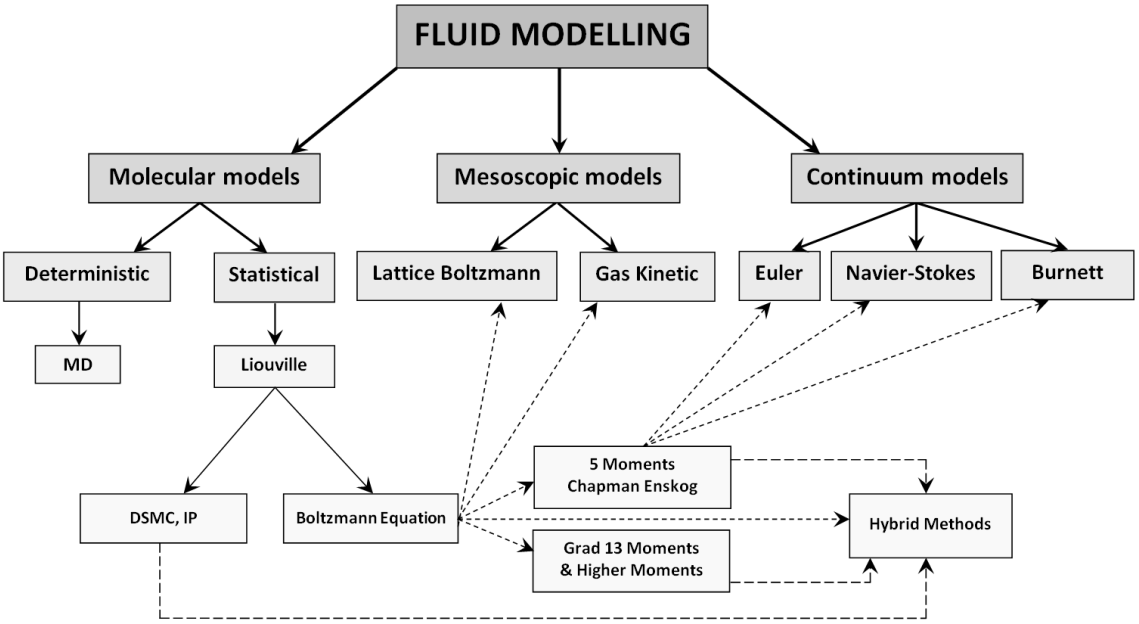

Figure 2.3: Fluid modelling classification.

Table 2.1: Knudsen number based flow regime and its fluid models.

Knudsen Number	Flow Regime	Fluid Model
$\mathrm{Kn} \to 0$	Continuum convective flow	Euler Equations
$\mathrm{Kn} \leq 10^{-3}$	Continuum convective and diffusive flow	Navier-Stokes equations with no slip boundary condition
$10^{-3} \leq \mathrm{Kn} \leq 10^{-1}$	Continuum slip flow	Navier Stokes with slip boundary condition Burnett equation with slip boundary condition (DSMC,IP, LB,Hybrid solvers)
$10^{-1} \leq \mathrm{Kn} \leq 10$	Transition flow	Burnett equation with slip boundary condition (DSMC,IP, LB, Hybrid solvers)
$\mathrm{Kn} > 10$	Free Molecular flow	Collisionless Boltzmann solver DSMC, Molecular Dynamics

room condition given by $\sqrt{2RT}$ of the order 10^3 m/s. If we require signal to be nine times larger than the noise then the sample size N required is around 10^9 to keep the standard deviation given as $\sqrt{2RT/N}$ to a small enough value (refer Shen [245] for details). Cercignani *et al.* [48] give this signal-to-noise ratio for a dilute gas as

$$\frac{u}{\delta u} = \mathrm{M}\sqrt{\gamma N} \tag{2.7}$$

where u is the characteristic flow velocity, δu is the statistical fluctuation, M is the Mach number, γ is the ratio of specific heat and N is the sample size. Thus DSMC becomes costly to simulate rarefied low speed gas flows encountered in MEMS and micro-channel flows. DSMC finds more application to many high speed flows. Fan and Shen [86, 87] proposed information preservation (IP) method to tackle this problem of large sample size. The thermal movement of the particles causes statistical scatter in DSMC while in IP method it surfaces only at the macroscopic information level. In IP method each simulated particle is assigned two velocities : thermal velocity c and information velocity (IP velocity) u_i. Thus, each simulated particle carries sum of the macroscopic velocity of a gas flow as well as velocity scatter with an aim to preserve and update the macroscopic information of a gas flow thereby reducing the statistical scatter. The major advantage of IP method is the considerable reduction in the sample size. For the example given earlier for the low speed flows the sample size for IP method is around 10^3 to 10^4. Another advantage of the IP method is the implementation of the boundary condition as macroscopic values of the flow field are known at each time step. Since IP method handles more information than the DSMC method hence it is more memory intensive and complicated in its implementation [270]. Another drawback of IP method is the issue of stability as the time step cannot be large and particle sample size cannot be small.

2.2.3.2 Direct numerical solution (DNS) of the Boltzmann equation

The modeling of the collision term poses a challenge because of its non-linear nature. The numerical methods should satisfy all the properties desired for a kinetic models described in Appendix B i.e. properties of locality and Galilean invariance, additive invariants, local entropy production, etc. There are broadly

three methods for direct numerical solution the Boltzmann equation [143] i) node to node (NtN) method, ii) Tcheremissine's method, and iii) node to closest node (NtCN) method. In the NtN method [97, 230, 273] a collision sphere in velocity space is wrapped around pre- and post collision velocities. The NtN method takes into account only those post-collisional velocities that fall exactly into the nodes of the velocity grid. Tcheremissine's method [274] is a generalization of the NtN method for more complex models of the collisions by taking into account inverse collisions that do not fall into the nodes of the velocity grid. NtCn method [66] on the other hand can be used for arbitrary interaction potentials and non-uniform grid in velocity space.

2.2.3.3 Hybrid solvers

DSMC becomes an expensive numerical method due to high sample size to keep the stochastic noise bounded to a lower value. DSMC also becomes impractical for time dependent flows as ensemble averaging becomes prohibitively expensive. Near the continuum regions it becomes unrealistic to apply DSMC as mean free time is very low. On the other hand continuum solvers like Navier-Stokes are not valid in the rarefied as well non-thermodynamic regions of shock. Many researchers [42, 143, 240] have used a hybrid approach to accommodate both the issues of accuracy and computational cost for problems that contain the disconnected rarefied and non-equilibrium kinetic regions in the continuum flow domain. DSMC due to its inherent statistical noise has been identified as an obstacle for the development of hybrid solvers [206]. Some group of researchers [143] have developed hybrid solvers which employs deterministic kinetic Boltzmann Solver instead of DSMC for rarefied and continuum gas flows. Tiwari and Klar [258], Tiwari *et. al* [261] have used particle method to carry out continuum and non-continuum coupling. Typical hybrid solver dynamically adapts the meshes with dynamic addition and deletion of kinetic patches to simulate the rarefied and non-continuum regions embedded in the continuum flow domain. The most crucial aspect of the hybrid codes are the : i)adequate continuum breakdown parameter, ii)identification of non-continuum regions, iii)method of domain decomposition, and iv)coupling strategy i.e. imposition of boundary conditions at the interface and procedure for information exchange. There are three

methods of domain decomposition. The first method is domain decomposition in physical space using appropriate continuum breakdown criteria. The second method is domain decomposition in velocity space where fast and slow particles are treated separately [58]. The third methods is hybrid of the two in which one solves kinetic and fluid equation in entire domain. For example, Beylich [34] interlaces the path-integral form of the kinetic equation (Boltzmann level) with the set of conservation equations (Navier-Stokes level). The coupling strategy between continuum and non-continuum domain can either be flux based coupling or state based coupling [42, 118]. In the flux based coupling strategy the fluxes of mass, momentum and energy are calculated according to non-continuum and continuum domains. In this method the fluxes at the interface are modified such that fluxes of continuum and non-continuum equate and conservation is insured in the transfer of information across the interface. State based coupling is inherently conservative; in this approach macroscopic state is obtained by using the average particle information in the non-continuum region and distribution of particles are generated from a macroscopic state on the other side of the interface in the continuum region. The major drawback of hybrid solvers is poor computational efficiency and the inability to simulate unsteady flows. Identification of non-continuum regions and implementation as well as synchronization of two separate methods for continuum and rarefied flow simulation makes the hybrid solver quite complex.

2.2.3.4 Slip modeling using higher order continuum equations

Higher order continuum equation based approaches are either based on i)5 moments based on expansion of distribution function (Chapman-Enskog series solution leading to Burnett or super-Burnett equations) or ii)higher moment based approach which include Grad's 13 moment, Struchtrup's regularized R13, etc. Lockerby *et. al* [163] have investigated most of the common higher order continuum equations, the study revealed that most of these approaches fail to resolve Knudsen layer structure in Kramers' problem shown in figure 2.4. Kramers' problem considers unidirectional isothermal motion of a gas over a stationary planar solid. In the Kramers' problem as the normal distance from the surface, $y \to \infty$

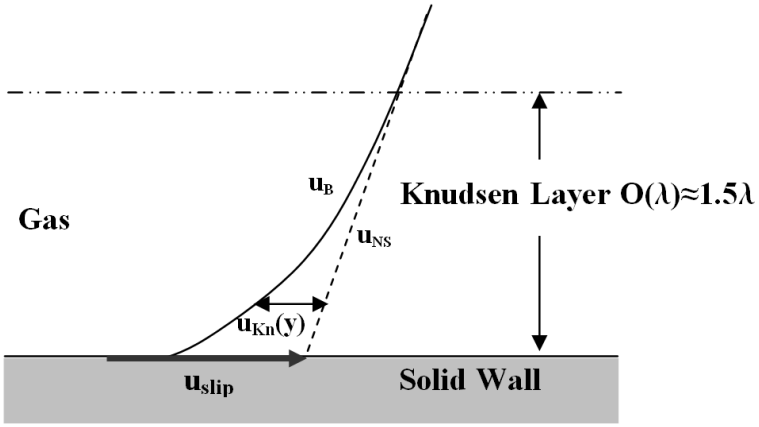

Figure 2.4: Knudsen layer in the Kramers' problem.

the bulk flow gradient du/dy becomes constant, where u is the tangential flow velocity. Let $u_B = u_{NS} + u_{\mathrm{Kn}}(y)$ be the true flow-field based on the Boltzmann solution where u_{NS} the Navier-Stokes based slip flow approximation and $u_{\mathrm{Kn}}(y)$ is the Knudsen layer correction [112, 169]. Similarly for temperature we can write $T_B = T_{NS} + T_{\mathrm{Kn}}(y)$ where T_{NS} the Navier-Stokes based temperature field approximation and $T_{\mathrm{Kn}}(y)$ is the Knudsen layer correction. The Knudsen layer correction $u_{\mathrm{Kn}}(y)$ and $T_{\mathrm{Kn}}(y)$ decays quickly as $y/\lambda \to \infty$. Hadjiconstantinou[112] estimates that $u_{\mathrm{Kn}}(y)$ decays to approximately 3% of its maximum value at $y = 1.5\lambda$ referred as effective width of the Knudsen layer. The Navier-Stokes solution reveals that the terms of order Kn^2 needs to be superimposed to the Navier-Stokes solution to resolve the true solution of the Boltzmann equation for the Kramers' problem. Investigation of Lockerby *et. al* [163] has revealed that for low-speed isothermal flows neither Burnett[52], super-Burnett [50], or Grad's 13 [102] moment equations can model the Knudsen layer. However, some of the higher order accurate continuum equations can qualitatively model the Knudsen layer. Modeling of Knudsen layer can be achieved either by introducing corrections based on kinetic theory or by wall function approach based on suitable scaling of stress-strain relationship. Table 2.2 gives the list of higher continuum models and their capabilities to capture Knudsen layer structure in Kramers' problem compiled from Lockerby *et. al* [163].

Table 2.2: Values of Knudsen layer thickness in Kramers' problem for various higher order continuum equations and kinetic theory based approaches (Refer [163] for details.)

Kinetic theory based models	Knudsen layer thickness
Burnett([52]), Super-Burnett([50]), Grad's 13 ([102]), Eu's GH([84]), Lumpkin's reduced Burnett ([174]) Woods ([291])	No Knudsen layer
Zhong's augmented Burnett ([302])	0.9λ
Linearized Boltzmann equation([45])	1.4λ
BGK model([172])	1.4λ
BGK Burnett([22])	2.1λ
R13([266])	2.8λ
Regularized Burnett([127])	4.9λ

2.2.3.5 Treatment of slip flow based on slip models and Navier-Stokes equation

Harley *et al.* [115], Arkilic *et al.* [12, 13], Beskok and Karniadakis [33] have shown that Navier-Stokes equations coupled with first order velocity slip and temperature jump boundary conditions effectively capture slip flow. One of the earliest model is the Maxwell's velocity slip [184] expressed in conventional form as

$$u_s - u_w = \pm \left(\frac{2-\sigma_v}{\sigma_v}\right) \lambda \left(\frac{\partial u_s}{\partial n}\right)_w + \frac{3}{4}\frac{\mu}{\rho T}\left(\frac{\partial T}{\partial s}\right)_w \tag{2.8}$$

This can be expressed in general form [162] as

$$u_s - u_w = \pm \left(\frac{2-\sigma_v}{\sigma_v}\right) \frac{\lambda \tau_{sn}}{\mu} - \frac{3}{4}\frac{\mathrm{Pr}(\gamma-1)}{\gamma P} q_s \tag{2.9}$$

where subscript n denotes the normal coordinate to the wall, s is the tangential coordinate,τ_{sn} is the component of shear stress, q_s is the component of heat flux vector, γ is the ratio of the specific heats, u_s is the slip velocity, u_w is

the reference wall velocity, Pr is the Prandtl number and σ_v is the tangential momentum accommodation coefficient. The second term on the right hand side of the equation is the thermal creep contribution to the slip velocity due to tangential temperature variation. Similarly, von Smoluchowski's temperature-jump boundary conditions [139] is given as

$$T_s - T_w = \left(\frac{2-\sigma_T}{\sigma_T}\right)\frac{2\gamma}{\mathrm{Pr}(\gamma+1)}\lambda\frac{\partial T}{\partial n} \tag{2.10}$$

where σ_T is the thermal accommodation coefficient. The accommodation coefficients depend upon specific gas and the surface quality and it models the momentum and energy exchange of gas molecules impinging on the walls. This velocity slip equation as described in equation 2.9 for a surface in two dimension can be written as [162] as follows

$$\vec{u}_{slip} - \vec{u}_w = -\left(\frac{2-\sigma_v}{\sigma_v}\right)\frac{\mu}{\rho(2RT_w/\pi)^{1/2}}\left(\frac{\partial u_s}{\partial n} + \frac{\partial u_n}{\partial s}\right) - \frac{3}{4}\frac{\mu}{\rho T_w}\frac{\partial T}{\partial s} \tag{2.11}$$

where u_s and u_n are the gas velocity components in the streamwise and normal to the wall, $\vec{u}_w$ is the wall velocity, and T_w is the wall temperature. s is the coordinate in the streamwise (tangential) direction and n is the coordinate in the normal direction to the wall. The second term in the equation 2.11 is associated with the thermal creep (transpiration) phenomena causing pressure variations in the streamwise direction in the presence of tangential temperature gradients.The value of tangential momentum accommodation coefficient (TMAC) can vary from zero for specular reflection to one for complete diffuse reflection.

These relations which are first order in Knudsen number for velocity slip and temperature jump are also expressed in literature as

$$u_s - u_w = \pm A_1\frac{\lambda\tau_{sn}}{\mu} - C_1\frac{\mathrm{Pr}(\gamma-1)}{\gamma\, p}q_s \tag{2.12}$$

$$T_s - T_w = B_1\frac{2\gamma}{\mathrm{Pr}(\gamma+1)}\lambda\frac{\partial T}{\partial n} \tag{2.13}$$

where coefficients $A_1 = \left(\frac{2-\sigma_v}{\sigma_v}\right)$, $C_1 = \frac{3}{4}$ are given by Maxwell and $B_1 = \left(\frac{2-\sigma_T}{\sigma_T}\right)$ is given by von Smoluchowski. These coefficients can also be estimated by solving the Boltzmann equation for slip coefficients for Bhatnagar-Gross-Krook (BGK)

model and Hard Sphere (HS) model i.e $A_1 = \delta(BGK/HS, \sigma_v = 1)\left(\frac{2}{\sqrt{\pi}}\right)$. Rigorous kinetic approach of Albertoni *et al.* [3], Loyalka *et al.* [172], Loyalka and Hickey [170], Loyalka and Tompson [171] have shown that $\delta(\sigma_v = 1)$ is 1.016191 for BGK molecules. The first order slip coefficient A_1 using kinetic approach for BGK molecular model can be written as

$$A_1 = \delta(BGK, \sigma_v = 1)\left(\frac{2}{\sqrt{\pi}}\right) = 1.14665 \tag{2.14}$$

Ohwada *et al.*[201] evaluates $\delta(\sigma_v = 1)$ as 0.98738 for HS molecules. The first order slip coefficient A_1 using kinetic approach for HS molecular model can be written as

$$A_1 = \delta(HS, \sigma_v = 1)\left(\frac{2}{\sqrt{\pi}}\right) = 1.114139 \tag{2.15}$$

The other coefficients C_1 and B_1 for fully accommodating surfaces $\sigma = \sigma_v = 1$ for BGK model are $C_1(BGK, \sigma = 1) = 1.149$ and $B_1(BGK, \sigma = 1) \approx 1.168$. For hard sphere (HS) model Ohwada *et al.* [201] evaluates these coefficients as $C_1(HS, \sigma = 1) = 1.015$ and $B_1(HS, \sigma = 1) = 1.13$. For isothermal flows of real gases the hard sphere model is more appropriate compared to BGK.

As described earlier the Knudsen layer correction $u_{\mathrm{Kn}}(y)$ over Navier-Stokes solution u_{NS} requires terms of order Kn^2 provided by second order velocity slip model. Higher order slip models are required to model rarefied flows [44, 67, 111, 172, 253], experimental studies [32, 85, 181] have also shown that first order slip model do not compare well with the experimental data beyond Kn>0.1. Most of the research is based on simple micro channel flow or flows in simple geometry without any flow separation. Thus, behavior of the slip model in the recirculation zone due to combined effect of rarefaction and reduction of Reynolds number forms a good validation test [2, 32]. Modeling the non-equilibrium layer close to the walls, known as the Knudsen layer is the most crucial aspect for obtaining a reliable higher-order slip model. Physics based empirical slip model of Beskok [32] predicts Knudsen's minimum, observed around Kn ≈ 1 as well as the flow rate, velocity profile, and the pressure distribution. Beskok [32] carried out detailed study of the slip model and validated it with DSMC results for classical backward facing step under combined effect of rarefaction and adverse pressure gradient on separated flows as a function of the Reynolds and Knudsen numbers.

Beskok [32] slip equation is based on tangential gas velocity one mean free path away from the wall surface as follows :

$$u_s = \frac{1}{2}\left[u_\lambda + (1-\sigma_v)u_\lambda + \sigma_v u_w\right] \tag{2.16}$$

where u_λ is the tangential gas velocity one mean free path away from the wall surface and u_s is the slip velocity. Using the Taylor series expansion of u_λ about u_s results in the following equation :

$$u_s = \frac{1}{2}(2-\sigma_v)\left[u_s + \lambda\left(\frac{\partial u}{\partial n}\right)_s + \frac{\lambda^2}{2}\left(\frac{\partial u}{\partial n}\right)_s + ...\right] + \frac{1}{2}\sigma_v u_w \tag{2.17}$$

Another example of higher order slip is linearized Maxwell-Burnett boundary condition obtained by Lockerby *et al.* [162] using the Burnett constitutive relations, the expressions of slip are as follows

$$\begin{aligned} u_s - u_w \quad &= \pm\left(\tfrac{2-\sigma_v}{\sigma_v}\right)\lambda\left(\tfrac{\partial u_s}{\partial n} + \tfrac{\partial u_n}{\partial s}\right)_w + \tfrac{3\mu}{4\rho T}\tfrac{\partial T}{\partial s} \pm \left(\tfrac{2-\sigma_v}{\sigma_v}\right)\lambda\left(2\tfrac{\mu}{\rho^2}\tfrac{\partial^2\rho}{\partial s\partial n} - \tfrac{\mu}{\rho T}\tfrac{\partial^2 T}{\partial s\partial n}\right)_w \\ &\quad + \tfrac{3\,\mathrm{Pr}}{16\pi}\left(\tfrac{\gamma-1}{\gamma}\right)\lambda^2\left((45\gamma-61)\tfrac{\partial^2 u_s}{\partial s^2} + (45\gamma-49)\tfrac{\partial^2 u_n}{\partial s\partial n} - 12\tfrac{\partial^2 u_s}{\partial n^2}\right)_w \end{aligned}$$

For stationary flow based on the linearized Maxwell-Burnett boundary condition, the thermal stress flow due to temperature gradients can be derived as

$$u_s - u_w \quad = \pm\left(\tfrac{2-\sigma_v}{\sigma_v}\right)\lambda\left(-\tfrac{\mu}{\rho T}\tfrac{\partial^2 T}{\partial s\partial n}\right)_w \tag{2.18}$$

Higher order slip condition in Knudsen number approaches the classical Maxwell's first order condition if we neglect second and higher order terms. A second or higher order slip boundary condition requires corresponding higher order continuum model i.e. second order slip condition will require Burnett equation. Struchtrup and Torrilhon [266, 267] have used R13 equations for the expression of the higher order slip boundary. Many researchers have used the generalized second-order velocity slip boundary condition, which in absence of thermal creep contribution can be expressed as

$$u_s - u_w = \pm A_1\lambda\left(\frac{\partial u_s}{\partial n}\right)_w - A_2\lambda^2\left(\frac{\partial^2 u_s}{\partial n^2}\right)_w \tag{2.19}$$

where A_1 and A_2 are the first and second order slip coefficients. For flow problems with small Knudsen number the solution of linearized Boltzmann equation using

asymptotic approaches can be used to obtain the second slip coefficient. For example Cercignani and Lorenzani [47] have obtained the solution of Navier-Stokes solution by using the second order slip boundary condition for Poiseuille mass flux problem as

$$S_{NS} = 1 + 6A_1\mathrm{Kn} + 12A_2\mathrm{Kn}^2 \tag{2.20}$$

Cercignani and Lorenzani [47] have used the variational technique to solve Boltzmann equation to get asymptotic near-continuum solution for the Poiseuille mass flux to obtain the slip coefficients. The Navier-Stokes solution reveals that the second order coefficient A_2 with the terms of order Kn^2 needs to be superimposed to the Navier-Stokes solution to capture the true solution of the Boltzmann equation. Thus, the Knudsen layer correction $u_{\mathrm{Kn}}(y)$ over Navier-Stokes solution u_{NS} requires a second order velocity slip model. With the second order slip coefficient the classical hydrodynamical equations can simulate rarefied flows beyond $\mathrm{Kn} = 0.1$ i.e. second order model extends its applicability beyond slip flow regime into the transition regime. Since the cost of solution of Navier-Stokes is negligible compared to the alternative methods hence large number of researchers have attempted to develop second order slip models that can be used beyond $\mathrm{Kn} = 0.1$. Table 2.3 gives the value of different slip coefficients proposed in the literature for gas micro flows. It can be inferred from the table that the first order slip coefficient is mildly dependent on molecular interaction model as compared to strong dependence seen in second order slip coefficient. Most of the theoretically derived second order slip models are derived under linearized conditions for flat walls, steady flow and small gradients. The real conditions can be quite different as geometries can be complex, flow can be time dependent, etc. The table reveals that with regards to the first order coefficient A_1 there is agreement amongst various researchers. However, there is a large discrepancy between the values of the second order coefficient, A_2 and there seems to be no consensus amongst the researchers even for the simple flows. It is also most likely that second order coefficient A_2 is geometry dependent. Under such a scenario boundary condition derived from set of Burnett equations [162] looks physically meaningful as it includes the terms of order Kn^2, shows reasonable agreement with experimental data and is simple to implement numerically.

Table 2.3: Value of slip coefficients proposed in the literature for gas micro flows for σ_v=1.

Source	A_1	A_2
Maxwell,1879 [184]	1.0	0.0
Schamberg 1947 [238]	1.0	1.308 ($5\pi/12$)
Albertoni *et al.* 1963[3]	1.1466	0.0
Cercignani[a] 1964 [44]	1.1466	0.647
Deissler [b], 1964 [67]	1.0	1.125 (9/8)
Sreekanth, 1969 [253]	1.1466	0.14
Loyalka *et al.* , 1975 [172]	1.1466	0.0
Lang[c] ,1976 [147]	1.007	0.75
Hsia and Domoto, 1983 [124]	1.0	0.5
Loyalka and Hickey, 1989 [170]	1.1019	0.4490
Mitsuya, 1993 [191]	1.0	2/9
Pan et al. 1999 [209]	1.125	0.0
Beskok [d], 2001 [32]	1.0	-0.5
Maurer *et al.*, 2003 [181] (Helium)	1.2±0.05	0.23±0.1
Maurer *et al.*, 2003 [181] (Nitrogen)	1.3±0.05	0.26±0.1
Cercignani et al. 2004 [48]	1.1366	0.6926
Hadjiconstantinou[e], 2005 [113]	1.11	0.31
Lockerby[f],2004 [162]	1.0	0.19 ($6/10\pi$)
Dongari *et al.* [g],2007 [77]	1.875	0.05
Ewart *et al.* 2007 [85]	1.26±0.02	0.17±0.02
Struchtrup *et al.* 2008 [267]	1.0	0.5303
Cercignani and Lorenzani 2010 [47]	1.209	0.2347

[a] After modification for hard sphere gas, refer Hadjiconstantinou [111] for details.

[b] Aubert and Colin [17] have also used Deissler's boundary conditions.

[c] $A_2 = 3\sigma_v/(4\,\mathrm{Pr})$ for BGK model. For Maxwell gas, $A_2 = 1.125$

[d] $A_2 = -\frac{2-\sigma_v}{2\sigma_v}$, where σ_v is the momentum accommodation coefficient.

[e] $A_2 = 0.31$ with Knudsen layer correction

[f] $A_2 = \frac{9\,\mathrm{Pr}}{4\pi}\left(\frac{\gamma-1}{\gamma}\right)$, based on Maxwell-Burnett boundary condition.

[g] $A_1 = 1.0, A_2 = 0$ for $\mathrm{Kn} \leq 0.1$, $A_1 = 1.4, A_2 = 0.7$ for $0.1 < \mathrm{Kn} \leq 1.0$, $A_1 = 1.875, A_2 = 0.05$ for $1.0 < \mathrm{Kn}$

Similarly, second order von Smoluchowski's temperature-jump boundary conditions can be expressed as

$$T_s - T_w = \frac{2\gamma}{\mathrm{Pr}(\gamma+1)}\left[B_1^T \lambda \left(\frac{\partial T}{\partial n}\right)_w + B_2^T \lambda^2 \left(\frac{\partial^2 T}{\partial n^2}\right)_w\right] \tag{2.21}$$

where B_1^T and B_2^T are the first and second order slip coefficients for temperature. Beskok's second order temperature jump condition[32] is as follows :

$$T_s = \frac{\left(\frac{(2-\sigma_T)}{\mathrm{Pr}}\right)\left(\frac{2\gamma}{(\gamma+1)}\right) T_\lambda + \sigma_T T_w}{\sigma_T + \left(\frac{(2-\sigma_T)}{\mathrm{Pr}}\right)\left(\frac{2\gamma}{(\gamma+1)}\right)} \tag{2.22}$$

Another approach for extending the Navier-Stokes equation to transition regime is to consider the rarefaction effects in calculating the Navier-Stokes viscosity coefficient. In order to include the rarefaction effects Karniadakis *et al.* [135] proposed the following viscosity coefficient relationship

$$\frac{\mu(\mathrm{Kn})}{\mu} = \frac{1}{1+\alpha_g \mathrm{Kn}} \tag{2.23}$$

Karniadakis *et al.*[135] uses only first order slip coefficient which is function of Knudsen number. While Roohi and Darbandi [232] have used second order slip formula coupled with viscosity coefficient correction evaluated using information preservation (IP) method expressed as

$$\frac{\mu(\mathrm{Kn})}{\mu} = \frac{1+0.75\mathrm{Kn}+19.98\mathrm{Kn}^2}{1+0.89\mathrm{Kn}+4.70\mathrm{Kn}^2} \tag{2.24}$$

Fichman and Hetsroni [88] found that there is reduction in viscosity in the Knudsen layer due to interaction of molecules with the wall. This reduction of viscosity leads to an increase in slip velocity as a consequence of increase of the flow gradient in the direction normal to the wall. The effective viscosity proposed by Fichman and Hetsroni [88] is

$$\frac{\mu(\bar{y},\sigma_v)}{\mu} = \begin{cases} \sigma_v/2 + (1-\sigma_v)\bar{y}, & \bar{y} \le 1 \\ 1, & \bar{y} > 1 \end{cases} \tag{2.25}$$

where $\bar{y} = y/\lambda$, y is the normal distance from the surface and λ is the mean free path. Fichman and Hetsroni [88] model fails to capture the asymptotic form of

the velocity profile in the Knudsen layer near the surface [154]. Lilley and Sader [154] have shown that flow exhibits a striking power-law dependence on distance from the solid surface where the velocity gradient is singular i.e. the effective viscosity is zero, under arbitrary thermal accommodation. The effective viscosity proposed by Lilley and Sader [154] for $\bar{y} < 1$ is

$$\frac{\mu(\bar{y}, \sigma_v)}{\mu} = \frac{\bar{y}^{1-\alpha(\sigma_v)}}{\alpha(\sigma_v) D(\sigma_v)} \tag{2.26}$$

Where $\alpha(\sigma_v)$ and $D(\sigma_v)$ are functions of momentum accommodation coefficient,σ_v given in [154].

2.2.3.6 Treatment of slip flow based on Lattice Boltzmann method.

The lattice Boltzmann (LB) method is a mesoscopic approach where details of the molecular motions are not required. An introduction to LB method and its theory may be obtained from reference [268]. Recently, Meng and Zhang [188] have shown that the nine-velocity square lattice D2Q9 model is not sufficient to capture flow characteristics in the Knudsen layer. Simulation of slip flows using LB method requires improvement in physics for high Knudsen flows to simulate nonlinear constitutive relations as well as proper method of slip boundary application. Researchers [8, 237] have used diffuse reflection boundary condition simulated as the combination of the bounce-back and specular reflection boundary condition (similar to procedures developed in continuum kinetic theory) to simulate slip flows in LB method. There are broadly two approaches in LB method to include the effect of high Knudsen number : i)choice of discreet velocity set with sufficient symmetry so that the discreet moments approximate its counterpart based on continuous Boltzmann equation, ii)the second approach makes use of an effective relaxation time to capture the Knudsen layer. Sbragaglia and Succi [237] suggested suitable modification of the construction of the body force in the LB model in order to obtain the second-order slip. Kim *et al* [141] have implemented modification to the non-equilibrium energy flux to capture the slip phenomena up to second order in the Knudsen number. Guo *et al* [109] have used multiple effective relaxation times with wall confinement effects to simulate the Knudsen layer. The LB framework's extension to non-equilibrium flows still

needs to evolve and mature to simulate transition regime [109]. The LB method are commonly used to simulate fluids with isothermal equations of state in a weakly compressible limit, it still needs development in the field of compressible high speed flows.

2.2.3.7 Treatment of slip based on Quasi-Gas-Dynamics (QGD) and hydrodynamic theory of Brenner

Galileo transform does not hold for the conservation equations based on spatial-time averages. Quasi-gas-dynamics (QGD) [81] and Quasi-hydrodynamic [248] approaches use the time-spatial averaging procedure for the definition of the main gas dynamic quantities: density, velocity, and temperature as compared to spatial averaging used in conventional Navier-Stokes theory. QGD introduces small diffusive velocity in the expression of mass flux such that time-spatial averages are invariant under Galileo transform. QGD approach[82] increases the domain of validity of the continuum approach up to Kn ~ 0.5. The mass flow rate for slip conditions using QGD approach also accounts for the flow rate increase due to self diffusion.
QGD approach is similar to modification in hydrodynamic theory proposed by Brenner [38] by introducing a new mass diffusion contribution to the continuity equation, more details are presented in section B.3 of Appendix B. Guo and Xu [108] studied gaseous micro flows using Brenner's hydrodynamic model and found that Brenner's model failed to give qualitative correct temperature profile.

2.2.3.8 Kinetic theory based slip modeling

According to kinetic theory velocity slip and temperature jump will always be present even in continuum flow regime [90, 265]. The slip flow simulation using the continuum solver can be carried out either by using slip models or by implementing kinetic wall boundary condition. Maxwell specular-diffuse reflection model is the most preferred gas-surface interaction model for engineering applications. In this model molecules partially undergo specular reflection and the remainder reflect in diffuse manner. The boundary conditions at the surface of the solid object define the distribution function of the reflected particles as a sum of diffuse

and specular reflections [189, 295]. It can be seen that there are large number of slip models existing in the literature, each with its own geometry specific slip coefficients and range of validity in Knudsen regime. Most of these slip models are for simple micro-channel flows. The first order slip model itself is not perfect as the slip velocity not only depends on the velocity gradient in the normal direction but also on the pressure gradient in the tangential flow direction [246]. Li *et al* [152] have used gas kinetic upwind method to carry out slip flow modeling for hypersonic flows. Agarwal *et al.* [1], Bao and Lin [24], and Lockerby and Reese [161] have used Burnett equations coupled with slip models. For example Bao and Lin [24] have adopted Beskok's slip model [32]. Researchers [153, 189, 295] have used kinetic wall boundary condition obtained using the distribution function. Velocity slip and temperature jump can also be derived using linearized Grad's moment method which is based on expansion of distribution function around local Maxwellian in terms of Hermite tensor polynomials. Accurate derivation of velocity slip and temperature jump using Grad's moment method requires at least thirteen equations [266]. Patterson [211] carried out derivation of velocity slip and temperature jump using Grad's moment method. Patterson's velocity slip condition is similar to Maxwell's velocity slip for curved surface [163]. However, Patterson's temperature boundary condition [211] is approximate as it is derived under assumption of negligible tangential variation and negligible magnitude of velocity compared to thermal speed of the molecules. Greenshields and Reese [104] have used velocity slip and temperature jump derived using Patterson [211] boundary conditions. Kinetic theory based methods in general have focused more on entropy condition and ignored the issues of non-equilibrium thermodynamics i.e. distribution of entropy for each thermodynamic force.

2.2.3.9 Kinetic theory and non-equilibrium thermodynamics based slip modeling

Waldmann [283] carried out analysis of boundary condition and was first to stress the need to incorporate features of non-equilibrium thermodynamics. Roldughin [231] and later on Zhdanov and Roldughin [300] established links between phenomenological approach of non-equilibrium thermodynamics and kinetic theory

for entropy production in the boundary layer, derivation of slip and jump conditions.

2.2.4 Potential area of research in slip modeling

The first order slip models not only depends on the velocity gradient in the normal direction but also on the pressure gradient in the tangential flow direction as most of theoretically derived slip models are derived under linearized conditions for flat walls, steady flow and small tangential gradients. It can be inferred from the literature review that the first order slip coefficient is mildly dependent on molecular interaction model as compared to strong dependence seen in second order slip coefficient. Literature survey also reveals that for Navier-Stokes based approach there is no consensus amongst researchers in usage of second order slip models. Compared to Navier-Stokes based approach kinetic theory based methods are more successful in resolving features of slip flow. Kinetic theory based methods in general have focused more on entropy condition and ignored the issues of non-equilibrium thermodynamics. *Literature review also revealed that there is virtually no reported upwind method based on linkage between kinetic theory and non-equilibrium thermodynamics for solving slip flows.*

2.3 Kinetic theory and Fluid Flow

The kinetic theory of gases is a very vast field which successfully explains the irreversible laws of fluid mechanics through a statistical description of a system composed of larger number of particles. For detailed description of kinetic theory of gases refer Appendix B.

2.3.1 Boltzmann equation

For a gas in absence of external force and without internal degrees of freedom, the Boltzmann equation with binary collisions term $J(f, f)$ is

$$\frac{\partial f}{\partial t} + \nabla_{\vec{x}} \cdot (\vec{v} f) = J(f, f) \tag{2.27}$$

The Boltzmann transport equation describes the transient molecular distribution $f(\vec{x}, \vec{v}, \mathbb{I}, t) : \mathbb{R}^D \times \mathbb{R}^D \times \mathbb{R}^+ \times \mathbb{R}^+ \rightarrow \mathbb{R}^+$ where D is the degree of freedom. For conservation of total energy instead of translational energy alone an additional internal energy variable $\mathbb{I} \in \mathbb{R}^+$ is added as polyatomic gas consists of particles with additional degree of freedom [69, 192]. Thus a molecule of a polyatomic gas is characterized by a $(2D + 1)$ dimensional space given by its position $\vec{x} \in \mathbb{R}^D$, molecular velocity vector $\vec{v} \in \mathbb{R}^D$ and internal energy $\mathbb{I} \in \mathbb{R}$. Distribution function expresses the probability of finding the molecules in the differential volume $d^D x d^D v d\mathbb{I}$ [1] of the phase space.

$$n(\vec{x}, t) = \int_{\mathbb{R}^+} \int_{\mathbb{R}^D} f(\vec{x}, \vec{v}, \mathbb{I}, t) d\vec{v} d\mathbb{I} \tag{2.28}$$

The equilibrium or Maxwellian distribution function for the polyatomic gas is given by

$$f_0 = \frac{\rho}{\mathbb{I}_o} \left(\frac{\beta}{\pi}\right)^{\frac{D}{2}} exp\left(-\beta(\vec{v} - \vec{u})^2 - \frac{\mathbb{I}}{\mathbb{I}_o}\right) \tag{2.29}$$

where $\beta = 1/2RT$ and $\mathbb{I}_o$ is given as

$$\mathbb{I}_o = \frac{< \mathbb{I}, f_0 >}{< f_0 >} = \frac{1}{\rho} \int_{\mathbb{R}^+} \int_{\mathbb{R}^D} \mathbb{I} f_0(\vec{x}, \vec{v}, \mathbb{I}, t) d\vec{v} d\mathbb{I} = \frac{2 - (\gamma - 1)D}{4(\gamma - 1)\beta} \tag{2.30}$$

2.3.2 Moments and hyperbolic conservation equations

The moment of a function, $\mathbf{\Psi} = \mathbf{\Psi}(\vec{v}, \mathbb{I}, t) : \mathbb{R}^D \times \mathbb{R}^+ \times \mathbb{R}^+ \rightarrow \mathbb{R}$ is defined as Hilbert space of functions generated by the inner product

$$\bar{\mathbf{\Psi}}(\vec{x}, t) = \langle \mathbf{\Psi}, f \rangle \equiv \int_{\mathbb{R}^+} \int_{\mathbb{R}^D} \Psi(\vec{v}, \mathbb{I}, t) f(\vec{x}, \vec{v}, \mathbb{I}, t) d\vec{v} d\mathbb{I} \tag{2.31}$$

The five moments function defined as $\mathbf{\Psi} = \left[1, \vec{v}, \mathbb{I} + \frac{1}{2}v^2\right]^T$ gives the macroscopic mass, momentum, and energy densities i.e. $\langle \mathbf{\Psi}, f \rangle = [\rho, \rho\vec{u}, \rho E]^T$, where $E = RT/(\gamma - 1) + \frac{1}{2}u^2$, $\vec{u}$ is the fluid velocity vector and γ is the specific heat ratio. When we take moments of the Boltzmann equation we get the hyperbolic

[1] For example when D=3 the polyatomic gas is characterized by a 7 dimensional space and the differential volume in phase space is $d^3x d^3v d\mathbb{I}$ where d^3x is $dxdydz$ and d^3v is $dv_x dv_y dv_z$.

conservation equation. For example with $f = f_0$ we get Euler equations that are set of inviscid compressible coupled hyperbolic conservation equations written as

$$\int_{\mathbb{R}^+}\int_{\mathbb{R}^D} \boldsymbol{\Psi}\left(\frac{\partial f_0}{\partial t} + \nabla_{\vec{x}}.(\vec{v}f_0) = 0\right) d\vec{v}d\mathbb{I} \equiv \frac{\partial \boldsymbol{U}}{\partial t} + \frac{\partial \boldsymbol{GX}_I}{\partial x} + \frac{\partial \boldsymbol{GY}_I}{\partial y} + \frac{\partial \boldsymbol{GZ}_I}{\partial z} = 0 \tag{2.32}$$

where $\boldsymbol{U} = [\rho, \rho\vec{u}, \rho E]^T = \langle \boldsymbol{\Psi}\ , f_0\rangle \equiv \int_{\mathbb{R}^+}\int_{\mathbb{R}^D} \boldsymbol{\Psi} f_0(\vec{x}, \vec{v}, \mathbb{I}, t)d\vec{v}d\mathbb{I}$ is the vector of conserved variable and $(\boldsymbol{GX}_I, \boldsymbol{GY}_I, \boldsymbol{GZ}_I)$ are the Cartesian components of the inviscid flux vector defined as

$$\boldsymbol{GX}_I = \int_{\mathbb{R}^+}\int_{\mathbb{R}^D} \boldsymbol{\Psi} v_x f_0(\vec{x}, \vec{v}, \mathbb{I}, t)d\vec{v}d\mathbb{I} \equiv \begin{bmatrix} \rho u_x \\ p + \rho u_x^2 \\ \rho u_x u_y \\ \rho u_x u_z \\ (\rho E + p)u_x \end{bmatrix} \tag{2.33}$$

$$\boldsymbol{GY}_I = \int_{\mathbb{R}^+}\int_{\mathbb{R}^D} \boldsymbol{\Psi} v_y f_0(\vec{x}, \vec{v}, \mathbb{I}, t)d\vec{v}d\mathbb{I} \equiv \begin{bmatrix} \rho u_y \\ \rho u_y u_x \\ p + \rho u_y^2 \\ \rho u_y u_z \\ (\rho E + p)u_y \end{bmatrix} \tag{2.34}$$

$$\boldsymbol{GZ}_I = \int_{\mathbb{R}^+}\int_{\mathbb{R}^D} \boldsymbol{\Psi} v_z f_0(\vec{x}, \vec{v}, \mathbb{I}, t)d\vec{v}d\mathbb{I} \equiv \begin{bmatrix} \rho u_z \\ \rho u_z u_x \\ \rho u_z u_y \\ p + \rho u_z^2 \\ (\rho E + p)u_z \end{bmatrix} \tag{2.35}$$

For an ideal law we have $p = \rho RT$ where R is the gas constant and T is the absolute temperature. No real gas follows the ideal gas law $p = \rho RT$ for all temperatures and pressures, similarly specific heat of many gases vary with temperature. Refer Appendix C for treatment of thermally and calorically imperfect gas.

The distribution function f can be expanded in terms Knudsen number, Kn as follows

$$f = f_0 + \mathrm{Kn}\bar{f}_1 + \mathrm{Kn}^2\bar{f}_2 + \cdots \tag{2.36}$$

With first order expansion $f = f_0 + \mathrm{Kn}\bar{f}_1$ we get Navier-Stokes equations, and with second order expansion $f = f_0 + \mathrm{Kn}\bar{f}_1 + \mathrm{Kn}^2\bar{f}_2$ we get a set of Burnett equations. The moments of the Boltzmann equation satisfy an infinite hierarchy

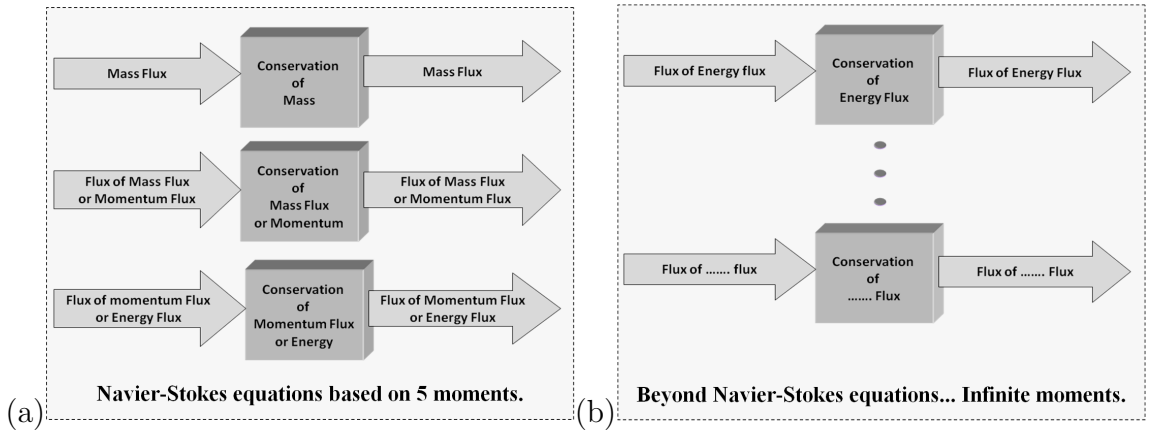

(a) (b)

Figure 2.5: Boltzmann equation with (a) 5 moments resulting in Navier-Stokes equations, (b) beyond Navier-Stokes with an infinite hierarchy of balance laws.

of balance laws such that from the continuum mechanics perspective the flux in an equation becomes the density at the next hierarchical level. In other words to conserve mass we require mass flux in the first hierarchy, now in order to conserve mass flux (which can be interpreted as momentum) we require momentum flux in the second hierarchy. In the second hierarchy we conserve the momentum for x, y and z directions using momentum flux (which can be interpreted as energy). This momentum flux or energy is conserved using flux of energy in the third hierarchy. Navier-Stokes ends in this third hierarchy with 5 equations conserving mass, three momentums and energy. But we still require conservation of energy flux which will require flux of energy flux in the fourth hierarchy. *Thus, we require infinite hierarchy or moments as shown in Figure 2.5.* It is evident that Navier-Stokes and Burnett equations are all obtained using the five moments and hence they do not have equations for evolution of shear stress tensor and heat flux vectors. There can be different set of moment equations based on entropy based closure or closure due to equilibrium solution, for further details refer section B.1.3 of Appendix B.

2.3.3 Kinetic Models

Boltzmann equation being a nonlinear integro-differential equation becomes difficult to handle. This requires some alternative simpler model to replace the

collision term. Such a model which replaces the Boltzmann collision integral is called a kinetic model. These models should preserve the basic properties and characteristics of the Boltzmann equation. In kinetic models, the Boltzmann collision term $J(f,f)$ is substituted by a relaxation expression $J_m(f,f_{ref})$ in terms of suitable reference distribution function, f_{ref} and mean collision frequency, ν which is inverse of relaxation time, t_R. The collision or kinetic model $J_m(f,f_{ref})$ should also satisfy the main properties of the Boltzmann collision integral. Some of the main properties are

1. Locality and Galilean invariance
   Since the Boltzmann equation is invariant under Galilean transformation hence the collision term $J_m(f,f_{ref})$ should depend only on peculiar velocity $\vec{c}=\vec{v}-\vec{u}$.

2. Additive invariants of the collision integral
   This property ensures conservation of mass, momentum and energy and is represented as
   $$\int_{\mathbb{R}^+}\int_{\mathbb{R}^D} J_m(f,f_{ref})\mathbf{\Psi}d\vec{v}d\mathbb{I}=0 \tag{2.37}$$

3. Uniqueness of equilibrium
   The zero point of kinetic model $J_m(f,f_{ref})=0$ representing collision term implies uniqueness of equilibrium. This condition is also known as condition of detailed balance.

4. Local entropy production inequality and Boltzmann H-theorem
   This property represents non-negative entropy production by the kinetic model representing collision term obtained using moment $\Psi_e=-Rlnf$.[1]
   $$\sigma(\vec{v},t)=-R\int_{\mathbb{R}^+}\int_{\mathbb{R}^D} lnfJ_m(f,f_0)d\vec{v}d\mathbb{I}=-R\frac{dH}{dt}\geq 0 \tag{2.38}$$

[1]When distribution function f is expressed in terms of number density as $\breve{f}$ then the moment $\Psi_e=-k_Blnf$ gives entropy production as
$\sigma(\vec{v},t)=-k_B\int_{\mathbb{R}^+}\int_{\mathbb{R}^D} ln\breve{f}J_m(\breve{f},\breve{f}_0)d\vec{v}d\mathbb{I}=-k_B\frac{dH}{dt}\geq 0$
where k_B is the Boltzmann's constant.

where H-function is given by

$$H = \int_{\mathbb{R}^+} \int_{\mathbb{R}^D} f ln f d\vec{v} d\mathbb{I} \tag{2.39}$$

5. Correct transport coefficients in the hydrodynamic limit
   In the hydrodynamic limit the kinetic model should generate correct transport coefficients such as viscosity, μ and thermal conductivity, κ and Prandtl number, Pr should be close to 2/3.

6. Positive distribution
   The H-function of the kinetic model should decay monotonically such that Boltzmann equation gives positive distribution leading towards the unique equilibrium solution.

For further details on properties of collision operator refer section B.2 of Appendix B. Literature review reveals Bhatnagar-Gross-Krook (BGK) model [35], Fokker-Planck model [148], Quasi-Equilibrium model [100] and several other kinetic models. The simplest of all the kinetic models which satisfies the Boltzmann H-theorem is the non-linear Bhatnagar-Gross-Krook (BGK) model.

2.3.3.1 Bhatnagar-Gross-Krook (BGK) Model

In this model the reference distribution function is simply Maxwellian i.e. $f_{ref} = f_0$. With this the BGK kinetic model [35] can be represented as

$$J_m(f, f_0) = -\nu(f - f_0) = -\frac{(f - f_0)}{t_R} \tag{2.40}$$

where ν is the collision frequency and t_R is the relaxation time. BGK is a non-linear function of the moments of f whereas the Boltzmann collision integral is non-linear in the distribution function itself. BGK model preserves most of the property of the collision integral but its evaluation in the hydrodynamic limit generates transport coefficients which cannot be adjusted to give the correct Prandtl number of 2/3. The BGK model gives viscosity, μ and thermal conductivity, κ and Prandtl number as follows

$$\mu = t_R p, \quad \kappa = p t_R R \tfrac{\gamma}{\gamma - 1}, \quad \text{Pr} = 1 \tag{2.41}$$

2.3.3.2 Morse-BGK model for polyatomic gases

In most of the cases translational, rotational and vibrational partition functions contribute to the thermodynamic properties in the temperature ranges encountered in engineering applications. As described earlier Maxwellian distribution function, f_0 for the polyatomic gas is given as

$$f_0 = \frac{\rho}{\mathbb{I}_o}\left(\frac{\beta}{\pi}\right)^{\frac{D}{2}} exp\left(-\beta(\vec{v}-\vec{u})^2 - \frac{\mathbb{I}}{\mathbb{I}_o}\right) \tag{2.42}$$

where $\mathbb{I}_o =< \mathbb{I}, f_0 > / < f_0 > = \frac{2-(\gamma-1)D}{4(\gamma-1)\beta}$ is the average internal energy parameter, $\beta = 1/2RT$. In Morse's model [192] relaxation time for elastic and inelastic collision is considered separately. Due to inelastic collision particles relax to equilibrium distribution in internal and translational state at same temperature as there is equipartition of energy between the internal and translational degree of freedom. Whereas, due to elastic collision particles relax to equilibrium for translational state at a temperature which is different from the temperature at which internal state attains its equilibrium. Elastic collisions do not contribute to equipartition of energy between translational and internal states. The relaxation model is parameterized by elastic and inelastic collision times. For inelastic collisions the Morse-BGK [192] relaxation time model for polyatomic gas is given by

$$J_m(f, f_0) = -\frac{f(\vec{x}, \vec{v}, \mathbb{I}, t)}{t_{R(f)}(\vec{x}, t)} + \frac{f_0(\vec{x}, \vec{v}, \mathbb{I}, t)}{t_{R(f_0)}(\vec{x}, t)} \tag{2.43}$$

where inelastic Maxwellian f_0 is

$$f_0 = \frac{\rho}{\mathbb{I}_o(T)}\left(\frac{\beta(T)}{\pi}\right)^{\frac{D}{2}} exp\left(-\beta(T)(\vec{v}-\vec{u})^2 - \frac{\mathbb{I}(T)}{\mathbb{I}_o(T)}\right) \tag{2.44}$$

Thus particles in non-equilibrium are replaced exponentially by particles in equilibrium with characteristic time $t_{R(f)}$ and $t_{R(f_0)}$ respectively. With an assumption $t_{R(f)}$=$t_{R(f_0)}$=t_R the Morse-BGK model becomes

$$J_m(f, f_0) = -\frac{f(\vec{x}, \vec{v}, \mathbb{I}, t) - f_0(\vec{x}, \vec{v}, \mathbb{I}, t)}{t_R(\vec{x}, t)} \tag{2.45}$$

Collision operator vanishes as f relaxes to f_0.

2.3.3.3 Drawbacks of BGK class of kinetic models

Morse-BGK model satisfies the Boltzmann H-theorem and preserves most of the property of the collision integral but its evaluation at the hydrodynamic limit generates transport coefficients which cannot be adjusted to give the correct Prandtl number of 2/3. The single relaxation time of the BGK class of kinetic model is defined by

$$t_R^{-1} = \left(\frac{RT_{ref}^{\delta o}}{\mu_{ref}} \right) \rho T^{1-\delta_o} \tag{2.46}$$

where μ_{ref} is the viscosity of the gas at the reference temperature, T_{ref}, δ_o is the exponent of the viscosity law of the gas, which depends on the molecular interaction potential and on the type of the gas. The single relaxation time in the BGK model used for the collision operator leads to incorrect values of the transport coefficients at the hydrodynamic limit. This approach gives Prandtl number as unity. Woods [291] suggested a method which appears to be *ad hoc* in which two distinct collision interval $t_{R,1}$ for momentum transport and $t_{R,2}$ for energy transport are adopted using the BGK model. These collision intervals are related as

$$t_{R,1} = \mathrm{Pr}\, t_{R,2} = \frac{2}{3} t_{R,2} \tag{2.47}$$

Chae *et al.* [49] and Xu [293] have suggested following modification of energy flux for accurate heat transfer prediction

$$[\rho E]_{corrected} = \rho E + \left(\frac{1}{\mathrm{Pr}} - 1 \right) \vec{q} \tag{2.48}$$

where $\vec{q}$ is the heat flux vector. May *et al.* [185] have proposed Prandtl number correction at the level of the partial differential equations without providing any physical basis. It is important to understand that there are very few models which respect each constraint of positivity, conservation of moments, and dissipation of entropy, while being computationally inexpensive.

2.3.4 Kinetic models with correct transport coefficients in the hydrodynamic limit

The incorrect value of the Prandtl number, can be corrected by kinetic models like Shakhov's model [241], the ellipsoidal statistical BGK (ES-BGK) model [6, 122].

The ellipsoidal statistical BGK (ES-BGK) model and the Shakhov's model or S-model is a generalization of the BGK model equation with correct relaxation of both the heat flux and stresses, leading thus to the correct continuum limit in the case of small Knudsen numbers. Model proposed by Shakhov provides reliable result for non-isothermal flows. Both the models are computationally expensive in comparison with BGK model. Zheng and Struchtrup [301] have carried out detailed study on kinetic models. Liu model [157], the BGK model with velocity dependent collision frequency ν(c)−BGK model of Mieussens and Struchtrup [190] also yield the proper Prandtl number.
Kinetic model in lattice Boltzmann (LB) method is represented as scattering matrix between various discrete-velocity distributions e.g. in lattice BGK (LBGK) scattering matrix is in diagonal form with single relaxation parameter. Kinetic model associated with multiple relaxation time (MRT) LB[74, 75] uses multiple relaxation to address the issue of fixed Prandtl number and fixed ratio between the kinematic and bulk viscosity while providing stability. Revised matrix LB model [134] uses a two-step relaxation BGK like model to strike a balance between enhanced stability and simplicity. Yong [298] proposed Onsager like relation as a requirement and guide to construct stable LB models.
Most of the kinetic models have either focused on Prandtl number fix or satisfaction of H-theorem or stability, and have ignored the crucial aspect of *non-equilibrium thermodynamics*. Almost all the models are expensive in terms of computational cost as compared to BGK model. The next sub-section describes ellipsoidal statistical BGK (ES-BGK) model and the Shakhov's model.

2.3.4.1 Ellipsoidal Statistical BGK Model

Holway [122] and Andries and Perthame[6] introduced the Ellipsoidal Statistical BGK (ES-BGK) model which predicts the correct value of transport coefficients and Prandtl number. Here the Maxwellian distribution which was the reference distribution function in BGK model is being replaced by the generalized Gaussian distribution given as

$$f_{ref} = f_{ES} = \frac{\rho}{[det(2\pi\Theta_{ij})]^{1/2}} exp(-\frac{1}{2} c_i \Theta_{ij}^{-1} c_j) \tag{2.49}$$

where Θ_{ij} is a function of symmetric temperature tensor given by p_{ij}/ρ defined as

$$\Theta_{ij} = RT\delta_{ij} + \xi\tau_{ij}/\rho = (1-\xi)RT\delta_{ij} + \xi p_{ij}/\rho \tag{2.50}$$

where factor ξ lies in the interval $[-1/2, 1]$ to ensure that Θ_{ij} is positive definite. The ES-BGK model gives viscosity, μ, thermal conductivity, κ and Prandtl number as follows

$$\mu = \tfrac{1}{1-\xi}\tfrac{p}{\nu}, \quad \kappa = \tfrac{5}{2}\tfrac{pR}{\nu}, \quad \mathrm{Pr} = \tfrac{1}{1-\xi} \tag{2.51}$$

Andries and Perthame [6] have also proved the validity of H-theorem for the ES-BGK model.

2.3.4.2 Shakhov Model

In Shakhov's model [241] we take f_{ref} as a function of peculiar velocity in the form represented by convoluted Hermitian polynomials as

$$f_{ref} = f_0\left(a^{(0)} + a_i^{(1)}c_i + a_{ij}^{(2)}\left(\frac{c_ic_j}{RT} - \delta_{ij}\right) + a_i^{(3)}c_i\left(\frac{c^2}{2RT} - \frac{5}{2}\right)\right) \tag{2.52}$$

By taking finite number of terms of the series to construct approximation of the reverse collision integral. We obtain

$$\begin{gathered} a^{(0)} = a_i^{(1)} = a_{ij}^{(2)} = 0 \\ a_1^{(3)} = \frac{1-\mathrm{Pr}_{ref}}{5}\frac{2q_i}{pRT}, \quad q_i = \int_{\mathbb{R}^D} c_ic^2 f d\vec{v} \end{gathered} \tag{2.53}$$

With the above approximation the reference distribution function, f_{ref} becomes

$$f_{ref} = f_M\left(1 + \frac{1-\mathrm{Pr}_{ref}}{5}\frac{2q_ic_i}{pRT}\left(\frac{c^2}{2RT} - \frac{5}{2}\right)\right) \tag{2.54}$$

If we take Pr_{ref} given in Shakhov's model as $2/3$ then this gives

$$\mu = \tfrac{p}{\nu}, \quad \kappa = \tfrac{15}{4}\tfrac{pR}{\nu}, \quad \mathrm{Pr} = \tfrac{2}{3} \tag{2.55}$$

The distribution function f might become negative for large values of the peculiar velocities.

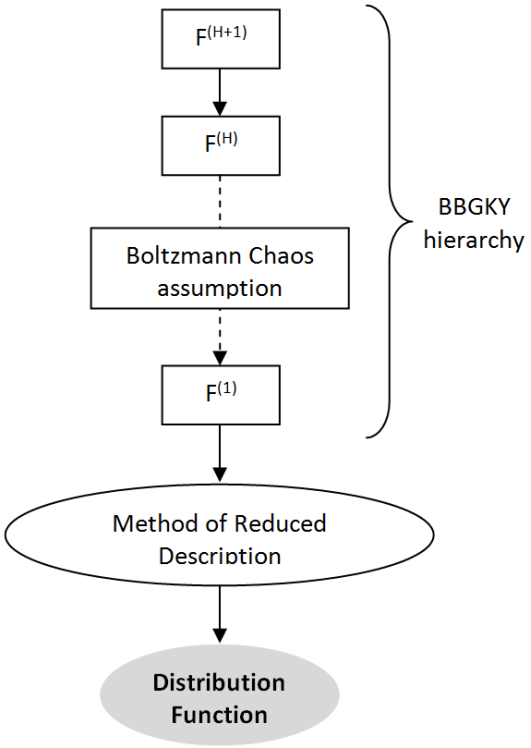

Figure 2.6: Method of reduced description.

2.3.5 Method of reduced description

The most detailed representation governed by Liouville equation leads to the BBGKY infinite hierarchy such that each chain in the hierarchy involves reduced distribution function $F^{(H)}$ and higher order distribution function $F^{(H+1)}$. Boltzmann's molecular chaos assumption gives a closed equation for $F^{(1)}$. The method of reduced description is required to find the closed set of equations. At each level of reduction the insignificant features are discarded for simplicity while retaining the essential physics. The closure problem becomes difficult because of the presence of higher order moments in the equation of lower order moment. Various methods have been developed to give a reduced description in terms of distribution function [45]. Some of the salient methods are: the Chapman-Enskog method [52], the Grad's method [102, 242], the quasi-equilibrium method, and the method of the invariant manifold [101]. In the Grad's method [242] Boltzmann equation is projected onto Hermite basis i.e. we seek solution of mass, momentum and energy conservation equation by expanding the distribution function $f(\vec{x}, \vec{v}, \mathbb{I}, t)$ in Hermite or Gram-Charlier polynomials. The unique feature of Hermite orthonormal polynomials forming the expansion basis is that its expansion coefficients correspond to the velocity moments. Thus, N^{th} order distribution function can be approximated by its projection onto a Hilbert subspace spanned by the first N Hermite polynomials. Instead of searching for a perturbative solution of the Boltzmann equation in the neighbourhood of equilibrium, the Chapman-Enskog method makes use of the time scales present in the equation of motion and expands it in terms of slow and fast components. As the evolution of distribution function in Boltzmann's equation happens on slower timescale τ_s due to slow process of spatial gradients and at faster timescale τ_f due to the process of collisions. The five moments corresponding to mass, momentum and energy densities evolve slowly through spatial gradients as they are unaffected by collisions, whereas all the higher moments which include momentum and energy fluxes evolve on the faster timescale of collisions. In van Kampen's procedure [278] the slow variables are kept unexpanded while the fast variables are expanded in power of τ_f/τ_s. The combination of any slow and fast variables will give rise to different, but asymptotically equivalent evolution equations for the slow variables at each stage

in procedure laid out by van Kampen [68]. Grad moment method and Chapman-Enskog are the most commonly used approaches. Fig. 2.6 shows the schematic of method of reduced description used in obtaining distribution function from the most detailed representation. Refer section B.4 of Appendix B for details on Grad moment method. In the present study we have followed Chapman-Enskog approach [52], this method instead of searching for a perturbative solution of the Boltzmann equation in the neighbourhood of equilibrium makes use of the time scales present in the Boltzmann equations and expands it in terms of slow and fast components.

2.3.5.1 Chapman-Enskog Expansion

Consider the Boltzmann equation with the BGK model as

$$\frac{\partial f}{\partial t} + \nabla_{\vec{x}} \cdot (\vec{v} f) = J_m(f, f_0) = -\frac{(f - f_0)}{t_R} \tag{2.56}$$

where f_0 is the Maxwellian. Boltzmann equation can also be written in a non-dimensional form [234] as

$$\mathrm{St}\left[\frac{\partial f}{\partial \hat{t}} + \nabla_{\vec{\hat{x}}} \cdot (\vec{\hat{v}} f)\right] = -\frac{1}{\mathrm{Kn}_L}\frac{(f - f_0)}{\hat{t}_R} \tag{2.57}$$

where $\vec{\hat{x}} = \vec{x}/L_0$, $\vec{\hat{v}} = \vec{v}/v_{th}$, $\hat{t}_R = t_R v_{th}/\lambda$, $\hat{t} = t/t_0$ based on reference macroscopic length scale, L_0, time scale, t_0 and most probable molecular thermal speed, $v_{th} = 1/\sqrt{\beta}$. Dimensionless form contains kinetic Strouhal number, St and local Knudsen number term, Kn_L. The local Knudsen number $\mathrm{Kn}_L = \lambda/L_0$ is defined as a ratio of mean free path, λ and length scale, L_0. The kinetic Strouhal number, St is given as

$$\mathrm{St} = \frac{L_0}{v_{th} t_0} \tag{2.58}$$

The distribution function f can be expressed as the Chapman-Enskog expansion in terms Knudsen number as follows

$$f = f_0 + \mathrm{Kn}\bar{f}_1 + \mathrm{Kn}^2\bar{f}_2 + \cdots \tag{2.59}$$

where f_0 is the Maxwellian. It should be noted that the perturbation terms satisfies the additive invariants property, expressed as

$$< \mathbf{\Psi}, \mathrm{Kn}^i \bar{f}_i >_{\forall i \geq 1} = 0 \tag{2.60}$$

In Chapman-Enskog expansion, the first term represents the Maxwellian equilibrium distribution function corresponding to the Euler equations. The first two terms in Chapman Enskog expansion, i.e., $(f_0 + \mathrm{Kn}\bar{f}_1)$ give a distribution function corresponding to the Navier-Stokes equations, which represent a first-order departure from equilibrium. Boltzmann equation with higher order Chapman-Enskog distribution will express higher order constitutive relationship for shear and heat transfer terms. The higher order terms are proportional to the corresponding power of Knudsen number, Kn hence higher order terms become important in the Knudsen number dominated rarefied regime. Higher order expansion gives Burnett equations [22, 127, 291], and super-Burnett equations [50]. Boltzmann equation with higher order Chapman-Enskog distribution will express higher order constitutive relationship for shear and heat transfer terms. Using the non-dimensionless Boltzmann equation and Chapman-Enskog perturbation expansion, higher order distribution is generated by virtue of iterative refinement as follows:

$$\bar{f}_i = -\frac{t_R}{\mathrm{Kn}}\left[\frac{\partial \bar{f}_{i-1}}{\partial t} + \nabla_{\vec{x}}.(\vec{v}\bar{f}_{i-1})\right] \tag{2.61}$$

where Kn is the Knudsen number with $\bar{f}_0 = f_0$.

2.3.6 Potential area of research in kinetic theory

Amongst researchers the Bhatnagar-Gross-Krook model (BGK) is the most preferred kinetic model because of the low computational cost even though it yields an inconsistent value of Prandtl number and fails to provide reliable results for non-isothermal flows. Morse-BGK model which is an extension of BGK model for polyatomic gases also gives inconsistent Prandtl number. The ellipsoidal statistical BGK (ES-BGK) model and the Shakhov's model give correct Prandtl number in the hydrodynamic limit but are computational expensive. *Literature survey reveals existence of a potential research area in the development of BGK like computationally inexpensive kinetic model for polyatomic gases which gives correct transport coefficients and Prandtl number in the hydrodynamic limit. It was also realized that extending Chapman-Enskog reduced description method for polyatomic gas could lead to a new contribution.*

2.4 Non-equilibrium thermodynamics

Non-equilibrium thermodynamics being a phenomenological theory gives the symmetry relationship between kinetic coefficients as well as general structure of equations describing the non-equilibrium phenomenon. Approximate solutions provided by kinetic theory has to comply with requirements of non-equilibrium thermodynamics like i)positive entropy production, ii)satisfaction of Onsager's relation. Thus non-equilibrium thermodynamics provides a tool for checking the correctness of the kinetic theory based solutions [300].

2.4.1 Onsager Reciprocity principle

Total entropy of a system described by N-state variables can be written as

$$\frac{d\rho_s}{dt} = \frac{d\rho_{s_{ex}}}{dt} + \frac{d\rho_{s_{in}}}{dt} \tag{2.62}$$

where the first term is because of entropy exchange between the system and the environment through the boundary and this can either be positive or negative. The second term is due to the rate of entropy production because of internal irreversible processes and it is always positive. The change in entropy due to irreversible processes with respect to time is given as

$$\frac{\partial \rho_s}{\partial t} + \nabla_{\vec{x}} \cdot (\vec{j_s}) = \sigma(t) \geq 0 \tag{2.63}$$

where ρ_s is the entropy density, $\vec{j_s}$ is the flux of entropy density and $\sigma(t)$ is the entropy production density. The entropy production is basically a characteristic of a non-equilibrium state as a consequence of the product of the thermodynamic force and conjugated fluxes. For the system described by N-state variables close to equilibrium there exists a linear relationship between its corresponding N fluxes $\boldsymbol{J}_i$ and associated thermodynamic forces $\boldsymbol{X}_j$ through the phenomenological tensor$\boldsymbol{L}_{ij}$ as

$$\boldsymbol{J}_i = \sum_{j=1}^{N} \boldsymbol{L}_{ij} \odot \boldsymbol{X}_j \tag{2.64}$$

Operator $\odot$ denotes full tensor contraction of forces and fluxes, which are of the same tensorial order following Curie principle. Linear relationship between thermodynamic forces and fluxes based on Onsager variational principle [204, 205] is

one of the corner stone of linear non-equilibrium thermodynamics. In isotropic media $\boldsymbol{L}_{ij}$ vanish if forces couple with fluxes of different tensor types. The phenomenological equation either obey Onsager's reciprocal relations $\boldsymbol{L}_{ij}$=$\boldsymbol{L}_{ji}$ or Casimir's one $\boldsymbol{L}_{ij}$=$-\boldsymbol{L}_{ji}$. The flux vanishes when the system is in equilibrium with respect to one of the corresponding state variables

$$\sum_{j=1}^{N} \boldsymbol{L}_{ij} \odot \boldsymbol{X}_j = 0 \tag{2.65}$$

The entropy production density is equal to the product of the thermodynamic force and conjugated fluxes as

$$\sigma(\boldsymbol{X}_i, \boldsymbol{J}_i) = \sum_{i=1}^{N} \boldsymbol{J}_i \odot \boldsymbol{X}_i \geq 0 \tag{2.66}$$

where $\odot$ denotes full tensor contraction. For example consider transport of mass flux and thermal energy flux between two vessels. Vessel-I is maintained at temperature T and pressure p and vessel-II is maintained at temperature $T + \Delta T$ and pressure $p + \Delta p$. Transport process due to mass flux $\boldsymbol{J}_m$ and the flux associated with heat flux vector, $\boldsymbol{J}_q$ is described by non equilibrium thermodynamic phenomenological relations [61]

$$\boldsymbol{J}_i = \sum \boldsymbol{L}_{ij} \odot \boldsymbol{X}_j \tag{2.67}$$

where the phenomenological coefficients $\boldsymbol{L}_{ij}$ form a positive matrix satisfying Onsager reciprocity condition $\boldsymbol{L}_{mq} = \boldsymbol{L}_{qm}$. The thermodynamic forces are given as [262]

$$\begin{aligned} \boldsymbol{X}_m &= -\tfrac{\Delta p}{T\rho} \\ \boldsymbol{X}_q &= -\tfrac{\Delta T}{T^2} \end{aligned} \tag{2.68}$$

where ρ is the fluid density. The entropy production density in this case is obtained as summation of each term of thermodynamic force and its conjugate flux as follows

$$\sigma(\boldsymbol{X}_i, \boldsymbol{J}_i) = \sum \boldsymbol{J}_i \odot \boldsymbol{X}_i \geq 0 \tag{2.69}$$

2.4.2 Maximum entropy production principle (MEPP)

Onsager variational principle was formulated in the space of thermodynamic fluxes, alternative formulation of Gyarmati[110] was proposed in the space of thermodynamic force. Ziegler [305] proposed that entropy production maximizes when actual fluxes satisfy Onsager reciprocity principle for prescribed irreversible force. Onsager [205] introduced dissipation function $\Phi(\boldsymbol{J}_i, \boldsymbol{J}_k)$ expressed as

$$\Phi(\boldsymbol{J}_i, \boldsymbol{J}_k) = \int_\Omega \phi_J(\boldsymbol{J}_i, \boldsymbol{J}_k) d\Omega = \frac{1}{2} \int_\Omega \sum_{i,k=1}^{N} \boldsymbol{R}_{ik}^J \odot \boldsymbol{J}_i \odot \boldsymbol{J}_k d\Omega \tag{2.70}$$

where $\boldsymbol{R}_{ik}^J$ is the symmetric tensor and $\phi_J(\boldsymbol{J}_i, \boldsymbol{J}_k)$ is dissipation function density in the flux space. Onsager variational principle can now be written as

$$\left[\frac{\partial \left(\sigma(\boldsymbol{X}_i, \boldsymbol{J}_i) - \phi_J(\boldsymbol{J}_i, \boldsymbol{J}_k) \right)}{\partial \boldsymbol{J}} \right]_{\boldsymbol{X}} = 0 \tag{2.71}$$

Physically it says that if values of irreversible forces $\boldsymbol{X}_i$ are assigned, true fluxes $\boldsymbol{J}_i$ maximize the expression $[\sigma(\boldsymbol{X}_i, \boldsymbol{J}_i) - \phi_J(\boldsymbol{J}_i, \boldsymbol{J}_k)]$, and expresses the principle of least dissipation of energy.

An alternative Gyarmati [110] formulation in force space can be written as

$$\left[\frac{\partial \left(\sigma(\boldsymbol{X}_i, \boldsymbol{J}_i) - \phi_X(\boldsymbol{X}_i, \boldsymbol{X}_k) \right)}{\partial \boldsymbol{X}} \right]_{\boldsymbol{J}} = 0 \tag{2.72}$$

$\phi_X(\boldsymbol{X}_i, \boldsymbol{X}_k)$ is dissipation function density in the force space given as

$$\phi_X(\boldsymbol{X}_i, \boldsymbol{X}_k) = \frac{1}{2} \int_\Omega \sum_{i,k=1}^{N} \boldsymbol{R}_{ik}^X \odot \boldsymbol{X}_i \odot \boldsymbol{X}_k d\Omega \tag{2.73}$$

where $\boldsymbol{R}_{ik}^X$ is the symmetric tensor. Gyarmati formulation says that for a prescribed thermodynamic fluxes $\boldsymbol{J}_i$ the actual irreversible forces $\boldsymbol{X}_i$ maximize the expression $[\sigma(\boldsymbol{X}_i, \boldsymbol{J}_i) - \phi_X(\boldsymbol{X}_i, \boldsymbol{X}_k)]$.

Ziegler [305] formulation is in flux space, it can be interpreted as maximization of entropy σ_J for prescribed irreversible force under constraint imposed on entropy production due to conservation laws [180, 282]. This can be mathematically written as

$$\begin{array}{ll} \text{Maximize} & \sigma_J(\boldsymbol{J}_i, \boldsymbol{J}_k) \\ \text{subject to} & (\sigma_J(\boldsymbol{J}_i, \boldsymbol{J}_k) - \sigma(\boldsymbol{X}_i, \boldsymbol{J}_i)) = 0 \end{array} \tag{2.74}$$

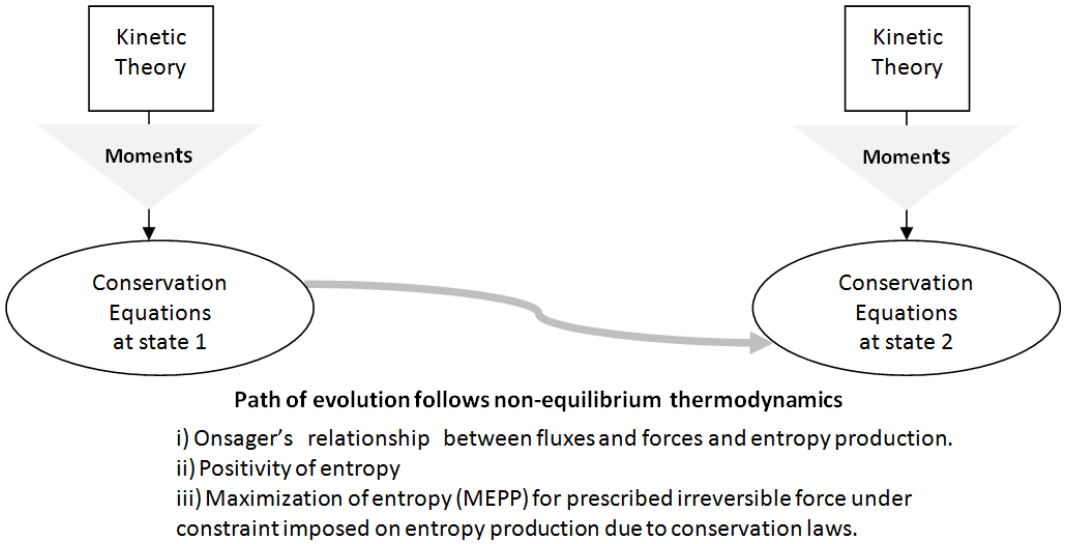

Figure 2.7: Linkage between kinetic theory and non-equilibrium thermodynamics.

where $\sigma(\boldsymbol{X}_i, \boldsymbol{J}_i) = \sum_i \boldsymbol{J}_i \odot \boldsymbol{X}_i$ is the entropy production density based on conservation law and $\sigma_J(\boldsymbol{J}_i, \boldsymbol{J}_k)$ is the entropy production density in terms of fluxes. Maximum entropy production principle (MEPP) represents an additional statement over the second law of thermodynamics that entropy production is not just positive but tends to a maximum. Maximization of the number of possible trajectories as the system evolves from a non-equilibrium state in the phase space probably leads to MEPP. Fig. 2.7 shows the linkage between kinetic theory and non-equilibrium thermodynamics. As the fluid system evolves from one conservation state to another it follows the path dictated by non-equilibrium thermodynamics satisfying Onsager's relationship which in turn leads to maximization of the entropy production. Figure 2.8 shows the schematic picture of the evolution of flow and entropy generation. The path which follows non-equilibrium thermodynamics (NET) generates maximum entropy. The path can also be interpreted in terms of entropy production in the flux space represented as surface $\sigma(\boldsymbol{J}_i, \boldsymbol{J}_k)$ [180]. Figure 2.9 shows a linear irreversible process and a simple dissipative surface σ for a case with two thermodynamic fluxes and forces. The flux $\boldsymbol{J}_i$ is generated corresponding to its conjugate thermodynamic force $\boldsymbol{X}_i$ which is orthogonal to surface $\sigma(\boldsymbol{J}_i, \boldsymbol{J}_k)$ intersected by the plane $\sum_i \boldsymbol{J}_i \odot \boldsymbol{X}_i$.

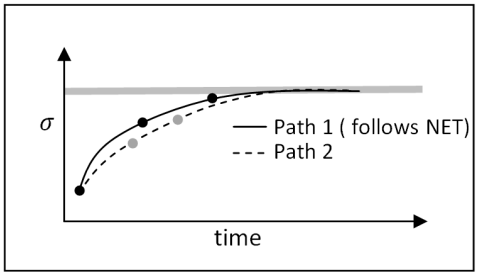

Figure 2.8: Maximum entropy production for the path which complies with the principles on non-equilibrium thermodynamics (NET).

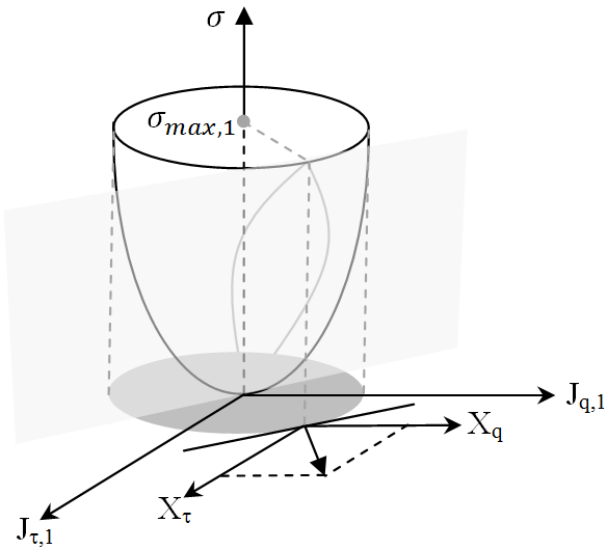

Figure 2.9: Simple dissipative surface for a path governed by two thermodynamic fluxes and forces.

2.4.3 Maximum entropy production, kinetic model and distribution function

The distribution can be linearized about a local Maxwellian as follows

$$f(\vec{x},\vec{v},\mathbb{I},t) = f_0(\vec{x},\vec{v},\mathbb{I},t)[1+\Phi(\vec{x},\vec{v},\mathbb{I},t)] \tag{2.75}$$

Neglecting the dependence of Φ on $\vec{x}$ and t we can write

$$f(\vec{x},\vec{v},\mathbb{I},t) = f_0(\vec{x},\vec{v},\mathbb{I},t)\,(1+\Phi(\vec{v},\mathbb{I})) \tag{2.76}$$

Let us consider another trial linearized distribution $f_{1,T} = f_0[1+\Phi_T]$ satisfying following conditions

- Distribution $f_{1,T}$ satisfies the additive invariants property

$$\langle \boldsymbol{\Psi}, f_0\Phi_T\rangle = 0 \tag{2.77}$$

- Distribution $f_{1,T}$ is not the solution of the Boltzmann equation

$$\frac{\partial f_0}{\partial t} + \nabla_{\vec{x}}\cdot(\vec{v}f_0) \neq -f_0\mathbb{J}\Phi_T \tag{2.78}$$

- Distribution $f_{1,T}$ produces entropy

$$\frac{\partial \rho_s}{\partial t} + \nabla_{\vec{x}}\cdot(j_s) = R\int_{\mathbb{R}^+}\int_{\mathbb{R}^D} f_0\Phi_T\mathbb{J}\Phi_T d\vec{v}d\mathbb{I} = \sigma_T(\vec{v},t) \geq 0 \tag{2.79}$$

  This condition requires

$$\int_{\mathbb{R}^+}\int_{\mathbb{R}^D}\Phi_T\left[\frac{\partial f_0}{\partial t} + \nabla_{\vec{x}}\cdot(\vec{v}f_0)\right]d\vec{v}d\mathbb{I} = -\int_{\mathbb{R}^+}\int_{\mathbb{R}^N} f_0\Phi_T\mathbb{J}\Phi_T d\vec{v}d\mathbb{I} \tag{2.80}$$

Based on the properties of the linear operator $\mathbb{J}$ we get

$$\int_{\mathbb{R}^+}\int_{\mathbb{R}^\mathbb{D}} f_0(\Phi-\Phi_T)\mathbb{J}(\Phi-\Phi_T)d\vec{v}d\mathbb{I} \geq 0 \tag{2.81}$$

Since the collision operator is linear and self-adjoint [180] we get

$$\int_{\mathbb{R}^+}\int_{\mathbb{R}^\mathbb{D}} f_0\Phi\mathbb{J}\Phi d\vec{v}d\mathbb{I} \geq \int_{\mathbb{R}^+}\int_{\mathbb{R}^\mathbb{D}} f_0\Phi_T\mathbb{J}\Phi_T d\vec{v}d\mathbb{I} \tag{2.82}$$

This proves that the distribution which maximizes the entropy is the solution of Boltzmann equation or in other words the solution of the Boltzmann equation is in accordance with the principle of maximum entropy production [180]. This exercise motivates us to device a non-equilibrium thermodynamics based distribution function. In order to investigate further on the subject it is essential to interpret linear Boltzmann collision operator from non-equilibrium thermodynamics point of view. Consider linearized Boltzmann equation in terms of linearized collision operator $\mathbb{J}\Phi$ with distribution $f = f_0[1 + \Phi]$ as follows

$$\frac{1}{f_0}\left(\frac{\partial f_0}{\partial t} + \nabla_{\vec{x}} \cdot (\vec{v} f_0)\right) = -\mathbb{J}\Phi \tag{2.83}$$

Wang Chang and Uhlenbeck [51] , Grad[102], Ikenberry and Truesdell [125], Gross and Jackson [107], and others have done extensive investigations on linearized Boltzmann equation. Researchers have tried to interpret the linear collision operator by i) either considering its spectrum that includes eigenvalues for which $\mathbb{J}\Phi = \lambda\Phi$ has eigensolutions within the Hilbert space, ii) or decomposing it in terms of fluid dynamic gradients, iii) or expanding it in terms of thermodynamic forces. For example Wang Chang and Uhlenbeck [51] interpreted Φ in terms of orthonormalized set of eigenfunctions written in separable form as tensor spherical harmonic and radial eigenfunctions, these eigenfunctions for Maxwell molecules can be written in terms of Laguerre-Sonine polynomials. Grad [102] interpreted Φ in terms of Hermitian tensor polynomials whereas Gross and Jackson [107] used eigenvalue-theory of Wang Chang and Uhlenbeck [51] to construct kinetic model by replacing higher order eigenvalues by a suitable constant at each lower order approximation. Loyalka [168] used linearized Boltzmann equation with perturbation based on pressure and temperature gradients to investigate the Onsager reciprocal relationship for slip flows. Lang [147] decomposed the perturbation into three parts and made use of variational technique to calculate symmetric Onsager's matrix for slip flows. Zhdanov and Roldughin [300] have investigated linkage between kinetic theory and non-equilibrium thermodynamics by expanding Φ in terms of tensor spherical harmonic and Sonine polynomials while McCourt *et al.* [186] incorporated non-equilibrium thermodynamics by interpreting Φ in term of flux and its conjugate thermodynamic force.

2.4.4 Eu's modified moment method.

In conventional moment method entropy, macroscopic variables are treated at par and Boltzmann equation is solved by expanding the distribution function. It is not guaranteed that this approximate distribution function will be able to meet all the requirements of thermodynamics. Eu [83] developed modified moment method in which the distribution function depends on microscopic molecular variables as well as entropy derivatives called as Gibbs variables. In Eu's modified moment method the distribution function depends on the thermodynamic information on the entropy surface, hence a close connection can be established between kinetic theory, transport processes, and irreversible thermodynamics. Eu's theory requires consistency condition to bring out the extended Gibbs relation for entropy change and expressions of thermodynamic forces. This consistency condition is expressed in terms of partial differential equation for entropy density.

2.4.5 Potential area of research in non-equilibrium thermodynamics.

Most of the research which links non-equilibrium thermodynamics with kinetic theory is still in the realm of physics. Approximate solutions provided by kinetic theory has to comply with requirements of non-equilibrium thermodynamics like following Onsager's principle and maximization of entropy production under constraint imposed due to conservation laws. *Thus, non-equilibrium thermodynamics provides a tool which can be used to check the correctness of the kinetic theory based flow solver. This opens up a major potential research area in incorporating phenomenological theory of non-equilibrium thermodynamics into kinetic theory based flow solver using the conventional moment method.*

2.5 Upwind methods

Gudunov and Boltzmann schemes are broadly two approaches to solve hyperbolic system of conservation laws. Godunov scheme uses sound waves and streamlines to propagate information while Boltzmann scheme uses trajectories of individual particles and its distribution [117, 279]. Godunov scheme relies on solving

a Riemann's initial value problem with characteristics of the Euler equation. In this approach interaction amongst the neighboring cells is through discrete, finite amplitude waves. The numerical technique using this incoming and the outgoing waves is called the *flux differencing splitting* scheme. Examples are the methods of Roe [229] and Osher [207]. While, in Boltzmann based approach interaction amongst the neighboring cells is through movement of the particles or its velocity distribution. The numerical technique based on this movement of incoming and outgoing particles is called *flux-vector splitting* scheme. One of the earliest example is the Beam scheme of Sanders and Prendergast [236] and Steger and Warming [256]. When it comes to resolution of boundary layers and calculation of adiabatic wall temperature the flux difference splitting is less dissipative compared to flux vector splitting [281].

2.5.1 Flux Vector Splitting Schemes

Sanders and Prendergast [236] developed Beam scheme for astrophysical computations which is based on velocity distribution consisting of delta-functions

$$f(v) = \rho_{sb}\delta[v - (u - u_\sigma)] + (\rho - 2\rho_{sb}\delta(v - u) + \rho_{sb}\delta[v - (u + u_\sigma)] \tag{2.84}$$

In the above equation ρ is the density, ρ_{sb} is the density of the particles in each side beam, u is the mass averaged velocity, and u_σ is a dispersion velocity greater than the sound velocity. For a special case when dispersion velocity equals the speed of sound the flux splitting becomes identical to the scheme of Steger and Warming [256]. Beam or Steger and Warming fluxes are not differentiable in sonic and stagnation points.

2.5.1.1 Flux Vector Splitting Schemes for Euler equations

Euler equation can be seen in two forms i)conservative form, ii)symmetric hyperbolic form. Consider Euler equation in conservative form as follows

$$\frac{\partial \boldsymbol{U}}{\partial t} + \frac{\partial \boldsymbol{G}(\boldsymbol{U})}{\partial \vec{x}} = 0 \tag{2.85}$$

where $\boldsymbol{U}$ is the state vector and $\boldsymbol{G}(\boldsymbol{U})$ is the flux vector. Euler equation satisfies the homogeneity property

$$\boldsymbol{G}(\boldsymbol{U}) = \boldsymbol{A}\boldsymbol{U} \tag{2.86}$$

where Jacobian matrix $\boldsymbol{A}$ is given as

$$\boldsymbol{A} = \frac{\partial \boldsymbol{G}(\boldsymbol{U})}{\partial \boldsymbol{U}} \tag{2.87}$$

The matrix $\boldsymbol{A}$ has real eigenvalues λ_i and complete set of eigenvectors. Flux vector splitting requires splitting flux into two components $\boldsymbol{G}(\boldsymbol{U})^+$ and $\boldsymbol{G}(\boldsymbol{U})^-$ such that

$$\boldsymbol{G}(\boldsymbol{U}) = \boldsymbol{G}(\boldsymbol{U})^+ + \boldsymbol{G}(\boldsymbol{U})^- \tag{2.88}$$

Because of homogeneity property splitting is easily accomplished by splitting the Jacobian matrix $\boldsymbol{A}$, which in turn is split by splitting of eigenvalues $\lambda_i{=}\lambda_i^+{+}\lambda_i^{-1}$, such that Jacobian $\partial \boldsymbol{G}^+/\partial \boldsymbol{U}$ has all positive eigenvalues and Jacobian $\partial \boldsymbol{G}^-/\partial \boldsymbol{U}$ has all the negative eigenvalues.
For approximating a first order system of conservation laws we require continuous differentiability of fluxes. Scheme of van Leer [279] provides split fluxes which are continuously differentiable, flux vector splitting can be used in a higher MUSCL-type code and can be considered as an approximate Riemann solver such as Roe's [229] and Osher's [207].

2.5.1.2 Flux Vector Splitting and Boltzmann type schemes

The symmetry of the Jacobian matrix occurring in the symmetric hyperbolic form establishes connection between symmetrizability, entropy function, and Roe linearization [116]. From physics point of view according to van Leer [280] the velocity distribution is not chosen to be Maxwellian, instead as a simplification it is assumed to be an instantaneous "equilibrium" uniform distribution with equivalent mass, momentum and energy as shown in figure 2.10. Solution of flux vector splitting for Euler equations can be interpreted as a solution of collisionless Boltzmann equation [117, 279, 280] and flux vector splitting is considered as a natural consequence of regarding a fluid as an ensemble of particles.

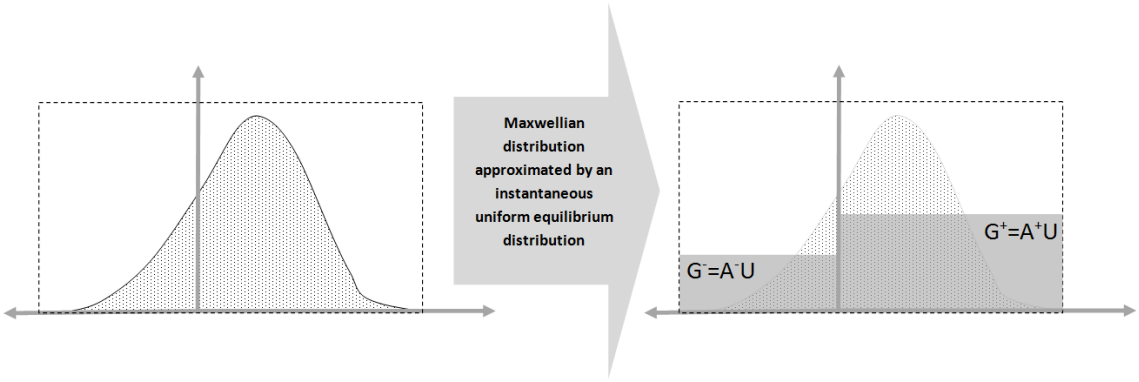

Figure 2.10: Flux vector splitting as a simplified solution of collisionless Boltzmann equation.

2.5.1.3 Dissipative properties of Flux Vector Splitting Schemes

Consider net traverse-momentum flux across the boundary layer using flux-vector splitting[280] as

$$\begin{aligned}\rho u_y u_x(i,j) &= G^{+}_{mass} u_x(i,j-1) + G^{-}_{mass} u_x(i,j+1) \\ &= (G^{+}_{mass}(i,j-1) + G^{-}_{mass}(i,j+1)) \, \tfrac{u_x(i,j-1)+u_x(i,j+1)}{2} \\ &- (G^{+}_{mass}(i,j-1) - G^{-}_{mass}(i,j+1)) \, \tfrac{u_x(i,j-1)-u_x(i,j+1)}{2}\end{aligned} \tag{2.89}$$

where $(i, j+1)$ denotes the top cell and $(i, j-1)$ denotes the bottom cell. When the net flux G_{mass}=$G^{+}_{mass}(i,j-1) + G^{-}_{mass}(i,j+1)$ vanishes the second term in the traverse momentum flux is still there and it becomes the cause of numerical diffusion. This dissipative property of flux vector splitting give rise to broadening of attached boundary layers and inaccurate adiabatic wall temperatures as compared to numerical solutions obtained with flux difference splitting of Roe [229] and Osher [207].

2.5.2 Kinetic Schemes

A few years later to the Beam scheme [236] Harten *et al.* [117] developed an approach to construct a scheme for general hyperbolic systems of conservation laws. Equilibrium flux method (EFM) of Pullin [221] initiated the development of kinetic schemes for compressible Euler system based on Maxwellian distribution. Just after development of EFM, Reitz [227] developed a kinetic scheme

using Boltzmann equation. Deshpande [70] proposed Kinetic Flux Vector Splitting (KFVS) scheme which was further developed by Mandal and Deshpande [179] for solving Euler problems. At the same time Perthame [214] developed kinetic scheme and Prendergast and Xu [219] proposed a scheme based on BGK simplification of the Boltzmann equation. Xu [293] and May *et al.* [185] modified and further developed this scheme. The exact solution of Boltzmann equation with BGK model $J(f, f_0) = -(f - f_0)/t_R$ is

$$f = \int_{\mathbb{R}^+} Exp(-\acute{t}/t_R) f_0(\vec{v}, \vec{x} - \vec{v}\acute{t}, t - \acute{t}) t_R^{-1} d\acute{t} \tag{2.90}$$

Physically it means that along the trajectory in the phase space, particles are replaced exponentially by particles in equilibrium with characteristics time t_R. The gas kinetic scheme of Xu [293, 294] uses this method of characteristics using BGK model and thus it differs from the KFVS scheme mainly in the inclusion of particle collisions in the gas evolution stage as it updates the distribution. Numerical fluxes are calculated in the gas evolution stage as time dependent gas distribution function is computed at the cell interface by making use of local integral solution of the BGK model. Raghurama and Deshpande [226] proposed a scheme based on peculiar velocity based upwind method which splits the flux vector into acoustic and the transport part. Macrossan [175] proposed a new method called the Relaxation Time Simulation Method (RTSM) based on Boltzmann equation with BGK kinetic model. Macrossan's RTSM (relaxation time simulation method) uses method of characteristics and BGK model to update distribution function, $f(\Delta t)$ after time $t = \Delta t$ as

$$f(\Delta t) = Exp(-\Delta t/t_R) f(0) - (1 - Exp(-\Delta t/t_R)) f_0 \tag{2.91}$$

where $f(0) = f(t = 0)$ is the initial distribution established by the streaming or convection phase just before the simulation of collision phase. In the collision phase the distribution function relaxes towards equilibrium Maxwellian distribution, f_0 after sufficient collisions with a time constant t_R. This pseudo-collision step or the relaxation step actually carries out the step of redistribution of the particles such that the resulting distribution is a mixture of the initial distribution, $f(0)$ and the final equilibrium distribution, f_0. Wang *et al.* [285] further

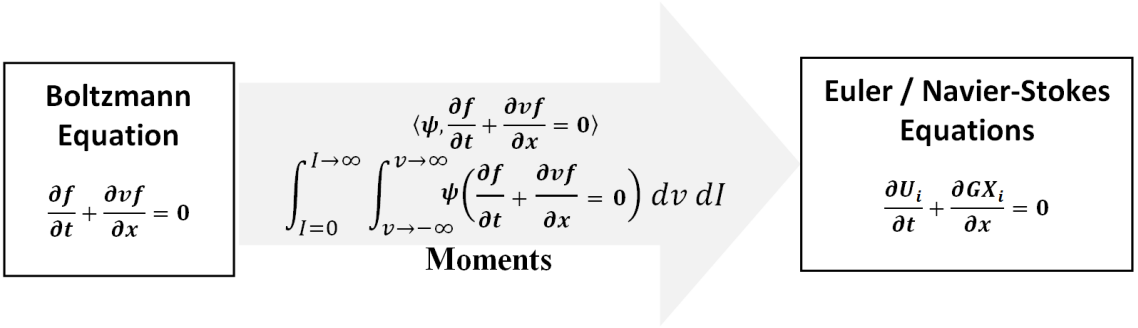

Figure 2.11: Moments of the Boltzmann equation.

improved RTSM by introducing the internal energy relaxation scheme. KFVS scheme for the viscous flows was proposed by Chou and Baganoff [54]. KFVS is based on moment-method strategy which operates in two levels: i) the Boltzmann level where upwind implementation is done, ii) the macroscopic (Euler or Navier-Stokes) level at which the state update operates. KFVS for viscous flows applies Courant splitting at the Boltzmann level followed by moment-method strategy using Chapman-Enskog distribution to obtain split Navier-Stokes fluxes based on the signs of the molecular velocity. Mahendra [177] used KFVS method proposed by Chou and Baganoff [54] for simulating compressible, viscous flows. KFVS has also been applied to quantum gas dynamics for Bose-Einstein and Fermi-Dirac gases [296].

2.5.3 Kinetic Flux Vector Splitting (KFVS)

Kinetic schemes exploits the connection between the Boltzmann equation and the governing conservation equations at the macroscopic level. As illustrated in Fig. 2.11 the moments of the Boltzmann equation lead to the Euler/ Navier-Stokes equations. Kinetic Flux Vector Splitting (KFVS) scheme [54, 70, 179] involves two steps : i)in the first step the Boltzmann equation is rendered into an upwind discretized form, ii)in the second step moments of the upwind discretized Boltzmann equation are taken to obtain upwind scheme for the macroscopic conservation equations. Fig.2.12 shows the two steps, implementation of upwinding in the Boltzmann (microscopic level) and mapping to the Euler or Navier-Stokes level (macroscopic level at which the state update operates) by taking $\mathbf{\Psi}$-moments.

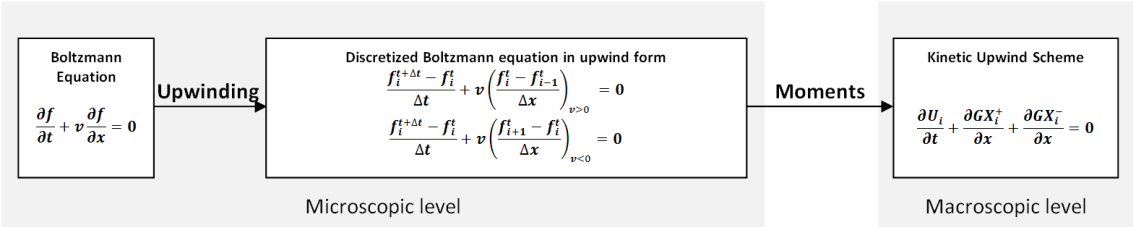

Figure 2.12: Kinetic Flux Vector Splitting Scheme operating at two levels.

Consider Boltzmann equation for one dimensional case in inertial frame of reference

$$\frac{\partial f}{\partial t} + v\frac{\partial f}{\partial x} = 0 \tag{2.92}$$

The 1-D Boltzmann equation can be interpreted as a linear scalar advection equation where $f(x,t)$ is a scalar function v is a positive constant. Consider that the spatial domain is unbounded i.e. $-\infty < x < \infty$, with initial condition being $f(x,0) = g(x)$. The solution to this linear advection equation [142] is

$$f(x, \Delta t) = g(x - v\Delta t) \tag{2.93}$$

The solution can be interpreted as a distribution similar to a wave traveling with speed v without a change of form. Similar to linear advection equation the propagation of information will depend on the signs of the molecular velocity v. For example when $v > 0$ then the information comes from the left of the node i i.e. solution at any point x_i is determined from the solution in the region $x < x_i$ at previous time level. Similarly, when $v < 0$ then the information comes from the right side of the node i i.e. solution at any point x_i is determined from the solution in the region $x > x_i$ at previous time level. The one dimensional Boltzmann equation in its upwind discretized form can be written as

$$\begin{array}{l} \frac{f_i^{t+\Delta t} - f_i^t}{\Delta t} + v\frac{f_i^t - f_{i-1}^t}{\Delta x} = 0 \quad if \quad v > 0 \\ \frac{f_i^{t+\Delta t} - f_i^t}{\Delta t} + v\frac{f_{i+1}^t - f_i^t}{\Delta x} = 0 \quad if \quad v < 0 \end{array} \tag{2.94}$$

The upwind discretized form in CIR split-form[1] can be written as

$$\frac{f_i^{t+\Delta t} - f_i^t}{\Delta t} + \frac{v + |v|}{2}\frac{f_i^t - f_{i-1}^t}{\Delta x} + \frac{v - |v|}{2}\frac{f_{i+1}^t - f_i^t}{\Delta x} = 0 \tag{2.95}$$

[1]In CIR (Courant, Isaacson and Rees) split-form $v = \frac{v+|v|}{2} + \frac{v-|v|}{2}$

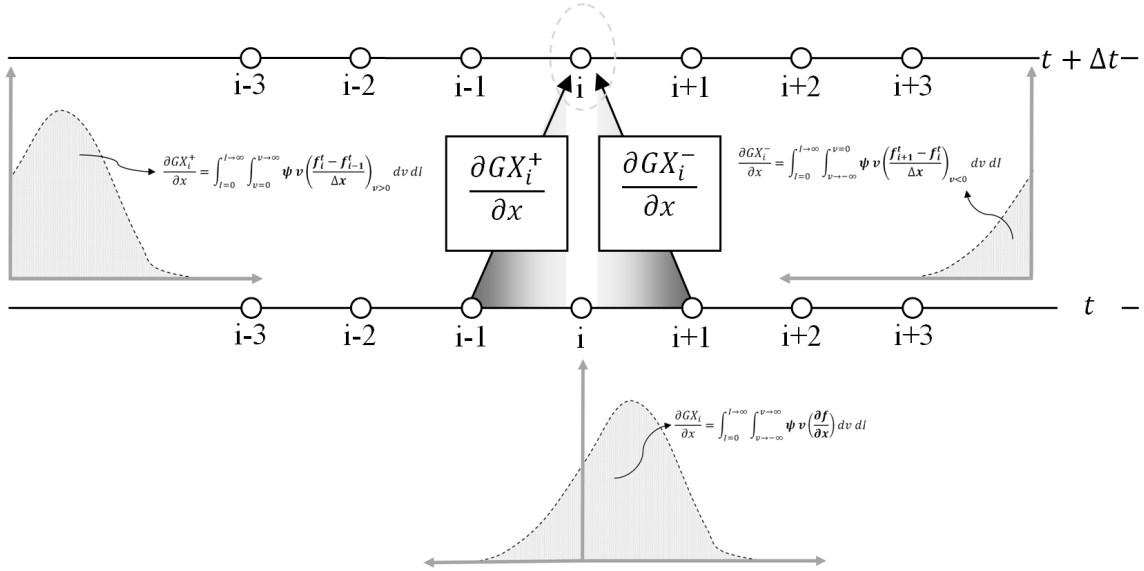

Figure 2.13: Kinetic Flux Vector Splitting based on moments of upwind discretized Boltzmann equation.

When scalar function f is a function of particle velocity v then the function needs splitting while undergoing upwinding. Fluid is regarded as an ensemble of particles moving in forward as well as in backward coordinate directions leading to split fluxes of mass, momentum and energy into positive fluxes (for positive velocity) and negative fluxes (for negative velocity). KFVS can also be interpreted as construction of the distribution function at time $t+\Delta t$ in a fluid domain based on half range distribution as follows

$$f_i^{t+\Delta t} = f_i^t - \Delta t \left[\left(\frac{\partial v f_i^+}{\partial x} \right)^t_{0<v<+\infty} + \left(\frac{\partial v f_i^-}{\partial x} \right)^t_{-\infty<v<0} \right] \tag{2.96}$$

where f_i^+ is the half-range first order distribution function for $0 < v < +\infty$ and f_i^- is the half-range distribution function for $-\infty < v < 0$. Consider $f = f_0$ as a Maxwellian distribution for one-dimensional case written as

$$f = f_0 = \rho \sqrt{\frac{\beta}{\pi}} exp\left(-\beta(v-u)^2 - \frac{\mathbb{I}}{\mathbb{I}_o} \right) \tag{2.97}$$

The moment function for one-dimensional case in terms of molecular velocity v and internal energy parameter $\mathbb{I}$ is

$$\boldsymbol{\Psi}(v,\mathbb{I}) = \begin{bmatrix} 1 \\ v \\ \mathbb{I} + \frac{1}{2}v^2 \end{bmatrix} \tag{2.98}$$

Taking moments of Boltzmann equation in upwind discretized form leads to

$$\frac{\boldsymbol{U}_i(t+\Delta t) - \boldsymbol{U}_i(t)}{\Delta t} + \frac{\boldsymbol{GX}_i^{+}(t) - \boldsymbol{GX}_{i-1}^{+}(t)}{\Delta x} + \frac{\boldsymbol{GX}_{i+1}^{-}(t) - \boldsymbol{GX}_i^{-}(t)}{\Delta x} = 0 \tag{2.99}$$

where

$$\boldsymbol{U} = \langle \boldsymbol{\Psi}, f \rangle = \int_0^{+\infty}\int_{-\infty}^{+\infty} \boldsymbol{\Psi} f dv d\mathbb{I} = \begin{bmatrix} \rho \\ \rho u \\ \rho E \end{bmatrix} \tag{2.100}$$

where $E = RT/(\gamma-1) + \frac{1}{2}u^2$, u is the fluid velocity vector and γ is the specific heat ratio. Fig. 2.13 shows the schematic of kinetic flux vector splitting method. The split fluxes are obtained as

$$\boldsymbol{GX}^{+} = \left\langle \boldsymbol{\Psi}, v f^{+} \right\rangle = \int_0^{+\infty}\int_0^{+\infty} \boldsymbol{\Psi} \frac{v+|v|}{2} f dv d\mathbb{I} \tag{2.101}$$

$$\boldsymbol{GX}^{-} = \left\langle \boldsymbol{\Psi}, v f^{-} \right\rangle = \int_0^{+\infty}\int_{-\infty}^{0} \boldsymbol{\Psi} \frac{v-|v|}{2} f dv d\mathbb{I} \tag{2.102}$$

The expression for split fluxes $\boldsymbol{GX}^{\pm}$ are

$$\boldsymbol{GX}^{\pm} = \begin{bmatrix} \frac{1}{2}(1 \pm Erf(u\sqrt{\beta}))\rho u \pm \rho \left(\frac{Exp(-\beta u^2)}{2\sqrt{\pi\beta}}\right) \\ \frac{1}{2}(1 \pm Erf(u\sqrt{\beta}))(p + \rho u^2) \pm \rho u \left(\frac{Exp(-\beta u^2)}{2\sqrt{\pi\beta}}\right) \\ \frac{1}{2}(1 \pm Erf(u\sqrt{\beta}))(pu + \rho u E) \pm \left(\frac{p}{2} + \rho E\right)\left(\frac{Exp(-\beta u^2)}{2\sqrt{\pi\beta}}\right) \end{bmatrix} \tag{2.103}$$

2.5.4 Modified KFVS for Euler equations

In modified KFVS for Euler equations, Anil *et al.* [7] introduce dissipation control function in order to resolve the discontinuity more sharply with less dissipation. The order of accuracy can be improved with the proper choice of dissipation

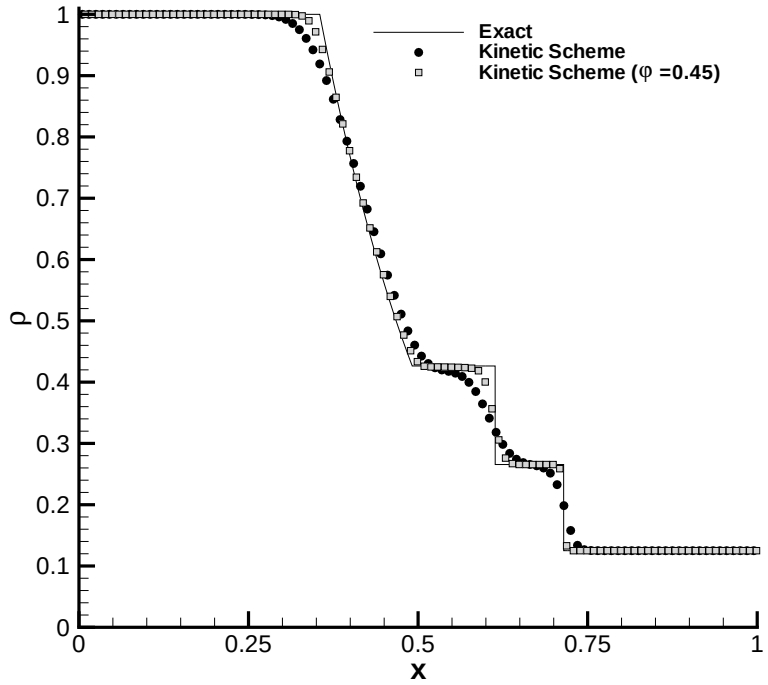

Figure 2.14: Comparison of density versus length plot with exact solution for kinetic scheme without dissipation control function and with dissipation control function, φ=0.45.

control function φ such that $0 < \varphi < 1$. Boltzmann equation in this modified Courant splitting is expressed as

$$\frac{f_i^{t+\Delta t} - f_i^t}{\Delta t} + \frac{v + \varphi|v|}{2}\left(\frac{f_i^t - f_{i-1}^t}{\Delta x}\right) + \frac{v - \varphi|v|}{2}\left(\frac{f_{i+1}^t - f_i^t}{\Delta x}\right) = 0 \tag{2.104}$$

Modified partial differential equation (MPDE) analysis for one dimensional Boltzmann equation reveals a numerical kinetic viscosity as

$$\mu_{num} = \frac{\Delta x}{2}\sqrt{\frac{\beta}{\pi}}\int_{\mathbb{R}^+}\int_{\mathbb{R}} |v|\,\varphi e^{-\beta(v-u)^2} dv d\mathbb{I} \tag{2.105}$$

With $\varphi = 0$ the formulation becomes central difference and with $\varphi = 1$ the formulation is in the KFVS upwind form. For the case when dissipation control function $\varphi = 1$ the numerical viscosity is maximum when molecular velocity v is closed to u. Analysis also revealed that particles with large peculiar velocity contribute little to the dissipation, hence Anil *et al.* [7] considered dissipation control function, φ to be function of molecular velocity.

2.5.4.1 One dimensional shock tube problem

Consider 1-D shock tube problem of unit length with a diaphragm at x_o =0.5 which separates left and the right regions which have different densities and pressure. The value of the left state is denoted by $(\rho, u, p)_L$=$(1.0, 0, 1.0)_L$, and the right state by $(\rho, u, p)_R$=$(0.125, 0, 0.1)_R$. The test case was simulated for t=0.1225 seconds. The computational domain of unit length with 200 mesh points and CFL no. of 0.9 with air as motive fluid ($\gamma = 1.4$) was used to evaluate 1-D shock test case. As explained earlier, the state update equation for kinetic scheme without dissipation control function is

$$\boldsymbol{U}_i(t + \Delta t) = \boldsymbol{U}_i(t) - \Delta t\left(\frac{\boldsymbol{GX}_i^+(t) - \boldsymbol{GX}_{i-1}^+(t)}{\Delta x} + \frac{\boldsymbol{GX}_{i+1}^-(t) - \boldsymbol{GX}_i^-(t)}{\Delta x}\right) \tag{2.106}$$

where expressions of $\boldsymbol{GX}^{\pm}$ are given by equation 2.103. In case of modified kinetic scheme the state update is written as

$$\boldsymbol{U}_i(t + \Delta t) = \boldsymbol{U}_i(t) - \Delta t\left(\frac{\tilde{\boldsymbol{GX}}_i^+(t) - \tilde{\boldsymbol{GX}}_{i-1}^+(t)}{\Delta x} + \frac{\tilde{\boldsymbol{GX}}_{i+1}^-(t) - \tilde{\boldsymbol{GX}}_i^-(t)}{\Delta x}\right) \tag{2.107}$$

The fluxes $\tilde{\boldsymbol{GX}}_i^{\pm}$ are based on dissipation control parameter φ given as

$$\tilde{\boldsymbol{GX}}^{\pm} = \frac{1}{2}\left[(\boldsymbol{GX}^{+} + \boldsymbol{GX}^{-}) \pm \varphi(\boldsymbol{GX}^{+} - \boldsymbol{GX}^{-})\right] \tag{2.108}$$

Figure 2.14 shows the exact solution of density variation with respect to length and its comparison with kinetic scheme without dissipation control function and with dissipation control function, φ=0.45.

2.5.5 Kinetic method and its connection with other upwind schemes

There are two different ways of incorporating hyperbolicity into numerical schemes. The first one is *flux difference splitting* where the flow variables which are held constant within a cell see a jump as it crosses a cell face. Riemann solver breaks these jumps into waves thus making cells interact with one and another through waves. In the second approach flux vector $\boldsymbol{G}$ is split into two parts $\boldsymbol{G}^{+}$, $\boldsymbol{G}^{-}$ such that the Jacobian $\partial\boldsymbol{G}^{+}/\partial\boldsymbol{U}$ has all positive eigenvalues and $\partial\boldsymbol{G}^{-}/\partial\boldsymbol{U}$ has all negative eigenvalues. Consider one dimensional Euler equation in primitive variables cast in matrix form as follows

$$\frac{\partial \boldsymbol{V}}{\partial t} + \tilde{\boldsymbol{A}}^{\mathcal{T}}\frac{\partial \boldsymbol{V}}{\partial x} + \tilde{\boldsymbol{A}}^{\mathcal{A}}\frac{\partial \boldsymbol{V}}{\partial x} = 0 \tag{2.109}$$

where,

$$\boldsymbol{V} = \begin{bmatrix} \rho \\ u \\ p \end{bmatrix}; \quad \tilde{\boldsymbol{A}}^{\mathcal{T}} = \begin{bmatrix} u & 0 & 0 \\ 0 & u & 0 \\ 0 & 0 & u \end{bmatrix}; \quad \tilde{\boldsymbol{A}}^{\mathcal{A}} = \begin{bmatrix} 0 & \rho & 0 \\ 0 & 0 & 1/\rho \\ 0 & \gamma p & 0 \end{bmatrix} \tag{2.110}$$

The matrix $\tilde{\boldsymbol{A}}^{\mathcal{T}}$ represents the transport part due to advection of fluid element along particle path $\tilde{\boldsymbol{A}}^{\mathcal{A}}$ represents the propagation of acoustic waves due to dilatation or contraction of fluid elements. The eigenvalues associated with the acoustic part of the matrix $\tilde{\boldsymbol{A}}^{\mathcal{A}}$ is $\lambda(\tilde{\boldsymbol{A}}^{\mathcal{A}})$=$0, \pm c$ where sonic speed $c = (\gamma p/\rho)^{1/2}$. Splitting of particle like transport part and wave like acoustic part leads to wave-particle splitting [71].

To understand this from kinetic theory point of view requires taking moments of Boltzmann equation written in terms of peculiar velocity, $c = v - u$, where v is the

molecular velocity and u is the macroscopic fluid velocity. Consider Boltzmann equation for one dimensional case in inertial frame of reference written in terms of peculiar velocity, as follows

$$\frac{\partial f}{\partial t} + u\frac{\partial f}{\partial x} + c\frac{\partial f}{\partial x} = 0 \tag{2.111}$$

When $f = f_0$ as a Maxwellian distribution for one-dimensional case, by taking moments we get one dimensional Euler equation in terms of transport and acoustic flux as

$$\frac{\partial \boldsymbol{U}}{\partial t} + \frac{\partial \boldsymbol{GX}^{\mathcal{T}}}{\partial x} + \frac{\partial \boldsymbol{GX}^{\mathcal{A}}}{\partial x} = 0 \tag{2.112}$$

where $\boldsymbol{U}$ represents the conserved vector, $\boldsymbol{GX}^{\mathcal{T}}$ the transport part of the flux vector, $\boldsymbol{GX}^{\mathcal{A}}$ the acoustic part of the flux vector given as

$$\boldsymbol{GX}^{\mathcal{T}} = \begin{bmatrix} \rho u \\ \rho u^2 \\ \rho u E \end{bmatrix}; \quad \boldsymbol{GX}^{\mathcal{A}} = \begin{bmatrix} 0 \\ p \\ pu \end{bmatrix} \tag{2.113}$$

The motion of the fluid can be thought as composed of u-part which is orderly, deterministic, unidirectional particle like and the c-part which is random and multi-directional and wave like due to thermal agitation following $N(0, 1/(2\beta))$ i.e. Normal distribution with zero mean and variance equal to $1/(2\beta)$. The Jacobian for $\boldsymbol{A}^{\mathcal{T}}$ and $\boldsymbol{A}^{\mathcal{A}}$ for the transport flux and acoustic flux can be written as

$$\begin{aligned} \boldsymbol{A}^{\mathcal{T}} &= \frac{\partial \boldsymbol{GX}^{\mathcal{T}}}{\partial \boldsymbol{U}} = \begin{bmatrix} 0 & 1 & 0 \\ -u^2 & 2u & 0 \\ -\frac{eu}{\rho} & \frac{e}{\rho} & u \end{bmatrix} \\ \boldsymbol{A}^{\mathcal{A}} &= \frac{\partial \boldsymbol{GX}^{\mathcal{A}}}{\partial \boldsymbol{U}} = \begin{bmatrix} 0 & 0 & 0 \\ \frac{(\gamma-1)}{2}u^2 & -(\gamma-1)u & (\gamma-1) \\ -\frac{pu}{\rho} + \frac{(\gamma-1)}{2}u^3 & -\frac{p}{\rho} - (\gamma-1)u^2 & (\gamma-1)u \end{bmatrix} \end{aligned} \tag{2.114}$$

The eigenvalues of the matrices are $\lambda(\boldsymbol{A}^{\mathcal{T}}) = [u, u, u]$ and $\lambda(\boldsymbol{A}^{\mathcal{A}}) = \left[0 \pm [(\gamma-1)/\gamma]^{\frac{1}{2}}\right]$. Due to mixed eigenvalue of acoustic flux the task of enforcing upwinding is complex. Hence upwind schemes can be constructed by carrying out separate treatment for transport and acoustic flux. For example scheme can do upwind differencing for the transport flux and apply splitting to the acoustic flux. Convection

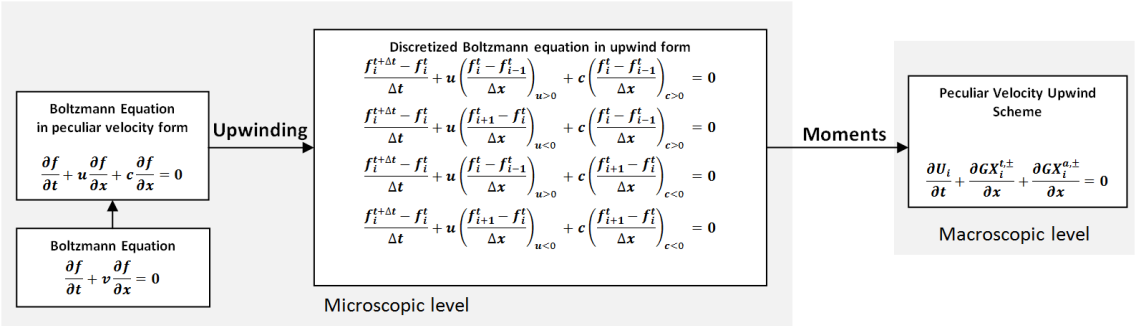

Figure 2.15: Peculiar Velocity upwind method operating at two levels.

Upwind and Split Pressure (CUSP) scheme of Jameson [126] and Advective Upstream Splitting Method (AUSM) of Liou and Steffen [155] split flux into two separate components i) convective which is similar to transport flux, and ii) pressure flux which is similar to acoustic flux and then each one undergoes upwinding. From kinetic theory point of view CUSP and AUSM schemes are related to upwind treatment of transport flux which is obtained using the macroscopic velocity u and acoustic flux which is obtained using peculiar velocity c.

2.5.6 Peculiar Velocity based Upwind Method (PVU)

Peculiar velocity based upwind (PVU) method [226] involves three steps : i) in the first step Boltzmann equation is written in terms of peculiar velocity , ii) in the second step Boltzmann equation is rendered into an upwind discretized form, iii) in the third step moments of the upwind discretized Boltzmann equation are taken to obtain upwind scheme for the macroscopic conservation equations. In KFVS upwind method propagation of information was based on the signs of the molecular velocity v, whereas in peculiar velocity based upwind (PVU) method propagation of information is based on the signs of the fluid velocity u and peculiar velocity c. Fig.2.15 shows the three steps, writing Boltzmann equation in terms of peculiar velocity, implementation of upwinding in the Boltzmann (microscopic level) and mapping to the Euler or Navier-Stokes level (macroscopic level at which the state update operates) by taking $\mathbf{\Psi}$-moments. The upwind discretized

form in CIR split-form can be written as

$$\begin{array}{l}\frac{f_i^{t+\Delta t}-f_i^t}{\Delta t}+\frac{u+|u|}{2}\left(\frac{f_i^t-f_{i-1}^t}{\Delta x}\right)+\frac{u-|u|}{2}\left(\frac{f_{i+1}^t-f_i^t}{\Delta x}\right)\\ +\frac{c+|c|}{2}\left(\frac{f_i^t-f_{i-1}^t}{\Delta x}\right)+\frac{c-|c|}{2}\left(\frac{f_{i+1}^t-f_i^t}{\Delta x}\right)=0\end{array} \tag{2.115}$$

Taking moments of Boltzmann equation in upwind discretized form leads to

$$\begin{array}{l}\frac{\boldsymbol{U}_i(t+\Delta t)-\boldsymbol{U}_i(t)}{\Delta t}+\frac{\boldsymbol{GX}_i^{\mathcal{T},+}(t)-\boldsymbol{GX}_{i-1}^{\mathcal{T},+}(t)}{\Delta x}+\frac{\boldsymbol{GX}_{i+1}^{\mathcal{T},-}(t)-\boldsymbol{GX}_i^{\mathcal{T},-}(t)}{\Delta x}\\ +\frac{\boldsymbol{GX}_i^{\mathcal{A},+}(t)-\boldsymbol{GX}_{i-1}^{\mathcal{A},+}(t)}{\Delta x}+\frac{\boldsymbol{GX}_{i+1}^{\mathcal{A},-}(t)-\boldsymbol{GX}_i^{\mathcal{A},-}(t)}{\Delta x}=0\end{array} \tag{2.116}$$

where $\boldsymbol{GX}^{\mathcal{T},\pm}$ and $\boldsymbol{GX}^{\mathcal{A},\pm}$ are given as

$$\boldsymbol{GX}^{\mathcal{T},+}=\left\langle\boldsymbol{\Psi},\frac{u+|u|}{2}f\right\rangle=\int_0^{+\infty}\int_0^{+\infty}\Psi\frac{u+|u|}{2}f\,dv\,d\mathbb{I} \tag{2.117}$$

$$\boldsymbol{GX}^{\mathcal{T},-}=\left\langle\boldsymbol{\Psi},\frac{u-|u|}{2}f\right\rangle=\int_0^{+\infty}\int_{-\infty}^{0}\Psi\frac{u-|u|}{2}f\,dv\,d\mathbb{I} \tag{2.118}$$

$$\boldsymbol{GX}^{\mathcal{A},+}=\left\langle\boldsymbol{\Psi},\frac{c+|c|}{2}f\right\rangle=\int_0^{+\infty}\int_0^{+\infty}\Psi\frac{c+|c|}{2}f\,dv\,d\mathbb{I} \tag{2.119}$$

$$\boldsymbol{GX}^{\mathcal{A},-}=\left\langle\boldsymbol{\Psi},\frac{c-|c|}{2}f\right\rangle=\int_0^{+\infty}\int_{-\infty}^{0}\Psi\frac{c-|c|}{2}f\,dv\,d\mathbb{I} \tag{2.120}$$

Peculiar velocity based method uses both the wave and particle model of the fluid flow.

2.5.6.1 PVU method for viscous flows

Peculiar Velocity based Upwind (PVU) method can be implemented into two forms PVU1 and PVU2 which differ from each other based on sequence of integration and differencing of the acoustic term. While implementing PVU2 scheme for the acoustic term, the integration step is completed first followed by the differencing step. The split acoustic flux expressions of PVU2 scheme do not involve any error functions or exponentials [225] hence PVU2 method is followed while implementing Peculiar Velocity based Upwind. The upwind viscous fluxes derived do not follows non-equilibrium thermodynamics, for example x-component of acoustic split mass flux can be derived as

$$GX^{\mathcal{A}^{\pm}}_{1}=\pm\frac{\rho}{2\sqrt{\pi\beta}}\mp\frac{\rho}{4\beta\sqrt{\pi\beta}}\tau_{xx} \tag{2.121}$$

The viscous part of the acoustic mass flux only contains terms of shear stress tensor the term associated with heat flux vector is missing. For effective capture of cross phenomena of thermal transpiration and the mechanocalorific effect the viscous part should also contain the terms of heat flux vector. *PVU method fails to comply with the principles of non-equilibrium thermodynamics.*

2.5.7 Kinetic method for strongly rotating flows.

For strongly rotating viscous compressible flows the gas is held under rigid-body rotation, in such flows the effective acceleration in the radial direction dominates the Earth's gravitational acceleration. There is an exponential density rise in the radial direction towards the periphery with thin boundary layers and a rarefied inner core [26, 40]. Numerical modeling of high speed rotating flows is a challenge as the regime changes from continuum at the periphery, slip, transition to non-continuum in the central core. Such a flow is of considerable interest and importance in the field of hydrodynamic bearings, rotating machinery and pumps. Numerical studies performed by researchers Dickinson and Jones [76], Park and Hyun [210] and Babarsky *et al.* [19] focused more on perturbative flows arising out of basic state of rigid body rotation. Most of the researchers have described such a strongly rotating flows using continuum hydrodynamics even though a large portion of the volume is rendered rarefied near to the free molecular region. It was first shown by Johnson and Stopford [128] that flow predicted by kinetic theory differs from the results obtained using continuum hydrodynamics. Johnson and Stopford [128] have used the Boltzmann equation in the presence of external force instead of Boltzmann equation with both centrifugal and Coriolis terms. Based on the Boltzmann equation Müller [195] concluded that in rotating systems a radial temperature gradient apart from leading to the radial heat flux also causes tangential heat flux which are related at the level of the Burnett approximation. Sharipov and Kremer[243] and Sharipov *et al.* [244] have investigated transport phenomena through a fluid confined between two coaxial cylinders over a wide range of gas rarefaction and observed that results based on kinetic approach do not follow from the Navier-Stokes equations of continuum mechanics. Taheri and Struchtrup [265] have used continuum approach as well

as regularized 13-moment (R13) equations to study the effects of rarefaction in micro flows between two rotating coaxial cylinders.
Rossby number and Ekman number are the two dimensionless numbers characterizing the rotating flow. The Rossby number is defined as the ratio between the inertial and the Coriolis forces, and the Ekman number is defined as the ratio of the viscous forces to the Coriolis forces. To understand rotating flow one needs to understand the rotating frame of reference as compared to the inertial frame of reference. The Boltzmann equation can be solved in two reference frames: i) non-inertial frame i.e. frame rotating with the body and ii) inertial frame i.e. in the laboratory frame in which the body rotates. It should be noted that the relation between heat flux and temperature gradient, stress and velocity gradient is frame dependent [195]. In most of the rotational problems the secondary flow features are embedded in a primary rotating flow field.

2.5.7.1 Validity of Navier-Stokes for strong rotations

Validity of the Navier-Stokes equation as well as diffusion equation requires sufficient collision of particles and relaxation of the distribution to weak spatial gradients and slow temporal variations. There are cases encountered in astrophysics when gradients are substantial on the scale of mean free path or temporal changes are relatively rapid compared to mean collision time. Causality is violated, since the particle flux is obviously limited by the finite particle speed. One way to proceed is to use Boltzmann equation which is strictly causal by taking higher moments with appropriate closure relations. Investigations by Narayan *et al.* [197] revealed that the shear stress depends on the shear amplitude as it reaches a maximum and then decreases as the velocity gradient increases. It should be noted that the shear amplitude for the non-inertial rotational problem should be observed in the correct frame of reference with variance reduction approach.

2.5.7.2 Kinetic scheme for axi-symmetric geometries

The velocity discretization of the transport operator is no longer trivial in the cylindrical system as inertia terms are velocity derivatives of the distribution function. The characteristic curves of this form of Boltzmann equation are curves

of $\mathbb{R}^4$ and certainly more complex compared to the Cartesian form [189]. The characteristic curves are defined by

$$\dot{z}(t) = v_z, \qquad \dot{r}(t) = v_r, \qquad \dot{v}_r(t) = \frac{v_\theta^2}{r}, \qquad \dot{v}_\theta(t) = -\frac{v_r v_\theta}{r} \tag{2.122}$$

Mieussens [189] and Sugimoto and Sone [269] have used variables ς and ω to replace (v_r, v_θ) by $(\varsigma\cos\omega, \varsigma\sin\omega)$ to obtain completely conservative form of Boltzmann equation as follows

$$\frac{\partial rf}{\partial t} + v_z\frac{\partial rf}{\partial z} + \varsigma\cos\omega\frac{\partial rf}{\partial r} - \varsigma\frac{\partial \sin\omega f}{\partial \omega} = rJ(f,f) \tag{2.123}$$

For axi-symmetric geometries the Boltzmann equation in the cylindrical coordinate system [243, 244] is as follows:

$$\frac{\partial f}{\partial t} + v_z\frac{\partial f}{\partial z} + v_r\frac{\partial f}{\partial r} + \frac{\partial v_r}{\partial t}\frac{\partial f}{\partial v_r} + \frac{\partial v_\theta}{\partial t}\frac{\partial f}{\partial v_\theta} = J(f,f) \tag{2.124}$$

Mieussens [189] has used discrete-velocity models for the collision and transport operators, for plane and axi-symmetric geometries satisfying positivity, entropy and conservation.

2.5.8 Potential area of research in kinetic upwind method

Kinetic upwind method make use of kinetic theory and moment method strategy to implement upwinding. Most of the kinetic upwind methods like gas kinetic scheme of Xu [293] and relaxation time simulation method (RTSM) [175] include particle collisions in the gas evolution stage by making use of local integral solution of the BGK model. Kinetic flux vector splitting (KFVS) method on the other hand uses fluxes based on the analytical evaluation, hence it is much easier to incorporate phenomenological theory of non-equilibrium thermodynamics. Kinetic flux vector splitting (KFVS) method complies with the principles of non-equilibrium thermodynamics as compared to peculiar velocity upwind method. *Literature review revealed that kinetic flux vector splitting method has not been extended to slip flows, strong rotation and axi-symmetric geometries. Development of kinetic upwind method which complies with requirements of non-equilibrium thermodynamics appears promising research area. Another potential area of research is to develop kinetic upwind method with dissipation control function and application of variance reduction techniques.*

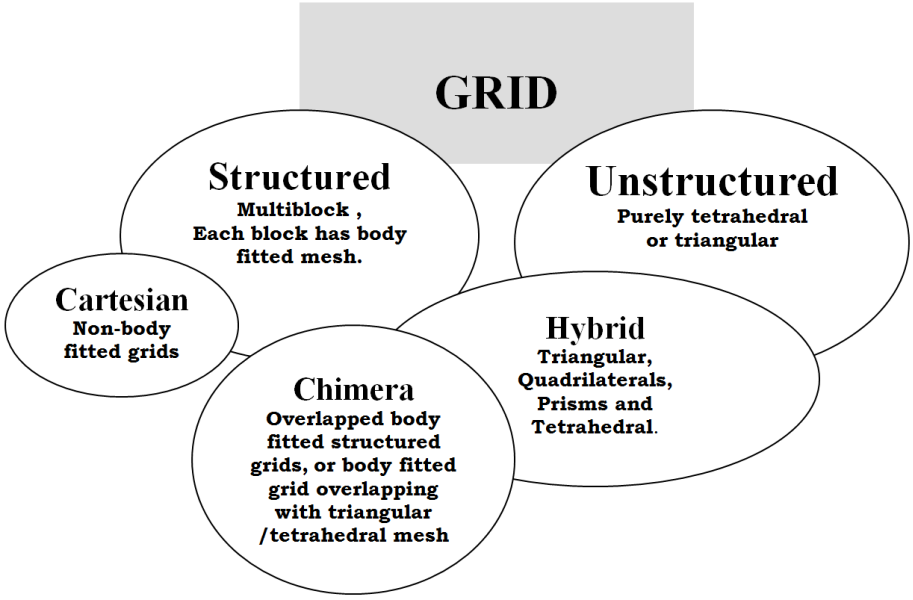

Figure 2.16: Taxonomy of grid.

2.6 Meshless method

For carrying out numerical simulation of Navier-Stokes equations for complex multibody configuration using conventional approach requires grids which include structured multi-block meshes, chimera or overset grids, unstructured grids, Cartesian grids and hybrid grids. Figure 2.16 shows the taxonomy of the different types of grids. Figure 2.17 shows typical multiblock structured and unstructured mesh for a pipe confined within a cylinder. In the multiblock approach the computational domain is composed of several blocks with either continuous (composite grids) or discontinuous (patched) block interfaces. Multiblock approach for complex geometries becomes very tedious due to large number of blocks of different orientation and sizes and their interfaces [257]. Difficulties associated with multiblock approach led to the development of more flexible method called chimera [29, 212]. In this approach the body fitted grids are generated for each component of a multibody configuration and the grids are allowed to overlap. Difficulty in this approach is in transferring information between regions and maintenance of conservation in the overlapped regions. The unstructured grid generation uses Delaunay methods [289], advancing front method [165] and octree based method

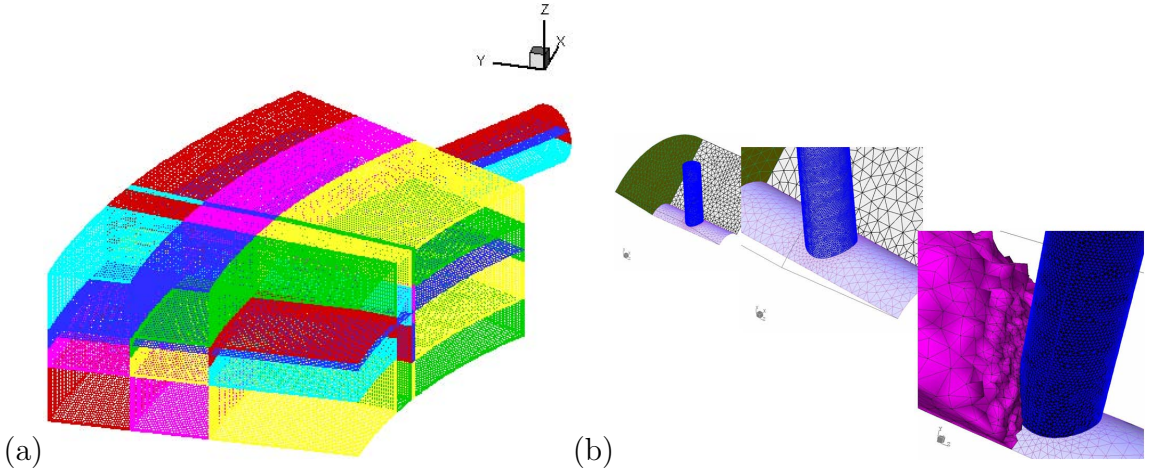

Figure 2.17: (a) Multiblock mesh (b) Unstructured mesh.

[239, 247]. For Navier-Stokes equation the main solution gradients occur in the direction normal to the surface and this requires cells with high aspect ratio. Generation of satisfactory tetrahedral cells for boundary layers is difficult [182]. The approach in Cartesian grid is different. Here the grids are aligned with respect to the Cartesian coordinates [73, 297]. Viscous flow simulations are difficult to be performed with Cartesian meshes [64]. The idea of making structured grids near the boundary and unstructured elsewhere to resolve the viscous flows led to the development of hybrid grids. Hybrid grids consisting of triangles and quadrilaterals in 2-D and tetrahedra and prisms in 3-D [15] provides the advantages of both structured and unstructured meshes. One of the important issue involved with hybrid grids is the smooth variation of sizes from one mesh to another and the treatment of the moving bodies. In real life generation of suitable grid for complex multibody configuration with many components becomes the bottleneck. Meshless methods is one of the approaches to circumvent the difficulty associated with the meshing process. Meshless or meshfree methods have become one of the topic of recent research in the area of computational fluid dynamics. Several meshless methods have been proposed over the last few decade, most of these methods can be defined either as radial basis functions (RBFs) or in terms of moving least squares (MLS) methods drawing motivations from applications in the field of mapping, meteorology, geophysics, etc. All meshless numerical

methods[28, 158] share a common feature that no mesh is needed and the solver is capable of operating on an arbitrary distribution of points. Meshfree methods originated with the work of Gingold and Monaghan [95], and Lucy [173] developing smooth particle hydrodynamics. Smooth particle hydrodynamics (SPH) is a Lagrangian method where the fluid is replaced with set of moving particles to model astrophysical phenomenon without boundaries, such as exploding stars and dust clouds. Finite point set [259, 260] is another meshless approach where finite points either move with fluid velocity (Lagrangian approach) or the flow information runs through the finite points if they are located constant in space (Eulerian approach) or a mixed approach (Arbitrary Lagrangian Eulerian, ALE) is followed. The finite points represents flow domain with particle like features and is extremely efficient for problems where free surfaces are involved or multiphase flows are to be handled. Liu *et al.* [159] proposed the Reproducing Kernel Particle Method (RKPM) to remove the inconsistency in SPH by correction function for kernels in both the discrete and continuous case. Combination of Reproducing Kernel Particle Method (RKPM) and Moving Least Squares (MLS) resulted in Moving Least Squares Reproducing Kernel Particle Method [160]. Nayroles *et al.* [198] developed Diffuse Element Method (DEM) by using the moving least squares (MLS) local interpolation in a Galerkin weak form. Belytschko *et al.* [28] developed Element Free Galerkin (EFG) which was an improvement over diffuse element method extending it to discontinuous approximations. Zhu and Atluri [16, 303] proposed Meshless Local Petrov Galerkin (MPLG) using Petrov-Galerkin weak form to compute integrals. Performance of MPLG deteriorates with high Peclet number flows. De and Bathe [60] introduced method of Finite Spheres which uses Partition of Unity [20] to construct approximation function. Griebel and Schweitzer [106] developed particle-partition of unity method for the solution of elliptic, parabolic, and hyperbolic problems. The method combines a particle approach and meshless method to generate the shape functions and adaptation of particles. Duarte and Oden [79] proposed meshfree $h - p$ cloud method based on h and p enrichment of the approximations. Other meshless methods include Boundary Element Method (BEM) [194] and Local Boundary Integral Method (LBIE) [304].

2.6.1 Meshless discretization for fluid flow

There are broadly three types of meshless discretization [137] followed in computational fluid dynamics : i) least square method based on Taylor series expansion, ii) least square method based on polynomial basis functions, and iii) local radial basis function based method. Batina [27] used least squares to carry out viscous flow simulation, Onãte *et al.* [202, 203] and Löhner *et al.* [166] developed Finite Point Method (FPM) for fluid flow problems. FPM used collocation point technique using polynomial basis with least square based trial functions. Ghosh and Deshpande [93] used least square based method based on Taylor series expansion [156] and developed Least Square Kinetic Upwind Method (LSKUM) for solving Euler flow problems. LSKUM was further developed by Ramesh[224], Praveen [217, 218] and Anandhanarayanan [4]. Sridar and Balakrishnan [254, 255] developed an upwind scheme based on least squares, Katz and Jameson[138] developed meshless method for overset grid system. Kansa [132, 133] was first to apply technique based on the direct collocation method and multiquadric Radial Basis Function (RBF) to solve fluid flow problem. Kansa method based on multiquadric RBF leads to global approximation resulting in a system of equations characterized by a dense stiffness matrix. Another approach called Local Multiquadric based on construction of approximation using sub-domains leads to local approximation resulting in a sparse stiffness matrix. Shu *et al.* [250] applied local radial basis function-based differential quadrature method to solve incompressible fluid flow problem. Shu *et al.* [251], Tota and Wang [276] applied RBF based meshless method for compressible inviscid flows. Barba *et. al.* [25] introduced meshless spatial adaption based on radial basis function interpolation for viscous vortex methods. Shu *et al.* [252] carried out study to compare meshless method based on least squares (LSQ) and radial basis function (RBF) in terms of their accuracy and efficiency for incompressible flow problems. The numerical experiments conducted by Shu *et al.* [252] using the same iterative solver under the similar conditions of node distribution and number of supporting points reveals that meshless method based on RBF give more accuracy while method based on LSQ require lesser iterations. Katz and Jameson[137] also carried out a comparative study using meshless method based on least squares with Taylor

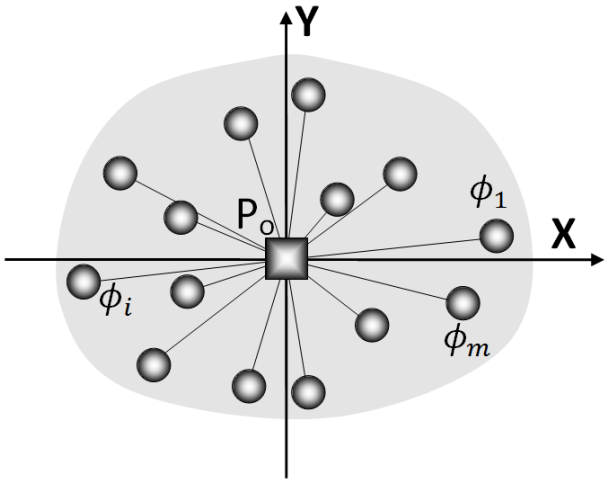

Figure 2.18: Point connectivity for least square based method.

series expansion, least squares using polynomial basis functions and Hardy multiquadric radial basis functions for Euler flow problems. Katz and Jameson[137] found that for flow problems with shocks the least square based methods was significantly better than radial basis method in terms of giving shock location and its magnitude. Chiu *et al.* [53] developed meshless formulation which possesses various conservation and mimetic properties at the discrete level.

2.6.2 Least square method based on Taylor series expansion

Let Ω be an open domain of $\mathbb{R}^n$, n= 1, 2, 3. Suppose that a continuous function ϕ :$\bar{\Omega}\rightarrow$ $\mathbb{R}$ is given at all nodes i.e. it is given at all points $P_i \in \bar{\Omega}$ in a cloud of nodes. Consider a reference node P_o surrounded by m points as shown in Figure 2.18 or with its set of local support or set of neighbours (also defined as connectivity, $N(P_o)$ =$\{\forall P_i : d(P_o, P_i) < h\ \}$.) We are interested in finding the derivatives of ϕ at all the nodes. The error at any point P_i in the neighbourhood of P_o for two dimensional case gives us,

$$E_i = \Delta\phi_i - \Delta x_i\phi_{xo} - \Delta y_i\phi_{yo} - \frac{\Delta x_i^2}{2}\phi_{xxo} - \frac{\Delta y_i^2}{2}\phi_{yyo} - \Delta x_i\Delta y_i\phi_{xyo} + \cdots \quad i = 1, \cdots, m \tag{2.125}$$

where $\Delta x_i = x_i - x_o$, $\Delta y_i = y_i - y_o$ and $\Delta\phi_i = \phi_i - \phi_o$. Terms ϕ_{xo}, ϕ_{yo} are the first order derivatives and ϕ_{xxo}, ϕ_{yyo} and ϕ_{xyo} are the second order derivatives. Thus, we can obtain following system of equations in matrix form as

$$\boldsymbol{A}_N \boldsymbol{\Phi}_o = \boldsymbol{\Delta\phi}_N \tag{2.126}$$

where $\boldsymbol{\Phi}_o = [\phi_{xo}, \phi_{yo}, \phi_{xxo}, \phi_{yyo}, \phi_{xyo}]^T \in \mathbb{R}^n$, observation $\boldsymbol{\Delta\phi}_N$=$[\Delta\phi_1, \cdots, \Delta\phi_m]^T$ $\in\mathbb{R}^m$ with data matrix $\boldsymbol{A}_N\in\mathbb{R}^{m\times n}$.The expressions $(\cdot)_N$ requires values evaluated using connectivity $N(P_o)$. Data matrix, $\boldsymbol{A}_N$ in this case is given as

$$\boldsymbol{A}_N = \begin{bmatrix} \Delta x_1 & \Delta y_1 & \frac{\Delta x_1^2}{2} & \frac{\Delta y_1^2}{2} & \Delta x_1 \Delta y_1 \\ \Delta x_2 & \Delta y_2 & \frac{\Delta x_2^2}{2} & \frac{\Delta y_2^2}{2} & \Delta x_2 \Delta y_2 \\ \cdots & \cdots & \cdots & \cdots & \cdots \\ \Delta x_m & \Delta y_m & \frac{\Delta x_m^2}{2} & \frac{\Delta y_m^2}{2} & \Delta x_m \Delta y_m \end{bmatrix} \tag{2.127}$$

Finding the derivative at point o is a least squares problem where error norm $\|E\|_2$ is to be minimized with respect to ϕ_{xo}, ϕ_{yo}, ϕ_{xxo}, ϕ_{yyo} and ϕ_{xyo} using stencil $N(P_o)$. Taylor series based least squares method uses the normal equations approach to find $\boldsymbol{\Phi}_o = [\phi_{xo}, \phi_{yo}, \phi_{xxo}, \phi_{yyo}, \phi_{xyo}]^T \in \mathbb{R}^n$ such that $\|\boldsymbol{A}_N\boldsymbol{\Phi}_o - \boldsymbol{\Delta\phi}_N\|_2$ is minimized. The normal equations approach uses smaller cross-product matrix $\boldsymbol{C} = \boldsymbol{A}_N^T\boldsymbol{A}_N \in \mathbb{R}^{n\times n}$ such that

$$\boldsymbol{C}\boldsymbol{\Phi}_o = \boldsymbol{A}_N^T\boldsymbol{A}_N\boldsymbol{\Phi}_o = \boldsymbol{A}_N^T\boldsymbol{\Delta\phi}_N \tag{2.128}$$

The derivatives can be obtained as

$$\boldsymbol{\Phi}_o = \boldsymbol{C}^{-1}\boldsymbol{A}_N^T\boldsymbol{\Delta\phi}_N = \left(\boldsymbol{A}_N^T\boldsymbol{A}_N\right)^{-1}\boldsymbol{A}_N^T\boldsymbol{\Delta\phi}_N \tag{2.129}$$

The cross product matrix $\boldsymbol{C}$ with $m > n$ has better condition number than the matrix $\boldsymbol{A}_N$. The matrix $\left(\boldsymbol{A}_N^T\boldsymbol{A}_N\right)^{-1}\boldsymbol{A}_N^T$ can be computed once and stored to evaluate the derivatives.The nodes near to the node P_o will have more influence compared to nodes further away in the connectivity set $N(P_o)$. In order to redistribute the error weights can be assigned based on the distance from the reference node P_o leading to weighted least squares. The derivatives in weighted least square method can be obtained as

$$\boldsymbol{\Phi}_o = \left(\boldsymbol{A}_N^T\boldsymbol{W}\boldsymbol{A}_N\right)^{-1}\boldsymbol{A}_N^T\boldsymbol{W}\boldsymbol{\Delta\phi}_N \tag{2.130}$$

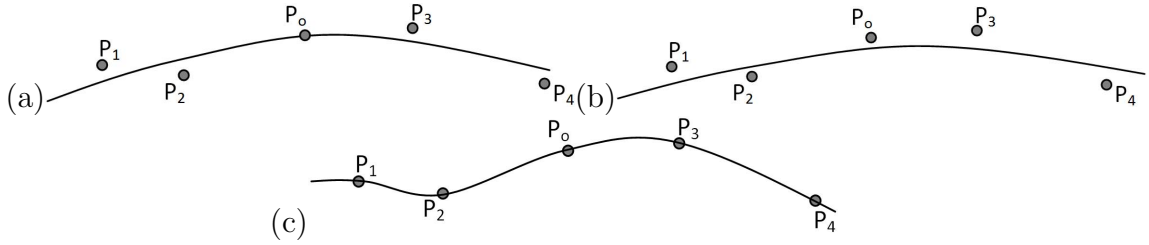

Figure 2.19: (a) Taylor series passes through reference node P_o, (b) Least Square Method based on Polynomial basis function does not pass through reference node P_o, and (c) Method based on Radial Basis Functions pass through all the points.

where $\boldsymbol{W}$ is a diagonal weight matrix given as

$$\boldsymbol{W} = \begin{bmatrix} w_1 & & & \\ & w_2 & & \\ & & \ddots & \\ & & & w_m \end{bmatrix} \tag{2.131}$$

Least square approach becomes unreliable for stretched distribution of nodes encountered in the boundary layer as nodes lying within a thin cylinder and disc leads to ill-conditioning [217, 218].

2.6.3 Least square method based on Polynomial Basis functions

Least square method based on polynomial basis fits a function to a discrete data and obtains partial derivatives after differentiation step whereas least square method based on Taylor series solves directly for the partial derivatives [137]. Fig 2.19 shows the subtle difference between the Taylor series based least square approach and least square approach based on polynomial basis function. It can be seen that in method based on Taylor series approach passes through the reference node compared to polynomial fit. As defined earlier let Ω be an open domain of $\mathbb{R}^n$, n= 1, 2, 3. Suppose that a continuous function $\phi : \bar{\Omega} \rightarrow \mathbb{R}$ is given at all nodes i.e. it is given at all points $P_i \in \bar{\Omega}$ in a cloud of nodes. For two dimensional case consider polynomial $P_k(x, y)$ represented as a linear combination of polynomial

basis function $b_i(x, y)$ given as

$$P_k(x, y) = \sum_{i=0}^{k} c_i b_i(x, y) \tag{2.132}$$

where c_i is the set of coefficients. For a 2D problem the polynomial basis, $\boldsymbol{b}^T$ for $k = 3$ can be expressed as $\boldsymbol{b}^T = [1, x, y]^T$ and $\boldsymbol{b}^T = [1, x, y, x^2, xy, y^2]^T$ for $k = 6$. We seek polynomial which minimizes

$$\|\phi - P_k\|_2 = \langle \phi - P_k, \phi - P_k \rangle^{\frac{1}{2}} \tag{2.133}$$

over the set of polynomials of degree $\leq k$. The optimal set of coefficients is obtained by using normal equations approach. The optimal set of coefficients using weighted least square approach are given as

$$\boldsymbol{C} = \left(\boldsymbol{V}_p^T \boldsymbol{W} \boldsymbol{V}_p\right)^{-1} \boldsymbol{V}_p^T \boldsymbol{W} \phi \tag{2.134}$$

where $\boldsymbol{W}$ is the weight matrix and $\boldsymbol{V}_p$ is the rectangular $m \times k$ Vandermonde matrix given as

$$\boldsymbol{V}_p = \begin{bmatrix} b_1(x_1, y_1) & b_2(x_1, y_1) & \cdots & b_k(x_1, y_1) \\ b_1(x_2, y_2) & b_2(x_2, y_2) & \cdots & b_k(x_2, y_2) \\ \vdots & \vdots \ddots & \vdots & \\ b_1(x_m, y_m) & b_2(x_m, y_m) & \cdots & b_k(x_m, y_m) \end{bmatrix} \tag{2.135}$$

2.6.4 Local Radial Basis Function based method

Unlike least square based method the radial basis function seeks to fit a function which passes through all points in the cloud of points. Figure 2.19 shows the comparison of radial basis function (RBF) based method with respect to least square based approach. Local radial basis function based method uses local cloud of points leading to sparse matrix. Radial basis function based approach can be considered as an extension of differential quadrature (DQ) technique for smooth functions [252]. In this approach partial derivative can be expressed as a weighted linear sum of function values at all points in the sub cloud. The p^{th} - order derivative with respect to independent variable x and y can be approximated by DQ as

$$\left.\frac{\partial^p \phi}{\partial x^{p-k} \partial y^k}\right|_{x_i, y_i} = \sum_{j=1}^{m} w_{ij}^{(p,k)} \phi(x_i, y_i) \tag{2.136}$$

where x_i, y_i are coordinates of the point $N(P_i)$, m is the number of points in the sub-cloud, $\phi(x_i, y_i)$ is the function value and $w_{ij}^{(p,k)}$ is the related weight which needs to be determined [252]. The weights can be evaluated using multivariate polynomial interpolation technique. But there are several issues like i) what mixed terms to be used in multivariate polynomial interpolation, ii) issue of singularity as polynomial interpolation for $\Omega \in \mathbb{R}^n$, for $n > 1$ is not well-posed [187]. Many of these issues can be resolved if RBF interpolation instead of polynomial basis is used to generate the weights. RBF are any function that satisfies

$$r(\vec{x}) = r(\|\vec{x}\|) \tag{2.137}$$

There are wide variety of RBF classified as i) piecewise smooth RBFs, and ii) infinitely smooth RBFs. Multiquadric RBF belonging to the class of infinitely smooth RBFs converges most rapidly and incurs least error compared to most of the RBFs used in the global scattered data interpolation. It is given as

$$r(x_i, y_i) = \sqrt{(x - x_i)^2 + (y - y_i)^2 + s^2} \tag{2.138}$$

where s is a free shape parameter which is empirically determined based on accuracy and convergence considerations. To improve consistency and to ensure non-singular approximation polynomial is appended to the radial basis function. The radial basis function with appended polynomial is given as

$$\bar{\phi}(x, y) = \sum_{i=1}^{m} d_i r_i(x, y) + \sum_{j=1}^{k} c_j b_j(x, y) = \boldsymbol{r}^T \boldsymbol{d} + \boldsymbol{b}^T \boldsymbol{c} \tag{2.139}$$

where $\boldsymbol{c}$=$[c_1, \cdots, c_k]^T$, $\boldsymbol{d}$=$[d_1, \cdots, d_m]^T$, $\boldsymbol{r}$ and $\boldsymbol{b}$ are the vectors of radial basis functions and polynomial basis as follows

$$\begin{array}{rcl} \boldsymbol{r}^T(x, y) & = & \left[\begin{array}{cccc} r_1(x, y) & r_2(x, y) & \cdots & r_m(x, y) \end{array} \right], \\ \boldsymbol{b}^T(x, y) & = & \left[\begin{array}{cccc} b_1(x, y) & b_2(x, y) & \cdots & b_k(x, y) \end{array} \right] \end{array} \tag{2.140}$$

Enforcing the interpolation condition

$$\bar{\phi}(x_i, y_i) = \phi(x_i, y_i) \;\; i = 1, \cdots, m \tag{2.141}$$

results in system of m linear equations in $m + k$ unknowns in vector $\boldsymbol{d}$ and $\boldsymbol{c}$, leading to k additional conditions

$$\sum_{i=1}^{m} d_i b_j(x, y) \;\; j = 1, \cdots, k \tag{2.142}$$

to ensure a unique solution. This amounts to solving system of linear equation of the form

$$\begin{bmatrix} \boldsymbol{r} & \boldsymbol{b} \\ \boldsymbol{b}^T & 0 \end{bmatrix} \begin{bmatrix} \boldsymbol{d} \\ \boldsymbol{c} \end{bmatrix} = \begin{bmatrix} \boldsymbol{\phi} \\ 0 \end{bmatrix} \tag{2.143}$$

where $\boldsymbol{\phi}$ is the vector of nodal values defined as $\boldsymbol{\phi}^T=[\phi_1, \cdots, \phi_m]$.

2.6.5 Potential area of research in meshless method

Literature review revealed that meshless approach based least square (LSQ) and radial basis function (RBF) are the two most potential methods for solving conservations laws. Review also revealed that RBF give more accuracy while method based on LSQ require lesser iterations [252]. For flow problems with shocks the least square based methods was significantly better than radial basis method in terms of giving shock location and its magnitude[137]. Least square approach for nodes lying within a thin cylinder and disc leads to ill-conditioning [217, 218], hence we require a new approach for developing least square based method for a highly stretched distribution of points required for viscous flow problems. *A potential area of research exists in developing least square based method which remains well conditioned for viscous flow problems which require highly stretched and clustered grid near the walls to resolve boundary layers.*

2.7 Parallelization of meshless method

For practical industrial problems with thin boundary layers and complex geometry we require large number of nodes or points for adequate resolution. Highly stretched grids near wall cause grid induced stiffness because allowed time step is dictated by the smallest h (i.e. grid size) and to resolve viscous as well as slip flow features we require scheme with higher order (p^{th} order). Thus, each solver is dictated by its $h-p$ adaptivity which in turn gives two measures of a code : i) rate of data processing (RDP), and ii) bytes per mesh point. Rate of data processing for a meshless code is defined as the time per iteration per mesh point for a given connectivity set. Memory required by a code is measured by bytes per mesh point for a given connectivity set. For real large scale problem the CPU

time for a meshless code becomes prohibitively large thus requiring its parallelization. The main goal of parallel computation is its performance and scalability. Parallelization can be implemented using i) a message based distributed memory model with MPI, ii) or shared memory programming model using OpenMP, iii) hybrid model[31]. Message passing based distributed memory model with domain decomposition or partitioning is the preferred parallelization strategy for most of the industrial solvers.

2.7.1 Domain decomposition

The computational domain comprises of nodes or elements at which similar computational tasks are performed. Such a domain is divided into many sub-domains, which are then assigned to different processors. In each sub-domain similar computational tasks are performed concurrently by their processors. Boundary conditions for each sub-domain are obtained from the data in the neighboring sub-domains thereby requiring communication with other processors by virtue of message passing. The main goal of parallel computation is its performance and scalability which depends on the following factors

- Numerical method and type of parallel architecture.
- Partitioning method.
- Dynamic load balancing.
- Scheduling of the message passing.
- Mapping of partitions to processors.

2.7.2 Partitioning methods

Mesh can be represented as a graph, namely, dual graph. The dual graph is defined to be consisting of an undirected, weighted graph $G = (V, E_e, w_v, w_e)$, where V is the set of vertices, E_e is the set of edges, w_v is a set of non-negative

vertex weights and w_e is a set of non-negative edge weights. For a set P of n processors, we can define a partition,

$$M_{part} : V \rightarrow P \tag{2.144}$$

The sub-domains defined by M_{part} gives the disjoint sub-sets of vertices, S_p as

$$S_p = \{v_i \in V : M_{part}(v_i) = p, p \in P\} \tag{2.145}$$

Thus a partition of the graph is a mapping of V into P disjoint sub-domains S_p such that the union of $S_p = V$ [120]. For a given partition M_{part}, the number of edges whose vertices belong to different subsets is called edge cut of the partition.The set of edge cuts, E_{cut} are defined as

$$E_{cut} = \{e_{ij} \in E_e : v_i \in S_p \rightarrow v_j \notin S_p\} \tag{2.146}$$

The graph partitioning seeks a partition which evenly balances the vertex weight in each sub-domain whilst minimizing the total weight of edge cut. Thus, one has to find M_{part} of a graph G which minimizes the bi-objective function f_1 and f_2

$$\begin{aligned} f_1 &= \left(S_p - \tfrac{V}{n}\right) \\ f_2 &= E_{cut} \end{aligned} \tag{2.147}$$

The graph partitioning algorithm is NP-complete i.e. there is no known algorithm that can provide an optimal solution for large variety of problems in a reasonable time. Mesh partitioning in general fall under the following five main approaches[130, 233].

- Bisection
- Greedy
- Probabilistic
- Local Migration
- Space filling curves

Most of the partitioning algorithms are either graph theory based [120, 136, 284] or based on geometric techniques [120, 129, 233]. Softwares for partitioning like Metis [136], Jostle [284], Chaco [120], Scotch [213] and Zoltan [37] are widely available.

2.7.3 Parallelization strategy for meshless method

Requirements of parallelization of meshless solver is quite similar to finite volume and finite element codes : i) balance of computational load among processor while minimizing the interprocessor communication. Literature review revealed that most of the parallelization strategy adopted for meshless method [59] use graph partitioning.

2.7.4 Communication scheduling

Complex problems require a large cluster of parallel system and in such cases performance depends highly on interprocessor communication time and message scheduling. Communication scheduling is an important aspect of parallelization in order to avoid memory contention and conflicts at the switches and maximize the performance. The most common approach for optimization of communication schedule are i) random scheduling, greedy approach, and iii) edge coloring algorithm. Surma *et al.*[272] have used collision graph model for optimal communication scheduling. For a given set of messages, a collision graph is defined as $G = (V, E_e)$ where V is the set of vertices representing messages M_1, M_1, $\cdots M_N$; and edges $E = \{(M_i, M_j)\}$, the paths of messages M_i and M_j intersect. Optimal schedule reduces to minimum edge orientation problem derived from collision graph model. Determination of minimum number of levels is equivalent to solving the NP-complete graph coloring problem [91].

2.7.5 Potential area of research in parallelization of meshless method

Literature review revealed that message passing based distributed memory model with domain decomposition or partitioning is the preferred parallelization strategy for most of the industrial solvers. Graph partitioning is the preferred parallelization strategy adopted for meshless method. *Parallelization of least square based meshless method using graph partitioning method and optimal communication schedule appears to be a potential area of new contribution.*

2.8 Multi-objective shape optimization for meshless method

Multi-objective problems are now common feature in many engineering problems. Shape optimization searches for the optimal shape that minimizes a certain objectives or cost functional while satisfying given constraints.

2.8.1 Optimization methods

Optimization methods can be broadly classified as

- Deterministic or Gradient based approaches.
  The gradient based approach requires the gradients of objectives with respect to design variables. Gradient based approach is further classified as
  - Quasi-Newton method.
    It uses the changes in gradient to carry out optimization.
  - Perturbation analysis and sensitivity analysis based methods.
    It is based on perturbation and sensitivity analysis using the gradients with respect to design variables.
  - Automatic differentiation based approach.
    This method is based on derivative information of user defined function with respect to the inputs based on the analysis codes.
  - Adjoint methods.
    Adjoint method was introduced by Pironneau [215] is motivated by control theory approach where system is defined by the conservation laws or partial differential equations of the flow, with boundary shape acts as the control.
- Stochastic or Non-Gradient based approaches.
  - Grid or random search.
    In this method the cost of searching the design space becomes very expensive for large set of design variables.

- Tabu search.
  Tabu search uses adaptive memory to guide its responsive search. In its responsive exploration it makes use of exploitation of good solution and exploration of new promising regions.
- Simulated annealing.
  This method simulates the annealing process and optimization follows the simulated path which minimizes the energy distribution.
- Genetic algorithms (GA).
  GA was introduced by Holland [121] in which each candidate design configuration is represented by a genetic string. The optimization method performs set of operations analogous to biological evolution theory.
- Ant colony optimization (ACO).
  ACO was developed by Dorigo [78] in which each candidate design configuration is represented by the path for trajectory taken by the ant.
- Particle swarm optimization (PSO).
  PSO was developed by Kennedy and Eberhart [140] in which each candidate design configuration is represented by its location.
- Nonlinear simplex.
  Nelder and Mead [199] introduced simplex method in which each vertex of the simplex represents the candidate design configuration.

Nearly all optimization method are constructed with elaborate permutation and combination of *hill climbing* and *random search*.

2.8.2 Shape parametrization

There are various parametrization approaches like discrete approach, domain element approach, polynomial and splines based, CAD based, free-form deformation and soft object animation based approach. The shape parametrization approach is problem specific and is of immense importance as it can bring drastic reduction

in the computational time. The sensitivity derivative or design velocity field of a response r with respect to the design vector, $\vec{x}$ [235] using chain rule can be written as

$$\frac{\partial r}{\partial \vec{x}} = \left(\frac{\partial r}{\partial m_f}\right)\left(\frac{\partial m_f}{\partial m_s}\right)\left(\frac{\partial m_s}{\partial m_g}\right)\left(\frac{\partial m_g}{\partial \vec{x}}\right) \tag{2.148}$$

where m_f is the field or volume mesh, m_s is the surface mesh, and m_g is the geometry. The term $\frac{\partial m_g}{\partial \vec{x}}$ is very vital as it denotes the geometry sensitivity derivatives with respect to design vector. Shape parametrization for multi-objective optimization is an active area of research[235].

2.8.3 Mesh handling strategy

As the boundary shape of the candidate design evolves during the optimization process, the location of the mesh points are moved or re-generated in order to conform to the new candidate design configuration. Automated re-meshing after every optimization step is a challenge as adequate quality of the mesh can fall. Alternatively, automated deformation for small deformation is more robust and inexpensive. Researchers in general have adopted algebraic mesh movement schemes [200] for structured meshes and automated re-meshing for unstructured meshes [55]. Rendall and Allen [228] have proposed radial basis functions (RBFs)-based mesh deformation method that preserves orthogonality and produces high quality of meshes and is independent of mesh type. Most of the mesh movement strategy either become expensive or fail when deformation is high when optimization demands large shape changes.

2.8.4 Cloud handling strategy for meshless method

As described earlier meshless method only require i) cloud of points in the computational domain, and ii) connectivity of each point in the computational domain. Combining meshless method with a stochastic algorithm is a very attractive possibility in fluid dynamic shape optimization. Genetic algorithm (GA), Ant colony optimization (ACO) and hybrid GA-ACO coupled with meshless solver [72, 145, 146] have all used node blanking method executed in following three steps : i)non-participating nodes are blanked off, ii)points only on the body

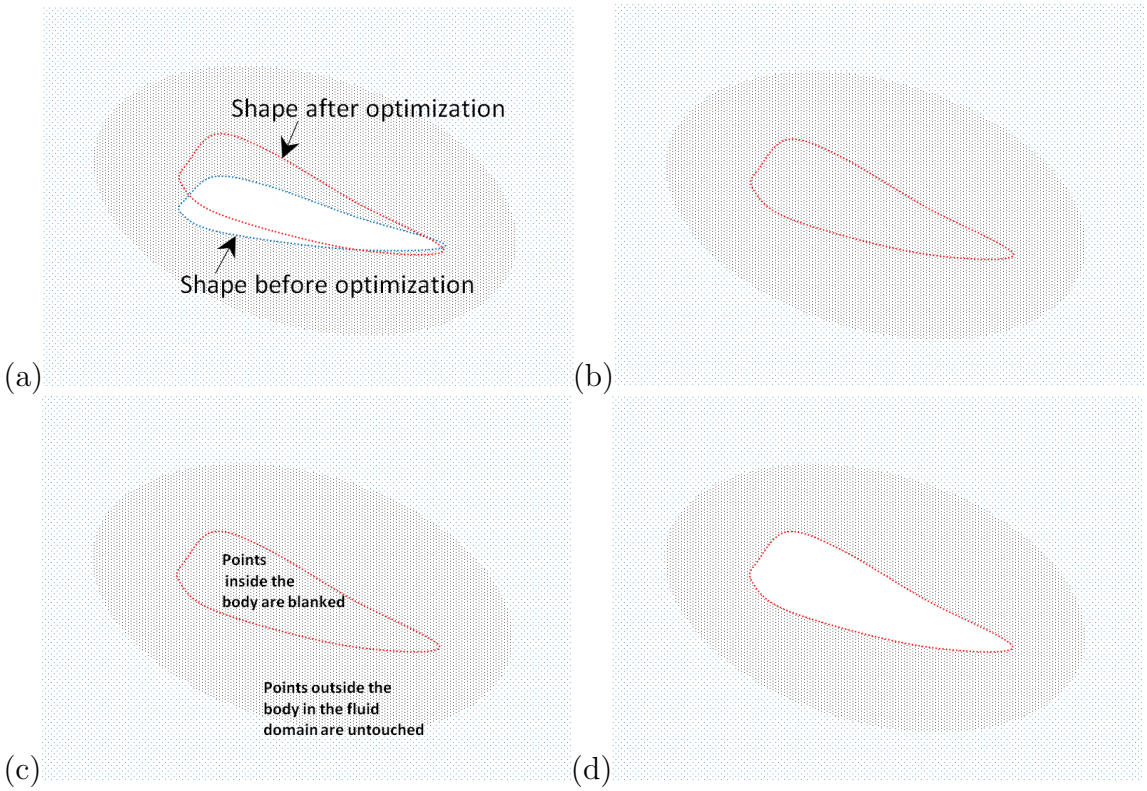

Figure 2.20: Node blanking method: (a) Shape before and after optimization step, points on the body move acting as a control, (b) New shape lying in the background cloud and dense body cloud, (c) assignment of flags with points inside the body being blanked off, and (d) connectivity generated based on participating points.

are changed, and iii)connectivity is generated. Salient features of node-blanking method shown in figure 2.20 can be described as follows:

- Points in the computational domain are assigned flags. As the optimizer suggests a new shape the points which go inside the body are blanked off and points which where previously blanked off but now are in the flow field are assigned flags.
- Points on the body acts as control points during optimization process. Only these points are allowed to change.
- Connectivity is generated for all points which are assigned flags. Points which are blanked off do not participate in flow solver and hence they are not the part of connectivity.

Essentially, this method does not generate any mesh point it either blanks "off" or flags "on" the existing points and generates connectivity for the "on" points.

2.8.5 Multi-objective optimization

Multi-objective problems are now common feature in many engineering problems. Let the functions $f_i(\vec{x}) \in Y \subset \mathbb{R}^m$ be the objective functions defining the m-dimensional objective space with its subset $\tilde{Y} \subset Y$ representing the feasible objective region. Similarly, let n-dimensional space $\mathbb{R}^n$ be called the parameter space dependent on the shape parametrization approach. The solution of such problem poses a challenge and requires a new notion of optimality as in most of the cases objectives tend to be in conflict with each other. There are variety of commonly used methods for multi-objective optimization. Three of the most commonly used methods can be stated as follows:

Method 1: Sum of weighted objectives

$$\begin{aligned} &\text{minimize } f = \textstyle\sum_i^m w_i f_i \\ &\text{subject to } \vec{x} \in \mathbb{R}^n;\ \text{where } w_i > 0 \text{ and } \textstyle\sum w_i = 1 \end{aligned} \tag{2.149}$$

Method 2: Lexicographic method

The multi-objective optimization is based on lexicographic ordering.

$$\vec{x}_1 \preceq \vec{x}_2 \tag{2.150}$$

$$\begin{aligned} &\text{if either } \vec{x}_1 = \vec{x}_2 \text{ or first non} - \text{zero component of } \vec{x}_1 - \vec{x}_2 < 0 \\ &\text{subject to } \vec{x}_1 \in \mathbb{R}^n \text{ and } \vec{x}_2 \in \mathbb{R}^n \end{aligned} \tag{2.151}$$

Objectives are ranked; the first objective is more important, the second one a bit less and so on.

Method 3: Increasing the constraint vector space

In this method one of the objective functions is taken as the most primary and the remaining objective functions are transformed into constraints.

$$\begin{aligned} &\text{minimize } f_1(\vec{x}) \\ &\text{subject to } f_2(\vec{x}) \leq c_2, ..., f_m(\vec{x}) \leq c_m \ \vec{x} \in \mathbb{R}^n; \\ &\text{where } \ c_i \text{ is the bound.} \end{aligned} \tag{2.152}$$

All these methods provide point solutions. Here parameter vector $\vec{x}$ is based on weights, objective value bounds, preferences based on experience, engineering judgment, etc. *Trade-offs in optimum solutions over a wide range of weights can give a better picture. In such a scenario optimization approaches based on game theory can be taken as the basis.* Methods based on game theory are : i) non-cooperative game theory using Nash Strategy, ii) cooperative game theory using Pareto Strategy, and iii) leader-follower based game theory using Stackelberg Strategy.

2.8.6 Pareto optimality

Dominance Pareto front technique [65, 96] is the most common approach used in multi-objective optimization, it uses non-dominated sorting coupled with the optimization algorithms. The dominance Pareto front technique moves the solution towards the Pareto front and does not suffer from convexity or scaling problems. In the non-dominated sorting approach Pareto optimality forms the basis of multi-objective optimization as it takes all the objectives into consideration simultaneously; every element in the Pareto front is a good solution. The concept of Pareto optimality can best be understood if we transform graphical solutions from n-dimensional parametric or design space X to m-dimensional objective or criterion space Y. The shaded portion $\tilde{Y}$ in Fig.2.21 represents feasible objective space Y and $\partial Y^{\prec}$ marks the Pareto optimal front bounded between $Y_1^{\prec}$

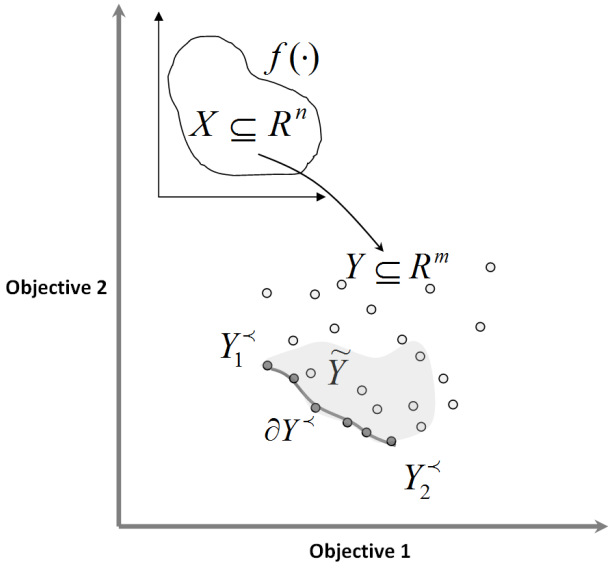

Figure 2.21: Mapping of the parameter space X to the objective function Y: shaded portion $\tilde{Y}$ represents feasible objective space Y and $\partial Y^{\prec}$ marks the Pareto optimal front.

and $Y_2^{\prec}$. The Pareto strategy uses dominance strategy where an optimum $\vec{x^*}$ is said to dominate $\vec{x}$ if and only if

$$\begin{cases} \forall \ i \in \{1, \cdots, m\}, f_i(\vec{x^*}) \leq f_i(\vec{x}) \\ \exists \ j \ \text{ such that } \ f_j(\vec{x^*}) < f_j(\vec{x}) \end{cases} \tag{2.153}$$

The $\vec{x^*}$ is said to be non-dominated and efficient solution if and only if there is no other feasible solution in the search space that dominates it. The Pareto front is a set of all such non-dominated solutions. The scheme for selecting the best solution along the Pareto front depends on the decision maker's overall preferences.

2.8.7 Potential area of research in multi-objective shape optimization for meshless method.

Literature review revealed several different issues like i)choice of optimization method, ii)shape parametrization, iii)mesh handling, and iv) multi-objective methodology. Survey also revealed numerous strategies for addressing these issues. *Potential area of research in the field of multi-objective shape optimization for meshless method includes i) development of new multi-objective and cloud handing*

strategy, ii)demonstrating the strategy for stochastic methods like GA, ACO and simplex method.

2.9 Summary

Development of a robust meshless solver for slip flow requires research work in wide variety of fields which include i) slip modeling, ii) kinetic theory, iii) non-equilibrium thermodynamics, iv) upwind methods, v) meshless methods, vi) parallelization, and vii) multi-objective shape optimization. Literature review was conducted and potential area of research identified in each field was taken up as follows

- Slip flow modeling
  Slip models not only depends on the velocity gradient in the normal direction but also on the pressure gradient in the tangential flow direction. Literature review also reveals that there is no consensus amongst researchers for second order slip models. Literature review further revealed that there is virtually no reported upwind method based on linkage between kinetic theory and non-equilibrium thermodynamics for solving slip flow.

- Kinetic theory
  Literature review reveals existence of a potential research area in the development of computationally inexpensive kinetic model for polyatomic gases which gives correct transport coefficients and Prandtl number in the hydrodynamic limit.

- Non-equilibrium thermodynamics
  Approximate solutions provided by kinetic theory has to comply with requirements of non-equilibrium thermodynamics There exists a major potential research area in incorporating phenomenological theory of non-equilibrium thermodynamics into kinetic theory based flow solver.

- Kinetic upwind method
  Literature review revealed that kinetic flux vector splitting method which

complies with requirements of non-equilibrium thermodynamics has not been extended to slip flows.

- Meshless method
  Literature review revealed that for flow problems with shocks the least square based methods was significantly better than the radial basis method in terms of giving shock location and its magnitude, but least square based methods fail when they encounter highly stretched distribution of points used in the boundary layer. Potential area of research exists in developing least square based method which remains well conditioned for viscous flow problems which require highly stretched and clustered grid near the walls to resolve boundary layers.

- Parallelization of meshless method
  Parallelization of least square based meshless method using graph partitioning method and optimal communication schedule appears to be a potential area of research.

- Multi-objective shape optimization for meshless method
  Potential area of research in the field of multi-objective shape optimization includes i) development of new multi-objective and cloud handing strategy, ii)demonstrating the strategy for stochastic methods like GA, ACO and simplex method.

Development of meshless solver requires formulation based on kinetic theory which complies with the principles of non-equilibrium thermodynamics. This will require i) development of a new kinetic model based on non-equilibrium thermodynamics, ii) development of kinetic scheme for viscous slip flow and its wall boundary condition, iii) development of new least square based meshless method for stretched distribution of nodes which retains simplicity of normal equations, iv)development of parallelization strategy and multi-objective optimization method for meshless solver.

Chapter 3

Onsager reciprocity principle based new kinetic model

3.1 Introduction

Boltzmann equation being a nonlinear integro-differential equation becomes difficult to handle and hence alternative simpler kinetic model is required to replace the collision term. The kinetic model should preserve the basic properties and characteristics of the Boltzmann equation and also comply with the principles of non-equilibrium thermodynamics. This chapter introduces maximum entropy production principle and investigates its relationship with Onsager's reciprocity principle and Boltzmann equation. The derivation of first order distribution function based on Morse-BGK model for polyatomic gas is presented. Morse-BGK model gives inconsistent value of Prandtl number, to overcome this problem a new kinetic model for polyatomic gas based on Onsager's reciprocity principle is proposed which gives correct Prandtl number and also complies with the requirements of non-equilibrium thermodynamics. This is followed by statistical representation of the new kinetic model by establishing relationship between entropy production and Mahalanobis distance. Finally derivations of first order distribution function, Euler and Navier-Stokes equations are presented.

3.2 Non-equilibrium thermodynamics

Non-equilibrium thermodynamics provides a tool which can be used to check the correctness of the kinetic theory based flow solver. Distribution function derived using kinetic theory has to comply with requirements of non-equilibrium thermodynamics like following Onsager's principle and maximization of entropy production under constraint imposed due to conservation laws. In the words of Clausius the second law of thermodynamics states that for an adiabatic process entropy of the final state is larger than or equal to entropy of the initial state. Maximum entropy production principle is an additional statement over the second law of thermodynamics telling us that the entropy production is not just positive, but tends to a maximum. Publications in this area is fragmented and still in the realm of physics [1]. In the first subsection we present a derivation of maximization of entropy which takes place within the imposed constraints of conservation laws. In the second section we have related Onsager's principle and Boltzmann equation.

3.2.1 Maximum entropy production and Onsager's principle for fluid flow

Derivation of maximum entropy production principle has been done by the physicists in many different ways. This subsection gives the derivation of the maximum entropy production principle from the point of view of a computational fluid dynamist. For any fluid flow process changing from one conservation state to another conservation state there is generation of entropy σ_J. *Maximum entropy production principle states that this entropy is not only positive it is also maximum. The maximization of entropy takes place for a prescribed irreversible force under constraint imposed on entropy production due to conservation laws.* This can be mathematically written as

$$\begin{array}{ll} \text{Maximize} & \sigma_J(\boldsymbol{J}_i, \boldsymbol{J}_k) \\ \text{subject to} & \sigma_J(\boldsymbol{J}_i, \boldsymbol{J}_k) - \sigma(\boldsymbol{J}_i, \boldsymbol{X}_i) = 0 \end{array} \tag{3.1}$$

[1] Refer to publication of Martyushev and Seleznev [180], and Beretta [30] for more details.

where $\sigma(\boldsymbol{J}_i, \boldsymbol{X}_i) = \sum_i \boldsymbol{J}_i \odot \boldsymbol{X}_i$ is the entropy production density based on conservation law and $\sigma_J(\boldsymbol{J}_i, \boldsymbol{J}_k)$ is the entropy production density in terms of fluxes. Operator $\odot$ denotes full tensor contraction of forces and fluxes, which are of the same tensorial order following Curie principle. The term $\boldsymbol{J}_i$ signifies flux and the term $\boldsymbol{X}_i$ signifies the thermodynamic force. The subscript "i" is not the index notation of the tensor, it signifies the type of thermodynamic force e.g $\boldsymbol{X}_\tau$ or $\boldsymbol{X}_q$ associated due to shear stress tensor or heat flux vector. Taylor expansion of the entropy production density σ_J in terms of fluxes for system close to equilibrium state gives

$$\sigma_J(\boldsymbol{J}_i, \boldsymbol{J}_k) = \alpha^0 + \sum_{i=1}^{N} \alpha_i^1 \boldsymbol{J}_i + \sum_{i,k=1}^{N} \boldsymbol{\alpha}_{ik}^2 \odot \boldsymbol{J}_i \odot \boldsymbol{J}_k + \cdots \tag{3.2}$$

where coefficients $\alpha^0, \alpha_i^1, \boldsymbol{\alpha}_{ik}^2, \cdots$, are properties of the system in equilibrium state. The first term on the right hand side vanishes since there is no entropy production in the equilibrium state. Coefficients associated with odd power of fluxes vanish i.e. $\alpha_i^1 = 0$ as entropy production is independent of the direction of flux flow. The coefficients $\boldsymbol{\alpha}_{rs}$, $\boldsymbol{\alpha}_{sr}$ vanish if flux $\boldsymbol{J}_r$ and $\boldsymbol{J}_s$ do not couple. Thus, entropy production density $\sigma_J(\boldsymbol{J}_i, \boldsymbol{J}_k)$ is bilinear function of fluxes given as

$$\sigma_J(\boldsymbol{J}_i, \boldsymbol{J}_k) = \sum_{i,k=1}^{N} \boldsymbol{\alpha}_{ik}^2 \odot \boldsymbol{J}_i \odot \boldsymbol{J}_k \tag{3.3}$$

The constrained maximization of $\sigma_J(\boldsymbol{J}_i, \boldsymbol{J}_k)$ leads to Lagrangian $\mathcal{L}(\boldsymbol{X}, \boldsymbol{J}, \lambda)$

$$\mathcal{L}(\boldsymbol{X}, \boldsymbol{J}, \lambda) = \left[\frac{\partial \left(\sum_{i,k=1}^{N} \boldsymbol{\alpha}_{ik}^2 \odot \boldsymbol{J}_i \odot \boldsymbol{J}_k - \lambda \left(\sum_{i,k=1}^{N} \boldsymbol{\alpha}_{ik}^2 \odot \boldsymbol{J}_i \odot \boldsymbol{J}_k - \sum_i^N \boldsymbol{J}_i \odot \boldsymbol{X}_i \right) \right)}{\partial \boldsymbol{J}_i} \right]_{\boldsymbol{X}} = 0 \tag{3.4}$$

where λ is a Lagrangian multiplier. The optimality conditions leads to KKT (Kharush-Kuhn-Tucker) equations $[\nabla_{\boldsymbol{J}} \mathcal{L}(\boldsymbol{X}, \boldsymbol{J}, \lambda)]_{\boldsymbol{X},\lambda} = 0$ and $[\nabla_{\lambda} \mathcal{L}(\boldsymbol{X}, \boldsymbol{J}, \lambda)]_{\boldsymbol{X},\boldsymbol{J}} = 0$.

$$\begin{aligned} \left[\frac{\partial \left(\sum_{i,k=1}^{N} \boldsymbol{\alpha}_{ik}^2 \odot \boldsymbol{J}_i \odot \boldsymbol{J}_k - \lambda \left(\sum_{i,k=1}^{N} \boldsymbol{\alpha}_{ik}^2 \odot \boldsymbol{J}_i \odot \boldsymbol{J}_k - \sum_i^N \boldsymbol{J}_i \odot \boldsymbol{X}_i \right) \right)}{\partial \boldsymbol{J}_i} \right]_{\boldsymbol{X},\lambda} &= 0 \\ \left[\frac{\partial \left(\sum_{i,k=1}^{N} \boldsymbol{\alpha}_{ik}^2 \odot \boldsymbol{J}_i \odot \boldsymbol{J}_k - \lambda \left(\sum_{i,k=1}^{N} \boldsymbol{\alpha}_{ik}^2 \odot \boldsymbol{J}_i \odot \boldsymbol{J}_k - \sum_i^N \boldsymbol{J}_i \odot \boldsymbol{X}_i \right) \right)}{\partial \lambda} \right]_{\boldsymbol{X},\boldsymbol{J}} &= 0 \end{aligned} \tag{3.5}$$

The first KKT condition $[\nabla_{\boldsymbol{J}} \mathcal{L}(\boldsymbol{X}, \boldsymbol{J}, \lambda)]_{\boldsymbol{X},\lambda} = 0$ gives

$$\boldsymbol{X}_i = \frac{2(\lambda - 1)}{\lambda} \sum_{k=1}^{N} \boldsymbol{\alpha}_{ik}^2 \odot \boldsymbol{J}_k \tag{3.6}$$

Using the second KKT condition we obtain $\lambda = 2$ and the Lagrangian becomes

$$\mathcal{L}(\boldsymbol{X}, \boldsymbol{J}) = \left[\frac{\partial\left(\sum_{i,k=1}^{N} \boldsymbol{\alpha}_{ik}^2 \odot \boldsymbol{J}_i \odot \boldsymbol{J}_k - 2\left(\sum_{i,k=1}^{N} \boldsymbol{\alpha}_{ik}^2 \odot \boldsymbol{J}_i \odot \boldsymbol{J}_k - \sum_i^N \boldsymbol{J}_i \odot \boldsymbol{X}_i\right)\right)}{\partial \boldsymbol{J}_i} \right]_{\boldsymbol{X}} = 0 \tag{3.7}$$

This Lagrangian can be recast in a form similar to Onsager's variational principle

$$\begin{aligned} &\left[\frac{\partial\left(\sum_i^N \boldsymbol{J}_i \odot \boldsymbol{X}_i - \frac{1}{2}\sum_{i,k=1}^{N} \boldsymbol{\alpha}_{ik}^2 \odot \boldsymbol{J}_i \odot \boldsymbol{J}_k\right)}{\partial \boldsymbol{J}} \right]_{\boldsymbol{X}} = 0 \\ \Leftrightarrow &\left[\frac{\partial(\sigma(\boldsymbol{J}_i, \boldsymbol{X}_i) - \phi_J(\boldsymbol{J}_i, \boldsymbol{J}_k))}{\partial \boldsymbol{J}} \right]_{\boldsymbol{X}} = 0 \end{aligned} \tag{3.8}$$

The derived entropy production is similar to Onsager's dissipative function described earlier in section 2.4.2 by equation 2.70 of Chapter 2.

$$\Phi(\boldsymbol{J}_i, \boldsymbol{J}_k) = \int_\Omega \sigma_J(\boldsymbol{J}_i, \boldsymbol{J}_k) d\Omega = \frac{1}{2} \int_\Omega \sum_{i,k=1}^{N} \boldsymbol{R}_{ik}^J \odot \boldsymbol{J}_i \odot \boldsymbol{J}_k d\Omega \tag{3.9}$$

and coefficients $\boldsymbol{\alpha}_{ik}^2 \equiv \boldsymbol{R}_{ik}^J$. *For a prescribed irreversible force $\boldsymbol{X}_i$ the actual flux $\boldsymbol{J}_i$ which satisfies Onsager's reciprocity principle $\sigma(\boldsymbol{X}_i, \boldsymbol{J}_i) = \sum_i \boldsymbol{J}_i \odot \boldsymbol{X}_i$ also maximizes the entropy production.*

3.2.2 Onsager's reciprocity principle and linearized Boltzmann equation

Consider linearized distribution $f_1 = f_0[1 + \Phi]$ with the further assumption that $|\Phi| \ll 1$ and both Maxwellian and unknown Φ vary slowly in space and time, with this assumption we can neglect the product of Φ with derivatives of Maxwellian f_0 as well as derivatives of Φ . With this the linearized Boltzmann equation[1] in terms of linearized collision operator $\mathbb{J}\Phi$ can be expressed as

$$\frac{1}{f_0}\left(\frac{\partial f_0}{\partial t} + \nabla_{\vec{x}} \cdot (\vec{v} f_0)\right) = -\mathbb{J}\Phi \tag{3.10}$$

The unknown Φ can be written as a sum of components Φ_i i.e. $\Phi = \sum_i \Phi_i$. The component of perturbation Φ_i appears due to thermodynamic force $\boldsymbol{X}_i$ such that all other thermodynamic forces are absent. This component can be expressed as follows

$$\Phi_i = (\Phi)_{\boldsymbol{X}_j = 0, \forall j \neq i} \tag{3.11}$$

[1]For further details on linearized Boltzmann equation refer section B.6 of Appendix B

The linearized Boltzmann equation corresponding thermodynamic force $\boldsymbol{X}_i$ becomes

$$\frac{1}{f_0}\left(\frac{\partial f_0}{\partial t}+\nabla_{\vec{x}}\cdot(\vec{v}f_0)\right)_{\boldsymbol{X}_j=0,\forall j\neq i}=-(\mathbb{J}\Phi)_i \tag{3.12}$$

The collision operator $(\mathbb{J}\Phi)_i$ will exists when the system is disturbed from the state of equilibrium due to some thermodynamic forces $\boldsymbol{X}_i$. Such a thermodynamic force will lead to its associated conjugate microscopic vector of heat and tensor of shear stress. Formulation of linearized collision operator in terms of thermodynamic force and its conjugate microscopic tensor is a first step towards establishing linkage between kinetic theory and non-equilibrium thermodynamics. For such a case linearized Boltzmann equation can be written as

$$\frac{1}{f_0}\sum\left(\frac{\partial f_0}{\partial t}+\nabla_{\vec{x}}\cdot(\vec{v}f_0)\right)_{\boldsymbol{X}_j=0,\forall j\neq i}=-\sum_i\bar{\boldsymbol{\Upsilon}}_i\odot\boldsymbol{X}_i \tag{3.13}$$

where $\odot$ denotes full tensor contraction, $\bar{\boldsymbol{\Upsilon}}_i$ is the reduced microscopic vector and tensor associated with heat and shear stress respectively, $\boldsymbol{X}_i$ is the conjugate thermodynamic force vector and tensor. For certain kinetic models we can invert the collision operator as the right hand side of the equation is in non-hydrodynamic subspace to obtain

$$\Phi_j=(\mathbb{J}^{-1}\bar{\boldsymbol{\Upsilon}})_j\odot\boldsymbol{X}_j \tag{3.14}$$

The thermodynamic flux $\boldsymbol{J}_i$ can be evaluated as

$$\boldsymbol{J}_i=R\langle\bar{\boldsymbol{\Upsilon}}_i,f_0\Phi\rangle=R\left\langle\bar{\boldsymbol{\Upsilon}}_i,f_0\sum_j\left((\mathbb{J}^{-1}\bar{\boldsymbol{\Upsilon}})_j\odot\boldsymbol{X}_j\right)\right\rangle \tag{3.15}$$

where R is the specific gas constant. The flux can also be written as

$$\boldsymbol{J}_i=\sum_j\boldsymbol{L}_{ij}\odot\boldsymbol{X}_j \tag{3.16}$$

where $\boldsymbol{L}_{ij}$ is the phenomenological tensor written as

$$\boldsymbol{L}_{ij}=R\langle\bar{\boldsymbol{\Upsilon}}_i,f_0(\mathbb{J}^{-1}\bar{\boldsymbol{\Upsilon}})_j\rangle \tag{3.17}$$

The phenomenological tensor either obeys Onsager's reciprocal relationship $\boldsymbol{L}_{ij}$ = $\boldsymbol{L}_{ji}$ or Casimir's $\boldsymbol{L}_{ij}$ = -$\boldsymbol{L}_{ji}$. If the reduced microscopic flux tensors $\bar{\boldsymbol{\Upsilon}}_r$ and

$\bar{\boldsymbol{\Upsilon}}_s$ do not couple then no cross effects will be present and phenomenological tensor of transport coefficients $\boldsymbol{L}_{rs} = \boldsymbol{L}_{sr}$ will vanish. For example in case of fluid flow described by Navier-Stokes-Fourier equations we have $\bar{\boldsymbol{\Upsilon}}_\tau$ associated with shear stress tensor and $\bar{\boldsymbol{\Upsilon}}_q$ associated with heat flux vector. For such a case $\boldsymbol{L}_{\tau q} = \boldsymbol{L}_{q\tau}$ vanish as $\bar{\boldsymbol{\Upsilon}}_\tau$ and $\bar{\boldsymbol{\Upsilon}}_q$ are of different tensorial order and hence do not couple. We get only two tensors $\boldsymbol{L}_{\tau\tau}$ and $\boldsymbol{L}_{qq}$ of transport coefficients which are equivalent to scalars because of isotropy due to the rotational invariance of the collision operator[1]. Viscosity and thermal conductivity coefficients can be extracted from the reduced matrix element $L_{\tau\tau}$ and L_{qq} respectively, where reduced matrix element L_{ii} for any tensor $\boldsymbol{L}_{ii}$ of rank t is defined as

$$L_{ii} = \frac{R\big\langle \bar{\boldsymbol{\Upsilon}}_i \odot, f_0(\mathbb{J}^{-1}\bar{\boldsymbol{\Upsilon}})_i \big\rangle}{2t+1} \tag{3.18}$$

In case of thermodynamic forces due to heat flux vector, $\boldsymbol{X}_q$ and species diffusion vector, $\boldsymbol{X}_d$ which is of the same tensorial order we get equality in Soret and Dufour coefficients due to Onsager symmetry. *Onsager-Casimir symmetry relationship* is a consequence of positive semi-definiteness and self-adjoint property of the linearized collision operator $\mathbb{J}$ arising from the microscopic reversibility condition due to the equality of the differential cross sections for direct and time reversed collision processes. The derivation of entropy production density quickly establishes the connection with linear irreversible thermodynamics as follows

$$\begin{aligned} \sigma(\boldsymbol{X}_i, \boldsymbol{J}_i) = \tfrac{\partial \rho_s}{\partial t} + \nabla_{\vec{x}} \cdot (\vec{j}_s) \quad &= R\langle ln(f), \mathbb{J}\Phi \rangle \geq 0 \\ &= R\langle (ln(f_0) + \Phi)\, \mathbb{J}\Phi \rangle \geq 0 \end{aligned} \tag{3.19}$$

This results in

$$\begin{aligned} \sigma(\boldsymbol{X}_i, \boldsymbol{J}_i) \quad &= R\langle f_0 \Phi \mathbb{J}\Phi \rangle \geq 0 \\ &= R\Big\langle f_0 \textstyle\sum_j (\mathbb{J}^{-1}\bar{\boldsymbol{\Upsilon}})_j \odot \boldsymbol{X}_j \sum_i \bar{\boldsymbol{\Upsilon}}_i \odot \boldsymbol{X}_i \Big\rangle \geq 0 \\ &= \textstyle\sum_i \Big(\sum_j \boldsymbol{L}_{ij} \odot \boldsymbol{X}_j \Big) \odot \boldsymbol{X}_i \geq 0 \\ &= \textstyle\sum_i \boldsymbol{J}_i \odot \boldsymbol{X}_i \geq 0 \end{aligned} \tag{3.20}$$

The connection with Onsager's theory of linear irreversible thermodynamics is quickly established. This exercise gives us the following guidance and directions

[1]The operator $\mathbb{J}$ has rotational invariance if $\mathbb{J} = \mathbb{O}^{-1}\mathbb{J}\mathbb{O}$ for any rotational operator $\mathbb{O}$.

- Kinetic model should be formulated based on the principles of non-equilibrium thermodynamics.
- The perturbation term Φ in such a case can be written as a sum of perturbation components Φ_i for each thermodynamic forces $\boldsymbol{X}_i$. The perturbation components Φ_i can be expressed as tensor contraction of reduced microscopic flux with its conjugate thermodynamic force following Onsager's relationship.
- Once the distribution function is formulated in the Onsager's form at the microscopic level it will also comply with the principles on non-equilibrium thermodynamics once it is projected to macroscopic Navier-Stokes level.

3.3 Derivation of first order distribution function using Morse-BGK model

Using the non-dimensionless Boltzmann equation with Morse-BGK kinetic model and Chapman-Enskog perturbation expansion, higher order distribution is generated by virtue of iterative refinement as follows:

$$\bar{f}_i = -\frac{t_R}{\mathrm{Kn}}\left[\frac{\partial \bar{f}_{i-1}}{\partial t} + \nabla_{\vec{x}} \cdot (\vec{v}\bar{f}_{i-1})\right] \tag{3.21}$$

where Kn is the Knudsen number, t_R is the relaxation time used in the Morse-BGK model with $\bar{f}_0 = f_0$. First order distribution is obtained by considering the first two terms of the Chapman-Enskog expansion given as

$$f_1 = f_0 + \mathrm{Kn}\bar{f}_1 \tag{3.22}$$

For Boltzmann equation in inertial frame

$$\frac{\bar{f}_1}{f_0} = -\frac{t_R}{\mathrm{Kn}}\left[\frac{\partial ln f_0}{\partial t} + v_x\frac{\partial ln f_0}{\partial x}\right] \tag{3.23}$$

In terms of total derivative $\frac{D}{Dt} = \frac{\partial}{\partial t} + \vec{u}.\nabla$ for inertial frame it can be written as

$$\frac{\bar{f}_1}{f_0} = -\frac{t_R}{\mathrm{Kn}}\left[\frac{D ln f_0}{Dt} + \vec{c}\frac{\partial ln f_0}{\partial x}\right] \tag{3.24}$$

which after simplification can be expressed as

$$\frac{\bar{f}_1}{f_0} = -\frac{t_R}{\mathrm{Kn}} \left[\begin{array}{l} \frac{1}{\rho}\frac{D\rho}{Dt} - 2\beta^2 R\left(\frac{D+2}{2\beta} - \frac{4(\gamma-1)\mathbb{I}}{2-D(\gamma-1)} - \sum_i^D c_i^2\right)\frac{DT}{Dt} \\ +2\beta\sum_j^D c_j\left(\frac{Du_j}{Dt} + \sum_i^D\left(c_i\frac{\partial u_i}{\partial s_j}\right)\right) \\ +\sum_j^D c_j\left\{\frac{1}{\rho}\frac{\partial\rho}{\partial s_j} - 2\beta^2 R\left(\frac{D+2}{2\beta} - \frac{4(\gamma-1)\mathbb{I}}{2-D(\gamma-1)} - \sum_i^D c_i^2\right)\frac{\partial T}{\partial s_j}\right\} \end{array} \right] \tag{3.25}$$

Where $c_i = v_i - u_i$ where $i = x, y, z$ with u_i and v_i being the fluid and molecular velocity. Parameters s_1, s_2 and s_3 are spatial coordinates x, y, z. While evaluating the above equation it is assumed that hydrodynamic scale and time scale are much larger than mean free path and the relaxation time. Thus spatio-temporal derivatives of molecular variables, $\vec{v}$ and $\mathbb{I}$ in the inertial framework vanish. After substitution of Euler equation we have

$$\int_{\mathbb{R}^+}\int_{\mathbb{R}^D} \mathbf{\Psi}\left(\frac{\partial f_0}{\partial t} + \nabla_{\vec{x}}\cdot(\vec{v}f_0) = 0\right) d\vec{v}d\mathbb{I} \Rightarrow \left.\begin{array}{l} \frac{D\rho}{Dt} = -\rho\frac{\partial u_i}{\partial s_i} \\ \frac{Du_i}{Dt} = \frac{\rho}{2\beta^2}\frac{\partial\beta\rho}{\partial s_i} \\ \frac{DT}{dt} = -(\gamma-1)T\frac{\partial u_i}{\partial s_i} \end{array}\right\} \tag{3.26}$$

The first-order Chapman-Enskog term can be written as

$$f_1 = f_0\left[1 - \frac{\xi_{1,\tau}}{p} - \frac{\xi_{1,q}}{p}\right] \tag{3.27}$$

where $\xi_{1,\tau}$ and $\xi_{1,q}$ are Chapman-Enskog polynomials associated with the shear stress tensor and heat flux vector. For 1D geometry this can be written as

$$\xi_{1,\tau} = pt_R\left[\frac{3\gamma-5}{2} + \frac{\mathbb{I}(1-\gamma)}{\mathbb{I}_o} + (3-\gamma)\beta c_x^2\right]\frac{\partial u_x}{\partial x} \tag{3.28}$$

$$\xi_{1,q} = 2\beta^2 R p t_R\left[\frac{5c_x}{2\beta} - \frac{c_x\mathbb{I}}{\mathbb{I}_o\beta} - c_x^3\right]\frac{\partial T}{\partial x} \tag{3.29}$$

where Navier Stokes stress τ_{xx} and heat flux q_x are given as follows

$$\tau_{xx} = 2pt_R\frac{\partial u_x}{\partial x} + (1-\gamma)\frac{p}{\nu}\frac{\partial u_x}{\partial x} \tag{3.30}$$

$$q_x = -pt_R R\frac{\gamma}{\gamma-1}\frac{\partial T}{\partial x} \tag{3.31}$$

For 2D geometry Chapman-Enskog polynomial associated with the shear stress tensor and heat flux vector can be written as

$$\begin{array}{rl} \xi_{1,\tau} & = pt_R\left[(2\gamma-3) + (1-\gamma)\frac{\mathbb{I}}{\mathbb{I}_o} + \beta(3-\gamma)c_x^2 + \beta(1-\gamma)c_y^2\right]\frac{\partial u_x}{\partial x} \\ & +pt_R\left[(2\gamma-3) + (1-\gamma)\frac{\mathbb{I}}{\mathbb{I}_o} + \beta(1-\gamma)c_x^2 + \beta(3-\gamma)c_y^2\right]\frac{\partial u_y}{\partial y} \\ & +pt_R\left[2\beta c_x c_y\frac{\partial u_x}{\partial y} + +2\beta c_x c_y\frac{\partial u_y}{\partial x}\right] \end{array} \tag{3.32}$$

$$\begin{aligned}\xi_{1,q} &= 2\beta^2 R p t_R \left[\frac{3c_x}{\beta} - \frac{c_x \mathbb{I}}{\mathbb{I}_o \beta} - c_x^3 - c_x c_y^2\right] \frac{\partial T}{\partial x} \\ &+2\beta^2 R p t_R \left[\frac{3c_y}{\beta} - \frac{c_y \mathbb{I}}{\mathbb{I}_o \beta} - c_x^2 c_y - c_y^3\right] \frac{\partial T}{\partial y}\end{aligned} \tag{3.33}$$

where Navier Stokes stress τ_{xx}, τ_{xy} and τ_{yy} and heat flux q_x and q_y are given as follows

$$\tau_{xx} = 2pt_R \frac{\partial u_x}{\partial x} + (1-\gamma) pt_R \left(\frac{\partial u_x}{\partial x} + \frac{\partial u_y}{\partial y}\right) \tag{3.34}$$

$$\tau_{yy} = 2pt_R \frac{\partial u_y}{\partial y} + (1-\gamma) pt_R \left(\frac{\partial u_x}{\partial x} + \frac{\partial u_y}{\partial y}\right) \tag{3.35}$$

$$\tau_{xy} = \tau_{yx} = 2\beta c_x c_y pt_R \left(\frac{\partial u_x}{\partial y} + \frac{\partial u_y}{\partial x}\right) \tag{3.36}$$

$$q_x = -pt_R R \frac{\gamma}{\gamma - 1} \frac{\partial T}{\partial x} \tag{3.37}$$

$$q_y = -pt_R R \frac{\gamma}{\gamma - 1} \frac{\partial T}{\partial y} \tag{3.38}$$

For 3D geometry it can be written as follows:

$$\begin{aligned}\xi_{1,\tau} &= pt_R \left[\frac{5\gamma-7}{2} - \frac{(\gamma-1)\mathbb{I}}{\mathbb{I}_o} + c_x^2(3-\gamma)\beta - c_y^2(\gamma-1)\beta - c_z^2(\gamma-1)\beta\right] \frac{\partial u_x}{\partial x} \\ &+pt_R \left[\frac{5\gamma-7}{2} - \frac{(\gamma-1)\mathbb{I}}{\mathbb{I}_o} - c_x^2(\gamma-1)\beta + c_y^2(3-\gamma)\beta - c_z^2(\gamma-1)\beta\right] \frac{\partial u_y}{\partial y} \\ &+pt_R \left[\frac{5\gamma-7}{2} - \frac{(\gamma-1)\mathbb{I}}{\mathbb{I}_o} - c_x^2(\gamma-1)\beta + c_y^2(\gamma-1)\beta - c_z^2(3-\gamma)\beta\right] \frac{\partial u_z}{\partial z} \\ &+pt_R \left[2\beta c_x c_y \left(\frac{\partial u_x}{\partial y} + \frac{\partial u_y}{\partial x}\right) + 2\beta c_y c_z \left(\frac{\partial u_y}{\partial z} + \frac{\partial u_z}{\partial y}\right) + 2\beta c_x c_z \left(\frac{\partial u_x}{\partial z} + \frac{\partial u_z}{\partial x}\right)\right]\end{aligned} \tag{3.39}$$

$$\begin{aligned}\xi_{1,q} = \; & -2\beta^2 R p t_R \left[\frac{7c_x}{2\beta} - \frac{c_x \mathbb{I}}{\mathbb{I}_o \beta} - c_x^3 - c_y^2 c_x - c_z^2 c_x\right] \frac{\partial T}{\partial x} \\ & -2\beta^2 R p t_R \left[\frac{7c_y}{2\beta} - \frac{c_y \mathbb{I}}{\mathbb{I}_o \beta} - c_x^2 c_y - c_y^3 - c_z^2 c_y\right] \frac{\partial T}{\partial y} \\ & -2\beta^2 R p t_R \left[\frac{7c_z}{2\beta} - \frac{c_z \mathbb{I}}{\mathbb{I}_o \beta} - c_x^2 c_z - c_y^2 c_z - c_z^3\right] \frac{\partial T}{\partial z}\end{aligned} \tag{3.40}$$

where Navier Stokes stress $\tau_{xx}, \tau_{xy}, \tau_{xz}, \cdots, \tau_{zy}, \tau_{zz}$ and heat flux q_x,q_y and q_z are given as follows

$$\tau_{xx} = 2pt_R \frac{\partial u_x}{\partial x} + (1-\gamma) pt_R \left(\frac{\partial u_x}{\partial x} + \frac{\partial u_y}{\partial y} + \frac{\partial u_z}{\partial z}\right) \tag{3.41}$$

$$\tau_{yy} = 2pt_R \frac{\partial u_y}{\partial y} + (1-\gamma) pt_R \left(\frac{\partial u_x}{\partial x} + \frac{\partial u_y}{\partial y} + \frac{\partial u_z}{\partial z}\right) \tag{3.42}$$

$$\tau_{zz} = 2pt_R \frac{\partial u_z}{\partial z} + (1-\gamma) pt_R \left(\frac{\partial u_x}{\partial x} + \frac{\partial u_y}{\partial y} + \frac{\partial u_z}{\partial z}\right) \tag{3.43}$$

$$\tau_{xy} = \tau_{yx} = pt_R \left(\frac{\partial u_x}{\partial y} + \frac{\partial u_y}{\partial x} \right) \tag{3.44}$$

$$\tau_{xz} = \tau_{zx} = pt_R \left(\frac{\partial u_x}{\partial z} + \frac{\partial u_z}{\partial x} \right) \tag{3.45}$$

$$\tau_{yz} = \tau_{zy} = pt_R \left(\frac{\partial u_y}{\partial z} + \frac{\partial u_z}{\partial y} \right) \tag{3.46}$$

$$q_x = -pt_R R \frac{\gamma}{\gamma - 1} \frac{\partial T}{\partial x} \tag{3.47}$$

$$q_y = -pt_R R \frac{\gamma}{\gamma - 1} \frac{\partial T}{\partial y} \tag{3.48}$$

$$q_z = -pt_R R \frac{\gamma}{\gamma - 1} \frac{\partial T}{\partial z} \tag{3.49}$$

From the above expression of distribution function, tensor of viscous stresses $\mathbf{\Pi}$ can be deduced as

$$\mathbf{\Pi} = \mu \left[(\nabla \otimes \vec{u}) + (\nabla \otimes \vec{u})^T - \frac{2}{3} \boldsymbol{I} \nabla \cdot \vec{u} \right] + \zeta \boldsymbol{I} \nabla \cdot \vec{u} \tag{3.50}$$

where $\boldsymbol{I}$ is the identity invariant tensor, ζ is the coefficient of bulk viscosity expressed as

$$\zeta = \mu \left(\frac{5}{3} - \gamma \right) \tag{3.51}$$

Macroscopic dynamic viscosity is directly related to molecular collision process by virtue of collision time. Chapman–Enskog expansion gives a viscosity coefficient of

$$\mu = t_R p \tag{3.52}$$

Similarly, heat flux vector, $\vec{q}$ can be deduced as

$$\vec{q} = -\kappa \nabla T \tag{3.53}$$

where thermal conductivity κ as

$$\kappa = t_R p R \frac{\gamma}{\gamma - 1} \tag{3.54}$$

This approach gives Prandtl number, Pr *as unity. The single relaxation time* t_R *used in the Morse-BGK model leads to incorrect values of the transport coefficients in the hydrodynamic limit.*

It is important to understand that there are very few models which respect each constraint of positivity, conservation of moments, and dissipation of entropy, while being computationally inexpensive. Hence research is required in the development of alternative kinetic model for polyatomic gas which retains the simplicity of the Morse-BGK model as well as complies with the principles of non-equilibrium thermodynamics.

3.3.1 Identification of thermodynamic forces and microscopic tensors

Important linkages with non-equilibrium thermodynamics can be drawn from the expression of the derived first order velocity distribution function, f_1 based on Morse-BGK model. Velocity distribution function f_1 can be written as

$$\begin{aligned} f_1 &= f_0 \left[1 - \tfrac{\xi_{1,\tau}}{p} - \tfrac{\xi_{1,q}}{p}\right] \\ &= f_0 - \textstyle\sum_j \boldsymbol{\Upsilon}_j \odot \boldsymbol{X}_j \\ &= f_0 - (\boldsymbol{\Upsilon}_\tau : \boldsymbol{X}_\tau + \boldsymbol{\Upsilon}_q \cdot \boldsymbol{X}_q) \end{aligned} \tag{3.55}$$

where $\odot$ denotes full tensor contraction, $\boldsymbol{\Upsilon}_j$ is the microscopic vector and tensor associated with heat and shear stress respectively, $\boldsymbol{X}_j$ is the conjugate thermodynamic force vector and tensor. Using the definition of perturbation term Φ the microscopic tensor $\boldsymbol{\Upsilon}_j$ can be expressed in terms of reduced microscopic tensor as follows

$$\boldsymbol{\Upsilon}_j = -f_0(\mathbb{J}^{-1}\bar{\boldsymbol{\Upsilon}})_j = -f_0 t_R \bar{\boldsymbol{\Upsilon}}_j \tag{3.56}$$

The linearized collision operator $\mathbb{J}$ is described by a single relaxation time t_R which is not affected by thermodynamic force. The microscopic tensor associated with the shear stress for D degree of freedom in terms of BGK's single relaxation time t_R is derived as

$$\boldsymbol{\Upsilon}_\tau = t_R f_0 \left[\vec{c} \otimes \vec{c} + \frac{1}{2}\{\frac{(2+D)\gamma - (4+D)}{2\beta} - \frac{\mathbb{I}(\gamma-1)}{\mathbb{I}_o\beta} - c^2(\gamma-1)\}\boldsymbol{I}\right] \tag{3.57}$$

where $\vec{c}$ is the peculiar velocity vector and $\boldsymbol{I}$ is the rank-D identity invariant tensor. The microscopic vector associated with heat transport in terms of BGK's single relaxation time t_R is derived as

$$\boldsymbol{\Upsilon}_q = t_R f_0 \left[\frac{4+D}{2\beta} - \frac{\mathbb{I}}{\mathbb{I}_o\beta} - c^2\right]\vec{c} \tag{3.58}$$

The thermodynamic force associated with shear stress tensor, $\boldsymbol{X}_\tau$ and heat vector, $\boldsymbol{X}_q$ can be expressed as

$$\begin{array}{ll} \boldsymbol{X}_\tau & = \beta[(\nabla \otimes \vec{u}) + (\nabla \otimes \vec{u})^T] \\ \boldsymbol{X}_q & = \nabla\beta \end{array} \tag{3.59}$$

For example components of microscopic tensor associated with shear stress, $\boldsymbol{\Upsilon}_\tau$ for 3D geometry can be expressed as

$$\Upsilon_\tau \equiv t_R f_0 \left[\begin{array}{lll} c_x^2 - \frac{1}{2}[c^2(\gamma-1) + I_\tau & c_x c_y & c_x c_z \\ c_x c_y & c_y^2 - \frac{1}{2}[c^2(\gamma-1) + I_\tau & c_y c_z \\ c_x c_z & c_y c_z & c_z^2 - \frac{1}{2}[c^2(\gamma-1) + I_\tau \end{array} \right] \tag{3.60}$$

where c^2=$c_x^2 + c_y^2 + c_z^2$ and

$$I_\tau \equiv \left(-\frac{\mathbb{I}(\gamma-1)}{\mathbb{I}_o\beta} + \frac{-7+5\gamma}{2\beta} \right) \tag{3.61}$$

Similarly, components of microscopic $\boldsymbol{\Upsilon}_q$ for 3D geometry can be expressed as

$$\Upsilon_q = t_R f_0 \left[\begin{array}{lll} c_x(-c^2 + I_q) & c_y(-c^2 + I_q) & c_z(-c^2 + I_q) \end{array} \right] \tag{3.62}$$

where

$$I_q = \frac{7}{2\beta} - \frac{\mathbb{I}}{\mathbb{I}_o\beta} \tag{3.63}$$

The components of thermodynamic force associated with shear stress tensor

$$\boldsymbol{X}_\tau \equiv \beta \left[\begin{array}{lll} 2\frac{\partial u_x}{\partial x} & (\frac{\partial u_x}{\partial y} + \frac{\partial u_y}{\partial x}) & (\frac{\partial u_x}{\partial z} + \frac{\partial u_z}{\partial x}) \\ (\frac{\partial u_x}{\partial y} + \frac{\partial u_y}{\partial x}) & 2\frac{\partial u_y}{\partial y} & (\frac{\partial u_z}{\partial y} + \frac{\partial u_y}{\partial z}) \\ (\frac{\partial u_x}{\partial z} + \frac{\partial u_z}{\partial x}) & (\frac{\partial u_z}{\partial y} + \frac{\partial u_y}{\partial z}) & 2\frac{\partial u_z}{\partial z} \end{array} \right] \tag{3.64}$$

The thermodynamic force associated with heat vector is

$$\begin{array}{ll} \boldsymbol{X}_q & \equiv \left[\begin{array}{lll} \frac{\partial\beta}{\partial x} & \frac{\partial\beta}{\partial y} & \frac{\partial\beta}{\partial z} \end{array} \right] \\ & \equiv -2R\beta^2 \left[\begin{array}{lll} \frac{\partial T}{\partial x} & \frac{\partial T}{\partial y} & \frac{\partial T}{\partial z} \end{array} \right] \end{array} \tag{3.65}$$

The exercise of derivation of distribution function of polyatomic gas using Morse-BGK model has led to following conclusions :

- Identification of $\boldsymbol{\Upsilon}_j$ microscopic vector and tensor associated with heat and shear stress.

- Identification of thermodynamic forces $\boldsymbol{X}_j$ for polyatomic gas.

- Distribution function contains terms of higher order moments $\boldsymbol{\Psi} = [\vec{v} \otimes \vec{v}, \left(\mathbb{I} + \frac{v^2}{2}\right)\vec{v}]^T$ as it contains pressure tensor and heat flux vector. The pressure tensor in terms of higher order moments are defined by

$$\boldsymbol{P} = \int_{\mathbb{R}^+}\int_{\mathbb{R}^D} \vec{c} \otimes \vec{c} f d\vec{v} d\mathbb{I} \tag{3.66}$$

  where $\vec{c}$ is the peculiar velocity. The heat flux vector in terms of higher order moments are defined by

$$\boldsymbol{q} = \int_{\mathbb{R}^+}\int_{\mathbb{R}^D} \left(\mathbb{I} + \frac{c^2}{2}\right)\vec{c} f d\vec{v} d\mathbb{I} \tag{3.67}$$

- Inference can be drawn that for each thermodynamic force there should be an associated relaxation time. *The construction of new kinetic model should have relaxation time for each thermodynamic force.*

3.4 New kinetic model

Distribution function should follow Onsager's reciprocity principle so as to satisfy principles of non-equilibrium thermodynamics. The polynomials associated with shear stress, $\xi_{1,\tau}$ and heat flux, $\xi_{1,q}$ will give rise to flux $\boldsymbol{J}_i$ expressed in terms of thermodynamic force $\boldsymbol{X}_j$ as follows

$$\boldsymbol{J}_i = \sum_j \boldsymbol{L}_{ij} \odot \boldsymbol{X}_j \tag{3.68}$$

where $\boldsymbol{L}_{ij}$ is the tensor of phenomenological coefficients such that entropy production $\sigma(\boldsymbol{X}_i, \boldsymbol{J}_i)$ satisfies the Onsager's reciprocity relations depicted as follows :

$$\sigma(\boldsymbol{X}_i, \boldsymbol{J}_i) = \sum_i \boldsymbol{J}_i \odot \boldsymbol{X}_i = \sum_{i,j} (\boldsymbol{L}_{ij} \odot \boldsymbol{X}_j) \odot \boldsymbol{X}_i \tag{3.69}$$

The subscript i and j denote the thermodynamic forces associated with shear stress tensor and heat flux vector. In order to derive a thermodynamically correct distribution function the kinetic model itself requires its foundation based on

principles of non-equilibrium thermodynamics. Assuming that the particles are in non-equilibrium due thermodynamic forces $\boldsymbol{X}_\tau$ and $\boldsymbol{X}_q$. The particles that are in non-equilibrium due to thermodynamic forces $\boldsymbol{X}_\tau$ are replaced exponentially by particles in equilibrium with characteristic time $t_{R(f,\tau)}$ and $t_{R(f_0,\tau)}$ respectively. Similarly, particles in non-equilibrium due to thermodynamic forces $\boldsymbol{X}_q$ are replaced exponentially by particles in equilibrium with characteristic time $t_{R(f,q)}$ and $t_{R(f_0,q)}$ respectively. In most cases the state of gas is not varying rapidly in the interval of relaxation time so $f-f_0$ is small, hence $t_{R(f,\tau)} = t_{R(f_0,\tau)} = t_{R(\tau)}$ and $t_{R(f,q)} = t_{R(f_0,q)} = tr_{R(q)}$, with this the new kinetic model becomes

$$J_m(f, f_0) = -\left(\frac{f(\vec{x}, \vec{v}, \mathbb{I}, t) - f_0(\vec{x}, \vec{v}, \mathbb{I}, t)}{t_{R(\tau)}(\vec{x}, t)}\right)_{\boldsymbol{X}_q=0} - \left(\frac{f(\vec{x}, \vec{v}, \mathbb{I}, t) - f_0(\vec{x}, \vec{v}, \mathbb{I}, t)}{t_{R(q)}(\vec{x}, t)}\right)_{\boldsymbol{X}_\tau=0} \tag{3.70}$$

In the proposed new kinetic model only inelastic collisions are considered such that particles relaxes to equilibrium distribution in internal and translational state at same temperature as there is equipartition of energy between the internal and translational degrees of freedom. Further, this inelastic collisions are in non-equilibrium due to thermodynamic forces $\boldsymbol{X}_\tau$ and $\boldsymbol{X}_q$. The part of distribution which is in non-equilibrium due thermodynamic forces $\boldsymbol{X}_\tau$ first relaxes to Maxwellian f_0 in characteristic time $t_{R(\tau)}$. Simultaneously the part of distribution which is in non-equilibrium due thermodynamic forces $\boldsymbol{X}_q$ relaxes to Maxwellian f_0 in characteristic time $t_{R(q)}$. Figure 3.1 shows the components of the new kinetic model for thermodynamic force $\boldsymbol{X}_\tau$ and $\boldsymbol{X}_q$ as non-equilibrium distribution f relaxes to equilibrium distribution f_0 in the phase plane of thermodynamic force $\boldsymbol{X}_\tau$ and $\boldsymbol{X}_q$. The relaxation step can also be cast as an eigenvalue problem $(\boldsymbol{\mathcal{A}} - \lambda \boldsymbol{I})\boldsymbol{\mathcal{X}}_{\tau q} = 0$ where $\boldsymbol{\mathcal{X}}_{\tau q}$ is a tensor with components $\{\boldsymbol{X}_\tau, \boldsymbol{X}_q\}$ such that positive semi-definiteness of the collision operator ensures non-negative entropy production, providing a Lyapunov criterion for the stability towards a equilibrium distribution. In a more generalized form Onsager-BGK model can be written as

$$J_m(f, f_0) = -\sum_j \left(\frac{f(\vec{x}, \vec{v}, \mathbb{I}, t) - f_0(\vec{x}, \vec{v}, \mathbb{I}, t)}{t_{R(j)}(\vec{x}, t)}\right)_{\boldsymbol{X}_i=0, \forall i \neq j} \tag{3.71}$$

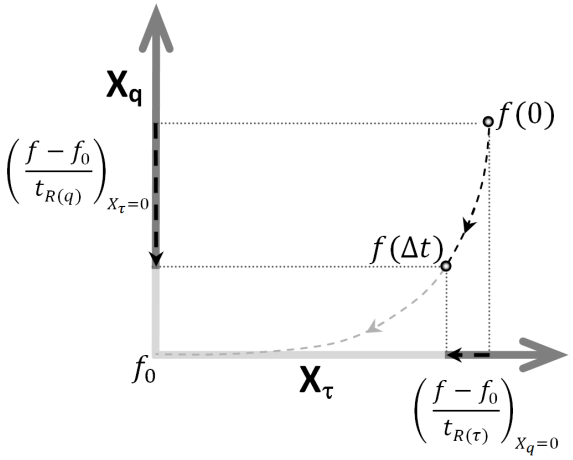

Figure 3.1: Components of the new kinetic model for thermodynamic force $\boldsymbol{X}_\tau$ and $\boldsymbol{X}_q$ as non-equilibrium distribution f relaxes to equilibrium distribution f_0.

where $t_{R(j)}$ is the relaxation time for thermodynamic force $\boldsymbol{X}_j$. Distribution function, $f(\Delta t)$ after time interval $t = \Delta t$ relaxes as

$$f(\Delta t) = \sum_j \left[f(0) Exp(-\Delta t / t_{R(j)}) - f_0 (1 - Exp(-\Delta t / t_{R(j)})) \right]_{\boldsymbol{X}_i = 0, i \neq j} \tag{3.72}$$

where $f(0) = f(t = 0)$ is the initial non-equilibrium distribution just after streaming or convection step while f_0 is the final equilibrium distribution to be reached after sufficient collisions[1]. Non-equilibrium thermodynamics based kinetic model can also be extended for gas mixtures, refer section B.7 in Appendix B for more details.

3.4.1 Distribution function for proposed new kinetic model

Using the non-dimensionless Boltzmann equation with BGK kinetic model and Chapman-Enskog perturbation expansion, higher order distribution is generated

[1]The present analysis can be made more physically meaningful by using modified moment method of Eu [83] in which the distribution function depends also on entropy derivatives called as Gibbs variables.

by virtue of iterative refinement as follows:

$$\bar{f}_i = -\frac{t_{R(\tau)}}{\mathrm{Kn}}\left[\frac{\partial \bar{f}_{i-1}}{\partial t} + \nabla_{\vec{x}} \cdot (\vec{v}\bar{f}_{i-1})\right]_{\boldsymbol{X}_q=0} - \frac{t_{R(q)}}{\mathrm{Kn}}\left[\frac{\partial \bar{f}_{i-1}}{\partial t} + \nabla_{\vec{x}} \cdot (\vec{v}\bar{f}_{i-1})\right]_{\boldsymbol{X}_\tau=0} \tag{3.73}$$

where Kn is the Knudsen number with $\bar{f}_0 = f_0$. Velocity distribution function f can be now be derived as

$$f_1 = f_0 - \sum_j \boldsymbol{\Upsilon}_j \odot \boldsymbol{X}_j = f_0 - (\boldsymbol{\Upsilon}_\tau : \boldsymbol{X}_\tau + \boldsymbol{\Upsilon}_q \cdot \boldsymbol{X}_q) \tag{3.74}$$

For the first order Chapman-Enskog expansion the microscopic tensor $\boldsymbol{\Upsilon}_j$ can be expressed in terms of reduced microscopic tensor $\bar{\boldsymbol{\Upsilon}}_j$ as follows

$$\boldsymbol{\Upsilon}_j = -f_0 t_{R(j)} \bar{\boldsymbol{\Upsilon}}_j = -f_0 t_{R(j)} \bar{\boldsymbol{\Upsilon}}_j \tag{3.75}$$

where linearized collision operator $\mathbb{J}$ has a dependence on the thermodynamic force i.e. it depends inversely with $t_{R(j)}$ which is the relaxation time associated with the thermodynamic force $\boldsymbol{X}_j$. The microscopic tensor associated with the shear stress for D degree of freedom is

$$\boldsymbol{\Upsilon}_\tau = t_{R(\tau)} f_0 \left[\vec{c} \otimes \vec{c} + \frac{1}{2}\{\frac{(2+D)\gamma - (4+D)}{2\beta} - \frac{\mathbb{I}(\gamma-1)}{\mathbb{I}_o\beta} - c^2(\gamma-1)\}\boldsymbol{I}\right] \tag{3.76}$$

where $\vec{c}$ is the peculiar velocity vector and $\boldsymbol{I}$ is the rank-D identity invariant tensor, the relaxation time associated with shear stress, $t_{R(\tau)}$ is given as

$$t_{R(\tau)} = \frac{\mu_{ref}}{p}\left(\frac{T}{T_{ref}}\right)^{\delta_o} \tag{3.77}$$

where μ_{ref} is the viscosity of the gas at reference temperature T_{ref}, δ_o is the exponent of the viscosity law and p is the pressure.
The microscopic vector associated with heat transport is

$$\boldsymbol{\Upsilon}_q = t_{R(q)} f_0 \left[\frac{4+D}{2\beta} - \frac{\mathbb{I}}{\mathbb{I}_o\beta} - c^2\right]\vec{c} \tag{3.78}$$

The relaxation time associated with heat transport, $t_{R(q)}$ is given as

$$t_{R(q)} = \frac{\kappa(\gamma-1)}{R\gamma p} = \frac{t_{R(\tau)}}{\mathrm{Pr}} \tag{3.79}$$

where κ is thermal conductivity and Pr is the Prandtl number. The thermodynamic force associated with shear stress tensor, $\boldsymbol{X}_\tau$ and heat vector, $\boldsymbol{X}_q$ are

$$\begin{array}{ll} \boldsymbol{X}_\tau & = \beta[(\nabla \otimes \vec{u}) + (\nabla \otimes \vec{u})^T] \\ \boldsymbol{X}_q & = \nabla\beta \end{array} \tag{3.80}$$

The perturbation term can be written as

$$\mathrm{Kn}\bar{f}_1 = -\sum_j \boldsymbol{\Upsilon}_j \odot \boldsymbol{X}_j \tag{3.81}$$

The perturbation terms satisfies the additive invariants property, expressed as

$$\left\langle \boldsymbol{\Psi}, \mathrm{Kn}\bar{f}_1 \right\rangle = \; -\textstyle\sum_j \left\langle \boldsymbol{\Psi}, \boldsymbol{\Upsilon}_j \right\rangle \odot \boldsymbol{X}_j = \; -\textstyle\sum_j \left(\int_{\mathbb{R}^+} \int_{\mathbb{R}^D} \boldsymbol{\Psi}\boldsymbol{\Upsilon}_j d\vec{v} d\mathbb{I} \right) \odot \boldsymbol{X}_j = 0 \tag{3.82}$$

where moment vector function is defined as $\boldsymbol{\Psi} = \left[1, \vec{v}, \mathbb{I} + \frac{1}{2}\vec{v}^T\vec{v}\right]^T$.

3.4.2 Statistical representation of new kinetic model

In statistics there are many varied approaches to measure divergence between two generalized probability density function $f_g(x)$ and $f_h(x)$. Kullback-Leibler divergence [144] is one such measure which provides relative entropy. Kullback-Leibler divergence is defined as follows

$$D(f_g \| f_h) = \int f_g(x) ln \frac{f_g(x)}{f_h(x)} dx \tag{3.83}$$

Kullback-Leibler divergence is asymmetric, always non-negative and becomes zero if and only if both the distributions are identical. Kullback-Leibler symmetric divergence can be written as

$$D(f_g, f_h) = D(f_g \| f_h) + D(f_h \| f_g) = \int (f_g(x) - f_h(x)) \, ln \frac{f_g(x)}{f_h(x)} dx \tag{3.84}$$

Kullback-Leibler symmetric divergence $D(f_g, f_h)$ equals Mahalanobis distance [176] when $f_g(x)$ and $f_h(x)$ are multivariate normal distributions with common variance-covariance matrix. Mahalanobis distance uses Galilean transformation and evaluates equivalent Euclidean distance under standard normal distribution. In the kinetic theory context $D(f, f_{ref})$ can be interpreted as Mahalanobis distance between two distributions f and f_{ref}.

3.4.2.1 Mahalanobis speed and entropy production

Consider Boltzmann H-function given by

$$H = \int_{\mathbb{R}^+} \int_{\mathbb{R}^D} f ln f d\vec{v} d\mathbb{I} \tag{3.85}$$

The time derivative of H-function can be cast as

$$\frac{\partial H}{\partial t} = \int_{\mathbb{R}^+} \int_{\mathbb{R}^D} J_m(f, f_0) ln f d\vec{v} d\mathbb{I} \tag{3.86}$$

Based on the additive invariant property due to conservation of mass, momentum and energy we can write

$$\int_{\mathbb{R}^+} \int_{\mathbb{R}^D} J_m(f, f_0) ln(f_0) d\vec{v} d\mathbb{I} = 0 \tag{3.87}$$

Using the above relationship the time derivative of Boltzmann H-function can also be written as

$$\frac{\partial H}{\partial t} = \int_{\mathbb{R}^+} \int_{\mathbb{R}^D} J_m(f, f_0) ln \frac{f}{f_0} d\vec{v} d\mathbb{I} \tag{3.88}$$

After substituting the kinetic model described by equation 3.70 we get

$$\begin{aligned} \frac{\partial H}{\partial t} &= -\frac{1}{t_{R(\tau)}} \left(\int_{\mathbb{R}^+} \int_{\mathbb{R}^D} (f - f_0) ln \frac{f}{f_0} d\vec{v} d\mathbb{I} \right)_{\boldsymbol{X}_q = 0} \\ &\quad -\frac{1}{t_{R(q)}} \left(\int_{\mathbb{R}^+} \int_{\mathbb{R}^D} (f - f_0) ln \frac{f}{f_0} d\vec{v} d\mathbb{I} \right)_{\boldsymbol{X}_\tau = 0} \\ &= -\frac{D(f, f_0)_{\boldsymbol{X}_q = 0}}{t_{R(\tau)}} - \frac{D(f, f_0)_{\boldsymbol{X}_\tau = 0}}{t_{R(q)}} \end{aligned} \tag{3.89}$$

where $D(f, f_0)_{\boldsymbol{X}_q = 0}$ and $D(f, f_0)_{\boldsymbol{X}_\tau = 0}$ are the Mahalanobis distance between distribution f and f_0 associated with thermodynamic force $\boldsymbol{X}_\tau$ and $\boldsymbol{X}_q$. This statistical representation helps us to draw analogy with Mahalanobis distance and its positivity property shows

$$\frac{\partial H}{\partial t} \leq 0 \tag{3.90}$$

this establishes an effortless proof of H-theorem for the new kinetic model. The entropy production can be written as

$$\begin{aligned} \sigma(f, f_0) &= -R \frac{\partial H}{\partial t} = R \frac{D(f, f_0)_{\boldsymbol{X}_q = 0}}{t_{R(\tau)}} + R \frac{D(f, f_0)_{\boldsymbol{X}_\tau = 0}}{t_{R(q)}} \\ &= \dot{M}_q + \dot{M}_\tau \end{aligned} \tag{3.91}$$

where $\dot{M}_q$ and $\dot{M}_\tau$ are defined in this thesis as Mahalanobis rate of generation of entropy or Mahalanobis speed for thermodynamic force $\boldsymbol{X}_\tau$ and $\boldsymbol{X}_q$. Mahalanobis speed $\dot{M}_i$ gives the component of entropy production rate, σ_i associated with the thermodynamic force $\boldsymbol{X}_i$.

3.4.2.2 Mahalanobis speed and Onsager's entropy relationship

Mahalanobis speed $\dot{M}_i$ associated with thermodynamic force $\boldsymbol{X}_i$ for first order distribution function can be written as

$$\begin{aligned}
\dot{M}_i &= R\left(\frac{D(f_1,f_0)}{t_{R(i)}}\right)_{\boldsymbol{X}_j=0,\forall j\neq i} = -R\left(\frac{\partial H}{\partial t}\right)_{\boldsymbol{X}_j=0,\forall j\neq i} \\
&= -R\int_{\mathbb{R}^+}\int_{\mathbb{R}^D} J_m(f,f_0)_{\boldsymbol{X}_j=0,\forall j\neq i} ln f d\vec{v} d\mathbb{I} \\
&= -R\int_{\mathbb{R}^+}\int_{\mathbb{R}^D}\left(\frac{\boldsymbol{\Upsilon}_i\odot\boldsymbol{X}_i}{t_{R(i)}}\right)_{\boldsymbol{X}_j=0,\forall j\neq i} ln f d\vec{v} d\mathbb{I} \\
&= R\left(\int_{\mathbb{R}^+}\int_{\mathbb{R}^D} f_0\bar{\boldsymbol{\Upsilon}}_i ln f d\vec{v} d\mathbb{I}\right)_{\boldsymbol{X}_j=0,\forall j\neq i}\odot\boldsymbol{X}_i \\
&= \boldsymbol{J}_i\odot\boldsymbol{X}_i
\end{aligned} \tag{3.92}$$

where $\boldsymbol{J}_i$ is the entropy flux associated with the thermodynamic force $\boldsymbol{X}_i$ as the physical state evolves with Mahalanobis speed $\dot{M}_i$ satisfying Onsager's relationship. Figure 3.2 shows Mahalanobis speed for thermodynamic force $\boldsymbol{X}_\tau$ and $\boldsymbol{X}_q$.

3.4.3 Derivation of Euler and Navier-Stokes equation

Euler and Navier-Stokes equation can be derived with an assumption that the departure from equilibrium is small and the first order Chapman-Enskog distribution is valid. Euler and Navier-Stokes equations are obtained by taking $\boldsymbol{\Psi}$-moments of the Boltzmann equation using the first order Chapman-Enskog distribution. Consider $\boldsymbol{\Psi}$-moments of the one-dimensional Boltzmann equation as follows

$$\left\langle \boldsymbol{\Psi}, \frac{\partial f_1}{\partial t} + \frac{\partial v f_1}{\partial x} = 0 \right\rangle \tag{3.93}$$

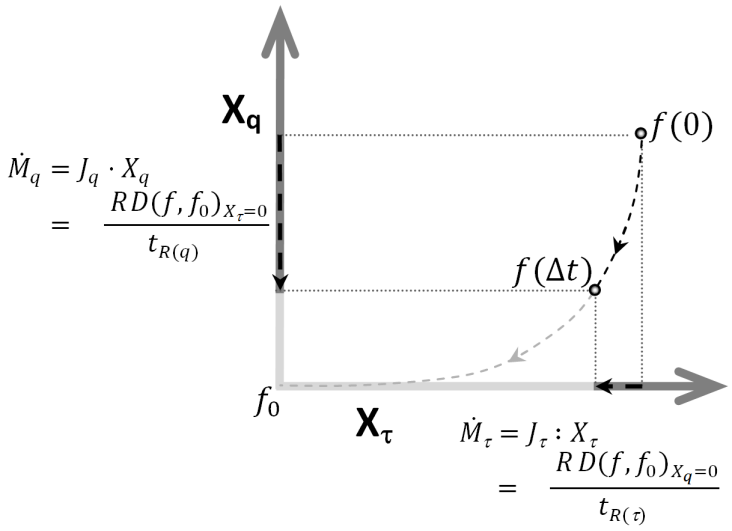

Figure 3.2: Mahalanobis speed for thermodynamic force $\boldsymbol{X}_\tau$ and $\boldsymbol{X}_q$ as non-equilibrium distribution f relaxes to equilibrium distribution f_0.

Substituting the first order Chapman-Enskog distribution based on new kinetic model, $f_1 = f_0 - \sum_j \boldsymbol{\Upsilon}_j \odot \boldsymbol{X}_j$ one can get

$$\left\langle \boldsymbol{\Psi}, \frac{\partial f_0 - \sum_j \boldsymbol{\Upsilon}_j \odot \boldsymbol{X}_j}{\partial t} \right\rangle + \left\langle \boldsymbol{\Psi}, \frac{\partial v(f_0 - \sum_j \boldsymbol{\Upsilon}_j \odot \boldsymbol{X}_j)}{\partial x} \right\rangle = 0 \tag{3.94}$$

This simplifies to

$$\frac{\partial \left\langle \boldsymbol{\Psi}, f_0 - \sum_j \boldsymbol{\Upsilon}_j \odot \boldsymbol{X}_j \right\rangle}{\partial t} + \frac{\partial \left\langle \boldsymbol{\Psi}, v f_0 \right\rangle}{\partial x} + \frac{\partial \left\langle \boldsymbol{\Psi}, -v \sum_j \boldsymbol{\Upsilon}_j \odot \boldsymbol{X}_j \right\rangle}{\partial x} = 0 \tag{3.95}$$

Due to additive invariants property the $\boldsymbol{\Psi}$ moments of the perturbation term does not contribute i.e.

$$\left\langle \boldsymbol{\Psi}, \sum_j \boldsymbol{\Upsilon}_j \odot \boldsymbol{X}_j \right\rangle = 0 \tag{3.96}$$

The $\boldsymbol{\Psi}$-moments of one dimensional Boltzmann equation simplifies to

$$\frac{\partial \left\langle \boldsymbol{\Psi}, f_0 \right\rangle}{\partial t} + \frac{\partial \left\langle \boldsymbol{\Psi}, v f_0 \right\rangle}{\partial x} + \frac{\partial - \sum_j \boldsymbol{\Lambda}_j \odot \boldsymbol{X}_j}{\partial x} = 0 \tag{3.97}$$

where macroscopic tensor $\boldsymbol{\Lambda}_j$ is defined as

$$\boldsymbol{\Lambda}_j = \langle \boldsymbol{\Psi}, v \boldsymbol{\Upsilon}_j \rangle \tag{3.98}$$

We get the one-dimensional Navier-Stokes equations as follows

$$\frac{\partial \boldsymbol{U}}{\partial t} + \frac{\partial \boldsymbol{GX_I}}{\partial x} + \frac{\partial \boldsymbol{GX_V}}{\partial x} = 0 \tag{3.99}$$

where $\boldsymbol{U}=(\rho, \rho u_x, \rho E)^T$ represent the conserved vector. $\boldsymbol{GX_I}$ is the x-component of the inviscid flux vector given as follows

$$\boldsymbol{GX}_I \;= \langle \boldsymbol{\Psi} v f_0 \rangle \;\equiv \int_{\mathbb{R}^+}\int_{\mathbb{R}} \boldsymbol{\Psi} v f_0 dv d\mathbb{I} \;= \begin{pmatrix} \rho u_x \\ p + \rho u_x^2 \\ \rho u_x E + u_x p \end{pmatrix} \tag{3.100}$$

$\boldsymbol{GX_V}$ is the x-component of the viscous flux vector given as follows

$$\begin{aligned} \boldsymbol{GX}_V \;&= -\textstyle\sum_j \boldsymbol{\Lambda}_j \odot \boldsymbol{X}_j = -\sum_j \langle \boldsymbol{\Psi} v \boldsymbol{\Upsilon}_j \rangle \odot \boldsymbol{X}_j \\ &\equiv -\sum_j \left(\int_{\mathbb{R}^+}\int_{\mathbb{R}} \boldsymbol{\Psi} v \boldsymbol{\Upsilon}_j dv d\mathbb{I} \right) \odot \boldsymbol{X}_j \end{aligned} \tag{3.101}$$

Components of macroscopic tensors $\boldsymbol{\Lambda}_\tau = [\Lambda_{1,\tau}, \Lambda_{2,\tau}, \Lambda_{3,\tau}]^T$ and $\boldsymbol{\Lambda}_q = [\Lambda_{1,q}, \Lambda_{2,q}, \Lambda_{3,q}]^T$ are given as follows

$$\begin{aligned} \Lambda_{1,\tau} &= [0], & \Lambda_{1,q} &= [0] \\ \Lambda_{2,\tau} &= \left[\tfrac{(3-\gamma)\mu\rho}{4p\beta^2}\right], & \Lambda_{2,q} &= [0] \\ \Lambda_{3,\tau} &= \left[u_x \tfrac{(3-\gamma)\mu\rho}{4p\beta^2}\right], & \Lambda_{3,q} &= \left[-\tfrac{\kappa\rho}{4pR\beta^3}\right] \end{aligned} \tag{3.102}$$

The thermodynamic forces are

$$\boldsymbol{X}_\tau = 2\beta \frac{\partial u_x}{\partial x}, \quad \boldsymbol{X}_q = -2R\beta^2 \tfrac{\partial T}{\partial x} \tag{3.103}$$

Using relation $\rho = 2p\beta$ the viscous fluxes are obtained as

$$\begin{aligned} \boldsymbol{GX}_V \;&= -\textstyle\sum_j \boldsymbol{\Lambda}_j \odot \boldsymbol{X}_j = -(\boldsymbol{\Lambda}_\tau : \boldsymbol{X}_\tau + \boldsymbol{\Lambda}_q \cdot \boldsymbol{X}_q) \\ &= \begin{pmatrix} 0 \\ -\tau_{xx} \\ -u_x \tau_{xx} + q_x \end{pmatrix} \end{aligned} \tag{3.104}$$

where shear stress tensor τ_{xx} based on kinetic theory is

$$\tau_{xx} = (3-\gamma)\mu \frac{\partial u_x}{\partial x} \tag{3.105}$$

and heat flux vector is

$$q_x = -\kappa \frac{\partial T}{\partial x} \tag{3.106}$$

3.4.3.1 Higher dimensional macroscopic tensors and validity of Stokes hypothesis

Macroscopic tensors $\mathbf{\Lambda}_\tau$, $\mathbf{\Lambda}_q$ satisfy Onsager's reciprocal principle and hence complies with the requirement of non-equilibrium thermodynamics. One dimensional derivation fails to provide a complete picture, hence a derivation for a higher dimensional case is required to illustrate the nature of the macroscopic tensors. Consider $\mathbf{\Psi}$-moments of a Boltzmann equation for a two dimensional fluid system as follows

$$\left\langle \mathbf{\Psi}, \frac{\partial f_1}{\partial t} + \frac{\partial v_x f_1}{\partial x} + \frac{\partial v_y f_1}{\partial y} = 0 \right\rangle \tag{3.107}$$

Substitution of the first order distribution for the polyatomic gas leads to

$$\begin{aligned} &\left\langle \mathbf{\Psi}, \frac{\partial f_0 - \sum_j \mathbf{\Upsilon}_j \odot \boldsymbol{X}_j}{\partial t} \right\rangle + \left\langle \frac{\partial v_x (f_0 - \sum_j \mathbf{\Upsilon}_j \odot \boldsymbol{X}_j)}{\partial x} \right\rangle \\ &+ \left\langle \frac{\partial v_y (f_0 - \sum_j \mathbf{\Upsilon}_j \odot \boldsymbol{X}_j)}{\partial y} \right\rangle = 0 \end{aligned} \tag{3.108}$$

After solving we get Navier-Stokes equation as follows

$$\frac{\partial \boldsymbol{U}}{\partial t} + \frac{\partial \boldsymbol{G X_I}}{\partial x} + \frac{\partial \boldsymbol{G X_V}}{\partial x} + \frac{\partial \boldsymbol{G Y_I}}{\partial y} + \frac{\partial \boldsymbol{G Y_V}}{\partial y} = 0 \tag{3.109}$$

where $\boldsymbol{U}=(\rho, \rho u_x, \rho u_y, \rho E)^T$ represent the conserved vector. As described earlier inviscid or Euler fluxes $\boldsymbol{GX}_I$,$\boldsymbol{GY}_I$ are based on Maxwellian, f_0 and viscous fluxes $\boldsymbol{GX}_V$, $\boldsymbol{GY}_V$ are based on perturbation $\mathrm{Kn}\bar{f}_1 = -(\sum_j \mathbf{\Upsilon}_j \odot \boldsymbol{X}_j)$. The mass, momentum and energy components of inviscid fluxes are

$$\begin{aligned} [GX_{I,i}, GY_{I,i}] &= [\langle \psi_i v_x f_0 \rangle, \langle \psi_i v_y f_0 \rangle] \\ &\equiv \int_{\mathbb{R}^+} \int_{\mathbb{R}^2} \psi_i \vec{v} f_0 d\vec{v} d\mathbb{I} \end{aligned} \tag{3.110}$$

where v_x and v_y are the Cartesian components of molecular velocity $\vec{v}$ and moment variable $\psi_i \in \mathbf{\Psi}$.

The mass, momentum and energy components of viscous fluxes are

$$[GX_{V,i}, GY_{V,i}] = [-\textstyle\sum_j \Lambda^x_{i,j} \odot \boldsymbol{X}_j, -\sum_j \Lambda^y_{i,j} \odot \boldsymbol{X}_j] \tag{3.111}$$

where $\Lambda^x_{i,j}$ and $\Lambda^y_{i,j}$ are the macroscopic tensors associated with heat flux vector and stress tensor expressed as

$$\begin{aligned} [\Lambda^x_{i,j}, \Lambda^y_{i,j}] &= [\langle \psi_i v_x \mathbf{\Upsilon}_j \rangle, \langle \psi_i v_y \mathbf{\Upsilon}_j \rangle] \\ &\equiv \int_{\mathbb{R}^+} \int_{\mathbb{R}^2} \psi_i \vec{v} \mathbf{\Upsilon}_j d\vec{v} d\mathbb{I} \end{aligned} \tag{3.112}$$

The components of macroscopic tensors $\mathbf{\Lambda}_{\tau}^{x}$ and $\mathbf{\Lambda}_{q}^{x}$ are obtained as

$$\begin{aligned}
\Lambda_{1,\tau}^{x} &= \begin{bmatrix} 0 & 0 \\ 0 & 0 \end{bmatrix}, & \Lambda_{1,q}^{x} &= \begin{bmatrix} 0 & 0 \end{bmatrix} \\
\Lambda_{2,\tau}^{x} &= \begin{bmatrix} \frac{(3-\gamma)\mu\rho}{4p\beta^2} & 0 \\ 0 & \frac{(1-\gamma)\mu\rho}{4p\beta^2} \end{bmatrix}, & \Lambda_{2,q}^{x} &= \begin{bmatrix} 0 & 0 \end{bmatrix} \\
\Lambda_{3,\tau}^{x} &= \begin{bmatrix} 0 & \frac{\mu\rho}{4p\beta^2} \\ \frac{\mu\rho}{4p\beta^2} & 0 \end{bmatrix}, & \Lambda_{3,q}^{x} &= \begin{bmatrix} 0 & 0 \end{bmatrix} \\
\Lambda_{4,\tau}^{x} &= \begin{bmatrix} u_x\frac{(3-\gamma)\mu\rho}{4p\beta^2} & u_y\frac{\mu\rho}{4p\beta^2} \\ u_y\frac{\mu\rho}{4p\beta^2} & u_x\frac{(1-\gamma)\mu\rho}{4p\beta^2} \end{bmatrix}, & \Lambda_{4,q}^{x} &= \begin{bmatrix} -\frac{\kappa\rho}{4pR\beta^3} & 0 \end{bmatrix}
\end{aligned} \tag{3.113}$$

Similarly, the components of macroscopic tensors $\mathbf{\Lambda}_{\tau}^{y}$ and $\mathbf{\Lambda}_{q}^{y}$ are obtained as

$$\begin{aligned}
\Lambda_{1,\tau}^{y} &= \begin{bmatrix} 0 & 0 \\ 0 & 0 \end{bmatrix}, & \Lambda_{1,q}^{y} &= \begin{bmatrix} 0 & 0 \end{bmatrix} \\
\Lambda_{2,\tau}^{y} &= \begin{bmatrix} 0 & \frac{\mu\rho}{4p\beta^2} \\ \frac{\mu\rho}{4p\beta^2} & 0 \end{bmatrix}, & \Lambda_{2,q}^{y} &= \begin{bmatrix} 0 & 0 \end{bmatrix} \\
\Lambda_{3,\tau}^{y} &= \begin{bmatrix} \frac{(1-\gamma)\mu\rho}{4p\beta^2} & 0 \\ 0 & \frac{(3-\gamma)\mu\rho}{4p\beta^2} \end{bmatrix}, & \Lambda_{3,q}^{y} &= \begin{bmatrix} 0 & 0 \end{bmatrix} \\
\Lambda_{4,\tau}^{y} &= \begin{bmatrix} u_y\frac{(1-\gamma)\mu\rho}{4p\beta^2} & u_x\frac{\mu\rho}{4p\beta^2} \\ u_x\frac{\mu\rho}{4p\beta^2} & u_y\frac{(3-\gamma)\mu\rho}{4p\beta^2} \end{bmatrix}, & \Lambda_{4,q}^{x} &= \begin{bmatrix} 0 & -\frac{\kappa\rho}{4pR\beta^3} \end{bmatrix}
\end{aligned} \tag{3.114}$$

Because of isotropy due to rotational invariance of the collision operator the macroscopic tensor associated with shear stress tensor follows the symmetry relationship by satisfying $\Lambda_{\tau}^{x,\psi_i}(r,s) = \Lambda_{\tau}^{x,\psi_i}(s,r)$ and $\Lambda_{\tau}^{y,\psi_i}(r,s) = \Lambda_{\tau}^{y,\psi_i}(s,r)$ where r, s are the component index of the tensor such that $s \neq r$. The thermodynamic forces are

$$\boldsymbol{X}_{\tau} \equiv \begin{pmatrix} 2\beta\frac{\partial u_x}{\partial x} & 2\beta\left(\frac{\partial u_y}{\partial x} + \frac{\partial u_x}{\partial y}\right) \\ 2\beta\left(\frac{\partial u_y}{\partial x} + \frac{\partial u_x}{\partial y}\right) & 2\beta\frac{\partial u_y}{\partial y} \end{pmatrix}, \quad \boldsymbol{X}_{q} \equiv \begin{pmatrix} -2R\beta^2\frac{\partial T}{\partial x} & -2R\beta^2\frac{\partial T}{\partial y} \end{pmatrix} \tag{3.115}$$

The viscous fluxes are obtained as

$$\begin{aligned}
\boldsymbol{G}\boldsymbol{X}_V &= -\textstyle\sum_j \mathbf{\Lambda}_j^x \odot \boldsymbol{X}_j \\
&= \begin{pmatrix} 0 \\ -\tau_{xx} \\ -\tau_{xy} \\ -u_x\tau_{xx} - u_y\tau_{xy} + q_x \end{pmatrix}
\end{aligned} \tag{3.116}$$

$$\begin{aligned} \boldsymbol{GY}_V &= -\sum_j \boldsymbol{\Lambda}_j^y \odot \boldsymbol{X}_j \\ &= \begin{pmatrix} 0 \\ -\tau_{xy} \\ -\tau_{yy} \\ -u_x\tau_{xy} - u_y\tau_{yy} + q_y \end{pmatrix} \end{aligned} \tag{3.117}$$

Here u_x and u_y are the velocity components in Cartesian frame, ρ is the density, T is the static temperature and p is the pressure which is calculated from equation of state of perfect gas. The heat flux vector is

$$\vec{q} = -\kappa \nabla T \tag{3.118}$$

Tensor of viscous stresses $\boldsymbol{\Pi}$ is given as

$$\boldsymbol{\Pi} = \mu \left[(\nabla \otimes \vec{u}) + (\nabla \otimes \vec{u})^T - \frac{2}{3} \boldsymbol{I} \nabla \cdot \vec{u} \right] + \zeta \boldsymbol{I} \nabla \cdot \vec{u} \tag{3.119}$$

where $\boldsymbol{I}$ is the rank-D identity invariant tensor, ζ is the coefficient of bulk viscosity expressed as

$$\zeta = \mu \left(\frac{5}{3} - \gamma \right) \tag{3.120}$$

From the expression of shear stress derived using kinetic theory it is evident that Stokes hypothesis is only valid for mono-atomic gases as $\gamma = 5/3$ *and* $\zeta = 0$. Otherwise, $\zeta > 0$ as $1 < \gamma < 5/3$. For polyatomic gas the concept of bulk viscosity term will change if elastic collisions are included e.g. when elastic and inelastic collision terms are of the same order Eucken correction to heat transfer coefficient and bulk viscosity may appear.

3.4.4 Realizability of moments for the first order distribution function

Local entropy production due to the collision term can be written as

$$\sigma(\vec{v}, t) = -R \int_{\mathbb{R}^+} \int_{\mathbb{R}^D} lnf J(f, f) d\vec{v} d\mathbb{I} \geq 0 \tag{3.121}$$

where R is specific gas constant. It follows from the Boltzmann equation that collisions between the molecules in the non-equilibrium state lead to entropy production. The Boltzmann H-theorem states that entropy production is positive

for all distributions. As described earlier the Chapman-Enskog expansion leads to f=$[1+\Phi]$ where Φ is perturbation term associated with the shear stress tensor and heat flux vector function of peculiar velocity and derivatives in space and time of temperature and velocity. The Chapman-Enksog distribution will become negative only when Φ<-1 for large value of peculiar velocity $\vec{c}$. Using the approach of Struchtrup[263] we fix a velocity bound c_{max} such that

$$\|\Phi\| < 1 \qquad for \qquad c < c_{max} \tag{3.122}$$

The entropy production after substituting the distribution with Chapman-Enskog distribution can be written as

$$\begin{aligned} \sigma(\vec{v},t) &= -R\int_{\mathbb{R}^+}\int_{\mathbb{R}^D} ln(f_0[1+\Phi])J_m(f,f_0)d\vec{v}d\mathbb{I} \\ &= -R\int_{\mathbb{R}^+}\int_{\mathbb{R}^D} ln[1+\Phi]J_m(f,f_0)d\vec{v}d\mathbb{I} \end{aligned} \tag{3.123}$$

Since the Chapman-Enskog polynomial is bounded by $\|\Phi\| < 1$, the entropy production can also be expressed by expanding the natural logarithm into a Taylor series as

$$\begin{aligned} \sigma(\vec{v},t) &= -R\int_{\mathbb{R}^+}\int_{\mathbb{R}^D} \left[\Phi - \frac{\Phi^2}{2} + \cdots\right] J_m(f,f_0)d\vec{v}d\mathbb{I} \\ &= -R\int_{\mathbb{R}^+}\int_{\mathbb{R}^D} \left[\mathrm{Kn}\xi_1 + \mathrm{Kn}^2(-\frac{1}{2}\xi_1^2 + \frac{\bar{f}_1}{f_0}\xi_2 + \cdots\right] J_m(f,f_0)d\vec{v}d\mathbb{I} \end{aligned} \tag{3.124}$$

The condition $\|\Phi\| < 1$ for the Chapman-Enskog expansion can also be interpreted as $\|\frac{\boldsymbol{\Upsilon}_\tau : \boldsymbol{X}_\tau}{f_0}\| \leq 1$ and $\|\frac{\boldsymbol{\Upsilon}_q \cdot \boldsymbol{X}_q}{f_0}\| \leq 1$. This leads to following condition

$$\begin{aligned} &\left[\tfrac{(2+D)\gamma-(4+D)}{2(2-(\gamma-1)D)} - \tfrac{\mathbb{I}}{4\beta\mathbb{I}_o^2} + \beta c_i^2\right]|\tau_{ii}| + 2\beta|c_i c_j \tau_{ij}| \leq 1 \\ &|\left[\tfrac{(4+D)}{2} - \tfrac{\mathbb{I}}{\mathbb{I}_o} - \beta c^2\right] c_i q_i| \leq 1 \end{aligned} \tag{3.125}$$

Entropy generation for the first order Chapman-Enskog distribution is

$$\begin{aligned} \sigma(\vec{v},t) &= -R\int_{\mathbb{R}^+}\int_{\mathbb{R}^D} \Phi J_m(f,f_0)d\vec{v}d\mathbb{I} \\ &= R\sum_i \left(\int_{\mathbb{R}^+}\int_{\mathbb{R}^D} f_0 \bar{\boldsymbol{\Upsilon}}_i ln f d\vec{v}d\mathbb{I}\right)_{\boldsymbol{X}_j=0,\forall j\neq i} \odot \boldsymbol{X}_i \\ &= \sum_i (\boldsymbol{J}_i \odot \boldsymbol{X}_i) \end{aligned} \tag{3.126}$$

Based on first order expansion the entropy generation is always positive and looks independent of velocity and temperature gradients involved in thermodynamic force $\boldsymbol{X}$. This is an incorrect interpretation as the very validity of first order Chapman-Enskog distribution is not ensured at higher gradients or when condition described by equation 3.125 i.e. $\|\frac{\boldsymbol{\Upsilon}_i \odot \boldsymbol{X}_i}{f_0}\| \leq 1$ is violated.

3.5 Summary

For a prescribed irreversible force $\boldsymbol{X}_i$ the actual flux $\boldsymbol{J}_i$ which satisfies Onsager's reciprocity principle maximizes the entropy production, $\sigma(\boldsymbol{X}_i, \boldsymbol{J}_i) = \sum_i \boldsymbol{J}_i \odot \boldsymbol{X}_i$. It is also shown that the perturbation term due to non-equilibrium distribution also follows Onsager's relationship as it can be expressed in terms of thermodynamic forces and its conjugate microscopic fluxes. Existing Morse-BGK model for polyatomic is single relaxation model that gives incorrect Prandtl number. A new kinetic model was proposed based on the principles of non-equilibrium thermodynamics. The new kinetic model is computationally inexpensive and gives correct Prandtl number in the hydrodynamic limit and follows Onsager's reciprocity principle. Kinetic model was also given statistical representation by relating entropy production with positivity of Mahalanobis distance, yielding an effortless proof of H-theorem. Chapman-Enskog procedure was extended for this new kinetic model to obtain distribution function which can be expressed in terms of thermodynamic force and its conjugate microscopic tensor. Euler and Navier-Stokes equations were also derived by taking $\boldsymbol{\Psi}$-moments of the Boltzmann equation using the first order Chapman-Enskog distribution, and nature of associated macroscopic tensors was also illustrated.

Chapter 4

Development of Kinetic Upwind method based on microscopic tensor splitting

4.1 Introduction

As the state update moves from one time step to another time step it decreases the thermodynamic forces and generates entropy which is the product of the thermodynamic forces and its conjugate fluxes. *All the research in the development of upwind scheme revolves around the methodology of adding the correct dissipation or entropy and its correct distribution for each thermodynamic force associated with shear stress tensor and heat flux vector.* In precise words the state update of a solver has to follow the path laid down by non-equilibrium thermodynamics. For example if the amount of dissipation is too less then the solver will fail to capture shocks and if the amount of dissipation is too high then natural viscous behavior will get overshadowed. The correct amount of dissipation and its distribution for each thermodynamic force depends on the physical process through which state update passes, hence it is difficult to have a single monolithic solver operating across the regime from rarefied flow to hypersonic continuum flow. If the solver follows and mimics the physics then we can have a single compressible flow solver serving the entire range from rarefied flow to continuum flow, creeping flow to flow with shocks. The research in the development of such a solver

will follows a rigorous procedure based on principles of kinetic theory incorporating phenomenological theory of non-equilibrium thermodynamics. The present research uses the approach of kinetic flux vector splitting using kinetic model and distribution function based on features of non-equilibrium thermodynamics. The present research also aims to have a single robust solver that naturally adds the necessary dissipation for each thermodynamic force and mimics the physics. This chapter describes kinetic flux vector splitting scheme based on microscopic tensor splitting which is entropy consistent and does not suffer from the many pathological behavior of other flux differencing / splitting schemes. The numerical dissipation in the kinetic scheme can be controlled by incorporating the modified Courant splitting based on dissipation control parameter. The chapter describes axi-symmetric formulation of kinetic scheme and also describes a novel scheme Variation Reduction Kinetic Flux Vector Splitting scheme (VRKFVS) which solves for the deviations over the chosen Maxwellian. Using this method the solver can capture very weak secondary flow features embedded in strong primary flow field.

4.2 Kinetic upwind method for Navier-Stokes equations

As explained earlier kinetic schemes exploits the connection between the Boltzmann equation and the governing conservation equations at the macroscopic level. Kinetic Flux Vector Splitting (KFVS) pioneered by Deshpande [70] extended by Chou and Baganoff [54] for Navier-Stokes equations involves two steps : i) in the first step the Boltzmann equation is rendered into an upwind discretized form, ii) in the second step $\mathbf{\Psi}$ moments of the upwind discretized Boltzmann equation are taken to obtain upwind scheme for the macroscopic conservation equations at which the state update operates.

4.2.1 Kinetic Flux Vector Splitting based on distribution splitting

Consider Boltzmann equation for one dimensional case with first order distribution function as follows

$$\frac{\partial f_1}{\partial t} + \frac{\partial v f_1}{\partial x} = 0 \tag{4.1}$$

The upwind CIR split-form for first order distribution function can be written as

$$\frac{\partial f_1}{\partial t} + \frac{\partial \frac{v+|v|}{2} f_1^+}{\partial x} + \frac{\partial \frac{v-|v|}{2} f_1^-}{\partial x} \tag{4.2}$$

where f_1^+ is the half-range first order distribution function for $0 < v < +\infty$ and f_1^- is the half-range distribution function for $-\infty < v < 0$. Thus in KFVS the distribution function at time $t + \Delta t$ in a fluid domain is constructed based on half range distribution as follows

$$f_1^{t+\Delta t} = f_1^t - \Delta t \left[\left(\frac{\partial v f_1^+}{\partial x} \right)^t_{0<v<+\infty} + \left(\frac{\partial v f_1^-}{\partial x} \right)^t_{-\infty<v<0} \right] \tag{4.3}$$

State update equation is obtained by taking $\boldsymbol{\Psi}$ moments as follows

$$\left\langle \boldsymbol{\Psi}, f_1^{t+\Delta t} \right\rangle = \left\langle \boldsymbol{\Psi}, f_1^t \right\rangle - \Delta t \begin{bmatrix} \left(\frac{\partial \left\langle \boldsymbol{\Psi}, v f_1^+ \right\rangle}{\partial x} \right)^t_{0<v<+\infty} \\ + \left(\frac{\partial \left\langle \boldsymbol{\Psi}, v f_1^- \right\rangle}{\partial x} \right)^t_{-\infty<v<0} \end{bmatrix} \tag{4.4}$$

Since the perturbation term satisfies the additive invariants property i.e. $\langle \boldsymbol{\Psi}, \mathrm{Kn}\bar{f}_1 \rangle = 0$, the one-dimensional Boltzmann equation in upwind form simplifies to

$$\left\langle \boldsymbol{\Psi}, f_0^{t+\Delta t} \right\rangle = \left\langle \boldsymbol{\Psi}, f_0^t \right\rangle - \Delta t \begin{bmatrix} \left(\frac{\partial \left\langle \boldsymbol{\Psi}, v f_1^+ \right\rangle}{\partial x} \right)^t_{0<v<+\infty} \\ + \left(\frac{\partial \left\langle \boldsymbol{\Psi}, v f_1^- \right\rangle}{\partial x} \right)^t_{-\infty<v<0} \end{bmatrix} \tag{4.5}$$

This leads to upwind equations in macroscopic form i.e. Navier-Stokes equations in kinetic upwind form as follows

$$\boldsymbol{U}(t + \Delta t) = \boldsymbol{U}(t) - \Delta t \left[\left(\frac{\partial \boldsymbol{G}\boldsymbol{X}^+(t)}{\partial x} \right)_{\Delta x<0} + \left(\frac{\partial \boldsymbol{G}\boldsymbol{X}^-(t)}{\partial x} \right)_{\Delta x>0} \right] \tag{4.6}$$

where $\boldsymbol{U} = [\rho, \rho u_x, \rho E]^T$ is the state update vector, where $E = RT/(\gamma - 1) + \frac{1}{2}u_x^2$, u_x is the macroscopic fluid velocity and γ is the specific heat ratio and split flux is $\boldsymbol{GX}^{\pm} = \langle \boldsymbol{\Psi}, v f_1^{\pm} \rangle$. Upwinding in macroscopic level is enforced using stencil subdivision. The derivative $\frac{\partial \boldsymbol{GX}^+}{\partial x}$ is evaluated using left side of the stencil $\Delta x < 0$ and derivative $\frac{\partial \boldsymbol{GX}^-}{\partial x}$ is evaluated using right side of the stencil $\Delta x > 0$.

4.2.2 KFVS based on microscopic tensor splitting

The new approach is guided by the principles of non-equilibrium thermodynamics and it differs from the approach of Chou and Baganoff [54]. In the new approach the viscous flux are split based on splitting of microscopic tensor associated with each thermodynamic force. The new method involves three steps : i) in the first step the Boltzmann equation is rendered into an upwind discretized form in terms of Maxwellian distribution and its perturbation term based on microscopic tensor and its conjugate thermodynamic forces , ii) in the second step inviscid or Euler fluxes are obtained by taking $\boldsymbol{\Psi}$ moments of split Maxwellian distribution, iii) in the third step viscous fluxes are obtained by taking moments and full tensor contraction of split microscopic tensors to obtain upwind scheme for macroscopic conservation equations. The method of obtaining inviscid or Euler fluxes by splitting the Maxwellian distribution in the new approach is similar to KFVS based on distribution splitting. *The method of evaluation of viscous split fluxes in the new approach differs from the KFVS extended by Chou and Baganoff [54] for Navier-Stokes which was based on distribution splitting. The new approach evaluates the viscous fluxes by taking moments of split microscopic tensors and subsequent full tensor contraction with its conjugate thermodynamic forces. The new approach gives the explicit contribution of entropy generation due to thermodynamic forces associated with shear stress tensor and heat flux vector and follows Onsager reciprocity principle.* Following sub-sections describes the three steps involved in the new upwind scheme.

4.2.2.1 Step 1 : Boltzmann equation in upwind form

Assuming that the departure from equilibrium is small we then use the first order Chapman-Enskog distribution, $f_1 = f_0 + \mathrm{Kn}\bar{f}_1$ to express Navier-Stokes equation

in upwind form as

$$\begin{aligned}\left\langle \boldsymbol{\Psi}, \{f_0 + \mathrm{Kn}\bar{f}_1\}^{t+\Delta t} \right\rangle &= \left\langle \boldsymbol{\Psi}, \{f_0 + \mathrm{Kn}\bar{f}_1\}^{t} \right\rangle \\ &-\Delta t \left[\begin{array}{l} \left(\frac{\partial \left\langle \boldsymbol{\Psi}, v\{f_0+\mathrm{Kn}\bar{f}_1\}^{+} \right\rangle}{\partial x} \right)^{t}_{0<v<+\infty} \\ + \left(\frac{\partial \left\langle \boldsymbol{\Psi}, v\{f_0+\mathrm{Kn}\bar{f}_1\}^{-} \right\rangle}{\partial x} \right)^{t}_{-\infty<v<0} \end{array} \right] \end{aligned} \tag{4.7}$$

The first order Chapman-Enskog distribution, $f_1{=}f_0 + \mathrm{Kn}\bar{f}_1{=}f_0 - \sum_j \boldsymbol{\Upsilon}_j \odot \boldsymbol{X}_j$. Taking $\boldsymbol{\Psi}$-moments of the one-dimensional Boltzmann equation in the upwind discretized form in terms of Maxwellian distribution and its perturbation term based on microscopic tensor and its conjugate thermodynamic forces, we get

$$\begin{aligned}\left\langle \boldsymbol{\Psi}, \{f_0 - \textstyle\sum_j \boldsymbol{\Upsilon}_j \odot \boldsymbol{X}_j\}^{t+\Delta t} \right\rangle &= \left\langle \boldsymbol{\Psi}, \{f_0 - \textstyle\sum_j \boldsymbol{\Upsilon}_j \odot \boldsymbol{X}_j\}^{t} \right\rangle \\ &-\Delta t \left[\begin{array}{l} \left(\frac{\partial \left\langle \boldsymbol{\Psi}, v\{f_0-\sum_j \boldsymbol{\Upsilon}_j \odot \boldsymbol{X}_j\}^{+} \right\rangle}{\partial x} \right)^{t}_{0<v<+\infty} \\ + \left(\frac{\partial \left\langle \boldsymbol{\Psi}, v\{f_0-\sum_j \boldsymbol{\Upsilon}_j \odot \boldsymbol{X}_j\}^{-} \right\rangle}{\partial x} \right)^{t}_{-\infty<v<0} \end{array} \right] \end{aligned} \tag{4.8}$$

The perturbation term $-\sum_j \boldsymbol{\Upsilon}_j \odot \boldsymbol{X}_j$ satisfies the additive invariants property

$$\left\langle \boldsymbol{\Psi}, -\sum_j \boldsymbol{\Upsilon}_j \odot \boldsymbol{X}_j \right\rangle = 0 \tag{4.9}$$

The Boltzmann equation after taking $\boldsymbol{\Psi}$-moments simplifies to

$$\begin{aligned}\left\langle \boldsymbol{\Psi}, f_0^{t+\Delta t} \right\rangle &= \langle \boldsymbol{\Psi}, f_0^{t} \rangle \\ &-\Delta t \left[\begin{array}{l} \left(\frac{\partial \left\langle \boldsymbol{\Psi}, v f_0^{+} \right\rangle}{\partial x} \right)^{t}_{0<v<+\infty} + \left(\frac{\partial - \sum_j \boldsymbol{\Lambda}_j^{+} \odot \boldsymbol{X}_j}{\partial x} \right)^{t}_{0<v<+\infty} \\ + \left(\frac{\partial \left\langle \boldsymbol{\Psi}, v f_0^{-} \right\rangle}{\partial x} \right)^{t}_{-\infty<v<0} + \left(\frac{\partial - \sum_j \boldsymbol{\Lambda}_j^{-} \odot \boldsymbol{X}_j}{\partial x} \right)^{t}_{-\infty<v<0} \end{array} \right] \end{aligned} \tag{4.10}$$

where positive macroscopic split tensor $\boldsymbol{\Lambda}_j^{+}$ is based on half range first order distribution function for $0 < v < +\infty$ as follows

$$\boldsymbol{\Lambda}_j^{+} = \left\langle \boldsymbol{\Psi}, v\boldsymbol{\Upsilon}_j^{+} \right\rangle \equiv \int_0^{+\infty} \int_0^{+\infty} \boldsymbol{\Psi} v \boldsymbol{\Upsilon}_j dv d\mathbb{I} \tag{4.11}$$

Similarly, negative macroscopic split tensor $\mathbf{\Lambda}_j^-$ is based on half-range distribution function for $-\infty < v < 0$ as follows

$$\mathbf{\Lambda}_j^- = \left\langle \mathbf{\Psi}, v\mathbf{\Upsilon}_j^- \right\rangle \equiv \int_0^{+\infty} \int_{-\infty}^{0} \mathbf{\Psi} v \mathbf{\Upsilon}_j dv d\mathbb{I} \tag{4.12}$$

This leads to upwind equations in macroscopic form i.e. Navier-Stokes equations in kinetic upwind form

$$\boldsymbol{U}(t+\Delta t) = \boldsymbol{U}(t) - \Delta t \left[\begin{array}{l} \left(\frac{\partial \boldsymbol{GX}_I^+(t)}{\partial x}\right)_{\Delta x<0} + \left(\frac{\partial \boldsymbol{GX}_I^-(t)}{\partial x}\right)_{\Delta x>0} \\ + \left(\frac{\partial \boldsymbol{GX}_V^+(t)}{\partial x}\right)_{\Delta x<0} + \left(\frac{\partial \boldsymbol{GX}_V^-(t)}{\partial x}\right)_{\Delta x>0} \end{array} \right] \tag{4.13}$$

Upwinding in macroscopic level is enforced using stencil sub-division. The flux is composed of inviscid, $\boldsymbol{GX}_I^{\pm}$ and viscous part $\boldsymbol{GX}_V^{\pm}$. The inviscid part of the flux component, $\boldsymbol{GX}_I^{\pm} = \langle \mathbf{\Psi}, v f_0^{\pm} \rangle$ and viscous part of the flux component $\boldsymbol{GX}_V^{\pm}$ $= \langle \mathbf{\Psi}, v\mathrm{Kn}\bar{f}_1^{\pm} \rangle$. The term $\boldsymbol{U}$ is the state update vector defined as

$$\boldsymbol{U} = \langle \mathbf{\Psi}, f_0 \rangle = \int_0^{+\infty} \int_{-\infty}^{+\infty} \mathbf{\Psi} f_0 dv d\mathbb{I} = \left[\begin{array}{l} \rho \\ \rho u_x \\ \rho E \end{array} \right] \tag{4.14}$$

where $E = RT/(\gamma - 1) + \frac{1}{2}u_x^2$, u_x is the macroscopic fluid velocity and γ is the specific heat ratio.

4.2.2.2 Step 2 : Evaluation of split inviscid fluxes based on split Maxwellian distribution

Like in KFVS the split Euler or inviscid fluxes are obtained based on split half range Maxwellian distribution i.e. split positive flux $\boldsymbol{GX}^+$ is evaluated using half range Maxwellian distribution f_0^+ for positive molecular velocities $0 < v < +\infty$ while split negative flux $\boldsymbol{GX}^-$ is evaluated using half range Maxwellian distribution f_0^- for negative molecular velocities $+\infty < v < 0$. Thus the inviscid part of the flux component, $\boldsymbol{GX}_I^{\pm}$ is defined as

$$\begin{aligned} \boldsymbol{GX}_I^+ &= \left\langle \mathbf{\Psi}, v f_0^+ \right\rangle = \int_0^{+\infty} \int_0^{\infty} \mathbf{\Psi} v f_0 dv d\mathbb{I} \\ \boldsymbol{GX}_I^- &= \left\langle \mathbf{\Psi}, v f_0^- \right\rangle = \int_0^{+\infty} \int_{-\infty}^{0} \mathbf{\Psi} v f_0 dv d\mathbb{I} \end{aligned} \tag{4.15}$$

The expression of inviscid flux $\boldsymbol{GX}_I^{\pm}$ is given as

$$\boldsymbol{GX}_I^{\pm} = \begin{bmatrix} \frac{1}{2}A^{\pm}\rho u_x + \rho\left(\frac{B^{\pm}}{2\sqrt{\pi\beta}}\right) \\ \frac{1}{2}A^{\pm}(p+\rho u_x^2) + \rho u_x\left(\frac{B^{\pm}}{2\sqrt{\pi\beta}}\right) \\ \frac{1}{2}A^{\pm}(pu_x+\rho u_x E) + \left(\frac{p}{2}+\rho E\right)\left(\frac{B^{\pm}}{2\sqrt{\pi\beta}}\right) \end{bmatrix} \tag{4.16}$$

where $A^{\pm}$ and $B^{\pm}$ are defined as

$$A^{\pm} = 1 \pm Erf(u_x\sqrt{\beta}), \quad B^{\pm} = \pm Exp(-\beta u_x^2) \tag{4.17}$$

4.2.2.3 Step 3 : Evaluation of split viscous fluxes based on split microscopic tensors

In the present upwind approach the viscous fluxes are evaluated based on full tensor contraction of split macroscopic tensors with its conjugate thermodynamic forces. The split macroscopic tensors are obtained by taking moments of the split microscopic tensors associated with the shear stress tensor and heat flux vector. Thus the viscous part of the flux component, $\boldsymbol{GX}_V^{\pm}$ is defined as

$$\begin{aligned} \boldsymbol{GX}_V^{+} &= -\sum_j \boldsymbol{\Lambda}_j^{+} \odot \boldsymbol{X}_j = -\sum_j \left(\int_0^{+\infty}\int_0^{\infty} \boldsymbol{\Psi} v \boldsymbol{\Upsilon}_j^{+} dv d\mathbb{I}\right) \odot \boldsymbol{X}_j \\ \boldsymbol{GX}_V^{-} &= -\sum_j \boldsymbol{\Lambda}_j^{-} \odot \boldsymbol{X}_j = -\sum_j \left(\int_0^{+\infty}\int_{-\infty}^{0} \boldsymbol{\Psi} v \boldsymbol{\Upsilon}_j^{-} dv d\mathbb{I}\right) \odot \boldsymbol{X}_j \end{aligned} \tag{4.18}$$

where $\boldsymbol{\Upsilon}^{+}$ is based on half-range Maxwellian distribution function for $0 < v < +\infty$. Similarly, $\boldsymbol{\Upsilon}^{-}$ is based on half-range Maxwellian distribution function for $-\infty < v < 0$. Components of macroscopic split tensors $\boldsymbol{\Lambda}_{\tau}^{\pm} = [\Lambda_{1,\tau}^{\pm}, \Lambda_{2,\tau}^{\pm}, \Lambda_{3,\tau}^{\pm}]^T$ and $\boldsymbol{\Lambda}_{q}^{\pm} = [\Lambda_{1,q}^{\pm}, \Lambda_{2,q}^{\pm}, \Lambda_{3,q}^{\pm}]^T$ are given as follows

$$\begin{aligned} \Lambda_{1,\tau}^{\pm} &= \left[\frac{B^{\mp}}{\sqrt{\pi}}\frac{(\gamma-3)\mu\rho}{8p\beta^{3/2}}\right], & \Lambda_{1,q}^{\pm} &= \left[-\frac{B^{\mp}}{\sqrt{\pi}}\frac{(\gamma-1)}{\gamma}\frac{\kappa\rho u_x}{4pR\beta^{3/2}}\right] \\ \Lambda_{2,\tau}^{\pm} &= \left[-\frac{(\gamma-3)\mu\rho A^{\pm}}{8p\beta^2}\right], & \Lambda_{2,q}^{\pm} &= \left[-\frac{B^{\mp}}{\sqrt{\pi}}\frac{(\gamma-1)}{\gamma}\frac{\kappa\rho}{4pR\beta^{5/2}}\right] \\ \Lambda_{3,\tau}^{\pm} &= \left[\frac{(\gamma-3)\mu\rho}{32p\beta^{5/2}}\left\{\frac{B^{\mp}}{\sqrt{\pi}}\frac{(3\gamma-1)}{(\gamma-1)} - 4u_x\sqrt{\beta}A^{\pm}\right\}\right], & \Lambda_{3,q}^{\pm} &= \left[\frac{\kappa\rho}{16pR\beta^3}\left\{\frac{B^{\mp}}{\sqrt{\pi}}\frac{u_x\sqrt{\beta}(\gamma-3)}{\gamma} - 2A^{\pm}\right\}\right] \end{aligned} \tag{4.19}$$

The viscous fluxes are obtained as

$$\boldsymbol{GX}_V^{\pm} = -\textstyle\sum_j \boldsymbol{\Lambda}_j^{\pm} \odot \boldsymbol{X}_j = -(\boldsymbol{\Lambda}_{\tau}^{\pm} : \boldsymbol{X}_{\tau} + \boldsymbol{\Lambda}_{q}^{\pm} \cdot \boldsymbol{X}_q) \tag{4.20}$$

Expression of viscous fluxes obtained after full tensor contraction with thermodynamic forces $\boldsymbol{X}_\tau = 2\beta\frac{\partial u_x}{\partial x}$ and $\boldsymbol{X}_q = -2R\beta^2\frac{\partial T}{\partial x}$ are

$$\boldsymbol{GX}_V^{\pm} = \begin{pmatrix} \frac{B^{\mp}}{\sqrt{\pi}}\frac{\rho}{4p\sqrt{\beta}}\left\{2u_x\beta q_x\frac{(\gamma-1)}{\gamma}+\tau_{xx}\right\} \\ \frac{\rho}{4p\beta}\left\{-2\frac{B^{\mp}}{\sqrt{\pi}}\sqrt{\beta}q_x\frac{(\gamma-1)}{\gamma}-A^{\pm}\tau_{xx}\right\} \\ \frac{\rho}{16p\beta^{3/2}}\left[\frac{B^{\mp}}{\sqrt{\pi}}\left\{2\beta u_x q_x\frac{(3-\gamma)}{\gamma}+\tau_{xx}\frac{(3\gamma-1)}{(\gamma-1)}\right\}+4A^{\pm}\sqrt{\beta}\left\{q_x-u_x\tau_{xx}\right\}\right] \end{pmatrix} \tag{4.21}$$

4.2.3 One dimensional test case: Argon shock structure

Examination of shock structure is one of the characteristic test case of non-equilibrium flow structure used for evaluating kinetic scheme along with its associated kinetic model. The present kinetic scheme uses microscopic tensor splitting and Onsager reciprocity principle based kinetic model. One dimensional code can be used to evaluate the performance of kinetic scheme and kinetic model by examining shock structure appearing due to discontinuity as the flow undergoes transition from uniform upstream flow to a uniform downstream flow. The shock wave has a finite thickness in terms of mean free path, λ and its profile as a function of Mach number and ω which is the exponent of viscosity law. Consider a argon shock structure simulation for shock of Mach 1.4 at 293 K with mean free path $\lambda = 1.3442 \times 10^{-2}$ m and Prandtl number, Pr = 2/3. The viscosity-temperature relationship used in the simulation is

$$\mu = \mu_{ref}\left(\frac{T}{T_{ref}}\right)^{\delta_o} \tag{4.22}$$

where exponent δ_o is 0.81 and reference viscosity [36] is evaluated as

$$\mu_{ref} = \frac{30}{(7-2\delta_o)(5-2\delta_o)}\frac{\rho\lambda\sqrt{2\pi RT}}{4} \tag{4.23}$$

The computational domain spans −0.3 m to 0.3 m with uniform spread of 300 nodes. The kinetic scheme based state update can be written as

$$\boldsymbol{U}(t+\Delta t) = \boldsymbol{U}(t) - \Delta t\begin{bmatrix} \left(\frac{\partial \boldsymbol{GX}_I^{+}(t)}{\partial x}\right)_{\Delta x<0} + \left(\frac{\partial \boldsymbol{GX}_I^{-}(t)}{\partial x}\right)_{\Delta x>0} \\ \left(\frac{\partial \boldsymbol{GX}_V^{+}(t)}{\partial x}\right)_{\Delta x<0} + \left(\frac{\partial \boldsymbol{GX}_V^{-}(t)}{\partial x}\right)_{\Delta x>0} \end{bmatrix} \tag{4.24}$$

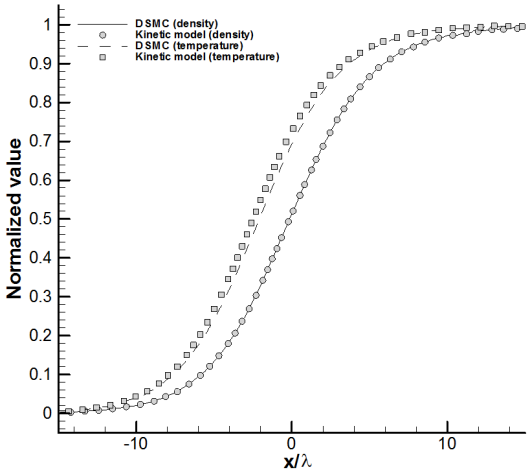

Figure 4.1: Density and temperature profile in argon for Mach 1.4.

Expressions for split inviscid Euler fluxes $\boldsymbol{GX}_I^{\pm}$ are given by Eq. 4.16 and split viscous fluxes $\boldsymbol{GX}_V^{\pm}$ are given by Eq. 4.21. The simulated results are compared with DSMC (Direct Simulation Monte Carlo) code *DSMC1S* provided by Bird [36]. Figure 4.1 shows the normalized density and temperature profile in argon for Mach 1.4. The normalized density $\bar{\rho}$ and normalized temperature $\bar{T}$ are defined as

$$\bar{\rho} = \frac{\rho - \rho_u}{\rho_d - \rho_u}, \quad \bar{T} = \frac{T - T_u}{T_d - T_u} \tag{4.25}$$

where subscripts u and d represents the upstream and downstream Rankine-Hugoniot values respectively. The results reveal that the kinetic scheme using Onsager's reciprocity principle based kinetic model preserves the shock structure accurately.

4.2.4 Two dimensional split fluxes and macroscopic tensors for new kinetic upwind method

One dimensional derivation fails to provide a complete picture, hence a derivation of higher dimensional case is required to illustrate the implementation of the new kinetic method, derivation of split macroscopic tensors and evaluation of split fluxes. The following subsection describes the procedure of obtaining split fluxes for two dimensional kinetic upwind method. Consider Boltzmann equation for

two dimensional case written in terms of first order distribution function as follows

$$\frac{\partial f_1}{\partial t} + \frac{\partial v_x f_1}{\partial x} + \frac{\partial v_y f_1}{\partial y} = 0 \tag{4.26}$$

In KFVS the distribution function at time $t+\Delta t$ in a fluid domain is constructed based on half range distribution as follows

$$f_1^{t+\Delta t} = f_1^t - \Delta t \begin{bmatrix} \left(\frac{\partial v_x f_1^{+\cdot}}{\partial x}\right)^t + \left(\frac{\partial v_x f_1^{-\cdot}}{\partial x}\right)^t \\ \left(\frac{\partial v_y f_1^{\cdot +}}{\partial y}\right)^t + \left(\frac{\partial v_y f_1^{\cdot -}}{\partial y}\right)^t \end{bmatrix} \tag{4.27}$$

Two-dimensional Boltzmann equation after taking $\boldsymbol{\Psi}$-moments simplifies to

$$\begin{aligned} \left\langle \boldsymbol{\Psi}, f_0^{t+\Delta t} \right\rangle &= \langle \boldsymbol{\Psi}, f_0^t \rangle \\ &-\Delta t \begin{bmatrix} \left(\frac{\partial \left\langle \boldsymbol{\Psi}, v_x f_0^{+\cdot} \right\rangle}{\partial x}\right)^t + \left(\frac{\partial -\sum_j \boldsymbol{\Lambda}_j^{+\cdot} \odot \boldsymbol{X}_j}{\partial x}\right)^t \\ + \left(\frac{\partial \left\langle \boldsymbol{\Psi}, v_x f_0^{-\cdot} \right\rangle}{\partial x}\right)^t + \left(\frac{\partial -\sum_j \boldsymbol{\Lambda}_j^{-\cdot} \odot \boldsymbol{X}_j}{\partial x}\right)^t \\ + \left(\frac{\partial \left\langle \boldsymbol{\Psi}, v_y f_0^{\cdot +} \right\rangle}{\partial y}\right)^t + \left(\frac{\partial -\sum_j \boldsymbol{\Lambda}_j^{\cdot +} \odot \boldsymbol{X}_j}{\partial y}\right)^t \\ + \left(\frac{\partial \left\langle \boldsymbol{\Psi}, v_y f_0^{\cdot -} \right\rangle}{\partial y}\right)^t + \left(\frac{\partial -\sum_j \boldsymbol{\Lambda}_j^{\cdot -} \odot \boldsymbol{X}_j}{\partial y}\right)^t \end{bmatrix} \end{aligned} \tag{4.28}$$

where the superscript over Maxwellian distribution represents its evaluation based on half range and full range components of molecular velocities as follows

$$\begin{array}{ll} f_0^{+\cdot} \equiv f_0^{(0<v_x<+\infty)(-\infty<v_y<+\infty)} & f_0^{-\cdot} \equiv f_0^{(-\infty<v_x<0)(-\infty<v_y<+\infty)} \\ f_0^{\cdot +} \equiv f_0^{(-\infty<v_x<+\infty)(0<v_y<+\infty)} & f_0^{\cdot -} \equiv f_0^{(-\infty<v_x<+\infty)(-\infty<v_y<0)} \end{array} \tag{4.29}$$

Similarly, split macroscopic tensors are denoted by superscript over macroscopic tensors which represents its evaluation based on half range and full range components of molecular velocities as follows

$$\begin{array}{ll} \boldsymbol{\Lambda}_j^{+\cdot} \equiv \boldsymbol{\Lambda}_j^{(0<v_x<+\infty)(-\infty<v_y<+\infty)} & \boldsymbol{\Lambda}_j^{-\cdot} \equiv \boldsymbol{\Lambda}_j^{(-\infty<v_x<0)(-\infty<v_y<+\infty)} \\ \boldsymbol{\Lambda}_j^{\cdot +} \equiv \boldsymbol{\Lambda}_j^{(-\infty<v_x<+\infty)(0<v_y<+\infty)} & \boldsymbol{\Lambda}_j^{\cdot -} \equiv \boldsymbol{\Lambda}_j^{(-\infty<v_x<+\infty)(-\infty<v_y<0)} \end{array} \tag{4.30}$$

Thus, positive macroscopic split tensor $\boldsymbol{\Lambda}_j^{+\cdot}$ is based half range of x-component of molecular velocity $0 < v_x < +\infty$ and full range of y-component of molecular

velocity $-\infty < v_y < +\infty$ as follows

$$\boldsymbol{\Lambda}_j^{+\cdot} = \left\langle \boldsymbol{\Psi}, v_x \boldsymbol{\Upsilon}_j^{+\cdot} \right\rangle \equiv \int_0^{+\infty} \int_{-\infty}^{+\infty} \int_0^{+\infty} \boldsymbol{\Psi} v_x \boldsymbol{\Upsilon}_j dv_x dv_y d\mathbb{I} \tag{4.31}$$

Similarly, negative macroscopic split tensor $\boldsymbol{\Lambda}_j^{-\cdot}$ is based on half range of x-component of molecular velocity $-\infty < v_x < 0$ and full range of y-component of molecular velocity $-\infty < v_y < +\infty$ as follows

$$\boldsymbol{\Lambda}_j^{-\cdot} = \left\langle \boldsymbol{\Psi}, v_x \boldsymbol{\Upsilon}_j^{-\cdot} \right\rangle \equiv \int_0^{+\infty} \int_{-\infty}^{+\infty} \int_{-\infty}^{0} \boldsymbol{\Psi} v_x \boldsymbol{\Upsilon}_j dv_x dv_y d\mathbb{I} \tag{4.32}$$

Similarly, macroscopic tensors $\boldsymbol{\Lambda}_j^{\cdot\pm}$ are based on full range of x-component of molecular velocity and half range of y-component of molecular velocity as follows

$$\boldsymbol{\Lambda}_j^{\cdot+} = \left\langle \boldsymbol{\Psi}, v_y \boldsymbol{\Upsilon}_j^{\cdot+} \right\rangle \equiv \int_0^{+\infty} \int_0^{+\infty} \int_{-\infty}^{+\infty} \boldsymbol{\Psi} v_y \boldsymbol{\Upsilon}_j dv_x dv_y d\mathbb{I} \tag{4.33}$$

$$\boldsymbol{\Lambda}_j^{\cdot-} = \left\langle \boldsymbol{\Psi}, v_y \boldsymbol{\Upsilon}_j^{\cdot-} \right\rangle \equiv \int_0^{+\infty} \int_{-\infty}^{0} \int_{-\infty}^{+\infty} \boldsymbol{\Psi} v_y \boldsymbol{\Upsilon}_j dv_x dv_y d\mathbb{I} \tag{4.34}$$

This leads to upwind equations in macroscopic form i.e. Navier-Stokes equations in kinetic upwind form

$$\boldsymbol{U}(t+\Delta t) = \boldsymbol{U}(t) - \Delta t \begin{bmatrix} \left(\frac{\partial \boldsymbol{GX}_I^+(t)}{\partial x}\right)_{\Delta x<0} + \left(\frac{\partial \boldsymbol{GX}_I^-(t)}{\partial x}\right)_{\Delta x>0} \\ + \left(\frac{\partial \boldsymbol{GX}_V^+(t)}{\partial x}\right)_{\Delta x<0} + \left(\frac{\partial \boldsymbol{GX}_V^-(t)}{\partial x}\right)_{\Delta x>0} \\ + \left(\frac{\partial \boldsymbol{GY}_I^+(t)}{\partial y}\right)_{\Delta y<0} + \left(\frac{\partial \boldsymbol{GY}_I^-(t)}{\partial y}\right)_{\Delta y>0} \\ + \left(\frac{\partial \boldsymbol{GY}_V^+(t)}{\partial y}\right)_{\Delta y<0} + \left(\frac{\partial \boldsymbol{GY}_V^-(t)}{\partial y}\right)_{\Delta y>0} \end{bmatrix} \tag{4.35}$$

Upwinding in macroscopic level is enforced using stencil sub-division. The term $\boldsymbol{U}$ is the state update vector defined as

$$\boldsymbol{U} = \langle \boldsymbol{\Psi}, f_0 \rangle = \int_0^{+\infty} \int_{-\infty}^{+\infty} \int_{-\infty}^{+\infty} \boldsymbol{\Psi} f_0 dv_x dv_y d\mathbb{I} = \begin{bmatrix} \rho \\ \rho u_x \\ \rho u_y \\ \rho E \end{bmatrix} \tag{4.36}$$

where $E = RT/(\gamma - 1) + \frac{1}{2}(u_x^2 + u_y^2)$, u_x, u_y are the x and y components of macroscopic fluid velocity and γ is the specific heat ratio.

4.2.4.1 Evaluation of split inviscid fluxes

Evaluation of split inviscid fluxes is similar to KFVS which is based on split half range Maxwellian distribution i.e. split positive flux $\boldsymbol{GX}_I^{\pm}$ is evaluated using half range Maxwellian distribution $f_0^{\pm\cdot}$ which is based on half range of x-component of molecular velocity $0 < v_x < +\infty$ or $-\infty < v_x < 0$ and full range of y-component of molecular velocity $-\infty < v_y < +\infty$. Thus the inviscid part of the flux component, $\boldsymbol{GX}_I^{\pm}$ is defined as

$$\begin{aligned}\boldsymbol{GX}_I^{+} &= \left\langle \boldsymbol{\Psi}, v_x f_0^{+\cdot} \right\rangle = \int_0^{+\infty}\int_{-\infty}^{+\infty}\int_0^{+\infty} \boldsymbol{\Psi} v_x f_0 dv_x dv_y d\mathbb{I} \\ \boldsymbol{GX}_I^{-} &= \left\langle \boldsymbol{\Psi}, v_x f_0^{-\cdot} \right\rangle = \int_0^{+\infty}\int_{-\infty}^{+\infty}\int_{-\infty}^{0} \boldsymbol{\Psi} v_x f_0 dv_x dv_y d\mathbb{I}\end{aligned} \tag{4.37}$$

Similarly, split negative flux $\boldsymbol{GY}_I^{-}$ is evaluated using half range Maxwellian distribution $f_0^{\cdot-}$ which is based on full range of x-component of molecular velocity $-\infty < v_x < +\infty$ and half range of y-component of molecular velocity $-\infty < v_y < 0$ or $0 < v_y < +\infty$. The expression of inviscid flux $\boldsymbol{GY}_I^{\pm}$ is given as

$$\begin{aligned}\boldsymbol{GY}_I^{+} &= \left\langle \boldsymbol{\Psi}, v_y f_0^{\cdot+} \right\rangle = \int_0^{+\infty}\int_0^{+\infty}\int_{-\infty}^{+\infty} \boldsymbol{\Psi} v_y f_0 dv_x dv_y d\mathbb{I} \\ \boldsymbol{GY}_I^{-} &= \left\langle \boldsymbol{\Psi}, v_y f_0^{\cdot-} \right\rangle = \int_0^{+\infty}\int_{-\infty}^{0}\int_{-\infty}^{+\infty} \boldsymbol{\Psi} v_y f_0 dv_x dv_y d\mathbb{I}\end{aligned} \tag{4.38}$$

The x-component of the inviscid split fluxes in 2-D is given by

$$\begin{aligned} GX_I^{\pm}(1) &= \tfrac{\rho}{2\sqrt{\beta}}\left(\tfrac{B_1^{\pm}}{\sqrt{\pi}} + s_x A_1^{\pm}\right) \\ GX_I^{\pm}(2) &= \tfrac{\rho}{2\beta}\left(\tfrac{B_1^{\pm}}{\sqrt{\pi}} s_x + \tfrac{(1+2s_x^2)}{2} A_1^{\pm}\right) \\ GX_I^{\pm}(3) &= \tfrac{\rho}{2\beta} s_y \left(\tfrac{B_1^{\pm}}{\sqrt{\pi}} + s_x A_1^{\pm}\right) \\ GX_I^{\pm}(4) &= \tfrac{\rho}{8\beta^{3/2}}\left(\tfrac{B_1^{\pm}}{\sqrt{\pi}} \tfrac{(1+\gamma+ds)}{(-1+\gamma)} + s_x \tfrac{(2\gamma+ds)}{(-1+\gamma)} A_1^{\pm}\right) \end{aligned} \tag{4.39}$$

The y-component of the inviscid split fluxes in 2-D is given by

$$\begin{aligned} GY_I^{\pm}(1) &= \tfrac{\rho}{2\sqrt{\beta}}\left(\tfrac{B_2^{\pm}}{\sqrt{\pi}} + s_y A_2^{\pm}\right) \\ GY_I^{\pm}(2) &= \tfrac{\rho}{2\beta} s_x \left(\tfrac{B_2^{\pm}}{\sqrt{\pi}} + s_y A_2^{\pm}\right) \\ GY_I^{\pm}(3) &= \tfrac{\rho}{2\beta}\left(\tfrac{B_2^{\pm}}{\sqrt{\pi}} s_y + \tfrac{(1+2s_y^2)}{2} A_2^{\pm}\right) \\ GY_I^{\pm}(4) &= \tfrac{\rho}{8\beta^{3/2}}\left(\tfrac{B_2^{\pm}}{\sqrt{\pi}} \tfrac{(1+\gamma+ds)}{(-1+\gamma)} + s_y \tfrac{(2\gamma+ds)}{(-1+\gamma)} A_2^{\pm}\right) \end{aligned} \tag{4.40}$$

where $s_x = \sqrt{\beta}u_x$, $s_y = \sqrt{\beta}u_y$, $dx = 2(-1+\gamma)s_x^2$, $dy = 2(-1+\gamma)s_y^2$, $ds = 2(-1+\gamma)(s_x^2 + s_y^2)$, $\eta = (-1+\gamma)/\gamma$, $B_1^{\pm} = \pm Exp[-s_x^2]$, $B_2^{\pm} = \pm Exp[-s_y^2]$, $A_1^{\pm} = 1 \pm Erf[s_x]$, $A_2^{\pm} = 1 \pm Erf[s_y]$.

4.2.4.2 Evaluation of split viscous fluxes based on split microscopic tensors

The split macroscopic tensors are obtained by taking moments of the split microscopic tensors associated with the shear stress tensor and heat flux vector. As described earlier the viscous fluxes are evaluated based on full tensor contraction of split macroscopic tensors with its conjugate thermodynamic forces. The viscous part of the flux component, $\boldsymbol{GX}_V^{\pm}$ and $\boldsymbol{GY}_V^{\pm}$ are defined as

$$\begin{array}{ll} \boldsymbol{GX}_V^{\pm} & = -\sum_j \boldsymbol{\Lambda}_j^{\pm\cdot} \odot \boldsymbol{X}_j = -(\boldsymbol{\Lambda}_\tau^{\pm\cdot} : \boldsymbol{X}_\tau + \boldsymbol{\Lambda}_q^{\pm\cdot} \cdot \boldsymbol{X}_q) \\ \boldsymbol{GY}_V^{\pm} & = -\sum_j \boldsymbol{\Lambda}_j^{\cdot\pm} \odot \boldsymbol{X}_j = -(\boldsymbol{\Lambda}_\tau^{\cdot\pm} : \boldsymbol{X}_\tau + \boldsymbol{\Lambda}_q^{\cdot\pm} \cdot \boldsymbol{X}_q) \end{array} \tag{4.41}$$

Conjugate thermodynamic forces, $\boldsymbol{X_\tau}$ and $\boldsymbol{X_q}$ are

$$\begin{aligned} X_\tau &\equiv \begin{bmatrix} 2\beta\frac{\partial u_x}{\partial x} & \beta(\frac{\partial u_x}{\partial y} + \frac{\partial u_y}{\partial x}) \\ \beta(\frac{\partial u_x}{\partial y} + \frac{\partial u_y}{\partial x}) & 2\beta\frac{\partial u_y}{\partial y} \end{bmatrix} \\ X_q &\equiv \left[-2R\beta^2\frac{\partial T}{\partial x}, -2R\beta^2\frac{\partial T}{\partial y}\right] \end{aligned} \tag{4.42}$$

The components of the macroscopic tensors $\boldsymbol{\Lambda}_\tau^{\pm\cdot}$, $\boldsymbol{\Lambda}_q^{\pm\cdot}$ associated with x split fluxes are given as follows

$$\Lambda_{1,\tau}^{\pm\cdot} = \left\langle \Psi_1, v_x \boldsymbol{\Upsilon}_\tau^{\pm\cdot} \right\rangle = \frac{\mu}{p} \begin{bmatrix} \frac{B_1^{\mp}(\gamma-3)\rho}{8\sqrt{\pi}\beta^{3/2}} & 0 \\ 0 & \frac{B_1^{\mp}(\gamma-1)\rho}{8\sqrt{\pi}\beta^{3/2}} \end{bmatrix} \tag{4.43}$$

$$\Lambda_{1,q}^{\pm\cdot} = \left\langle \Psi_1, v_x \boldsymbol{\Upsilon}_q^{\pm\cdot} \right\rangle = \frac{(\gamma-1)}{\gamma}\frac{\kappa}{pR} \begin{bmatrix} -\frac{B_1^{\mp}u_x\rho}{4\sqrt{\pi}\beta^{3/2}} & 0 \end{bmatrix} \tag{4.44}$$

$$\Lambda_{2,\tau}^{\pm\cdot} = \left\langle \Psi_2, v_x \boldsymbol{\Upsilon}_\tau^{\pm\cdot} \right\rangle = \frac{\mu}{p} \begin{bmatrix} -\frac{A_1^{\pm}(\gamma-3)\rho}{8\beta^2} & 0 \\ 0 & -\frac{A_1^{\pm}(\gamma-1)\rho}{8\beta^2} \end{bmatrix} \tag{4.45}$$

$$\Lambda_{2,q}^{\pm\cdot} = \left\langle \Psi_2, v_x \boldsymbol{\Upsilon}_q^{\pm\cdot} \right\rangle = \frac{(\gamma-1)}{\gamma}\frac{\kappa}{pR} \begin{bmatrix} \frac{B_1^{\mp}\rho}{4\sqrt{\pi}\beta^{5/2}} & 0 \end{bmatrix} \tag{4.46}$$

$$\Lambda_{3,\tau}^{\pm\cdot} = \left\langle \Psi_3, v_x \boldsymbol{\Upsilon}_\tau^{\pm\cdot} \right\rangle = \frac{\mu}{p} \begin{bmatrix} \frac{B_1^{\mp} u_y (\gamma-3)\rho}{8\sqrt{\pi}\beta^{3/2}} & \frac{A_1^{\pm}\rho}{8\beta^2} \\ \frac{A_1^{\pm}\rho}{8\beta^2} & \frac{B_1^{\mp} u_y (\gamma-1)\rho}{8\sqrt{\pi}\beta^{3/2}} \end{bmatrix} \tag{4.47}$$

$$\Lambda_{3,q}^{\pm\cdot} = \left\langle \Psi_3, v_x \boldsymbol{\Upsilon}_q^{\pm\cdot} \right\rangle = \frac{(\gamma-1)}{\gamma} \frac{\kappa}{pR} \begin{bmatrix} -\frac{B_1^{\mp} u_x u_y \rho}{4\sqrt{\pi}\beta^{3/2}} & \frac{B_1^{\mp}\rho}{8\sqrt{\pi}\beta^{5/2}} \end{bmatrix} \tag{4.48}$$

$$\Lambda_{4,\tau}^{\pm\cdot} = \left\langle \Psi_4, v_x \boldsymbol{\Upsilon}_\tau^{\pm\cdot} \right\rangle = \frac{\mu}{p} \begin{bmatrix} -\frac{(\gamma-3)C_1^{\pm}\rho}{32\sqrt{\pi}\beta^{5/2}(\gamma-1)} & \frac{A_1^{\pm} u_y \rho}{8\beta^2} \\ \frac{A_1^{\pm} u_y \rho}{8\beta^2} & -\frac{C_1^{\pm}\rho}{32\sqrt{\pi}\beta^{5/2}} \end{bmatrix} \tag{4.49}$$

$$\Lambda_{4,q}^{\pm\cdot} = \left\langle \Psi_4, v_x \boldsymbol{\Upsilon}_q^{\pm\cdot} \right\rangle = \frac{(\gamma-1)}{\gamma} \frac{\kappa}{pR} \begin{bmatrix} -\frac{(B_1^{\mp}\sqrt{\beta} u_x (3+2{u_y}^2\beta(\gamma-1)-\gamma)+2A_1^{\pm}\sqrt{\pi}\gamma)\rho}{16\sqrt{\pi}\beta^3(\gamma-1)} & \frac{B_1^{\mp} u_y \rho}{8\sqrt{\pi}\beta^{5/2}} \end{bmatrix} \tag{4.50}$$

Similarly, the components of the macroscopic tensors $\boldsymbol{\Lambda}_\tau^{\cdot\pm}$, $\boldsymbol{\Lambda}_q^{\cdot\pm}$ associated with y split fluxes are given as follows

$$\Lambda_{1,\tau}^{\cdot\pm} = \left\langle \Psi_1, v_y \boldsymbol{\Upsilon}_\tau^{\cdot\pm} \right\rangle = \frac{\mu}{p} \begin{bmatrix} \frac{B_2^{\mp}(\gamma-1)\rho}{8\sqrt{\pi}\beta^{3/2}} & 0 \\ 0 & \frac{B_2^{\mp}(\gamma-3)\rho}{8\sqrt{\pi}\beta^{3/2}} \end{bmatrix} \tag{4.51}$$

$$\Lambda_{1,q}^{\cdot\pm} = \left\langle \Psi_1, v_y \boldsymbol{\Upsilon}_q^{\cdot\pm} \right\rangle = \frac{(\gamma-1)}{\gamma} \frac{\kappa}{pR} \begin{bmatrix} 0 & -\frac{B_2^{\mp} u_y \rho}{4\sqrt{\pi}\beta^{3/2}} \end{bmatrix} \tag{4.52}$$

$$\Lambda_{2,\tau}^{\cdot\pm} = \left\langle \Psi_2, v_y \boldsymbol{\Upsilon}_\tau^{\cdot\pm} \right\rangle = \frac{\mu}{p} \begin{bmatrix} \frac{B_2^{\mp} u_x (\gamma-1)\rho}{8\sqrt{\pi}\beta^{3/2}} & \frac{A_2^{\pm}\rho}{8\beta^2} \\ \frac{A_2^{\pm}\rho}{8\beta^2} & \frac{B_2^{\mp} u_x (\gamma-3)\rho}{8\sqrt{\pi}\beta^{3/2}} \end{bmatrix} \tag{4.53}$$

$$\Lambda_{2,q}^{\cdot\pm} = \left\langle \Psi_2, v_y \boldsymbol{\Upsilon}_q^{\cdot\pm} \right\rangle = \frac{(\gamma-1)}{\gamma} \frac{\kappa}{pR} \begin{bmatrix} \frac{B_2^{\mp}\rho}{8\sqrt{\pi}\beta^{5/2}} & -\frac{B_2^{\mp} u_x u_y \rho}{4\sqrt{\pi}\beta^{3/2}} \end{bmatrix} \tag{4.54}$$

$$\Lambda_{3,\tau}^{\cdot\pm} = \left\langle \Psi_3, v_y \boldsymbol{\Upsilon}_\tau^{\cdot\pm} \right\rangle = \frac{\mu}{p} \begin{bmatrix} -\frac{A_2^\pm(\gamma-1)\rho}{8\beta^2} & 0 \\ 0 & -\frac{A_2^\pm(\gamma-3)\rho}{8\beta^2} \end{bmatrix} \tag{4.55}$$

$$\Lambda_{3,q}^{\cdot\pm} = \left\langle \Psi_3, v_y \boldsymbol{\Upsilon}_q^{\cdot\pm} \right\rangle = \frac{(\gamma-1)}{\gamma}\frac{\kappa}{pR} \begin{bmatrix} 0 & \frac{B_2^\mp \rho}{4p\sqrt{\pi}\beta^{5/2}} \end{bmatrix} \tag{4.56}$$

$$\Lambda_{4,\tau}^{\cdot\pm} = \left\langle \Psi_4, v_y \boldsymbol{\Upsilon}_\tau^{\cdot\pm} \right\rangle = \frac{\mu}{p} \begin{bmatrix} -\frac{C_2^\pm \rho}{32\sqrt{\pi}\beta^{5/2}} & \frac{A_2^\pm u_x \rho}{8\beta^2} \\ \frac{A_2^\pm u_x \rho}{8\beta^2} & -\frac{(\gamma-3)C_2^\pm \rho}{32\sqrt{\pi}\beta^{5/2}} \end{bmatrix} \tag{4.57}$$

$$\Lambda_{4,q}^{\cdot\pm} = \left\langle \Psi_4, v_y \boldsymbol{\Upsilon}_q^{\cdot\pm} \right\rangle = \frac{(\gamma-1)}{\gamma}\frac{\kappa}{pR} \begin{bmatrix} \frac{B_2^\mp u_x \rho}{8p\sqrt{\pi}\beta^{5/2}} & \frac{(-B_2^\mp u_y \sqrt{\beta}(3+2{u_x}^2\beta(\gamma-1)-\gamma)+2A_2^\pm\sqrt{\pi}\gamma)\rho}{16\sqrt{\pi}\beta^3(\gamma-1)} \end{bmatrix} \tag{4.58}$$

where $A_1^\pm = 1 \pm Erf(u_x\sqrt{\beta})$, $A_2^\pm = 1 \pm Erf(u_y\sqrt{\beta})$, $B_1^\pm = \pm exp(-\beta u_x^2)$, $B_2^\pm = \pm exp(-\beta u_y^2)$ and

$$\begin{aligned} C_1^\pm &= 4A_1^\pm u_x\sqrt{\beta}\sqrt{\pi}(\gamma-1) + B_1^\mp(1-2u_y^2\beta(\gamma-1)-3\gamma) \\ C_2^\pm &= 4A_2^\pm u_y\sqrt{\beta}\sqrt{\pi}(\gamma-1) + B_2^\mp(1-2u_x^2\beta(\gamma-1)-3\gamma) \end{aligned} \tag{4.59}$$

The x-component of the viscous split fluxes in 2-D is given by

$$\begin{aligned} GX_V(1)^\pm &= -\frac{\rho}{4p\sqrt{\beta}}\frac{B_1^\pm}{\sqrt{\pi}}(2\sqrt{\beta}\eta q_x s_x + \tau_{xx}) \\ GX_V(2)^\pm &= \frac{\rho}{4p\beta}(\frac{B_1^\pm}{\sqrt{\pi}}2\sqrt{\beta}\eta q_x - A_1^\pm\tau_{xx}) \\ GX_V(3)^\pm &= \frac{\rho}{4p\beta}(\frac{B_1^\pm}{\sqrt{\pi}}(\sqrt{\beta}\eta(q_y - 2q_x s_x s_y) - s_y\tau_{xx}) - A_1^\pm\tau_{xy}) \\ GX_V(4)^\pm &= \frac{\rho}{16p\beta^{3/2}} \begin{pmatrix} \frac{B_1^\pm}{\sqrt{\pi}}(4\sqrt{\beta}\eta q_y s_y + 2\sqrt{\beta}q_x s_x\frac{(-3+\gamma-dy)}{\gamma} + \frac{(1-3\gamma-dy)}{-1+\gamma}\tau_{xx}) \\ +4(\sqrt{\beta}q_x - s_x\tau_{xx} - s_y\tau_{xy})A_1^\pm \end{pmatrix} \end{aligned} \tag{4.60}$$

The y-component of the viscous split fluxes in 2-D is given by

$$
\begin{aligned}
GY_V(1)^{\pm} &= -\tfrac{\rho}{4p\sqrt{\beta}}\tfrac{B_2^{\pm}}{\sqrt{\pi}}(2\sqrt{\beta}\eta q_y s_y + \tau_{yy}) \\
GY_V(2)^{\pm} &= \tfrac{\rho}{4p\beta}(\tfrac{B_2^{\pm}}{\sqrt{\pi}}(\sqrt{\beta}\eta(q_x - 2q_y s_x s_y) - s_x\tau_{yy}) - A_2^{\pm}\tau_{xy}) \\
GY_V(3)^{\pm} &= \tfrac{\rho}{4p\beta}(\tfrac{B_2^{\pm}}{\sqrt{\pi}}2\sqrt{\beta}\eta q_y - A_2^{\pm}\tau_{yy}) \\
GY_V(4)^{\pm} &= \tfrac{\rho}{16p\beta^{3/2}}\begin{pmatrix} \tfrac{B_2^{\pm}}{\sqrt{\pi}}(4\sqrt{\beta}\eta q_x s_x + 2\sqrt{\beta}q_y s_y\tfrac{(-3+\gamma-dx)}{\gamma} + \tfrac{(1-3\gamma-dx)}{-1+\gamma}\tau_{yy}) \\ +4(\sqrt{\beta}q_y - s_x\tau_{xy} - s_y\tau_{yy})A_2^{\pm} \end{pmatrix}
\end{aligned}
\tag{4.61}
$$

where $s_x = \sqrt{\beta}u_x$, $s_y = \sqrt{\beta}u_y$, $dx = 2(-1+\gamma)s_x^2$, $dy = 2(-1+\gamma)s_y^2$, $ds = 2(-1+\gamma)(s_x^2 + s_y^2)$, $\eta = (-1+\gamma)/\gamma$, $B_1^{\pm} = \pm Exp[-s_x^2]$, $B_2^{\pm} = \pm Exp[-s_y^2]$, $A_1^{\pm} = 1 \pm Erf[s_x]$, $A_2^{\pm} = 1 \pm Erf[s_y]$.

4.2.5 Three dimensional split fluxes and macroscopic tensors for new kinetic upwind method

The procedure of obtaining split fluxes for three dimensional kinetic upwind method is similar to two dimensional method. Three-dimensional Boltzmann equation after taking $\mathbf{\Psi}$-moments simplifies to

$$
\begin{aligned}
\left\langle \mathbf{\Psi}, f_0^{t+\Delta t} \right\rangle &= \langle \mathbf{\Psi}, f_0^t \rangle \\
&\quad -\Delta t \begin{bmatrix} \left(\frac{\partial \left\langle \mathbf{\Psi}, v_x f_0^{\pm\cdot\cdot} \right\rangle}{\partial x}\right)^t + \left(\frac{\partial - \sum_j \mathbf{\Lambda}_j^{\pm\cdot\cdot} \odot \boldsymbol{X}_j}{\partial x}\right)^t \\ + \left(\frac{\partial \left\langle \mathbf{\Psi}, v_y f_0^{\cdot\pm\cdot} \right\rangle}{\partial y}\right)^t + \left(\frac{\partial - \sum_j \mathbf{\Lambda}_j^{\cdot\pm\cdot} \odot \boldsymbol{X}_j}{\partial y}\right)^t \\ + \left(\frac{\partial \left\langle \mathbf{\Psi}, v_z f_0^{\cdot\cdot\pm} \right\rangle}{\partial z}\right)^t + \left(\frac{\partial - \sum_j \mathbf{\Lambda}_j^{\cdot\cdot\pm} \odot \boldsymbol{X}_j}{\partial z}\right)^t \end{bmatrix}
\end{aligned}
\tag{4.62}
$$

where the superscript "$\pm$" over Maxwellian distribution f_0 and macroscopic tensors $\mathbf{\Lambda}_j$ represents evaluation based on half range component of molecular velocities. Similarly, the superscript "$\cdot$" over Maxwellian distribution f_0 and macroscopic tensors $\mathbf{\Lambda}_j$ represents evaluation based on full range components of molec-

ular velocities as follows

$$\begin{aligned} f_0^{+\cdot\cdot} &\equiv f_0^{(0<v_x<+\infty)(-\infty<v_y<+\infty)(-\infty<v_z<+\infty)} & f_0^{-\cdot\cdot} &\equiv f_0^{(-\infty<v_x<0)(-\infty<v_y<+\infty)(-\infty<v_z<+\infty)} \\ f_0^{\cdot+\cdot} &\equiv f_0^{(-\infty<v_x<+\infty)(0<v_y<+\infty)(-\infty<v_z<+\infty)} & f_0^{\cdot-\cdot} &\equiv f_0^{(-\infty<v_x<+\infty)(-\infty<v_y<0)(-\infty<v_z<+\infty)} \\ f_0^{\cdot\cdot+} &\equiv f_0^{(-\infty<v_x<+\infty)(-\infty<v_y<+\infty)(0<v_z<+\infty)} & f_0^{\cdot\cdot-} &\equiv f_0^{(-\infty<v_x<+\infty)(-\infty<v_y<+\infty)(-\infty<v_z<0)} \end{aligned} \tag{4.63}$$

Similarly, split macroscopic tensors are denoted by superscript over macroscopic tensors which represents its evaluation based on half range and full range components of molecular velocities as follows

$$\begin{aligned} \boldsymbol{\Lambda}_j^{+\cdot\cdot} &\equiv \boldsymbol{\Lambda}_j^{(0<v_x<+\infty)(-\infty<v_y<+\infty)(-\infty<v_z<+\infty)} & \boldsymbol{\Lambda}_j^{-\cdot\cdot} &\equiv \boldsymbol{\Lambda}_j^{(-\infty<v_x<0)(-\infty<v_y<+\infty)(-\infty<v_z<+\infty)} \\ \boldsymbol{\Lambda}_j^{\cdot+\cdot} &\equiv \boldsymbol{\Lambda}_j^{(-\infty<v_x<+\infty)(0<v_y<+\infty)(-\infty<v_z<+\infty)} & \boldsymbol{\Lambda}_j^{\cdot-\cdot} &\equiv \boldsymbol{\Lambda}_j^{(-\infty<v_x<+\infty)(-\infty<v_y<0)(-\infty<v_z<+\infty)} \\ \boldsymbol{\Lambda}_j^{\cdot\cdot+} &\equiv \boldsymbol{\Lambda}_j^{(-\infty<v_x<+\infty)(-\infty<v_y<+\infty)(0<v_z<+\infty)} & \boldsymbol{\Lambda}_j^{\cdot\cdot-} &\equiv \boldsymbol{\Lambda}_j^{(-\infty<v_x<+\infty)(-\infty<v_y<+\infty)(-\infty<v_z<0)} \end{aligned} \tag{4.64}$$

Thus, macroscopic split tensor $\boldsymbol{\Lambda}_j^{\pm\cdot\cdot}$ is based on half range of x-component of molecular velocity and full range of y-component and z-component of molecular velocity $-\infty < v_y < +\infty$ as follows

$$\begin{aligned} \boldsymbol{\Lambda}_j^{+\cdot\cdot} &= \left\langle \boldsymbol{\Psi}, v_x \boldsymbol{\Upsilon}_j^{+\cdot\cdot} \right\rangle \equiv \int_0^{+\infty}\int_{-\infty}^{+\infty}\int_{-\infty}^{+\infty}\int_0^{+\infty} \boldsymbol{\Psi} v_x \boldsymbol{\Upsilon}_j dv_x dv_y dv_z d\mathbb{I} \\ \boldsymbol{\Lambda}_j^{-\cdot\cdot} &= \left\langle \boldsymbol{\Psi}, v_x \boldsymbol{\Upsilon}_j^{-\cdot\cdot} \right\rangle \equiv \int_0^{+\infty}\int_{-\infty}^{+\infty}\int_{-\infty}^{+\infty}\int_{-\infty}^{0} \boldsymbol{\Psi} v_x \boldsymbol{\Upsilon}_j dv_x dv_y dv_z d\mathbb{I} \end{aligned} \tag{4.65}$$

Similarly, macroscopic split tensor $\boldsymbol{\Lambda}_j^{\cdot\pm\cdot}$ is based on half range of y-component of molecular velocity as follows

$$\begin{aligned} \boldsymbol{\Lambda}_j^{\cdot+\cdot} &= \left\langle \boldsymbol{\Psi}, v_y \boldsymbol{\Upsilon}_j^{\cdot+\cdot} \right\rangle \equiv \int_0^{+\infty}\int_{-\infty}^{+\infty}\int_0^{+\infty}\int_{-\infty}^{+\infty} \boldsymbol{\Psi} v_y \boldsymbol{\Upsilon}_j dv_x dv_y dv_z d\mathbb{I} \\ \boldsymbol{\Lambda}_j^{\cdot-\cdot} &= \left\langle \boldsymbol{\Psi}, v_y \boldsymbol{\Upsilon}_j^{\cdot-\cdot} \right\rangle \equiv \int_0^{+\infty}\int_{-\infty}^{+\infty}\int_{-\infty}^{0}\int_{-\infty}^{+\infty} \boldsymbol{\Psi} v_y \boldsymbol{\Upsilon}_j dv_x dv_y dv_z d\mathbb{I} \end{aligned} \tag{4.66}$$

Macroscopic split tensors $\boldsymbol{\Lambda}_j^{\cdot\cdot\pm}$ are based on half range of z component of molecular velocity as follows

$$\begin{aligned} \boldsymbol{\Lambda}_j^{\cdot\cdot+} &= \left\langle \boldsymbol{\Psi}, v_z \boldsymbol{\Upsilon}_j^{\cdot\cdot+} \right\rangle \equiv \int_0^{+\infty}\int_0^{+\infty}\int_{-\infty}^{+\infty}\int_{-\infty}^{+\infty} \boldsymbol{\Psi} v_z \boldsymbol{\Upsilon}_j dv_x dv_y dv_z d\mathbb{I} \\ \boldsymbol{\Lambda}_j^{\cdot\cdot-} &= \left\langle \boldsymbol{\Psi}, v_z \boldsymbol{\Upsilon}_j^{x+} \right\rangle \equiv \int_0^{+\infty}\int_{-\infty}^{0}\int_{-\infty}^{+\infty}\int_{-\infty}^{+\infty} \boldsymbol{\Psi} v_z \boldsymbol{\Upsilon}_j dv_x dv_y dv_z d\mathbb{I} \end{aligned} \tag{4.67}$$

This leads to upwind equations in macroscopic form i.e. Navier-Stokes equations in kinetic upwind form

$$\boldsymbol{U}(t+\Delta t) = \boldsymbol{U}(t) - \Delta t \begin{bmatrix} \frac{\partial \boldsymbol{GX}_I^{\pm}(t)}{\partial x} + \frac{\partial \boldsymbol{GX}_V^{\pm}(t)}{\partial x} \\ + \frac{\partial \boldsymbol{GY}_I^{\pm}(t)}{\partial y} + \frac{\partial \boldsymbol{GY}_V^{\pm}(t)}{\partial y} \\ + \frac{\partial \boldsymbol{GZ}_I^{\pm}(t)}{\partial z} + \frac{\partial \boldsymbol{GZ}_V^{\pm}(t)}{\partial z} \end{bmatrix} \tag{4.68}$$

where $\boldsymbol{U}$ is the state update vector defined as

$$\boldsymbol{U} = \langle \boldsymbol{\Psi}, f_0 \rangle = \int_0^{+\infty} \int_{-\infty}^{+\infty} \int_{-\infty}^{+\infty} \int_{-\infty}^{+\infty} \boldsymbol{\Psi} f_0 dv_x dv_y dv_z d\mathbb{I} = \begin{bmatrix} \rho \\ \rho u_x \\ \rho u_y \\ \rho u_z \\ \rho E \end{bmatrix} \tag{4.69}$$

where $E = RT/(\gamma - 1) + \frac{1}{2}(u_x^2 + u_y^2 + u_z^2)$, u_x, u_y and u_z are the x, y and z components of macroscopic fluid velocity and γ is the specific heat ratio.

4.2.5.1 Evaluation of split inviscid fluxes

As described earlier split inviscid fluxes are evaluated based on distribution splitting in a similar way to KFVS. The inviscid part of the flux component, $\boldsymbol{GX}_I^{\pm}$ is defined as

$$\begin{aligned} \boldsymbol{GX}_I^{+} &= \left\langle \boldsymbol{\Psi}, v_x f_0^{+\cdots} \right\rangle = \int_0^{+\infty} \int_{-\infty}^{+\infty} \int_{-\infty}^{+\infty} \int_0^{+\infty} \boldsymbol{\Psi} v_x f_0 dv_x dv_y dv_z d\mathbb{I} \\ \boldsymbol{GX}_I^{-} &= \left\langle \boldsymbol{\Psi}, v_x f_0^{-\cdots} \right\rangle = \int_0^{+\infty} \int_{-\infty}^{+\infty} \int_{-\infty}^{+\infty} \int_{-\infty}^{0} \boldsymbol{\Psi} v_x f_0 dv_x dv_y dv_z d\mathbb{I} \end{aligned} \tag{4.70}$$

Similarly, split fluxes $\boldsymbol{GY}_I^{\pm}$ and $\boldsymbol{GZ}_I^{\pm}$ are evaluated as

$$\begin{aligned} \boldsymbol{GY}_I^{+} &= \left\langle \boldsymbol{\Psi}, v_y f_0^{\cdot+\cdot} \right\rangle = \int_0^{+\infty} \int_{-\infty}^{+\infty} \int_0^{+\infty} \int_{-\infty}^{+\infty} \boldsymbol{\Psi} v_y f_0 dv_x dv_y dv_z d\mathbb{I} \\ \boldsymbol{GY}_I^{-} &= \left\langle \boldsymbol{\Psi}, v_y f_0^{\cdot-\cdot} \right\rangle = \int_0^{+\infty} \int_{-\infty}^{+\infty} \int_{-\infty}^{0} \int_{-\infty}^{+\infty} \boldsymbol{\Psi} v_y f_0 dv_x dv_y dv_z d\mathbb{I} \end{aligned} \tag{4.71}$$

$$\begin{aligned} \boldsymbol{GZ}_I^{+} &= \left\langle \boldsymbol{\Psi}, v_z f_0^{\cdot\cdot+} \right\rangle = \int_0^{+\infty} \int_0^{+\infty} \int_{-\infty}^{+\infty} \int_{-\infty}^{+\infty} \boldsymbol{\Psi} v_z f_0 dv_x dv_y dv_z d\mathbb{I} \\ \boldsymbol{GZ}_I^{-} &= \left\langle \boldsymbol{\Psi}, v_z f_0^{\cdot\cdot-} \right\rangle = \int_0^{+\infty} \int_{-\infty}^{0} \int_{-\infty}^{+\infty} \int_{-\infty}^{+\infty} \boldsymbol{\Psi} v_z f_0 dv_x dv_y dv_z d\mathbb{I} \end{aligned} \tag{4.72}$$

The expressions for fluxes are given in the Appendix D.

4.2.5.2 Evaluation of split viscous fluxes based on split microscopic tensors

The split macroscopic tensors are obtained by taking moments of the split microscopic tensors associated with the shear stress tensor and heat flux vector. As described earlier the viscous fluxes are evaluated based on full tensor contraction of split macroscopic tensors with its conjugate thermodynamic forces. The viscous part of the flux component, $\boldsymbol{GX}_V^{\pm}$, $\boldsymbol{GY}_V^{\pm}$ and $\boldsymbol{GZ}_V^{\pm}$ are defined as

$$\begin{array}{ll} \boldsymbol{GX}_V^{\pm} & = -\sum_j \boldsymbol{\Lambda}_j^{\pm\cdot\cdot} \odot \boldsymbol{X}_j = -(\boldsymbol{\Lambda}_\tau^{\pm\cdot\cdot} : \boldsymbol{X}_\tau + \boldsymbol{\Lambda}_q^{\pm\cdot\cdot} \cdot \boldsymbol{X}_q) \\ \boldsymbol{GY}_V^{\pm} & = -\sum_j \boldsymbol{\Lambda}_j^{\cdot\pm\cdot} \odot \boldsymbol{X}_j = -(\boldsymbol{\Lambda}_\tau^{\cdot\pm\cdot} : \boldsymbol{X}_\tau + \boldsymbol{\Lambda}_q^{\cdot\pm\cdot} \cdot \boldsymbol{X}_q) \\ \boldsymbol{GZ}_V^{\pm} & = -\sum_j \boldsymbol{\Lambda}_j^{\cdot\cdot\pm} \odot \boldsymbol{X}_j = -(\boldsymbol{\Lambda}_\tau^{\cdot\cdot\pm} : \boldsymbol{X}_\tau + \boldsymbol{\Lambda}_q^{\cdot\cdot\pm} \cdot \boldsymbol{X}_q) \end{array} \tag{4.73}$$

Expressions for components of the macroscopic tensors $\boldsymbol{\Lambda}_\tau^{\pm\cdot\cdot}$, $\boldsymbol{\Lambda}_q^{\pm\cdot\cdot}$ associated with x-split fluxes, $\boldsymbol{\Lambda}_\tau^{\cdot\pm\cdot}$, $\boldsymbol{\Lambda}_q^{\cdot\pm\cdot}$ associated with y-split fluxes and $\boldsymbol{\Lambda}_\tau^{\cdot\cdot\pm}$, $\boldsymbol{\Lambda}_q^{\cdot\cdot\pm}$ associated with z-split fluxes are given in Appendix D. Expression of conjugate thermodynamic forces, $\boldsymbol{X_\tau}$ and $\boldsymbol{X_q}$ and expressions of split viscous fluxes $\boldsymbol{GX}_V^{\pm}$, $\boldsymbol{GY}_V^{\pm}$ and $\boldsymbol{GZ}_V^{\pm}$ are also given in the Appendix D.

4.3 Linkage of non-equilibrium thermodynamics with the new kinetic scheme

As the state update moves from one time step to another time step in order to decrease the thermodynamic forces, the path of evolution follows non-equilibrium thermodynamics by generating entropy which is the product of the thermodynamic forces and its conjugate fluxes. As derived earlier the path traced out maximizes the entropy under the constraint imposed due to conservation laws and satisfies the Onsager's variational principle. Most of the solver require fixes and tuning if they have to operate from low speed to hypersonic rarefied flow or from creeping flows to high speed continuum flow. This is because of two unknown factors, i) the correct amount of entropy generation, and ii) distribution of entropy generation for each thermodynamic force i.e. in what proportion the thermodynamic forces associated with shear stress tensor and heat flux vector contribute. While the present scheme generates entropy for each thermodynamic

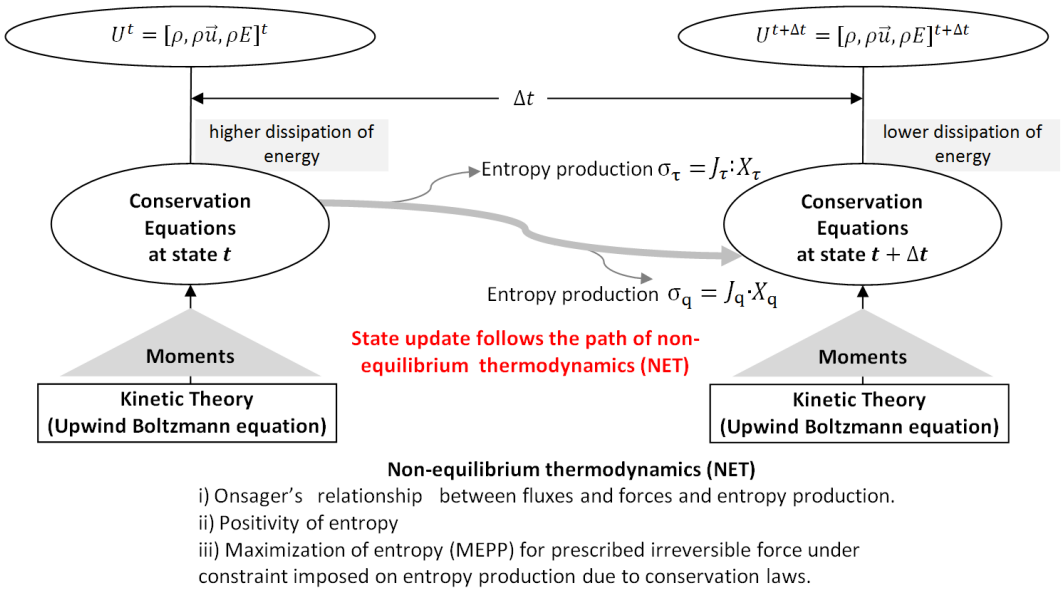

Figure 4.2: State update of the kinetic method follows non-equilibrium thermodynamics.

force e.g. $\sigma_\tau = \boldsymbol{J}_\tau : \boldsymbol{X}_\tau$ with respect to thermodynamic force associated with the shear stress tensor and entropy, $\sigma_q = \boldsymbol{J}_q \cdot \boldsymbol{X}_q$ with respect to thermodynamic force associated with the heat flux vector. *Linkage with non-equilibrium thermodynamics ensures correct division of entropy generation for each thermodynamic force as the state update moves from one conservation state to another.* The kinetic upwind method developed in the thesis mimics the actual physics as the state update follows the path laid down by non-equilibrium thermodynamics as shown in Figure 4.2. The present kinetic upwind scheme can be used to simulate the entire range from rarefied flow to continuum flow, creeping flow to flow with shocks as it is derived using kinetic theory incorporating phenomenological theory of non-equilibrium thermodynamics. Figure 4.3(a) shows the schematic picture of the evolution of flow and entropy generation for two different kinetic schemes : one following non-equilibrium thermodynamics (NET)and other non-NET based. The flow trajectory leaves the surface representing infinite-dimensional manifold of locally Maxwellian distribution as shown in the Fig. 4.3(a). The flow trajectory represents Boltzmann flow which after leaving the manifold is brought back on this infinite-dimensional manifold of locally Maxwellian distribution gen-

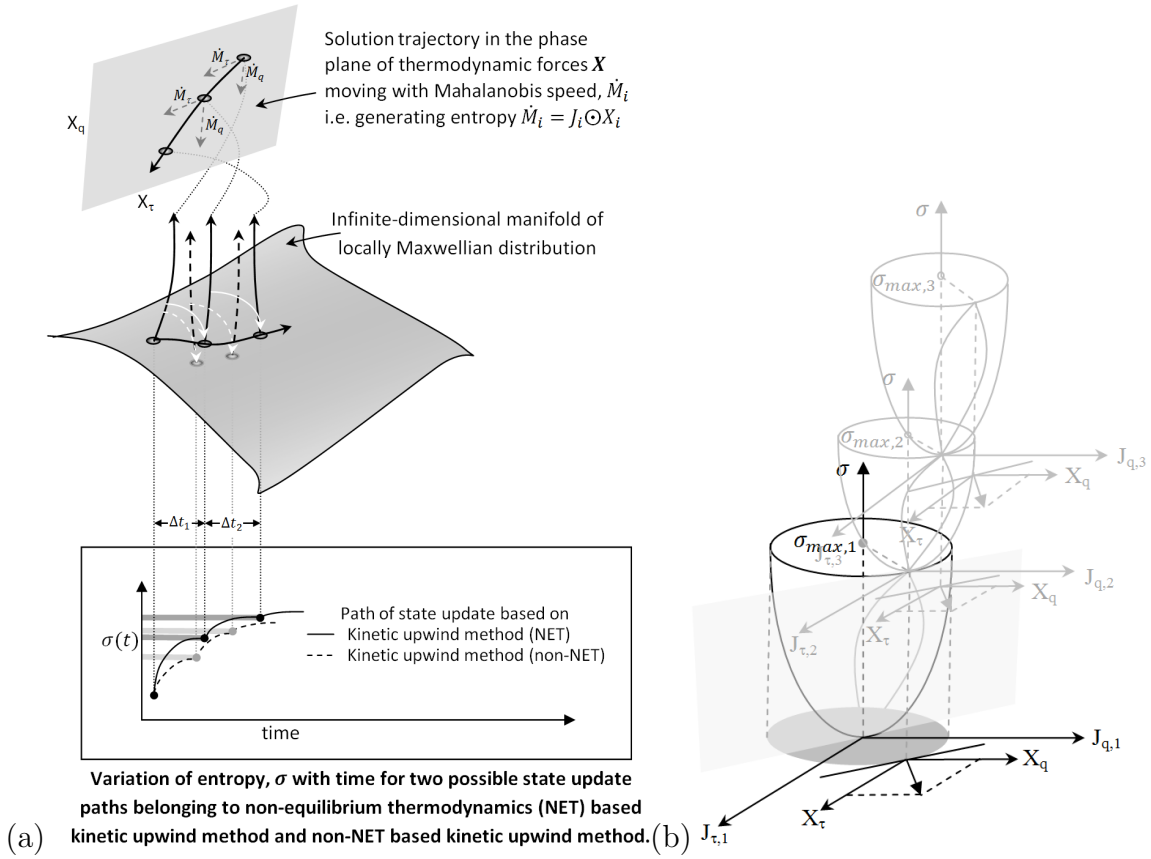

Variation of entropy, σ with time for two possible state update paths belonging to non-equilibrium thermodynamics (NET) based kinetic upwind method and non-NET based kinetic upwind method.

Figure 4.3: Schematic picture of the (a) evolution of flow and entropy generation for non-equilibrium thermodynamics (NET) based kinetic scheme and non-NET based kinetic upwind method. (b) entropy generation based on Onsager's principle for NET based kinetic scheme for two thermodynamic fluxes.

erating irreversibility and entropy as a consequence. Each kinetic scheme will have its own path or trajectory of evolution of flow as well as entropy generation. This trajectory can also be observed in the phase plane of thermodynamic forces where it moves with Mahalanobis speed $\dot{M}_i$ i.e. generating entropy for each thermodynamic force $\boldsymbol{X}_i$ following Onsager's relationship. The movement of this trajectory can also be interpreted in terms of entropy production in the flux space represented as surface $\sigma(\boldsymbol{J}_i, \boldsymbol{J}_k)$. Figure 4.3(b) shows a linear irreversible process and a dissipative surface of entropy for a case with two thermodynamic fluxes and forces. As the flow trajectory leaves the manifold the flux $\boldsymbol{J}_i$ is generated corresponding to its conjugate thermodynamic force $\boldsymbol{X}_i$ which is orthogonal to surface $\sigma(\boldsymbol{J}_i, \boldsymbol{J}_k)$ intersected by the plane $\sum_i \boldsymbol{J}_i \odot \boldsymbol{X}_i$.
It is the split flux not the full flux which participates in actual physical process. Split fluxes based on new kinetic model also follow non-equilibrium thermodynamics, for example entropy based on the split non-equilibrium flux $\sigma^{\pm}(\boldsymbol{J}_i, \boldsymbol{X}_i)$ is expressed as

$$\sigma^{\pm}(\boldsymbol{J}_i, \boldsymbol{X}_i) = \sum_i \boldsymbol{J}_i^{\pm} \odot \boldsymbol{X}_i \tag{4.74}$$

where non-equilibrium split flux $\boldsymbol{J}_i^{\pm}$ are kinetic non-equilibrium split flux conjugate to its thermodynamic force $\boldsymbol{X}_i$. Non-equilibrium split fluxes involve terms of higher moments $\psi_j \notin \boldsymbol{\Psi}$, thus it modifies the idea of extended thermodynamics

4.4 Moments and extended thermodynamics due to kinetic split fluxes

The moments of the Boltzmann equation satisfy an infinite hierarchy of balance laws, the macroscopic state vector at the $k+1^{th}$ hierarchy is based on the flux vector $\boldsymbol{J}_i^k = \sum_j \boldsymbol{L}_{ij}^k \odot \boldsymbol{X}_j$ in the k^{th} hierarchy where Onsager's phenomenological tensor at k^{th} hierarchy, $\boldsymbol{L}_{ij}^k$ is obtained using $\boldsymbol{L}_{ij}^{k-1}$ as $\boldsymbol{L}_{ij}^k = \left\langle \boldsymbol{\Psi}, \vec{v}\boldsymbol{L}_{ij}^{k-1} \right\rangle$. Higher order transport equations can be seen as a fractal entity based on Onsager's phenomenological tensor emerging through Maxwellian iteration. Navier-Stokes equations is a limiting case of extended thermodynamics (ET) when relaxation times of diffusive fluxes are neglected[196].

In actual physical process it is split fluxes which participates in the conservation hence the moments of the Boltzmann equation should satisfy an infinite hierarchy of balance laws in terms of split fluxes. At the k^{th} hierarchy the macroscopic state vector $\boldsymbol{U}_{m_1 m_2 \cdots m_k}$ and split flux vector $\boldsymbol{G}^{\pm}_{m_1 m_2 \cdots m_k}$ are based on the k^{th} component of the vector of collision invariant, $\boldsymbol{\Psi}_{m_1 m_2 \cdots m_k}$ given as

$$\boldsymbol{U}_{m_1 m_2 \cdots m_k} = \int_{\mathbb{R}^+} \int_{\mathbb{R}^D} \boldsymbol{\Psi}_{m_1 m_2 \cdots m_k} f d\vec{v} d\mathbb{I} \tag{4.75}$$

$$\boldsymbol{G}^{\pm}_{m_1 m_2 \cdots m_k} = \int_{\mathbb{R}^+} \int_{\mathbb{R}^{D^{\pm}}} \boldsymbol{\Psi}_{m_1 m_2 \cdots m_k} \vec{v} f d\vec{v} d\mathbb{I} \tag{4.76}$$

Unlike the idea of rational extended thermodynamics[196] it is the split flux terms in an equation which becomes the density in the next one as follows

$$\begin{array}{c} \frac{\partial \boldsymbol{U}_{m_1}}{\partial t} + \frac{\partial \boldsymbol{G}^{\pm}_{m_1}}{\partial \vec{x}} = 0 \\ \swarrow \\ \frac{\partial \boldsymbol{U}_{m_1 m_2}}{\partial t} + \frac{\partial \boldsymbol{G}^{\pm}_{m_1 m_2}}{\partial \vec{x}} = 0 \\ \swarrow \\ \vdots \end{array} \tag{4.77}$$

The state vector $\boldsymbol{U}_{m_1 m_2 \cdots m_k m_{k+1}}$ in the $(k+1)^{th}$ hierarchy is based on the split flux $\boldsymbol{G}^{\pm}_{m_1 m_2 \cdots m_k}$ based on half range distribution function defined in k^{th} hierarchy. For example, consider one dimensional case where split mass flux composed of inviscid and viscous contribution, $GX^{\pm}(\psi_1)$ evaluated using $\psi_1 \in \boldsymbol{\Psi}$ is given as

$$GX^{\pm}(\psi_1) = \tfrac{1}{2}\rho \left(A^{\pm} u_x + \tfrac{B^{\pm}}{\sqrt{\pi\beta}} \right) - \tfrac{\rho}{4p\sqrt{\beta}} \tfrac{B^{\pm}}{\sqrt{\pi}} \left(2u_x \beta q_x \tfrac{(\gamma-1)}{\gamma} + \tau_{xx} \right) \tag{4.78}$$

where $A^{\pm} = 1 \pm Erf(u_x\sqrt{\beta})$ and $B^{\pm} = \pm Exp(-\beta u_x^2)$. The split mass flux contain terms of momentum, shear stress tensor and heat flux vector. These terms involve i)$\vec{v}$, ii) $\vec{v} \otimes \vec{v}$, and iii) $\left(\mathbb{I} + \frac{1}{2}\vec{v}^T\vec{v}\right)\vec{v}$ components of collision invariants. Thus, 5 moments based on $\boldsymbol{\Psi}=\left[1, \vec{v}, \mathbb{I} + \frac{1}{2}\vec{v}^T\vec{v}\right]^T$ are inadequate as vector of collision invariant should include $\boldsymbol{\Psi}=\left[1, \vec{v}, \mathbb{I} + \frac{1}{2}\vec{v}^T\vec{v}, \vec{v} \otimes \vec{v}, \left(\mathbb{I} + \frac{1}{2}\vec{v}^T\vec{v}\right)\vec{v}\right]^T$ giving rise to at-least 13 moment equations such that split mass flux becomes density in the second step and split momentum flux becomes density in the third step. This set of 13-moment Grad like system[102] includes evolution of shear stress tensor and heat flux vector. However, the present 5 moments based formulation is adequate for the simulation of most of the engineering slip flow problems which

lie in the regime of linear irreversible thermodynamics. The present approach will not be adequate for cases that involve large Mach number in shock waves, high frequencies for sound waves, etc. It should also be noted that the approach based on non-equilibrium thermodynamics may also modify Levermore [149] procedure which generates hierarchy of closed systems of moment equations that ensures every member of the hierarchy is symmetric hyperbolic with an entropy, and formally recovers to Euler limit. The finite dimensional linear subspace Ξ of functions of $\vec{v}$ in Levermore procedure should ensure that entropy generation follows Onsager's reciprocity principle.

In real media it is the split flux which participates in any physical process and for non-equilibrium flows the split fluxes contain dissipative terms. For example split flux associated with mass flow contains contribution of viscous terms. It is also interesting to note that the presence of dissipative terms due to thermodynamic forces in the split fluxes brings out its relationship and difference with the hydrodynamic theory of Brenner [38] and Quasi-gas dynamics [81] where dissipative terms were introduced in un-split flux terms such that time-spatial averages are invariant under Galileo transform.

4.5 Kinetic upwind method for axi-symmetric geometries and strongly rotating flows

As described earlier in chapter two that the numerical modeling of high speed rotating flows is a challenge as the regime changes from continuum at the periphery, slip, transition to non-continuum in the central core. The another difficult aspect of strongly rotating flows is to effectively capture the weak secondary flow feature (measured by Rossby number) embedded in a strongly rotating primary flow field. This section gives the new way of implementing kinetic upwind method for axi-symmetric geometries. This section also presents a novel approach using variance reduction technique and kinetic flux vector splitting method for resolving weak secondary flow present in a primary strong rotating flow field.

4.5.1 Continuum breakdown in rotating flow field

Rossby number, ε can also be defined as the deviation from equilibrium rigid body rotation, expressed as

$$\varepsilon = \frac{\int_{\mathbb{R}^+}\int_{\mathbb{R}^D}\psi_i(f_1 - f_{RB})d\vec{v}d\mathbb{I}}{\int_{\mathbb{R}^+}\int_{\mathbb{R}^D}\psi_i f_{RB}d\vec{v}d\mathbb{I}} \tag{4.79}$$

where moment variable $\psi_i \in \mathbf{\Psi} \equiv \{1, \vec{v}, \vec{v}^T\vec{v}\}$ or any other admissible $\psi_i \in \mathbf{\Psi} \equiv \{1, \vec{v}, \vec{v}\otimes\vec{v}, \cdots\}$. The term f_{RB} is Maxwellian distribution function based on rigid body rotation condition, and f_1 is the first order distribution function corresponding to the Navier-Stokes equation. Continuum breakdown parameter, NS_L based on the degree of departure from the non-equilibrium flow state is expressed as

$$NS_L = \frac{\int_{\mathbb{R}^+}\int_{\mathbb{R}^D}\psi_i(f - f_1)d\vec{v}d\mathbb{I}}{\int_{\mathbb{R}^+}\int_{\mathbb{R}^D}\psi_i(f_1 - f_{RB})d\vec{v}d\mathbb{I}} \tag{4.80}$$

where f is a higher order distribution function. Continuum breakdown parameter, NS_L for a rotating flow field based on the degree of departure from the non-equilibrium flow state will then be a function of Rossby number, ε as follows

$$NS_L = \frac{\int_{\mathbb{R}^+}\int_{\mathbb{R}^D}\psi_i(f - f_1)d\vec{v}d\mathbb{I}}{\varepsilon\int_{\mathbb{R}^+}\int_{\mathbb{R}^D}\psi_i f_{RB}d\vec{v}d\mathbb{I}} \tag{4.81}$$

4.5.2 Kinetic upwind method for axi-symmetric geometries

For axi-symmetric geometries the Boltzmann equation in the cylindrical coordinate system is given as follows:

$$\frac{\partial f}{\partial t} + v_z\frac{\partial f}{\partial z} + \frac{v_r}{r}\frac{\partial rf}{\partial r} + \left\{\frac{-fv_r}{r} + \frac{v_\theta^2}{r}\frac{\partial f}{\partial v_r} - \frac{v_r v_\theta}{r}\frac{\partial f}{\partial v_\theta}\right\} = J(f,f) \tag{4.82}$$

The terms in the curly bracket correspond to the source terms obtained in stationary frame of reference. Applying the modified kinetic flux vector splitting of the axi-symmetric formulation and taking $\mathbf{\Psi}$ moments of the Boltzmann equation with dissipation control function, φ

$$\begin{aligned}\left\langle \Psi, \frac{\partial f_1}{\partial t} + \frac{\partial\left(\frac{v_z+\varphi|v_z|}{2}\right)f_1}{\partial z} + \frac{\partial\left(\frac{v_z-\varphi|v_z|}{2}\right)f_1}{\partial z} + \frac{1}{r}\frac{\partial r\left(\frac{v_r+\varphi|v_r|}{2}\right)f_1}{\partial r} + \frac{1}{r}\frac{\partial r\left(\frac{v_r-\varphi|v_r|}{2}\right)f_1}{\partial r}\right\rangle \\ + \left\langle \Psi, \left\{\frac{-f_1 v_r}{r} + \frac{v_\theta^2}{r}\frac{\partial f_1}{\partial v_r} - \frac{v_r v_\theta}{r}\frac{\partial f_1}{\partial v_\theta}\right\}\right\rangle = 0\end{aligned} \tag{4.83}$$

For axi-symmetric geometries the dissipation control function, φ can either be a function of molecular velocity or any suitable macroscopic parameter depending on the type of flow. This leads to kinetic upwind axi-symmetric formulation of Navier-Stokes equations as

$$\frac{\partial \boldsymbol{U}}{\partial t} + \frac{\partial \boldsymbol{GZ}^{+}}{\partial z} + \frac{\partial \boldsymbol{GZ}^{-}}{\partial z} + \frac{1}{r}\frac{\partial r\boldsymbol{GR}^{+}}{\partial r} + \frac{1}{r}\frac{\partial r\boldsymbol{GR}^{-}}{\partial r} + \boldsymbol{S} = 0 \tag{4.84}$$

where $\boldsymbol{GZ}^{\pm}$ and $\boldsymbol{GR}^{\pm}$ represents axial and radial split fluxes and un-split source term $\boldsymbol{S}$ is expressed as

$$\boldsymbol{S} = \left[0, 0, -\frac{p}{r} - \frac{\rho u_{\theta}^{2}}{r} - \frac{\tau_{\theta\theta}}{r}, \frac{\rho u_{r} u_{\theta}}{r} + \frac{\tau_{r\theta}}{r}, 0\right]^{T} \tag{4.85}$$

4.5.3 Variance Reduction Kinetic Flux Vector Splitting (VRKFVS)

The shear amplitude for the non-inertial rotational problem should be observed in the correct frame of reference with variance reduction approach. A new method variance reduction kinetic flux vector splitting (VRKFVS) was developed to resolve weak secondary flow embedded in strong primary flow. In the variance reduction approach Boltzmann equation is written as a perturbation from its state of equilibrium. This method basically evaluates the *variance-reduced* form of the collision integral as in the variance reduction technique of Baker and Hadjiconstantinou [21] and Homolle and Hadjiconstantinou [123] used in direct simulation Monte Carlo (DSMC). The collision integral can also be expressed as

$$\begin{aligned} J(f,f) \quad &= \frac{1}{2}\int_{0}^{\pi/2}\int_{0}^{2\pi}\int_{\mathbb{R}^{+}}\int_{\mathbb{R}^{+}}\int_{\mathbb{R}^{D}}\int_{\mathbb{R}^{D}}\cdots \\ &\quad (\delta_1^a + \delta_2^a - \delta_1 - \delta_2)\, f^{(1)} f^{(2)} g\, \bar{\Pi}\, d\vec{v}_1 d\vec{v}_2 d\mathbb{I}_1 d\mathbb{I}_2 d\varrho d\Theta \end{aligned} \tag{4.86}$$

where $\delta_1^a = \delta^3(\vec{v}_1^a - \vec{v})$, $\delta_2^a = \delta^3(\vec{v}_2^a - \vec{v})$, $\delta_1 = \delta^3(\vec{v}_1 - \vec{v})$ and $\delta_2 = \delta^3(\vec{v}_2 - \vec{v})$, δ is the Dirac delta function and subscript 'a' denotes after collision state. Integration is performed with respect to scattering angle ϱ which goes from 0 to 2π, while angle Θ varies from 0 (head-on collisions) to $\pi/2$ (grazing collisions), $\bar{\Pi}$ is the molecular collision cross section, g is the magnitude of the relative velocity of the particles before collision relative to path of the centre of gravity of the system consisting of two particles. For further details on binary collisions refer section

B.1 in Appendix B. If the distributions $f^{(1)} = f_0 + \Delta f^{(1)}$ and $f^{(2)} = f_M + \Delta f^{(2)}$ are perturbations around Maxwellians f_0 and f_M, then the collision integral in the variance-reduced form can be expressed as

$$\begin{aligned} J(f,f) &= \frac{1}{2}\int_0^{\pi/2}\int_0^{2\pi}\int_{\mathbb{R}^+}\int_{\mathbb{R}^+}\int_{\mathbb{R}^D}\int_{\mathbb{R}^D}\cdots \\ &\quad (\delta_1^a + \delta_2^a - \delta_1 - \delta_2)\,(2f_0\Delta f^{(2)} + \Delta f^{(1)}\Delta f^{(2)})g\;\bar{\Pi}\;d\vec{v}_1 d\vec{v}_2 d\mathbb{I}_1 d\mathbb{I}_2 d\varrho d\Theta \\ &= L(\Delta f) + \Gamma(\Delta f, \Delta f) \end{aligned} \tag{4.87}$$

Thus the integral can be written as the sum of linear $L(\Delta f)$ and a quadratic $\Gamma(\Delta f, \Delta f)$ term.

In this variant of kinetic flux vector splitting the Boltzmann equation uses distribution in a Chapman-Enskog perturbative form. The Boltzmann equation with distribution function written in Chapman-Enskog perturbative form with respect to Maxwellian f_0 is expressed as

$$\frac{\partial\left(f_0 + \sum_i^\infty \mathrm{Kn}^i \bar{f}_i\right)}{\partial t} + \frac{\partial\vec{v}\left(f_0 + \sum_i^\infty \mathrm{Kn}^i \bar{f}_i\right)}{\partial\vec{x}} = 0 \tag{4.88}$$

Assuming that f in the vicinity of f_0 as well as another chosen Maxwellian f_M. In such a case the Boltzmann equation can also be written based on Chapman-Enskog perturbative form with respect to f_M

$$\frac{\partial\left(f_M + \sum_i^\infty \mathrm{Kn}^i \bar{f}_i^M\right)}{\partial t} + \frac{\partial\vec{v}\left(f_M + \sum_i^\infty \mathrm{Kn}^i \bar{f}_i^M\right)}{\partial\vec{x}} = 0 \tag{4.89}$$

Taking $\mathbf{\Psi}$ moment of the difference of these two Boltzmann equations we get

$$< \mathbf{\Psi}, \frac{\partial\left(\Delta f\right)}{\partial t} + \frac{\partial\vec{v}\left(\Delta f + \sum_i^\infty \mathrm{Kn}^i \bar{f}_i - \sum_i^\infty \mathrm{Kn}^i \bar{f}_i^M\right)}{\partial\vec{x}} = 0 > \tag{4.90}$$

The term $\Delta f = f_0 - f_M$ is the difference in the Maxwellians. It should be noted that the terms $\sum_i^\infty \mathrm{Kn}^i \bar{f}_i$and $\sum_i^\infty \mathrm{Kn}^i \bar{f}_i^M$associated with time derivative vanishes as these perturbation terms satisfy the additive invariants property, expressed as

$$< \mathbf{\Psi}, \mathrm{Kn}^i \bar{f}_i >_{\forall i\geq 1} =< \Psi, \mathrm{Kn}^i \bar{f}_i^M >_{\forall i\geq 1} = 0 \tag{4.91}$$

The difference in the perturbation terms for the two Maxwellians can be simplified for first order distribution as

$$\mathrm{Kn}\bar{f}_1 - \mathrm{Kn}\bar{f}_1^M = -t_{R0}\left[\frac{\partial f_0}{\partial t} + \nabla_{\vec{x}}\cdot(\vec{v}f_0)\right] + t_{RM}\left[\frac{\partial f_M}{\partial t} + \nabla_{\vec{x}}\cdot(\vec{v}f_M)\right] \tag{4.92}$$

where t_{R0} and t_{RM} are relaxation time for f_0 and f_M. Assuming $t_R = t_{R0} = t_{RM}$ as the chosen distribution f_0 is in the vicinity off_M. With this the difference in the perturbation terms can be approximated for the first order expansion as

$$\mathrm{Kn}\Delta\bar{f}_1 = \mathrm{Kn}\bar{f}_1 - \mathrm{Kn}\bar{f}_1^M \approx -t_R\left[\frac{\partial \Delta f}{\partial t} + \nabla_{\vec{x}}\cdot(\vec{v}\Delta f)\right] \tag{4.93}$$

where $\Delta\bar{f}_1 = \bar{f}_1 - \bar{f}_1^M$and with its substitution the Boltzmann equation in this variance reduction form based on first order distribution is expressed as

$$\frac{\partial(\Delta f)}{\partial t} + \frac{\partial \vec{v}(\Delta f_1)}{\partial \vec{x}} = 0 \quad \text{or} \quad \frac{\partial\left(\Delta\hat{f}\right)}{\partial t} + \frac{\partial \vec{v}(\Delta f_1)}{\partial \vec{x}} = 0 \tag{4.94}$$

where $\Delta f_1 = \Delta f + \mathrm{Kn}\Delta\bar{f}_1 = \Delta f - \sum_j \boldsymbol{\Upsilon}_j \odot \boldsymbol{X}_j$ and $\Delta\hat{f} = f_1 - f_M$ and$f_1 = f_0 + \mathrm{Kn}\bar{f}_1 = f_0 - \sum_j \boldsymbol{\Upsilon}_j \odot \boldsymbol{X}_j$ as $\langle \boldsymbol{\Psi}, \sum_j \boldsymbol{\Upsilon}_j \odot \boldsymbol{X}_j\rangle = 0$.
In Variance Reduction Kinetic Flux Vector Splitting (VRKFVS) for Navier-Stokes upwinding is implemented in a similar way as in KFVS using Courant split Boltzmann equation as follows :

$$\frac{\partial\Delta\hat{f}}{\partial t} + \frac{\partial(\frac{v_x \pm |v_x|}{2})\Delta f_1}{\partial x} + \frac{\partial(\frac{v_y \pm |v_y|}{2})\Delta f_1}{\partial y} + \frac{\partial(\frac{v_z \pm |v_z|}{2})\Delta f_1}{\partial z} = 0 \tag{4.95}$$

Taking $\boldsymbol{\Psi}$ moments of the resulting variant of Boltzmann equation leads to Navier-Stokes equation based on Variance Reduction Kinetic Flux Vector Splitting (VRKFVS) as follows

$$\begin{array}{ll} \frac{\partial}{\partial t}(\Delta \boldsymbol{U}) & +\frac{\partial}{\partial x}\left[\Delta\left(\boldsymbol{G}\boldsymbol{X}_I^{\pm}\right) + \left(\boldsymbol{G}\boldsymbol{X}_V^{\pm}\right)_{\Delta}\right] + \frac{\partial}{\partial y}\left[\Delta\left(\boldsymbol{G}\boldsymbol{Y}_I^{\pm}\right) + \left(\boldsymbol{G}\boldsymbol{Y}_V^{\pm}\right)_{\Delta}\right] \\ & +\frac{\partial}{\partial z}\left[\Delta\left(\boldsymbol{G}\boldsymbol{Z}_I^{\pm}\right) + \left(\boldsymbol{G}\boldsymbol{Z}_V^{\pm}\right)_{\Delta}\right] = 0 \end{array} \tag{4.96}$$

where $\Delta\boldsymbol{U} = \boldsymbol{U} - \boldsymbol{U}_M$ is the deviation of the state update vector $\boldsymbol{U}$ over $\boldsymbol{U}_M$ based on Maxwellian distribution,f_M. The inviscid fluxes are also deviations over the inviscid fluxes based on the chosen distribution,f_M. Thus $\Delta\left(\boldsymbol{G}\boldsymbol{X}_I^{\pm}\right) = \left(\boldsymbol{G}\boldsymbol{X}_I^{\pm}\right) - \left(\boldsymbol{G}\boldsymbol{X}_I^{\pm}\right)_M$, $\Delta\left(\boldsymbol{G}\boldsymbol{Y}_I^{\pm}\right) = \left(\boldsymbol{G}\boldsymbol{Y}_I^{\pm}\right) - \left(\boldsymbol{G}\boldsymbol{Y}_I^{\pm}\right)_M$ and $\Delta\left(\boldsymbol{G}\boldsymbol{Z}_I^{\pm}\right) = \left(\boldsymbol{G}\boldsymbol{Z}_I^{\pm}\right) - \left(\boldsymbol{G}\boldsymbol{Z}_I^{\pm}\right)_M$, where $\left(\boldsymbol{G}\boldsymbol{X}_I^{\pm}\right)_M$, $\left(\boldsymbol{G}\boldsymbol{Y}_I^{\pm}\right)_M$ and $\left(\boldsymbol{G}\boldsymbol{Z}_I^{\pm}\right)_M$ are the inviscid split fluxes based on the Maxwellian distribution, f_M associated with the chosen state of equilibrium. The viscous fluxes$\left(\boldsymbol{G}\boldsymbol{X}_V^{\pm}\right)_{\Delta}$, $\left(\boldsymbol{G}\boldsymbol{Y}_V^{\pm}\right)_{\Delta}$ and $\left(\boldsymbol{G}\boldsymbol{Z}_V^{\pm}\right)_{\Delta}$ are computed based on relative velocity field over the chosen Maxwellian f_M. Thus we solve for the deviations over a state vector, $\boldsymbol{U}_M$ using the fluxes over a relative flow

field based on chosen Maxwellian, f_M. The selection of the state of equilibrium, f_M can be based on i) free stream condition, or ii) wall conditions, or iii) the mean equilibrium based on the neighborhood values, or iv) combination of all the three in the solution domain. This variant of KFVS based on variance reduction form of BGK-Boltzmann equation was found extremely useful in capturing weak secondary flow in a strong flow field environment.

4.5.3.1 VRKFVS scheme for one dimensional case

In a presence of thermodynamic force $\boldsymbol{X}$ the one dimensional Boltzmann equation can be written in terms of first order distribution functionf_1 as follows

$$\frac{\partial f_1}{\partial t} + \frac{\partial v f_1}{\partial x} = 0 \tag{4.97}$$

In absence of any thermodynamic force the system is in equilibrium and there can be many possible equilibrium states. Consider an equilibrium state based on space varying Maxwellian f_M which is closest to distribution f_1. The one dimensional Boltzmann equation in its variance reduction form for such a case can be written as

$$\frac{\partial\left(\Delta\hat{f}\right)}{\partial t} + \frac{\partial\vec{v}\left(\Delta f_1\right)}{\partial\vec{x}} = 0 \tag{4.98}$$

where $\Delta f_1 = \Delta f - \sum_j \boldsymbol{\Upsilon}_j \odot \boldsymbol{X}_j$ and $\Delta\hat{f} = f_1 - f_M$ and $f_1 = f_0 - \sum_j \boldsymbol{\Upsilon}_j \odot \boldsymbol{X}_j$ as $\langle \boldsymbol{\Psi}, \sum_j \boldsymbol{\Upsilon}_j \odot \boldsymbol{X}_j \rangle = 0$. Thus in VRKFVS the distribution function at time $t + \Delta t$ in a fluid domain is constructed based on half range perturbation over Maxwellian distribution as follows

$$f_1^{t+\Delta t} = f_M - \Delta t \left[\left(\frac{\partial v \Delta f_1^+}{\partial x} \right)^t_{0<v<+\infty} + \left(\frac{\partial v \Delta f_1^-}{\partial x} \right)^t_{-\infty<v<0} \right] \tag{4.99}$$

Figure 4.4 shows a schematic of variance reduction kinetic flux vector splitting. State update equation is obtained by taking $\boldsymbol{\Psi}$ moments as follows

$$\left\langle \boldsymbol{\Psi}, f_1^{t+\Delta t} \right\rangle = \langle \boldsymbol{\Psi}, f_M \rangle - \Delta t \left[\begin{array}{l} \left(\frac{\partial \left\langle \boldsymbol{\Psi}, v \Delta f_1^+ \right\rangle}{\partial x} \right)^t_{0<v<+\infty} \\ + \left(\frac{\partial \left\langle \boldsymbol{\Psi}, v \Delta f_1^- \right\rangle}{\partial x} \right)^t_{-\infty<v<0} \end{array} \right] \tag{4.100}$$

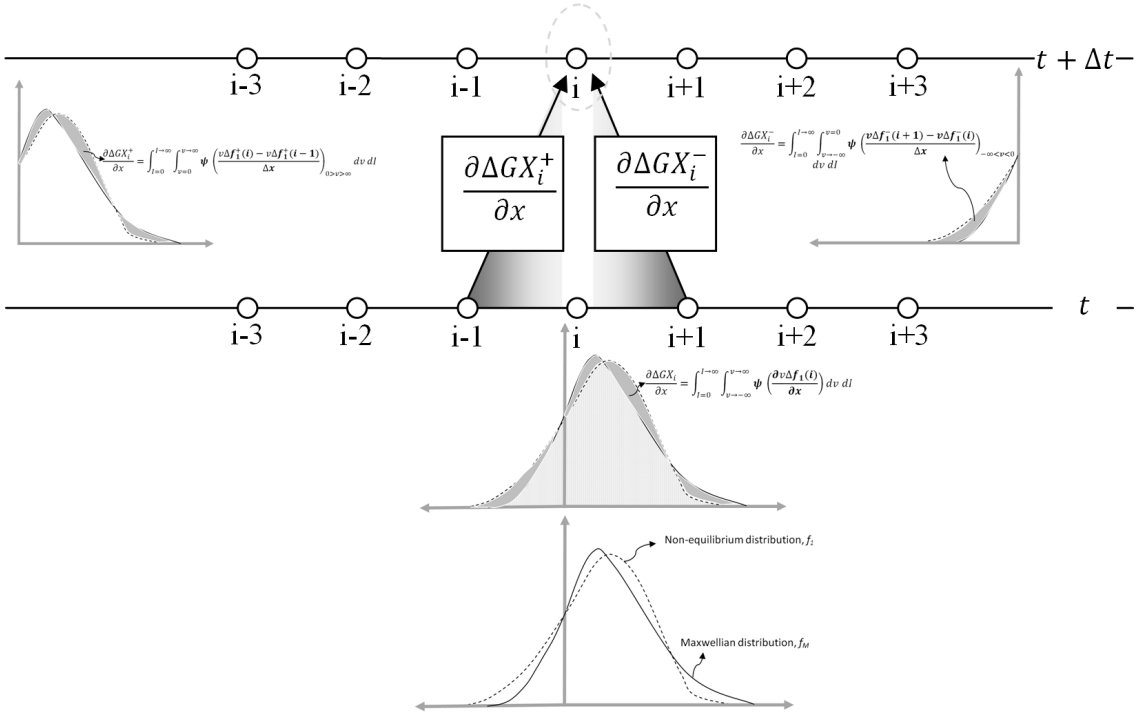

Figure 4.4: Variance reduction kinetic flux vector splitting based on moments of upwind discretized Boltzmann equation using perturbation over a chosen Maxwellian distribution.

The first order Chapman-Enskog distribution, $f_1 = f_0 - \sum_j \boldsymbol{\Upsilon}_j \odot \boldsymbol{X}_j$. The one-dimensional Boltzmann equation in the upwind discretized form after taking $\boldsymbol{\Psi}$-moments is

$$\begin{aligned}\left\langle \boldsymbol{\Psi}, \{f_0 - \textstyle\sum_j \boldsymbol{\Upsilon}_j \odot \boldsymbol{X}_j\}^{t+\Delta t} \right\rangle &= \langle \boldsymbol{\Psi}, f_M \rangle \\ &-\Delta t \left[\begin{array}{l} \left(\frac{\partial \left\langle \boldsymbol{\Psi}, v\{f_0 - \sum_j \boldsymbol{\Upsilon}_j \odot \boldsymbol{X}_j\}^+ \right\rangle}{\partial x} \right)^t_{0<v<+\infty} \\ - \left(\frac{\partial \left\langle \boldsymbol{\Psi}, v\Delta f_M^+ \right\rangle}{\partial x} \right)_{0<v<+\infty} \\ + \left(\frac{\partial \left\langle \boldsymbol{\Psi}, v\{f_0 - \sum_j \boldsymbol{\Upsilon}_j \odot \boldsymbol{X}_j\}^- \right\rangle}{\partial x} \right)^t_{-\infty<v<0} \\ - \left(\frac{\partial \left\langle \boldsymbol{\Psi}, v f_M^- \right\rangle}{\partial x} \right)_{-\infty<v<0} \end{array} \right]\end{aligned} \tag{4.101}$$

The perturbation term $-\sum_j \boldsymbol{\Upsilon}_j \odot \boldsymbol{X}_j$ satisfies the additive invariants property

$$\left\langle \boldsymbol{\Psi}, \sum_j \boldsymbol{\Upsilon}_j \odot \boldsymbol{X}_j \right\rangle = 0 \tag{4.102}$$

The upwind discretized Boltzmann equation after taking $\boldsymbol{\Psi}$-moments simplifies to

$$\begin{aligned}\left\langle \boldsymbol{\Psi}, f_0^{t+\Delta t} \right\rangle &= \langle \boldsymbol{\Psi}, f_M \rangle \\ &-\Delta t \left[\begin{array}{l} \left(\frac{\partial \left\langle \boldsymbol{\Psi}, v(f_0^+ - f_M^+) \right\rangle}{\partial x} \right)^t_{0<v<+\infty} + \left(\frac{\partial - \sum_j \boldsymbol{\Lambda}_j^+ \odot \bar{\boldsymbol{X}}_j}{\partial x} \right)^t_{0<v<+\infty} \\ + \left(\frac{\partial \left\langle \boldsymbol{\Psi}, v(f_0^- - f_M^+) \right\rangle}{\partial x} \right)^t_{-\infty<v<0} + \left(\frac{\partial - \sum_j \boldsymbol{\Lambda}_j^- \odot \bar{\boldsymbol{X}}_j}{\partial x} \right)^t_{-\infty<v<0} \end{array} \right]\end{aligned} \tag{4.103}$$

where tensor of thermodynamic force $\bar{\boldsymbol{X}}$ are computed based on relative velocity field $\vec{v} - \vec{v}_M$ and temperature field $T - T_M$ where $\vec{v}_M$ and T_M are the velocity and temperature field of the chosen Maxwellian f_M. This leads to Navier-Stokes equation based on Variance Reduction Kinetic Flux Vector Splitting (VRKFVS)

$$\frac{\partial}{\partial t}(\Delta \boldsymbol{U}) + \frac{\partial \Delta \boldsymbol{G}\boldsymbol{X}^+}{\partial x} + \frac{\partial \Delta \boldsymbol{G}\boldsymbol{X}^-}{\partial x} = 0 \tag{4.104}$$

where $\Delta \boldsymbol{U} = \boldsymbol{U} - \boldsymbol{U}_M$ is the deviation of the state update vector $\boldsymbol{U}$ over $\boldsymbol{U}_M$ based on Maxwellian distribution,f_M.The flux $\Delta \boldsymbol{GX}^{\pm}$ is expressed as

$$\Delta \boldsymbol{GX}^{\pm} = \Delta \boldsymbol{GX}_I^{\pm} + \left(\boldsymbol{GX}_V^{\pm}\right)_{\Delta} \tag{4.105}$$

The inviscid flux $\Delta\left(\boldsymbol{GX}_I^{\pm}\right) = \left(\boldsymbol{GX}_I^{\pm}\right) - \left(\boldsymbol{GX}_I^{\pm}\right)_M$ where $\left(\boldsymbol{GX}_I^{\pm}\right)_M$ is the inviscid split fluxes based on the Maxwellian distribution, f_M associated with the chosen state of equilibrium. The inviscid fluxes are also deviations over the inviscid fluxes based on the chosen distribution,f_M. The viscous fluxes $\left(\boldsymbol{GX}_V^{\pm}\right)_{\Delta}$ is computed based on tensor of thermodynamic force $\bar{\boldsymbol{X}}$ evaluated using relative velocity field $\vec{v} - \vec{v}_M$ and temperature field $T - T_M$.

4.5.3.2 Variance Reduction approach and treatment for strong rotation

Gas under isothermal condition with temperature $T = T_o$ uniformly rotating with angular velocity ω in a cylinder of radius r_{wall} can be described by rigid body rotation. The flow variables with rigid body condition are expressed as

$$[v_z, v_r, v_\theta,\ T, \rho]_{\mathrm{RB}} \equiv \left[0, 0, \omega\, r, T_o, \rho_{wall}\ Exp\left(\frac{\omega^2}{2RT_o}(r^2 - r_{wall}^2)\right)\right] \tag{4.106}$$

where the subscript $_{\mathrm{RB}}$ denotes the state of rigid body rotation. Boltzmann equation observed in the rigid body rotational frame leads to a very interesting result as velocity distribution associated with the rigid body solution satisfies both the inviscid as well as viscous solution. The velocity distribution associated with this rigid body rotation, f_{RB} is a Maxwellian. This variant of BGK-Boltzmann equation is then expressed in the variance reduction form as

$$\frac{\partial\left(\Delta f\right)}{\partial t} + \frac{\partial \vec{v}\left(\Delta f_1\right)}{\partial \vec{x}} = 0 \quad \text{or} \quad \frac{\partial\left(\Delta \hat{f}\right)}{\partial t} + \frac{\partial \vec{v}\left(\Delta f_1\right)}{\partial \vec{x}} = 0 \tag{4.107}$$

where $\Delta f_1 = \Delta f + \mathrm{Kn}\Delta \bar{f}_1 = \Delta f - \sum_j \boldsymbol{\Upsilon}_j \odot \boldsymbol{X}_j$, $\Delta f = f_0 - f_{RB}$, $\Delta \bar{f}_1 = \bar{f}_1 - \bar{f}_1^{RB}$ and $\Delta \hat{f} = f_1 - f_{RB}$. The term $\bar{f}_1^{RB}$ is the first order perturbation term for Maxwellian, f_{RB} associated with rigid body rotation. The term $\mathrm{Kn}\Delta \bar{f}_1$ is expressed as

$$\mathrm{Kn}\Delta \bar{f}_1 \approx -t_R\left[\frac{\partial \Delta f}{\partial t} + \nabla_{\vec{x}} \cdot \left(\vec{v}\Delta f\right)\right] \tag{4.108}$$

The steep gradients observed in stationary inertial frame now appear to be a weak perturbation. Taking $\boldsymbol{\psi}$ moments of the resulting variant of Boltzmann equation leads to upwind Navier-Stokes equation based on Variance Reduction Kinetic Flux Vector Splitting (VRKFVS) form as

$$\begin{array}{ll} \frac{\partial}{\partial t}\left(\boldsymbol{U}-\boldsymbol{U}_{RB}\right) & +\frac{\partial}{\partial x}\left[\left(\boldsymbol{GX}_I^{\pm}\right)-\left(\boldsymbol{GX}_I^{\pm}\right)_{RB}+\left(\boldsymbol{GX}_V^{\pm}\right)_{\Delta}\right] \\ & +\frac{\partial}{\partial y}\left[\left(\boldsymbol{GY}_I^{\pm}\right)-\left(\boldsymbol{GY}_I^{\pm}\right)_{RB}+\left(\boldsymbol{GY}_V^{\pm}\right)_{\Delta}\right] \\ & +\frac{\partial}{\partial z}\left[\left(\boldsymbol{GZ}_I^{\pm}\right)-\left(\boldsymbol{GZ}_I^{\pm}\right)_{RB}+\left(\boldsymbol{GZ}_V^{\pm}\right)_{\Delta}\right]=0 \end{array} \tag{4.109}$$

where $\boldsymbol{U}_{RB}$ is the state update vector at rigid body rotation condition, $\left(\boldsymbol{GX}_I^{\pm}\right)_{RB}$, $\left(\boldsymbol{GY}_I^{\pm}\right)_{RB}$ and $\left(\boldsymbol{GZ}_I^{\pm}\right)_{RB}$ are the split fluxes based on rigid body rotation. The viscous fluxes $\left(\boldsymbol{GX}_V^{\pm}\right)_{\Delta}$, $\left(\boldsymbol{GY}_V^{\pm}\right)_{\Delta}$ and $\left(\boldsymbol{GZ}_V^{\pm}\right)_{\Delta}$ are computed based on relative velocity field over the rigid body rotation. Rossby number which gives relative importance of inertial with respect to Coriolis forces is also a measure of departure from the rigid body solution. Small perturbation defined by Rossby number based on perturbation due to rotation $\varepsilon=\frac{\Delta\omega}{\omega}$ or temperature as $\varepsilon=\frac{\Delta T}{T}$ can be used to expand the solution as a Taylor series in ε about rigid body rotation. For a case where the departure from the rigid body distribution f_{RB} is small, the first order distribution is $f_1=f_{RB}(1-\sum_j \boldsymbol{\Upsilon}_j\odot\boldsymbol{X}_j)$ the Rossby number in such as case can also be expressed as

$$\varepsilon=\frac{\langle\Psi_i,f_1-f_{RB}\rangle}{\langle\Psi_i,f_{RB}\rangle}=\frac{\left\langle\Psi_i,\sum_j\boldsymbol{\Upsilon}_j\odot\boldsymbol{X}_j\right\rangle}{\langle\Psi_i,f_{RB}\rangle} \tag{4.110}$$

This local Rossby number, ε is used as a measure of departure from the rigid body solution, for example if $\varepsilon<\varepsilon_s$ the solver switches to VRKFVS scheme otherwise solver uses default KFVS based scheme.

4.6 Summary

It is difficult to find a single solver serving the entire regime from low speed to hypersonic rarefied flow or from creeping flows to high speed continuum flow. All the research in the development of upwind scheme revolves around the methodology of i) adding the correct amount of dissipation or entropy generation, and ii) distribution of dissipation or entropy generation for each thermodynamic force

i.e. in what proportion the thermodynamic forces associated with shear stress tensor and heat flux vector contribute to this entropy gain. The state update of a solver has to follow the path laid down by non-equilibrium thermodynamics. The path traced out maximizes the entropy under the constraint imposed due to conservation laws and satisfies the Onsager's variational principle. The new upwind scheme for macroscopic conservation equations involves three steps : i) in the first step the Boltzmann equation is rendered into an upwind discretized form, ii) in the second step inviscid fluxes are obtained by taking moments of split Maxwellian distribution, iii) in the third step viscous fluxes are obtained by taking moments of split microscopic tensors and subsequent full tensor contraction with its conjugate thermodynamic forces, hence it differs from KFVS extended by Chou and Baganoff [54]. The present method only requires split microscopic tensor and its conjugate thermodynamic forces, for example it can easily be extended for solving species transport problem by splitting the microscopic tensor associated with it. The new kinetic method apart from giving physically correct dissipation also gives the contribution to this dissipation made by the thermodynamic forces associated with shear stress tensor and heat flux vector. The new kinetic theory based scheme has a potential to be a monolithic solver for simulating the entire range from rarefied slip flow to continuum flow, creeping flow to flow with shocks as it is derived using kinetic theory incorporating phenomenological theory of non-equilibrium thermodynamics. The new kinetic scheme was also formulated for axi-symmetric case and in its variance reduced form.

Chapter 5

Development of Kinetic wall boundary conditions

5.1 Introduction

Wall boundary condition is an important part in simulation of fluid flow. Experimental studies as well as theoretical analysis corroborate the efficacy of a given boundary condition. No-slip and slip condition at the wall provide a realistic boundary condition used for the solution of Navier-Stokes equation in the continuum and rarefied regime respectively. Kinetic theory based methods in general have focused more on entropy condition and ignored the crucial aspect of non-equilibrium thermodynamics. Apart from entropy condition boundary condition based on kinetic method should also satisfy the Onsager's reciprocity relationship. The formulation of Maxwell velocity slip and von Smoluchowski temperature jump fail when flow variations tangential to surface are significant. The kinetic theory based formulation which constructs velocity distribution using half range distribution following Onsager's reciprocity relationship is better suited to resolve features associated with slip flow as well as continuum flow. *One of the motivations of the thesis is to derive a unified wall boundary condition which satisfies Onsager's relationship and can simulate both continuum and rarefied slip flow within Navier-Stokes equation in order to avoid extremely costly multi-scale simulation.*

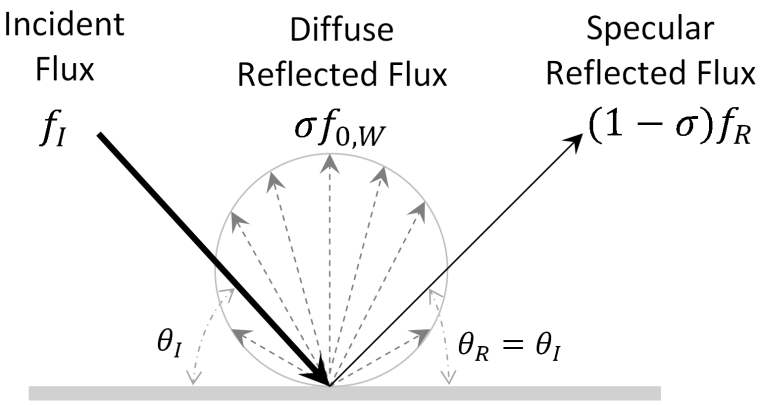

Figure 5.1: Maxwell model based on specular and diffuse reflection.

This chapter gives the derivation of kinetic wall boundary condition using non-equilibrium thermodynamics based distribution and Maxwell model. The first section describes the implementation of Maxwell's model used in the research. Second section carries out the derivation of velocity slip and temperature jump conditions using the non-equilibrium thermodynamics based distribution function for cases with negligible fluid dynamical variations in the tangential direction. Slip boundary conditions are derived using first order distribution based on Chapman-Enskog approach in the present research work. The third section gives the derivation of flux based wall boundary conditions which being more exact remains valid even for strong gradients in the tangential directions. The fourth section gives the treatment for slip flow near the transition regime using Burnett based second order model as well as a new method based on collision probability function.

5.2 Treatment of slip boundary condition using Maxwell model.

In the present approach Maxwell model is used for gas-surface interaction for both continuum as well as slip flow regime. In this model molecules partially undergo specular reflection and the remainder reflect in diffuse manner as shown in figure 5.1 such that the distribution function is a sum of diffuse and specular

reflections. With a accommodation coefficient σ, distribution function can be written as

$$f_{\Sigma}= f_I+(1-\sigma)f_R+\sigma f_{0,W} \tag{5.1}$$

where f_{Σ} is the distribution function which is a sum of f_I incident distribution, f_R specularly reflected distribution and $f_{0,W}$ which is the diffuse reflected Maxwellian distribution evaluated at the wall conditions. For example the specularly reflected distribution, f_R is reconstructed from incident distribution, f_I for 2D geometry as follows

$$f_R(v_x,v_y,\mathbb{I}) = \begin{array}{ll} f_I(v_x,v_y,\mathbb{I}) & for \quad v_y<0 \\ f_I(v_x,-v_y,\mathbb{I}) & for \quad v_y>0 \end{array} \tag{5.2}$$

Similarly, for for 3D geometry the specularly reflected distribution, f_R is reconstructed from incident distribution, f_I as follows

$$f_R(v_x,v_y,v_z,\mathbb{I}) = \begin{array}{ll} f_I(v_x,v_y,v_z,\mathbb{I}) & for \quad v_z<0 \\ f_I(v_x,v_y,-v_z,\mathbb{I}) & for \quad v_z>0 \end{array} \tag{5.3}$$

5.3 Derivation of density jump for negligible tangential gradients.

The conservation of mass at the wall for 2-D geometry can be simplified as

$$\int_{\mathbb{R}^+}\int_{\mathbb{R}^-}\int_{\mathbb{R}} v_y f_I^{\cdot -} dv_x dv_y d\mathbb{I} + \int_{\mathbb{R}^+}\int_{\mathbb{R}^+}\int_{\mathbb{R}} v_y f_{0,W}^{\cdot +} dv_x dv_y d\mathbb{I} = 0 \tag{5.4}$$

where $f_I^{\cdot -}$ is the half-range incident distribution function for $-\infty < v_x < +\infty$ and $-\infty < v_y < 0$ and similarly $f_{0,W}^{\cdot +}$ is the half-range Maxwellian distribution function for $-\infty < v_x < +\infty$ and $0 < v_y < \infty$.

Solving the mass conservation using first order distribution at the boundary $f_{1,I}^{\cdot -}=f_{0,I}^{\cdot -}-\sum_j \boldsymbol{\Upsilon}_{I,j}^{\cdot -} \odot \boldsymbol{X_j}$, the resultant flux due to incident and specular reflection can be simplified as

$$\begin{aligned} &\int_{\mathbb{R}^+}\int_{\mathbb{R}^-}\int_{\mathbb{R}} v_y f_{1,I}^{\cdot -} dv_x dv_y d\mathbb{I} \\ &= \int_{\mathbb{R}^+}\int_{\mathbb{R}^-}\int_{\mathbb{R}} v_y \left(f_{0,I}^{\cdot -} - \sum_j \boldsymbol{\Upsilon}_{I,j}^{\cdot -} \odot \boldsymbol{X_j} \right) dv_x dv_y d\mathbb{I} \\ &= \frac{\rho}{\sqrt{\beta}} \left[\begin{array}{l} \frac{1}{2}\left(\frac{-B_y}{\sqrt{\pi}} + s_y A_y^-\right) - \frac{\tau_{xx}}{4p}\left(\frac{-B_y}{\sqrt{\pi}} + s_y A_y^-\right) + \frac{\tau_{yy}}{2p}\left(\frac{-B_y}{\sqrt{\pi}} - \frac{s_y A_y^-}{2}\right) \\ + \frac{\tau_{xx}+\tau_{yy}}{4p}\left(\frac{-B_y}{\sqrt{\pi}} + s_y A_y^-\right) + q_y \eta \sqrt{\beta} \frac{s_y B_y}{2\sqrt{\pi}} \end{array} \right] \end{aligned} \tag{5.5}$$

where

$$\begin{array}{l} A_y^{\pm} = 1 \pm Erf(s_y) \\ B_y = Exp(-s_y^2) \\ s_y = u_y\sqrt{\beta} \\ \eta = \frac{\gamma-1}{\gamma} \end{array} \tag{5.6}$$

The flux due to diffuse reflection is a contribution of Maxwellian flux based on wall condition, this can be expressed as

$$\begin{array}{l} \int_{\mathbb{R}^+}\int_{\mathbb{R}^+}\int_{\mathbb{R}} v_y f_{0,W}^{\cdot\cdot+}(\rho_w, v_x, v_y, \mathbb{I})dv_x dv_y d\mathbb{I} \\ = \frac{\rho_w}{2\sqrt{\beta_w}}\left[\ \frac{B_{w,y}}{\sqrt{\pi}} + s_{w,y}A_{w,y}^{+}\ \right] \end{array} \tag{5.7}$$

where β_w, $B_{w,y}$, $s_{w,y}$ and $A_{w,y}^{+}$ are evaluated with wall condition as follows

$$\begin{array}{l} A_{w,y}^{+} = 1 + Erf(s_{w,y}) \\ B_{w,y} = Exp(-s_{w,y}^2) \\ s_{w,y} = u_{w,y}\sqrt{\beta_w} \end{array} \tag{5.8}$$

Near the wall $u_y \rightarrow 0$, with this $s_y \rightarrow 0$, $B_y \rightarrow$ and $A_y^{\pm} \rightarrow 1$. For stationary wall $u_{w,y}= 0$, with this $s_{w,y} = 0$, $B_{w,y} = 1$ and $A_{w,y}^{+} = 1$. The conservation of mass at the wall can now be expressed as

$$\frac{\rho}{2\sqrt{\pi}\sqrt{\beta}}\left[-1 + \frac{\tau_{xx}}{2p}\frac{\tau_{yy}}{p} - \frac{\tau_{xx}+\tau_{yy}}{2p}\right] + \frac{\rho_w}{2\sqrt{\pi}\sqrt{\beta_w}} = 0 \tag{5.9}$$

This leads to density jump at the wall as

$$\rho_w = \frac{\rho\sqrt{\beta_w}}{\sqrt{\beta}}\left[1 - \frac{\tau_{yy}}{2p}\right] = \rho\sqrt{\frac{T}{T_w}}\left(1 - \frac{\tau_{yy}}{2p}\right) \tag{5.10}$$

where T_w is the wall temperature.

5.3.1 Derivation of density jump for 3D geometry

The conservation of mass at the wall can be simplified as

$$\int_{\mathbb{R}^+}\int_{\mathbb{R}^-}\int_{\mathbb{R}}\int_{\mathbb{R}} v_z f_I^{\cdot\cdot-} dv_x dv_y dv_z d\mathbb{I} + \int_{\mathbb{R}^+}\int_{\mathbb{R}^+}\int_{\mathbb{R}}\int_{\mathbb{R}} v_z f_{0,W}^{\cdot\cdot+} dv_x dv_y dv_z d\mathbb{I} = 0 \tag{5.11}$$

where $f_I^{\cdot\cdot-}$ is the half-range incident distribution function for $-\infty < v_x < +\infty$, $-\infty < v_y < +\infty$ and $-\infty < v_z < 0$. The distribution $f_{0,W}^{\cdot\cdot+}$ is the half-range

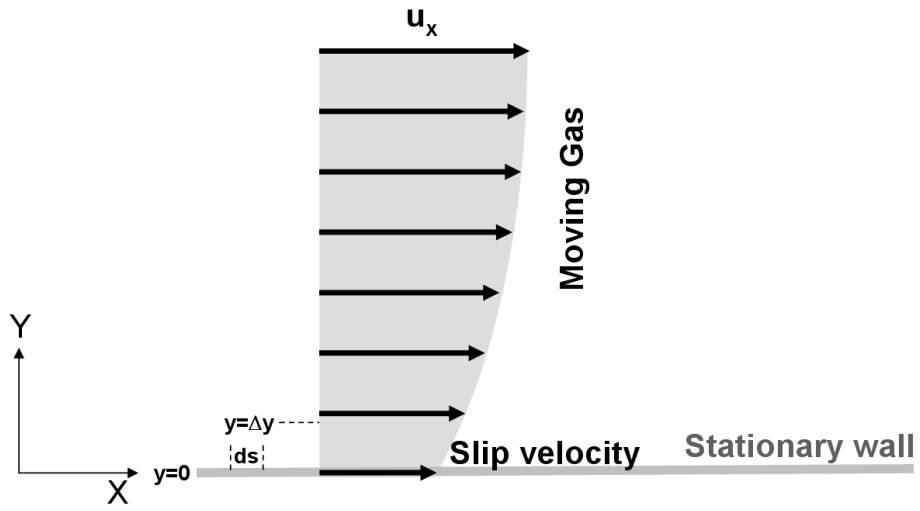

Figure 5.2: Shearing stress on infinitesimal area on the wall

Maxwellian distribution function for $-\infty < v_x < +\infty$, $-\infty < v_y < +\infty$ and $0 < v_z < \infty$.

This leads to density jump at the wall as

$$\rho_w = \frac{\rho\sqrt{\beta_w}}{\sqrt{\beta}}\left[1 - \frac{\tau_{zz}}{2p}\right] = \rho\sqrt{\frac{T}{T_w}}\left(1 - \frac{\tau_{zz}}{2p}\right) \tag{5.12}$$

where T_w is the wall temperature.

5.4 Derivation of slip velocity and temperature jump for negligible tangential gradients.

The expression of Maxwell velocity slip and von Smoluchowski's temperature jump available in the literature are derived under conditions of negligible fluid dynamical variations in the tangential directions. This section revisits the derivation of Maxwell velocity slip and von Smoluchowski temperature jump using the non-equilibrium thermodynamics based distribution function.

5.4.1 Derivation of slip velocity

Let us consider an infinitesimal area ds on the surface of the wall and an elementary strip of gas extending above the wall in the y-direction from the elementary

area ds as shown in Fig.5.2. The strip reaches the imaginary plane set at $y = \Delta y$ and the momentum flux, $\mathbb{M}$ passing through it based on linearized distribution f_1 is given as

$$\mathbb{M}_{y=\Delta y}= \int_{\mathbb{R}^+}\int_{\mathbb{R}}\int_{\mathbb{R}}(f_0 - \sum_j \boldsymbol{\Upsilon}_j \odot \boldsymbol{X}_j)v_x v_y dv_x dv_y d\mathbb{I}= \rho u_x u_y - \tau_{xy} \tag{5.13}$$

The contributing momentum component at the wall where y=0 is expressed as

$$\mathbb{M}_{y=0}ds \;\; = \sigma \left[\begin{array}{l} \int_{\mathbb{R}^+}\int_{\mathbb{R}^-}\int_{\mathbb{R}}(f^{\cdot -}_{0,I} - \sum_j \boldsymbol{\Upsilon}^{\cdot -}_{I,j} \odot \boldsymbol{X}_j)v_x v_y dv_x dv_y d\mathbb{I} \\ +\int_{\mathbb{R}^+}\int_{\mathbb{R}^+}\int_{\mathbb{R}} f^{\cdot +}_{0,W} v_x v_y dv_x dv_y d\mathbb{I} \end{array} \right] \tag{5.14}$$

where $\boldsymbol{\Upsilon}^{\cdot -}_{I,j}$ is evaluated for $-\infty < v_x < +\infty$ and $-\infty < v_y < 0$ corresponding to incident distribution. The momentum flux on the infinitesimal surface ds at the wall $y = 0$ can be equated with the momentum flux on the infinitesimal surface ds as $\Delta y \to 0$.
With the definition, tensor of viscous stresses $\boldsymbol{\Pi}=\mu\left[(\nabla \otimes \vec{u}) + (\nabla \otimes \vec{u})^T - \frac{2}{3}\boldsymbol{I}\nabla \cdot \vec{u}\right] + \zeta \boldsymbol{I}\nabla\cdot\vec{u}$ where coefficient of bulk viscosity $\zeta = \mu\left(\frac{5}{3} - \gamma\right)$, heat flux vector $\vec{q}=-\kappa\nabla T$ the conservation of momentum flux becomes

$$-\tau_{xy} = \sigma\left[-\frac{\rho}{4\beta p\sqrt{\pi}}\left(\sqrt{\pi}\tau_{xy} + \sqrt{\beta}(\eta q_x - \tau_{yy}u_x)\right) - \frac{1}{2\sqrt{\pi}}\left(\rho u_x - \rho_w u_{w,x}\right)\right] \tag{5.15}$$

where $u_{w,x}$ is the x component of the wall velocity and $\eta = (\gamma - 1)/\gamma$. After substituting the viscosity based mean free path, $\lambda=\frac{\mu}{2p}\sqrt{\frac{\pi}{\beta}}$, the slip velocity u_x for stationary wall condition can be expressed as

$$\begin{aligned} u_x &= \left[\left(\frac{2-\sigma}{\sigma}\right)\frac{\tau_{xy}}{2p}\frac{\sqrt{\pi}}{\beta} - \frac{q_x\eta}{2p}\right]\phi \\ &= \left[\left(\frac{2-\sigma}{\sigma}\right)\tau_{xy}\frac{\lambda}{\mu} - \left(\frac{\gamma-1}{\gamma}\right)\frac{q_x}{2p}\right]\phi \end{aligned} \tag{5.16}$$

We get the new expression of velocity slip which is named in this research work as Onsager-Maxwell slip velocity, it differs from Maxwell's expression [163] by an extra term $\phi = (1 - \tau_{yy}/2p)^{-1}$ due to density jump.

5.4.1.1 Expressions of velocity slip for 3D geometry

For three dimensional case there are two slip velocities u_x and u_y if the surface normal points towards z direction. For stationary surface the two slip velocities are derived as

$$u_x = \left[\left(\frac{2-\sigma}{\sigma}\right)\tau_{xz}\frac{\lambda}{\mu} - \left(\frac{\gamma-1}{\gamma}\right)\frac{q_x}{2p}\right]\left(1-\frac{\tau_{zz}}{2p}\right)^{-1} \tag{5.17}$$

$$u_y = \left[\left(\frac{2-\sigma}{\sigma}\right)\tau_{yz}\frac{\lambda}{\mu} - \left(\frac{\gamma-1}{\gamma}\right)\frac{q_y}{2p}\right]\left(1-\frac{\tau_{zz}}{2p}\right)^{-1} \tag{5.18}$$

5.4.2 Derivation of temperature jump

Similarly, we can carry out energy conservation by equating the energy flux on the strip ds at $y = \Delta y$ and $y = 0$ as shown in Fig.5.2. The energy flux, $\mathbb{Q}$ at $y = \Delta y$ based on linearized distribution is given as

$$\mathbb{Q}_{y=\Delta y} = \int_{\mathbb{R}^+}\int_{\mathbb{R}}\int_{\mathbb{R}}(f_0 - \textstyle\sum_j \boldsymbol{\Upsilon}_j \odot \boldsymbol{X}_j)(\mathbb{I}+\frac{v^2}{2})v_y dv_x dv_y d\mathbb{I} \tag{5.19}$$

This gets simplified as

$$\mathbb{Q}_{y=\Delta y} = \frac{\rho}{2p\beta}\left[\ q_y - u_x\tau_{xy} + u_y(-\tau_{yy} + \beta p u_x^2 + \beta p u_y^2 + \tfrac{p\gamma}{\gamma-1})\ \right] \tag{5.20}$$

The energy flux at the wall where $y = 0$ can be expressed as

$$\mathbb{Q}_{y=0} = \sigma\left[\begin{array}{l}\displaystyle\int_{\mathbb{R}^+}\int_{\mathbb{R}_-}\int_{\mathbb{R}}(\dot{f}^-_{0,I} - \textstyle\sum_j \dot{\boldsymbol{\Upsilon}}^-_{I,j} \odot \boldsymbol{X}_j)(\mathbb{I}+\frac{v^2}{2})v_y dv_x dv_y d\mathbb{I} \\ \displaystyle+\int_{\mathbb{R}^+}\int_{\mathbb{R}_+}\int_{\mathbb{R}}\dot{f}^+_{0,W}(\mathbb{I}+\frac{v^2}{2})v_y dv_x dv_y d\mathbb{I}\end{array}\right] \tag{5.21}$$

After substituting the value of slip velocity u_x and wall density ρ_w this expression simplifies as

$$\begin{aligned}\mathbb{Q}_{y=0} &= \frac{\rho(\gamma+1)(2p^2 - 3p\tau_{yy} - \tau_{yy}^2)\sigma}{\beta_w \mathcal{B}} \\ &+\frac{\rho}{2\beta\mathcal{B}\sigma}\left[\begin{array}{l}-8(\gamma-1)\pi\tau_{xy}^2 \\ +\sigma^2\left(\begin{array}{l}-4(\gamma+1)p^2 + 2(\gamma-1)(\sqrt{\beta}\eta q_x + \sqrt{\pi}\tau_{xy})^2 \\ -4\sqrt{\beta}\eta\gamma\sqrt{\pi}q_y\tau_{yy} + \tau_{yy}^2 - 3\gamma\tau_{yy}^2 \\ +8\gamma p(\sqrt{\beta}\eta\sqrt{\pi}q_y + \tau_{yy})\end{array}\right)\end{array}\right]\end{aligned} \tag{5.22}$$

where $\mathcal{B} = 8\sqrt{\beta}(\gamma-1)p\sqrt{\pi}(2p-\tau_{yy})$. The energy flux at the wall, $y=0$ is being balanced by the energy flux as $\Delta y \to 0$. The conservation leads to

$$\frac{\rho}{2\beta\beta_w\mathcal{B}}\left[\begin{array}{l} 2\beta(\gamma+1)(2p^2-3p\tau_{yy}+\tau_{yy}^2)\sigma^2 \\ +\beta_w\left(\begin{array}{l} 2(\gamma-1)\pi\tau_{xy}^2(\sigma-2)^2 \\ +4\sqrt{\beta}\eta\sqrt{\pi}(-q_x\tau_{xy}+\gamma(2pq_y+q_x\tau_{xy}-q_y\tau_{yy}))\sigma(\sigma-2) \\ +(4(\gamma+1)p^2+2\beta\eta^2(\gamma-1)q_x^2+8\gamma p\tau_{yy}-(3\gamma-1)\tau_{yy}^2)\sigma^2 \end{array}\right) \end{array}\right] = 0 \tag{5.23}$$

For small temperature jump we can replace pressure in terms of mean free path, λ using relation $p = \mu\sqrt{\pi}/(2\lambda\sqrt{\beta})$. In this case we get balance equations for 2D geometry case in β as follows

$$\left[\begin{array}{l} 2\beta^2(\beta_w\eta^2(\gamma-1)q_x^2+(\gamma+1)\tau_{yy}^2)\lambda^2\sigma^2 \\ +4\sqrt{\beta}\beta_w\gamma\sqrt{\pi}\tau_{yy}\lambda\mu\sigma^2-\beta_w(\gamma+1)\pi\mu^2\sigma^2 \\ +\beta\sqrt{\beta}\sqrt{\pi}\lambda\sigma(4\beta_w\eta((\gamma-1)q_x\tau_{xy}-\gamma q_y\tau_{yy})\lambda(\sigma-2) \\ -3(\gamma+1)\tau_{yy}\mu\sigma)+\beta(\gamma+1)\pi\mu^2\sigma^2 \\ +\beta\beta_w\lambda\left(\begin{array}{l} -(3\gamma-1)\tau_{yy}^2\lambda\sigma^2 \\ +2\pi(\sigma-2)((\gamma-1)\tau_{xy}^2\lambda(\sigma-2)+2\eta\gamma q_y\mu\sigma) \end{array}\right) \end{array}\right] = 0 \tag{5.24}$$

This expression can be further simplified by neglecting terms associated with τ_{yy} and q_x to get

$$(\beta-\beta_w)(\gamma+1)\pi\mu^2\sigma^2+\beta_w(2\beta_w\pi\lambda(\sigma-2)((\gamma-1)\tau_{xy}^2\lambda(\sigma-2)+2\eta\gamma q_y\mu\sigma)) = 0 \tag{5.25}$$

After solving for β we get

$$\beta = \frac{\beta_w(\gamma+1)\mu^2\sigma^2}{(\gamma+1)\mu^2\sigma^2+2\beta_w\lambda(\sigma-2)((\gamma-1)\tau_{xy}^2\lambda(\sigma-2)+2\eta\gamma q_y\mu\sigma)} \tag{5.26}$$

After substituting the following expressions for β, β_w given as

$$\beta = \frac{1}{2RT} = \frac{\gamma}{2T(\gamma-1)c_p} \tag{5.27}$$

$$\beta_w = \frac{1}{2RT_w} = \frac{\gamma}{2T_w(\gamma-1)c_p} \tag{5.28}$$

The solution leads to

$$T = T_w + \left(\frac{2-\sigma}{\sigma}\right)^2\frac{\gamma\lambda^2\tau_{xy}^2}{c_p(\gamma+1)\mu^2} - \left(\frac{2-\sigma}{\sigma}\right)\frac{2\gamma\lambda q_y}{c_p(\gamma+1)\mu} \tag{5.29}$$

We get a new expression of temperature jump which is named in this research work as Onsager-von Smoluchowski's temperature jump as it contains both the

terms of heat flux vector and shear stress tensor following Onsager's reciprocity relationship. With an additional assumption that shear stress term τ_{xy} is negligible we get the von Smoluchowski's temperature jump boundary condition in terms of Prandtl number Pr as

$$T = T_w - \left(\frac{2-\sigma}{\sigma}\right)\frac{2\gamma\lambda q_y}{c_p(1+\gamma)\mu} = T_w + \frac{(2-\sigma)}{\sigma}\frac{2}{\mathrm{Pr}}\frac{\gamma}{(\gamma+1)}\lambda\frac{\partial T}{\partial y} \tag{5.30}$$

This condition is obtained with an assumption that tangential variations, terms q_x, τ_{yy} and τ_{xy} are negligible and temperature jump is mild.
For large temperature jump the mean free path may vary significantly, in such cases the compressibility effect is accounted by using ideal gas law where pressure depends on density as $p = \rho/2\beta$. The energy balance equation for such a case becomes

$$\begin{aligned}
&4\beta^{5/2}\beta_w\eta\sqrt{\pi}((\gamma-1)q_x\tau_{xy} - \gamma q_y\tau_{yy})(\sigma-2)\sigma \\
&+(\beta-\beta_w)(1+\gamma)\rho^2\sigma^2 + 2\beta^3(\beta_w\eta^2(\gamma-1)q_x^2 + (\gamma+1)\tau_{yy}^2)\sigma^2 \\
&+\beta\rho\sigma(4\sqrt{\beta}\beta_w\eta\gamma\sqrt{\pi}q_y(\sigma-2) + 4\beta_w\gamma\tau_{yy}\sigma - 3\beta(\gamma+1)\tau_{yy}\sigma) \\
&+\beta^2\beta_w(2-(\gamma-1)\pi\tau_{xy}^2(\sigma-2)^2 + (1-3\gamma)\tau_{yy}^2\sigma^2) = 0
\end{aligned} \tag{5.31}$$

The energy balance equation for such a case can be solved when τ_{yy}, q_x and τ_{xy} is negligible to get temperature jump for compressible flow as

$$T = \frac{3\beta_w^2\gamma\mathcal{S}^2\vartheta}{c_p(\gamma-1)(2^{1/3}(2-12\beta_w^3\mathcal{S}^2+2^{1/3}\vartheta^2)+2\vartheta)} \tag{5.32}$$

where

$$\mathcal{S} = -\left(\frac{2-\sigma}{\sigma}\right)\frac{4(\gamma-1)\sqrt{\pi}}{\rho(\gamma+1)}q_y \tag{5.33}$$

$$\vartheta = \left(2 - 18\beta_w^3\mathcal{S}^2 + 27\beta_w^6\mathcal{S}^4 + 3\beta_w^4\mathcal{S}^3\sqrt{81\beta_w^4\mathcal{S}^2 - 12\beta_w}\right)^{1/3} \tag{5.34}$$

It is should be noted that these expressions are valid only in slip flow regime when there are insignificant fluid dynamic variations in the tangential direction.

5.4.2.1 Expressions of temperature jump for 3D geometry

For 3D case after substituting the slip velocity u_x and u_y the balance equations are

$$\frac{\rho}{2\beta\beta_w\mathcal{B}}\left[\begin{array}{l}\beta(\gamma+1)(2p-\tau_{zz})^2\sigma^2\\ +\beta_w\left(\begin{array}{l}2(\gamma-1)\pi(\tau_{xz}^2+\tau_{yz}^2)(\sigma-2)^2\\ +4\sqrt{\beta}\eta\sqrt{\pi}\left(\begin{array}{l}-q_x\tau_{xz}-q_y\tau_{yz}\\ +\gamma(2pq_z+q_x\tau_{xz}+q_y\tau_{yz}-q_z\tau_{zz})\end{array}\right)\sigma(\sigma-2)\\ +\left(\begin{array}{ll}4(\gamma+1)p^2+2\beta\eta^2(\gamma-1)(q_x^2+q_y^2) & l\\ +8\gamma p\tau_{zz}-(3\gamma-1)\tau_{zz}^2 & \end{array}\right)\sigma^2\end{array}\right)\end{array}\right]=0 \tag{5.35}$$

where $\mathcal{B}=8\sqrt{\beta}(\gamma-1)p\sqrt{\pi}(2p-\tau_{zz})$.
As described before for small temperature jump we can replace pressure in terms of mean free path, λ using relation $p=\mu\sqrt{\pi}/(2\lambda\sqrt{\beta})$. In this case we get balance equations for 3D case in terms of β as follows

$$\left[\begin{array}{l}2\beta^2(\beta_w\eta^2(\gamma-1)(q_x^2+q_y^2)+(\gamma+1)\tau_{zz}^2)\lambda^2\sigma^2\\ +4\sqrt{\beta}\beta_w\gamma\sqrt{\pi}\tau_{zz}\lambda\mu\sigma^2-\beta_w(\gamma+1)\pi\mu^2\sigma^2\\ +\beta\sqrt{\beta}\sqrt{\pi}\lambda\sigma_T\left(\begin{array}{l}4\beta_w\eta((\gamma-1)(q_x\tau_{xz}+q_y\tau_{yz})\\ -\gamma q_z\tau_{zz})\lambda(\sigma-2)-(\gamma+1)\tau_{zz}\mu\sigma\end{array}\right)\\ +\beta(\gamma+1)\pi\mu^2\sigma^2\\ +\beta\beta_w\lambda\left(\begin{array}{l}-(3\gamma-1)\tau_{zz}^2\lambda\sigma^2\\ +2\pi(\sigma-2)\left(\begin{array}{l}(\gamma-1)\tau_{xz}^2\lambda(\sigma-2)\\ +(\gamma-1)\tau_{yz}^2\lambda(\sigma-2)\\ +2\eta\gamma q_z\mu\sigma\end{array}\right)\end{array}\right)\end{array}\right]=0 \tag{5.36}$$

This expression can be further simplified by neglecting terms associated with τ_{zz}, q_x and q_y to get

$$(\beta-\beta_w)(\gamma+1)\pi\mu^2\sigma^2+\beta_w(2\beta_w\pi\lambda(\sigma-2)((\gamma-1)(\tau_{xz}^2+\tau_{yz}^2)\lambda(\sigma-2)+2\eta\gamma q_z\mu\sigma))=0 \tag{5.37}$$

After solving for β we get

$$\beta=\frac{\beta_w(\gamma+1)\mu^2\sigma^2}{(\gamma+1)\mu^2\sigma^2+2\beta_w\lambda(\sigma-2)((\gamma-1)(\tau_{xz}^2+\tau_{yz}^2)\lambda(\sigma-2)+2\eta\gamma q_z\mu\sigma)} \tag{5.38}$$

substituting the following expressions for β, β_w the solution leads to

$$T=T_w+\left(\frac{2-\sigma}{\sigma}\right)^2\frac{\gamma\lambda^2(\tau_{xz}^2+\tau_{yz}^2)}{c_p(\gamma+1)\mu^2}-\left(\frac{2-\sigma}{\sigma}\right)\frac{2\gamma\lambda q_z}{c_p(\gamma+1)\mu} \tag{5.39}$$

We get the expression of Onsager-von Smoluchowski's temperature jump for 3D geometry. With an additional assumption that shear stress terms τ_{xz} and τ_{yz} are negligible we get the von Smoluchowski's temperature jump boundary condition in terms of Prandtl number Pr as

$$T = T_w - \left(\frac{2-\sigma}{\sigma}\right)\frac{2\gamma\lambda q_z}{c_p(1+\gamma)\mu} = T_w + \frac{(2-\sigma)}{\sigma}\frac{2}{\mathrm{Pr}}\frac{\gamma}{(\gamma+1)}\lambda\frac{\partial T}{\partial z} \tag{5.40}$$

This condition is obtained with an assumption that tangential variations, terms q_x, q_y, τ_{zz}, τ_{xz} and τ_{yz} are negligible and temperature jump is mild.
For large temperature jump the compressibility effect is accounted by using ideal gas law where pressure depends on density as $p = \rho/2\beta$. The energy balance equation for such a case becomes

$$\begin{aligned}
&4\beta^{5/2}\beta_w\eta\sqrt{\pi}((\gamma-1)(q_x\tau_{xz}+q_y\tau_{yz})-\gamma q_z\tau_{zz})(\sigma-2)\sigma\\
&+(\beta-\beta_w)(1+\gamma)\rho^2\sigma^2+2\beta^3(\beta_w\eta^2(\gamma-1)(q_x^2+q_y^2)+(\gamma+1)\tau_{zz}^2)\sigma^2\\
&+\beta\rho\sigma(4\sqrt{\beta}\beta_w\eta\gamma\sqrt{\pi}q_z(\sigma-2)+4\beta_w\gamma\tau_{zz}\sigma-2\beta(\gamma+1)\tau_{zz}\sigma)\\
&+\beta^2\beta_w(2(\gamma-1)\pi(\tau_{xz}^2+\tau_{yz}^2)(\sigma-2)^2+(1-3\gamma)\tau_{zz}^2\sigma^2)=0
\end{aligned} \tag{5.41}$$

The energy balance equation for such a case can be solved when τ_{zz}, τ_{xz}, τ_{yz}, q_x and q_y are negligible to get temperature jump for compressible flow similar to 2D case as

$$T = \frac{3\beta_w^2\gamma\mathcal{S}^2\vartheta}{c_p(\gamma-1)(2^{1/3}(2-12\beta_w^3\mathcal{S}^2+2^{1/3}\vartheta^2)+2\vartheta)} \tag{5.42}$$

where

$$\mathcal{S} = -\left(\frac{2-\sigma}{\sigma}\right)\frac{4(\gamma-1)\sqrt{\pi}}{\rho(\gamma+1)}q_z \tag{5.43}$$

$$\vartheta = \left(2-18\beta_w^3\mathcal{S}^2+27\beta_w^6\mathcal{S}^4+3\beta_w^4\mathcal{S}^3\sqrt{81\beta_w^4\mathcal{S}^2-12\beta_w}\right)^{1/3} \tag{5.44}$$

It is should be noted that these expressions are valid only in slip flow regime when there are insignificant fluid dynamic variations in the tangential direction.

5.5 Kinetic upwind based wall boundary condition

The approach of continuum solver coupled with Maxwell's velocity slip boundary condition [184] and von Smoluchowski's temperature jump boundary condition

[139] is the most popular as it is computationally the least expensive. Most of the applications slip are simple micro-channel flows. It is should be noted that these expressions are valid only in slip flow regime when there are insignificant fluid dynamic variations in the tangential direction. Literature review has already revealed that the first order slip velocity not only depends on the velocity gradient in the normal direction but also on the pressure gradient in the tangential flow direction. Thus we require an approach which is computationally cheap and takes the slip velocity dependence on the fluid dynamic variations in the tangential direction. Using the Maxwell model for gas-surface interaction and accounting the kinetic split fluxes in the tangential direction a more accurate estimate of slip velocity and temperature jump can be made. As described earlier net first order distribution function at time $t + \Delta t$ in terms of accommodation coefficient σ can be written as

$$\begin{aligned} f_{1,\Sigma}(\vec{v}, \mathbb{I}, t + \Delta t) \quad &= f_{1,I}(\vec{v}, \mathbb{I}, t + \Delta t) \\ &+(1 - \sigma) f_{1,R}(\vec{v}, \mathbb{I}, t + \Delta t) + \sigma f_{0,W}(\vec{v}, \mathbb{I}, t + \Delta t) \end{aligned} \tag{5.45}$$

where $f_{1,\Sigma}(\vec{v}, \mathbb{I}, t + \Delta t)$ is the total distribution resulting due to Maxwell model, $f_{1,I}(\vec{v}, \mathbb{I}, t + \Delta t)$ and $f_{1,R}(\vec{v}, \mathbb{I}, t + \Delta t)$ are the incident and specularly reflected first order distribution respectively and $f_{0,W}(\vec{v}, \mathbb{I}, t + \Delta t)$ is the diffuse reflected Maxwellian distribution evaluated using wall conditions. The specularly reflected first order distribution $f_{1,R}(\vec{v}, \mathbb{I}, t + \Delta t)$ is written as

$$f_R(\vec{v}, \mathbb{I}, t + \Delta t) = \begin{array}{ll} f_I(\vec{v}, \mathbb{I}, t + \Delta t) & for \quad \vec{i_n} \cdot \vec{v} < 0 \\ f_I(\vec{v} - 2\vec{i_n}\vec{i_n} \cdot \vec{v}, \mathbb{I}, t + \Delta t) & for \quad \vec{i_n} \cdot \vec{v} > 0 \end{array} \tag{5.46}$$

molecules are reflected away from the boundary ($\vec{i_n} \cdot \vec{v} > 0$) where $\vec{i_n}$ is the surface normal. The specular reflected distribution is constructed using $\vec{v} - 2\vec{i_n}\vec{i_n} \cdot \vec{v}$ i.e. with reverse sign of normal component of velocity.

The total distribution satisfies Boltzmann equation and hence at time $t + \Delta t$ it is constructed as follows

$$f_{1,\Sigma}(\vec{v}, \mathbb{I}, t + \Delta t) = f_{1,\Sigma}(\vec{v}, \mathbb{I}, t) - \Delta t \nabla_{\vec{x}} \cdot (\vec{v} f_{1,\Sigma}(\vec{v}, \mathbb{I}, t)) \tag{5.47}$$

5.5.1 Wall boundary condition for 2-D case

After upwind discretization for the two dimensional case the distribution at time $t + \Delta t$ at the boundary simplifies as

$$f_{1,\Sigma}(t + \Delta t) = f_{1,\Sigma}(t) - \Delta t \left[\frac{\partial v_x f_{1,\Sigma}^{+-}(t)}{\partial x} + \frac{\partial v_x f_{1,\Sigma}^{--}(t)}{\partial x} + \frac{\partial v_y f_{1,\Sigma}^{\cdot -}(t)}{\partial y} \right] \tag{5.48}$$

where f_1^{+-} is the half-range total distribution function for $0 < v_x < \infty$ and $-\infty < v_y < 0$ and f_1^{--} is the half-range total distribution function for $-\infty < v_x < 0$ and $-\infty < v_y < 0$. After taking $\boldsymbol{\Psi}$ moment we can obtain state update equation expressed as

$$\boldsymbol{U}(t + \Delta t) = \boldsymbol{U}(t) - \Delta t \left[\begin{array}{l} \left(\frac{\partial \widehat{\boldsymbol{GX}}^{+-}(t)}{\partial x} \right)_{\Delta x<0} + \left(\frac{\partial \widehat{\boldsymbol{GX}}^{--}(t)}{\partial x} \right)_{\Delta x>0} \\ + \left(\frac{\partial \widehat{\boldsymbol{GY}}^{\cdot -}(t)}{\partial y} \right)_{\Delta y>0} \end{array} \right] \tag{5.49}$$

where $\boldsymbol{U}$=$[\rho, \rho\boldsymbol{u}, \rho E]^T$ is the state vector and Δt is the time step.
The y component of state vector is not updated as $U_{i=3}$=ρu_y= 0. $\widehat{\boldsymbol{GX}}^{\pm -}$ represents the flux based on half range distributions $f_{1,\Sigma}^{\pm -}$. $\widehat{\boldsymbol{GY}}^{\cdot -}$ is the flux resulting from half range distribution $f_{1,\Sigma}^{\cdot -}$. Derivatives of $\widehat{\boldsymbol{GX}}^{+-}$, $\widehat{\boldsymbol{GX}}^{--}$ and $\widehat{\boldsymbol{GY}}^{\cdot -}$ are evaluated using mesh points on the left, right and upward side. The mass, momentum and energy components of x-directional flux $\widehat{\boldsymbol{GX}}^{\pm -}$ can be written as sum of inviscid or Euler part $\widehat{\boldsymbol{GX}}_I^{\pm -}$ and viscous part $\widehat{\boldsymbol{GX}}_V^{\pm -}$ as follows

$$\widehat{\boldsymbol{GX}}^{\pm -} = \widehat{\boldsymbol{GX}}_I^{\pm -} + \widehat{\boldsymbol{GX}}_V^{\pm -} = \left\langle v_x \boldsymbol{\Psi} f_{0,\Sigma}^{\pm -} \right\rangle - \textstyle\sum_j \boldsymbol{\Lambda}_j^{\pm -} \odot \boldsymbol{X}_j \tag{5.50}$$

Similarly, components of y-directional flux $\widehat{\boldsymbol{GY}}^{\cdot -}$ can be written as sum of inviscid part and viscous part as follows

$$\widehat{\boldsymbol{GY}}^{\cdot -} = \widehat{\boldsymbol{GY}}_I^{\cdot -} + \widehat{\boldsymbol{GY}}_V^{\cdot -} = \left\langle v_y \boldsymbol{\Psi} f_{0,\Sigma}^{\cdot -} \right\rangle - \textstyle\sum_j \boldsymbol{\Lambda}_j^{\cdot -} \odot \boldsymbol{X}_j \tag{5.51}$$

The viscous fluxes are obtained using macroscopic tensors $\boldsymbol{\Lambda}_j^{\pm -}$ and $\boldsymbol{\Lambda}_j^{\cdot -}$ associated with shear stress tensor and heat flux vector following Onsager's reciprocal relationship so as to maximize the entropy production. The fluxes $\widehat{\boldsymbol{GX}}^{\pm -}$ and $\widehat{\boldsymbol{GY}}^{\cdot -}$ can also be written in alternative form as

$$\begin{array}{l} \widehat{\boldsymbol{GX}}^{\pm -} = (2 - \sigma)(\boldsymbol{GX}_I^{\pm -} + \boldsymbol{GX}_V^{\pm -}) + \sigma \boldsymbol{GX}_I^{\pm -}(\rho, u_{w,x}, T_w) \\ \widehat{\boldsymbol{GY}}^{\cdot -} = (2 - \sigma)(\boldsymbol{GY}_I^{\cdot -} + \boldsymbol{GY}_V^{\cdot -}) + \sigma \boldsymbol{GY}_I^{\cdot -}(\rho, u_{w,x}, T_w) \end{array} \tag{5.52}$$

where $\boldsymbol{GX}_I^{\pm-}$, $\boldsymbol{GX}_V^{\pm-}$, $\boldsymbol{GY}_I^{-}$ and $\boldsymbol{GY}_V^{-}$ are evaluated based on fluid conditions while $\boldsymbol{GX}_I^{\pm-}(\rho, u_{w,x}, T_w)$ and $\boldsymbol{GY}_I^{-}(\rho, u_{w,x}, T_w)$ are the inviscid flux based on Maxwellian distribution which are evaluated using fluid density ρ, wall temperature T_w and wall velocity $\boldsymbol{u}_w \equiv (u_{w,x}, 0)$.

The expressions for $\boldsymbol{GX_I^{\pm-}}$, $\boldsymbol{GX_V^{\pm-}}$, $\boldsymbol{GY_I^{-}}$ and $\boldsymbol{GY_V^{-}}$ fluxes are given below

$$GX_{I,1}^{\pm-} = \frac{\rho}{4\sqrt{\beta}} A_2^- \left(\frac{B_1^\pm}{\sqrt{\pi}} + \sqrt{\beta} u_x A_1^\pm \right)$$

$$GX_{V,1}^{\pm-} = \frac{\rho}{8p\sqrt{\beta}} \begin{pmatrix} \frac{B_1^\pm}{\sqrt{\pi}} \begin{pmatrix} 2\sqrt{\beta}\frac{B_2^-}{\sqrt{\pi}} u_y (2\beta\eta q_y u_y + \tau_{yy}) \\ -(2\beta\eta q_x u_x + \tau_{xx}) A_2^- \end{pmatrix} \\ -2\frac{B_2^-}{\sqrt{\pi}} \begin{pmatrix} \beta\eta q_y u_x (1 - 2\beta u_y^2) + \tau_{xy} \\ +\beta u_y (\eta q_x - u_x \tau_{yy}) \end{pmatrix} A_1^\pm \end{pmatrix}$$

$$GX_{I,2}^{\pm-} = \frac{\rho}{8\beta} A_2^- \left(\frac{B_1^\pm}{\sqrt{\pi}} 2\sqrt{\beta} u_x + (1 + 2\beta u_x^2) A_1^\pm \right)$$

$$GX_{V,2}^{\pm-} = \frac{\rho}{8p\beta} \begin{pmatrix} 2\frac{B_1^\pm}{\sqrt{\pi}} \begin{pmatrix} -\frac{B_2^-}{\sqrt{\pi}} (\beta\eta q_y u_x (1 - 2\beta u_y^2) + 2\tau_{xy} + \beta u_y (2\eta q_x - u_x \tau_{yy})) \\ +\sqrt{\beta}\eta q_x A_2^- \end{pmatrix} \\ + \begin{pmatrix} \sqrt{\beta}\frac{B_2^-}{\sqrt{\pi}} \begin{pmatrix} \eta q_y (1 + 2\beta(u_y^2 + u_x^2(-1 + 2\beta u_y^2))) \\ -4u_x(\beta\eta q_x u_y + \tau_{xy}) + (1 + 2\beta u_x^2) u_y \tau_{yy} \end{pmatrix} \\ -\tau_{xx} A_2^- \end{pmatrix} A_1^\pm \end{pmatrix}$$

$$GX_{I,4}^{\pm-} = \frac{\rho}{16\beta^{3/2}} \begin{pmatrix} \frac{B_1^\pm}{\sqrt{\pi}} \left(-\frac{2\sqrt{\beta} B_2^- u_y}{\sqrt{\pi}} + \frac{(1+\bar{u}^2+\gamma) A_2^-}{\gamma - 1} \right) \\ + \left(-\frac{2\beta B_2^- u_x u_y}{\sqrt{\pi}} + \frac{\sqrt{\beta}(\bar{u}^2 + 2\gamma) u_x A_2^-}{\gamma - 1} \right) A_1^\pm \end{pmatrix}$$

$$GX_{V,4}^{\pm-} = \frac{\rho}{32p\beta^{3/2}} \begin{pmatrix} \frac{B_1^\pm}{\sqrt{\pi}} \begin{pmatrix} -2\sqrt{\beta}\frac{B_2^-}{\sqrt{\pi}} \begin{pmatrix} \frac{q_y(-4\gamma + \bar{u}_x^2 + 2\beta(-2 - \bar{u}_x^2) u_y^2)}{\gamma} \\ +(u_y(8\beta\eta q_x u_x + \tau_{xx}) + 6u_x \tau_{xy}) \\ -\frac{(2+\bar{u}_x^2) u_y \tau_{yy}}{\gamma - 1} \end{pmatrix} \\ + \begin{pmatrix} 4\beta\eta q_y u_y + \frac{2\beta q_x u_x (-3 + \gamma - \bar{u}_y^2)}{\gamma} \\ +\frac{(1 - 3\gamma - \bar{u}_y^2)\tau_{xx}}{\gamma - 1} \end{pmatrix} A_2^- \end{pmatrix} \\ +2 \begin{pmatrix} \frac{B_2^-}{\sqrt{\pi}} \begin{pmatrix} -\frac{\beta q_x (1 + \gamma + 3\bar{u}_x^2) u_y}{\gamma} \\ +\frac{\beta q_y u_x (-1 + 3\gamma - \bar{u}_x^2 + (2\beta(1+\gamma) + 2\beta\bar{u}_x^2) u_y^2)}{\gamma} \\ +\frac{(1 - 3\gamma - 3\bar{u}_x^2)\tau_{xy} + \beta u_x (1 + \gamma + \bar{u}_x^2) u_y \tau_{yy}}{\gamma - 1} \end{pmatrix} \\ +2\sqrt{\beta}(q_x - (u_x \tau_{xx} + u_y \tau_{xy})) A_2^- \end{pmatrix} A_1^\pm \end{pmatrix}$$

$$GY_{I,1}^{-} = \frac{\rho}{2\sqrt{\beta}} \left(\frac{B_2^-}{\sqrt{\pi}} + \sqrt{\beta} u_y A_2^- \right)$$

$$GY_{V,1}^{-} = -\frac{\rho}{4p\sqrt{\beta}} \frac{B_2^-}{\sqrt{\pi}} (2\beta\eta q_y u_y + \tau_{yy})$$

$$GY_{I,2}^{-} = \frac{\rho}{2\sqrt{\beta}} u_x \left(\frac{B_2^-}{\sqrt{\pi}} + \sqrt{\beta} u_y A_2^- \right)$$

$$GY_{V,2}^{-} = \frac{\rho}{4p\beta} \left(\sqrt{\beta} \frac{B_2^-}{\sqrt{\pi}} (\eta(q_x - 2\beta q_y u_x u_y) - u_x \tau_{yy}) - A_2^- \tau_{xy} \right)$$

$$GY_{I,4}^{-} = \frac{\rho}{8\beta^{3/2}} \left(\frac{B_2^-}{\sqrt{\pi}} \frac{(1+\gamma+\bar{u}^2)}{(\gamma-1)} + \sqrt{\beta} u_y \frac{(2\gamma+\bar{u}^2)}{(\gamma-1)} A_2^- \right)$$

$$GY^{-}_{V,4} = \frac{\rho}{16p\beta^{3/2}} \begin{pmatrix} \frac{B_2^-}{\sqrt{\pi}}(4\beta\eta q_x u_x + 2\beta q_y u_y \frac{(\gamma-3-\bar{u}_x^2)}{\gamma} + \frac{(1-3\gamma-\bar{u}_x^2)}{\gamma-1}\tau_{yy}) \\ +4\sqrt{\beta}(q_y - u_x\tau_{xy} - u_y\tau_{yy})A_2^- \end{pmatrix}$$

where $\bar{u}_x^2 = 2\beta(\gamma-1)u_x^2$, $\bar{u}_y^2 = 2\beta(\gamma-1)u_y^2$, $\bar{u}^2 = 2\beta(\gamma-1)(u_x^2+u_y^2)$, $\eta = (\gamma-1)/\gamma$, $B_1^{\pm} = \pm Exp[-\beta u_x^2]$, $B_2^{\pm} = \pm Exp[-\beta u_y^2]$, $A_1^{\pm} = 1 \pm Erf[\sqrt{\beta}u_x]$ and $A_2^{\pm} = 1 \pm Erf[\sqrt{\beta}u_y]$. The y component of state vector is not updated as $U_{i=3}$=ρu_y= 0, hence fluxes $GX^{\pm-}_{I,3}$, $GX^{\pm-}_{V,3}$, $GY^{-}_{I,3}$,$GY^{-}_{V,3}$ are not evaluated.

5.5.2 Wall boundary condition for 3-D case

Similarly upwind discretization for the three dimensional case the distribution at time $t+\Delta t$ at the boundary is obtained as

$$f_{1,\Sigma}(t+\Delta t) = f_{1,\Sigma}(t) - \Delta t \begin{bmatrix} \frac{\partial v_x f^{+\cdot-}_{1,\Sigma}(t)}{\partial x} + \frac{\partial v_x f^{-\cdot-}_{1,\Sigma}(t)}{\partial x} \\ \frac{\partial v_y f^{\cdot+-}_{1,\Sigma}(t)}{\partial y} + \frac{\partial v_y f^{\cdot--}_{1,\Sigma}(t)}{\partial y} \\ +\frac{\partial v_z f^{\cdot\cdot-}_{1,\Sigma}(t)}{\partial z} \end{bmatrix} \tag{5.53}$$

where distribution $f_1^{+\cdot-}$ is the half-range total distribution function for $0 < v_x < \infty$, $-\infty < v_y < \infty$ and $-\infty < v_z < 0$. The distribution $f_1^{-\cdot-}$ is the total distribution function for $-\infty < v_x < 0$, $-\infty < v_y < \infty$ and $-\infty < v_z < 0$. The distribution $f_1^{\cdot\cdot-}$ is the total distribution function for $-\infty < v_x < \infty$, $-\infty < v_y < \infty$ and $-\infty < v_z < 0$. After taking $\boldsymbol{\Psi}$ moment we can obtain state update equation expressed as

$$\boldsymbol{U}(t+\Delta t) = \boldsymbol{U}(t) - \Delta t \begin{bmatrix} \left(\frac{\partial \widehat{\boldsymbol{GX}}^{+\cdot-}(t)}{\partial x}\right)_{\Delta x<0} + \left(\frac{\partial \widehat{\boldsymbol{GX}}^{-\cdot-}(t)}{\partial x}\right)_{\Delta x>0} \\ \left(\frac{\partial \widehat{\boldsymbol{GY}}^{\cdot+-}(t)}{\partial y}\right)_{\Delta y<0} + \left(\frac{\partial \widehat{\boldsymbol{GY}}^{\cdot--}(t)}{\partial y}\right)_{\Delta y>0} \\ + \left(\frac{\partial \widehat{\boldsymbol{GZ}}^{\cdot\cdot-}(t)}{\partial z}\right)_{\Delta z>0} \end{bmatrix} \tag{5.54}$$

where $\boldsymbol{U}$=$[\rho, \rho\boldsymbol{u}, \rho E]^T$ is the state vector and Δt is the time step.
The z component of state vector is not updated as $U_{i=4}$=ρu_z= 0. $\widehat{\boldsymbol{GX}}^{\pm\cdot-}$ represents the flux based on half range distributions $f^{\pm\cdot-}_{1,\Sigma}$. $\widehat{\boldsymbol{GY}}^{\cdot\pm-}$ represents the flux based on half range distributions $f^{\cdot\pm-}_{1,\Sigma}$. $\widehat{\boldsymbol{GZ}}^{\cdot\cdot-}$ is the flux resulting from half range distribution $f^{\cdot\cdot-}_{1,\Sigma}$. The mass, momentum and energy components of x-directional

flux $\widehat{\boldsymbol{GX}}^{\pm\cdot-}$ can be written as sum of inviscid or Euler part $\widehat{\boldsymbol{GX}}_I^{\pm\cdot-}$ and viscous part $\widehat{\boldsymbol{GX}}_V^{\pm\cdot-}$ as

$$\widehat{\boldsymbol{GX}}^{\pm\cdot-} = \widehat{\boldsymbol{GX}}_I^{\pm\cdot-} + \widehat{\boldsymbol{GX}}_V^{\pm\cdot-} = \left\langle v_x \boldsymbol{\Psi} f_{0,\Sigma}^{\pm\cdot-} \right\rangle - \textstyle\sum_j \boldsymbol{\Lambda}_j^{\pm\cdot-} \odot \boldsymbol{X}_j \tag{5.55}$$

Components of y-directional flux $\widehat{\boldsymbol{GY}}^{\cdot\pm-}$ can be written as sum of inviscid part and viscous part as follows

$$\widehat{\boldsymbol{GY}}^{\cdot\pm-} = \widehat{\boldsymbol{GY}}_I^{\cdot\pm-} + \widehat{\boldsymbol{GY}}_V^{\cdot\pm-} = \left\langle v_y \boldsymbol{\Psi} f_{0,\Sigma}^{\cdot\pm-} \right\rangle - \textstyle\sum_j \boldsymbol{\Lambda}_j^{\cdot\pm-} \odot \boldsymbol{X}_j \tag{5.56}$$

Similarly, components of z-directional flux $\widehat{\boldsymbol{GZ}}^{\cdot\cdot-}$ can be written as sum of inviscid part and viscous part as follows

$$\widehat{\boldsymbol{GZ}}^{\cdot\cdot-} = \widehat{\boldsymbol{GZ}}_I^{\cdot\cdot-} + \widehat{\boldsymbol{GZ}}_V^{\cdot\cdot-} = \left\langle v_z \boldsymbol{\Psi} f_{0,\Sigma}^{\cdot\cdot-} \right\rangle - \textstyle\sum_j \boldsymbol{\Lambda}_j^{\cdot\cdot-} \odot \boldsymbol{X}_j \tag{5.57}$$

The viscous fluxes are obtained using macroscopic tensors $\boldsymbol{\Lambda}_j^{\pm\cdot-}$, $\boldsymbol{\Lambda}_j^{\cdot\pm-}$ and $\boldsymbol{\Lambda}_j^{\cdot\cdot-}$ associated with shear stress tensor and heat flux vector following Onsager's reciprocal relationship so as to maximize the entropy production. The fluxes $\widehat{\boldsymbol{GX}}^{\pm\cdot-}$, $\widehat{\boldsymbol{GY}}^{\cdot\pm-}$ and $\widehat{\boldsymbol{GZ}}^{\cdot\cdot-}$ can also be written in alternative form as

$$\begin{aligned}
\widehat{\boldsymbol{GX}}^{\pm\cdot-} &= (2-\sigma)(\boldsymbol{GX}_I^{\pm\cdot-} + \boldsymbol{GX}_V^{\pm\cdot-}) + \sigma \boldsymbol{GX}_I^{\pm-}(\rho, \vec{u}_w, T_w) \\
\widehat{\boldsymbol{GY}}^{\cdot\pm-} &= (2-\sigma)(\boldsymbol{GY}_I^{\cdot\pm-} + \boldsymbol{GY}_V^{\cdot\pm-}) + \sigma \boldsymbol{GY}_I^{\cdot\pm-}(\rho, \vec{u}_w, T_w) \\
\widehat{\boldsymbol{GZ}}^{\cdot\cdot-} &= (2-\sigma)(\boldsymbol{GZ}_I^{-} + \boldsymbol{GZ}_V^{-}) + \sigma \boldsymbol{GZ}_I^{-}(\rho, \vec{u}_w, T_w)
\end{aligned} \tag{5.58}$$

where $\boldsymbol{GX}_I^{\pm\cdot-}$, $\boldsymbol{GX}_V^{\pm\cdot-}$, $\boldsymbol{GY}_I^{\cdot\pm-}$ $\boldsymbol{GY}_V^{\cdot\pm-}$, $\boldsymbol{GZ}_I^{-}$ and $\boldsymbol{GZ}_V^{-}$ are evaluated based on fluid conditions while $\boldsymbol{GX}_I^{\pm\cdot-}(\rho, \vec{u}_w, T_w)$, $\boldsymbol{GY}_I^{\cdot\pm-}(\rho, \vec{u}_w, T_w)$ and $\boldsymbol{GZ}_I^{-}(\rho, \vec{u}_w, T_w)$ are the inviscid flux based on Maxwellian distribution which are evaluated using fluid density ρ, wall temperature T_w and wall velocity $\vec{u}_w \equiv (u_{w,x}, u_{w,y}, 0)$. The final expressions of these fluxes are given in section D.3.3 of Appendix D.

5.6 Treatment of slip flow near transition regime.

For modeling slip near transition regime ideally we require an approach which is computationally cheap and takes the slip velocity dependence on the fluid dynamic variations in the tangential direction. The approach also requires inclusion of the terms of order Kn^2 for its validity in the non-continuum slip bordering

the transition region (Kn ≈ 0.1). In the present study we have implemented slip boundary based on kinetic approach. By using the higher order Chapman-Enskog distribution the kinetic treatment of slip can be extended to higher Knudsen number, Kn>0.1 by adding the Burnett split flux terms. Full kinetic approach with the addition of Burnett split fluxes associated with second order Chapman-Enskog will make the computation quite costly. This section discusses various approaches for the treatment of slip flow near transition regime

5.6.1 Kinetic upwind method using second order Chapman-Enskog perturbation expansion

For example consider second order Chapman-Enskog perturbation expansion for Morse-BGK model written as

$$\begin{aligned} f &= f_0 + \mathrm{Kn}\bar{f}_1 + \mathrm{Kn}^2\bar{f}_2 \\ &= f_0 + \mathrm{Kn}f_0\xi_1 + \mathrm{Kn}^2\bar{f}_1\xi_2 \end{aligned} \tag{5.59}$$

where Kn is the Knudsen number and $\xi_1$and ξ_2 are the first and second order Chapman-Enskog polynomials.[1] Expressing in terms of substantiative derivative $\frac{D}{Dt} = \frac{\partial}{\partial t} + \vec{u}.\nabla$ and relaxation time t_R using the procedure of iterative refinement

[1]Chapman-Enskog theory and the physical models are based on an inappropriate definition of the peculiar velocity leading to frame dependence of the Burnett equations [291].

for one dimensional geometry we get

$$\begin{aligned}
\frac{\mathrm{Kn}^2\bar{f}_2}{f_0} &= t_R^2\left[\begin{array}{l}
\left[\left(\frac{25}{4\beta^2}-\frac{\mathbb{I}^2}{\beta^2\mathbb{I}_o^2}-\frac{5\mathbb{I}}{\beta^2\mathbb{I}_o}\right)c_x^2+\left(\frac{2\mathbb{I}}{\beta\mathbb{I}_o}-\frac{5}{\beta}\right)c_x^4+c_x^6\right]\left(\frac{\partial\beta}{\partial x}\right)^2\\
+2\left[\begin{array}{l}\left(\frac{5(3\gamma-5)}{4\beta}-\frac{(4\gamma-5)\mathbb{I}}{\beta\mathbb{I}_o}+\frac{(\gamma-1)\mathbb{I}^2}{\beta\mathbb{I}_o^2}\right)c_x+\\ \left((10-4\gamma)+\frac{(2\gamma-4)\mathbb{I}}{\mathbb{I}_o}\right)c_x^3-(3-\gamma)\beta c_x^5\end{array}\right]\left(\frac{\partial\beta}{\partial x}\right)\left(\frac{\partial u_x}{\partial x}\right)\\
+\left[\begin{array}{l}\left(\frac{(3\gamma-5)^2}{4}-\frac{(3\gamma-5)(\gamma-1)\mathbb{I}}{\mathbb{I}_o}-\frac{(\gamma-1)^2\mathbb{I}^2}{\mathbb{I}_o^2}\right)+\\ \left((3-\gamma)(3\gamma-5)\beta-\frac{(\gamma-1)(3-\gamma)2\beta\mathbb{I}}{\mathbb{I}_o}\right)c_x^2+(3-\gamma)^2\beta^2c_x^4\end{array}\right]\left(\frac{\partial u_x}{\partial x}\right)^2
\end{array}\right]\\
&+t_R^2\left[\begin{array}{l}
\left(\frac{5c_x}{2\beta}-\frac{\mathbb{I}c_x}{\mathbb{I}_o\beta}-c_x^3\right)\frac{D}{Dt}\left(\frac{\partial\beta}{\partial x}\right)+\left\{\begin{array}{l}\left(-\frac{5}{2\beta}+\frac{\mathbb{I}}{\mathbb{I}_o\beta}+3c_x^2\right)\frac{Du_x}{Dt}\\ -\frac{5c_x}{2\beta^2}\frac{D\beta}{Dt}\end{array}\right\}\left(\frac{\partial\beta}{\partial x}\right)\\
+\left((3-\gamma)\beta c_x^2-\frac{(\gamma-1)\mathbb{I}}{\mathbb{I}_o}c_x+\frac{(3\gamma-5)}{2}\right)\frac{D}{Dt}\left(\frac{\partial u_x}{\partial x}\right)+\\
\left\{\left((3-\gamma)c_x^2-\frac{(\gamma-1)}{\beta\mathbb{I}_o}\right)\frac{D\beta}{Dt}-2(3-\gamma)\beta c_x\frac{Du_x}{Dt}\right\}\left(\frac{\partial u_x}{\partial x}\right)
\end{array}\right]\\
&+t_R^2\left[\begin{array}{l}
\left(\frac{5c_x^2}{2\beta}-\frac{\mathbb{I}c_x^2}{\mathbb{I}_o\beta}-c_x^4\right)\frac{\partial^2\beta}{\partial x^2}+\left(\begin{array}{l}-\frac{5c_x}{2\beta}\frac{\partial u_x}{\partial x}+\frac{\mathbb{I}c_x}{\mathbb{I}_o\beta}\frac{\partial u_x}{\partial x}+3c_x^3\frac{\partial u_x}{\partial x}\\ -\frac{5c_x^2}{2\beta^2}\frac{\partial\beta}{\partial x}\end{array}\right)\frac{\partial\beta}{\partial x}\\
+\left((3-\gamma)\beta c_x^3-\frac{(\gamma-1)\mathbb{I}}{\mathbb{I}_o}c_x+\frac{(3\gamma-5)}{2}c_x\right)\frac{\partial^2u_x}{\partial x^2}+\\
\left(-2(3-\gamma)\beta\frac{\partial u_x}{\partial x}+(3-\gamma)c_x^2\frac{\partial\beta}{\partial x}-\frac{(\gamma-1)\mathbb{I}}{\beta\mathbb{I}_o}\frac{\partial\beta}{\partial x}\right)\left(\frac{\partial u_x}{\partial x}\right)
\end{array}\right]
\end{aligned} \tag{5.60}$$

This perturbation term has to satisfy the additive invariants property, expressed as

$$< \mathbf{\Psi}, \mathrm{Kn}^i\bar{f}_i >_{1\le i\le 2} = 0 \tag{5.61}$$

More-so-ever evaluation shows that $< \mathbf{\Psi}, \mathrm{Kn}^2\bar{f}_2 > \neq 0$ so we require additional moment closure terms thus making the determination of f_2 non-unique. Refer section B.5 of Appendix B for closure coefficients for second order Chapman-Enskog distribution. This derivation illustrates that expressions even for one dimensional second order distribution based on Morse-BGK model become very unwieldy and unmanageable. Hence we require an alternative simpler treatment for modeling slip near transition regime.

5.6.2 Transition-slip velocity treatment based on Burnett constitutive relations

One of the simplest way to extend the kinetic based slip boundary condition is by further updating the slip velocity using the second order Kn^2 terms associated

with the Burnett constitutive relations [162].

$$(u_s)^{n+1}_{2^{nd}Order} = (u_s)^{n+1}_{kinetic} + (\Delta u_s)^{n+1}_{Burnett} \tag{5.62}$$

The second order Kn^2 Burnett correction terms given by Lockerby *et al.* [162] is expressed as

$$\begin{aligned}(\Delta u_s)^{n+1}_{Burnett} = &\left(\tfrac{2-\sigma_v}{\sigma_v}\right)\lambda\left(2\tfrac{\mu}{\rho^2}\tfrac{\partial^2\rho}{\partial s\partial n} - \tfrac{\mu}{\rho T}\tfrac{\partial^2 T}{\partial s\partial n}\right)^n_w \\ &+ \tfrac{3\,\mathrm{Pr}}{16\pi}\left(\tfrac{\gamma-1}{\gamma}\right)\lambda^2\left((45\gamma-61)\tfrac{\partial^2 u_s}{\partial s^2} + (45\gamma-49)\tfrac{\partial^2 u_n}{\partial s\partial n} - 12\tfrac{\partial^2 u_s}{\partial n^2}\right)^n_w\end{aligned} \tag{5.63}$$

It should be noted that for polyatomic molecules this correction requires a modification as Burnett coefficients are different. In this approach second order treatment based on addition of Burnett correction terms is only applied to the velocity slip. This treatment is thermodynamically incorrect and violates Onsager's reciprocity principle as there is no contribution made to the thermal terms.

5.6.3 Treatment of transition-slip flow based on collision probability function

Near the wall at a normal distance of order $O(\lambda) = \lambda_e$ there exists a Knudsen layer parametrized by λ_e which is the effective mean free path depending on the effective viscosity and wall conditions. In the Knudsen layer some molecules may collide more with the wall and may not suffer as much collisions with the molecules as compared to the molecules above the Knudsen layer. Figure 5.3 shows the incident molecules and the reflected molecules in the Knudsen layer. For modeling slip near transition regime ideally we require an approach which is computationally cheap includes higher moments thereby terms of order Kn^2. It should be noted that validity of Chapman-Enskog expansion procedure can only be said for $\mathrm{Kn} \leq 1$, the more correct way to obtain non-linear distribution has to be based on extended irreversible thermodynamics (EIT) by expanding the distribution function in terms of microscopic tensors and thermodynamic forces as follows

$$f = f_0 - \sum_j \boldsymbol{\Upsilon}_j \odot \boldsymbol{X}_j - \sum_{jk} \bar{\boldsymbol{\Upsilon}}_{jk} \odot \boldsymbol{X}_j \odot \boldsymbol{X}_k + \cdots \tag{5.64}$$

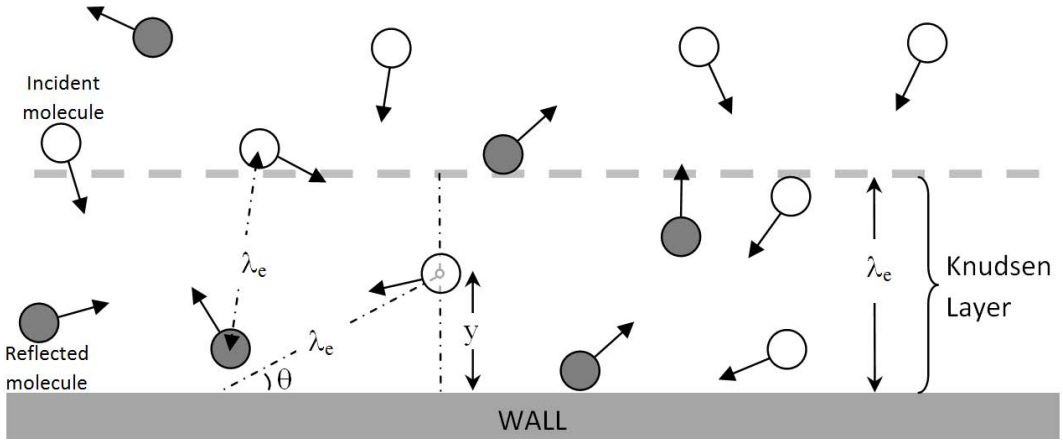

Figure 5.3: Collision probability function in the Knudsen layer

From non-equilibrium thermodynamics point of view linear irreversible thermodynamics (LIT) is no longer valid in the Knudsen layer as fluxes are no longer linear functions of its conjugate force, regime shifts to extended irreversible thermodynamics (EIT) described by $\boldsymbol{J}_i = \sum_j \boldsymbol{L}_{ij} \odot \boldsymbol{X}_j + \frac{1}{2}\sum_{jk} \boldsymbol{L}_{ijk} \odot \boldsymbol{X}_j \odot \boldsymbol{X}_k + \cdots$. Simplest approach may be to approximate EIT based flux as a function of LIT based flux by using suitable scaling function. Consider a function $\mathbb{P}(\bar{y})$[1] as a measure of probability of collision at any normal distance $\bar{y}=\frac{y}{\lambda_e} \leq 1$ such that non-equilibrium EIT based flux, $\boldsymbol{J}_i$ can be approximated in terms of $\mathbb{P}(\bar{y})$ for curvature free surface as $\boldsymbol{J}_i \approx \mathbb{P}(\bar{y}) \sum_j \boldsymbol{L}_{ij} \odot \boldsymbol{X}_j$. In the present study we have used the following form of the collision probability function

$$\mathbb{P}(\bar{y}) = \begin{cases} \frac{\bar{y}}{2} + \frac{\sin^{-1}(\bar{y})}{\pi}, & \bar{y} \leq 1 \\ 1, & \bar{y} > 1 \end{cases} \tag{5.65}$$

where factor $\frac{\bar{y}}{2}$ is probability of molecules in the Knudsen layer moving in upward direction i.e. it is proportional to volume of molecules below the dimensionless normal distance. Similarly the factor $\frac{\sin^{-1}(\bar{y})}{\pi}$ is the probability of collision due to downward traveling molecules. The single particle reduced description of the velocity distribution $f_1(\bar{y})$ in the Knudsen layer at any normal dimensionless

[1]For two dimensional symmetry problems collision probability function, $\mathbb{P}(\bar{y})$ will also depend on the curvature of the surface as it is a volume dependent parameter related to Onsager's dissipation function.

distance $\bar{y}=\frac{y}{\lambda_e} \leq 1$ can be expressed as

$$f_1(\bar{y}) = f_0 + \mathbb{P}(\bar{y})\Phi f_0 \tag{5.66}$$

where $\mathbb{P}(\bar{y})$ is the collision probability function, f_0 is the Maxwellian, Φ can be in terms of first order tensorial Hermite polynomials or Chapman-Enskog polynomials. In the present case the distribution function at normal dimensionless distance $\bar{y}$ is expressed as

$$f_1(\bar{y}) = f_0 - \mathbb{P}(\bar{y}) \sum_j \boldsymbol{\Upsilon}_j \odot \boldsymbol{X}_j \tag{5.67}$$

Using the Maxwell model the total distribution function, $f_{1,\Sigma}$ at the wall in terms of accommodation coefficient σ can be written as

$$f_{1,\Sigma}(\bar{y}=0) \quad = f_{1,I}(\bar{y}=0)_{v_z<0} + (1-\sigma) f_{1,I}(\bar{y}=0)_{v_z>0} + \sigma f_{0,W}(\bar{y}=0)_{v_z>0} \tag{5.68}$$

where $f_{1,\Sigma}(\vec{v},\mathbb{I})$ is the total, $f_{1,I}(\vec{v},\mathbb{I})$ is the incident as well as the specularly reflected Chapman-Enskog distribution and $f_{0,W}(\vec{v},\mathbb{I})$ is the diffuse reflected Maxwellian distribution evaluated at the wall conditions. At the wall the velocity gradient is singular as Maxwellian distribution prevails i.e. the effective viscosity becomes zero similar to the findings of Lilley and Sader [154].
The Boltzmann equation in the Knudsen layer in terms of new kinetic model can be interpreted as

$$\frac{\partial f}{\partial t} + \nabla_{\vec{x}} \cdot (\vec{v} f) = -\left(\frac{f-f_0}{\mathbb{P}(\bar{y}) t_{R(\tau)}}\right)_{\boldsymbol{X}_q=0} - \left(\frac{f-f_0}{\mathbb{P}(\bar{y}) t_{R(q)}}\right)_{\boldsymbol{X}_\tau=0} \tag{5.69}$$

This can also be interpreted as new kinetic model with varying relaxation time expressed as

$$\frac{\partial f}{\partial t} + \nabla_{\vec{x}} \cdot (\vec{v} f) = -\left(\frac{f-f_0}{\tilde{t}_{R(\tau)}(\bar{y})}\right)_{\boldsymbol{X}_q=0} - \left(\frac{f-f_0}{\tilde{t}_{R(q)}(\bar{y})}\right)_{\boldsymbol{X}_\tau=0} \tag{5.70}$$

The relaxation time varies with the normal distance from the wall based on the collision probability function, $\mathbb{P}(\bar{y})$ as

$$\tilde{t}_{R(j)} = \mathbb{P}(\bar{y}) t_{R(j)} \tag{5.71}$$

The kinetic upwind equations in the macroscopic form is

$$\boldsymbol{U}(t+\Delta t) = \boldsymbol{U}(t) - \Delta t \begin{bmatrix} \frac{\partial \boldsymbol{G}\boldsymbol{X}_I^{\pm}(t)}{\partial x} + \frac{\partial \bar{\boldsymbol{G}}\boldsymbol{X}_V^{\pm}(t)}{\partial x} \\ + \frac{\partial \boldsymbol{G}\boldsymbol{Y}_I^{\pm}(t)}{\partial y} + \frac{\partial \bar{\boldsymbol{G}}\boldsymbol{Y}_V^{\pm}(t)}{\partial y} \\ + \frac{\partial \boldsymbol{G}\boldsymbol{Z}_I^{\pm}(t)}{\partial z} + \frac{\partial \bar{\boldsymbol{G}}\boldsymbol{Z}_V^{\pm}(t)}{\partial z} \end{bmatrix} \tag{5.72}$$

This kinetic method is quite easy to implement as the viscous fluxes are just multiplied by the collision function $\mathbb{P}(\bar{y})$. The viscous part of the flux component, $\bar{\boldsymbol{G}}\boldsymbol{X}_V^{\pm}$, $\bar{\boldsymbol{G}}\boldsymbol{Y}_V^{\pm}$ and $\bar{\boldsymbol{G}}\boldsymbol{Z}_V^{\pm}$ are obtained as

$$\begin{array}{ll} \bar{\boldsymbol{G}}\boldsymbol{X}_V^{\pm} & = \mathbb{P}(\bar{y})\boldsymbol{G}\boldsymbol{X}_V^{\pm} = -\mathbb{P}(\bar{y}) \sum_j \boldsymbol{\Lambda}_j^{\pm\cdot\cdot} \odot \boldsymbol{X}_j \\ \bar{\boldsymbol{G}}\boldsymbol{Y}_V^{\pm} & = \mathbb{P}(\bar{y})\boldsymbol{G}\boldsymbol{Y}_V^{\pm} = -\mathbb{P}(\bar{y}) \sum_j \boldsymbol{\Lambda}_j^{\cdot\pm\cdot} \odot \boldsymbol{X}_j \\ \bar{\boldsymbol{G}}\boldsymbol{Z}_V^{\pm} & = \mathbb{P}(\bar{y})\boldsymbol{G}\boldsymbol{Z}_V^{\pm} = -\mathbb{P}(\bar{y}) \sum_j \boldsymbol{\Lambda}_j^{\cdot\cdot\pm} \odot \boldsymbol{X}_j \end{array} \tag{5.73}$$

Expressions for components of the macroscopic tensors $\boldsymbol{\Lambda}_\tau^{\pm\cdot\cdot}$, $\boldsymbol{\Lambda}_q^{\pm\cdot\cdot}$ associated with x-split fluxes, $\boldsymbol{\Lambda}_\tau^{\cdot\pm\cdot}$, $\boldsymbol{\Lambda}_q^{\cdot\pm\cdot}$ associated with y-split fluxes and $\boldsymbol{\Lambda}_\tau^{\cdot\cdot\pm}$, $\boldsymbol{\Lambda}_q^{\cdot\cdot\pm}$ associated with z-split fluxes are given in section D.2 of Appendix D.

5.7 Summary

The chapter derives gradient and flux based kinetic wall boundary condition using new non-equilibrium thermodynamics based distribution function. Gradient based velocity slip and temperature jump boundary conditions were derived using half range distribution function for cases with negligible tangential variations. Expressions of gradient based velocity slip and temperature jump derived using non-equilibrium based distribution were compared with the expressions of Maxwell velocity slip and von Smoluchowski temperature jump. A unified kinetic theory and non-equilibrium thermodynamics based wall boundary condition which satisfies Onsager's relationship was also derived, this boundary condition is flux based and can simulate both continuum and rarefied slip flow within Navier-Stokes equation in order to avoid extremely costly multi-scale simulation. In order to extend the slip flow simulation near the transition regime a new method based on collision probability function was also suggested.

Chapter 6

Development of meshless kinetic upwind solver

6.1 Introduction

In this chapter we present a novel meshless kinetic upwind solver which can work for highly stretched distribution of points required for viscous and slip flow simulations. The first section describes least square method using normal equations approach to carry out a test for highly stretched distribution of points. The second section describes the novel least square method based on stencil spitting, the third section describes the pre-processing tools used in the split stencil least square based method. An illustrative numerical example of a function simulating boundary layer over stretched distribution of points is presented to show the merit of the novel least square approach. The fourth section describes the implementation of kinetic upwind scheme based on split stencil least square meshless method. The fifth section describes the parallelization strategy and the last section describes the implementation of multi-objective optimization methodology for meshless solver.

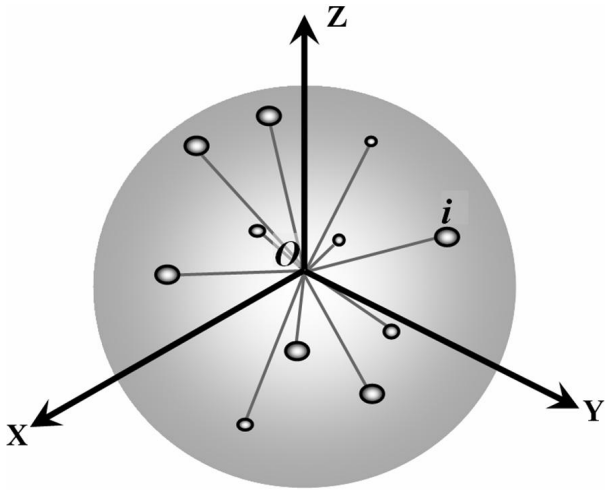

Figure 6.1: Point connectivity for LSKUM

6.2 Least square based method and stretched distribution of points

Consider a reference node P_o surrounded by m points defined as connectivity $N(P_o) = \{\forall P_i : d(P_o, P_i) < h\ \}$ as shown in Figure 6.1. We are interested in finding the derivatives of ϕ at all the nodes. The derivatives are obtained in the following way. Error at any point P_i in the neighbourhood of P_o in terms of derivatives ϕ_{xo}, ϕ_{yo} and ϕ_{zo} gives us,

$$E_i = \Delta\phi_i - \Delta x_i\phi_{xo} - \Delta y_i\phi_{yo} - \Delta z_i\phi_{zo} \quad i = 1, ..., m \tag{6.1}$$

where $\Delta x_i = x_i - x_o$, $\Delta y_i = y_i - y_o$, $\Delta z_i = z_i - z_o$ and $\Delta\phi_i = \phi_i - \phi_o$. Finding the derivative at point P_o is a least squares problem where error norm $\|E\|_2$ is to be minimized with respect to ϕ_{xo}, ϕ_{yo} and ϕ_{zo} using stencil $N(P_o)$. In the normal equations approach we find $\boldsymbol{\Phi}_o = [\phi_{xo}, \phi_{yo}, \phi_{zo}]^T \in \mathbb{R}^n$ such that $\|\boldsymbol{A}_N\boldsymbol{\Phi}_o - \boldsymbol{\Delta\phi}_N\|_2$ is minimized where data matrix $\boldsymbol{A}_N \in \mathbb{R}^{m\times n}$ and observation $\boldsymbol{\Delta\phi}_N = [\Delta\phi_1, \Delta\phi_2, \cdots, \Delta\phi_m]^T \in \mathbb{R}^m$. As described earlier the normal equations approach uses smaller cross-product matrix $\boldsymbol{C} = \boldsymbol{A}_N^T\boldsymbol{A}_N \in \mathbb{R}^{n\times n}$. In the least

square approach the matrices $\boldsymbol{A}_N^T$ and $\boldsymbol{A}_N$ are expressed as

$$\begin{aligned} \boldsymbol{A}_N^T &= \begin{bmatrix} \Delta x_1 & \Delta x_2 & \cdots & \Delta x_m \\ \Delta y_1 & \Delta y_2 & \cdots & \Delta y_m \\ \Delta z_1 & \Delta z_2 & \cdots & \Delta z_m \end{bmatrix} \\ \boldsymbol{A}_N &= \begin{bmatrix} \Delta x_1 & \Delta y_1 & \Delta z_1 \\ \Delta x_2 & \Delta y_2 & \Delta z_2 \\ \cdots & \cdots & \cdots \\ \Delta x_m & \Delta y_m & \Delta z_m \end{bmatrix} \end{aligned} \tag{6.2}$$

Thus, cross matrix product $\boldsymbol{C} = \boldsymbol{A}_N^T \boldsymbol{A}_N$ for sub-stencil $N_x(P_o)$ is given as

$$\boldsymbol{C} = \boldsymbol{A}_N^T \boldsymbol{A}_N = \begin{bmatrix} (\sum \Delta x_i^2)_N & (\sum \Delta x_i \Delta y_i)_N & (\sum \Delta x_i \Delta z_i)_N \\ (\sum \Delta x_i \Delta y_i)_N & (\sum \Delta y_i^2)_N & (\sum \Delta y_i \Delta z_i)_N \\ (\sum \Delta x_i \Delta z_i)_N & (\sum \Delta y_i \Delta z_i)_N & (\sum \Delta z_i^2)_N \end{bmatrix} \tag{6.3}$$

The expressions $(\cdot)_N$ require values evaluated using stencils $N(P_o)$. The derivatives in least square method can be obtained as

$$\boldsymbol{\Phi}_o = \left(\boldsymbol{A}_N^T \boldsymbol{A}_N\right)^{-1} \boldsymbol{A}_N^T \boldsymbol{\Delta\phi}_N = \boldsymbol{C}^{-1} \boldsymbol{A}_N^T \boldsymbol{\Delta\phi}_N \tag{6.4}$$

For a two dimensional case this can be written as

$$\begin{bmatrix} \phi_{xo} \\ \phi_{yo} \end{bmatrix} = \begin{bmatrix} (\sum \Delta x_i^2)_N & (\sum \Delta x_i \Delta y_i)_N \\ (\sum \Delta x_i \Delta y_i)_N & (\sum \Delta y_i^2)_N \end{bmatrix}^{-1} \begin{bmatrix} (\sum \Delta \phi_i \Delta x_i)_N \\ (\sum \Delta \phi_i \Delta y_i)_N \end{bmatrix} \tag{6.5}$$

The expressions of the derivatives after solution based on normal equations approach is as follows

$$\phi_{xo} = \frac{(\sum \Delta y_i^2)_N (\sum \Delta \phi_i \Delta x_i)_N - (\sum \Delta x_i \Delta y_i)_N (\sum \Delta \phi_i \Delta y_i)_N}{(\sum \Delta x_i^2)_N (\sum \Delta y_i^2)_N - (\sum \Delta x_i \Delta y_i)_N (\sum \Delta x_i \Delta y_i)_N} \tag{6.6}$$

$$\phi_{yo} = \frac{(\sum \Delta x_i^2)_N (\sum \Delta \phi_i \Delta y_i)_N - (\sum \Delta x_i \Delta y_i)_N (\sum \Delta \phi_i \Delta x_i)_N}{(\sum \Delta x_i^2)_N (\sum \Delta y_i^2)_N - (\sum \Delta x_i \Delta y_i)_N (\sum \Delta x_i \Delta y_i)_N} \tag{6.7}$$

The selection of connectivity set $N(P_o)$ is the most crucial aspect. With this method degeneracy takes place when the distribution of points is highly stretched.

6.2.1 Condition number and highly stretched distribution of points

Important question is how least square based method based on normal equations approach handle highly stretched distribution of points. One of the good measure

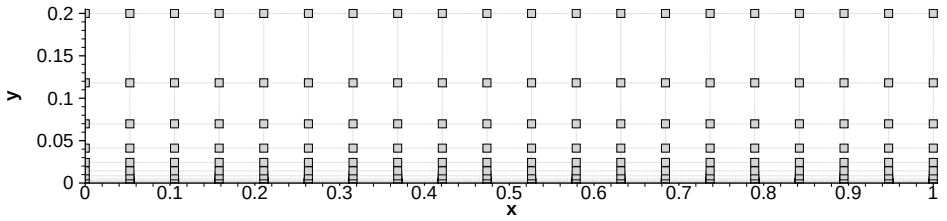

Figure 6.2: Highly stretched distribution of points.

is the condition number of the cross product matrix evaluated for highly stretched cloud of points. To illustrate this consider a test case with highly stretched distribution of point generated using uniform clustering parallel to x-axis and exponential clustering parallel to y-axis as follows

$$\begin{aligned} x_i &= x_{max}\left(\frac{i-1}{imax-1}\right) \\ y_i &= y_{max}\left(\frac{exp\left(\beta\frac{j-1}{jmax-1}\right)-1}{exp(\beta)-1}\right) \end{aligned} \tag{6.8}$$

Following parameters are used in this test case

$$\beta = 10. \quad i_{max} = 20 \quad , j_{max} = 20 \quad x_{max} = 1.0 \quad y_{max} = 0.2 \tag{6.9}$$

Fig. 6.2 shows the distribution of points, aspect ratio of the distribution of points near the wall is $\frac{\Delta x}{\Delta y} = 8367$. For 2-D geometry the cross matrix product $\boldsymbol{C} = \boldsymbol{A}_N^T \boldsymbol{A}_N$ is

$$\boldsymbol{C} = \boldsymbol{A}_N^T \boldsymbol{A}_N = \begin{bmatrix} (\sum \Delta x_i^2)_N & (\sum \Delta x_i \Delta y_i)_N \\ (\sum \Delta x_i \Delta y_i)_N & (\sum \Delta y_i^2)_N \end{bmatrix} \tag{6.10}$$

Fig. 6.3 shows the contour plot of condition number of the cross matrix product $\boldsymbol{C}$. Near the wall the condition number rises up to an order 9×10^7. The least square based approach leads to ill-conditioning near the wall due to highly stretched distribution of points required for resolving the viscous flow features.

6.2.2 QR approach

The most reliable approach is reduction of matrix A_N to various canonical forms via orthogonal transformations [98] and QR approach is one of the ways to com-

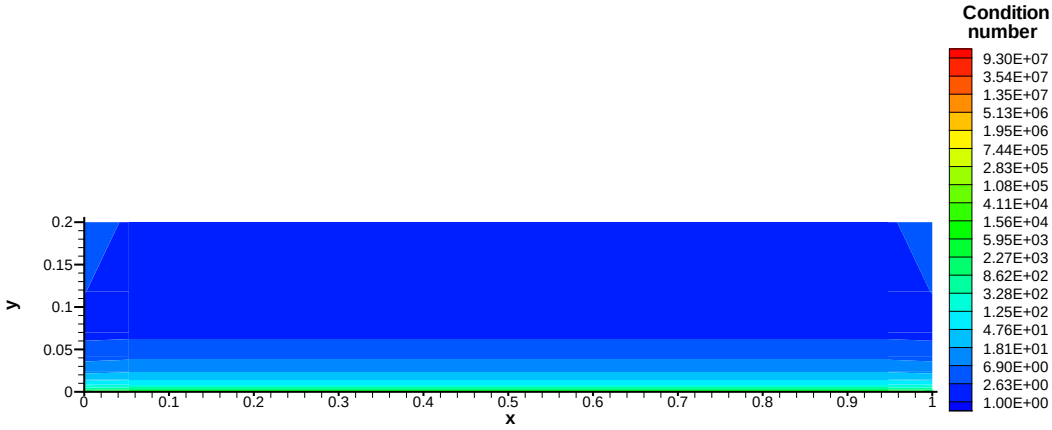

Figure 6.3: Condition number plot for highly stretched distribution of points.

pute orthonormal basis for a set of vectors. Any matrix can be decomposed in $\boldsymbol{Q}$ which is orthonormal and $\boldsymbol{R}$ which is upper triangular. QR factorization transforms the linear least square problem into a triangular least squares. Not all ill effects inherent in the normal equation approach can be avoided by using orthogonal transformation as condition number is still relevant to some extent [99].

6.2.3 Numerical test

Consider a 2-D test case to evaluate gradients of a function,ϕ simulating viscous boundary layer. The function ϕ chosen for this test case is

$$\phi = 1.5\left(\frac{y}{\delta}\right) - 0.5\left(\frac{y}{\delta}\right)^3 \tag{6.11}$$

where δ is given as

$$\delta = \frac{5.2x}{\sqrt{\mathrm{Re}}} \tag{6.12}$$

where Reynold's number, Re = 1000. The clouds of points are generated using highly stretched grid described in the previous section. Fig. 6.4(a) and Fig. 6.4(b) show comparison of derivatives $\frac{\partial \phi}{\partial x}$ and $\frac{\partial \phi}{\partial y}$ using normal equations and QR based least square method with respect to analytical evaluation. The cross-product

matrix, $\boldsymbol{C}$ in normal equations based least square method becomes ill-conditioned when the distribution of points is highly stretched. Because of clustering in y direction the derivative $\frac{\partial \phi}{\partial y}$ is quite accurate. While derivative $\frac{\partial \phi}{\partial x}$ suffers due to ill-conditioning of matrix $\boldsymbol{C}$ caused by stretched distribution. Approach of normal equations as well as QR produces inaccurate results when applied to ill-conditioned problem [98]. *Numerical test conducted to check the accuracy of the least square based meshless method revealed that for a stretched distribution of points, least square approach based on normal equations and QR leads to ill-conditioning. Thus, we require a formulation which remains well conditioned even for highly stretched distribution of points.*

6.2.4 Why least square method fails ?

Consider a two-dimensional case with reference node P_o surrounded by m points defined by its connectivity $N(P_o)$ with node point P_j lying close to x-axis such that Δy_j is very small, and node point P_k lying close to y-axis such that Δx_k is very small as shown in Figure 6.5 The derivative ϕ_{xo} and ϕ_{yo} based on Taylor series can be written for any node point P_i as follows

$$\phi_{xo} = \frac{\Delta \phi_i}{\Delta x_i} - \frac{\Delta y_i}{\Delta x_i}\phi_{yo} - \frac{E_i}{\Delta x_i} \quad i = 1, ..., m \tag{6.13}$$

$$\phi_{yo} = \frac{\Delta \phi_i}{\Delta y_i} - \frac{\Delta x_i}{\Delta y_i}\phi_{xo} - \frac{E_i}{\Delta y_i} \quad i = 1, ..., m \tag{6.14}$$

For point P_k which lies close to y-axis the term $\frac{\Delta y_k}{\Delta x_k}$ becomes singular as Δx_k approaches y-axis, thus evaluation of ϕ_{xo} will become erroneous due to presence of all the similar points like P_k which are close to y-axis. Similarly, For point P_j which lies close to x-axis the term $\frac{\Delta x_j}{\Delta y_j}$ becomes singular as Δy_j approaches x-axis, thus evaluation of ϕ_{yo} will become erroneous due to presence of all the similar points like P_j which are close to x-axis. *Hence we require a method which filters off all the points close to y-axis while evaluating x-derivative ϕ_{xo} and filters off all the points close to x-axis while evaluating y-derivative ϕ_{yo}.*

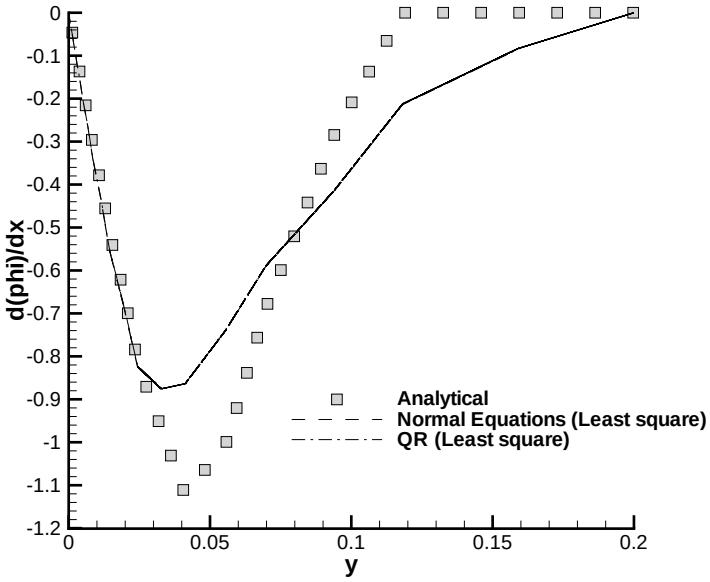

(a)

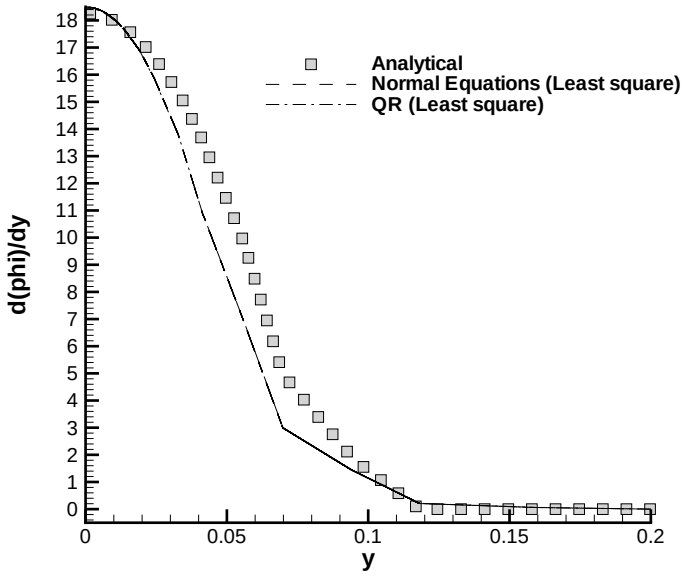

(b)

Figure 6.4: Comparison of (a) derivative $\frac{\partial \phi}{\partial x}$, and (b) derivative $\frac{\partial \phi}{\partial y}$ with respect to analytical result.

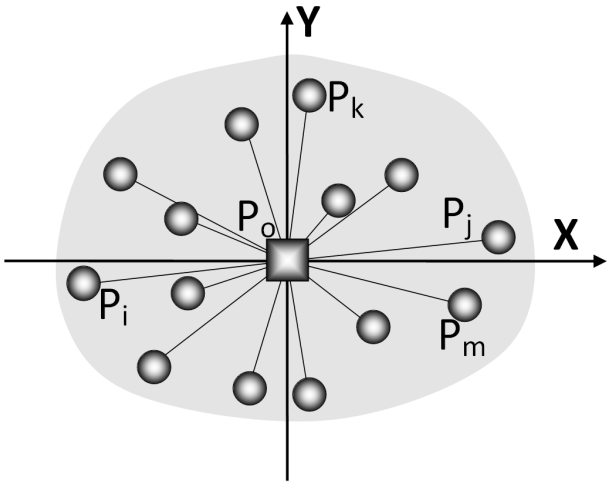

Figure 6.5: A typical connectivity for a two dimensional least square method.

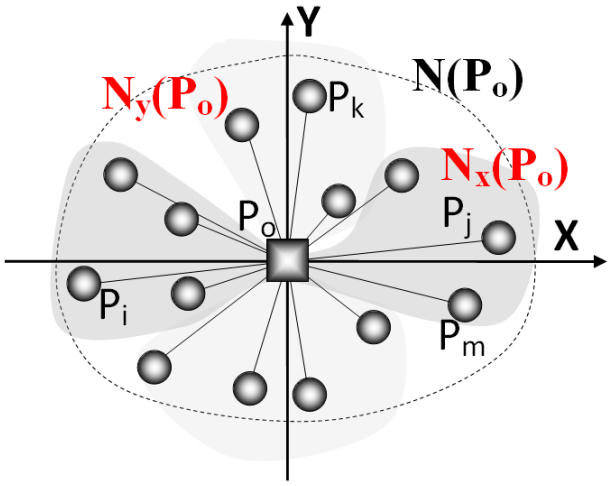

Figure 6.6: Connectivity $N(P_o)$ split into two parts $N_x(P_o)$ and $N_y(P_o)$.

6.3 Split-stencil least square kinetic upwind method (SLKNS)

This section presents a novel way to avoid ill-conditioning of the cross-product matrix while retaining the simplicity of normal equations approach. Consider a two-dimensional case with reference node P_o surrounded by m points defined by its split connectivity $N_x(P_o)$ and $N_y(P_o)$ as shown in Figure 6.6. By splitting the connectivity we will get error for x-split connectivity $N_x(P_o)$ with m_x points as well as y-split connectivity $N_y(P_o)$ with m_y points. For example error at any point P_i in the neighbourhood of P_o for $N_x(P_o)$ in terms of derivatives ϕ_{xo} and ϕ_{yo} gives us

$$Ex_i = \Delta\phi_i - \Delta x_i\phi_{xo} - \Delta y_i\phi_{yo} \;\; i = 1, \cdots, m_x \tag{6.15}$$

where $\Delta x_i = x_i - x_o$, $\Delta y_i = y_i - y_o$ and $\Delta\phi_i = \phi_i - \phi_o$. The x-split connectivity $N_x(P_o)$ is defined as

$$N_x(P_o) = \left\{ \forall P_i : P_i \in N(P_o) \exists \frac{\Delta y_i}{\Delta x_i} \leq 1 \right\} \tag{6.16}$$

such that m_x are the number of nodes contained in $N_x(P_o)$. Similarly, error at any point P_i in the neighbourhood of P_o for $N_y(P_o)$ gives us

$$Ey_i = \Delta\phi_i - \Delta x_i\phi_{xo} - \Delta y_i\phi_{yo} \;\; i = 1, \cdots, m_y \tag{6.17}$$

where m_y are the number of nodes contained in y-split connectivity $N_y(P_o)$ defined as

$$N_y(P_o) = \left\{ \forall P_i : P_i \in N(P_o) \exists \frac{\Delta x_i}{\Delta y_i} \leq 1 \right\} \tag{6.18}$$

Finding the derivative at point P_o now differs from the usual normal equations approach as error norms $\|Ex\|_2$ and $\|Ey\|_2$ are to be minimized with respect to ϕ_{xo} and ϕ_{yo} using stencils $N_x(P_o)$ and $N_y(P_o)$. Solution for this can be written as

$$\begin{bmatrix} \phi_{xo} \\ \phi_{yo} \end{bmatrix} = \begin{bmatrix} (\sum \Delta x_i^2)_{N_x} & (\sum \Delta x_i \Delta y_i)_{N_x} \\ (\sum \Delta x_i \Delta y_i)_{N_y} & (\sum \Delta y_i^2)_{N_y} \end{bmatrix}^{-1} \begin{bmatrix} (\sum \Delta\phi_i \Delta x_i)_{N_x} \\ (\sum \Delta\phi_i \Delta y_i)_{N_y} \end{bmatrix} \tag{6.19}$$

The expressions of the derivatives are as follows

$$\phi_{xo} = \frac{(\sum \Delta y_i^2)_{N_y}(\sum \Delta\phi_i \Delta x_i)_{N_x} - (\sum \Delta x_i \Delta y_i)_{N_x}(\sum \Delta\phi_i \Delta y_i)_{N_y}}{(\sum \Delta x_i^2)_{N_x}(\sum \Delta y_i^2)_{N_y} - (\sum \Delta x_i \Delta y_i)_{N_x}(\sum \Delta x_i \Delta y_i)_{N_y}} \tag{6.20}$$

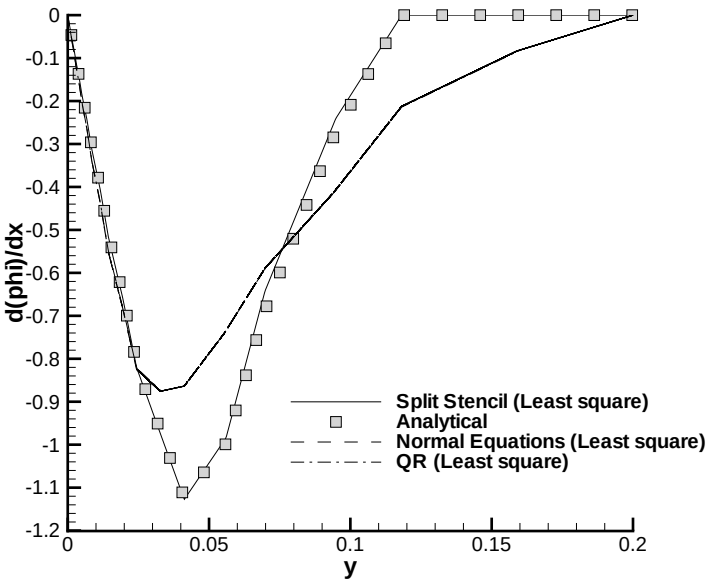

Figure 6.7: Comparison of derivative $\frac{\partial \phi}{\partial x}$ with respect to analytical result.

$$\phi_{yo} = \frac{(\sum \Delta x_i^2)_{N_x}(\sum \Delta\phi_i \Delta y_i)_{N_y} - (\sum \Delta x_i \Delta y_i)_{N_y}(\sum \Delta\phi_i \Delta x_i)_{N_x}}{(\sum \Delta x_i^2)_{N_x}(\sum \Delta y_i^2)_{N_y} - (\sum \Delta x_i \Delta y_i)_{N_x}(\sum \Delta x_i \Delta y_i)_{N_y}} \tag{6.21}$$

Consider a 2-D test case described in section 6.2.3 using highly stretched grid to evaluate gradients of a function,ϕ simulating viscous boundary layer described earlier. As observed earlier because of clustering in y direction the derivative $\frac{\partial \phi}{\partial y}$ is quite accurate. While derivative $\frac{\partial \phi}{\partial x}$ suffers due to ill-conditioning of matrix $\boldsymbol{C}$ caused by stretched distribution. The new method based on split stencil least square gives the most accurate result as it filters off all the points close to y-axis while evaluating x-derivative ϕ_{xo} and filters off all the points close to x-axis while evaluating y-derivative ϕ_{yo}. Fig. 6.7 shows the comparison of derivatives $\frac{\partial \phi}{\partial x}$ using normal equations, QR based least square method and new method using split stencil least square with respect to analytical evaluation. *The present method based on split stencils successfully overcomes the ill-conditioning due to stretched distribution of points while retaining the simplicity of normal equations approach.*

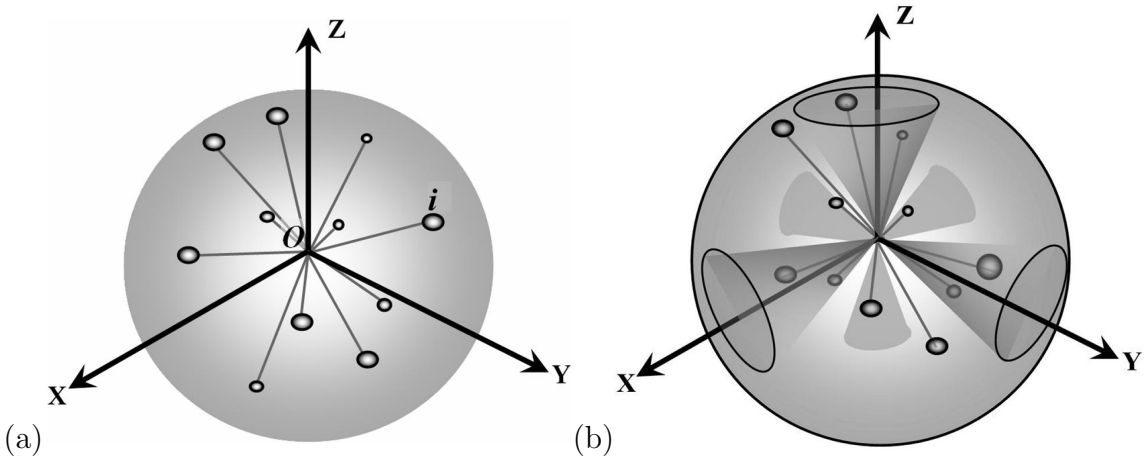

Figure 6.8: Point connectivity for (a)Normal equations based least Square method, and (b)Split-stencil based least Square method

6.3.1 Selection of sub-stencils

Let us consider Ω to be an open domain of $\mathbb{R}^n$, n= 3. Suppose that a continuous function ϕ :$\bar{\Omega}\rightarrow$ $\mathbb{R}$ i.e. it is given at all points $P_i \in \bar{\Omega}$ in a cloud of nodes and ϕ is any function of x, y and z. Also consider a reference node P_o surrounded by m points defined as connectivity $N(P_o)$ =$\{\forall P_i : d(P_o, P_i) < h \}$ as shown in Figure 6.8(a). The new method splits the set of neighbours $N(P_o)$ for node P_o so as to resolve the derivatives for highly stretched cloud of points. We are interested in finding the derivatives of ϕ at all the nodes. As described earlier, existing least square method follows normal equations approach where $\|\boldsymbol{A}_N\boldsymbol{\Phi}_o-\boldsymbol{\Delta\phi}_N\|_2$ is minimized for stencil $N(P_o)$. Whereas, the new method using split stencils minimizes $\|\boldsymbol{A}_{N_x}\boldsymbol{\Phi}_o - \boldsymbol{\Delta\phi}_{N_x}\|_2$, $\|\boldsymbol{A}_{N_y}\boldsymbol{\Phi}_o - \boldsymbol{\Delta\phi}_{N_y}\|_2$ and $\|\boldsymbol{A}_{N_z}\boldsymbol{\Phi}_o - \boldsymbol{\Delta\phi}_{N_z}\|_2$ with respect to ϕ_{xo}, ϕ_{yo} and ϕ_{zo} respectively for each carefully selected sub-stencils $N_x(P_o) \in \mathbb{R}^{m_x}$, $N_y(P_o) \in \mathbb{R}^{m_y}$, $N_z(P_o) \in \mathbb{R}^{m_z}$ and $\boldsymbol{\Delta\phi}_{N_\alpha} = [\Delta\phi_1, \Delta\phi_2, \cdots, \Delta\phi_{m_\alpha}]^T \in \mathbb{R}^{m_\alpha}$ where α= x,y and z. For example matrix $\boldsymbol{A}_{N_x} \in \mathbb{R}^{m_x\times n} \subset \boldsymbol{A}_N$ contains entries of only those nodes which have Δy and Δz tending to zero such that sub-stencil $N_x(P_o) \subset N(P_o)$ contains m_x nodes. Similarly, sub-stencil $N_y(P_o) \subset N(P_o)$ contains m_y nodes forms matrix $\boldsymbol{A}_{N_y} \in \mathbb{R}^{m_y\times n} \subset \boldsymbol{A}_N$ and sub-stencil $N_z(P_o) \subset N(P_o)$ contains m_z nodes forms matrix $\boldsymbol{A}_{N_z} \in \mathbb{R}^{m_z\times n} \subset \boldsymbol{A}_N$. Expressing $\|\boldsymbol{A}_{N_\alpha}\boldsymbol{\Phi}_o-\boldsymbol{\Delta\phi}_{N_\alpha}\|_2$ where α= x,y and z as a dot-product in terms of transpose and matrix multipli-

cation

$$\begin{aligned}&(\boldsymbol{A}_{N_\alpha}\boldsymbol{\Phi}_o - \boldsymbol{\Delta\phi}_{N_\alpha})^T(\boldsymbol{A}_{N_\alpha}\boldsymbol{\Phi}_o - \boldsymbol{\Delta\phi}_{N_\alpha})\\ = \boldsymbol{A}_{N_\alpha}^T\boldsymbol{\Phi}_o^T\boldsymbol{A}_{N_\alpha}\boldsymbol{\Phi}_o - \boldsymbol{A}_{N_\alpha}^T\boldsymbol{\Phi}_o^T\boldsymbol{\Delta\phi}_{N_\alpha} - \boldsymbol{\Delta\phi}_{N_\alpha}^T\boldsymbol{A}_{N_\alpha}\boldsymbol{\Phi}_o + \boldsymbol{\Delta\phi}_{N_\alpha}^T\boldsymbol{\Delta\phi}_{N_\alpha}\end{aligned} \tag{6.22}$$

Minimization of the 2-norm $(\boldsymbol{A}_{N_\alpha}\boldsymbol{\Phi}_o - \boldsymbol{\Delta\phi}_{N_\alpha})^T(\boldsymbol{A}_{N_\alpha}\boldsymbol{\Phi}_o - \boldsymbol{\Delta\phi}_{N_\alpha})$ with respect to its gradient $\phi_{\alpha o}$ where α= x,y and z using matrix calculus leads to

$$\left(\sum_\alpha \boldsymbol{\Lambda}_\alpha \boldsymbol{A}_{N_\alpha}^T\boldsymbol{A}_{N_\alpha}\right)\boldsymbol{\Phi}_o = \sum_\alpha \boldsymbol{\Lambda}_\alpha\boldsymbol{A}_{N_\alpha}^T\boldsymbol{\Delta\phi}_{N_\alpha} \Leftrightarrow \boldsymbol{C}\boldsymbol{\Phi}_o = \boldsymbol{\Delta\phi}_{N_{xyz}} \tag{6.23}$$

where $\boldsymbol{C} = \boldsymbol{\Lambda}_x\boldsymbol{A}_{N_x}^T\boldsymbol{A}_{N_x} + \boldsymbol{\Lambda}_y\boldsymbol{A}_{N_y}^T\boldsymbol{A}_{N_y} + \boldsymbol{\Lambda}_z\boldsymbol{A}_{N_z}^T\boldsymbol{A}_{N_z}$ and $\boldsymbol{\Delta\phi}_{N_{xyz}} = \boldsymbol{\Lambda}_x\boldsymbol{A}_{N_x}^T\boldsymbol{\Delta\phi}_{N_x}$ $+ \boldsymbol{\Lambda}_y\boldsymbol{A}_{N_y}^T\boldsymbol{\Delta\phi}_{N_y} + \boldsymbol{\Lambda}_z\boldsymbol{A}_{N_z}^T\boldsymbol{\Delta\phi}_{N_z}$ with diagonal matrices $\boldsymbol{\Lambda}_x$, $\boldsymbol{\Lambda}_y$ and $\boldsymbol{\Lambda}_z \in \mathbb{R}^{n\times n}$. The diagonal matrices are subsets of Identity matrix, $\boldsymbol{I}$ such that $\boldsymbol{\Lambda}_x$+$\boldsymbol{\Lambda}_y$+$\boldsymbol{\Lambda}_z$ = $\boldsymbol{I}$ with $\boldsymbol{\Lambda}_x \equiv diag(1,0,0)$, $\boldsymbol{\Lambda}_y \equiv diag(0,1,0)$ and $\boldsymbol{\Lambda}_z \equiv diag(0,0,1)$. For example matrices $\boldsymbol{\Lambda}_x\boldsymbol{A}_{N_x}^T$ and $\boldsymbol{A}_{N_x}$ can be expressed as

$$\begin{aligned}\boldsymbol{\Lambda}_x\boldsymbol{A}_{N_x}^T &= \begin{bmatrix}\Delta x_1 & \Delta x_2 & \cdots & \Delta x_{m_x}\\ 0 & 0 & \cdots & 0\\ 0 & 0 & \cdots & 0\end{bmatrix}\\ \boldsymbol{A}_{N_x} &= \begin{bmatrix}\Delta x_1 & \Delta y_1 & \Delta z_1\\ \Delta x_2 & \Delta y_2 & \Delta z_2\\ \cdots & \cdots & \cdots\\ \Delta x_{m_x} & \Delta y_{m_x} & \Delta z_{m_x}\end{bmatrix}\end{aligned} \tag{6.24}$$

Matrices $\boldsymbol{\Lambda}_y\boldsymbol{A}_{N_y}^T$ and $\boldsymbol{A}_{N_y}$ can be expressed as

$$\begin{aligned}\boldsymbol{\Lambda}_x\boldsymbol{A}_{N_y}^T &= \begin{bmatrix}0 & 0 & \cdots & 0\\ \Delta y_1 & \Delta y_2 & \cdots & \Delta y_{m_y}\\ 0 & 0 & \cdots & 0\end{bmatrix}\\ \boldsymbol{A}_{N_y} &= \begin{bmatrix}\Delta x_1 & \Delta y_1 & \Delta z_1\\ \Delta x_2 & \Delta y_2 & \Delta z_2\\ \cdots & \cdots & \cdots\\ \Delta x_{m_y} & \Delta y_{m_y} & \Delta z_{m_y}\end{bmatrix}\end{aligned} \tag{6.25}$$

Similarly, matrices $\boldsymbol{\Lambda}_z\boldsymbol{A}_{N_z}^T$ and $\boldsymbol{A}_{N_z}$ can be expressed as

$$\begin{aligned}\boldsymbol{\Lambda}_z\boldsymbol{A}_{N_z}^T &= \begin{bmatrix}0 & 0 & \cdots & 0\\ 0 & 0 & \cdots & 0\\ \Delta z_1 & \Delta z_2 & \cdots & \Delta z_{m_z}\end{bmatrix}\\ \boldsymbol{A}_{N_z} &= \begin{bmatrix}\Delta x_1 & \Delta y_1 & \Delta z_1\\ \Delta x_2 & \Delta y_2 & \Delta z_2\\ \cdots & \cdots & \cdots\\ \Delta x_{m_z} & \Delta y_{m_z} & \Delta z_{m_z}\end{bmatrix}\end{aligned} \tag{6.26}$$

The cross product matrix $\boldsymbol{C} = \boldsymbol{\Lambda}_x \boldsymbol{A}_{N_x}^T \boldsymbol{A}_{N_x} + \boldsymbol{\Lambda}_y \boldsymbol{A}_{N_y}^T \boldsymbol{A}_{N_y} + \boldsymbol{\Lambda}_z \boldsymbol{A}_{N_z}^T \boldsymbol{A}_{N_z}$ is given as

$$\boldsymbol{C} = \begin{bmatrix} (\sum \Delta x_i^2)_{N_x} & (\sum \Delta x_i \Delta y_i)_{N_x} & (\sum \Delta x_i \Delta z_i)_{N_x} \\ (\sum \Delta x_i \Delta y_i)_{N_y} & (\sum \Delta y_i^2)_{N_y} & (\sum \Delta y_i \Delta z_i)_{N_y} \\ (\sum \Delta x_i \Delta z_i)_{N_z} & (\sum \Delta y_i \Delta z_i)_{N_z} & (\sum \Delta z_i^2)_{N_z} \end{bmatrix} \tag{6.27}$$

The expressions $(\cdot)_{N_x}$, $(\cdot)_{N_y}$ and $(\cdot)_{N_z}$ requires values evaluated using sub-stencils $N_x(P_o)$, $N_y(P_o)$ and $N_z(P_o)$. With the proper choice of sub-stencils N_x, N_y and N_z we can make the matrix $\boldsymbol{C}$ diagonally dominant and off-diagonal terms very small.

When upwind scheme is implemented based on positive and negative stencil split to account signal propagation we have to further split the stencil. Thus in upwind split stencil based least square method the basic stencil $N(P_o)$ gets divided into 6 different kind of upwind sub-stencils : $N_x^+(P_o)$, $N_x^-(P_o)$, $N_y^+(P_o)$, $N_y^-(P_o)$, $N_z^+(P_o)$ and $N_z^-(P_o)$ as shown in Fig. 6.8(b). For example connectivity parameters $\mathbb{S}_{yx}$ and $\mathbb{S}_{zx}$ define conical sub-stencils $N_x^{\pm}(P_o)$ such that $\left|\frac{\Delta y_i}{\Delta x_i}\right| = s_{yx_i} \leq \mathbb{S}_{yx}$ and $\left|\frac{\Delta z_i}{\Delta x_i}\right| = s_{zx_i} \leq \mathbb{S}_{zx}$ as follows:

$$\begin{aligned} N_x^+(P_o) =& \left\{ \forall P_i : P_i \in N(P_o) \exists \Delta x_i \leq 0, s_{yx_i} \leq \mathbb{S}_{yx}, s_{zxi} \leq \mathbb{S}_{zx} \right\} \\ N_x^-(P_o) =& \left\{ \forall P_i : P_i \in N(P_o) \exists \Delta x_i \geq 0, s_{yx_i} \leq \mathbb{S}_{yx}, s_{zxi} \leq \mathbb{S}_{zx} \right\} \end{aligned} \tag{6.28}$$

Connectivity parameters $\mathbb{S}_{xy}$ and $\mathbb{S}_{zy}$ define conical sub-stencils $N_y^{\pm}(P_o)$ such that $\left|\frac{\Delta x_i}{\Delta y_i}\right| = s_{xy_i} \leq \mathbb{S}_{xy}$ and $\left|\frac{\Delta z_i}{\Delta y_i}\right| = s_{zy_i} \leq \mathbb{S}_{zy}$. Conical sub-stencils $N_y^{\pm}(P_o)$ is defined as follows

$$\begin{aligned} N_y^+(P_o) =& \left\{ \forall P_i : P_i \in N(P_o) \exists \Delta y_i \leq 0, s_{xy_i} \leq \mathbb{S}_{xy}, s_{zy_i} \leq \mathbb{S}_{zy} \right\} \\ N_y^-(P_o) =& \left\{ \forall P_i : P_i \in N(P_o) \exists \Delta y_i \geq 0, s_{xy_i} \leq \mathbb{S}_{xy}, s_{zy_i} \leq \mathbb{S}_{zy} \right\} \end{aligned} \tag{6.29}$$

Similarly, connectivity parameters $\mathbb{S}_{xz}$ and $\mathbb{S}_{yz}$ define conical sub-stencils $N_z^{\pm}(P_o)$ such that $\left|\frac{\Delta x_i}{\Delta z_i}\right| = s_{xzi} \leq \mathbb{S}_{xz}$ and $\left|\frac{\Delta y_i}{\Delta z_i}\right| = s_{yz_i} \leq \mathbb{S}_{yz}$. Conical sub-stencils $N_z^{\pm}(P_o)$ is defined as follows

$$\begin{aligned} N_z^+(P_o) =& \left\{ \forall P_i : P_i \in N(P_o) \exists \Delta z_i \leq 0, s_{xzi} \leq \mathbb{S}_{xz}, s_{yz_i} \leq \mathbb{S}_{yz} \right\} \\ N_z^-(P_o) =& \left\{ \forall P_i : P_i \in N(P_o) \exists \Delta z_i \geq 0, s_{xzi} \leq \mathbb{S}_{xz}, s_{yz_i} \leq \mathbb{S}_{yz} \right\} \end{aligned} \tag{6.30}$$

Minimization of the $\|\boldsymbol{A}_{N_\alpha}\boldsymbol{\Phi}_o - \boldsymbol{\Delta\phi}_{N_\alpha}\|_2$ with respect to its gradient $\boldsymbol{\phi}_{\alpha o}$ where α= x,y and z leads to $\boldsymbol{C\Phi}_o = \boldsymbol{\Delta\phi}_{N_{xyz}}$ as follows:

$$\underbrace{\Delta r_{xyz}\begin{bmatrix} 1 & \frac{\left(\sum \Delta x_i^2 s_{yx\,i}\right)_{N_x^\pm}}{\left(\sum \Delta x_i^2\right)_{N_x^\pm}} & \frac{\left(\sum \Delta x_i^2 s_{zx\,i}\right)_{N_x^\pm}}{\left(\sum \Delta x_i^2\right)_{N_x^\pm}} \\ \frac{\left(\sum \Delta y_i^2 s_{xy\,i}\right)_{N_y^\pm}}{\left(\sum \Delta y_i^2\right)_{N_y^\pm}} & 1 & \frac{\left(\sum \Delta y_i^2 s_{zy\,i}\right)_{N_y^\pm}}{\left(\sum \Delta y_i^2\right)_{N_y^\pm}} \\ \frac{\left(\sum \Delta z_i^2 s_{xz\,i}\right)_{N_z^\pm}}{\left(\sum \Delta z_i^2\right)_{N_z^\pm}} & \frac{\left(\sum \Delta z_i^2 s_{yz\,i}\right)_{N_z^\pm}}{\left(\sum \Delta z_i^2\right)_{N_z^\pm}} & 1 \end{bmatrix}}_{\boldsymbol{C}} \underbrace{\begin{bmatrix} \phi_{xo} \\ \phi_{yo} \\ \phi_{zo} \end{bmatrix}}_{\boldsymbol{\Phi}_o} = \underbrace{\begin{bmatrix} \left(\sum \Delta\phi_i \Delta x_i\right)_{N_x^\pm} \\ \left(\sum \Delta\phi_i \Delta y_i\right)_{N_y^\pm} \\ \left(\sum \Delta\phi_i \Delta z_i\right)_{N_z^\pm} \end{bmatrix}}_{\boldsymbol{\Delta\phi}_{N_{xyz}}} \tag{6.31}$$

where $\Delta r_{xyz} = \left(\sum \Delta x_i^2\right)_{N_x^\pm}\left(\sum \Delta y_i^2\right)_{N_y^\pm}\left(\sum \Delta z_i^2\right)_{N_z^\pm}$. The expressions $(\cdot)_{N_x^\pm}$, $(\cdot)_{N_y^\pm}$ and $(\cdot)_{N_z^\pm}$ requires values evaluated using split stencils $N_x^\pm(P_o)$, $N_y^\pm(P_o)$ and $N_z^\pm(P_o)$. When these connectivity parameters $\mathbb{S}_{yx}$, $\mathbb{S}_{zx}$, $\mathbb{S}_{xy}$, $\mathbb{S}_{zy}$, $\mathbb{S}_{xz}$ and $\mathbb{S}_{yz}$ all tend to zero, then the matrix $\boldsymbol{C}$ as shown in Eq. (6.31) is always diagonally dominant and well conditioned as off diagonal terms are very small. When all the connectivity parameters tend to zero split stencil based least square method becomes less dissipative as it approaches the Taylor series based finite difference method.

The new proposed method uses a different approach to solve a least squares problem as it generates the non-symmetric cross-product matrix $\boldsymbol{C} \neq \boldsymbol{A}_N^T\boldsymbol{A}_N$ by suitable selection of sub-stencils such that the matrix is diagonally dominant and well conditioned. In other words split stencil based least square while retaining the simplicity of normal equations approach avoids the ill-conditioning of the matrix $\boldsymbol{C}$ which is the weakness of normal equations approach. The present method like normal equations approach requires $(m+n/3)n^2$ flops as against $2(m-n/3)n^2$ flops required in QR approach for a full rank least squares problem. For large $m \gg n$ the split stencil least square provides stable results involving about half the arithmetic. The kinetic upwind scheme based on least square method using split stencil is called as split stencil least square kinetic upwind method or SLKNS in short.

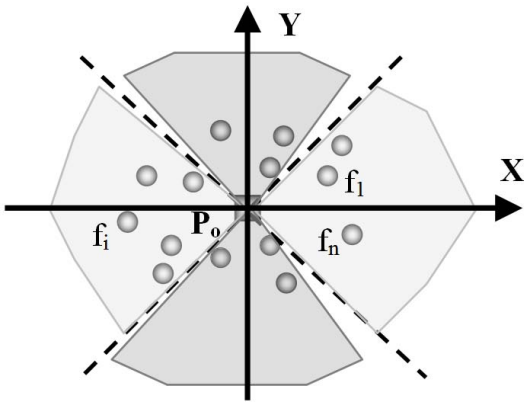

Figure 6.9: Typical split connectivity around point Po

6.3.2 Modified split stencil method (m-SLKNS)

In modified split stencil based least square method the error is normalized by distance component such that error at any point i in the neighbourhood of o gives us

$$ex_i = \frac{e_i}{\Delta x_i} = \frac{\Delta\phi_i}{\Delta x_i} - \phi_{xo} - \frac{\Delta y_i}{\Delta x_i}\phi_{yo} - \frac{\Delta z_i}{\Delta x_i}\phi_{zo} + \cdots \quad i = 1, \cdots, m_x \tag{6.32}$$

$$ey_i = \frac{e_i}{\Delta y_i} = \frac{\Delta\phi_i}{\Delta y_i} - \frac{\Delta x_i}{\Delta y_i}\phi_{xo} - \phi_{yo} - \frac{\Delta z_i}{\Delta y_i}\phi_{zo} + \cdots \quad i = 1, \cdots, m_y \tag{6.33}$$

$$ez_i = \frac{e_i}{\Delta z_i} = \frac{\Delta\phi_i}{\Delta z_i} - \frac{\Delta x_i}{\Delta z_i}\phi_{xo} - \frac{\Delta y_i}{\Delta z_i}\phi_{yo} - \phi_{zo} + \cdots \quad i = 1, \cdots, m_z \tag{6.34}$$

where $\Delta x_i = x_i - x_o$, $\Delta y_i = y_i - y_o$, $\Delta z_i = z_i - z_o$ and $\Delta\phi_i = \phi_i - \phi_o$. Modified split stencil minimizes $\sum \|ex\|_2$, $\sum \|ey\|_2$ and $\sum \|ez\|_2$ with respect to ϕ_{xo}, ϕ_{yo} and ϕ_{zo} respectively for each carefully selected sub-stencils $N_x(P_o) \in \mathbb{R}^{m_x}$, $N_y(P_o) \in \mathbb{R}^{m_y}$ and $N_z(P_o) \in \mathbb{R}^{m_z}$. Thus, modified split stencil is similar to split stencil least square as the basic stencil $N(P_o)$ gets divided into 6 different kind of upwind sub-stencils : $N_x^+(P_o)$, $N_x^-(P_o)$, $N_y^+(P_o)$, $N_y^-(P_o)$, $N_z^+(P_o)$ and $N_z^-(P_o)$ defined by connectivity parameters. To illustrate the derivative calculation consider ϕ to be any function of x, y in two-dimensions with cloud of points with split stencils as shown in Fig. 6.9. Error ex_i for any point P_i using connectivity set $N_x(P_o)$ based on Taylor series around P_o is defined as

$$ex_i = \frac{e_i}{\Delta x_i} = \left(\Delta\phi_i - \phi_{xo} - \frac{\Delta y_i}{\Delta x_i}\phi_{yo}\right) + \cdots \tag{6.35}$$

Similarly, error ey_i for connectivity set $N_y(P_o)$ is defined as

$$ey_i = \frac{e_i}{\Delta y_i} = \left(\Delta\phi_i - \frac{\Delta x_i}{\Delta y_i}\phi_{xo} - \phi_{yo}\right) + \cdots \tag{6.36}$$

Thus we have two sets of the square of error $\sum \|ex\|_2$and $\sum \|ey\|_2$ defined as

$$\sum \|ex\|_2 = \sum_{i=1}^{m_x}\left(\frac{\Delta\phi_i}{\Delta x_i} - \phi_{xo} - \phi_{yo}\frac{\Delta y_i}{\Delta x_i}\right)^2 = \sum_{i=1}^{m_x}\left(\frac{\Delta\phi_i}{\Delta x_i} - \phi_{xo} - \phi_{yo}\eta_i\right)^2 \tag{6.37}$$

$$\sum \|ey\|_2 = \sum_{i=1}^{m_y}\left(\frac{\Delta\phi_i}{\Delta y_i} - \phi_{xo}\frac{\Delta x_i}{\Delta y_i} - \phi_{yo}\right)^2 = \sum_{i=1}^{m_y}\left(\frac{\Delta\phi_i}{\Delta y_i} - \phi_{xo}\frac{1}{\eta_i} - \phi_{yo}\right)^2 \tag{6.38}$$

where slope $\eta_i = \frac{\Delta y_i}{\Delta x_i}$. Minimizing the sum of the squares of error $\sum \|ex\|_2$ and $\sum \|ey\|_2$ with respect to ϕ_{xo} and ϕ_{yo}will lead to $\boldsymbol{C}\boldsymbol{\Phi}_o = \boldsymbol{\Delta\Phi}_{xy}$

$$\boldsymbol{C} = \begin{bmatrix} 1. & \frac{1}{\mathrm{m_x}}\sum_{i=1}^{\mathrm{m_x}}\eta_{\mathrm{i}} \\ \frac{1}{\mathrm{m_y}}\sum_{\mathrm{i}=1}^{m_y}(\eta_i)^{-1} & 1. \end{bmatrix}, \boldsymbol{\Phi}_o = \begin{bmatrix} \phi_{xo} \\ \phi_{yo} \end{bmatrix}, \quad \boldsymbol{\Delta\Phi}_{xy} = \begin{bmatrix} \frac{1}{\mathrm{m_x}}\sum_{i=1}^{m_x}\frac{\Delta\phi_i}{\Delta x_i} \\ \frac{1}{\mathrm{m_y}}\sum_{i=1}^{m_y}\frac{\Delta\phi_i}{\Delta y_i} \end{bmatrix} \tag{6.39}$$

The derivatives ϕ_{xo} and ϕ_{yo}will lead to

$$\begin{aligned} \phi_{xo} &= \frac{\frac{1}{\mathrm{m_x}}\sum_{i=1}^{m_x}\frac{\Delta\phi_i}{\Delta x_i} - \left(\frac{1}{\mathrm{m_x}}\sum_{i=1}^{\mathrm{m_x}}\eta_{\mathrm{i}}\right)\left(\frac{1}{\mathrm{m_y}}\sum_{i=1}^{m_y}\frac{\Delta\phi_i}{\Delta y_i}\right)}{1. - \left(\frac{1}{\mathrm{m_x}}\sum_{i=1}^{\mathrm{m_x}}\eta_{\mathrm{i}}\right)\left(\frac{1}{\mathrm{m_y}}\sum_{\mathrm{i}=1}^{m_y}(\eta_i)^{-1}\right)} \\ \phi_{yo} &= \frac{\frac{1}{\mathrm{m_y}}\sum_{i=1}^{m_y}\frac{\Delta\phi_i}{\Delta y_i} - \left(\frac{1}{\mathrm{m_y}}\sum_{\mathrm{i}=1}^{m_y}\frac{1}{\eta_{\mathrm{i}}}\right)\left(\frac{1}{\mathrm{m_x}}\sum_{i=1}^{m_x}\frac{\Delta\phi_i}{\Delta x_i}\right)}{1. - \left(\frac{1}{\mathrm{m_x}}\sum_{i=1}^{\mathrm{m_x}}\eta_{\mathrm{i}}\right)\left(\frac{1}{\mathrm{m_y}}\sum_{\mathrm{i}=1}^{m_y}(\eta_i)^{-1}\right)} \end{aligned} \tag{6.40}$$

Two eigen values are

$$\lambda_E^{\pm} = 1 \pm \sqrt{\frac{1}{\mathrm{m_x}}\sum_{i=1}^{\mathrm{m_x}}\eta_{\mathrm{i}}\frac{1}{\mathrm{m_y}}\sum_{\mathrm{i}=1}^{m_y}(\eta_i)^{-1}} \tag{6.41}$$

If the chosen split connectivity stencils $N_x(P_o)$ and $N_y(P_o)$ are bounded within a 45 degree line then in such case $\eta_{\mathrm{i}} \leq 1$ for $N_x(P_o)$ and $(\eta_{\mathrm{i}})^{-1} \leq 1$ for $N_y(P_o)$, thus the matrix $\boldsymbol{C}$ is always well-conditioned. Advantage of this method is its low storage requirement as we are only storing the off diagonal terms of the matrix $\boldsymbol{C}$. The second advantage is for each sub-stencils we can assign separate weights. The kinetic upwind scheme is based on this modified form of split stencil based least square method is called as modified split stencil least square kinetic upwind method or m-SLKNS in short.

6.3.3 Higher order of accuracy through defect correction

As described earlier Taylor series expansion of any function ϕ_i at node P_i in the neighbourhood of node P_o will give

$$\begin{aligned}\phi_i = \quad & \phi_o + \Delta x_i\phi_{xo} + \Delta y_i\phi_{yo} + \Delta z_i\phi_{zo} \\ & + \tfrac{\Delta x_i^2}{2}\phi_{xxo} + \tfrac{\Delta y_i^2}{2}\phi_{yyo} + \tfrac{\Delta z_i^2}{2}\phi_{zzo} \\ & + \Delta x_i\Delta y_i\phi_{xyo} + \Delta x_i\Delta z_i\phi_{xzo} + \Delta y_i\Delta z_i\phi_{yzo} + O(h^3)\end{aligned} \tag{6.42}$$

where $O(h)\equiv O(\Delta x, \Delta y, \Delta z)$. For first order accurate derivatives Taylor series is retained upto first order terms as follows

$$\Delta\phi_i^{(0)} = \phi_i - \phi_o = \Delta x_i\phi_{xo} + \Delta y_i\phi_{yo} + \Delta z_i\phi_{zo} + O(h^2) \tag{6.43}$$

The present method of obtaining higher order accuracy using multi-step defect correction over first order derivative is extension of defect correction procedure of Ghosh [92]. In the first step $\mathbf{\Phi}_o^{(1)}$ obtained for node P_o as

$$\underbrace{\begin{bmatrix}\phi_{xo}^{(1)}\\ \phi_{yo}^{(1)}\\ \phi_{zo}^{(1)}\end{bmatrix}}_{\mathbf{\Phi}_o^{(1)}} = \boldsymbol{C}^{-1}\underbrace{\begin{bmatrix}\left(\sum\Delta\phi_i^{(0)}\Delta x_i\right)_{N_x^{\pm}}\\ \left(\sum\Delta\phi_i^{(0)}\Delta y_i\right)_{N_y^{\pm}}\\ \left(\sum\Delta\phi_i^{(0)}\Delta z_i\right)_{N_z^{\pm}}\end{bmatrix}}_{\boldsymbol{\Delta\phi}_{N_{xyz}}^{(0)}} \tag{6.44}$$

The derivatives $\phi_{xi}^{(1)}$, $\phi_{yi}^{(1)}$ and $\phi_{zi}^{(1)}$ can also be expanded in Taylor series as follows

$$\begin{aligned}\Delta\phi_{xi}^{(1)} = \phi_{xi}^{(1)} - \phi_{xo}^{(1)} &= \Delta x_i\phi_{xxo} + \Delta y_i\phi_{xyo} + \Delta z_i\phi_{xzo} + O(h^2)\\ \Delta\phi_{yi}^{(1)} = \phi_{yi}^{(1)} - \phi_{yo}^{(1)} &= \Delta x_i\phi_{yxo} + \Delta y_i\phi_{yyo} + \Delta z_i\phi_{yzo} + O(h^2)\\ \Delta\phi_{zi}^{(1)} = \phi_{zi}^{(1)} - \phi_{zo}^{(1)} &= \Delta x_i\phi_{zxo} + \Delta y_i\phi_{zyo} + \Delta z_i\phi_{zzo} + O(h^2)\end{aligned} \tag{6.45}$$

Using the Taylor series expansion expressed in equation 6.45 we can approximate the second order accurate Taylor series expansion as follows

$$\Delta\phi_i^{(1)} = \Delta\phi_i^{(0)} - \frac{1}{2}\left[\Delta x_i\phi_{xi}^{(1)} + \Delta y_i\phi_{yi}^{(1)} + \Delta z_i\phi_{zi}^{(1)}\right] + O(h^3) \tag{6.46}$$

Once the first order derivatives $\phi_{xi}^{(1)}$, $\phi_{yi}^{(1)}$ and $\phi_{zi}^{(1)}$ are available we calculate the defect corrected first order accurate $\Delta\phi_i^{(1)}$ to obtain second order accurate deriva-

tives as follows

$$\underbrace{\begin{bmatrix} \phi_{xo}^{(2)} \\ \phi_{yo}^{(2)} \\ \phi_{zo}^{(2)} \end{bmatrix}}_{\boldsymbol{\Phi}_o^{(2)}} = \boldsymbol{C}^{-1} \underbrace{\begin{bmatrix} \left(\sum \Delta\phi_i^{(1)} \Delta x_i\right)_{N_x^{\pm}} \\ \left(\sum \Delta\phi_i^{(1)} \Delta y_i\right)_{N_y^{\pm}} \\ \left(\sum \Delta\phi_i^{(1)} \Delta z_i\right)_{N_z^{\pm}} \end{bmatrix}}_{\boldsymbol{\Delta\phi}_{N_{xyz}}^{(1)}} \tag{6.47}$$

Thus, second order accuracy in split stencil is achieved through a two-step defect procedure with inner iterations. The inner iterations further improves the spectral property as well as second order accuracy of the derivative. The defect corrected first order accurate $\Delta\phi_i^{(1),k}$ after k iterations is

$$\Delta\phi_i^{(1),k} = \Delta\phi_i^{(0)} - \frac{1}{2}\left[\Delta x_i \phi_{xi}^{(2),k-1} + \Delta y_i \phi_{yi}^{(2),k-1} + \Delta z_i \phi_{zi}^{(2),k-1}\right] + O(h^3) \tag{6.48}$$

The second order accurate derivative with improved spectral property after k iterations is evaluated as follows

$$\underbrace{\begin{bmatrix} \phi_{xo}^{(2),k} \\ \phi_{yo}^{(2),k} \\ \phi_{zo}^{(2),k} \end{bmatrix}}_{\boldsymbol{\Phi}_o^{(2),k}} = \boldsymbol{C}^{-1} \underbrace{\begin{bmatrix} \left(\sum \Delta\phi_i^{(1),k} \Delta x_i\right)_{N_x^{\pm}} \\ \left(\sum \Delta\phi_i^{(1),k} \Delta y_i\right)_{N_y^{\pm}} \\ \left(\sum \Delta\phi_i^{(1),k} \Delta z_i\right)_{N_z^{\pm}} \end{bmatrix}}_{\boldsymbol{\Delta\phi}_{N_{xyz}}^{(1),k}} \tag{6.49}$$

In order to evaluate third order accurate derivative we need to calculate the Hessian matrix, $\boldsymbol{H}(\phi_0^{(1),k})$ of second order derivatives after k iterations given as follows

$$\underbrace{\begin{bmatrix} \phi_{xxo}^{(1),k} & \phi_{xyo}^{(1),k} & \phi_{xzo}^{(1),k} \\ \phi_{yxo}^{(1),k} & \phi_{yyo}^{(1),k} & \phi_{yzo}^{(1),k} \\ \phi_{zxo}^{(1),k} & \phi_{zyo}^{(1),k} & \phi_{zzo}^{(1),k} \end{bmatrix}}_{\boldsymbol{H}(\phi_0^{(1),k})}$$
$$= \boldsymbol{C}^{-1} \underbrace{\begin{bmatrix} \left(\sum \Delta\phi_{xi}^{(2),k} \Delta x_i\right)_{N_x^{\pm}} & \left(\sum \Delta\phi_{yi}^{(2),k} \Delta x_i\right)_{N_x^{\pm}} & \left(\sum \Delta\phi_{zi}^{(2),k} \Delta x_i\right)_{N_x^{\pm}} \\ \left(\sum \Delta\phi_{xi}^{(2),k} \Delta y_i\right)_{N_y^{\pm}} & \left(\sum \Delta\phi_{yi}^{(2),k} \Delta y_i\right)_{N_y^{\pm}} & \left(\sum \Delta\phi_{zi}^{(2),k} \Delta y_i\right)_{N_y^{\pm}} \\ \left(\sum \Delta\phi_{xi}^{(2),k} \Delta z_i\right)_{N_z^{\pm}} & \left(\sum \Delta\phi_{yi}^{(2),k} \Delta z_i\right)_{N_z^{\pm}} & \left(\sum \Delta\phi_{zi}^{(2),k} \Delta z_i\right)_{N_z^{\pm}} \end{bmatrix}}_{\boldsymbol{\Delta\Phi}_{N_{xyz}}^{(2),k}} \tag{6.50}$$

The defect corrected second accurate $\Delta\phi_i^{(2),k}$ is expressed as

$$\begin{aligned}\Delta\phi_i^{(2),k} &= \Delta\phi_i^{(0)} - \tfrac{1}{2}\left[\Delta x_i\phi_{xi}^{(2),k} + \Delta y_i\phi_{yi}^{(2),k} + \Delta z_i\phi_{zi}^{(2),k}\right] \\ &+\tfrac{1}{12}\left[\Delta x_i^2\phi_{xxi}^{(1),k} + \Delta y_i^2\phi_{yyi}^{(1),k} + \Delta z_i^2\phi_{zzi}^{(1),k}\right] \\ &+\tfrac{1}{6}\left[\Delta x_i\Delta y_i\frac{\phi_{xyi}^{(1),k}+\phi_{yxi}^{(1),k}}{2} + \Delta y_i\Delta z_i\frac{\phi_{yzi}^{(1),k}+\phi_{zyi}^{(1),k}}{2} + \Delta x_i\Delta z_i\frac{\phi_{xzi}^{(1),k}+\phi_{zxi}^{(1),k}}{2}\right] + O(h^4)\end{aligned} \tag{6.51}$$

It should be noted that cross derivatives ϕ_{xyi}, ϕ_{xzi} are evaluated using stencil $N_x^{\pm}$ whereas ϕ_{yxi} and ϕ_{yzi} is evaluated using stencil $N_y^{\pm}$. Similarly, cross derivatives ϕ_{zxi} and ϕ_{zyi} are evaluated using stencil $N_z^{\pm}$. Third order accurate derivatives after k inner iterations can now be written as

$$\underbrace{\begin{bmatrix}\phi_{xo}^{(3),k}\\ \phi_{yo}^{(3),k}\\ \phi_{zo}^{(3),k}\end{bmatrix}}_{\boldsymbol{\Phi}_o^{(3),k}} = \boldsymbol{C}^{-1}\underbrace{\begin{bmatrix}\left(\sum\Delta\phi_i^{(2),k}\Delta x_i\right)_{N_x^{\pm}}\\ \left(\sum\Delta\phi_i^{(2),k}\Delta y_i\right)_{N_y^{\pm}}\\ \left(\sum\Delta\phi_i^{(2),k}\Delta z_i\right)_{N_z^{\pm}}\end{bmatrix}}_{\boldsymbol{\Delta\phi}_{Nxyz}^{(2),k}} \tag{6.52}$$

6.3.4 Implementation of SLKNS

The following subsection describes the implementation of split-stencil least square kinetic upwind method (SLKNS). To illustrate the implementation of SLKNS two dimensional case has been taken up as one dimensional derivation fails to provide a complete picture. As described earlier in kinetic upwind method the distribution function at time $t+\Delta t$ in a fluid domain for two dimensional case with first order Chapman-Enskog distribution is constructed based on half range distribution using x-split and y-split stencils as follows

$$f_1^{t+\Delta t} = f_1^t - \Delta t\begin{bmatrix}\left(\frac{\partial v_x f_1^{+\cdot}}{\partial x}\right)_{N_x^{+\cdot}(P_o)}^t + \left(\frac{\partial v_x f_1^{-\cdot}}{\partial x}\right)_{N_x^{-\cdot}(P_o)}^t\\ +\left(\frac{\partial v_y f_1^{\cdot+}}{\partial y}\right)_{N_y^{\cdot+}(P_o)}^t + \left(\frac{\partial v_y f_1^{\cdot-}}{\partial y}\right)_{N_y^{\cdot-}(P_o)}^t\end{bmatrix} \tag{6.53}$$

where the superscript over first order distribution f_1 represents its evaluation based on half range and full range components of molecular velocities. The propagation of information to node P_o depends upon location of node P_i relative to P_o and the signs of v_x and v_y . If $v_x > 0$ then only the nodes to the left of P_o

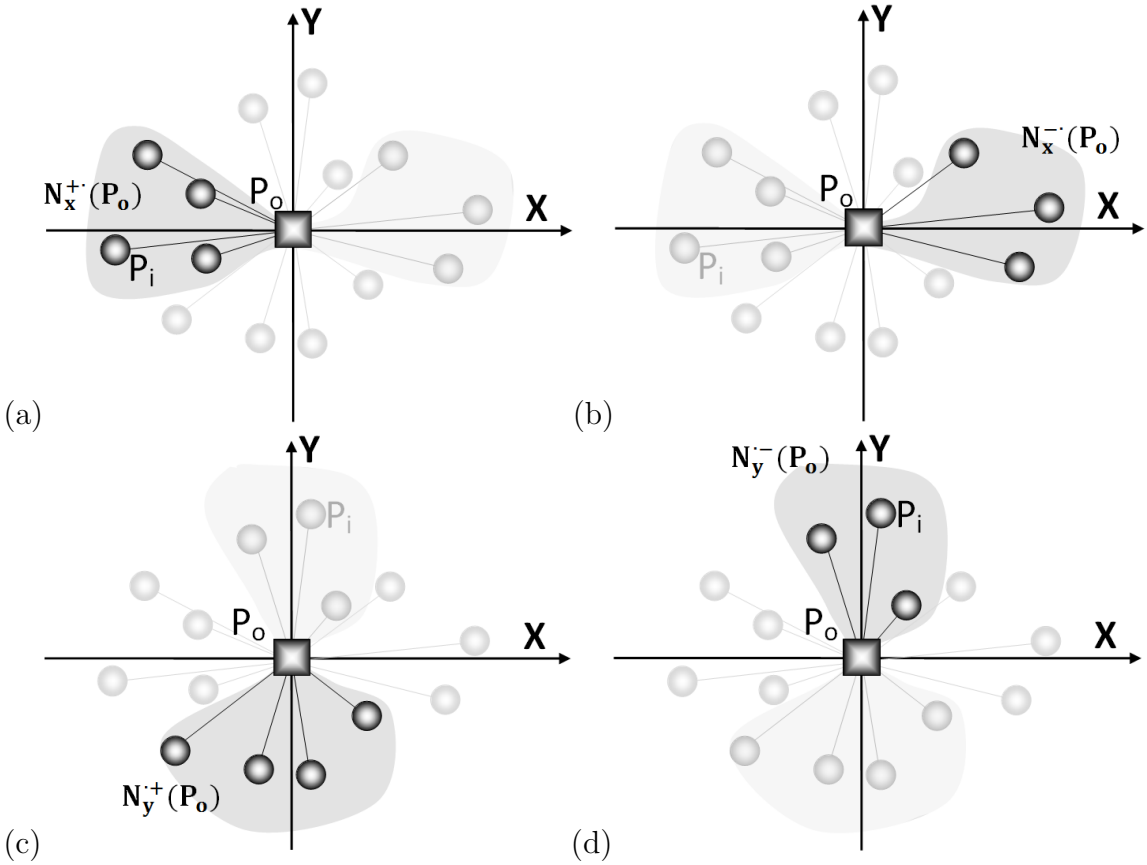

Figure 6.10: Split-stencil least square kinetic upwind method (SLKNS) (a) positive x-split, (b) negative x-split, (c) positive y-split, and (d) negative y-split connectivity for upwind implementation.

belonging to connectivity $N_x^{+\cdot}(P_o)$ will influence the solution at P_o as shown in Figure 6.10(a). Similarly, if $v_x < 0$ then only the nodes to the right of P_o belonging to connectivity $N_x^{-\cdot}(P_o)$ will influence the solution at P_o as shown in Figure 6.10(b). Similar arguments show that for $v_y > 0$ the node below P_o and for $v_y < 0$ the node above P_o will influence the solution at P_o belonging to connectivity sets $N_y^{\cdot+}(P_o)$ and $N_y^{\cdot-}(P_o)$ respectively as shown in Figure 6.10(c) and (d). Kinetic upwind scheme accounts this signal propagation property, two-dimensional upwind discretized Boltzmann equation after taking $\boldsymbol{\Psi}$-moments simplifies to

$$\begin{aligned}\left\langle \boldsymbol{\Psi}, f_1^{t+\Delta t} \right\rangle &= \langle \boldsymbol{\Psi}, f_1^t \rangle \\ &-\Delta t \left[\begin{array}{l} \left(\frac{\partial \left\langle \boldsymbol{\Psi}, v_x f_1^{+\cdot} \right\rangle}{\partial x} \right)^t_{N_x^{+\cdot}(P_o)} + \left(\frac{\partial \left\langle \boldsymbol{\Psi}, v_x f_1^{-\cdot} \right\rangle}{\partial x} \right)^t_{N_x^{-\cdot}(P_o)} \\ + \left(\frac{\partial \left\langle \boldsymbol{\Psi}, v_y f_1^{\cdot+} \right\rangle}{\partial y} \right)^t_{N_y^{\cdot+}(P_o)} + \left(\frac{\partial \left\langle \boldsymbol{\Psi}, v_y f_1^{\cdot-} \right\rangle}{\partial y} \right)^t_{N_y^{\cdot-}(P_o)} \end{array} \right] \end{aligned} \tag{6.54}$$

Taking Ψ moment leads to split flux Navier-Stokes state update equations for iteration $k+1$ as follows

$$\boldsymbol{U}^{k+1} = \boldsymbol{U}^k - \Delta t \left[\begin{array}{l} \left(\frac{\partial \boldsymbol{GX}^{+\cdot}}{\partial x} \right)^k_{N_x^{+\cdot}(P_o)} + \left(\frac{\partial \boldsymbol{GX}^{-\cdot}}{\partial x} \right)^k_{N_x^{-\cdot}(P_o)} \\ + \left(\frac{\partial \boldsymbol{GY}^{\cdot+}}{\partial y} \right)^k_{N_y^{\cdot+}(P_o)} + \left(\frac{\partial \boldsymbol{GY}^{\cdot-}}{\partial y} \right)^k_{N_y^{\cdot-}(P_o)} \end{array} \right] \tag{6.55}$$

where split fluxes $\boldsymbol{GX}^{\pm\cdot}$ and $\boldsymbol{GY}^{\cdot\pm}$ are represented as $\boldsymbol{GX}^{\pm}$ and $\boldsymbol{GY}^{\pm}$ respectively for the sake of brevity. The expressions of these flux terms are given in Appendix D. The state update can also be expressed as

$$\boldsymbol{U}^{k+1} = \boldsymbol{U}^k - \Delta t \left[\begin{array}{l} \left(\frac{\partial \boldsymbol{GX}^{+}}{\partial x} \right)^k_{\Delta x<0} + \left(\frac{\partial \boldsymbol{GX}^{-}}{\partial x} \right)^k_{\Delta x>0} \\ + \left(\frac{\partial \boldsymbol{GY}^{+}}{\partial y} \right)^k_{\Delta y<0} + \left(\frac{\partial \boldsymbol{GY}^{-}}{\partial y} \right)^k_{\Delta y>0} \end{array} \right] \tag{6.56}$$

The upwind treatment of the viscous term is required for effective capture of cross phenomena of thermal transpiration or thermal creep and the mechanocalorific effect.

Similarly, 3-D split flux Navier-Stokes state update equations for iteration $k+1$

can be written as

$$\boldsymbol{U}^{k+1} = \boldsymbol{U}^k - \Delta t \left[\begin{array}{l} \left(\frac{\partial \boldsymbol{GX}^{+\cdot\cdot}}{\partial x}\right)^k_{N_x^{+\cdot\cdot}(P_o)} + \left(\frac{\partial \boldsymbol{GX}^{-\cdot\cdot}}{\partial x}\right)^k_{N_x^{-\cdot\cdot}(P_o)} \\ + \left(\frac{\partial \boldsymbol{GY}^{\cdot+\cdot}}{\partial y}\right)^k_{N_y^{\cdot+\cdot}(P_o)} + \left(\frac{\partial \boldsymbol{GY}^{\cdot-\cdot}}{\partial y}\right)^k_{N_y^{\cdot-\cdot}(P_o)} \\ + \left(\frac{\partial \boldsymbol{GZ}^{\cdot\cdot+}}{\partial z}\right)^k_{N_z^{\cdot\cdot+}(P_o)} + \left(\frac{\partial \boldsymbol{GZ}^{\cdot\cdot-}}{\partial z}\right)^k_{N_y^{\cdot\cdot-}(P_o)} \end{array} \right] \tag{6.57}$$

where split fluxes $\boldsymbol{GX}^{\pm\cdot\cdot}$, $\boldsymbol{GY}^{\cdot\pm\cdot}$ and $\boldsymbol{GZ}^{\cdot\cdot\pm}$ are represented as $\boldsymbol{GX}^{\pm}$, $\boldsymbol{GY}^{\pm}$ and $\boldsymbol{GZ}^{\pm}$ respectively for the sake of brevity. The state update can also be expressed as

$$\boldsymbol{U}^{k+1} = \boldsymbol{U}^k - \Delta t \left[\begin{array}{l} \left(\frac{\partial \boldsymbol{GX}^{+}}{\partial x}\right)^k_{\Delta x<0} + \left(\frac{\partial \boldsymbol{GX}^{-}}{\partial x}\right)^k_{\Delta x>0} \\ + \left(\frac{\partial \boldsymbol{GY}^{+}}{\partial y}\right)^k_{\Delta y<0} + \left(\frac{\partial \boldsymbol{GY}^{-}}{\partial y}\right)^k_{\Delta y>0} \\ + \left(\frac{\partial \boldsymbol{GZ}^{+}}{\partial z}\right)^k_{\Delta z<0} + \left(\frac{\partial \boldsymbol{GZ}^{-}}{\partial z}\right)^k_{\Delta z>0} \end{array} \right] \tag{6.58}$$

In order to maintain the stability during explicit time integration the CFL time step is determined by inviscid, viscous and slip time steps as follows

$$\Delta t \leq \left[\frac{1}{\Delta t_I} + \frac{1}{\Delta t_V} + \frac{1}{\Delta t_S} \right]^{-1} \tag{6.59}$$

where Δt_I is the inviscid time step based on detailed stability analysis [92]

$$\Delta t_I \leq \underset{i \in N(P_o)}{Min} \; | \frac{d(P_i, P_o)}{(\sqrt{u_x^2 + u_y^2 + u_z^2 + 3RT})_i} | \tag{6.60}$$

where $d(P_i, P_o)$ is the distance between points P_i and P_o. The viscous time step Δt_V is adapted for meshless method given as

$$\Delta t_V = \frac{\rho \, \mathrm{Pr} \, d(P_i, P_o)_{min}}{4\mu\gamma} \tag{6.61}$$

where Pr is the Prandtl number and $d(P_i, P_o)_{min}$ is the minimum distance between points P_i and P_o. The slip time step is given by

$$\Delta t_S = \frac{\lambda}{v_{th}} \tag{6.62}$$

where λ is the mean free path and $v_{th} = 1/\sqrt{\beta}$ is the most probable molecular thermal speed.

The Navier-Stokes equations in the unsteady state form is obtained by marching in time till residual falls below a specified tolerance. For an equation

$$\frac{d\boldsymbol{U}}{dt} = \mathcal{R}(\boldsymbol{U}^k) \tag{6.63}$$

A single stage Euler time step gives

$$\boldsymbol{U}^{k+1} = \boldsymbol{U}^k + \Delta t \mathcal{R}(\boldsymbol{U}^k) \tag{6.64}$$

The linear stability requirement for the hyperbolic problems leads to a bounded ratio between the time step Δt and the spatial mesh size Δx. As a consequence regardless of higher order spatial accuracy one gets only global first order accuracy for the scheme. Higher order accuracy in time is required while still maintaining this stability. For this we require a strong stability preserving (SSP) and positivity preserving high order time discretization method. SSP time discretization is also required for hyperbolic problems with shocks because each intermediate stage solution is non-oscillatory. The present work also uses a 3-stage scheme of Shu and Osher [249] which is one such SSP higher order time discretization written as follows

$$\begin{aligned}
\boldsymbol{U}^{(0)} &= \boldsymbol{U}^k \\
\boldsymbol{U}^{(1)} &= \boldsymbol{U}^k + \Delta t \mathcal{R}(\boldsymbol{U}^{(0)}) \\
\boldsymbol{U}^{(2)} &= \tfrac{3}{4}\boldsymbol{U}^k + \tfrac{1}{4}\left(\boldsymbol{U}^{(1)} + \Delta t \mathcal{R}(\boldsymbol{U}^{(1)})\right) \\
\boldsymbol{U}^{(3)} &= \tfrac{1}{3}\boldsymbol{U}^k + \tfrac{2}{3}\left(\boldsymbol{U}^{(2)} + \Delta t \mathcal{R}(\boldsymbol{U}^{(2)})\right) \\
\boldsymbol{U}^{k+1} &= \boldsymbol{U}^{(3)}
\end{aligned} \tag{6.65}$$

where Δt is the CFL time step. It can be observed that each stage in the scheme is a convex combination of an explicit Euler step, thus it retains strong stability properties. Convergence is evaluated as L_2 norm of change in state vector as follows

$$Res_2^k = \frac{1}{N_{cloud}} \sum_{i=1}^{N_{cloud}} \left(\frac{1}{D+2} \sum_{j}^{D+2} (U_j^{k+1}(i) - U_j^k(i))^2 \right)^{1/2} \tag{6.66}$$

where Res_2^k is the residue based on L_2 norm at k^{th} iteration, N_{cloud} is the number of points in the cloud, $D + 2$ is number of components of the state vector $\boldsymbol{U}$

e.g. for 2D geometry we have 4 components of the state vector and for 3D we have 5 components. The term $U_j^k(i)$ is the j^{th} component of the state vector at iteration k for point i. For convergence residue Res_2^k as well as normalized residue $\bar{Res}_2^k = Res_2^k/Res_2^0$ are monitored and time stepping is continued till the residue undergoes atleast 5 decades fall or it falls below a specified tolerance.

6.3.5 Implementation of SLKNS for kinetic slip boundary condition.

As described earlier with an accommodation coefficient σ, distribution function can be written as

$$f_\Sigma = f_I + (1-\sigma) f_R + \sigma f_{0,W} \tag{6.67}$$

where f_Σ is the distribution function which is a sum of f_I incident distribution, f_R specularly reflected distribution and $f_{0,W}$ which is the diffuse reflected Maxwellian distribution evaluated at the wall conditions. For example the specularly reflected distribution, f_R is reconstructed from incident distribution, f_I for 2-D geometry is as follows

$$f_R(v_x, v_y, \mathbb{I}) = \begin{array}{ll} f_I(v_x, v_y, \mathbb{I}) & for \quad v_y < 0 \\ f_I(v_x, -v_y, \mathbb{I}) & for \quad v_y > 0 \end{array} \tag{6.68}$$

The distribution $f_{0,W}$ is constructed based on conservation of mass at the wall written as

$$\int_{\mathbb{R}^+}\int_{\mathbb{R}^-}\int_{\mathbb{R}} v_y f_I^{\cdot -} dv_x dv_y d\mathbb{I} + \int_{\mathbb{R}^+}\int_{\mathbb{R}^+}\int_{\mathbb{R}} v_y f_{0,W}^{\cdot +} dv_x dv_y d\mathbb{I} = 0 \tag{6.69}$$

where $f_I^{\cdot -}$ is the half-range incident distribution function for $-\infty < v_x < +\infty$ and $-\infty < v_y < 0$ and similarly $f_{0,W}^{\cdot +}$ is the half-range Maxwellian distribution function for $-\infty < v_x < +\infty$ and $0 < v_y < \infty$. The distribution function at time $t + \Delta t$ at the boundary for two dimensional case with first order Chapman-Enskog distribution is constructed based on half range distribution using x-split and y-split stencils as follows

$$f_{1,\Sigma}^{t+\Delta t} = f_{1,\Sigma}^{t} - \Delta t \left[\begin{array}{l} \left(\frac{\partial v_x f_{1,\Sigma}^{+-}}{\partial x}\right)^t_{N_x^{+-}(P_o)} + \left(\frac{\partial v_x f_{1,\Sigma}^{--}}{\partial x}\right)^t_{N_x^{--}(P_o)} \\ + \left(\frac{\partial v_y f_{1,\Sigma}^{\cdot -}}{\partial y}\right)^t_{N_y^{\cdot -}(P_o)} \end{array} \right] \tag{6.70}$$

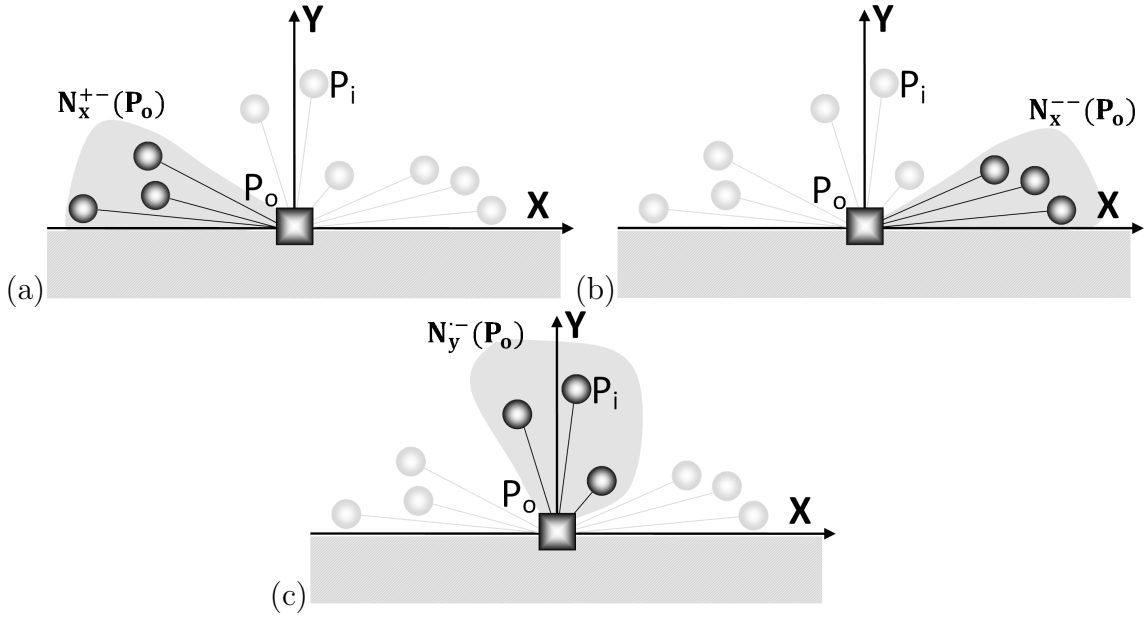

Figure 6.11: Split-stencil least square kinetic upwind method (SLKNS) for boundary points (a) positive x-split, (b) negative x-split, and (c) negative y-split connectivity for upwind implementation.

where $f_{1,\Sigma}^{+-}$ is half-range distribution function for for $0 < v_x < +\infty$ and $-\infty < v_y < 0$, $f_{1,\Sigma}^{--}$ is half-range distribution function for for $-\infty < v_x < 0$ and $-\infty < v_y < 0$ and $f_{1,\Sigma}^{\cdot-}$ is the half-range incident distribution function for $-\infty < v_x < +\infty$ and $-\infty < v_y < 0$. The propagation of information to node P_o depends upon location of node P_i relative to P_o and the signs of v_x and v_y . If $v_x > 0$ then only the nodes to the left of P_o belonging to connectivity $N_x^{+-}(P_o)$ will influence the solution at P_o as shown in Figure 6.11(a). Similarly, if $v_x < 0$ then only the nodes to the right of P_o belonging to connectivity $N_x^{--}(P_o)$ will influence the solution at P_o as shown in Figure 6.11(b). Since the distribution of reflected molecules are written in terms of incident molecules hence the node above P_o will influence the solution at P_o belonging to connectivity set $N_y^{\cdot-}(P_o)$ as shown in Figure 6.11(c). Two-dimensional Boltzmann equation for the boundary node

after taking $\boldsymbol{\Psi}$-moments simplifies to

$$\begin{aligned}\left\langle \boldsymbol{\Psi}, f_{1,\Sigma}^{t+\Delta t} \right\rangle &= \left\langle \boldsymbol{\Psi}, f_{1,\Sigma}^{t} \right\rangle \\ &-\Delta t \left[\begin{array}{l} \left(\frac{\partial \left\langle \boldsymbol{\Psi}, v_x f_{1,\Sigma}^{+-} \right\rangle}{\partial x} \right)_{N_x^{+\cdot}(P_o)}^{t} + \left(\frac{\partial \left\langle \boldsymbol{\Psi}, v_x f_{1,\Sigma}^{--} \right\rangle}{\partial x} \right)_{N_x^{-\cdot}(P_o)}^{t} \\ + \left(\frac{\partial \left\langle \boldsymbol{\Psi}, v_y f_{1,\Sigma}^{\cdot -} \right\rangle}{\partial y} \right)_{N_y^{\cdot -}(P_o)}^{t} \end{array} \right] \end{aligned} \tag{6.71}$$

SLKNS implementation is performed in locally rotated frame such that surface normal of the boundary coincides with the y-axis. Taking $\boldsymbol{\Psi}$ moment leads to the kinetic split flux boundary state update equations for iteration $k+1$ as follows

$$\begin{aligned}\boldsymbol{U}^{k+1} &= \boldsymbol{U}^{k} - \Delta t \left[\begin{array}{l} \left(\frac{\partial \widehat{\boldsymbol{GX}}^{+-}}{\partial x} \right)_{N_x^{+-}(P_o)}^{k} + \left(\frac{\partial \widehat{\boldsymbol{GX}}^{--}}{\partial x} \right)_{N_x^{--}(P_o)}^{k} \\ + \left(\frac{\partial \widehat{\boldsymbol{GY}}^{\cdot -}}{\partial y} \right)_{N_y^{\cdot -}(P_o)}^{k} \end{array} \right] \end{aligned} \tag{6.72}$$

where $\widehat{\boldsymbol{GX}}^{\pm -}$ and $\widehat{\boldsymbol{GY}}^{\cdot -}$ represents the split inviscid and viscous fluxes described in section 5.5.1. Expressions of the wall split fluxes are given in Appendix D. This state update can also be expressed as

$$\begin{aligned}\boldsymbol{U}^{k+1} &= \boldsymbol{U}^{k} - \Delta t \left[\begin{array}{l} \left(\frac{\partial \widehat{\boldsymbol{GX}}^{+-}}{\partial x} \right)_{\Delta x<0}^{k} + \left(\frac{\partial \widehat{\boldsymbol{GX}}^{--}}{\partial x} \right)_{\Delta x>0}^{k} \\ + \left(\frac{\partial \widehat{\boldsymbol{GY}}^{\cdot -}}{\partial y} \right)_{\Delta y>0}^{k} \end{array} \right] \end{aligned} \tag{6.73}$$

Similarly, for 3-D geometry SLKNS implementation is performed in locally rotated frame such that surface normal of the boundary coincides with the z-axis. The kinetic split flux boundary state update equations for iteration $k+1$ is

$$\begin{aligned}\boldsymbol{U}^{k+1} &= \boldsymbol{U}^{k} - \Delta t \left[\begin{array}{l} \left(\frac{\partial \widehat{\boldsymbol{GX}}^{+\cdot -}}{\partial x} \right)_{N_x^{+\cdot -}(P_o)}^{k} + \left(\frac{\partial \widehat{\boldsymbol{GX}}^{-\cdot -}}{\partial x} \right)_{N_x^{-\cdot -}(P_o)}^{k} \\ + \left(\frac{\partial \widehat{\boldsymbol{GY}}^{\cdot +-}}{\partial y} \right)_{N_y^{\cdot +-}(P_o)}^{k} + \left(\frac{\partial \widehat{\boldsymbol{GY}}^{\cdot --}}{\partial y} \right)_{N_y^{\cdot --}(P_o)}^{k} \\ + \left(\frac{\partial \widehat{\boldsymbol{GZ}}^{\cdot \cdot -}}{\partial z} \right)_{N_z^{\cdot \cdot -}(P_o)}^{k} \end{array} \right] \end{aligned} \tag{6.74}$$

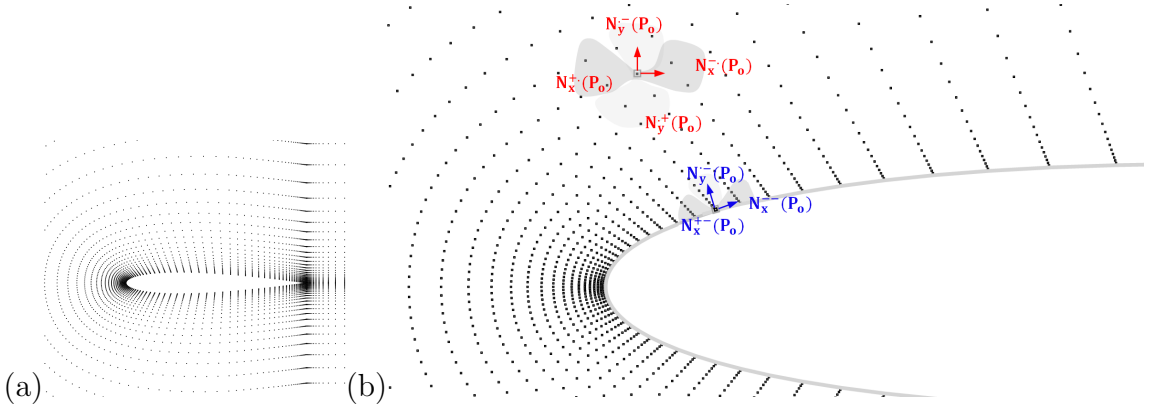

Figure 6.12: Split-stencil least square kinetic upwind method (SLKNS) for supersonic flow past NACA airfoil (a) cloud of points, (b) split connectivity in the flow domain and the boundary for upwind implementation.

where $\widehat{\boldsymbol{GX}}^{\pm\cdot-}$, $\widehat{\boldsymbol{GY}}^{\cdot\pm-}$ and $\widehat{\boldsymbol{GZ}}^{\cdot\cdot-}$ represents the split inviscid and viscous fluxes described in section 5.5.2. Expressions of the wall split fluxes are given in Appendix D. This state update can also be expressed as

$$\boldsymbol{U}^{k+1} = \boldsymbol{U}^k - \Delta t \left[\begin{array}{l} \left(\frac{\partial \widehat{\boldsymbol{GX}}^{+\cdot-}}{\partial x}\right)^k_{\Delta x<0} + \left(\frac{\partial \widehat{\boldsymbol{GX}}^{-\cdot-}}{\partial x}\right)^k_{\Delta x>0} \\ + \left(\frac{\partial \widehat{\boldsymbol{GY}}^{\cdot+-}}{\partial y}\right)^k_{\Delta y<0} + \left(\frac{\partial \widehat{\boldsymbol{GY}}^{\cdot--}}{\partial y}\right)^k_{\Delta y>0} \\ + \left(\frac{\partial \widehat{\boldsymbol{GZ}}^{\cdot\cdot-}}{\partial z}\right)^k_{\Delta z>0} \end{array} \right] \tag{6.75}$$

6.3.6 Implementation of SLKNS : Example supersonic flow past NACA0012 airfoil

Consider free stream supersonic flow at M = 1.5 past a NACA0012 airfoil at an angle of attack $\alpha = 0$ deg. The Reynolds number based on the airfoil chord is 10000. Total 10143 cloud of points were generated using C-type mesh of size 207×49 shown in Figure 6.12(a). This test case was solved using SLKNS solver with dissipation control, the state update for node P_o in the flow domain is

implemented as

$$\boldsymbol{U}(t+\Delta t) = \boldsymbol{U}(t) - \Delta t \left[\begin{array}{l} \left(\frac{\partial \boldsymbol{GX}^{+}(t)}{\partial x}\right)_{N_x^{+\cdot}(P_o)} + \left(\frac{\partial \boldsymbol{GX}^{-}(t)}{\partial x}\right)_{N_x^{-\cdot}(P_o)} \\ + \left(\frac{\partial \boldsymbol{GY}^{+}(t)}{\partial y}\right)_{N_y^{\cdot+}(P_o)} + \left(\frac{\partial \boldsymbol{GY}^{-}(t)}{\partial y}\right)_{N_y^{\cdot-}(P_o)} \end{array} \right] \tag{6.76}$$

The upwinding at node P_o is enforced using split flux and its associated split connectivity sets $N_x^{\pm\cdot}(P_o)$ and $N_y^{\cdot\pm}(P_o)$ as shown in Figure 6.12(b). where flux derivatives are calculated using SLKNS as follows

$$\left(\frac{\partial \boldsymbol{GX}^{\pm}(t)}{\partial x}\right)_{N_x^{\pm\cdot}(P_o)} = \frac{(\sum \Delta y_i^2)_{N_y^{\pm\cdot}(P_o)} (\sum \Delta \boldsymbol{GX}_i^{\pm}(t) \Delta x_i)_{N_x^{\pm\cdot}(P_o)} - (\sum \Delta x_i \Delta y_i)_{N_x^{\pm\cdot}(P_o)} (\sum \Delta \boldsymbol{GX}_i^{\pm} \Delta y_i)_{N_y^{\pm\cdot}(P_o)}}{(\sum \Delta x_i^2)_{N_x^{\pm\cdot}(P_o)} (\sum \Delta y_i^2)_{N_y^{\pm\cdot}(P_o)} - (\sum \Delta x_i \Delta y_i)_{N_x^{\pm\cdot}(P_o)} (\sum \Delta x_i \Delta y_i)_{N_y^{\pm\cdot}(P_o)}} \tag{6.77}$$

$$\left(\frac{\partial \boldsymbol{GY}^{\pm}(t)}{\partial y}\right)_{N_y^{\cdot\pm}(P_o)} = \frac{(\sum \Delta x_i^2)_{N_x^{\cdot\pm}(P_o)} (\sum \Delta \boldsymbol{GY}_i^{\pm}(t) \Delta y_i)_{N_y^{\cdot\pm}(P_o)} - (\sum \Delta x_i \Delta y_i)_{N_y^{\cdot\pm}(P_o)} (\sum \Delta \boldsymbol{GY}_i^{\pm}(t) \Delta x_i)_{N_x^{\cdot\pm}(P_o)}}{(\sum \Delta x_i^2)_{N_x^{\cdot\pm}(P_o)} (\sum \Delta y_i^2)_{N_y^{\cdot\pm}(P_o)} - (\sum \Delta x_i \Delta y_i)_{N_x^{\cdot\pm}(P_o)} (\sum \Delta x_i \Delta y_i)_{N_y^{\cdot\pm}(P_o)}} \tag{6.78}$$

where $\Delta \boldsymbol{GX}_i^{\pm}(t) = \boldsymbol{GX}_i^{\pm}(t) - \boldsymbol{GX}_o^{\pm}(t)$ and $\Delta \boldsymbol{GY}_i^{\pm}(t) = \boldsymbol{GY}_i^{\pm}(t) - \boldsymbol{GY}_o^{\pm}(t)$ are the flux differences between node P_i and P_o. The expressions of split fluxes are given in Appendix D. For boundary nodes SLKNS implementation is done in a locally rotated frame of reference such that surface normal and tangents coincide with the coordinate axes as shown in Figure 6.12(b). The state update for node P_o in the boundary is as follows

$$\boldsymbol{U}(t+\Delta t) \quad = \boldsymbol{U}(t) - \Delta t \left[\begin{array}{l} \left(\frac{\partial \widehat{\boldsymbol{GX}}^{+-}(t)}{\partial x}\right)_{N_x^{+-}(P_o)} + \left(\frac{\partial \widehat{\boldsymbol{GX}}^{--}(t)}{\partial x}\right)_{N_x^{--}(P_o)} \\ + \left(\frac{\partial \widehat{\boldsymbol{GY}}^{\cdot-}(t)}{\partial y}\right)_{N_y^{\cdot-}(P_o)} \end{array} \right] \tag{6.79}$$

where $N_x^{\pm-}(P_o)$ and $N_y^{\cdot-}(P_o)$ are the associated split connectivity sets for split fluxes $\widehat{\boldsymbol{GX}}^{\pm-}$ and $\widehat{\boldsymbol{GY}}^{\cdot-}$ described in section 5.5.1 of chapter 5. In this example no-slip boundary condition is used i.e. $U_2 = 0$ and $U_3 = 0$ using explicit Euler time stepping based on global CFL time step described by equation 6.59. Figure 6.13(b) shows the solution trajectory and the stability point reached by the two different solver points one located near the NACA airfoil wall boundary and the other located near the freestream boundary. The phase plane portrait of the solution trajectory is shown in the state space defined by the magnitude of

thermodynamic forces associated with heat flux vector and shear stress tensor. Figure 6.13(a) shows the unstable focus of the solution trajectory in the initial phase of the iterations. The phase-plane analysis provides physical insight about the qualitative behaviour of the solver, for example in the initial iterations, the eigenvalue solution with respect to magnitude of the thermodynamic forces is complex with positive real parts which gradually approaches a stable node at the end of the iterations. The trajectory speed in the phase plane can also be used to ascertain convergence. The present research uses residue plot to ascertain convergence, for example residue plot depicted in Figure 6.14 shows the 5 decades fall of the normalized residue $\bar{Res}_2^k = Res_2^k/Res_2^0$, where residue Res_2^k is based on the average L_2 norm of all the components across the domain at k^{th} iteration evaluated as follows

$$Res_2^k = \frac{1}{10143}\sum_{i=1}^{10143}\left(\frac{1}{4}\sum_{j}^{4}(U_j^{k+1}(i) - U_j^k(i))^2\right)^{1/2} \tag{6.80}$$

where $U_j^k(i)$ is the j^{th} component of the state vector at iteration k for point i. The computation reveals shock ahead of the body as well as a fish tail shock shown in Figure 6.15.

6.4 Meshless pre-processor

One of the greatest advantages of meshless solver is its ability to work on any type of grid or on an arbitrary distribution of points. In present meshless method the points are generated around each component of the multibody configuration using simple grid generator and then the points around each components are merged to form the cloud of points. Meshless method in this case requires cloud of points and its connectivity. The meshless pre-processing requires i) pre-processing of cloud of points, and ii) connectivity generation

6.4.1 Generation of cloud of points

The task of generating suitable grid for a complex multi-body configuration can be accomplished by breaking down a geometrically complex object as a union of

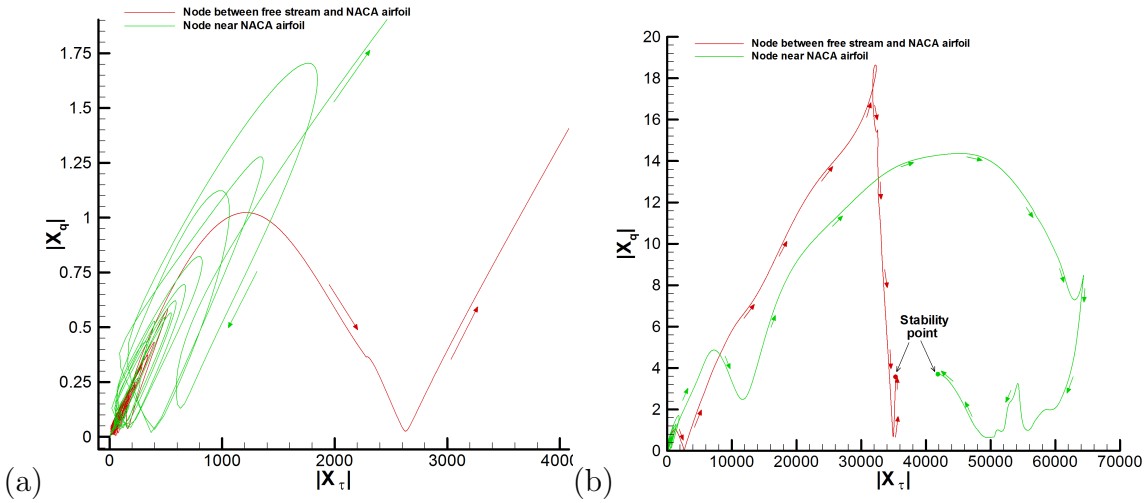

Figure 6.13: Solution trajectory shown in the state space defined by the magnitude of thermodynamic forces associated with heat flux vector and shear stress tensor (a) unstable focus in the initial iteration phase, (b) and stability point reached at the end of the iteration.

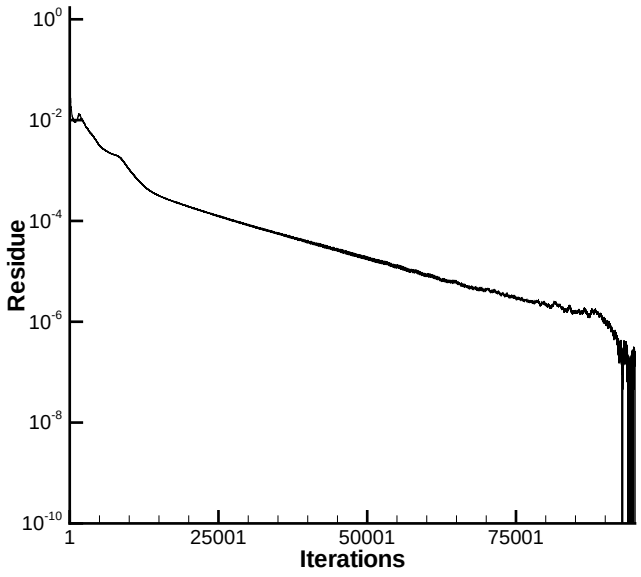

Figure 6.14: Residue plot for supersonic flow at M=1.5 past a NACA0012 airfoil.

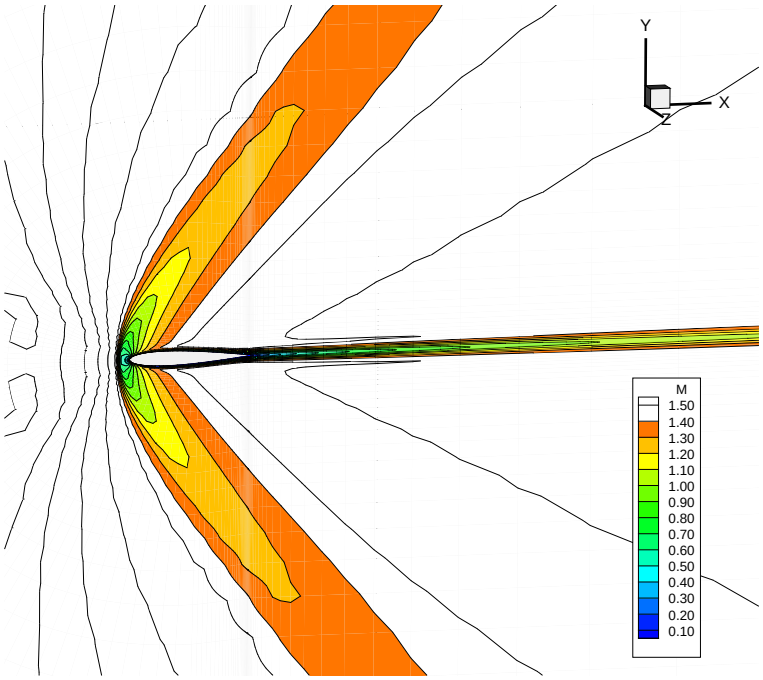

Figure 6.15: Supersonic flow at M=1.5 past a NACA0012 airfoil.

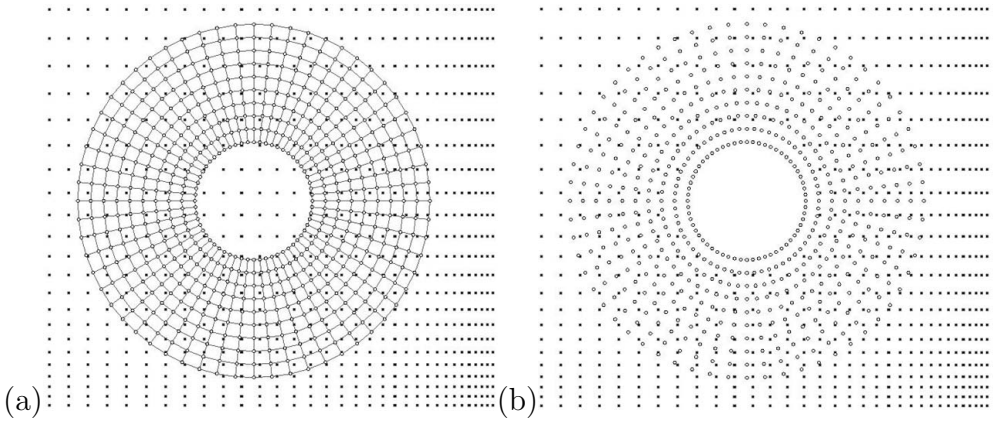

Figure 6.16: Pre-processing of cloud of points (a) merging of simple sub-cloud, (b)node deletion of sub-cloud.

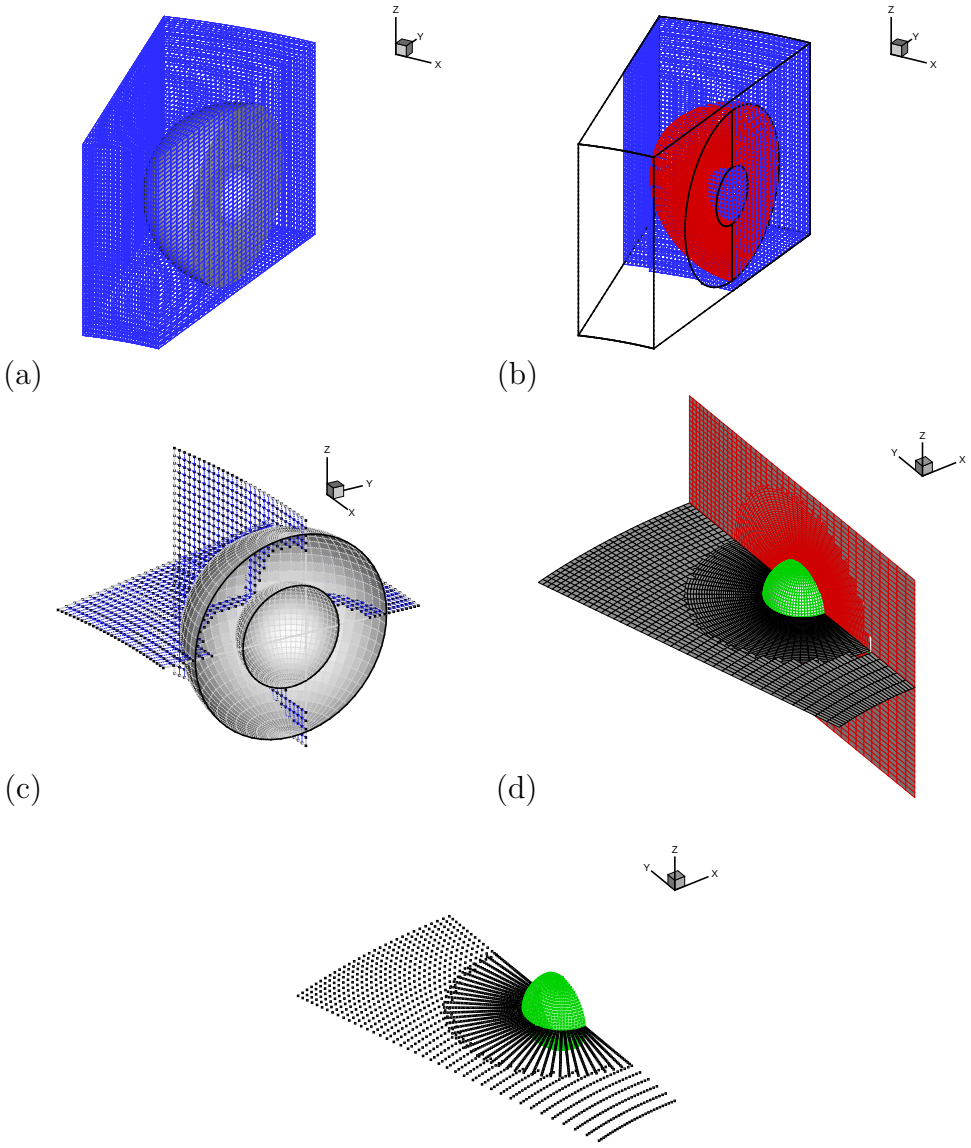

Figure 6.17: Pre-processing of cloud of points (a) merging of hemispherical sub-cloud, (b) sectional view (c) view after node deletion of background cloud (d) view showing grid tesselation after pre-processing phase (e) cloud of points after pre-processing

several geometrically simple objects, generating grid around each simple object and then finally merging all the grid points into a *cloud* of points enveloping the complex multi-body configuration. We need an appropriate pre-processor to carry out merging of points and then generating connectivity. Let us define nodes generated around simple objects as *sub-clouds* that will merge to form the cloud. For example define sub-clouds around a circle shaped body as α sub-cloud which is to be merged with background β sub-cloud. A pre-processor is required to merge many sub-clouds as shown in Figure 6.16. The union of two sub-clouds can be written as

$$sC(\alpha) \cup sC(\beta) = sC(\alpha) + sC(\beta) - sC(\alpha) \cap sC(\beta) - sC^{C}(\alpha) - sC^{C}(\beta) \quad (6.81)$$

where

$$sC(\alpha) \cap sC(\beta) = \{\forall P_i : P_i \in sC(\alpha), \forall P_j : P_j \in sC(\beta) \exists\, d(P_i, P_j) \leq h_{\min}\} \quad (6.82)$$

$$sC^{C}(\alpha) = \{\forall P_i : P_i | P_i \notin sC(\alpha), P_i \in Bc(\alpha)\} \quad (6.83)$$

$$sC^{C}(\beta) = \{\forall P_i : P_i | P_i \notin sC(\beta), P_i \in Bc(\beta)\} \quad (6.84)$$

The term $sC(\alpha) \cap sC(\beta)$denote nodes belonging to sub-clouds $sC(\alpha)$ of object α and sub-cloud $sC(\beta)$of object β which are very close to each other i.e. within the minimum tolerance $h_{\min}$ specified by the user. While $Bc(\alpha)$ and $Bc(\beta)$ denote blank nodes i.e. nodes which will perform no computation. $Bc(\alpha)$ can also be defined as a set of sub-clouds lying inside the body or in any other non-computing domain of α and similarly $Bc(\beta)$ can be defined as a set of sub-clouds lying inside the body or in any other non-computing domain of β. Thus, the term $sC^{C}(\alpha)$and $sC^{C}(\beta)$ denote the set of all the nodes which do not belong to sub-clouds $sC(\alpha)$, $sC(\beta)$ and these nodes lie inside the body or in any other non-computing domain of α and β respectively. The term $sC(\alpha) \cup sC(\beta)$ denotes the merging phase where the nodes that lie inside the body or in any other non-computing domain are deleted by ray-tracing algorithm. The merging phase also deletes the nodes based on the criterion $d(P_i, P_j) \leq h_{\min}$. The parameter $d(P_i, P_j)$ gives the Euclidean distance between P_i and P_j. Similarly, for a three dimensional problem figure 6.17 shows the steps involved in pre-processing of cloud of points.

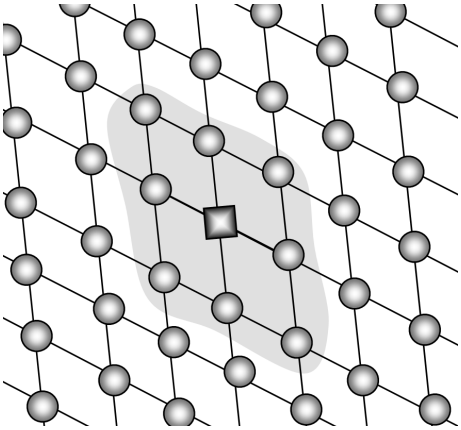

Figure 6.18: Connectivity data by moving along coordinate directions for a structured grid.

6.4.2 Connectivity generation

Connectivity or neighbourhood information for cloud of points generated using structured mesh as shown in Fig.6.18 can easily be obtained by by selecting the nodes along the co-ordinate directions. For unstructured cloud of points as shown in Fig.6.19 the connectivity is generated using edge based data structure. For example for a grid generated using triangulation, the edge based data structure is generated using the Voronoi information. Distribution of points can be obtained by multiple sources and there can be multiple bodies in such cases it is desirable to have a method which would operate on any type of distribution of points independent of the way the cloud of points is generated. Quad-tree and Oct-tree based methods are commonly used in generating connectivity. Connectivity is an important issue and it should possess following certain minimum attributes :

- Each quadrant also should have adequate number of points for implementing upwinding by stencil sub-division.
  Care should be taken to avoid extreme case of a quadrant being empty. For the boundary points where locally rotated frame are used it is essential that the above criterion be applied to quadrants of rotated frame.

- Connectivity for points near or on body should only contain aerodynamic points.

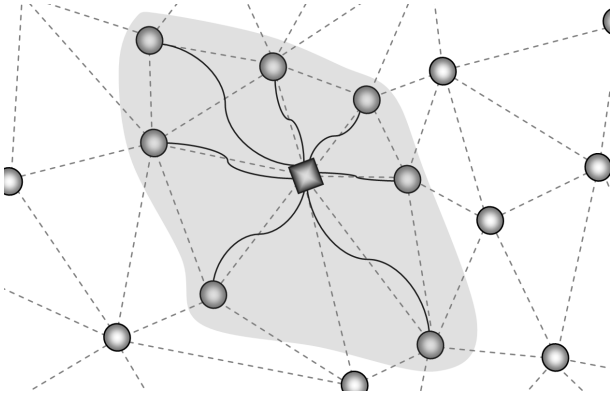

Figure 6.19: Connectivity data using edge based data structure for an unstructured grid.

Consider a point P_o is shown lying on lower side of the body as shown in in Fig. 6.20 where its split neighbourhood is defined as $N_x(P_o)$ and $N_y(P_o)$. The split neighborhoods of P_o lie inside a ball of radius h and it can easily be seen that all the points contained within this ball are not aerodynamically connected i.e. some of the points lie on the upper side of the body. Such points should not participate in the solution process or influence the solution update at P_o. Define set of edges that connect all points of the connectivity data to point P_o and all the points connected to those edges that intersect the body define the forbidden region as shown in the Fig. 6.20. This forbidden region should be excluded or removed from the connectivity set, $N_x(P_o)$ or $N_y(P_o)$. The pre-processor while generating the connectivity data deletes the points lying in the forbidden regions. The final connectivity so obtained is shown in Fig. 6.20 where points retained are solid circles, represented by the edges joining the point P_o to all the valid nodes in the connectivity.

Connectivity is generated by quad-tree / oct-tree method in the fluid domain far away from the body. For points near the body edge based data structure is used so as to get the aerodynamically connected neighbors. We require enough connectivity such that the problem remains overdetermined we also require that the cross-product matrix remains well-conditioned. The matrix becomes ill-conditioned when all the points in the connectivity set lie on a straight line that passes

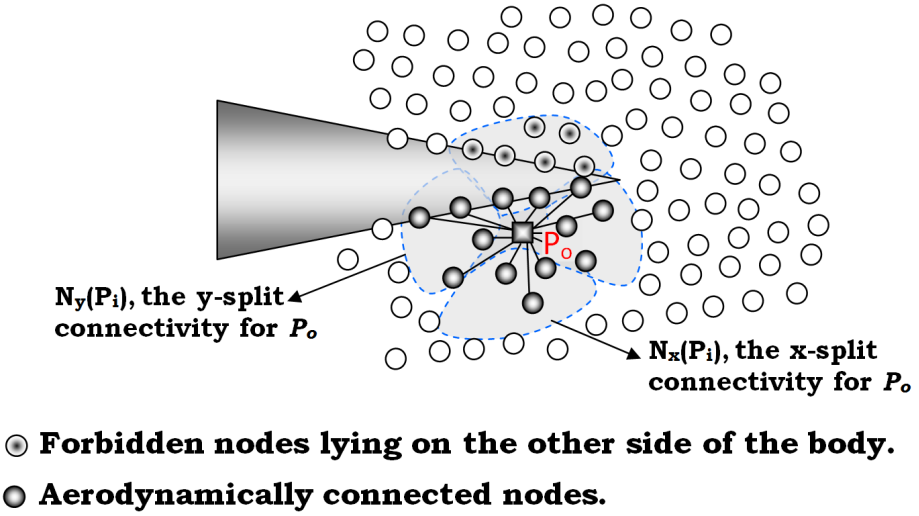

Figure 6.20: Aerodynamically connected neighbours and definition of eclipsed region

Figure 6.21: Degenerate cases of neighbours lying within a thin pencil

through the node P_o as illustrated in Fig. 6.21. This eventuality is an example of degeneracy of connectivity. For a 3-D case the denominator will become zero when all the points in the connectivity set lie on a plane. For a 2-D case even when the points lie approximately on a straight line, that is forming a thin pencil also contributes a case of degeneracy and can cause solution divergence or large error. While generating connectivity data one should ensure that degeneracy is avoided.

6.5 Parallelization of SLKNS

For practical industrial problems with thin boundary layers and rapid density and pressure variation large number of nodes or points are required for adequate resolution. Highly stretched grids near wall cause grid induced stiffness because allowed time step is dictated by the smallest h (i.e. grid size) and to resolve viscous as well as slip flow features we require scheme with higher order (p^{th} or-

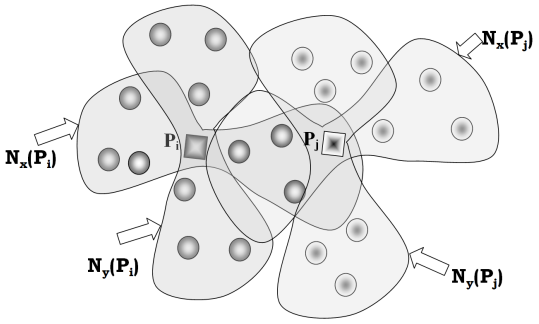

Figure 6.22: Asymmetric connectivity

der). For real large scale problem the CPU time for a SLKNS code then becomes prohibitively large thus requiring its parallelization. The main goal of parallel computation is its performance and scalability, the present parallelization strategy employs domain decomposition. In the present research METIS was found to be quite superior in terms of speed and partitioning performance as compared to partitioning by Recursive Co-ordinate Bisection (RCB), Recursive Spectral Bisection(RSB). METIS offers a variety of codes to partition graphs, meshes, convert meshes into graphs. There are two codes *pmetis* and *kmetis* for partitioning an unstructured graph into k equal size parts. The code *pmetis* is based on multilevel recursive bisection, whereas the code *kmetis* is based on multilevel k-way partitioning. METIS also supports the minimization of total communication volume using subroutine $METIS\_PartGraphVKway$ and $METIS\_PartGraphKway$. In the present work *pmetis* was found to provide better domain decomposition for SLKNS code.

6.5.1 Graph partitioning for SLKNS

The graph to be partitioned requires an adjacency list. METIS operates only on symmetric adjacency list. Symmetry relation requires that if P_i is the neighbour of P_j then P_j should be a neighbour of P_i. Consider a node P_i with a split connectivity set $N_x(P_i)$, $N_y(P_i)$ and node $P_j \in N_x(P_i)$ with split connectivity set $N_x(P_j)$ and $N_y(P_j)$. Then symmetry requires that $P_i \in N_x(P_j)$ and $P_j \in N_x(P_i)$. Fig. 6.22 shows a case where this condition is violated. For this case $P_i \in N_x(P_j)$ but $P_j \notin N_x(P_i)$. Consider only x-split stencil and a new set $SN_x(P_j)$ called

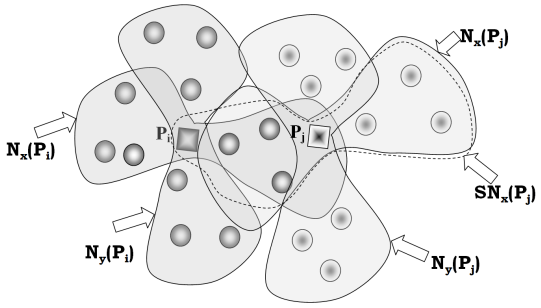

Figure 6.23: Symmetric connectivity for interior point

symmetric x-split connectivity set of P_j defined by

$$SN_x(P_j) = N_x(P_j) \cup P_i : P_j \in N_x(P_i) \tag{6.85}$$

This new connectivity set satisfies the symmetry relation

$$\forall P_i \in SN_x(P_j) \exists P_j \in SN_x(P_i) \tag{6.86}$$

Fig. 6.23 shows a symmetric connectivity set, $SN_x(P_j)$ shown by a dotted line. Here point P_i has been appended to x-split connectivity set of P_j .This symmetric connectivity $SN_x(P_j)$ forms the x-split adjacency list of point P_j. Similarly, symmetric connectivity set for y-split stencil is created. METIS requires the symmetric connectivity set $SN(P_i)$ which is union of symmetric split connectivity sets $SN_x(P_i)$ and $SN_y(P_i)$ i.e. $SN(P_i) = SN_x(P_i) \cup SN_y(P_i)$.

6.5.2 Mapping global grid data structure to the local sub-domains

After decomposition we get many sub-domains that are assigned to different processors to perform almost identical computational tasks. At the boundary of sub-domains some nodes can have neighbours which can lie in many neighbouring sub-domains. Thus, at the interface boundary we have a set of nodes that have to communicate information with neighboring sub-domains. Each sub-domain is assigned to a particular processor and hence it is given a label corresponding to the processor number. Boundary conditions for each sub-domain are obtained from the data in the neighboring sub-domains thereby requiring communication

with the other processors by virtue of message passing. Within a sub-domain, a node is assigned a unique integer i.d. between 1 and the total number of nodes. A node that is shared between several processors is stored in all the processors that share it to avoid additional communication overhead. Thus, the total number of nodes for a particular sub-domain includes both the computation nodes and the communication nodes that lie in other sub-domain. Nodes are renumbered within each sub-domain and assigned a local index having a correspondence with global index. Furthermore, each sub-domain maintains two arrays, one for sending the information and other for receiving it. Each send and receive array is a two dimensional array which keeps the list of processor that communicates and the i.d. of the node. This enables any sub-domain to exchange data with its neighboring sub-domain. It should be noted that for asymmetric neighborhood the send array is not identical to receive array.

6.5.3 Parallelization pre-processing

To illustrate the pre-processing step consider a flow domain Ω with total number of nodes as m and total number of processors as np. After domain decomposition we will have np domains Ω_i each containing m_i nodes with b_i communicating boundaries $\partial\Omega_1$,$\cdots$,$\partial\Omega_{b_i}$. The parallelization pre-processing can be illustrated as follows

- (a) Domain Decomposition

$$\Omega = \sum_{i=1}^{np} \Omega_i \tag{6.87}$$

  Flow domain $\Omega\{1, 2, \cdots, m\}$ is decomposed into np domains Ω_i.

- (b) Renumber domains
  Each domain is renumbered locally e.g. $\Omega_i\{1, 2, \cdots, m_i\}$.

- Construct Global/Local mapping function

$$\mathcal{G}(\Omega_i, p) \subset \Omega, \quad where \quad \mathcal{G} : \Omega_i \mapsto \Omega \tag{6.88}$$

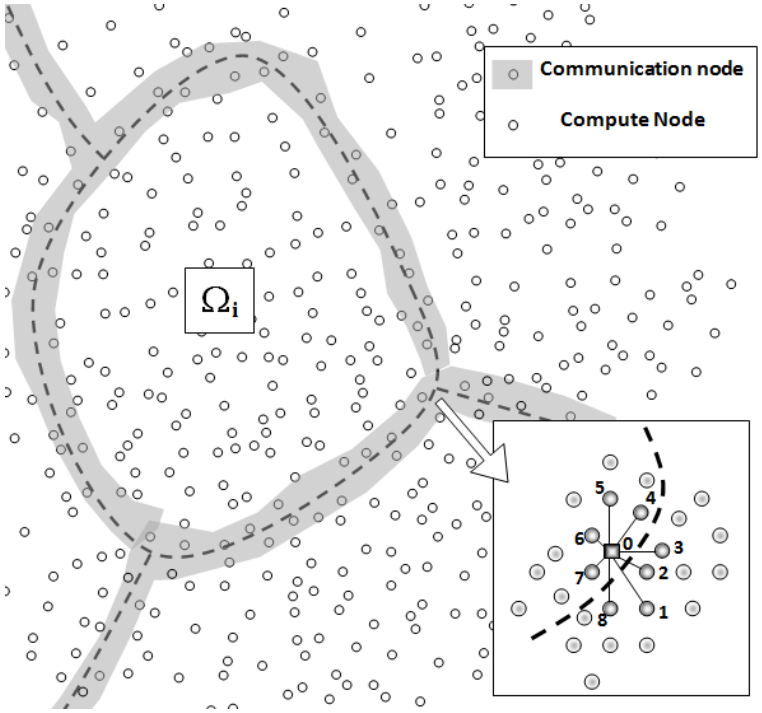

Figure 6.24: Compute nodes and Communication nodes due to part of connectivity lying outside the domain.

The global mapping function $\mathcal{G}$ maps the domain $\Omega_i\{1, 2, \cdots, m_i\}$ into the global grid $\Omega\{1, 2, \cdots, m\}$. Similarly constructing np local mapping functions $\mathcal{L}$ which maps the domain global flow domain,Ω to local decomposed domains Ω_i.

$$\mathcal{L}(\Omega, p) \subset \Omega, \quad where \quad \mathcal{L} : \Omega \mapsto \Omega_i \tag{6.89}$$

- Compute send and receive data

  Some part of the connectivity set may lie in the neighbouring domain forming the communication nodes which needs to be received or send by the neighbouring domain. Figure 6.24 shows the compute as well as communication nodes. Receive communication data consists of static data as well as dynamic data.

$$\Omega_i^R = \sum_{j=1}^{b_i} \Omega_{i,j}^{R,s} + \sum_{j=1}^{b_i} \Omega_{i,j}^{R,d} \tag{6.90}$$

where $\Omega_{i,j}^{R,s}$ is the static receive data (or data which is not changing with the iterations) from domain i to domain j, similarly $\Omega_{i,j}^{R,d}$ is the dynamic receive data i.e. fluid dynamic data from domain i to domain j. The send communication data can also be expressed as

$$\Omega_i^S = \sum_{j=1}^{b_i} \Omega_{i,j}^{S,s} + \sum_{j=1}^{b_i} \Omega_{i,j}^{S,d} \tag{6.91}$$

where $\Omega_{i,j}^{S,s}$ is the static send data from domain i to domain j, similarly $\Omega_{i,j}^{R,d}$ is the dynamic send data from domain i to domain j.

- Domain Augmentation
  The domain Ω_i is augmented with the static receive communication data to avoid repeated communications after every iterations.

$$\tilde{\Omega}_i = \Omega_i + \sum_{j=1}^{b_i} \Omega_i^{R,s} \tag{6.92}$$

- Communication matrix Optimization
  For any np number of processors there are $np-1$ parallel set of communications that avoid collision of messages. Basic communication matrix is prepared based on Latin hyper cube described by the following pseudo code

```
for i = 0 to np-2
for j = 0 to np-2
cm(i,j) = (i+j) mod (n-1)
next j
next i
for i = 0 to np-1
for j = 0 to np-1
  if cm(i,j) =0  then
     cm(i,j) = np-1
  end if
 if i = j then
    cm(i,np-1) = cm(i,j)
    cm(np-1,i) = cm(i,j)
```

```
    cm(i,j) = 0
 end if
next j
next i
```

For example for the case of $np = 8$, the communication matrix $\boldsymbol{C}_M$ is

$$\boldsymbol{C}_M = \begin{bmatrix} 0 & 1 & 2 & 3 & 4 & 5 & 6 & 7 \\ 1 & 0 & 3 & 4 & 5 & 6 & 7 & 2 \\ 2 & 3 & 0 & 5 & 6 & 7 & 1 & 4 \\ 3 & 4 & 5 & 0 & 7 & 1 & 2 & 6 \\ 4 & 5 & 6 & 7 & 0 & 2 & 3 & 1 \\ 5 & 6 & 7 & 1 & 2 & 0 & 4 & 3 \\ 6 & 7 & 1 & 2 & 3 & 4 & 0 & 5 \\ 7 & 2 & 4 & 6 & 1 & 3 & 5 & 0 \end{bmatrix} \tag{6.93}$$

At communication step $C_M(i, j)$ the i^{th} domain sends data to j^{th} domain for all $i > j$. Similarly at communication step $C_M(i, j)$ the i^{th} domain receives data from j^{th} domain for all $i < j$. Consider domain decomposition of flow domain of 7200 nodes around NACA0012 airfoil decomposed into $np = 8$ domains as shown in Fig. 6.25. This decomposition generates an adjacency matrix, $\boldsymbol{A}_M$ based on neighbourhood of decomposed domains. For example in this particular case the matrix $\boldsymbol{A}_M$ can be expressed as

$$\boldsymbol{A}_M = \begin{bmatrix} 0 & 1 & 0 & 0 & 0 & 0 & 0 & 1 \\ 1 & 0 & 1 & 1 & 0 & 1 & 0 & 1 \\ 0 & 1 & 0 & 1 & 1 & 0 & 0 & 0 \\ 0 & 1 & 1 & 0 & 1 & 1 & 1 & 0 \\ 0 & 0 & 1 & 1 & 0 & 0 & 1 & 1 \\ 1 & 1 & 0 & 1 & 0 & 0 & 1 & 0 \\ 0 & 0 & 0 & 1 & 1 & 1 & 0 & 1 \\ 1 & 0 & 0 & 0 & 1 & 0 & 1 & 0 \end{bmatrix} \tag{6.94}$$

Within each $np - 1$ parallel set of communications there are some communications that may be empty depending on the neighborhood of partitions or domains. Thus, within these 7 sets of communication in this example there are some communications that are empty e.g. domain Ω_1 can only communicate to two domains i.e Ω_2 and Ω_8. Hence after domain decomposition the optimal communication scheduling will depend on its adjacency

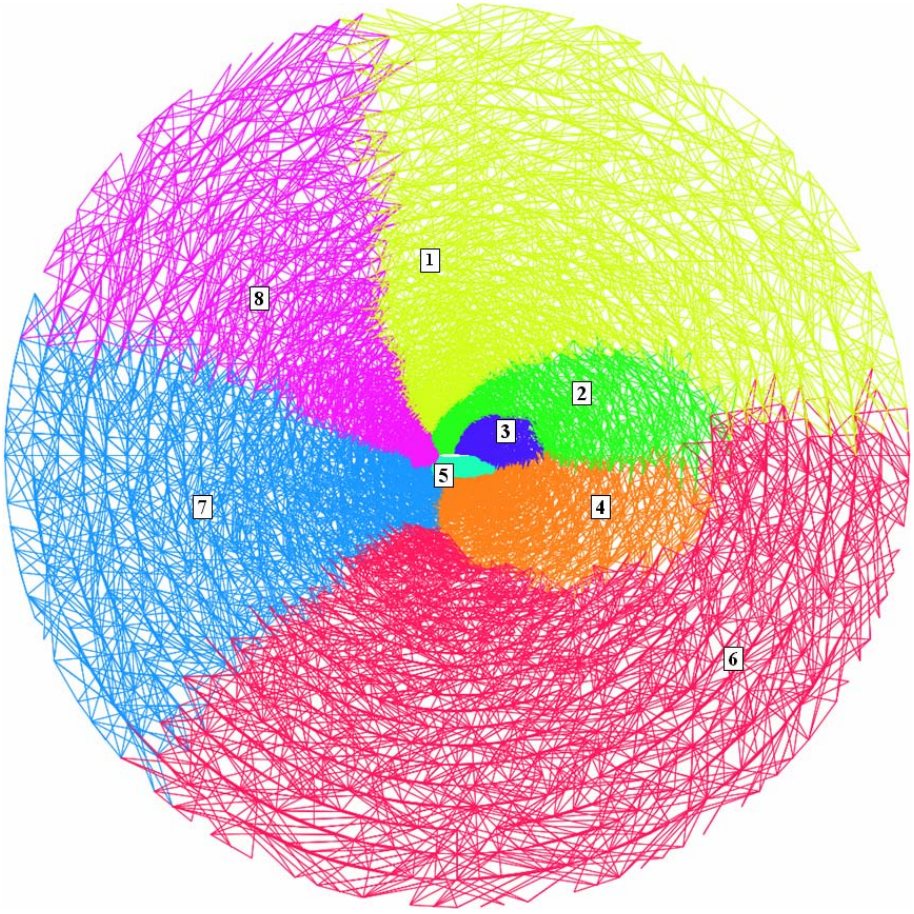

Figure 6.25: Flow domain around NACA0012 airfoil decomposed into $np = 8$ domains based on its symmetric connectivity.

Table 6.1: Communication Schedule based on Communication matrix $\boldsymbol{C}_M$

Communication Step	Set 1	Set 2	Set 3	Set 4
Step 1	$1 \leftrightarrow 2$	$3 \leftrightarrow 7$	$4 \leftrightarrow 6$	$5 \leftrightarrow 8$
Step 2	$1 \leftrightarrow 3$	$2 \leftrightarrow 8$	$4 \leftrightarrow 7$	$5 \leftrightarrow 6$
Step 3	$1 \leftrightarrow 4$	$2 \leftrightarrow 3$	$5 \leftrightarrow 7$	$6 \leftrightarrow 8$
Step 4	$1 \leftrightarrow 5$	$2 \leftrightarrow 4$	$3 \leftrightarrow 8$	$6 \leftrightarrow 7$
Step 5	$1 \leftrightarrow 6$	$2 \leftrightarrow 5$	$3 \leftrightarrow 4$	$7 \leftrightarrow 8$
Step 6	$1 \leftrightarrow 7$	$2 \leftrightarrow 6$	$3 \leftrightarrow 5$	$4 \leftrightarrow 8$
Step 7	$1 \leftrightarrow 8$	$2 \leftrightarrow 7$	$3 \leftrightarrow 6$	$4 \leftrightarrow 5$

matrix. The modified communication matrix $\tilde{\boldsymbol{C}}_M$ is evaluated based on neighbourhood of decomposed domains, it is expressed as

$$\tilde{\boldsymbol{C}}_M = \begin{bmatrix} 0 & 1 & 0 & 0 & 0 & 0 & 0 & 7 \\ 1 & 0 & 3 & 4 & 0 & 6 & 0 & 2 \\ 0 & 3 & 0 & 5 & 6 & 0 & 0 & 0 \\ 0 & 4 & 5 & 0 & 7 & 1 & 2 & 0 \\ 0 & 0 & 6 & 7 & 0 & 0 & 3 & 1 \\ 5 & 6 & 0 & 1 & 0 & 0 & 4 & 0 \\ 0 & 0 & 0 & 2 & 3 & 4 & 0 & 5 \\ 7 & 0 & 0 & 0 & 1 & 0 & 5 & 0 \end{bmatrix} \tag{6.95}$$

Table 6.1 and table 6.2 shows the communication schedule based on matrix $\boldsymbol{C}_M$ and $\tilde{\boldsymbol{C}}_M$ respectively. Fig. 6.26 shows the communication between the domains.Optimal communication schedule of 3 pairs in only 5 steps can be obtained based on the modified Communication matrix $\tilde{\boldsymbol{C}}_M$ and tabu search as shown in Table 6.3. Fig. 6.27 shows the optimized communication between the processors reduced from 7 steps to 5 steps.

6.5.4 Coarse-medium-fine cloud sequencing

As iterations proceeds the high frequency part of the error gets removed but low frequency part reduces slowly. Convergence requires prohibitive $O(N^2)$ iterations and coarse-medium-fine cloud sequencing is one of the method to hasten the

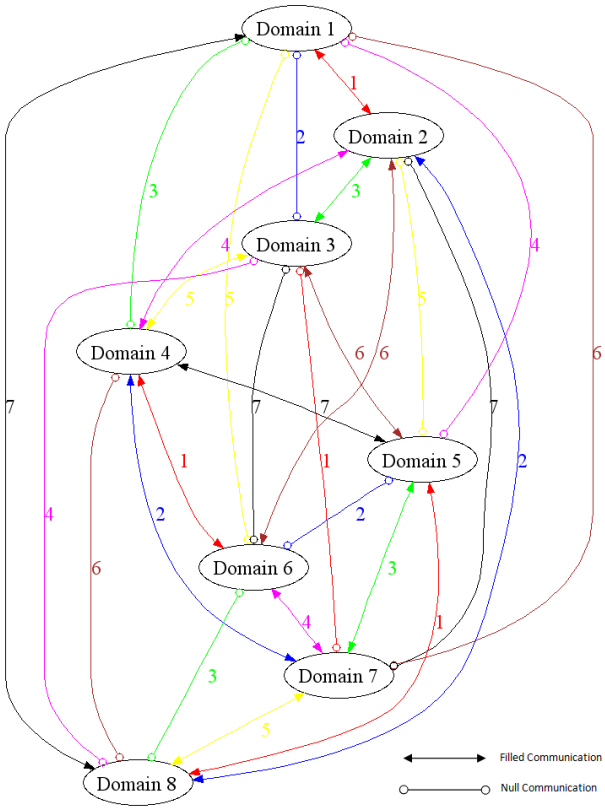

Figure 6.26: Communication schedule between domains.

Table 6.2: Communication Schedule based on modified Communication matrix $\tilde{C}_M$

Communication Step	Set 1	Set 2	Set 3	Set 4
Step 1	$1 \leftrightarrow 2$		$4 \leftrightarrow 6$	$5 \leftrightarrow 8$
Step 2		$2 \leftrightarrow 8$	$4 \leftrightarrow 7$	
Step 3		$2 \leftrightarrow 3$	$5 \leftrightarrow 7$	
Step 4		$2 \leftrightarrow 4$		$6 \leftrightarrow 7$
Step 5			$3 \leftrightarrow 4$	$7 \leftrightarrow 8$
Step 6		$2 \leftrightarrow 6$	$3 \leftrightarrow 5$	
Step 7	$1 \leftrightarrow 8$			$4 \leftrightarrow 5$

Table 6.3: Optimized communication schedule

Communication Step	Set 1	Set 2	Set 3
Step 1	$2 \leftrightarrow 8$	$4 \leftrightarrow 6$	$5 \leftrightarrow 7$
Step 2	$2 \leftrightarrow 4$	$5 \leftrightarrow 8$	$6 \leftrightarrow 7$
Step 3	$1 \leftrightarrow 2$	$3 \leftrightarrow 4$	$7 \leftrightarrow 8$
Step 4	$2 \leftrightarrow 6$	$3 \leftrightarrow 5$	$4 \leftrightarrow 7$
Step 5	$1 \leftrightarrow 8$	$2 \leftrightarrow 3$	$4 \leftrightarrow 5$

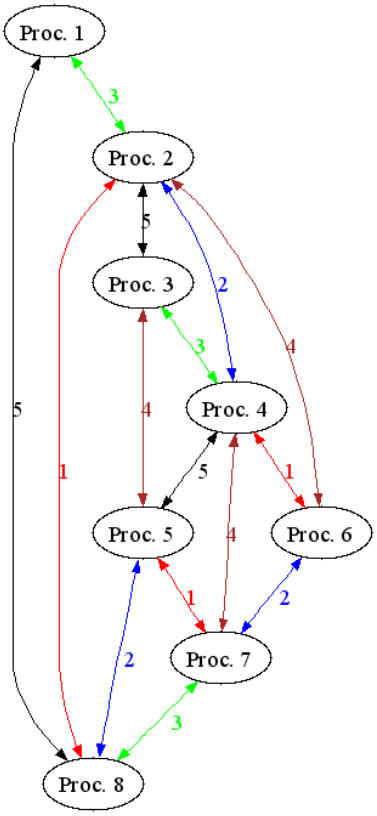

Figure 6.27: Optimized Communication schedule between processors.

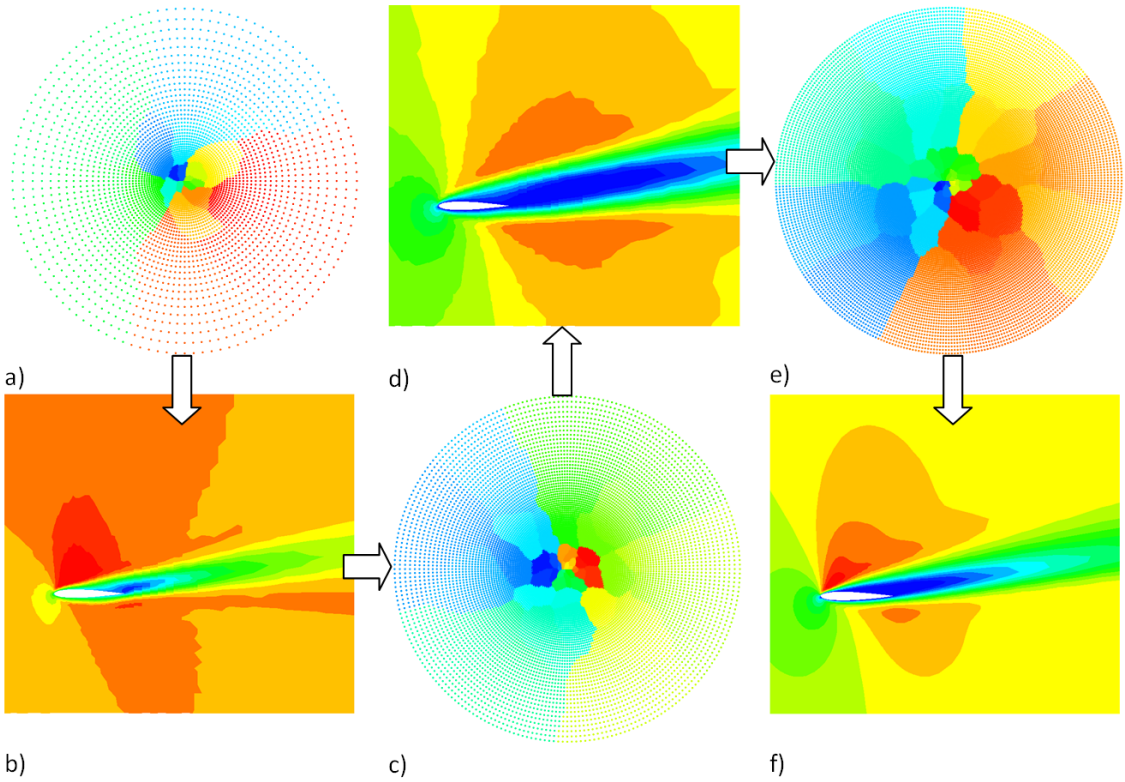

Figure 6.28: Coarse-medium-fine cloud sequencing.

convergence. In this multi-cloud approach coarse cloud solution is mapped to medium cloud and then finally to fine cloud. The coarse cloud sieves out low frequency part of error observed in fine grid. The coarse cloud is solved in parallel by decomposing its domain as shown in Figure 6.28(a). After few thousand iterations the solution as shown in Figure 6.28(b) is mapped to the medium cloud as shown in Figure 6.28(c). The parallel solution from the medium cloud as shown in Figure 6.28(d) is mapped to the fine cloud as shown in Figure 6.28(e) and solved to obtain the final solution as shown in Figure 6.28(f).

6.5.5 Construction of the parallel code

The parallel SLKNS code contains three codes i) pre-processor code, ii) solver code, and iii)post-processor code. The details of each code is as follows:

- Pre-processor code
  At the start pre-processor is run to decompose the domain, prepare optimized communication look-up table and information regarding receiving and sending processors, amount of nodes in each one of them. The pre-processor also augments the cloud Ω_i for each processor with static send and receive data. The augmented cloud $\tilde{\Omega}_i = \Omega_i + \sum_{j=1}^{b_i} \Omega_i^{R,s}$ for each processor is written as a separate file. Where $\Omega_{i,j}^{R,s}$ is the static receive data (or data which is not changing with the iterations) from domain i to domain j. Each augmented cloud $\tilde{\Omega}_i$ is written as a separate file with its boundary flags, connectivity set and fluid dynamic state vectors. This set of files form a part of I/O (input/output) parallelization.

- SLKNS code
  The parallel code reads the augmented cloud data $\tilde{\Omega}_i$=Ω_i+$\sum_{j=1}^{b_i} \Omega_i^{R,s}$ in *subroutine cloud_data*. The optimized communication schedule as a look-up table is read by *subroutine read_par_info*, this subroutine also reads information regarding receiving and sending processors, amount of nodes in each one of them. The computation of inviscid fluxes at a node P_i lying in the domain Ω_i will require only the state vector of the node P_i. On the other hand the computation of viscous fluxes will require the evaluation of velocity and

temperature gradients at all the neighbouring nodes $P_j \in \{N_x(P_i), N_y(P_i), N_z(P_i)\}$ belonging to the communication band Ω_i^R of the augmented cloud $\tilde{\Omega}_i$. Since the computation of fluxes is more computationally intensive hence the split fluxes of all the node P_j is communicated instead of transferring the gradients. The *subroutine par_comm_split_fluxes* performs this task of communicating the send and receive split fluxes. Similarly the derivatives of fluxes are transfered by *subroutine par_comm_split_fluxes_derivatives* to carry out higher order accurate calculation.

- Post-processor code
  This routine plots the residue and reconstructs the data from the decomposed domain for plotting and data extraction.

The SLKNS code uses domain decomposition and I/O (input/output) parallelization to read and write data for a large scale parallel computing. The present parallel implementation uses "master-slave" paradigm with parallel optimized communication with I/O parallelization. Structure of the FORTRAN based SLKNS code is as follows

```
C-------------------------------------------------------------
        include 'params.h'
        include 'mpif.h'
C     MPI initialize calls
        call mpi_init (anumpi_err)
        call mpi_comm_rank (MPI_COMM_WORLD, anumpi_myid, anumpi_err)
        call mpi_comm_size (MPI_COMM_WORLD, anumpi_nproc, anumpi_err)
C     Open all files
        call open_file
C     Read augmented grid and solver parameters
        call input_parameters
C     Initialize constants and allocate memory
        call constants_and_allocate_memory
C     Read augmented cloud data
        call cloud_data
C     Initialize flow field
        call init_flow
C     Read parallel information i.e. send / receive arrays, etc.
```

```
        call read_par_info
C     Evaluate parameters of  cross-product C matrix
C    for least square method
        call c_matrix
C     Implement the time stepping
        do iter = itmin+1,itmax
C     Evaluate the split inviscid fluxes based on Maxwellian distribution
                call inviscid_split_fluxes
C     Evaluate the thermodynamic force tensors using
C     velocity and temperature gradients
                call thermo_force_tensor
C     Perform tensor contraction to get split viscous fluxes
                call split_tensor_contraction
C     Parallel communication of inviscid/viscous split fluxes
C     using  mpi_send, mpi_recv calls.
                call par_comm_split_fluxes
C     Evaluate first order flux derivatives using SLKNS routine
C    for points in the fluid domain
                call first_order_SLKNS
C     Evaluate boundary flux and its derivatives using SLKNS routine
C    for points in the boundary
                call boundary_flux_SLKNS
C     Evaluate time steps for each nodes in the cloud
                call delta_time
C     Do the first order based state vector update
                call update_first_order
C    Check flag for higher order accuracy using
C    defect correction
                if ( iorder .gt. 1 ) then
C     Parallel communication of  split fluxes derivatives
C     using  mpi_send, mpi_recv calls.
                call par_comm_split_flux_derivatives
C     Carry out defect correction to get the higher order accuracy
                 call higher_order_SLKNS
C     Do the state vector update for higher order points in the cloud
                call update_higher_order
```

```
                end if
C     Parallel communication of  state vector U
C    using  mpi_send, mpi_recv calls.
                call par_comm_state_vector
C    Evaluate L-2 norm, L-infinity residue and send it for plotting
                call residue
C    Write output and post-processing data after iprn iterations
                if((iter/iprn)*iprn.eq.iter) then
                        call output
                end if
        end do
C     Close all files, deallocate memory.
        call clsfil
C     MPI finalize call
                call mpi_finalize (anumpi_err)
        stop
        end
C-------------------------------------------------------------
```

The slave code differs from the master code in the *subroutine open_file*. The slave code opens its processor's specific file for reading cloud and fluid dynamic data.

6.6 Multi-objective optimization methodology for SLKNS

The meshless method only require boundary data, cloud of points and its connectivity. As mentioned earlier the existing method reported in the literature carry out optimization for meshless method by flagging off the blank nodes and generating connectivity of the participating nodes. In the present research we have used a novel approach for cloud handling for meshless method. In this method the sub-cloud around the body is generated after every optimization step and this new sub-cloud is merged with the background cloud. This methodology can be described in following steps as shown in the Figure 6.29

- Hole creation in the background cloud.
  Hole is created in the background cloud by blanking nodes in the vicinity of

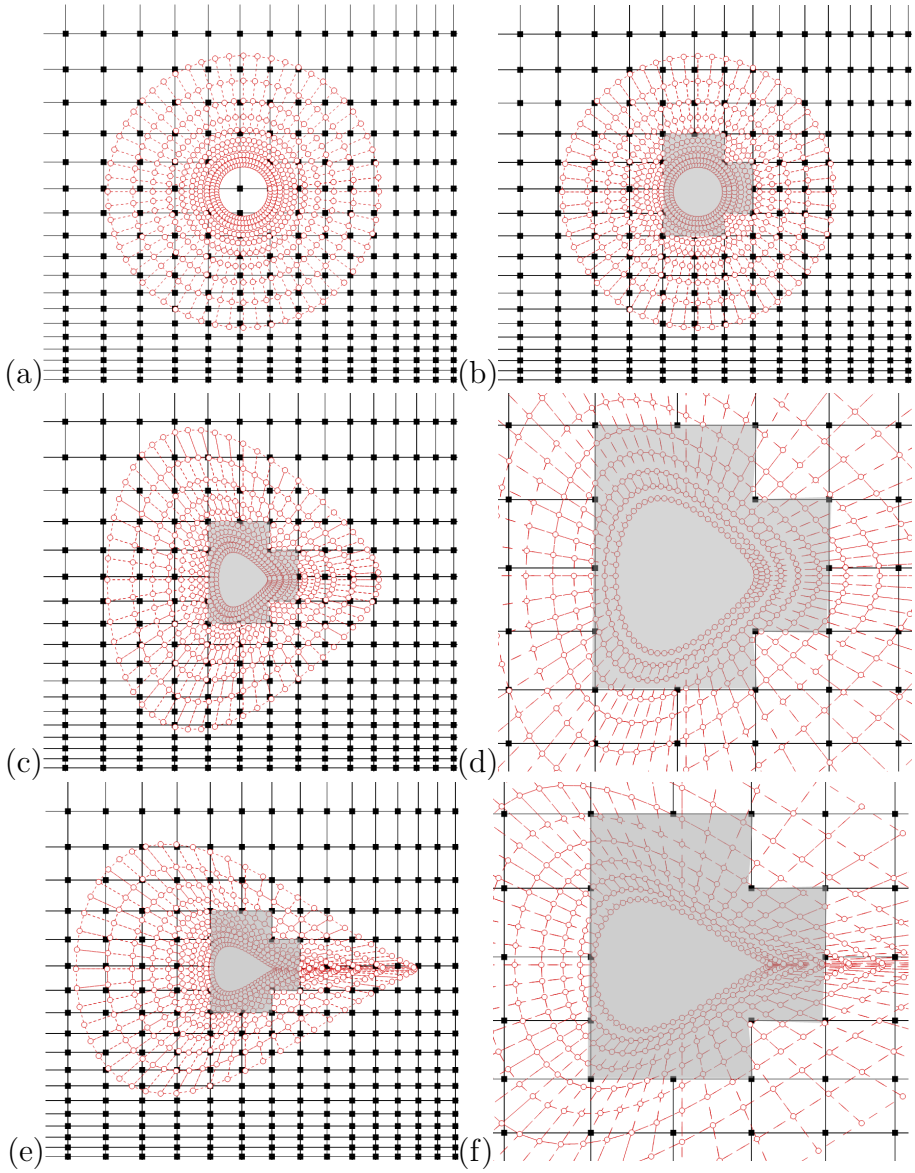

Figure 6.29: Cloud handling methodology for shape optimization.

the body which need optimization. The size of the hole is made large enough such that the body undergoing optimization remains bounded. This step is shown in Figure 6.29(b) in which nodes are blanked off around the body as shown in Figure 6.29 (a). Hole creation in the background cloud helps in avoiding the time-consuming node-deletion phase of pre-processing. During the optimization process the shape of the body may change drastically for such cases the optimization module can have many a priori different kind of holes so as to contain the shape of the body within its limit.

- Generation of sub-cloud around the body.
  The sub-cloud is generated around the new shape based on the suggestion of the optimization step. This is illustrated in Figure 6.29(c) and Figure 6.29(e) for two different shapes to illustrate that the body remains confined within the hole created in the background cloud. Figure Figure 6.29(d) and Figure 6.29(f) shows the zoomed view of the cloud around the body.

- Merging of background and sub-cloud.
  In this step the sub-cloud around the body and the background are merged to form a single cloud.

- Connectivity generation.
  The connectivity is only generated for the nodes lying in the vicinity of the body.

- Mapping of the fluid dynamic data.
  The fluid dynamic data is mapped from cloud-body configuration to another cloud-body configuration as shown in Figure 6.30 (a) and (b). This helps in quick convergence of the solution for the new body shape suggested by the optimization step.

6.6.1 Multi-objective optimization and parametrization

The shape of the body depends on its parametrization. As described earlier there are various parametrization approaches like discrete approach, domain element approach, polynomial and splines based, CAD based, free-form deformation and soft object animation based approach. The shape parametrization approach is

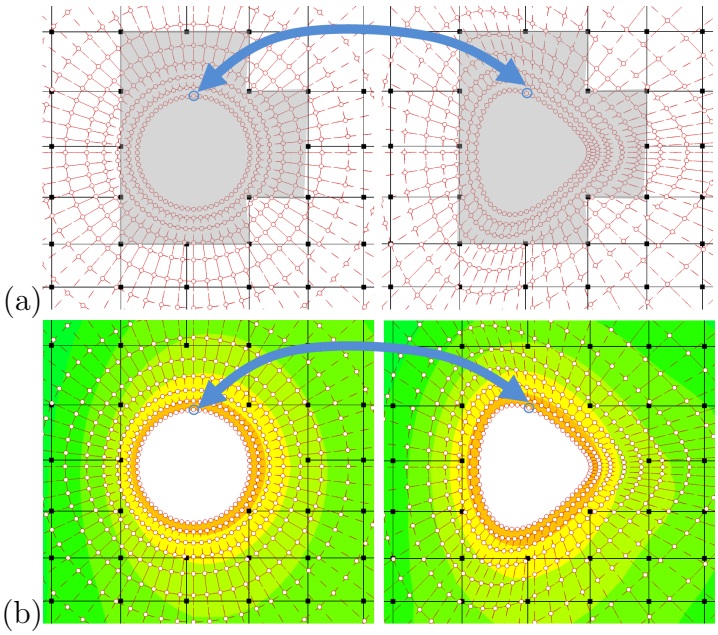

Figure 6.30: Mapping of the fluid dynamic data from one cloud to another.

problem specific and is of immense importance as it can bring drastic reduction in the computational time. Consider a simple shape parametrization based on four parameters i.e. x_1, x_2, x_3 and x_4 as shown in Figure 6.31. The parameter x_1 gives the length of the body, parameter x_2 gives the camber at the mid-body, parameter x_3 and x_4 are the two control points at two pre-determined positions. The optimization routine only requires the set of parameters $\vec{x}\in\mathbb{R}^n$ called the n-dimensional parameter space. The task of optimization is to get the best shape or $\vec{x}$ so as optimize m objective functions $f_i(\vec{x})\in Y\subset\mathbb{R}^m$. Solutions to these objective

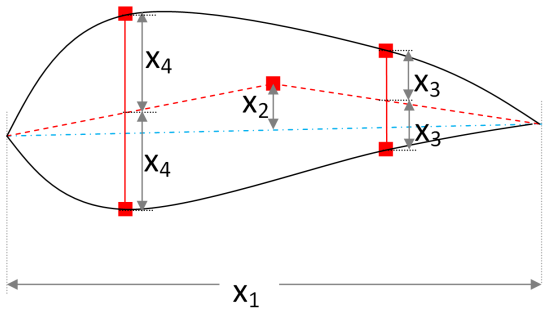

Figure 6.31: Shape parametrization.

functions defining the m-dimensional objective space with its subset $\tilde{Y} \subset Y$ represents the feasible objective region. Since the real world is dotted with multi-modal noisy search space fractured with discontinuities hence calculus based methods fails to reach the global solution as they are local in scope, require strict continuity and derivability. In the present study three stochastic or non-gradient based methods have been considered namely i) Nonlinear simplex, ii) Genetic algorithm (GA), and iii) Ant Colony Optimization (ACO). Figure 6.32 shows the $\vec{x}$ containing the shape parameters of the candidate design configuration and its relation with the optimization method. Nonlinear simplex method starts by forming a simplex which is simply a polytope of $n+1$ vertices in n-dimensions. Each vertex of the simplex is given by the parametric shape vector as shown in Figure 6.32. The simplex undergoes reflection, expansion, contraction and shrinkage to move towards the best solution. In genetic algorithm (GA) the parameter involved in shape parametrization denotes a gene as shown in Figure 6.32 and genetic string denotes the shape or the candidate design which undergoes optimization. The basic building block of genetic algorithm is its i)Parameterization and Coding, (ii) Population, (iii) Crossover, (iv) Mutation and (v)Selection. In ant colony optimization (ACO) each parameter is discretized into finite number of levels such that the ant path contains the level of each parameter. In this method the path taken by the ant denotes a shape or candidate design configuration participating in the optimization as shown in Figure 6.32.

6.6.2 New approach using scalarization based ϵ-dominance

The solution of muti-objective problem poses a challenge and requires a new notion of optimality as in most of the cases objectives tend to be in conflict with each other. The present research gives a novel approach based on the concept of Pareto optimality and scalarization based ϵ-dominance as the basis for the multiple objective optimizations. In the present algorithm the concept of multiple objective optimizations is achieved using the goal vector (or reference point) optimization strategy[290] by applying scalarization. This method translates the multi-objective function into a single objective. The ranking is done using scalarization based ϵ-dominance with L_p metric strategy. The minimization of the maximum distance from the goal vector drives the solution closer to the goal

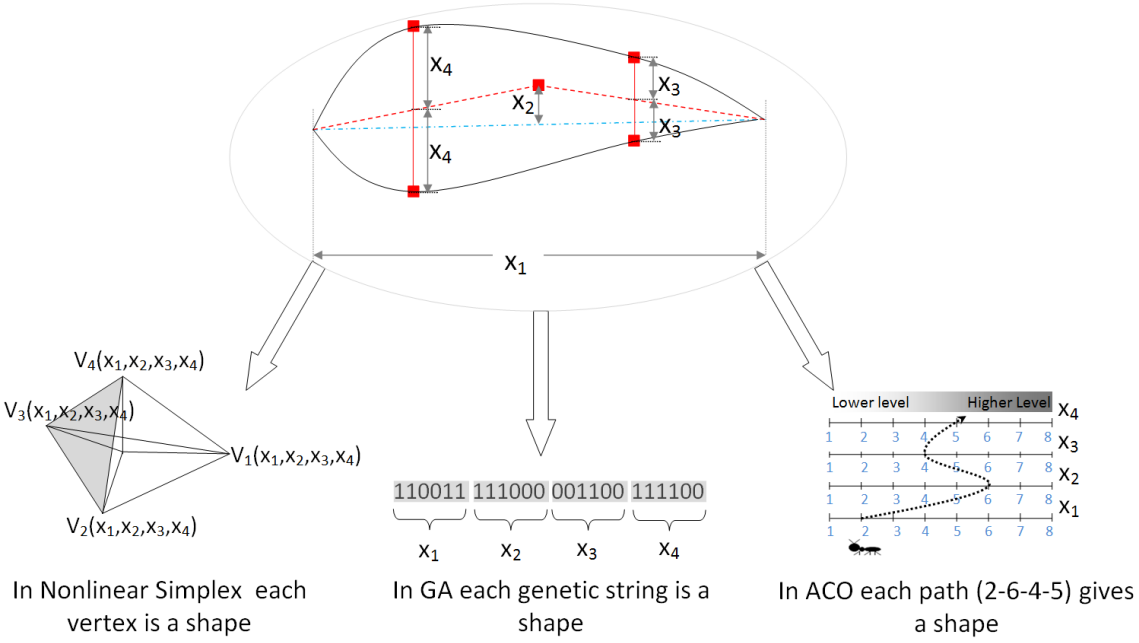

Figure 6.32: Parameterization coding in the optimization methods : i)Nonlinear Simplex, ii) Genetic algorithm, and iii) Ant colony optimization.

vector.

The method of determining ranking is based on either (i) non-dominated sorting (Pareto based), or (ii) sorting based on ϵ-dominance. In the non-dominated sorting approach Pareto optimality forms the basis of multi-objective optimization as it takes all the objectives into consideration simultaneously; every element in the Pareto front is a good solution. *Pareto-optimality only tells us which decisions to avoid.* This non-uniqueness of Pareto-optimal solution can be turned into advantage by using scalarizing function which projects the reference vector $\vec{q}^{g} \in \mathbb{R}^m$ onto the Pareto optimal front. This approach transforms the multi-objective problem into a single objective problem. There are many scalarizing function $s : Q \times Y \rightarrow \mathbb{R}^1$ which are strictly order preserving. Min-max optimization can be used by selecting Pareto point chosen by minimizing its weighted maximum deviation from the *ideal point (utopia point)* or the *demand point.* described earlier. The scalarization step is implemented by weighted L_p-problem as

$$\min_{\vec{x} \in \mathbb{R}^n} L_p^{(\vec{f},\vec{w},\vec{q}^*)}(\vec{x}) = \left(\sum_{i=1}^{m} w_i |f_i(\vec{x}) - q_i^*|^p \right)^{1/p} \tag{6.96}$$

where $\vec{q}^*$ is the goal or reference vector. Most of the multi-objective methods use Pareto based non-dominated ranking shown in figure. 6.33 and given as follows

$$\vec{f}^* \prec \vec{f} :\Leftrightarrow \underset{i\in 1,2,\dots m}{\forall}(f_i(\vec{x}^*) \leq f_i(\vec{x})) \wedge \underset{i\in 1,2,\cdots,m}{\exists}(f_i(\vec{x}^*) < f_i(\vec{x})) \tag{6.97}$$

where $\vec{f}^*$ is the non-dominated solution. The present research uses a new approach of sorting using scalarization based ϵ-dominance with L_p metric strategy [178] described by equation 6.98

$$\begin{aligned}\vec{f}^* \prec \vec{f} :\Leftrightarrow \underset{i\in 1,2,\dots m}{\forall}(f_i(\vec{x}^*) \leq f_i(\vec{x}) - \epsilon_i) \wedge \underset{i\in 1,2,\cdots,m}{\exists}(f_i(\vec{x}^*) < f_i(\vec{x}) - \epsilon_i) \\ \exists L_p^{(\vec{f},\vec{w},\vec{q}^*)}(\vec{x}) < L_p^{(\vec{f}-\epsilon_i,\vec{w},\vec{q}^*)}(\vec{x}) \ ; \ \epsilon_i = \zeta(f_i^{max} - f_i^{min}); \ \zeta \in (0,1)\end{aligned} \tag{6.98}$$

where ζ is a user defined parameter which determines the ϵ-dominance zone as illustrated in Fig. 6.33. The points on the curve 1 belong to the Pareto optimal (non-dominated) solutions. Similarly curves 2 and 3 represent less non-dominated sets. For the purpose of ranking using non-dominated sorting we construct curves 1,2 and 3 from the given data. Solutions on curve 1 are given highest priority, next preference is given to curve 2 then to curve 3. The sorting using ϵ-dominance described by equation 6.98, this is also shown in form of loops in Fig. 6.33. The distance of a solution from goal vector is L_p metric used by the scalarization function. The solutions within a zone are sorted from rest of them. We see that the ϵ-dominance zone contains solutions belonging to multiple levels of non-dominated Pareto solutions. As the value of ζ increases the size of the loop increases. Smaller loop reduces the optimization time, but may run into the risk of not reaching the global optimum.

6.6.2.1 Scalarization in absence of goal vector

In absence of the prescribed goal vector or reference vector $\vec{q}^g \in Q \subset \mathbb{R}^m$ we consider an ideal vector $\vec{q}_i^* \equiv \{f_i(\vec{x}), \cdots, f_m(\vec{x})\}$ defined as an individual maximum of each component of a vector obtained during the course of optimization after k evaluations of the problem as follows

$$q_i^* = \underset{\vec{x}\in\mathbb{R}^n}{min}\{(f_i(\vec{x}))^1, \cdots, (f_i(\vec{x}))^k\} \tag{6.99}$$

Thus the goal vector is the minimum value of the function obtained during course of optimization after k simulation runs.

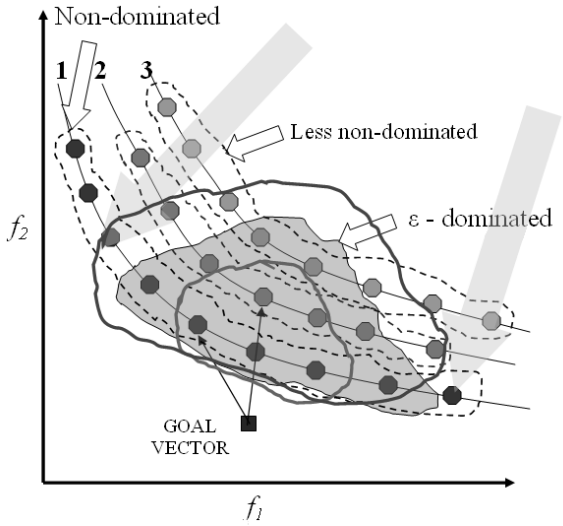

Figure 6.33: Sorting using scalarization based ϵ-dominance with L_p metric strategy.

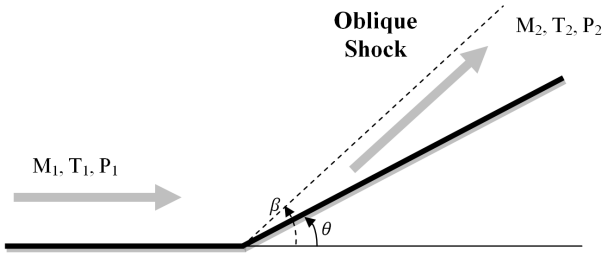

Figure 6.34: Oblique shock test case.

6.6.3 Multi-objective optimization example

Two examples are taken to illustrate the multi-objective optimization methodology. The first example is multi-objective optimization for oblique shock test case, the second example is aerodynamic shape optimization of an airfoil in a meshless framework.

6.6.3.1 Oblique shock test case

Consider a example test case of a oblique shock problem involving compressible frictionless irrotational flow of air. The inlet pressure and temp being 95720 Pa and 273 K respectively. Figure 6.34 describes the example test case in which air

moving in a supersonic speed $M_1 = 3$ approaches a ramp which is at an angle θ to the horizontal. After production of an oblique shock (at an angle β to the horizontal) the pressure, temperature changes to after shock condition. To simplify assume that the Rankine-Hugoniot (R-H) jump conditions relate the pre-shock and post-shock situations. The optimization problem is now formulated as follows: Given the inlet flow conditions i.e. Mach (M_1), Pressure (P_1), Temperature (T_1) and angle of shock β optimize the $n = 3$ parameters of post shock conditions i.e. pressure P_2, temperature T_2 and ramp angle θ. The $m = 3$ objective functions which are to be optimized are entropy change ΔS, enthalpy change ΔH across the shock and the ramp angle θ given as

$$\begin{aligned} f_1(\vec{x}) &= \Delta S = C_p\ ln(T_2/T_1) - R\ ln(P_2/P_1) \\ f_2(\vec{x}) &= \Delta H = C_p\ (T_2 - T_1) \\ f_3(\vec{x}) &= \theta = Tan^{-1}(2cot\beta \tfrac{M_1^2 sin^2\beta - 1}{M_1^2(\gamma + cos2\beta) + 2}) \end{aligned} \tag{6.100}$$

For a given goal vector $\vec{q}^* \equiv (\Delta S_m, \Delta H_m, \theta_m)$ the scalarizing function $s : Q \times Y \rightarrow R^1$ is defined by the L_2 metric. This L_2 metric based normalized distance from the goal vector scalarizes the multi-objectives to a single function described by

$$s = \|(\Delta S, \Delta H, \beta) - (\Delta S_m, \Delta H_m, \beta_m)\|_2 \tag{6.101}$$

Multi-objective nonlinear simplex (MNS), multi-objective ant colony (MACO) , multi-objective genetic algorithm (MGA) was run with the goal vector ($\Delta S_m = 168.75, \Delta H_m = 275860, \theta_m = 0.5237$). The exercise shows that multi-objective nonlinear simplex (MNS) converges faster than multi-objective ant colony (MACO) and multi-objective genetic algorithm (MGA) for this case as shown in Figure 6.35. It is found that MNS took 404 function calls compared to 2125 function calls for MACO to converge to 7 decade fall whereas MGA took 4900 function calls for 5 decade fall of L_2 metric based normalized distance from the goal vector. Multi-objective nonlinear simplex (MNS) and multi-objective ant colony (MACO) are attractive choice of methods which can be used in conjunction with the meshless SLKNS code to carry out multi-objective shape optimization. [1] In

[1] Studies conducted over various test cases have shown that MACO and MNS both are promising methods for shape optimization as they require minimum function calls or CFD runs [178]. These studies are not reported in the present work as they are beyond the scope of the thesis.

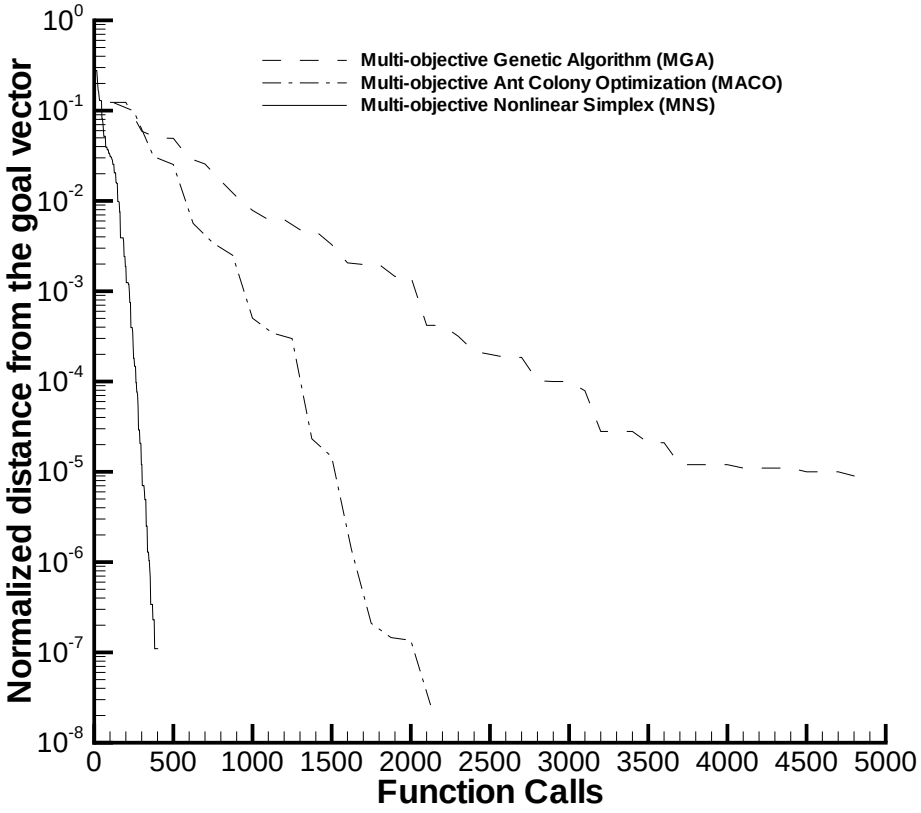

Figure 6.35: L_2 metric versus function calls for multi-objective nonlinear simplex, ant colony optimization and genetic algorithm.

the present research multi-objective nonlinear simplex (MNS) method is preferred over multi-objective ant colony (MACO) method as MNS takes less number of CFD calls.

6.6.3.2 Aerodynamic shape optimization using SLKNS

Consider two objective functions based an aerodynamic shape optimization problem involving viscous subsonic flow around an airfoil at Mach = 0.7 and 5×10^6 Reynolds number. In this test case of multi-objective aerodynamic shape optimization, the objective functions are

$$Objective\ Functions\ f_1 = C_l\ ,\ f_2 = C_d \tag{6.102}$$

and scalarization function is given as

$$Scalarization\ function = \|(C_l, C_d) - (C_{l,m}, C_{d,m})\|_2 \tag{6.103}$$

where $(C_{l,m}, C_{d,m})$ are the components of the goal vector taken as

$$\vec{q}^* \equiv (C_{l,m} = 1.2, C_{d,m} = 0.09) \tag{6.104}$$

The meshless SLKNS solver was run to evaluate the lift coefficient C_l and drag coefficient C_d and carry out optimization. The shape of the airfoil was constructed using NACA 4-digit airfoil formula. Parameterization consists of 3 shape controls and one flow control parameter. The shape parameters are 1) Maximum thickness of airfoil (THK), 2) Maximum camber (MC) and 3) Position of maximum camber (PMC). The flow control parameter used was 4) Angle of attack (AOA). In this test case, constraint concerning the thickness of airfoil was imposed by fixing it's minimum value. Shape optimization was carried out using ACO and meshless SLKNS solver. Figure 6.36 shows a schematic of SLKNS based multi-objective shape optimization process. Only the control parameters are allowed to change as the optimization proceeds. Each of the parameter's domain was discretized into 5 levels and 125 ant paths were chosen randomly. Each ant path defines the shape of the airfoil as well as AOA at which it should be solved. Figure 6.37 shows the discretized parameter domain and the ant paths. For example each path taken gives a shape of the airfoil as shown in Figure 6.37 where an ant e.g. *ANT01* traces out a path $1-3-1-2$ which gives the value of angle of attack (AOA),

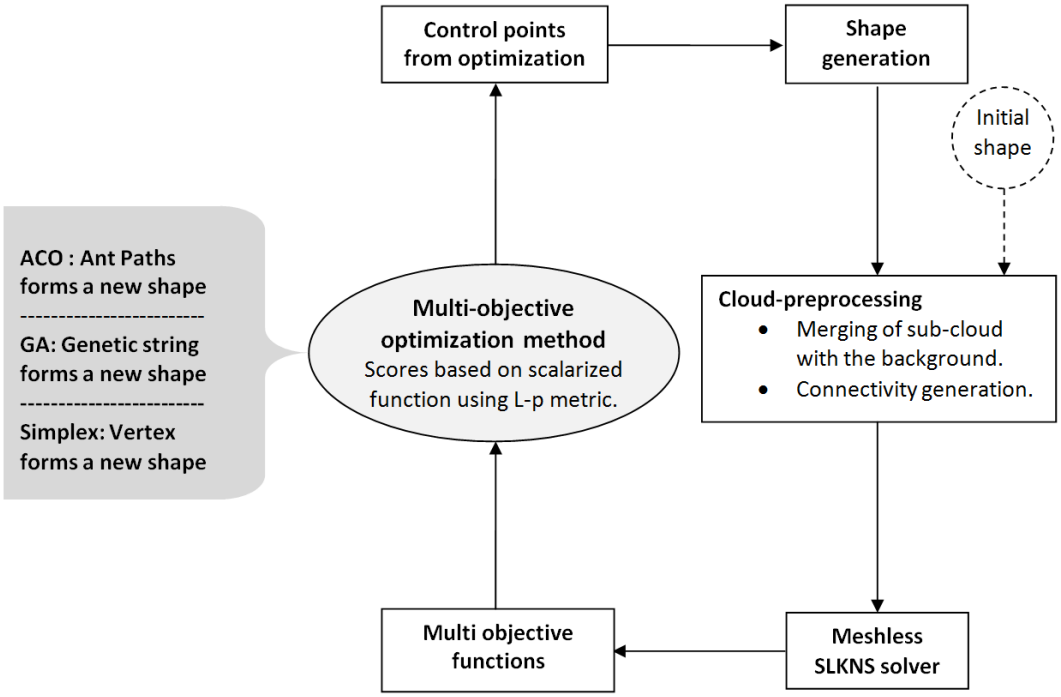

Figure 6.36: Schematic of a SLKNS based multi-objective shape optimization process.

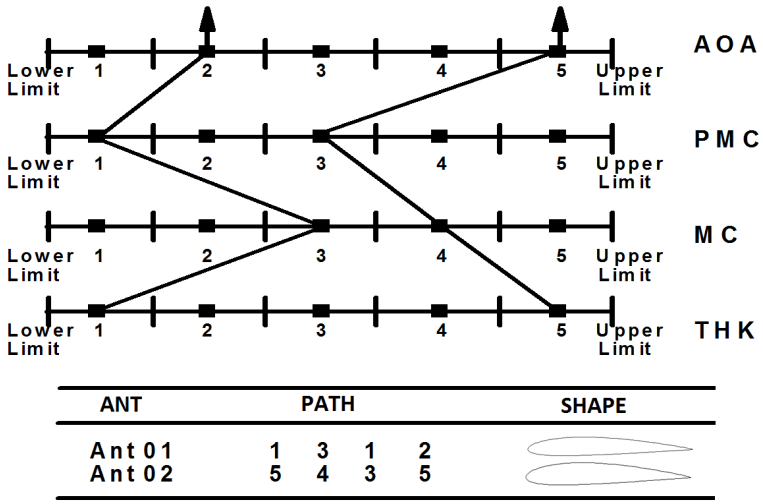

Figure 6.37: Ant paths and shape parametrization.

Table 6.4: Comparison of Initial and optimized results for goal vector $\vec{q}$

MACO parameters	*Initial range*	*Optimization result*
THK	[10 , 15]	[10.40, 10.82]
MC	[0.0 , 4.0]	[2.15, 2.43]
PMC	[0.2 , 0.4]	*[0.25, 0.45]*
AOA	[0.0 , 5.0]	*[4.90, 5.62]*
Optimum C_l, C_d	–	(1.214,0.087)
No. of CFD runs	–	875

position of maximum camber (PMC), maximum camber (MC) and thickness of the airfoil (THK). Using this we get the shape as well as angle of attack to carry out next optimization step. After carrying out cloud pre-processing step which involves cloud merging and connectivity generation we proceed with the optimization. Trials and scores were evaluated at each discretized point of the parametric domain using the L_2 metric. For each ant path in the study, one CFD call is needed. A large number of CFD calls are required for the entire shape optimization. It should be noted that the time taken by the flow solver was very high compared to the time taken by ACO. Table 6.4 shows the initial and final range after convergence for the parameters for goal vector $\vec{q} \equiv (C_{l,m} = 1.2, C_{d,m} = 0.09)$ The optimization case was also run with multi-objective nonlinear simplex (MNS) in order to compare it with multi-objective ACO. MNS took nearly four times less CFD runs but failed to converge to a lower value of L_2 metric while multi-objective ant colony optimization took nearly 875 CFD calls and converges to a much lower value of L_2 metric as ACO goes outside the range provided by the user. *It should be noted that the parameters PMC and AOA converge to a range outside the initial range supplied by the user - an advantage of using ACO based multi-objective optimization.* Figure 6.38(a) shows the change in airfoil shape and Figure 6.38(b) shows the convergence in terms of scalarization based L_2 metric with respect to CFD calls as the optimization proceeds.

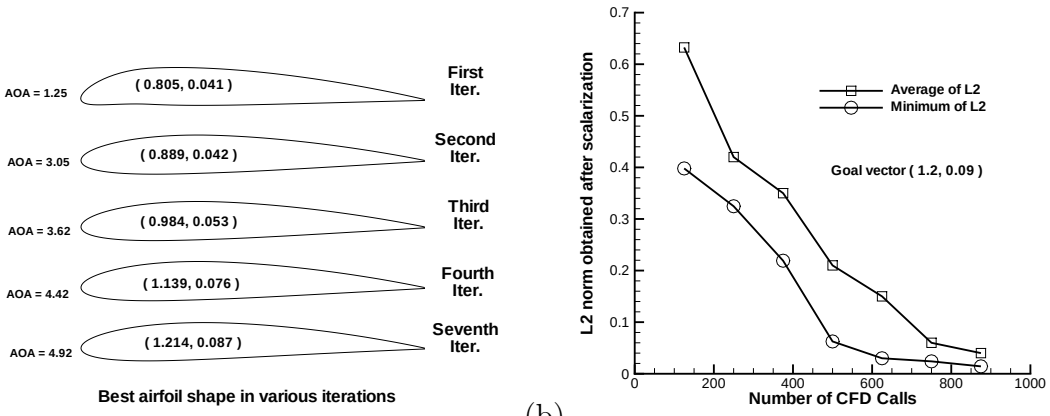

(a) (b)

Figure 6.38: ACO based aerodynamic shape optimization (a) change of shape with iterations, and (b)convergence for goal vector $\vec{q}$.

6.7 Summary

Normal equations as well as QR approach used in least square method produces inaccurate results when applied to stretched distribution of points required to resolve boundary layers of a viscous slip flow problem. The present approach overcomes the limitations due to the ill-conditioning which is the weakness of normal equations by using a novel concept of stencil splitting. The present method like normal equations approach requires $(m+n/3)n^2$ flops and provides stable results for highly stretched distribution of points involving about half the arithmetic as compared to QR approach. A new meshless method, SLKNS based on kinetic theory retains the simplicity of normal equations approach and achieves higher order accuracy through multi step procedure of defect correction. SLKNS uses symmetric connectivity to generate graph required for domain decomposition. Parallelization of SLKNS was carried out using optimized contention free communication. By using coarse-medium-fine cloud sequencing the SLKNS solver can be further accelerated. SLKNS can also be readily used for optimization by generating cloud over the candidate body after each optimization step and merging its sub-cloud. SLKNS was tested for carrying out multi-objective optimization using scalarization based ϵ-dominance strategy coupled with ant colony and simplex method. Ant colony optimization (ACO) can venture outside the

range provided by the user while exploring the optima at a cost of higher number of CFD calls as compared to nonlinear-simplex. Multi-objective nonlinear simplex (MNS) because of lesser CFD calls is more attractive, hence it is used in the present research work to demonstrate multi-objective optimization within meshless framework.

Chapter 7

Results and Discussions

7.1 Introduction

Based on the formulations described in chapter 6, SLKNS code has been developed. The code uses kinetic flux vector splitting based boundary condition for non-continuum slip flow as well as continuum flow. SLKNS code also has an option of no-slip, Maxwell velocity slip and von Smoluchowski temperature jump boundary conditions. In this code the time integration is based on local time step as well as global time step. By default SLKNS code uses global time step with 3-stage scheme of Shu and Osher [249]. In the present study local time step with explicit first order Euler is used only for test cases based on 3-D problems and test cases for carrying out optimization studies in order to cut down computational time for faster convergence to steady solutions. The code implements dynamic allocation of memory for each node based on its connectivity.

This chapter describes the validation of meshless SLKNS solver for a variety of test cases including continuum flows and non-continuum slip flows. Validation test cases include experimental pressure drop example, sets of numerical case studies with slip flow features, supersonic flows and test cases with typical features of the strongly rotating flows characterized by steep density gradient and thin boundary layers. Multi-objective optimization test case is in addition included to describe cloud handling methodology and non-linear simplex with ϵ-dominance strategy within meshless framework.

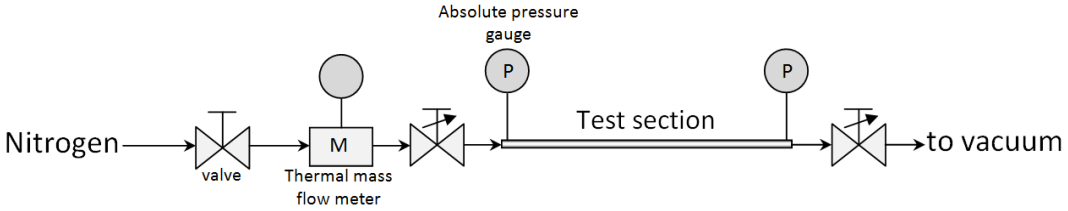

Figure 7.1: Experimental setup

7.2 Validation with experimental data

Literature review revealed large scale availability of slip flow data for micro-slip flows but scanty data was available for rarefied slip flow. More so ever to carry out accurate simulation we require the correct value of tangential momentum accommodation coefficient i.e. the factor which identifies the fraction of molecules reflecting in a diffuse way. In most of the reported experimental methods the tangential momentum accommodation coefficient, σ are derived under an assumption that pressure gradient along the test specimen is negligible. Hence, it was planned to carry out in house experiments for validation of the SLKNS code with an experimental pressure drop versus flow rate data for two pipes with different geometries and surface finish.

Fig. 7.1 shows the experimental setup which consists of thermal mass flow meter and capacitance based absolute pressure gauge. The test section chosen was a pipe, motive gas chosen was nitrogen and experiment was conducted for varying mass flow rate and its corresponding inlet and outlet pressures were measured. The test section was baked and out-gassed. The setup was made leak tight by carrying out the Helium leak detection test. An extra valve was placed just after the test section for pressure throttling and rarefied condition was maintained using diffusion and roots pump. Experiments were conducted for two different tubes of varying surface finish with following dimensions : i) 0.25 inch outer diameter (OD) with inner diameter(ID) 0.475 cm and length 54 cm, and ii) 0.50 inch OD with ID 1.205 cm and length 100.8 cm. Experiments revealed that the rarefaction acts to increase the observed mass flow rate for a given inlet and outlet pressure condition. The effect of slip makes a more significant contribution to the mass flow.

7.2.1 Analytical determination of mass flow rate

In the present case Maxwell model is used for gas-surface interaction. Maxwell model uses tangential momentum accommodation coefficient (TMAC), σ. The value of TMAC, σ depends upon the surface roughness of the wall as well as particular solid and gas involved. For specular reflection TMAC, σ is zero and for fully diffuse reflection σ becomes unity. Under fully developed conditions the flow can be described by axial momentum equation as

$$\mu\left(\frac{d^2u}{dr^2}+\frac{1}{r}\frac{du}{dr}\right)=\frac{dp}{dz} \tag{7.1}$$

The solution of Eq.7.1 gives a parabolic velocity profile equation as

$$u_t(r,z)=A(z)r^2+B(z)r+C(z) \tag{7.2}$$

The boundary condition is provided by the tangential slip velocity written in terms of TMAC, σ as

$$u_t(r,z)=-\frac{2-\sigma}{\sigma}\lambda\left(\frac{\partial u}{\partial r}\right)_{r=a} \tag{7.3}$$

where a is the radius of the pipe and λ is the mean free path. By substituting the expressions of the derivatives the factors $A(z)$, $B(z)$ and $C(z)$ can be derived as

$$A(z)=\frac{1}{4\mu}\frac{dp}{dz} \tag{7.4}$$

$$B(z)=0 \tag{7.5}$$

$$C(z)=-\frac{1}{4\mu}\frac{dp}{dz}\left(a^2+2a\frac{2-\sigma}{\sigma}\lambda\right) \tag{7.6}$$

Substituting these factors we can obtain the axial velocity profile across the pipe as

$$u(r,z)=-\frac{1}{4\mu}\frac{dp}{dz}\left(a^2-r^2+2a\frac{2-\sigma}{\sigma}\lambda\right) \tag{7.7}$$

The average velocity can be written as

$$\begin{aligned}\bar{u}(z) &= \frac{1}{\pi a^2}\int_0^a u(r,z)2\pi r dr\\ &= -\frac{a^2}{8\mu}\frac{dp}{dz}\left(1+4\frac{2-\sigma}{\sigma}\frac{\lambda}{a}\right)\\ &= -\frac{a^2}{8\mu}\frac{dp}{dz}\left(1+8\frac{2-\sigma}{\sigma}\mathrm{Kn}\right)\end{aligned} \tag{7.8}$$

where Kn is the Knudsen number defined as

$$\mathrm{Kn} = \frac{\lambda}{2a} = \frac{\mu}{2a}\sqrt{\frac{\pi}{2\rho p}} = \frac{\mu}{2ap}\sqrt{\frac{\pi RT}{2}} \tag{7.9}$$

The mass flow rate (generally measured in units of $mbar - liter/s$) can be expressed as

$$\begin{aligned} \dot{m} &= \pi a^2 \bar{u}(z) p \\ &= -\frac{\pi a^4}{8\mu} p \frac{dp}{dz}\left(1 + 4\frac{2-\sigma}{\sigma}\frac{\lambda}{a}\right) \\ &= -\frac{\pi a^4}{8\mu} p \frac{dp}{dz}\left(1 + 8\frac{2-\sigma}{\sigma}\mathrm{Kn}\right) \end{aligned} \tag{7.10}$$

The ratio of mass flow rate in slip flow regime, $\dot{m}$ with respect to mass flow rate in continuum flow regime, $\dot{m}_{NS}$ can be expressed as

$$\frac{\dot{m}}{\dot{m}_{NS}} = \left(1 + 8\tfrac{2-\sigma}{\sigma}\mathrm{Kn}\right) \tag{7.11}$$

Thus the mass flow rate depends also on the pressure and its axial gradient. The axial pressure gradient does not remain constant with respect to axial position. This pressure gradient can be derived in two steps [13] : i) by obtaining the radial velocity profile using the continuity equation, ii) deriving the pressure equation based on the boundary condition of radial velocity at the wall. For isothermal case we can write the continuity equation at steady state as

$$\frac{1}{r}\frac{\partial p(z) v(r,z) r}{\partial r} + \frac{\partial p(z) u(r,z)}{\partial z} = 0 \tag{7.12}$$

where $v(r,z)$ is the radial component of the velocity. After substitution of tangential velocity we get the following expression

$$\frac{1}{r}\frac{\partial p(z) v(r,z) r}{\partial r} = \frac{1}{8\mu}\frac{d^2p^2}{dz^2}(a^2 - r^2) + \frac{a}{2}\frac{2-\sigma}{\sigma}\sqrt{\frac{\pi RT}{2}}\frac{d^2p}{dz^2} \tag{7.13}$$

The radial component of the velocity, $v(r,z)$ can be evaluated as

$$\begin{aligned} v(r,z) &= \frac{1}{rp(z)}\int r\frac{\partial p(z) u(r,z)}{\partial z} dr \\ &= \frac{1}{rp(z)}\left(\frac{1}{8\mu}\frac{d^2p^2}{dz^2}\left(\frac{a^2r^2}{2} - \frac{r^4}{4}\right) + \frac{ar^2}{4}\frac{2-\sigma}{\sigma}\sqrt{\frac{\pi RT}{2}}\frac{d^2p}{dz^2} + C_1\right) \end{aligned} \tag{7.14}$$

where C_1 is the integration constant. Using symmetry boundary condition at the centre of the pipe where $v(r,z) = 0$ at $r = 0$. With this $C_1 = 0$ and radial velocity $v(r,z)$ can be written as

$$v(r,z) \quad = \frac{1}{p(z)} \left(\frac{1}{8\mu} \frac{d^2p(z)^2}{dz^2} (\frac{a^2 r}{2} - \frac{r^3}{4}) + \frac{ar}{4} \frac{2-\sigma}{\sigma} \sqrt{\frac{\pi RT}{2}} \frac{d^2p(z)}{dz^2} \right) \tag{7.15}$$

Using boundary condition at the wall where normal velocity is zero i.e. $v(r,z) = 0$ at $r = a$ we get the pressure condition

$$\frac{d^2p(z)^2}{dz^2} + \frac{8\mu}{a} \frac{2-\sigma}{\sigma} \sqrt{\frac{\pi RT}{2}} \frac{d^2p(z)}{dz^2} = 0 \tag{7.16}$$

This can also be written in terms of Knudsen number $\overline{\mathrm{Kn}}$ defined on the basis of average pressure $\bar{p}$=$(p_i + p_o)/2$ of the pipe as

$$\overline{\mathrm{Kn}} = \frac{\bar{\lambda}}{2a} = \frac{\mu}{2a\bar{p}} \sqrt{\frac{\pi RT}{2}} \tag{7.17}$$

The pressure variation equation can now be expressed as

$$\frac{d^2p(z)^2}{dz^2} + 16\overline{\mathrm{Kn}}\bar{p} \frac{2-\sigma}{\sigma} \frac{d^2p(z)}{dz^2} = 0 \tag{7.18}$$

Using pressure boundary conditions i)$p = p_i$ at $z = 0$, and ii)$p = p_o$ at $z = L$ we can solve for pressure as

$$p(z) = -f_{slip} + \sqrt{(p_i + f_{slip}\bar{p})^2 + (p_o - p_i)(p_i + p_o + 2f_{slip}\bar{p}) \frac{z}{L}} \tag{7.19}$$

The pressure gradient can be derived as

$$\frac{dp(z)}{dz} = \frac{(p_i - p_o)(p_i + p_o + 2f_{slip}\bar{p})}{2\sqrt{L(L(p_i + f_{slip}\bar{p})^2 + (p_o - p_i)(p_i + p_o + 2f_{slip}\bar{p})z)}} \tag{7.20}$$

where factor f_{slip} is expressed as

$$f_{slip} = 8\overline{\mathrm{Kn}} \frac{2-\sigma}{\sigma} \tag{7.21}$$

The pressure gradient at the inlet and outlet can be written as

$$\begin{aligned} \left(\frac{dp(z)}{dz} \right)_{z=0} &= \frac{(p_i - p_o)(p_i + p_o + 2f_{slip}\bar{p})}{2L(p_i + f_{slip}\bar{p})} \\ \left(\frac{dp(z)}{dz} \right)_{z=L} &= \frac{(p_i - p_o)(p_i + p_o + 2f_{slip}\bar{p})}{2L(p_o + f_{slip}\bar{p})} \end{aligned} \tag{7.22}$$

The average pressure gradient can be written as

$$\frac{d\bar{p}(z)}{dz} = \frac{(p_i - p_o)(p_i + p_o + 2f_{slip}\bar{p})^2}{4L(p_i + f_{slip}\bar{p})(p_o + f_{slip}\bar{p})} \tag{7.23}$$

The mass flow rate, $\dot{m}$ for a short pipe in terms of average pressure and its gradient can be expressed as

$$\begin{aligned} \dot{m} &= -\frac{\pi a^4}{8\mu}\bar{p}\frac{d\bar{p}}{dz}(1 + f_{slip}) \\ &= \frac{\pi a^4}{8\mu}\bar{p}\frac{\Delta p}{L}\bar{\phi_p}(1 + f_{slip}) \end{aligned} \tag{7.24}$$

where

$$\bar{p}\frac{\Delta p}{L} = \left(\frac{p_i + p_o}{2}\right)\frac{(p_i - p_o)}{L} \tag{7.25}$$

and $\bar{\phi_p}$ is

$$\bar{\phi_p} = \frac{(p_i + p_o + 2f_{slip}\bar{p})^2}{4(p_i + f_{slip}\bar{p})(p_o + f_{slip}\bar{p})} \tag{7.26}$$

7.2.2 Validation with pressure drop and flow rate data

In order to validate the SLKNS code with the experimental data we require the tangential momentum accommodation coefficient (TMAC) which identifies fraction of molecules undergoing diffuse reflection. Refer Appendix E for the experimental determination of tangential momentum accommodation coefficient (TMAC). In the present study, axi-symmetric SLKNS code was used to calculate mass flow rate for a given pressure drop for 0.25 inch OD pipe and 0.50 inch OD pipe with TMAC evaluated using method-III described in the Appendix E. The state update using axi-symmetric SLKNS is given as

$$\boldsymbol{U}(t + \Delta t) = \boldsymbol{U}(t) - \Delta t \left[\begin{array}{l} \left(\frac{\partial \boldsymbol{GZ}^+(t)}{\partial z}\right)_{\Delta z<0} + \left(\frac{\partial \boldsymbol{GZ}^-(t)}{\partial z}\right)_{\Delta z>0} \\ + \left(\frac{1}{r}\frac{\partial r\boldsymbol{GR}^+(t)}{\partial r}\right)_{\Delta r<0} + \frac{1}{r}\left(\frac{\partial r\boldsymbol{GR}^-(t)}{\partial r}\right)_{\Delta r>0} + \boldsymbol{S} \end{array} \right] \tag{7.27}$$

where expressions of z and r component of the split fluxes $\boldsymbol{GZ}^{\pm}$, $\boldsymbol{GR}^{\pm}$ and source term $\boldsymbol{S}$ are given in section D.4 of Appendix D. Figure 7.2 shows the validation of SLKNS code along with the selected experimental data and analytical expression for flow rate versus average pressure for 0.50 and 0.25 inch OD pipe.

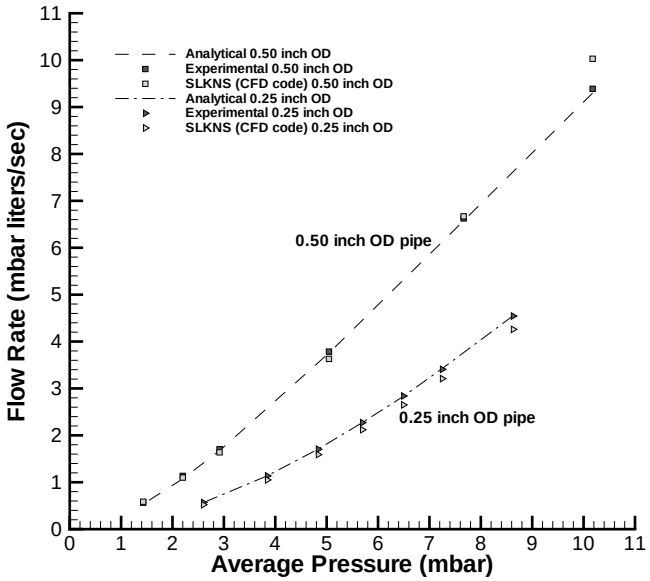

Figure 7.2: Validation of SLKNS code using experimental data and analytical expression for flow rate versus average pressure for 0.50 and 0.25 inch OD pipe.

7.3 Validations with numerical test cases

This section presents set of twelve test cases to validate SLKNS, this also includes two test cases chosen to validate the robustness and versatility of the meshless solver for carrying out multi-objective optimization. The test cases are described as follows :

- Continuum transonic flow over NACA0012 airfoil to validate wall boundary condition using SLKNS solver.
- Hypersonic rarefied flow over a flat plate to validate kinetic wall boundary conditions and its comparison with gradient based slip boundary conditions.
- Rarefied transonic flow over NACA0012 airfoil to validate the slip boundary condition.
- Velocity distribution in a cylindrical annuli to validate slip boundary condition.
- Concentric Couette flow to validate slip under rotation and axi-symmetric solving capability of the solver. This test case was also solved with SLKNS solver using r-θ plane.
- Rarefied flow in a rotating annulus to validate the axi-symmetric rarefied flow solving capability.
- Optimization of slowly moving ring in a rotating annulus to validate the optimization capability for axi-symmetric problems.
- Flow field around a stationary body in the rotating subsonic and supersonic flow field.
- Rarefied near transition flow in a rotating eccentric cylinder to validate the slip modeling abilities of the solver under rarefied condition beyond slip and near transition regime with adverse pressure gradient.
- Rarefied supersonic flow over a hemisphere to validate SLKNS for 3-D flow and slip boundary.

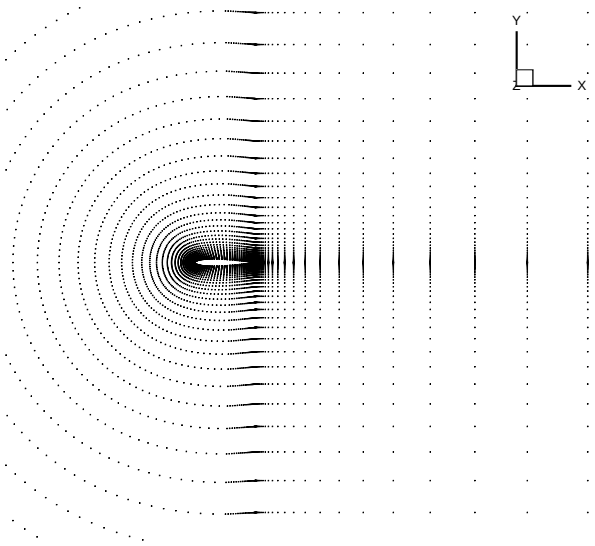

Figure 7.3: Cloud of points around NACA0012 aero foil

- Stationary hemisphere in strongly rotating flow field to validate SLKNS for rarefied core boundary condition.
- Multi-objective optimization of stationary body in a strongly rotating flow field to demonstrate the optimization method in meshless framework.

7.3.1 Transonic viscous flow over NACA0012 airfoil and wall boundary condition

Consider a test case of transonic continuum flow of air at Mach 0.8 past a NACA0012 airfoil at 10 degrees angle of attack at Reynolds number of 500 with Knudsen number of 2.4×10^{-3} based on chord length. This test case is simulated using C-type mesh of size 207 $\times$ 49 shown in Fig. 7.3 using no-slip and adiabatic wall boundary condition. This test case was solved using SLKNS solver with dissipation control, the state update for this case is written as

$$\boldsymbol{U}(t+\Delta t) = \boldsymbol{U}(t) - \Delta t \left[\begin{array}{c} \left(\frac{\partial \tilde{\boldsymbol{GX}}^{+}(t)}{\partial x}\right)_{\Delta x<0} + \left(\frac{\partial \tilde{\boldsymbol{GX}}^{-}(t)}{\partial x}\right)_{\Delta x>0} \\ + \left(\frac{\partial \tilde{\boldsymbol{GY}}^{+}(t)}{\partial y}\right)_{\Delta y<0} + \left(\frac{\partial \tilde{\boldsymbol{GY}}^{-}(t)}{\partial y}\right)_{\Delta y>0} \end{array} \right] \tag{7.28}$$

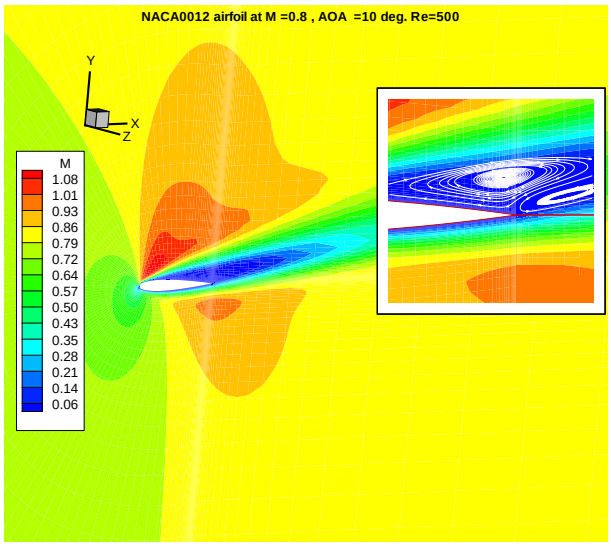

Figure 7.4: Transonic flow past NACA0012 airfoil at Mach=0.8,AOA=10 deg., Re=500

The fluxes based on dissipation control parameter φ are

$$\begin{aligned} \tilde{\boldsymbol{GX}}^{\pm} &= \tfrac{1}{2}\left[(\boldsymbol{GX}^{+} + \boldsymbol{GX}^{-}) \pm \varphi(\boldsymbol{GX}^{+} - \boldsymbol{GX}^{-})\right] \\ \tilde{\boldsymbol{GY}}^{\pm} &= \tfrac{1}{2}\left[(\boldsymbol{GY}^{+} + \boldsymbol{GY}^{-}) \pm \varphi(\boldsymbol{GY}^{+} - \boldsymbol{GY}^{-})\right] \end{aligned} \tag{7.29}$$

when dissipation control parameter φ=1 the formulation becomes in KFVS form. In this study the dissipation control parameter φ is a function of average cloud space or grid spacing in the connectivity. Fig.7.4 shows the Mach contours with two counter rotating vortices. Figure 7.5 and Figure 7.6 show plots of pressure coefficient and skin friction coefficient for SLKNS solver and a finite volume laminar viscous solver of Furtunato and Magi [89]. The skin friction coefficient plot also shows comparison with results of Catalano *et al.* [43] obtained using the grid size of $257 \times 65 = 16705$ nodes. SLKNS code was run for coarse, medium and fine cloud and its results in terms of lift and drag coefficients are compared in table 7.1. The table shows that the results improve as the cloud becomes fine. Results for fine cloud lies within the range reported in GAMM workshop [39]. Figure 7.7 shows plot of skin friction coefficient for coarse, medium and fine cloud using SLKNS solver. In this test case, the solver uses a 3-stage scheme of Shu and Osher [249] based on global CFL time step. The residue plot in Figure 7.8 shows the fall of normalized residue for coarse, medium and fine clouds. The

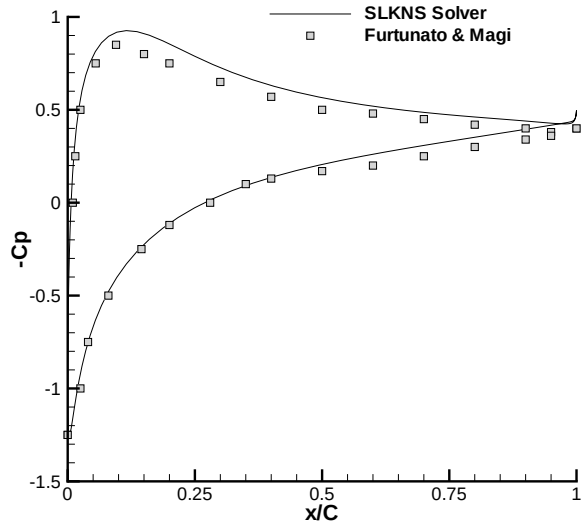

Figure 7.5: Pressure distribution plot for transonic flow past NACA0012 airfoil at Mach=0.8,AOA=10 deg., Re=500.

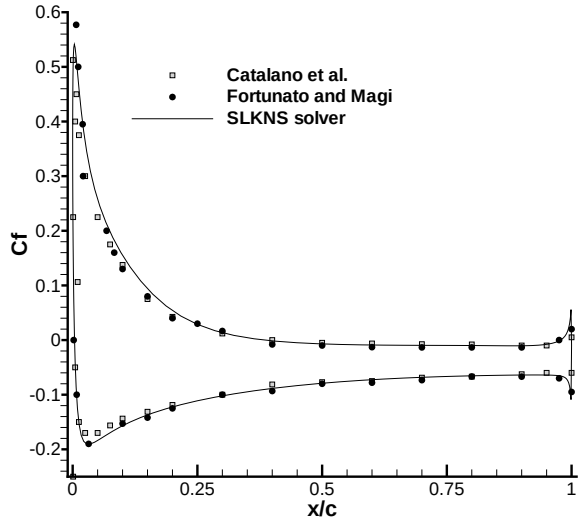

Figure 7.6: Skin friction plot for transonic flow past NACA0012 airfoil at Mach=0.8,AOA=10 deg., Re=500.

Table 7.1: Comparison of lift and drag coefficients for transonic flow past NACA0012 airfoil with coarse, medium and fine cloud.

Cloud	C_l	C_d
64×16	0.6992	0.3417
128×32	0.5520	0.3110
257×65	0.4642	0.2812
GAMM	0.4145 0.5170	0.2430 0.2868

normalized residue $\bar{Res}_2^k = Res_2^k/Res_2^0$, where residue Res_2^k is based on the average L_2 norm of all the state vector components across the domain at k^{th} iteration as described in section 6.3.4 of chapter 6. Kinetic schemes work more efficiently for high speed flows; this is evident if we compare the fall of residue of transonic flow past NACA0012 airfoil with respect to supersonic flow for the same cloud of points as shown in section 6.3.6.

7.3.1.1 Validity of no-slip boundary condition

Based on results of continuum theory no-slip condition prevails at the wall. On the other hand results of kinetic theory reveals that the velocity slip and temperature jump will always be present even in continuum flow regime [90, 265]. The slip taking place is of the order of mean free path which cannot be validated experimentally or deduced without some kind of dependence of classical Navier-Stokes equations. More-so-ever in gases no slip is achieved only when the molecules simulate wettability condition i.e. molecules are adsorbed onto solid surface for a considerable amount of time. Watanabe *et al.* [288] and Tretheway & Meinhart [277] have reported that that slip exists in liquids when wettability is not achieved. Discussions about this subject is beyond the scope of the thesis but the kinetic theory based derivations reported in the next subsection shows that slip is always present. Slip becomes negligibly small and approaches no-slip condition as the flow condition approaches continuum.

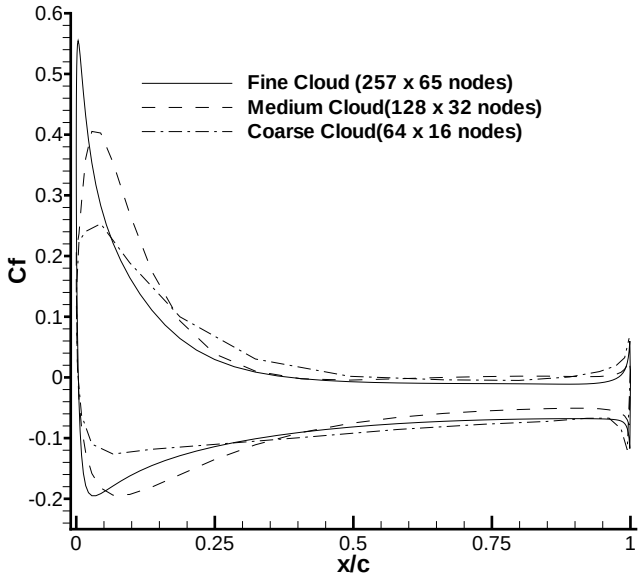

Figure 7.7: Skin friction plot for transonic flow past NACA0012 airfoil at Mach=0.8,AOA=10 deg., Re=500 for coarse, medium and fine cloud.

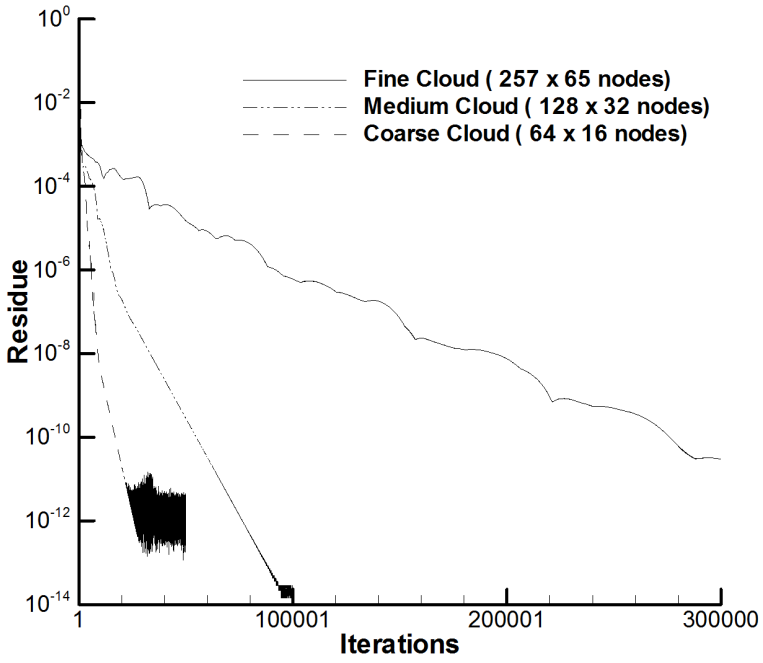

Figure 7.8: Residue plot for transonic flow past NACA0012 airfoil with coarse, medium and fine cloud.

7.3.1.2 No-slip and kinetic wall boundary condition

For continuum flow conditions the stationary solid wall will have to satisfy no-slip boundary condition that is $u_x = 0$, $u_y = 0$ and temperature is required to satisfy isothermal or adiabatic boundary condition. The adiabatic boundary condition for temperature is obtained by solving $\vec{s}_n \cdot \nabla T = 0$, where $\vec{s}_n$ is the surface normal. It is found advantageous to update pressure at the wall (instead of density) by using normal momentum equation. The momentum flux can be written as $\rho\ \vec{u} \otimes \vec{u} - \boldsymbol{P}$. At the wall in continuum regime $\vec{u}$=0 hence pressure for no slip boundary can be obtained using $\nabla \cdot \boldsymbol{P} = 0$. The term $\boldsymbol{P}$ is the pressure tensor defined as $\boldsymbol{P} = \boldsymbol{\Pi} - p\boldsymbol{I}$ where $\boldsymbol{I}$ is the identity invariant tensor and $\boldsymbol{\Pi}$ is the tensor of viscous stresses. Primarily very close to the wall the balance is between pressure gradient and viscous stress gradient terms.

The alternative route based on kinetic theory differs from the treatment of boundary based on no-slip condition. Kinetic boundary condition solves the conservation of distribution at the boundary based on the tangential momentum / energy accommodation coefficient. Kinetic theory results show that the velocity slip and

temperature jump, however small is always be present in the continuum flow regime.

7.3.1.3 Continuum test case with kinetic wall boundary condition

Consider the same test case of transonic continuum flow of air at Mach 0.8 past a NACA0012 airfoil at 10 degrees angle of attack at Re=500. The Knudsen number in terms of Mach number, rmM and Reynolds number, Re can be written as

$$\mathrm{Kn} = \sqrt{\frac{\pi\gamma}{2}}\frac{\mathrm{M}}{\mathrm{Re}} \tag{7.30}$$

The Knudsen number, Kn evaluated for such a case is 2.4×10^{-3} based on chord length. This test case is simulated using the kinetic boundary condition with fully diffuse reflecting wall i.e. the accommodation coefficient, σ =1. The kinetic boundary condition treats the continuum region in the same way as the non-continuum region admitting velocity slip and temperature jump which becomes negligibly small in the continuum region. The slip velocity not only depends on the velocity gradient in the normal direction but also on the tangential flow gradients. As described earlier when variations in tangential directions are substantial then distribution at time $t + \Delta t$ at the boundary can be constructed as follows

$$f_{1,\Sigma}(t+\Delta t) = f_{1,\Sigma}(t) - \Delta t\left[\frac{\partial v_x f_{1,\Sigma}^{+-}(t)}{\partial x} + \frac{\partial v_x f_{1,\Sigma}^{--}(t)}{\partial x} + \frac{\partial v_y f_{1,\Sigma}^{\cdot-}(t)}{\partial y}\right] \tag{7.31}$$

where f_1^{+-} is the half-range first order distribution function for $0 < v_x < \infty$ and $-\infty < v_y < 0$ and f_1^{--} is the half-range first order distribution function for $-\infty < v_x < 0$ and $-\infty < v_y < 0$. After taking $\boldsymbol{\Psi}$ moment we can obtain state update equation expressed as

$$\boldsymbol{U}(t+\Delta t) = \boldsymbol{U}(t) - \Delta t\left[\begin{array}{l}\left(\frac{\partial \widehat{\boldsymbol{GX}}^{+-}(t)}{\partial x}\right)_{\Delta x<0} + \left(\frac{\partial \widehat{\boldsymbol{GX}}^{--}(t)}{\partial x}\right)_{\Delta x>0} \\ + \left(\frac{\partial \widehat{\boldsymbol{GY}}^{\cdot-}(t)}{\partial y}\right)_{\Delta y>0}\end{array}\right] \tag{7.32}$$

where $\boldsymbol{U}=[\rho, \rho\boldsymbol{u}, \rho E]^T$ is the state vector and Δt is the time step. $\widehat{\boldsymbol{GY}}^{\cdot-}$ is the flux resulting from half range distribution $f_{1,\Sigma}^{\cdot-}$. Derivatives of $\widehat{\boldsymbol{GX}}^{+-}$, $\widehat{\boldsymbol{GX}}^{--}$

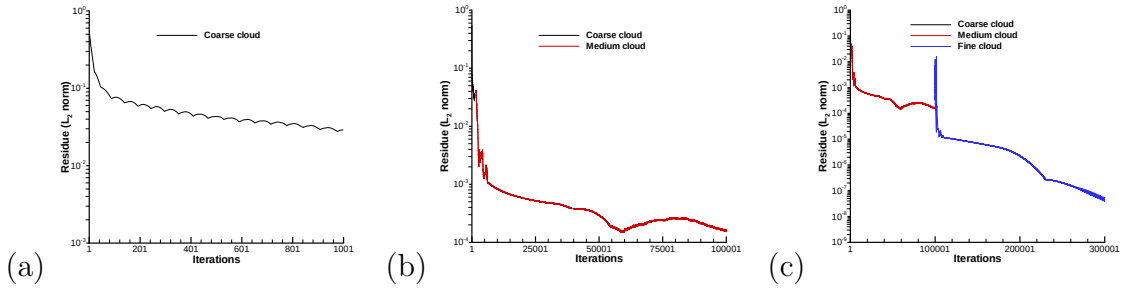

(a) (b) (c)

Figure 7.9: Residue plot for continuum transonic flow past NACA0012 airfoil with kinetic wall boundary condition: (a)Coarse cloud, (b)coarse-medium cloud sequence, and (c)coarse-medium-fine cloud sequence.

and $\widehat{\boldsymbol{GY}}^{\cdot-}$ are evaluated using mesh points on the left, right and upward side. The fluxes $\widehat{\boldsymbol{GX}}^{\pm-}$ and $\widehat{\boldsymbol{GY}}^{-}$ are given as

$$\begin{aligned}\widehat{\boldsymbol{GX}}^{\pm-} &= (2-\sigma)(\boldsymbol{GX}_I^{\pm-} + \boldsymbol{GX}_V^{\pm-}) + \sigma \boldsymbol{GX}_I^{\pm-}(\rho, u_{w,x}, T_w) \\ \widehat{\boldsymbol{GY}}^{\cdot-} &= (2-\sigma)(\boldsymbol{GY}_I^{\cdot-} + \boldsymbol{GY}_V^{\cdot-}) + \sigma \boldsymbol{GY}_I^{\cdot-}(\rho, u_{w,x}, T_w)\end{aligned} \tag{7.33}$$

where $\boldsymbol{GX}_I^{\pm-}$, $\boldsymbol{GX}_V^{\pm-}$, $\boldsymbol{GY}_I^{\cdot-}$ and $\boldsymbol{GY}_V^{\cdot-}$ are evaluated based on fluid conditions while $\boldsymbol{GX}_I^{\pm-}(\rho, u_{w,x}, T_w)$ and $\boldsymbol{GY}_I^{\cdot-}(\rho, u_{w,x}, T_w)$ are the inviscid flux based on Maxwellian distribution which are evaluated using fluid density ρ, wall temperature T_w and wall velocity $\boldsymbol{u}_w \equiv (u_{w,x}, 0)$. The final expressions of these fluxes are given in Appendix D.

With the implementation of kinetic wall boundary condition we require smaller time step and as a consequence the code converges slowly and number of iterations increases many fold for resolving slip flow feature. In the present approach the code is accelerated using cloud sequencing described earlier by running SLKNS on a coarse cloud of size 64×16 for a limited amount of iterations after one decade fall in the residue and then the result is mapped into a medium cloud of size 128×32 . The solver runs on the medium cloud for 3 decade fall of residue and results are mapped to a fine cloud of size 257×65. Figure 7.9 shows the plot of the normalized residue for coarse, medium and fine cloud used in cloud sequencing.

Fig. 7.10 (a) shows the plot of coefficient of friction compared with SLKNS solver with kinetic wall boundary condition, SLKNS with no-slip boundary condition and fluctuation splitting LDA scheme [43] using no-slip boundary condition. Dip in coefficient of friction near the leading edge can be observed due to slip flow.

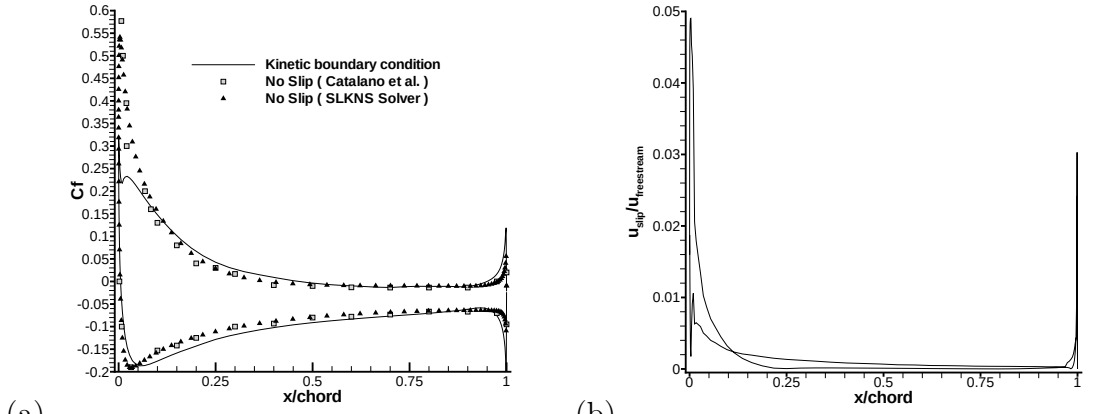

(a) (b)

Figure 7.10: Continuum transonic flow past NACA0012 airfoil with kinetic wall boundary condition: (a)Coefficient of friction plot, (b) velocity slip along the surface of NACA0012 airfoil.

Fig. 7.10 (b) shows the small velocity slip existing on the surface. Temperature jump for this case was found to be very negligible. This continuum flow test case using kinetic wall boundary condition confirms the observation made by Struchtrup [265] that temperature jump and velocity slip will be present for all dissipative walls even in continuum regime.

7.3.2 Hypersonic rarefied flow over a flat plate

Hypersonic rarefied flow over a flat plate is one of the fundamental problem as it generates wide range of flow phenomena extending from highly non-equilibrium flow near the leading edge through the merged layer to strong and weak interaction regimes to a classical boundary layer flow at the downstream. Figure 7.11 shows a schematic of fluid flow phenomena near the leading edge. Kinetic flow region exists very near the leading edge caused by collisions between free stream and body reflected molecules. Near the leading edge non-continuum non-equilibrium viscous region exists where molecule-molecule and molecule-body collisions dominate the flow and as a consequence the distribution function is far away from Maxwellian. Further downstream in the transition region molecule-molecule collisions dominate the flow, this is followed by merged layer region in which wall

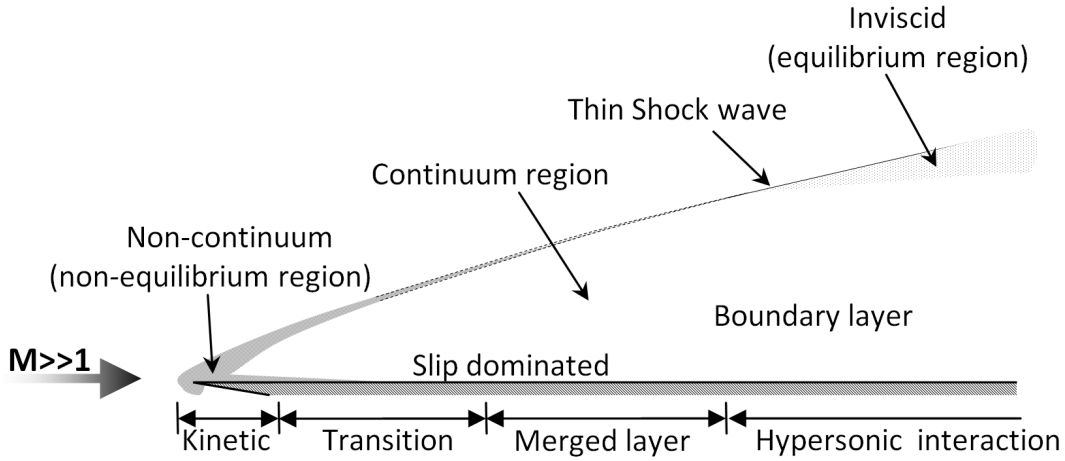

Figure 7.11: Schematic of fluid phenomena near the leading edge for hypersonic rarefied flow over a flat plate[222].

boundary layer merges with the a non-Rankine-Hugoniot shock [222]. Consider a test case of hypersonic flow of argon at free stream velocity of $(1893.7, 0, 0)$ m/s, with pressure of 3.73 Pascal at temperature of 64.5 K over a flat-plate held at uniform temperature $T_w = 292$ K at 0 deg angle of attack [104]. The test case used in this thesis consists of flat plate 45 cm long placed along the x-axis in a flow domain of 25 cm $\times$ 50 cm as shown in Figure 7.12. The CFD simulation used a mesh of 70 $\times$ 100 graded from $\Delta y \approx 0.13$ mm at the plate surface to $\Delta x \approx 0.21$ mm ahead of the plate tip. The kinetic slip boundary condition is flux based and its state update is given as

$$\boldsymbol{U}(t+\Delta t) = \boldsymbol{U}(t) - \Delta t \left[\begin{array}{l} \left(\frac{\partial \widehat{\boldsymbol{GX}}^{+-}(t)}{\partial x} \right)_{\Delta x<0} + \left(\frac{\partial \widehat{\boldsymbol{GX}}^{--}(t)}{\partial x} \right)_{\Delta x>0} \\ + \left(\frac{\partial \widehat{\boldsymbol{GY}}^{\cdot-}(t)}{\partial y} \right)_{\Delta y>0} \end{array} \right] \tag{7.34}$$

Figure 7.13 shows the profile of the tangential velocity in the boundary layer at x=25 mm from the plate tip. Figure 7.14 shows the profile of the temperature in the boundary layer at x=25 mm from the plate tip. Figure 7.15 shows the profile of the density in the boundary layer at x=25 mm from the plate tip. The hypersonic test case was run for 500 iterations using SLKNS solver with no-slip boundary condition, thereafter SLKNS was used with kinetic wall boundary condition. Figure 7.16 shows plot of density with iterations at a location x= 5

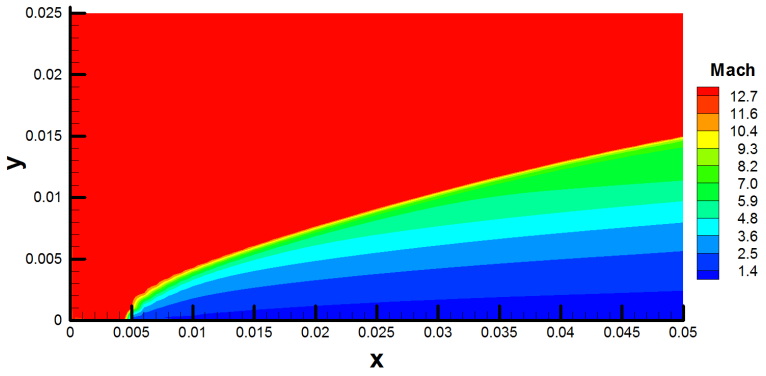

Figure 7.12: Hypersonic flow over a flat plate, Mach contours based on SLKNS solver.

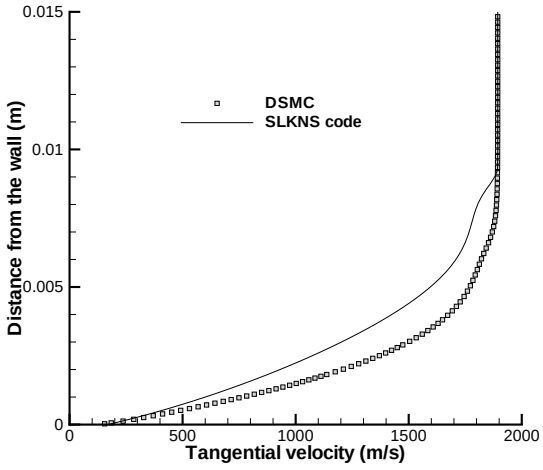

Figure 7.13: Tangential velocity at cross-section x=25 mm from the plate tip.

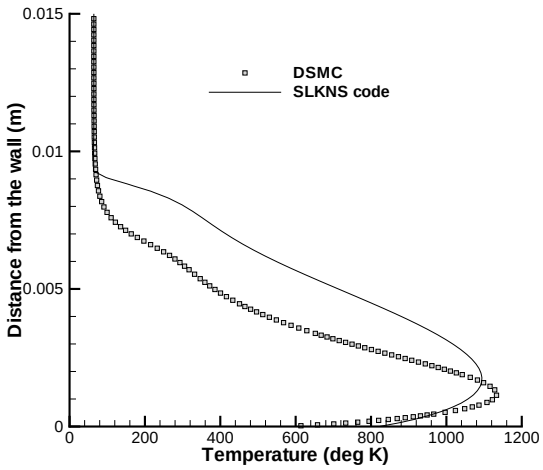

Figure 7.14: Temperature at cross-section x=25 mm from the plate tip.

mm and y=2 mm from the plate tip.

7.3.2.1 Comparison with various slip boundary conditions

In this test case of the hypersonic flat plate problem various slip and jump boundary conditions are compared with the results of flux based kinetic wall boundary condition using SLKNS solver and DSMC (Direct Simulation Monte Carlo) [36]. Maxwell velocity slip [163] given as

$$u_x = \left[\left(\frac{2-\sigma}{\sigma}\right)\frac{\tau_{xy}}{2p}\frac{\sqrt{\pi}}{\beta} - \frac{q_x\eta}{2p}\right] \tag{7.35}$$

and von Smoluchowski's temperature jump boundary condition given as

$$T = T_w - \left(\frac{2-\sigma}{\sigma}\right)\frac{2\gamma\lambda q_y}{c_p(1+\gamma)\mu} \tag{7.36}$$

Apart from this we have also used the new velocity slip and temperature jump conditions based on present research work derived using non-equilibrium distribution based on the new kinetic model as described in sections 5.4.1 and 5.4.2 of chapter 5. The derived velocity slip expression called Onsager-Maxwell slip velocity is

$$u_x = \left[\left(\frac{2-\sigma}{\sigma}\right)\frac{\tau_{xy}}{2p}\frac{\sqrt{\pi}}{\beta} - \frac{q_x\eta}{2p}\right](1-\tau_{yy}/2p)^{-1} \tag{7.37}$$

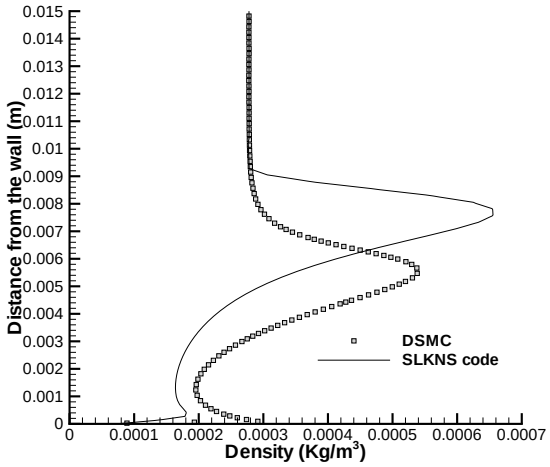

Figure 7.15: Density at cross-section x=25 mm from the plate tip.

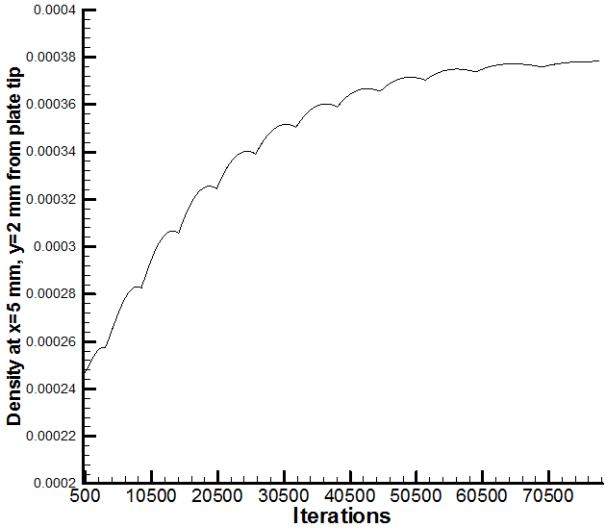

Figure 7.16: Plot of density variation with iterations at a location x= 5 mm and y=2 mm from the plate tip.

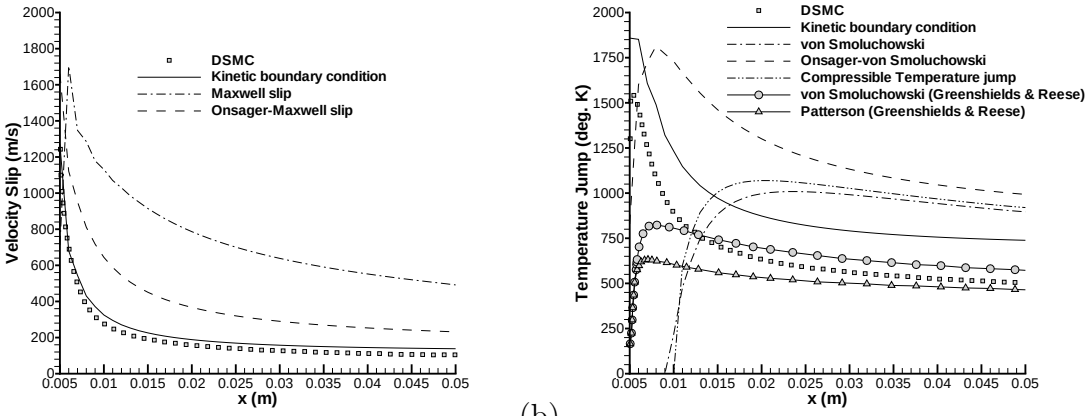

(a) (b)

Figure 7.17: Variation of (a)Velocity slip and (b)Temperature jump along the surface of flat plate for various boundary conditions.

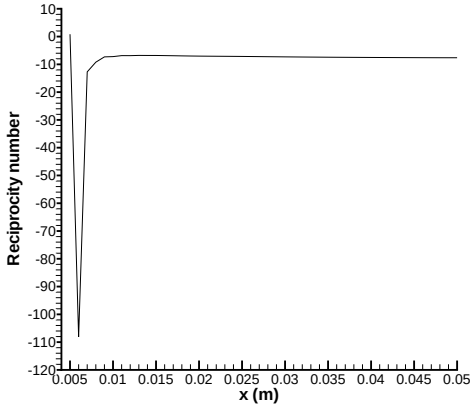

Figure 7.18: Variation of the *Rp* term along the surface of the flat plate.

The derived temperature jump condition called Onsager-von Smoluchowski's temperature jump is

$$T = T_w + \left(\frac{2-\sigma}{\sigma}\right)^2 \frac{\gamma\lambda^2\tau_{xy}^2}{c_p(\gamma+1)\mu^2} - \left(\frac{2-\sigma}{\sigma}\right)\frac{2\gamma\lambda q_y}{c_p(\gamma+1)\mu} \tag{7.38}$$

In the present simulation we have also used derived compressible temperature jump condition as

$$T = \frac{3\beta_w^2\gamma\mathcal{S}^2\vartheta}{c_p(\gamma-1)(2^{1/3}(2-12\beta_w^3\mathcal{S}^2+2^{1/3}\vartheta^2)+2\vartheta)} \tag{7.39}$$

where β_w is given as

$$\beta_w = \frac{1}{2RT_w} = \frac{\gamma}{2T_w(\gamma-1)c_p} \tag{7.40}$$

and

$$\mathcal{S} = -\left(\frac{2-\sigma}{\sigma}\right)\frac{4(\gamma-1)\sqrt{\pi}}{\rho(\gamma+1)}q_y \tag{7.41}$$

$$\vartheta = \left(2 - 18\beta_w^3\mathcal{S}^2 + 27\beta_w^6\mathcal{S}^4 + 3\beta_w^4\mathcal{S}^3\sqrt{81\beta_w^4\mathcal{S}^2 - 12\beta_w}\right)^{1/3} \tag{7.42}$$

All of these boundary conditions are compared with the flux based kinetic boundary condition and results of DSMC. Figure 7.17(a) shows the plot of velocity slip for DSMC, kinetic boundary condition, Maxwell slip and Onsager-Maxwell slip. Figure 7.17(b) shows the plot of temperature jump for DSMC, kinetic, von Smoluchowski, Onsager-von Smoluchowski boundary condition and temperature jump for compressible flow. Temperature jump for compressible flow and von Smoluchowski temperature jump gave unphysical temperature jump near the leading edge, hence they were evaluated based on DSMC field data to compare it with kinetic boundary condition. Kinetic boundary condition was found to give better agreement with the results of DSMC. As also observed by Greenshields & Reese [104] there is discrepancy between the results of DSMC and boundary conditions of Maxwell and von Smoluchowski. This discrepancy is because of two factors: i)missing features of non-equilibrium thermodynamics, ii)as well as due to the fact that these expressions are derived under condition of negligible tangential variations. The mass flux due to slip on the surface of the plate is governed both by the tangential as well as normal components of shear stress tensor and heat flux vector. In order to estimate the order of importance of cross phenomenon involved in tangential flow a new term called reciprocity number Rp was derived

using the contribution of thermodynamic forces on viscous split fluxes. Rp is expressed as the ratio of slip mass flux due to shear stress tensor and heat flux vector derived using half range distribution for this case as follows

$$Rp = \frac{\boldsymbol{\Lambda}^{+-}_{1,\tau} : \boldsymbol{X}_{\tau}}{\boldsymbol{\Lambda}^{+-}_{1,q} \cdot \boldsymbol{X}_{q}} = \frac{2\tau_{xy}A_1^+ - \tau_{xx}B_1^+}{2\beta\eta u_{slip}(q_y A_1^+ - q_x B_1^+)} \tag{7.43}$$

where expressions of A_1^+ and B_1^+ are given in Appendix D. The plot of Rp in Figure 7.18 shows a sudden variation in the ratio of contribution of shear stress tensor and heat flux vector near the leading edge. Near the leading edge the flow is dominated by the cross-coupling due to thermodynamic forces based on heat flux vector and shear stress tensor. Tangential variations become insignificant as we move away from the zone of sudden dip.

7.3.3 Rarefied transonic viscous flow over NACA0012 airfoil

This test consists of free stream rarefied transonic flow at Mach, $rmM = 0.8$, density $1.116 \times 10^{-4}\ kg/m^3$ and temperature 257 K past a NACA0012 airfoil at zero angle of attack [270]. The Reynolds number based on the airfoil chord is 73 and Knudsen number is 0.014. The chord length is $0.04m$ and wall of the airfoil is at 290 K. The density contours shown in Fig. 7.19 reveals rise of density near stagnation point and rarefaction towards the tail where the density drops down. The viscosity based mean free path depends on the density, ρ as follows

$$\lambda = \mu\sqrt{\frac{\pi}{2\rho p}} \tag{7.44}$$

The mean free path becomes large near the tail. Fig. 7.20 shows the contours of mean free path. The rise in the mean free path near the tail makes the slip influence more pronounced which results in sudden rise of slip velocity. The state update equation for interior flow solver node is expressed as

$$\boldsymbol{U}(t+\Delta t) = \boldsymbol{U}(t) - \Delta t \left[\begin{array}{c} \left(\frac{\partial \boldsymbol{GX}^+(t)}{\partial x}\right)_{\Delta x<0} + \left(\frac{\partial \boldsymbol{GX}^-(t)}{\partial x}\right)_{\Delta x>0} \\ + \left(\frac{\partial \boldsymbol{GY}^+(t)}{\partial y}\right)_{\Delta y<0} + \left(\frac{\partial \boldsymbol{GY}^-(t)}{\partial y}\right)_{\Delta y>0} \end{array} \right] \tag{7.45}$$

where $\boldsymbol{U}=[\rho, \rho\boldsymbol{u}, \rho E]^T$ is the state vector and Δt is the time step. Expressions of split fluxes $\boldsymbol{GX}^{\pm}$ and $\boldsymbol{GY}^{\pm}$ are given in Appendix D. The state update for the

boundary node is expressed as

$$\boldsymbol{U}(t+\Delta t) = \boldsymbol{U}(t) - \Delta t \left[\begin{array}{l} \left(\frac{\partial \widehat{\boldsymbol{GX}}^{+-}(t)}{\partial x} \right)_{\Delta x<0} + \left(\frac{\partial \widehat{\boldsymbol{GX}}^{--}(t)}{\partial x} \right)_{\Delta x>0} \\ + \left(\frac{\partial \widehat{\boldsymbol{GY}}^{\cdot -}(t)}{\partial y} \right)_{\Delta y>0} \end{array} \right] \tag{7.46}$$

where $\widehat{\boldsymbol{GY}}^{\cdot -}$ is the flux resulting from half range distribution $f^{\cdot -}_{1,\Sigma}$. Derivatives of $\widehat{\boldsymbol{GX}}^{+-}$, $\widehat{\boldsymbol{GX}}^{--}$ and $\widehat{\boldsymbol{GY}}^{\cdot -}$ are evaluated using mesh points on the left, right and upward side. The fluxes $\widehat{\boldsymbol{GX}}^{\pm -}$ and $\widehat{\boldsymbol{GY}}^{-}$ are given as

$$\begin{aligned} \widehat{\boldsymbol{GX}}^{\pm -} &= (2-\sigma)(\boldsymbol{GX}^{\pm -}_{I} + \boldsymbol{GX}^{\pm -}_{V}) + \sigma \boldsymbol{GX}^{\pm -}_{I}(\rho, u_{w,x}, T_w) \\ \widehat{\boldsymbol{GY}}^{\cdot -} &= (2-\sigma)(\boldsymbol{GY}^{\cdot -}_{I} + \boldsymbol{GY}^{\cdot -}_{V}) + \sigma \boldsymbol{GY}^{\cdot -}_{I}(\rho, u_{w,x}, T_w) \end{aligned} \tag{7.47}$$

where $\boldsymbol{GX}^{\pm -}_{I}$, $\boldsymbol{GX}^{\pm -}_{V}$, $\boldsymbol{GY}^{\cdot -}_{I}$ and $\boldsymbol{GY}^{\cdot -}_{V}$ are evaluated based on fluid conditions while $\boldsymbol{GX}^{\pm -}_{I}(\rho, u_{w,x}, T_w)$ and $\boldsymbol{GY}^{\cdot -}_{I}(\rho, u_{w,x}, T_w)$ are the inviscid flux based on Maxwellian distribution which are evaluated using fluid density ρ, wall temperature T_w and wall velocity $\boldsymbol{u}_w \equiv (u_{w,x}, 0)$. The final expressions of these fluxes are given in Appendix D.

Fig. 7.21 shows the comparison of the slip velocity distribution for rarefied flow past NACA0012 airfoil based on SLKNS solver and DSMC on a coarse cloud. The simulation was carried out using 7200 cloud of points generated using mesh of size 120×60 as shown in Fig. 7.22. DSMC gave better results for nearly same grid size. Fig. 7.23 shows the plot of normalized residue using SLKNS solver using explicit first order Euler time stepping based on global time step.

7.3.4 Slip flow in an annulus

Avci and Aydin [18] investigated laminar slip flow in a micro-annulus between two concentric cylinders of inner radius r_i and outer radius r_o. They considered a slip flow with fully diffuse reflection and found out a relationship in terms of dimensionless radius $r_d = r_i/r_o$ for dimensionless velocity distribution as

$$\frac{u_z}{u_{z_{\max}}} = \frac{2\left[1 - \left(\frac{r}{r_o}\right)^2 + r_m^2 \ln\left(\frac{r}{r_o}\right) + A\right]}{B} \tag{7.48}$$

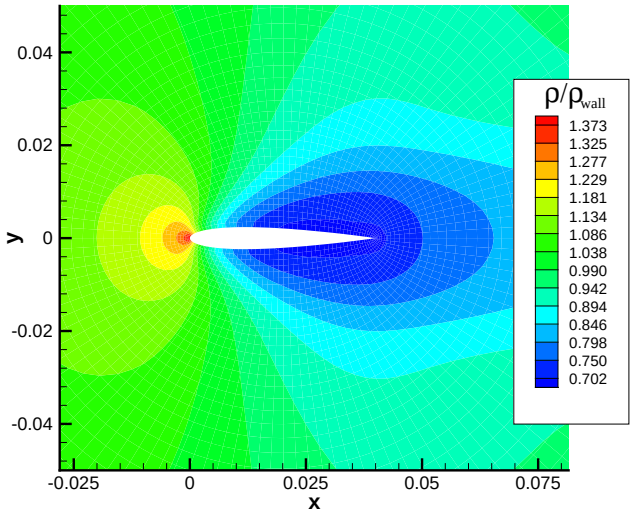

Figure 7.19: Contours of $\frac{\rho}{\rho_{wall}}$ for rarefied flow past NACA0012 airfoil at Mach=0.8, Re=73., Kn=0.014

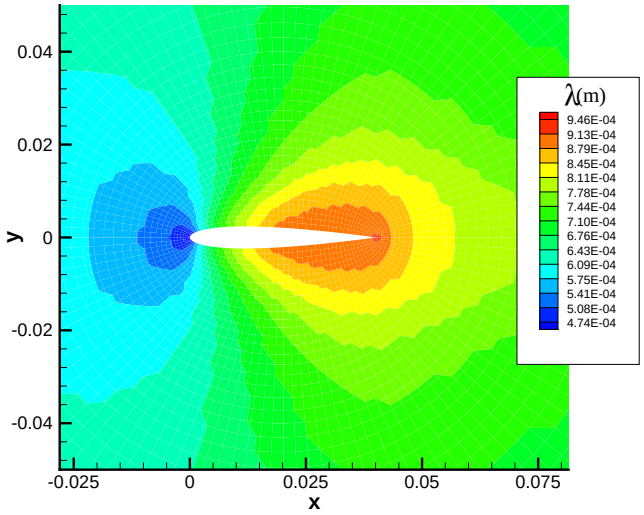

Figure 7.20: Contours of mean free path for rarefied flow past NACA0012 airfoil at Mach=0.8, Re=73., Kn=0.014

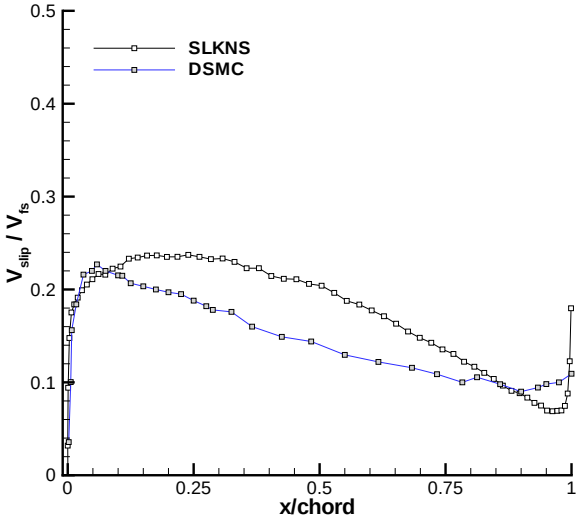

Figure 7.21: Comparision of the slip velocity distribution for rarefied flow past NACA0012 airfoil at Mach=0.8, Re=73., Kn=0.014

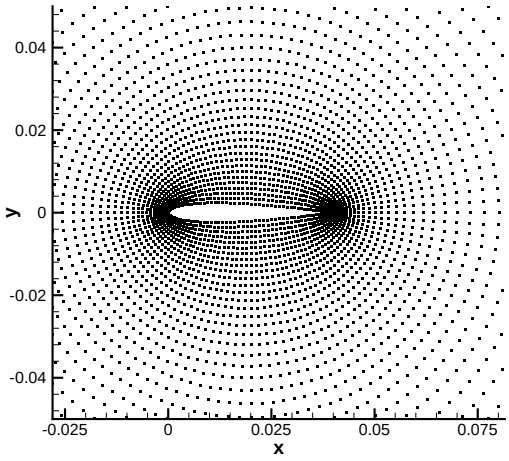

Figure 7.22: Cloud of points around NACA0012 airfoil

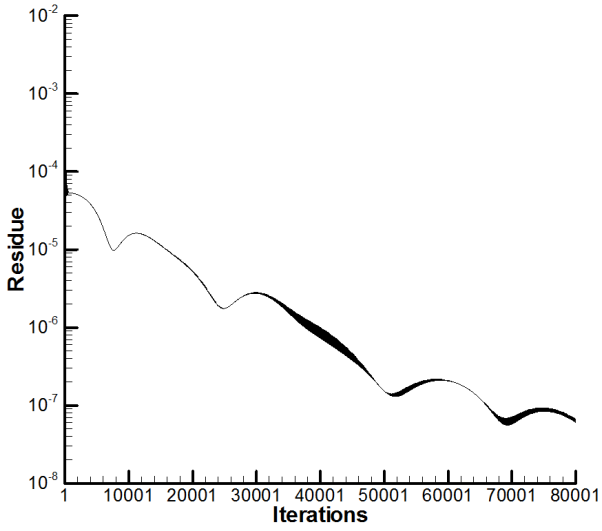

Figure 7.23: Residue plot for rarefied transonic viscous flow over NACA0012 airfoil

where A, B and r_m are, respectively given as

$$\begin{aligned} A &= 4\mathrm{Kn}(1-r_d)(1-r_m^2) \\ B &= \left[1 - r_d^2 - 4r_m^2\left(\tfrac{1}{2} + \tfrac{r_d^2}{1-r_d^2}\ln(r_d)\right) + 2A\right] \\ r_m &= \frac{r_m}{r_o} = \left[\frac{(1-r_d^2)(1+4\mathrm{Kn})}{2\ln(\frac{1}{r_d}) - 4\mathrm{Kn}(\frac{r_d^2-1)}{r_d^2}}\right]^{1/2} \end{aligned} \tag{7.49}$$

Here Knudsen number,Kn $= \lambda/d_h$ is defined with respect to hydraulic diameter of the annuli as

$$d_h = 2(r_o - r_i) \tag{7.50}$$

In this test case we considered cylindrical annuli with inner radius of 0.02 m and outer radius of 0.1 m with argon flowing at an average pressure of 2 pascals. The meshless solver m-SLKNS described in section 6.3.2 was used for this slip flow case at Kn = 0.0227. The 900 node size cloud was generated using r-z mesh of 30 × 30. The state update using axi-symmetric SLKNS is given as

$$\boldsymbol{U}(t+\Delta t) = \boldsymbol{U}(t) - \Delta t\left(\frac{\partial \boldsymbol{GZ}^{\pm}}{\partial z} + \frac{1}{r}\frac{\partial r\boldsymbol{GR}^{\pm}}{\partial r} + \boldsymbol{S}\right) \tag{7.51}$$

Figure 7.24(a) shows the plot of dimensionless velocity which compared well with the analytical results of Avci and Aydin [18]. The plot in Figure 7.24(b) shows

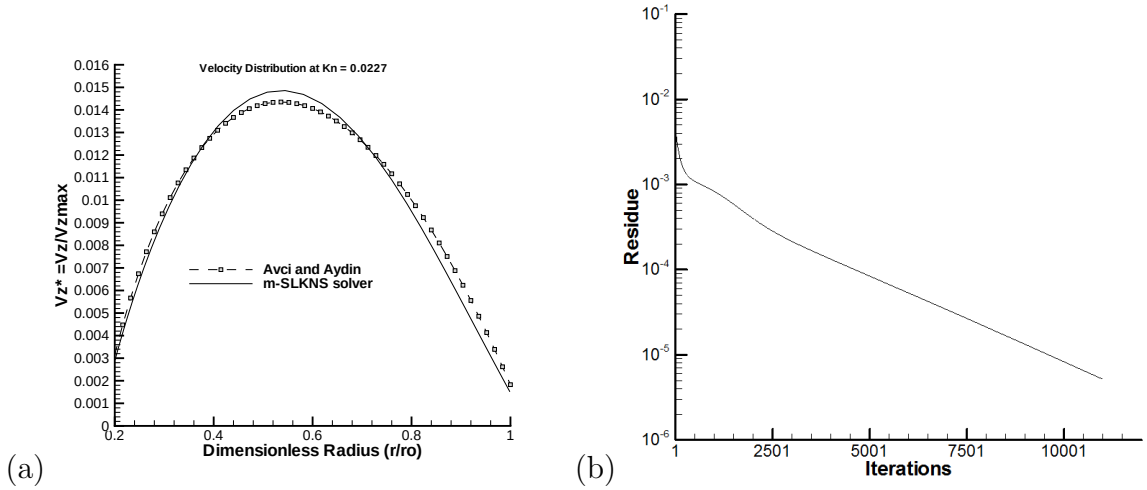

Figure 7.24: Slip flow in a micro-annulus at Kn = 0.0227 (a)plot of velocity distribution, (b) residue plot.

the fall of normalized residue, $\bar{Res}_2^k = Res_2^k/Res_2^0$, where residue Res_2^k is based on the average L_2 norm of all the components across the domain at k^{th} iteration as described in section 6.3.4 of chapter 6.

7.3.5 Concentric Couette flow

Couette flow between concentric inner rotating and outer stationary cylinders is one of a classical fluid dynamics problem. However, under certain conditions of rarefaction and wall boundary (when accommodation coefficient is small the wall become more specular), the velocity profile inverts i.e. the gas rotates faster near the stationary wall. This phenomenon was first predicted by Einzel *et al.* [80]. Many researchers [9, 162, 275] have carried out analytical and DSMC studies to explain this anomalous behavior. In this test case Argon gas is confined between inner and outer cylinder that have tangential momentum accommodation coefficient of *0.1* and radii of 3λ and 5λ respectively, where mean free path, $\lambda = 6.25 \times 10^{-8}$ m. Inner cylinder rotates with angular speed, $\omega = 5.17 \times 10^8$ rad/s and outer cylinder is held stationary [275].

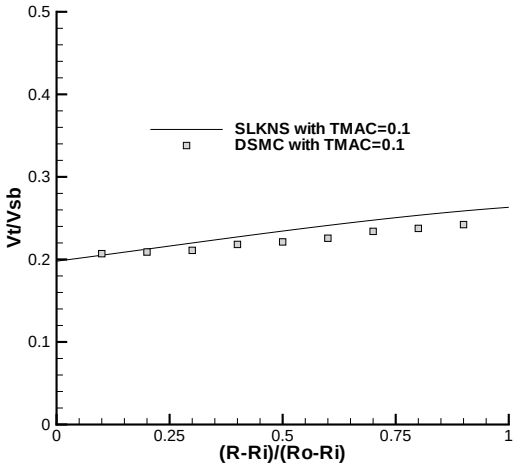

Figure 7.25: Comparison of the non-dimensional tangential velocity for SLKNS simulation on r-z plane and DSMC

7.3.5.1 SLKNS simulation on r-z plane

Meshless solver SLKNS was able to capture this anomalous behavior of velocity inversion with axi-symmetric version of the code using r-z plane with a cloud of size 60 $\times$ 30. The state update for interior node using axi-symmetric SLKNS is given as

$$\boldsymbol{U}(t+\Delta t) = \boldsymbol{U}(t) - \Delta t \left[\begin{array}{l} \left(\frac{\partial \boldsymbol{GZ}^{+}(t)}{\partial z}\right)_{\Delta z<0} + \left(\frac{\partial \boldsymbol{GZ}^{-}(t)}{\partial z}\right)_{\Delta z>0} \\ + \left(\frac{1}{r}\frac{\partial r\boldsymbol{GR}^{+}(t)}{\partial r}\right)_{\Delta r<0} + \frac{1}{r}\left(\frac{\partial r\boldsymbol{GR}^{-}(t)}{\partial r}\right)_{\Delta r>0} + \boldsymbol{S} \end{array} \right] \quad (7.52)$$

where expressions of z and r component of the split fluxes $\boldsymbol{GZ}^{\pm}$ and $\boldsymbol{GR}^{\pm}$ and source term $\boldsymbol{S}$ are given in section D.4 of Appendix D. Fig.7.25 shows the plot of the non-dimensional tangential velocity with respect to non-dimensional radial distance for SLKNS and Direct Simulation Monte Carlo(DSMC) [36]. From physical point of view the rotating cylinder imparts the circumferential momentum to the molecules undergoing diffuse reflection. At smaller Knudsen number most of the momentum transfer is due to molecular collisions. When the outer cylinder is specularly reflecting then no circumferential momentum is transferred to the outer cylinder [9]. As a consequence the gas accelerates and reaches the stationary state of rigid body rotation (the distribution function is a Maxwellian),

satisfying the Onsager's principle of least dissipation of energy valid for processes close to equilibrium.

7.3.5.2 SLKNS simulation on r-θ plane

Similar test case was also verified with the analytical results of Sun *et al.* [271]. Consider rarefied flow with a mean free path, λ of 0.00625 m confined in a rotating inner cylinder of radius 3λ and stationary outer cylinder of radius 5λ. The motive gas chosen is argon with initial uniform density of $1.867819 \times 10^{-5}\ kg/m^3$ and inner cylinder held at 300 K, rotates at frequency of 1000π radians/sec. The tangential momentum accommodation coefficient and thermal accommodation coefficient were taken as unity. The tangential velocity derived by Sun *et al.* [271] can be written as

$$u_\theta(r) = ar + \frac{b}{r} \tag{7.53}$$

where factors a and b can be written as

$$a = \frac{A}{A-B}\omega \tag{7.54}$$

$$b = \frac{1}{B-A}\omega \tag{7.55}$$

parameters A and B are as follows

$$A = \frac{1}{r_o^2}\left(1 - \frac{2-\sigma_o}{\sigma_o}\frac{2\lambda}{r_o}\right) \tag{7.56}$$

$$B = \frac{1}{r_i^2}\left(1 + \frac{2-\sigma_i}{\sigma_i}\frac{2\lambda}{r_i}\right) \tag{7.57}$$

where r_i and r_o are the inner and outer radius, σ_i and σ_o are the accommodation factors at the inner and outer cylinder. The dimensionless velocity with respect to circumferential rotating inner cylinder u_θ^* can be written as

$$u_\theta^* = \frac{u_\theta}{\omega r_i} = \frac{1}{(A-B)r_i}\left(Ar - \frac{1}{r}\right) \tag{7.58}$$

The state update equation for interior flow solver node using r-θ plane is expressed as

$$\boldsymbol{U}(t+\Delta t) = \boldsymbol{U}(t) - \Delta t \left[\begin{array}{c} \left(\frac{\partial \boldsymbol{GX}^+(t)}{\partial x}\right)_{\Delta x<0} + \left(\frac{\partial \boldsymbol{GX}^-(t)}{\partial x}\right)_{\Delta x>0} \\ + \left(\frac{\partial \boldsymbol{GY}^+(t)}{\partial y}\right)_{\Delta y<0} + \left(\frac{\partial \boldsymbol{GY}^-(t)}{\partial y}\right)_{\Delta y>0} \end{array} \right] \tag{7.59}$$

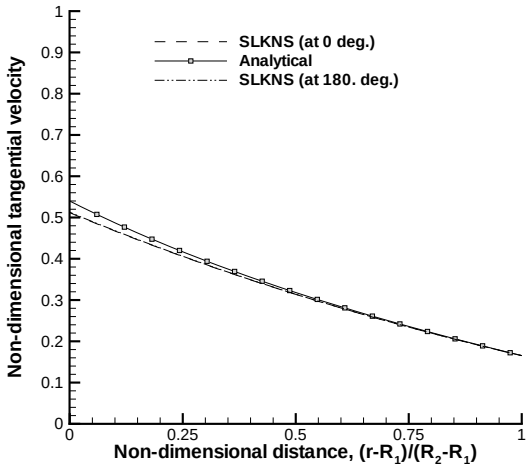

Figure 7.26: Comparison of the non-dimensional tangential velocity for SLKNS simulation on r-θ plane and analytical result [271].

where expressions of split fluxes $\boldsymbol{GX}^{\pm}$ and $\boldsymbol{GY}^{\pm}$ are given in Appendix D. A cloud of size 120 $\times$ 200 was used to carry out simulation using SLKNS. Fig.7.26 shows the plot of the non-dimensional tangential velocity with respect to non-dimensional radial distance for SLKNS solver using r-θ plane and analytical results. The analytical results are obtained using isothermal condition and uniform density. It should be noted that the density dips near the inner cylinder and increases near the outer cylinder as shown in figures 7.27 and 7.28. Figure 7.29 shows the contour of temperature which breaks the symmetry. It should be noted that analytical result is based on axi-symmetric solution which may no longer be accurate as symmetry breaks due to slip flow. SLKNS converges very fast as it is based on VRKFVS scheme which solves for the perturbation over the Maxwellian distribution. Figure 7.30 shows the plot of residue fall with iterations for coarse, medium and fine cloud, here the residue is based on the average L_2 norm of all the components across the domain at k^{th} iteration as described in section 6.3.4 of chapter 6. Figure 7.31 shows the variation of dimensionless velocity with respect to non-dimensional radial distance for coarse cloud of size 1500 nodes, medium cloud of size 6000 nodes and fine cloud of size 24000 nodes, and its comparison with analytical result.

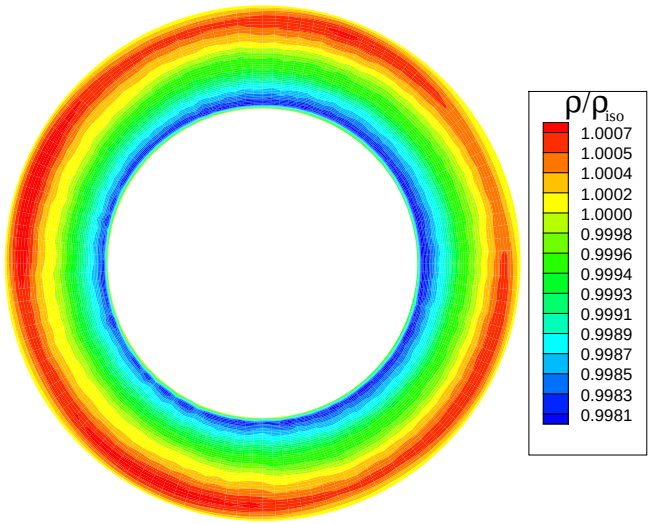

Figure 7.27: Contours of dimensionless density based on SLKNS simulation on r-θ plane.

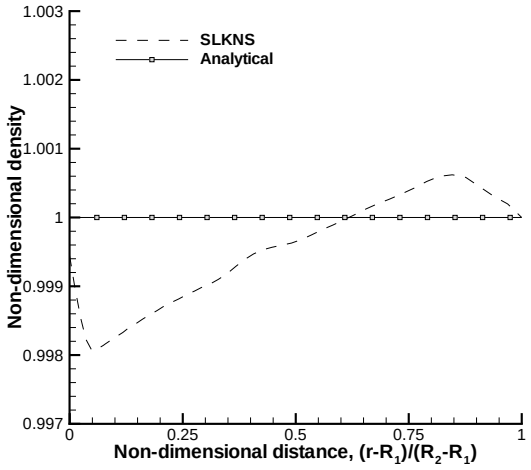

Figure 7.28: Variation of dimensionless density with respect to non-dimensional radial distance based on simulation on r-θ plane.

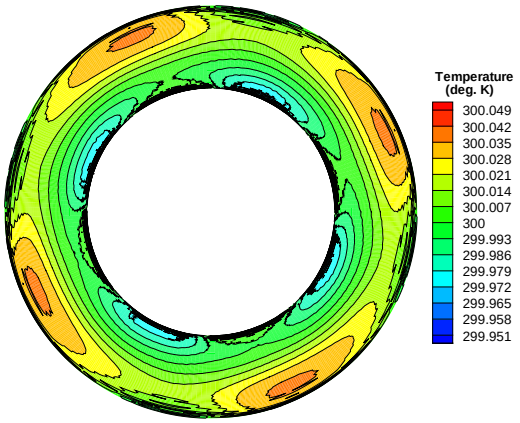

Figure 7.29: Contours of temperature based on simulation on r-θ plane.

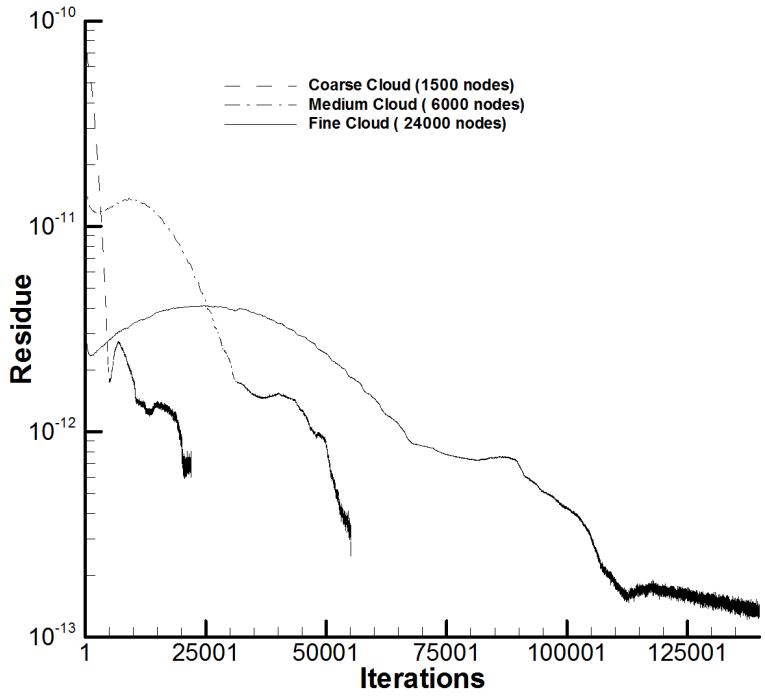

Figure 7.30: Residue plot for coarse, medium and fine cloud for concentric couette flow based on simulation on r-θ plane.

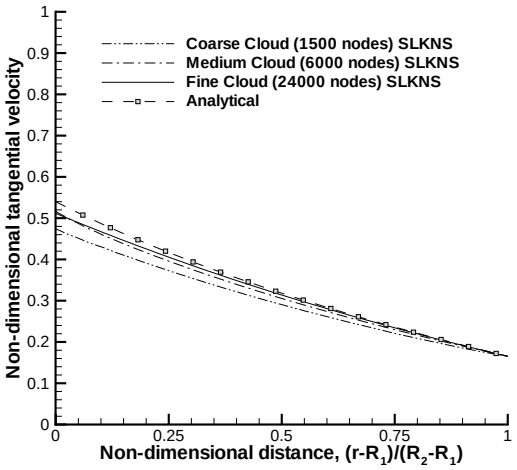

Figure 7.31: Variation of dimensionless velocity with respect to non-dimensional radial distance for coarse, medium and fine cloud simulation on r-θ plane and analytical result.

7.3.6 Flow in a rotating annulus

In this test case we present result for argon gas with a stream density of 1.4×10^{21} $molecules/m^3$ in rotating cylindrical annulus of inner radius 0.1 m and outer radius of 0.2 m and height of 0.1 m with top lid held at 310 deg K and bottom at 290 deg K. Figure 7.32 shows the comparison between Direct Simulation Monte Carlo(DSMC) simulation with 100×100 mesh and axi-symmetric SLKNS results with cloud of 14400 nodes. The distance between first node and the bottom wall and peripheral side wall was kept at 1.65×10^{-4} m so as to resolve the viscous boundary layers encountered in the rotating flows.

7.3.6.1 Boundary layer in rotating flows

A simple scaling analysis [105] of the flow close to side wall and bottom wall gives three types of boundary layers i.e. two vertical Stewartson layers to bring azimuthal velocity to wall velocity and axial velocity to rest and horizontal Ekman layer to bring radial velocity to rest. The thickness of the three layers are given by

$$\delta_{layer} = \bar{H} E_k^{\alpha} \tag{7.60}$$

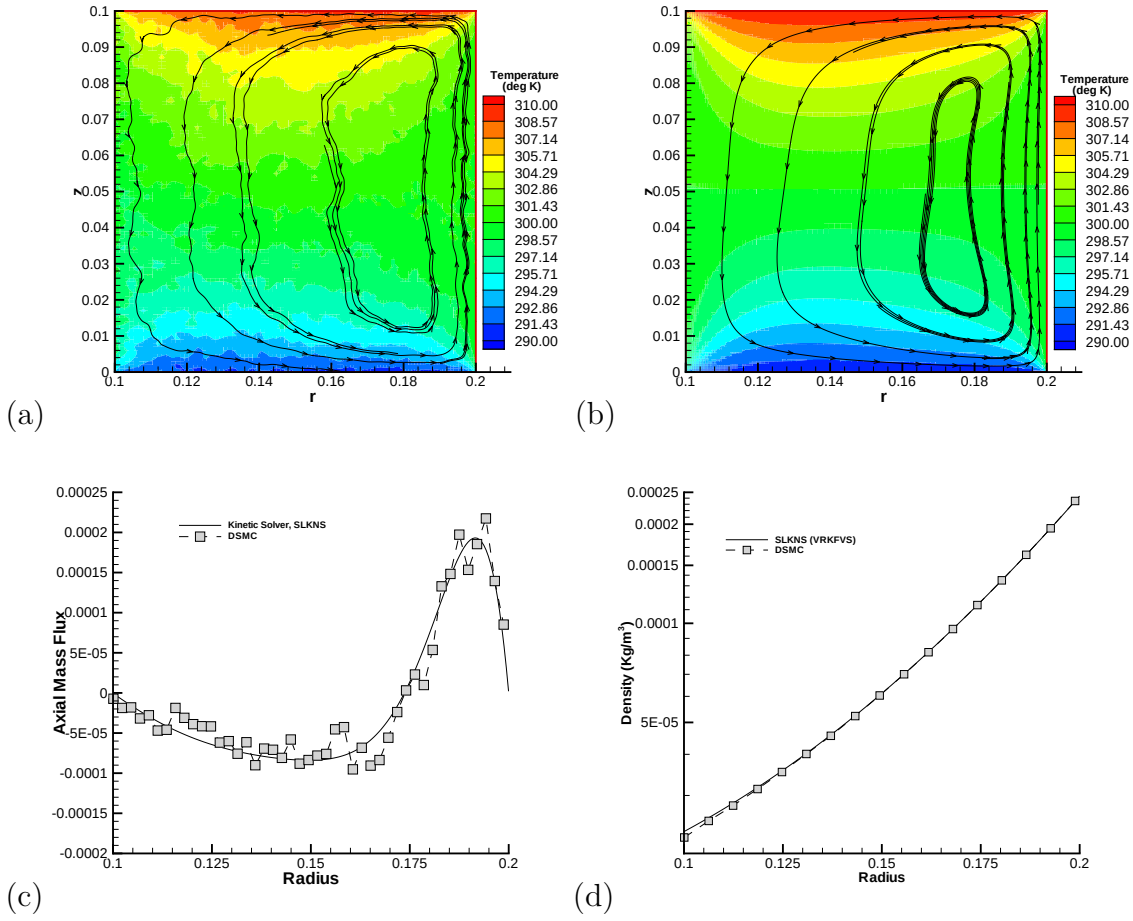

Figure 7.32: Comparison of SLKNS and DSMC results for flow in rotating annulus:(a)DSMC;(b)SLKNS; (c)axial mass flux (kg m/s) with respect to radius (m) for DSMC and SLKNS solver; and (d) density variation for DSMC and SLKNS.

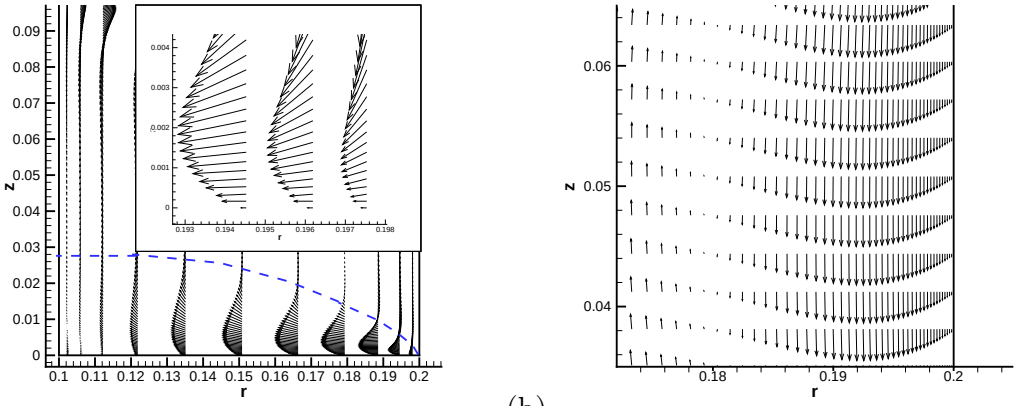

(a) (b)

Figure 7.33: Velocity boundary layers computed using SLKNS code for flow in rotating annulus:(a)Horizontal radial velocity Ekman layer with slip velocity in the inset figure(b) Vertical axial velocity Stewartson layer.

where $\bar{H}$ is the half height of the cylinder, E_k is the Ekman number and α is the exponent based on type of layer. The Ekman number E_k is given by

$$E_k = \frac{\mu}{\rho \Omega \bar{H}^2} \tag{7.61}$$

where Ω is the angular speed in radians. The thickness of the layers are given as

- $\delta_{Stewartsonlayer} = \bar{H} E_k^{1/3}$
  This gives the thickness of the vertical Stewartson 1/3 boundary layer which brings the axial velocity to rest.
- $\delta_{Stewartsonlayer} = \bar{H} E_k^{1/4}$
  This gives the thickness of the vertical Stewartson 1/4 boundary layer which brings the azimuthal velocity to wall's rigid body rotation.
- $\delta_{Ekmanlayer} = \bar{H} E_k^{1/2}$
  This gives the thickness of the horizontal Ekman boundary layer which brings the radial and azimuthal velocities to rest.

SLKNS was able to resolve both the layers. Figure 7.33(a) shows the horizontal Ekman layer for bringing radial velocity to rest, the inset figure shows the zoomed view with small slip velocity developed at the wall. Figure 7.33(b) shows the vertical Stewartson layer for bringing axial velocity to rest.

7.3.6.2 Weak secondary flow in a strong primary flow field

Apart from capturing flow features associated with strong rotation SLKNS solver was also able to capture a weak axial flow of the order 2 ms^{-1} with maximum wall velocity of around 628 ms^{-1}. In this validation test case variance reduction kinetic flux vector scheme (VRKFVS) was used. As described earlier the SLKNS solver based on VRKFVS uses only the perturbation fluxes over the rigid body rotation as follows

$$\begin{aligned}\frac{\partial}{\partial t}\left(\boldsymbol{U}-\boldsymbol{U}_{RB}\right) \quad & +\frac{\partial}{\partial z}\left[\left(\boldsymbol{GZ}_I^{\pm}\right)-\left(\boldsymbol{GZ}_I^{\pm}\right)_{RB}+\left(\boldsymbol{GZ}_V^{\pm}\right)_{\Delta}\right] \\ & +\frac{1}{r}\frac{\partial}{\partial r}\left[\left(r\boldsymbol{GR}_I^{\pm}\right)-r\left(\boldsymbol{GR}_I^{\pm}\right)_{RB}+r\left(\boldsymbol{GR}_V^{\pm}\right)_{\Delta}\right]+\boldsymbol{S}-\boldsymbol{S}_{RB}=0\end{aligned} \tag{7.62}$$

where $\boldsymbol{U}_{RB}$ is the state update vector , $\left(\boldsymbol{GR}_I^{\pm}\right)_{RB}$ and $\left(\boldsymbol{GZ}_I^{\pm}\right)_{RB}$ are the split fluxes based on rigid body rotation. The viscous fluxes $\left(\boldsymbol{GR}_V^{\pm}\right)_{\Delta}$ and $\left(\boldsymbol{GZ}_V^{\pm}\right)_{\Delta}$ are computed based on relative velocity field over the rigid body rotation. The source term $\boldsymbol{S}$ is subtracted with $\boldsymbol{S}_{RB}$ evaluated with rigid body rotation condition. Cloud convergence study was done using a coarse cloud of 900 nodes, medium cloud of 3600 nodes and a fine cloud of 14400 nodes. Figure 7.34 shows the plot of axial mass flux for coarse, medium and fine cloud. Figure 7.35 shows the plot of normalized residue for the coarse, medium and fine cloud based on VRKFVS and KFVS schemes using macroscopic tensor splitting. Normalized residue is defined as $\bar{Res}_2^k = Res_2^k/Res_2^0$, where residue Res_2^k is based on the average L_2 norm of all the components across the domain at k^{th} iteration as described in section 6.3.4 of chapter 6. From the residue plot it is evident that the scheme based on VRKFVS converges much faster and at the same time resolves the weak secondary flow.

7.3.6.3 Comparison of SLKNS solver with DSMC

It is difficult to truly compare time and memory requirements of DSMC and SLKNS solver as it depends on the speed memory trade-off and level of rarefaction. Typically, SLKNS solver based on VRKFVS takes around 20 to 30 times less computational time with fraction of memory requirement as compared to DSMC. In this particular problem DSMC solver has taken nearly 6.5 K Bytes/meshpoint compared to 1.2 K Bytes/node for SLKNS solver.

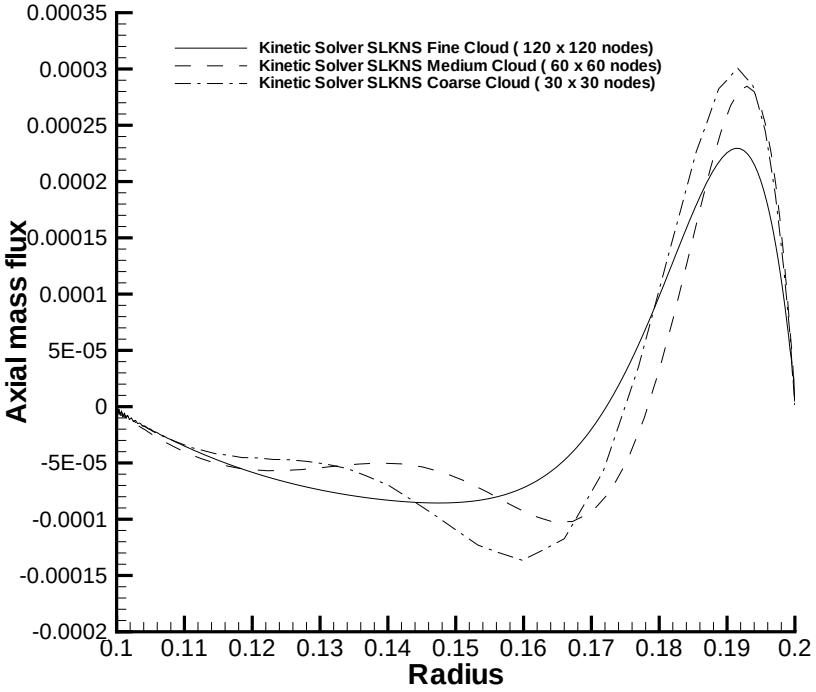

Figure 7.34: Plot of axial mass flux (kg m/s) with respect to radius (m) for cloud convergence study using coarse, medium and fine cloud for flow in rotating annulus.

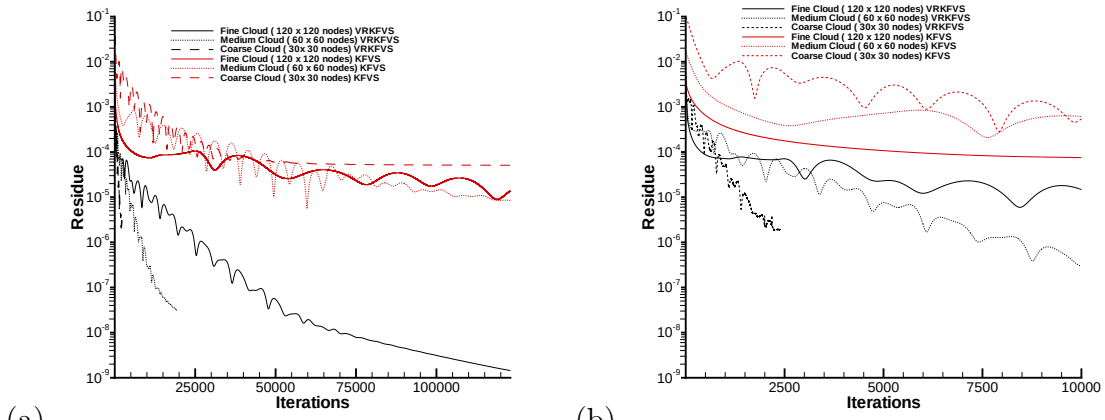

(a) (b)

Figure 7.35: Flow in rotating annulus: (a) Residue plot for coarse, medium and fine cloud for SLKNS solver based on VRKFVS and KFVS schemes using macroscopic tensor splitting, (b) and its zoomed view.

7.3.6.4 Symmetry breaking due to slip flow

It should be noted that rigid body rotation does not hold for rarefied gas confined in a rotating annulus. Fig. 7.36 shows a symmetry breaking in temperature contour due to slip flow solved with SLKNS solver on r-θ plane. In this case the inner and outer walls are rotating with the same frequency, walls are held at temperature of 300 K and Knudsen no. based on radius of inner cylinder is 0.01. Due to rotation the gas becomes rarefied near the inner cylinder causing slip flow which produces instability mechanism due to shear-thinning finally leading to symmetry breaking. Thus we require 3D solver instead of axi-symmetric solver to simulate gas confined in a rotating cylindrical annulus. The cloud requirement to simulate such a flow using a 3D solver will be enormous in order to resolve thin boundary layers, slip effects and exponential rise in density towards the peripheral wall.

7.3.7 Shape optimization of slowly moving ring in a rotating annulus

We present a third case of argon gas in a cylindrical annulus of inner radius of 0.3 m, outer radius of 1.0 m, height of 1.0 m with a ring of radius 0.01 m located at

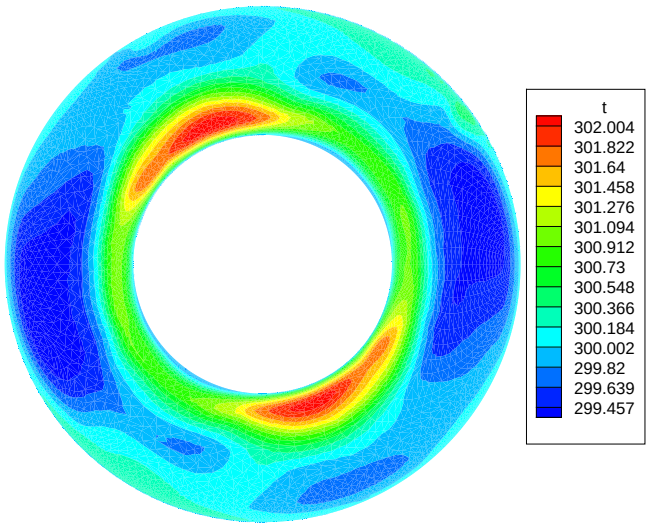

Figure 7.36: Symmetry breaking in temperature contour due to slip flow observed using SLKNS solver on r-θ plane.

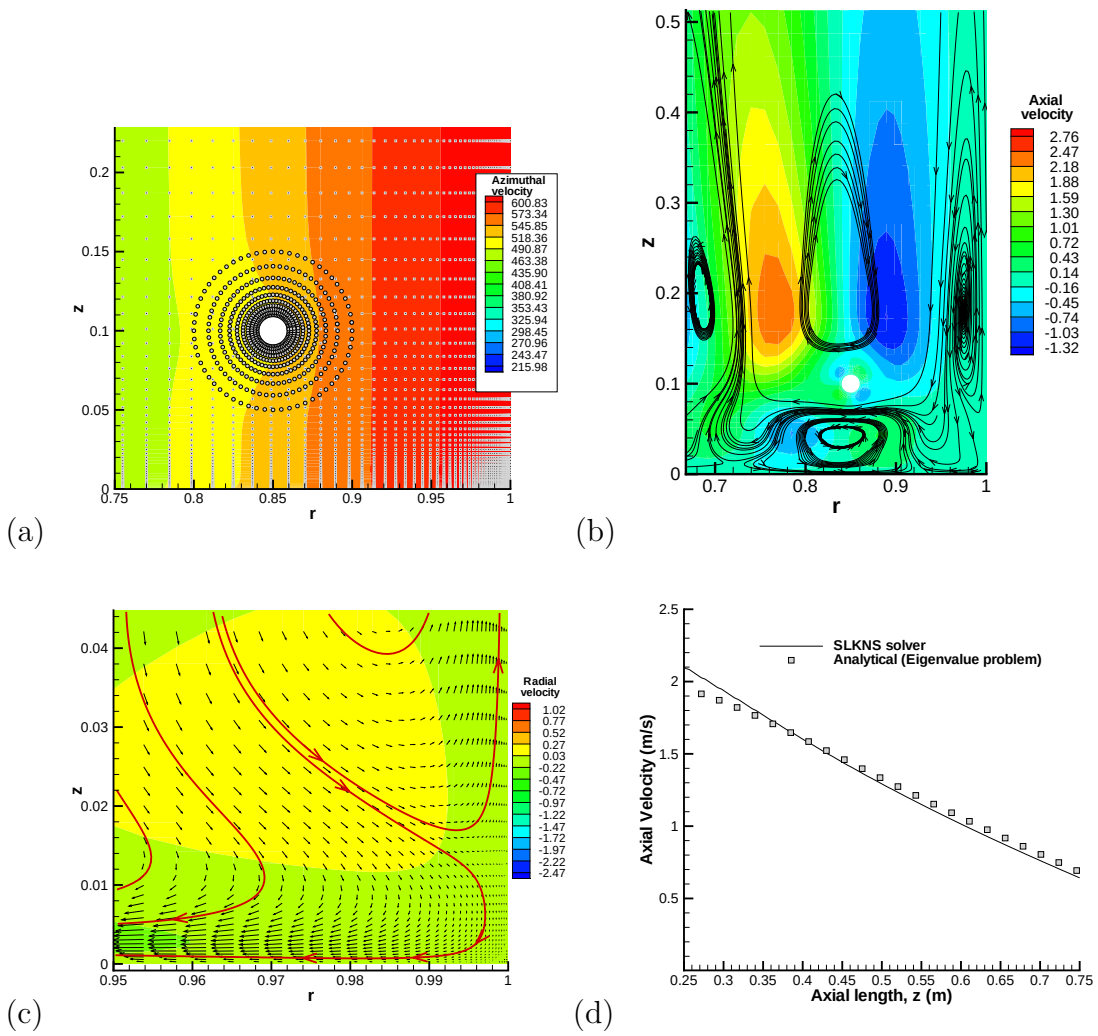

Figure 7.37: Rotating cylindrical annulus with a slowly rotating ring: (a)Cloud of points; (b)recirculation in Stewartson layer; (c)velocity vector in Ekman and Stewartson layers; and (d)axial decay of axial flow at radius=0.77 m

a radius of 0.85 m and axial location of 0.1 m from bottom. Initial density at the wall being 0.0528 Kg/m^3 is held at 300 deg K and rotates with 100 revolutions per second. Ring which is also held at 300 deg K rotates at angular speed of 95 revolutions per second. The total number of nodes in the cloud was 15010. The solver with normal equations based least square approach as well as QR based approach failed with this highly stretched connectivity at the wall. SLKNS solver on the other hand was able to capture weak secondary flow. Figure 7.37 shows the cloud of points, streamline plot and vectors in Ekman and Stewartson layers. Variation of axial flow profile can be cast as an eigenvalue problem for unknown decay rates λ_i. Thus the axial flow variation can be expressed as series of decaying exponentials e.g. $v_z = \sum_i f_i(r)e^{-\lambda_i z}$ [19]. The decay of axial flow at radial location $r = 0.77$ m predicted by SLKNS solver compares well with the theoretical result as shown in figure 7.37(d). Drag of such a body varies with the radius as the density increases exponentially towards the wall leading to presence of vortex in Stewartson layer as shown in Fig. 7.37(b). The simulation was carried out using a global time step with 3-stage scheme of Shu and Osher [249]. For temporal accuracy, time step smaller than the CFL time step was chosen for getting unsteady transient solution. It was observed that the axial velocity oscillates between two values with iterations as shown in Figure 7.38(a) and 7.38(b). Figure 7.39(a) shows the plot of convergence history of the residue based on axial flux, U_z defined as

$$Res_2^k = \frac{1}{N_{cloud}} \sum_{i=1}^{N_{cloud}} \left(|U_z^{k+1}(i) - U_z^k(i)| \right) \tag{7.63}$$

where Res_2^k is the residue based on L_2 norm at k^{th} iteration of axial flux $U_z = \rho u_z$ with u_z as the axial velocity and N_{cloud} as the number of points in the cloud. Residue oscillation can be observed in Figure 7.39(a) and 7.39(b) due to unsteady nature of the problem, similar to vortex shedding past cylindrical bodies observed in linear flows. However, performance of the solver shows a converging trend towards a asymptotic residue with minor oscillation due to fluid mechanics of rotating flow and slowly rotating ring. Figure 7.39(b) shows the zoomed view of the convergence plot.

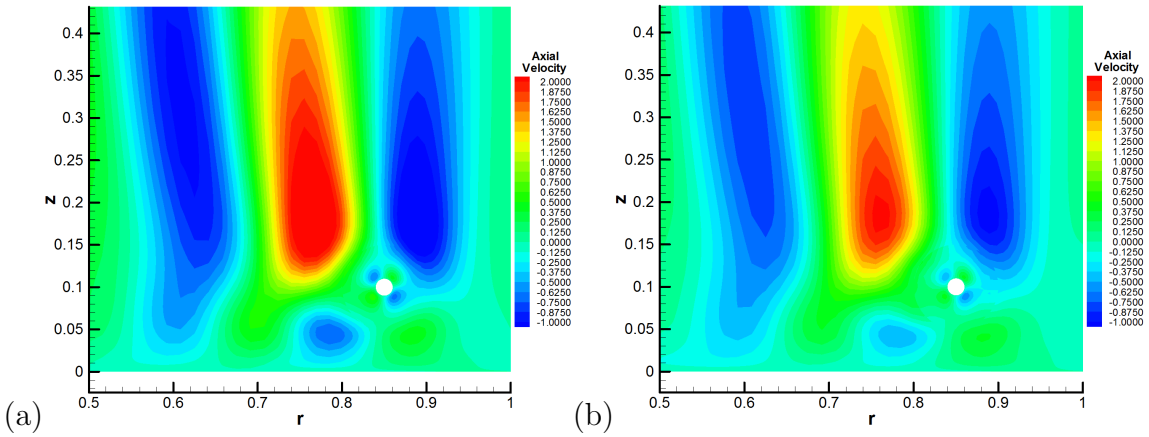

Figure 7.38: Plot of axial velocity (m/s) at (a) iteration 1.3×10^7 and (b) iteration 1.35×10^7 for rotating cylindrical annulus with a slowly rotating ring.

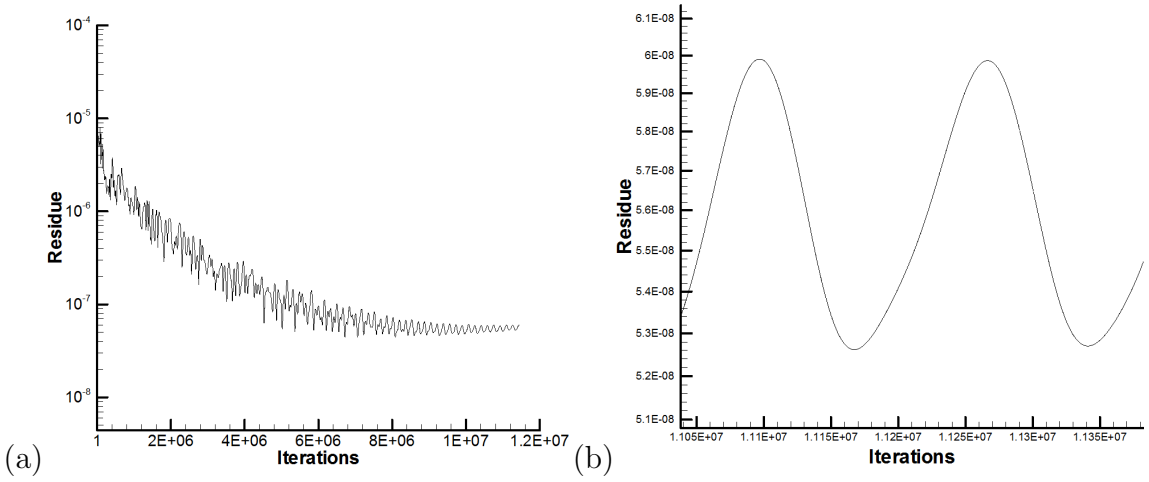

Figure 7.39: Plot of (a)Convergence history, (b) zoomed view showing oscillations for rotating cylindrical annulus with a slowly rotating ring.

7.3.7.1 Shape parametrization and optimization method

One may aspire to optimize the shape of the slowly rotating ring such that the strength of the vortex weakens. Such a shape optimization will require repeated grid generation and a solver which can capture features of high speed flow, slip flow features and weak secondary flow. The cost of optimization depends on the choice of shape parametrization and optimization method. The present approach uses simplex (Nelder-Mead) method based optimization strategy as it takes minimum function calls or CFD runs. The boundary of the body is created using Fourier descriptors[299] i.e. trigonometric functions based on sine and cosine as it requires minimum parameters and at the same time it can be rendered as a smooth function. In this case the boundary of the body is created using trigonometric function $g_t(\vec{x})$ based on parametric vector $\vec{x} \equiv (x_1, x_2) \in \mathbb{R}^2$ as follows

$$\begin{aligned} bx_i &= g_t(\vec{x}) Cos(\theta_i) \\ by_i &= g_t(\vec{x}) Sin(\theta_i) \end{aligned} \tag{7.64}$$

where bx_i and by_i are the coordinates of the body and function $g_t(\vec{x})$ is given as

$$g_t(\vec{x}) = x_1 \left(\frac{1 - Cos(\theta_i)}{2} \right) \left(1 - x_2 \frac{1 - Cos(\theta_i)}{2} \right) \tag{7.65}$$

Figure 7.40 shows shape of the ring and its associated cloud of points after deletion and merging phase of pre-processor. In non-linear simplex approach parameters x_1 and x_2 are the coordinates of the simplex. The single objective function $f \in \mathbb{R}$ is given by the drag of the ring. By carrying out shape optimization we basically search the two dimensional parametric space in order to minimize the drag of the ring so as to weaken the vortex in the Stewartson layer. Fig 7.41 shows the streamline plot and contours of axial velocity for certain shapes of the ring. Total 67 CFD runs using SLKNS code with local time stepping were required while using the optimization routine for 35 iterations based on single simplex. This test case shows that the present meshless solver is capable of carrying out shape optimization for axi-symmetric problems.

7.3.8 Stationary body in the rotating flow field

Consider a stationary cylinder of radius *0.01* m placed at a radial location of *0.075* m within a rotating flow confined between outer isothermal rotating cylinders of

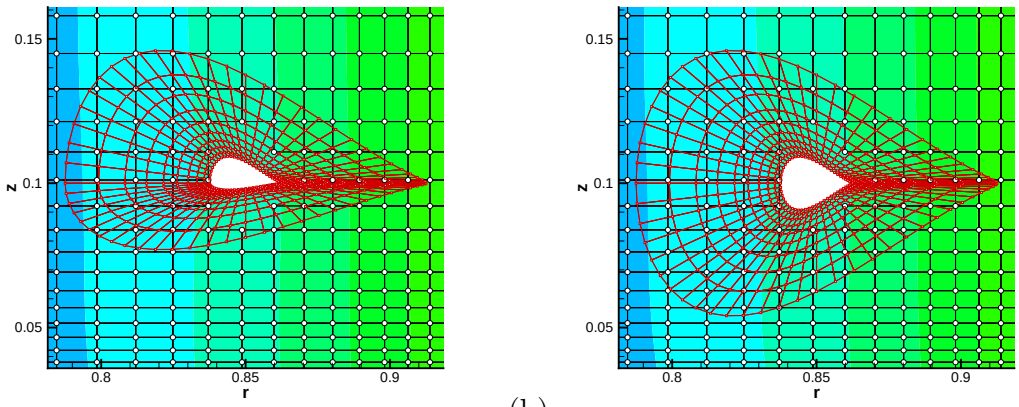

(a) (b)

Figure 7.40: Shape of the ring and its cloud of points : (a) Asymmetric shape, and (b) Symmetric shape

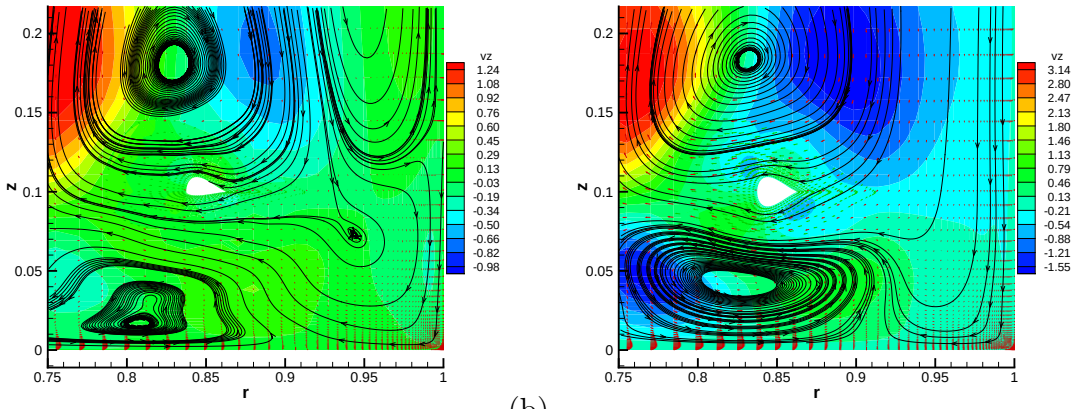

(a) (b)

Figure 7.41: Variation of shape of vortex in the Stewartson layer for (a) Asymmetric shape of the ring, and (b) Symmetric shape of the ring .

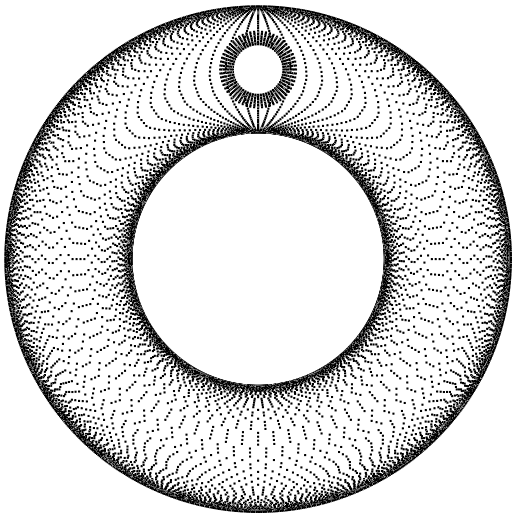

Figure 7.42: Cloud of points in the flow domain to simulate stationary body in the rotating flow field

radius *0.1* m and inner isothermal stationary cylinder of radius *0.05* m. Two cases with subsonic wall speed (Mach=*0.5*) and supersonic wall speed (Mach=*2.0*) with argon gas are chosen for simulation. Figure 7.42 shows the total 20807 points in the flow domain. For the case with wall speed of Mach=0.5 we can observe the spread of the stagnation temperature against the flow and towards the radial direction; it almost covers the whole domain. This is because here the body faces its own wake. The flow accelerates between the rotating cylinder and the stationary cylinder on the expense of the internal energy, thereby cooling the gas. Fig. 7.43 shows the plot of the temperature contour. Fig.7.44 shows the Mach contour. Fig. 7.45 shows the stream line plot near the stationary body. For the case with supersonic wall speed with Mach=2.0 a vortex ahead of the stationary body in the subsonic pocket can be observed. Fig. 7.46 shows the Mach contour and a vortex ahead of the body. At higher speed this vortex becomes weak. It should be noted that the pressure is function of density and entropy per unit mass. If $\nabla\rho \times \nabla p \neq 0$ or $\nabla T \times \nabla s \neq 0$ then, this baroclinic effect creates the

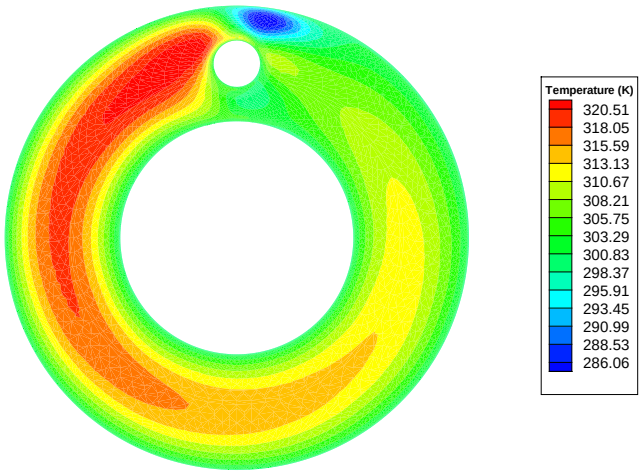

Figure 7.43: Temperature contour observed for stationary body in the rotating flow field.

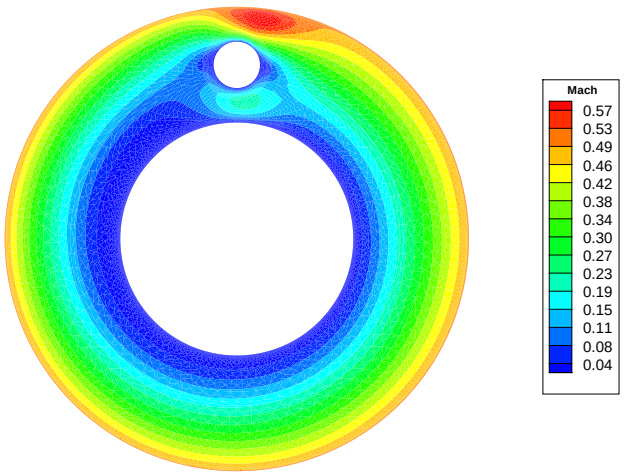

Figure 7.44: Mach contour for subsonic case observed for stationary body in the rotating flow field.

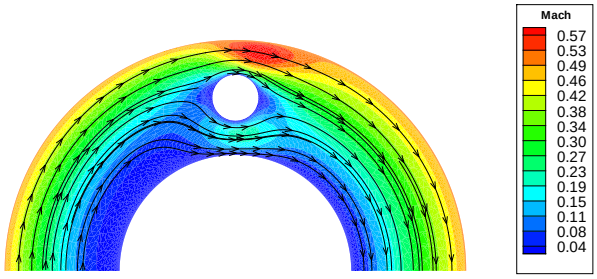

Figure 7.45: Stream line plot near the stationary body for subsonic rotating flow.

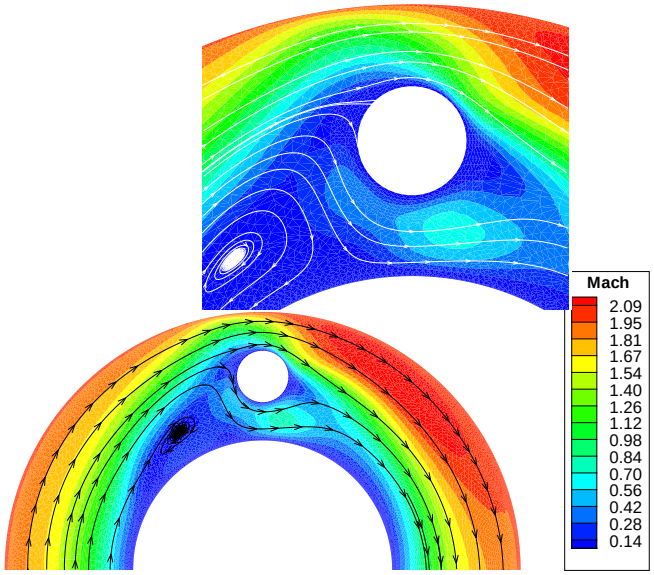

Figure 7.46: Mach contour observed for stationary body in the supersonic rotating flow field, the zoom view near the stationary body shows the vortex.

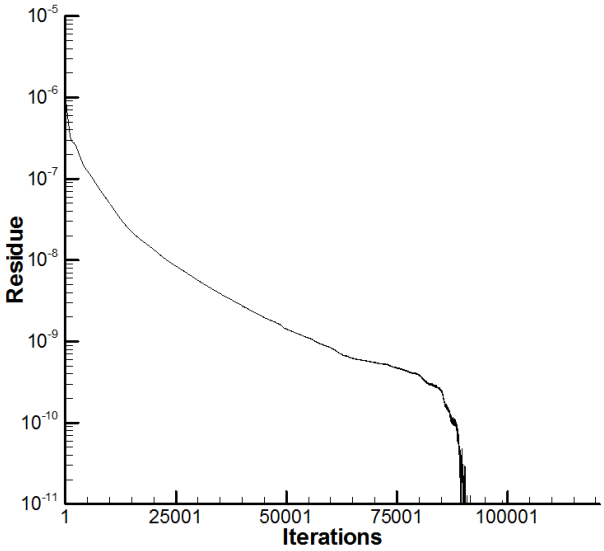

Figure 7.47: Residue plot for stationary body in supersonic rotating flow.

vorticity in the subsonic pocket. The baroclinic term, χ is derived by taking the curl of the pressure gradient in the Navier-Stokes equation

$$\chi = \nabla \times \left(-\frac{1}{\rho} \nabla p \right) = \frac{1}{\rho^2} \nabla \rho \times \nabla p \tag{7.66}$$

The size of the sub-sonic pocket becomes small at very high rotational speed. As a consequence a very fine grid is required to capture the weak vortex at very high rotational speed. It should be noted that as the wall speed increases, the central core becomes rarefied and non-continuum region starts appearing. Figure 7.47 show the plot of fall of residue with iterations. In this case residue, Res_2^k is based on the average L_2 norm of all the components across the domain at k^{th} iteration as described in section 6.3.4 of chapter 6.

7.3.9 Rarefied near transition flow in a rotating eccentric cylinder

The flow confined between two eccentric cylinders is much more complex than the axi-symmetric case. This flow even though confined within such a simple geometry generates myriad nonlinearities associated with the Navier-Stokes equation. Consider a flow of argon confined between outer rotating and inner stationary

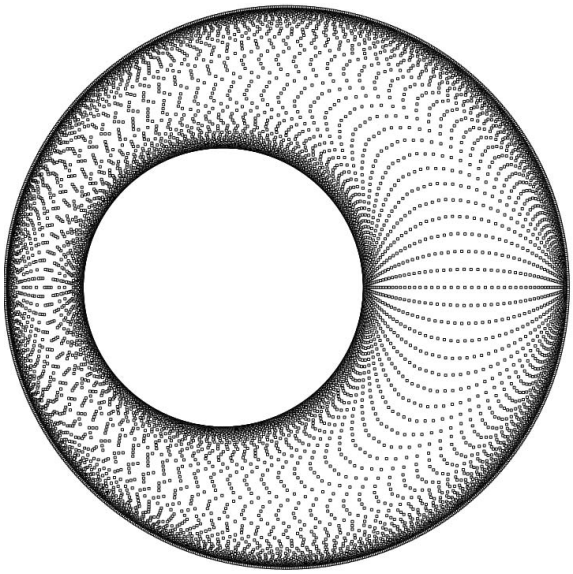

Figure 7.48: Cloud of points for simulating rarefied flow in a rotating eccentric cylinder.

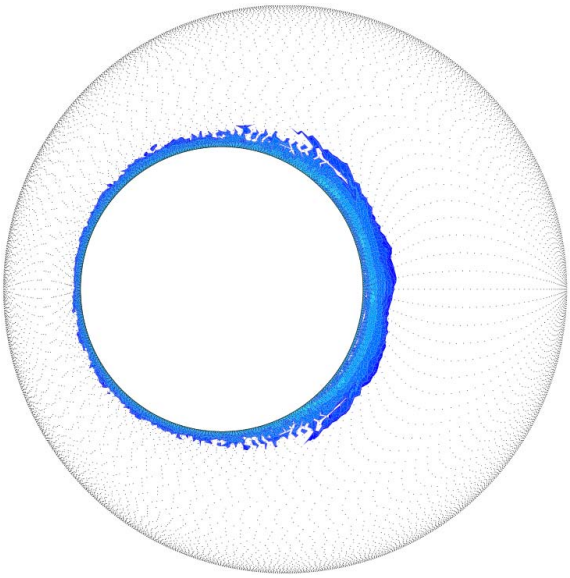

Figure 7.49: Shaded portion shows the region of Navier-Stokes breakdown for rarefied flow in a rotating eccentric cylinder for Mach=0.5 based on gradient length Knudsen number.

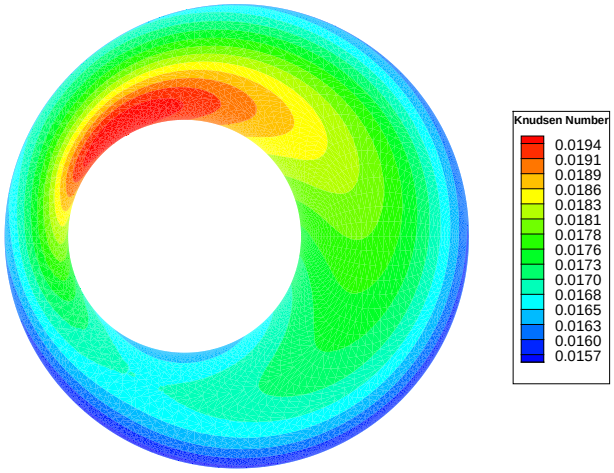

Figure 7.50: Plot of local Knudsen number with region showing separation of flow at Kn=0.0175 for rarefied flow in a rotating eccentric cylinder.

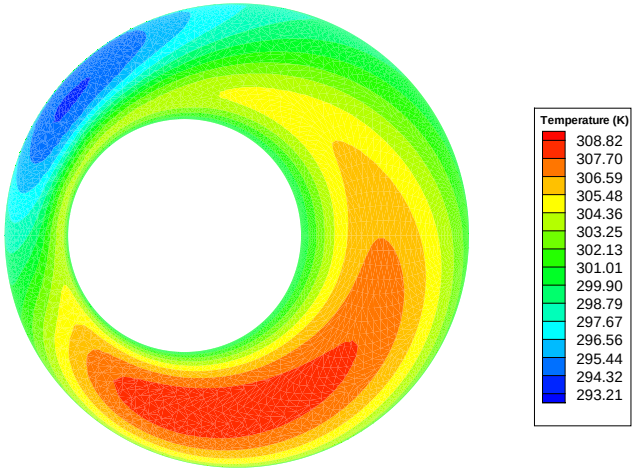

Figure 7.51: Temperature contour for Mach =0.5, eccentricity =0.45, Kn=0.1 for rarefied flow in a rotating eccentric cylinder.

eccentric isothermal cylinders. Researchers [131, 287] have given approximate closed form solution to describe such a flow, others have used approximate analytical solutions by either using an eccentricity parameter [292] or the Reynolds number [23]. Numerical techniques were also developed [5, 10, 223] to simulate continuum flows for this eccentric geometry. Socio and Marino [62, 63] studied this problem using direct simulation Monte-Carlo (DSMC) and carried out detailed study by taking effects of eccentricity and different wall rotational speed for different gas rarefaction for wide range of Knudsen number. The determination of non-continuum region in the present investigation is carried out using a local continuum breakdown parameter called the gradient-length Knudsen number, defined as

$$\mathrm{Kn}_{GL,\varsigma} = \frac{\lambda}{\varsigma} |\nabla \varsigma| \tag{7.67}$$

where ς is the parameter of interest, such as density(ρ), bulk velocity magnitude ($|u| = \sqrt{u_x^2 + u_y^2 + u_z^2}$), or temperature (T). The actual continuum breakdown parameter is maximum of these, that is:

$$\mathrm{Kn}_{GL} = \max(\mathrm{Kn}_{\rho}, \mathrm{Kn}_{|u|}, \mathrm{Kn}_{T}) \tag{7.68}$$

The local Knudsen number, Kn is defined as

$$\mathrm{Kn} = \frac{\lambda}{(r_o - r_i)} \tag{7.69}$$

where r_o is the outer radius and r_i is the inner radius. For example take a case with eccentricity of 0.45 at Mach=0.5 for Kn=0.0175 with isothermal wall held at temperature of *300* K using14962 points in the cloud as shown in Fig. 7.48. Fig. 7.49 shows the region of continuum breakdown based on gradient length Knudsen number Kn_{GL}. Fig. 7.50 shows the plot of local Knudsen number contours for Kn=0.0175.

The present test case explores the validity of kinetic boundary condition derived using first order Chapman-Enskog for rarefied near transition flow with Kn=0.1. Numerical simulation for eccentricity of 0.45 at Mach=0.5, Kn=0.1 with isothermal wall held at temperature of *300* K was carried out using cloud of 14962 points. This test case was solved using boundary condition based on Burnett correction term as well as collision probability function using Variance Reduction

Kinetic Flux Vector Splitting (VRKFVS) and m-SLKNS solver described in section 6.3.2. Upwind Navier-Stokes equation based on Variance Reduction Kinetic Flux Vector Splitting (VRKFVS) form is written as

$$\begin{array}{ll} \frac{\partial}{\partial t}\left(\boldsymbol{U}-\boldsymbol{U}_{RB}\right) & +\frac{\partial}{\partial x}\left[\left(\boldsymbol{GX}_{I}^{\pm}\right)-\left(\boldsymbol{GX}_{I}^{\pm}\right)_{RB}+\left(\boldsymbol{GX}_{V}^{\pm}\right)_{\Delta}\right] \\ & +\frac{\partial}{\partial y}\left[\left(\boldsymbol{GY}_{I}^{\pm}\right)-\left(\boldsymbol{GY}_{I}^{\pm}\right)_{RB}+\left(\boldsymbol{GY}_{V}^{\pm}\right)_{\Delta}\right]=0 \end{array} \tag{7.70}$$

where $\boldsymbol{U}_{RB}$ is the state update vector at rigid body rotation condition, $\left(\boldsymbol{GX}_{I}^{\pm}\right)_{RB}$ and $\left(\boldsymbol{GY}_{I}^{\pm}\right)_{RB}$ are the split fluxes based on rigid body rotation. The viscous fluxes $\left(\boldsymbol{GX}_{V}^{\pm}\right)_{\Delta}$ and $\left(\boldsymbol{GY}_{V}^{\pm}\right)_{\Delta}$ are computed based on relative velocity field over the rigid body rotation. VRKFVS based method is more accurate and applicable in regions where solution is in vicinity of rigid body state.

7.3.9.1 Treatment based on Burnett correction

One of the simplest way to extend the kinetic based slip boundary condition is by further updating the slip velocity using the second order Kn^2 terms associated with the Burnett constitutive relations as described in section 5.6.2 in chapter 5. This correction $(\Delta u_s)_{Burnett}$ over slip velocity, $(u_s)_{kinetic}$ calculated by SLKNS is as follows

$$(u_s)_{2^{nd}Order}^{n+1}=(u_s)_{kinetic}^{n+1}+(\Delta u_s)_{Burnett}^{n+1} \tag{7.71}$$

Flux derivatives are calculated with at-least third order accuracy, the Burnett correction to the slip velocity is under-relaxed by factor, rf which is below 0.1 such that

$$(\Delta u_s)_{Burnett}^{n+1}=(\Delta u_s)_{Burnett}^{n}+rf\left[(\Delta u_s)_{Burnett}^{n+1}-(\Delta u_s)_{Burnett}^{n}\right] \tag{7.72}$$

Fig. 7.51 revealed contours of temperature similar to observed in DSMC for the case with Kn=0.1. In this case the maximum temperature observed is 308.82 K and minimum temperature is 293.21 K using m-SLKNS solver based on VRKFVS scheme with Burnett correction. Thus, maximum temperature ratio is 1.029 and minimum temperature ratio is 0.977 ratio. Socio and Marino [63] have observed as maximum temperature ratio as 1.033 and minimum at 0.979 using DSMC Simulation. This second order treatment based on addition of Burnett correction terms does not comply with the Onsager's reciprocity principle as there is no contribution made to the thermal terms.

7.3.9.2 Treatment based on collision probability function

As described earlier near the wall at a normal distance of order $O(\lambda) = \lambda_e$ there exists a Knudsen layer where some molecules may not suffer as much collisions as compared to the molecules above the Knudsen layer. The term λ_e is the effective mean free path depending on the viscosity and wall conditions. In this case the distribution function at normal dimensionless distance $\bar{y} = \frac{y}{\lambda_e} \leq 1$ is expressed as

$$f_1(\bar{y}) = f_0 - \mathbb{P}(\bar{y}) \sum_j \boldsymbol{\Upsilon}_j \odot \boldsymbol{X}_j \tag{7.73}$$

The collision probability function used in the simulation is

$$\mathbb{P}(\bar{y}) = \begin{cases} \frac{\bar{y}}{2} + \frac{\sin^{-1}(\bar{y})}{\pi}, & \bar{y} \leq 1 \\ 1, & \bar{y} > 1 \end{cases} \tag{7.74}$$

where factor $\frac{\bar{y}}{2}$ is probability of molecules in the Knudsen layer moving in upward direction i.e. it is proportional to volume of molecules below the dimensionless normal distance. For surface with curvature $\mathbb{P}(\bar{y})$ is multiplied with additional surface dependent weight e.g. in this case weight is based on its radius. This kinetic method is quite easy to implement as the viscous fluxes are just multiplied by the collision function $\mathbb{P}(\bar{y})$. The viscous part of the flux component, $\left(\bar{\boldsymbol{G}\boldsymbol{X}}_V^{\pm}\right)_\Delta$ and $\left(\bar{\boldsymbol{G}\boldsymbol{Y}}_V^{\pm}\right)_\Delta$ are obtained as

$$\begin{aligned} \left(\bar{\boldsymbol{G}\boldsymbol{X}}_V^{\pm}\right)_\Delta &= \mathbb{P}(\bar{y}) \left(\boldsymbol{G}\boldsymbol{X}_V^{\pm}\right)_\Delta = -\mathbb{P}(\bar{y}) \textstyle\sum_j \boldsymbol{\Lambda}_j^{\pm\cdot} \odot \bar{\boldsymbol{X}}_j \\ \left(\bar{\boldsymbol{G}\boldsymbol{Y}}_V^{\pm}\right)_\Delta &= \mathbb{P}(\bar{y}) \left(\boldsymbol{G}\boldsymbol{Y}_V^{\pm}\right)_\Delta = -\mathbb{P}(\bar{y}) \textstyle\sum_j \boldsymbol{\Lambda}_j^{\cdot\pm} \odot \bar{\boldsymbol{X}}_j \end{aligned} \tag{7.75}$$

where tensor of thermodynamic force $\bar{\boldsymbol{X}}$ is evaluated based on relative velocity field and temperature over the rigid body rotation condition. Using SLKNS solver based on VRKFVS scheme with slip flow model based collision probability function $\mathbb{P}(\bar{y})$ the maximum temperature observed is 309.01 K and minimum temperature is 291.59 K as shown in Fig. 7.52 and Fig. 7.53 shows the plot of residue based on the average L_2 norm of all the components across the domain at k^{th} iteration as described in section 6.3.4 of chapter 6. The maximum temperature ratio is 1.030 and minimum temperature ratio is 0.972 ratio observed with slip flow model based on Onsager's reciprocity principle and collision probability function is much closer to DSMC.

DSMC simulation carried out by Socio and Marino [63] revealed that the onset of vortex was being helped by the eccentricity while gas rarefaction had an opposite influence in subsiding the vortex. The disappearance of the vortex for eccentricity of 0.45 at Mach =0.5 was observed at Kn=0.72 using SLKNS with Burnett correction, this disappearance of vortex happens at Kn=0.8 using slip flow model based on Onsager's reciprocity principle and collision probability function while Socio and Marino [63] observed it at Kn=1.0 using DSMC. It should be noted that Socio and Marino [62, 63] employed the bi-polar coordinate system to simplify the geometric representation at the cost of complications introduced due to the rectilinear trajectories of the particles. The density contour plot reveals the density rises exponentially towards the periphery. The bipolar coordinate system used in DSMC leads to large size cells towards the rotating peripheral region where density rises sharply. While in m-SLKNS solver the cloud of points were more clustered radially towards the peripheral wall as well as in the azimuthal region.

7.3.9.3 Performance of SLKNS solver for rarefied transition flow

The vortex for eccentricity of 0.45 at Mach =0.5 subsides at much lower Knudsen number and does not compare well with the DSMC prediction[63] at Kn=1.0. One of the reasons of disagreement is due to the extension of the present first order distribution based kinetic boundary condition to higher Knudsen number flow using corrections with Kn^2 order Burnett terms and usage of collision probability function. More-so-ever the present 5 moments based formulation is inadequate for the simulation of rarefied flow beyond slip regime, in order to resolve features of transition flow we need to extend the formulation to 13-moment Grad system [102].

7.3.10 Rarefied supersonic flow over a hemisphere

Consider a 3D test case of rarefied supersonic flow of air of density 1.40706×10^{-5} kg/m^3 at 300 K impinging a hemisphere of radius 0.1 m with a speed of 1000. m/s. The Knudsen number based on hemisphere radius is 0.0535 with fully diffuse wall held at 300 K. Fig 7.54 shows the Mach and density contour at Knudsen number 0.0535 calculated using SLKNS solver. SLKNS solver was run using

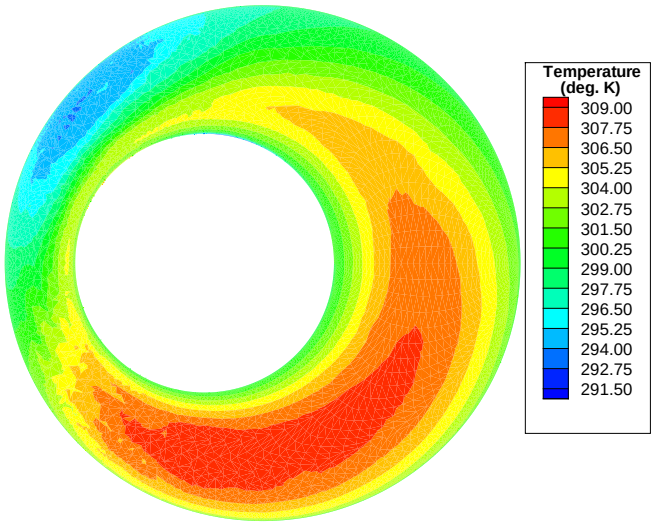

Figure 7.52: Temperature contour for Mach =0.5, eccentricity =0.45, Kn=0.1 for rarefied flow in a rotating eccentric cylinder with slip flow model based collision probability function.

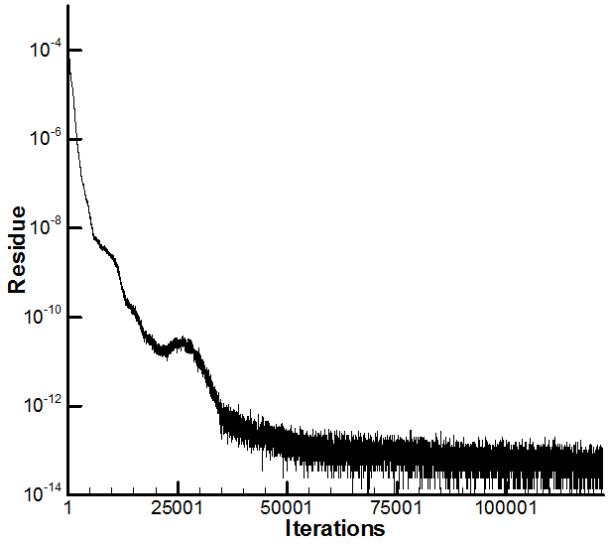

Figure 7.53: Residue plot for rarefied flow in a rotating eccentric cylinder with Mach =0.5, eccentricity =0.45, Kn=0.1 using VRKFVS scheme and collision probability function.

23657 cloud of points generated using $25 \times 25 \times 41$ grid in spherical coordinate system. The number of cloud of points were chosen based on grid points used in DSMC simulation with which results of SLKNS is to be compared. Fig 7.55 shows the variation of slip velocity expressed in Mach as well as density on the surface of the hemisphere with respect to angle from the stagnation point. Fig 7.56 shows the variation of Mach number as well as density with respect to distance from the hemisphere. For nearly similar number of points DSMC was more accurate, SLKNS was not able to capture the shock structure as described by DSMC. The state update for interior flow solver nodes is expressed as

$$\boldsymbol{U}^{k+1} = \boldsymbol{U}^{k} - \Delta t \left[\begin{array}{l} \left(\frac{\partial \boldsymbol{GX}^{+}}{\partial x}\right)^{k}_{\Delta x<0} + \left(\frac{\partial \boldsymbol{GX}^{-}}{\partial x}\right)^{k}_{\Delta x>0} \\ + \left(\frac{\partial \boldsymbol{GY}^{+}}{\partial y}\right)^{k}_{\Delta y<0} + \left(\frac{\partial \boldsymbol{GY}^{-}}{\partial y}\right)^{k}_{\Delta y>0} \\ + \left(\frac{\partial \boldsymbol{GZ}^{+}}{\partial z}\right)^{k}_{\Delta z<0} + \left(\frac{\partial \boldsymbol{GZ}^{-}}{\partial z}\right)^{k}_{\Delta z>0} \end{array} \right] \tag{7.76}$$

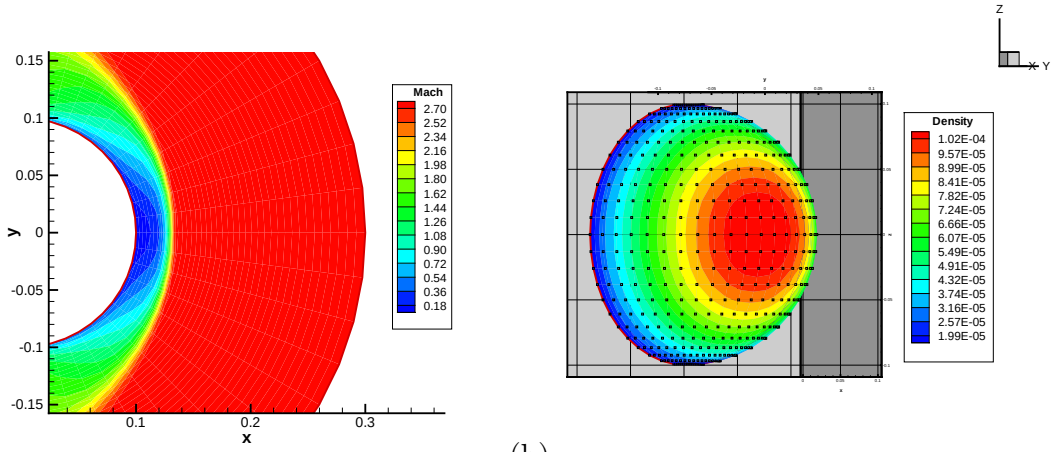

(a) (b)

Figure 7.54: Mach contours and density contour at Kn = 0.0535 of flow of air at 1000 m/s over a hemisphere based on SLKNS solver

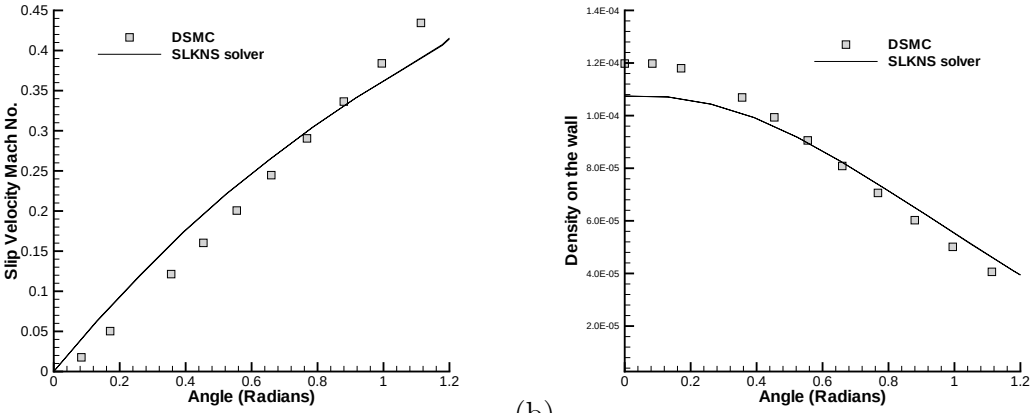

(a) (b)

Figure 7.55: Slip velocity and density variation at Kn = 0.0535 of flow of air at 1000 m/s over a hemisphere based on SLKNS solver and DSMC

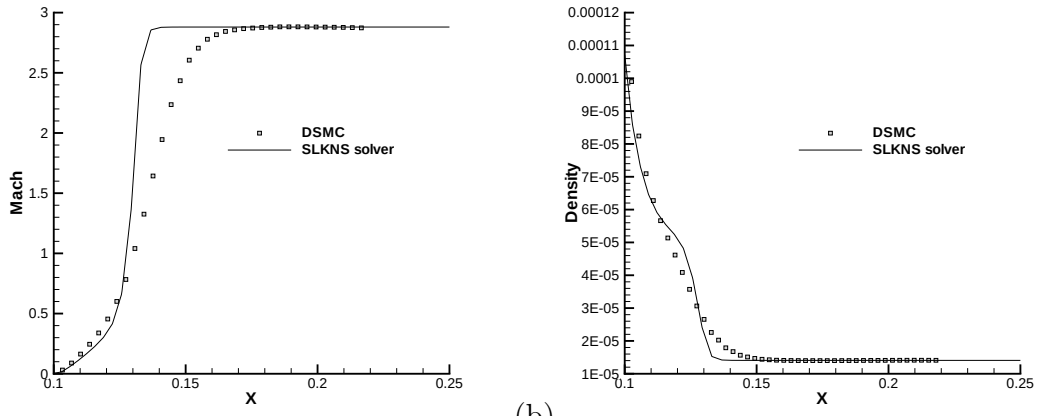

(a) (b)

Figure 7.56: Mach and density variation at Kn = 0.0535 of flow of air at 1000 m/s over a hemisphere based on SLKNS solver and DSMC with respect to distance x in meters.

where expressions of split fluxes $\boldsymbol{GX}^{\pm}$, $\boldsymbol{GY}^{\pm}$ and $\boldsymbol{GZ}^{\pm}$ are given in Appendix D. The sate update for wall boundary nodes is expressed

$$\boldsymbol{U}^{k+1} = \boldsymbol{U}^{k} - \Delta t \left[\begin{array}{l} \left(\frac{\partial \widehat{\boldsymbol{GX}}^{+\cdot-}}{\partial x}\right)^{k}_{\Delta x<0} + \left(\frac{\partial \widehat{\boldsymbol{GX}}^{-\cdot-}}{\partial x}\right)^{k}_{\Delta x>0} \\ + \left(\frac{\partial \widehat{\boldsymbol{GY}}^{\cdot+-}}{\partial y}\right)^{k}_{\Delta y<0} + \left(\frac{\partial \widehat{\boldsymbol{GY}}^{\cdot--}}{\partial y}\right)^{k}_{\Delta y>0} \\ + \left(\frac{\partial \widehat{\boldsymbol{GZ}}^{\cdot\cdot-}}{\partial z}\right)^{k}_{\Delta z>0} \end{array} \right] \tag{7.77}$$

where expressions of split fluxes $\widehat{\boldsymbol{GX}}^{\pm\cdot-}$, $\widehat{\boldsymbol{GY}}^{\cdot\pm-}$ and $\widehat{\boldsymbol{GZ}}^{\cdot\cdot-}$ are given in Appendix D. This test once again revealed that DSMC required lesser computing nodes as compared to SLKNS. The size of cloud in the present analysis was fixed based on the requirement of cells required by DSMC used in this test case for validation. For doing cloud convergence study we will require a medium cloud of 2562 nodes using $12 \times 12 \times 21$ grid in spherical coordinate system. Generation of coarse cloud in this case will not be a feasible. In order to carry out cloud convergence analysis a fine cloud of 127551 nodes was generated using $51 \times 51 \times 51$ grid in spherical coordinate system. Medium cloud of 15002 nodes using $25 \times 25 \times 26$ grid and coarse cloud of 1586 nodes using $12 \times 12 \times 13$ grid was generated. Fig 7.57

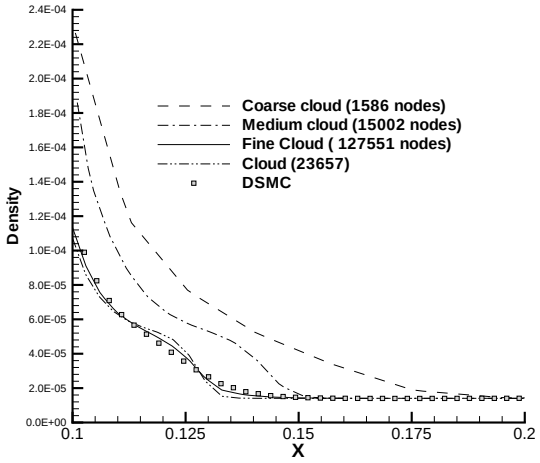

Figure 7.57: Density variation at Kn = 0.0535 of flow of air at 1000 m/s based on SLKNS solver for coarse, medium and fine cloud.

shows the variation of density with respect to distance from the hemisphere for coarse, medium and fine cloud as compared to cloud with 23657 nodes and results of DSMC. SLKNS solver uses explicit first order Euler time integration based on local time step to cut down the computational time. Fig 7.58 shows the residue plot for coarse, medium and fine cloud of points. The residue, Res_2^k in this particular case is based on the average L_2 norm of all the components across the domain at k^{th} iteration as described in section 6.3.4 of chapter 6. Because of local time-stepping this 3-D test case converges much faster compared to test cases with global time stepping.

7.3.11 Stationary hemisphere in a strongly rotating flow field

Consider another 3D test case in which a stationary hemisphere of radius 0.005 m is placed mid way at a radius of 0.075 m in a annular cylindrical sector of outer radius 0.1 m and inner radius of 0.05 m and height of 0.035 m. The wall of the annular cylindrical sector is rotating at 2000 revolutions per second. The top lid and the rear side of the hemisphere have an outflow boundary as shown in Fig. 7.59 with the rotating bottom boundary. Fig. 7.60 shows the points

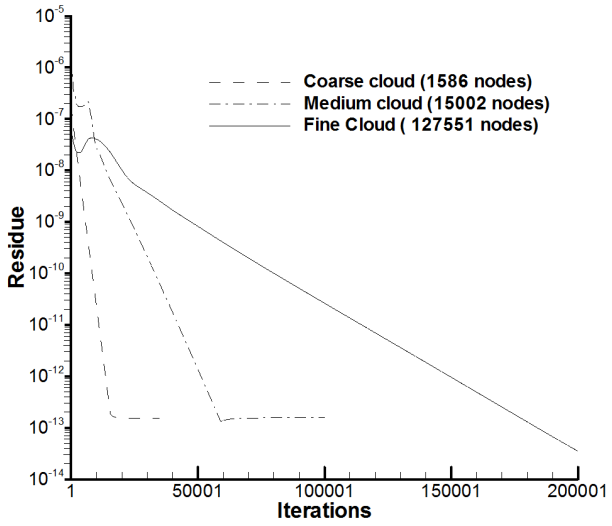

Figure 7.58: Residue plot for coarse, medium and fine cloud of points for rarefied supersonic flow over a hemisphere.

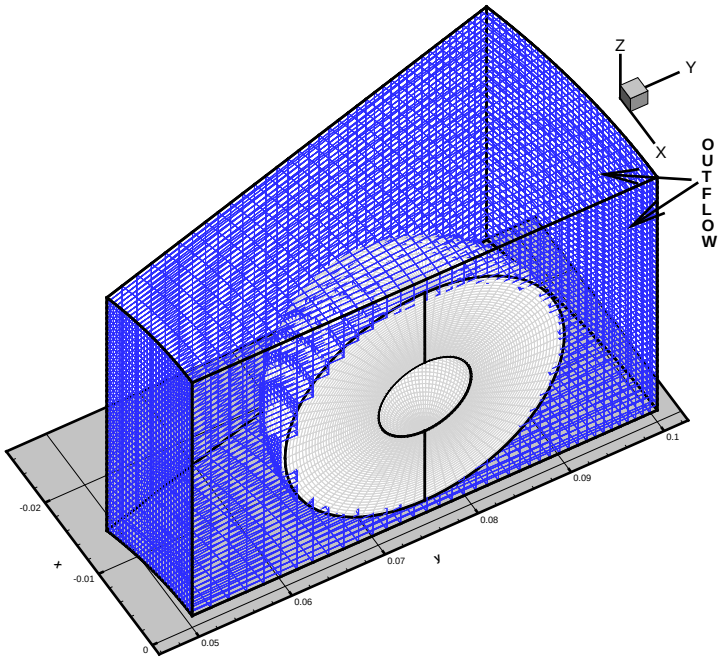

Figure 7.59: Cloud of points and outflow boundary for stationary hemisphere placed a strongly rotating flow field.

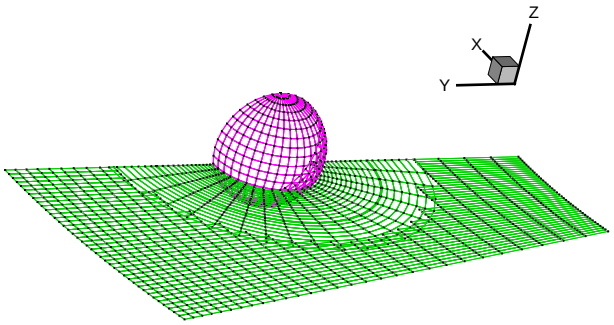

Figure 7.60: Cloud of points generated using cylindrical and spherical mesh for stationary hemisphere placed a strongly rotating flow field.

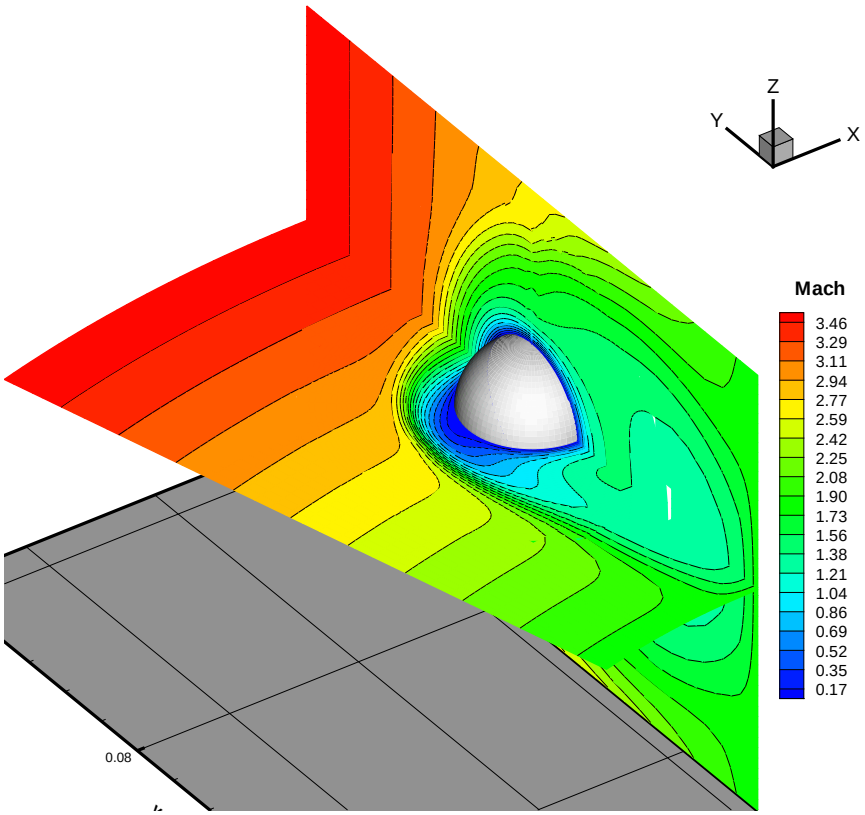

Figure 7.61: Mach contours Hemisphere facing a rotating flow.

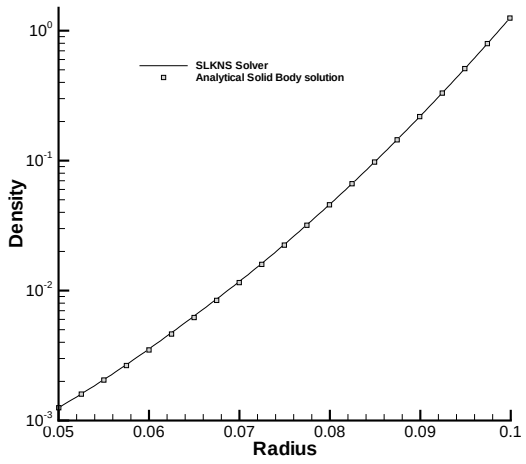

Figure 7.62: Density variation at the bottom lid of the outflow based on SLKNS and analytical solid body solution for stationary hemisphere placed a strongly rotating flow field.

generated using cylindrical and spherical meshes, the total number of points in the cloud was 122921. Fig.7.61 shows a curved shock with strong radially inward flow as the rotating flow hits the stationary hemisphere. The density of air at wall is taken as *1.271* Kg/m^3 for this case. Fig.7.62 shows comparison between SLKNS and analytical result near the bottom boundary. The exponential rise in the density compared well with the analytical result given as $\rho_r = \rho_{wall} \exp\left(\frac{1}{2RT}\left((v_\theta^2)_r - (v_\theta^2)_{wall}\right)\right)$.

7.3.11.1 Rarefied case

Consider a rarefied rotating flow with density of air at wall being *0.01271* Kg/m^3. SLKNS solver using VRKFVS scheme as well as KFVS scheme is used to solve this test case. Upwind Navier-Stokes equation based on Variance Reduction Kinetic Flux Vector Splitting (VRKFVS) form is written as

$$\begin{aligned} \frac{\partial}{\partial t}\left(\boldsymbol{U}-\boldsymbol{U}_{RB}\right) \quad & +\frac{\partial}{\partial x}\left[\left(\boldsymbol{GX}_I^{\pm}\right)-\left(\boldsymbol{GX}_I^{\pm}\right)_{RB}+\left(\boldsymbol{GX}_V^{\pm}\right)_{\Delta}\right] \\ & +\frac{\partial}{\partial y}\left[\left(\boldsymbol{GY}_I^{\pm}\right)-\left(\boldsymbol{GY}_I^{\pm}\right)_{RB}+\left(\boldsymbol{GY}_V^{\pm}\right)_{\Delta}\right] \\ & +\frac{\partial}{\partial z}\left[\left(\boldsymbol{GZ}_I^{\pm}\right)-\left(\boldsymbol{GZ}_I^{\pm}\right)_{RB}+\left(\boldsymbol{GZ}_V^{\pm}\right)_{\Delta}\right]=0 \end{aligned} \tag{7.78}$$

where $\boldsymbol{U}_{RB}$ is the state update vector at rigid body rotation condition, $\left(\boldsymbol{GX}_I^{\pm}\right)_{RB}$, $\left(\boldsymbol{GY}_I^{\pm}\right)_{RB}$ and $\left(\boldsymbol{GZ}_I^{\pm}\right)_{RB}$ are the split fluxes based on rigid body rotation. The viscous fluxes $\left(\boldsymbol{GX}_V^{\pm}\right)_{\Delta}$, $\left(\boldsymbol{GY}_V^{\pm}\right)_{\Delta}$ and $\left(\boldsymbol{GZ}_V^{\pm}\right)_{\Delta}$ are computed based on relative velocity field over the rigid body rotation. VRKFVS based method is more accurate and applicable in regions where solution is in vicinity of rigid body state. Rossby number which gives relative importance of inertial with respect to Coriolis forces is also a measure of departure from the rigid body solution. In the present research work we have defined the local Rossby number, ε based on z-component of vorticity vector Ω_z as

$$\varepsilon = \left| 1 - \frac{\Omega_z}{(\Omega_z)_{RB}} \right| \tag{7.79}$$

where $(\Omega_z)_{RB}$ is the z-component of vorticity vector for rigid body rotation. The domain is decomposed based on this local Rossby number which is used as a measure of departure from the rigid body solution. For example in the present case if $\varepsilon < \varepsilon_s$=0.1 the flow domain uses VRKFVS scheme and when $\varepsilon > \varepsilon_s$ then the solver switches back to KFVS scheme. Fig. 7.63(a) shows a typical VRKFVS domain where $\varepsilon < 0.1$ and Fig. 7.63(b) shows remaining KFVS domain where KFVS solver updates the solution. The KFVS and VRKFVS regions are dynamically defined at every iteration based on the local Rossby number.

Fig.7.64 shows the non-continuum transition region due to the development of rarefied core at high speed based on gradient length Knudsen number, $\mathrm{Kn}_\rho = \frac{\lambda}{L_\rho}$, where λ is the mean free path and characteristic length scale, L_ρ is defined in terms of the density gradient as $L_\rho = \rho / \frac{\partial \rho}{\partial r}$ with r as the radius. This non-continuum rarefied region which is near transition regime i.e. $\mathrm{Kn}_\rho \geq 0.1$ requires coupling with either Burnett equation or DSMC solver. In the present case rarefied core boundary condition was used and interior rarefied core was coupled with Maxwellian distribution. At the rarefied core the distribution is Maxwellian, $f_{0,\infty}$ as near free molecular flow prevails. This Maxwellian is split into two parts based on the direction of propagation. Similarly, the Chapman-Enskog distribution, f_1 is split into two parts i.e. part escaping out of the flow domain and the part which remains in the flow domain as shown in figure 7.65. If $v_z > 0$ then the molecules belonging to the Maxwellian, $f_{0,\infty}$ enter into the computational domain from the rarefied core. If $v_z < 0$ then the molecules are coming from the computational domain. Thus, distribution function $f_{1,\Sigma}(v_x, v_y, v_z, \mathbb{I})$ at the rarefied

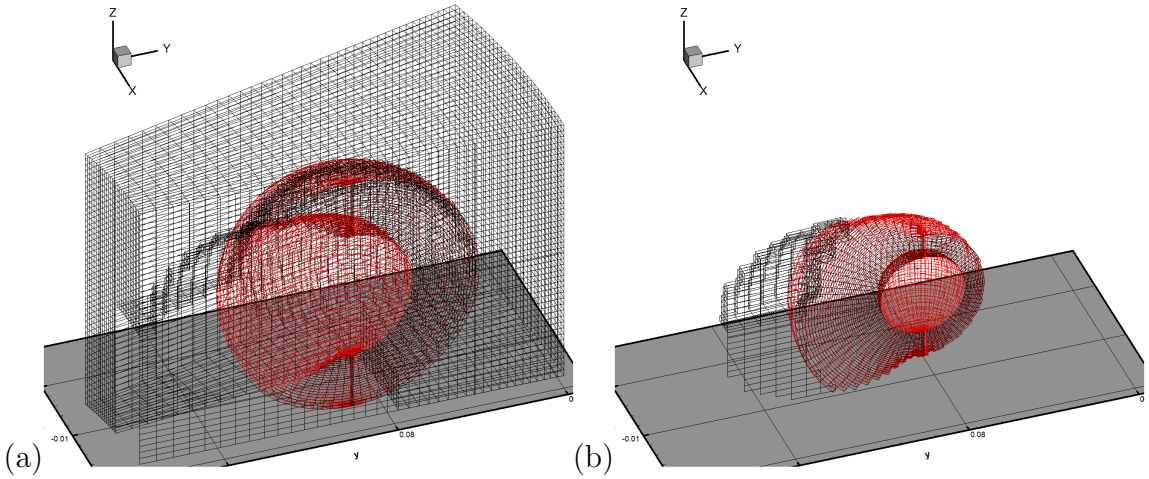

Figure 7.63: Domain decomposition based on Rossby number for stationary hemisphere placed a strongly rotating flow field: (a) VRKFVS domain where $\varepsilon < 0.1$, (b) remaining KFVS domain. Regions based on cylindrical and spherical mesh are shown by black and red colour respectively.

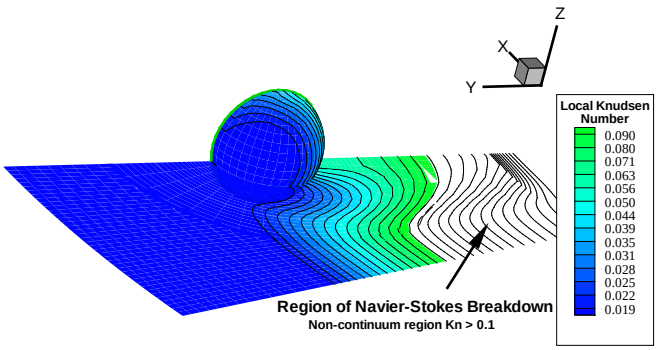

Figure 7.64: Region of Navier-Stokes breakdown based on gradient length Knudsen number, Kn_ρ for stationary hemisphere placed a strongly rotating flow field.

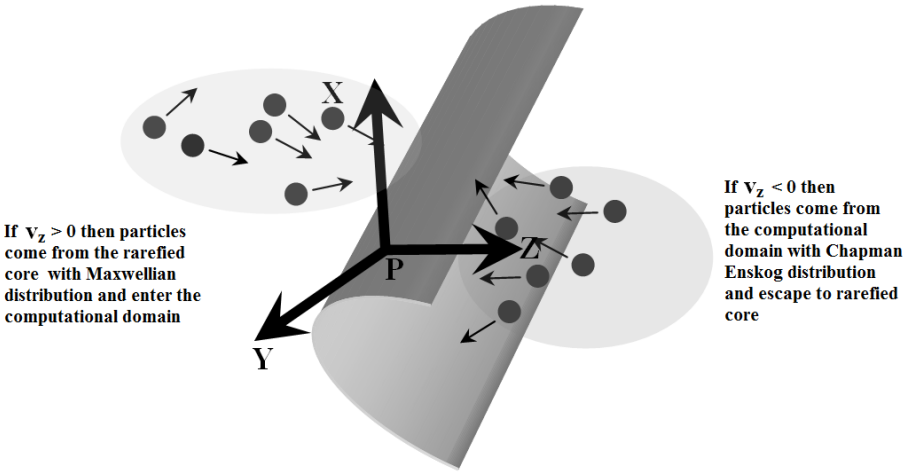

Figure 7.65: Distribution function at the rarefied core constructed from the truncated Maxwellian from the rarefied core and Chapman-Enskog distribution from the flow domain

core is constructed as the union of a Maxwellian distribution $f_{0,\infty}(v_x, v_y, v_z, \mathbb{I})$ corresponding to the incoming particle from the rarefied domain and first order Chapman-Enskog distribution $f_1(v_x, v_y, v_z, \mathbb{I})$ corresponding to outgoing particles from the computing domain.

$$f_{1,\Sigma}(v_x, v_y, v_z, \mathbb{I}) = f_{0,\infty}(v_x, v_y, v_z, \mathbb{I})_{v_z>0} \cup f_1(v_x, v_y, v_z, \mathbb{I})_{v_z<0} \tag{7.80}$$

where $f_1 = f_0 - \sum_j \boldsymbol{\Upsilon}_j \odot \boldsymbol{X}_j$. The state update based on KFVS implementation at the rarefied core boundary after taking $\boldsymbol{\Psi}$ moment and writing in terms of inner product at time $t + \Delta t$ can be expressed as

$$\boldsymbol{U}(t + \Delta t) = \bar{\boldsymbol{U}}(t) - \Delta t \left[\frac{\partial \boldsymbol{GX}(t)}{\partial x}^{\pm\cdot-} + \frac{\partial \boldsymbol{GY}(t)}{\partial y}^{\cdot\pm-} + \frac{\partial \boldsymbol{GZ}(t)}{\partial z}^{-} \right] \tag{7.81}$$

where

$$\bar{\boldsymbol{U}} = \int_{\mathbb{R}^D} \int_{\mathbb{R}^+} \boldsymbol{\Psi} f_{1,\Sigma} d\vec{v} d\mathbb{I} \tag{7.82}$$

The $\boldsymbol{GX}^{\pm\cdot-}$, $\boldsymbol{GY}^{\cdot\pm-}$ and $\boldsymbol{GZ}^{-}$ fluxes can be written as sum of inviscid or Euler part and viscous part as follows

$$\boldsymbol{GX}^{\pm\cdot-} = \boldsymbol{GX}_I^{\pm\cdot-} + \boldsymbol{GX}_V^{\pm\cdot-} = \left\langle v_x \boldsymbol{\Psi} f_0^{\pm\cdot-} \right\rangle - \textstyle\sum_j \boldsymbol{\Lambda}_j^{\pm\cdot-} \odot \boldsymbol{X}_j \tag{7.83}$$

$$\boldsymbol{GY}^{\cdot\pm-} = \boldsymbol{GY}_I^{\cdot\pm-} + \boldsymbol{GY}_V^{\cdot\pm-} = \left\langle v_y \boldsymbol{\Psi} f_0^{\cdot\pm-} \right\rangle - \textstyle\sum_j \boldsymbol{\Lambda}_j^{\cdot\pm-} \odot \boldsymbol{X}_j \tag{7.84}$$

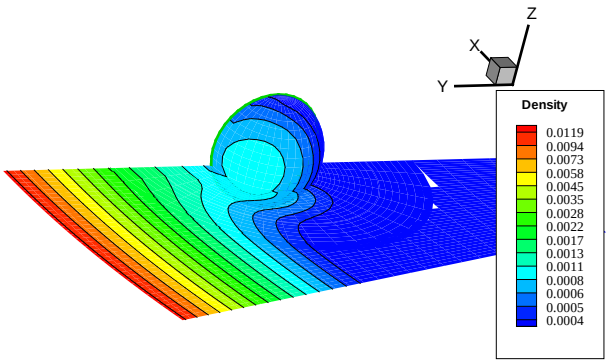

Figure 7.66: Plot of density contour for stationary hemisphere placed a strongly rotating flow field.

$$\boldsymbol{GZ}^{-} = \boldsymbol{GZ}_I^{-} + \boldsymbol{GZ}_V^{-} = \left\langle v_z \boldsymbol{\Psi} f_0^{\cdot\cdot -} \right\rangle - \sum_j \boldsymbol{\Lambda}_j^{\cdot\cdot -} \odot \boldsymbol{X}_j \tag{7.85}$$

Fig. 7.66 and Fig.7.67 shows density and Mach contours. In the three dimensional case due to relieving effect of flow moving out axially the effect of shock is not so severe. Fig. 7.67 also shows that the subsonic pocket is much smaller and the shock is smeared due to coarse distribution of points. In this case SLKNS was used with local time stepping to cut down the computational time. Fig 7.68 shows the plot of residue, Res_2^k based on the average L_2 norm of all the components across the domain at k^{th} iteration as described in section6.3.4 of chapter 6.
The cloud used in the present test case is also used for carrying out multi-objective optimization presented in the next sub-section. The purpose of using a coarse cloud in this test case is to demonstrate the robustness of the SLKNS solver in handling the supersonic region to rarefied non-continuum regions as well as to cut down the computation time for carrying out multi-objective optimization which requires repeated solver runs.

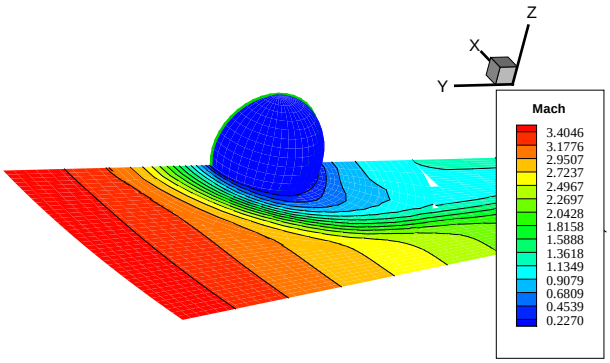

Figure 7.67: Plot of Mach contour

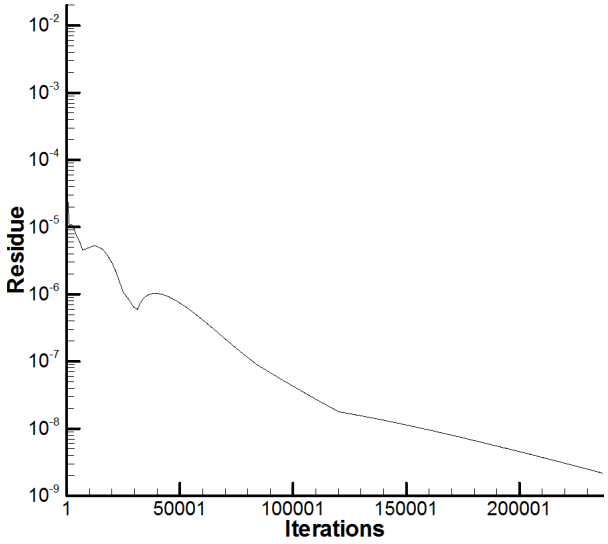

Figure 7.68: Residue plot for stationary hemisphere placed a strongly rotating flow field.

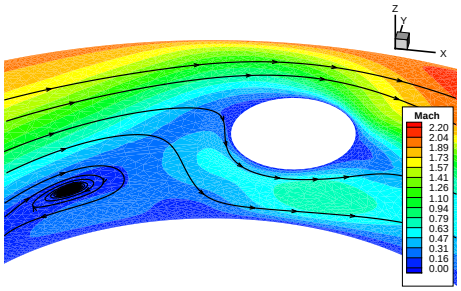

Figure 7.69: Vortex ahead of the cylinder facing strongly rotating flow

7.3.12 Shape optimization of stationary body in a rotating flow

This test case demonstrates the multi-objective optimization capability of the SLKNS solver. As described earlier, Fig 7.69 shows the vortex ahead of the cylindrical body placed in strongly rotating flow of air computed using SLKNS solver. The presence of vortex is due to baroclinic term because of entropy gain as pressure and density are no longer isentropically related. Thus, one may aspire to have an optimum shape which minimizes this baroclinic effect, minimizes the maximum temperature on the body and maximizes the axial mass flux under certain constraints. Consider the same test conditions and geometry as described in previous subsection for a stationary hemisphere in a rotating flow. Let the functions $f_i(\vec{x}) \in Y \subset \mathbb{R}^m$ be the objective functions defining the m-dimensional objective space with its subset $\tilde{Y} \subset Y$ representing the feasible objective region. Similarly, let n-dimensional space $\mathbb{R}^n$ be called the parameter space dependent on the shape parametrization approach. Multi-objective shape optimization of stationary body (initial shape being a hemisphere) in a high speed rotating flow will require repeated grid generation and a solver capable of capturing high speed flow features like shocks, weak secondary flow in the axial direction and in slip flow region. As described earlier only the cloud of points enveloping the object as shown in Figure 7.70 are modified during the course of optimization while the background cloud of points are dynamically flagged or blanked off where body is present. Multiples holes are created in the background cloud. Based on the shape

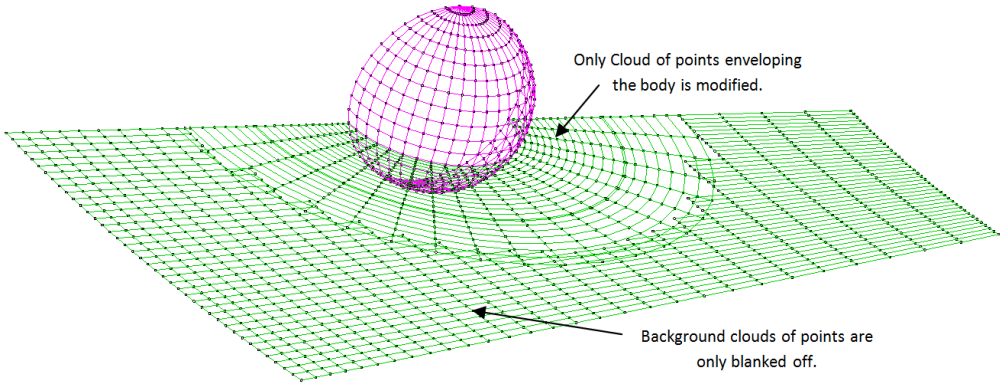

Figure 7.70: Modification of cloud of points around the body to be optimized.

of body suggested by optimization algorithm a hole which can contain the body with a minimum gap is selected from a priori sets of hole. The fluid dynamic data is extrapolated where hole was earlier existing. Figure 7.71 shows the merging of sub-cloud around the body and the background cloud.

7.3.12.1 Shape parametrization and optimization method.

As described earlier there are various parametrization approaches like discrete approach, domain element approach, polynomial and splines based, CAD based, free-form deformation and soft object animation based approach. The shape parametrization approach is problem specific and is of immense importance as it can bring drastic reduction in the computational time. The present study uses shape parametrization based on Fourier descriptors[299] and meshless strategy. The shape parametrization based on Fourier descriptors require smaller parametric space. The spherical coordinate system is used for parametrization of the body. The shape of the body is generated by deforming the sphere of radius r_s with its origin at $(bx_{ref}, by_{ref}, bz_{ref})$ by multiplying its height by a trigonometric function $g_t(\vec{x})$ using $\vec{x} \equiv (x_1, x_2) \in \mathbb{R}^2$ i.e. based on two parameters x_1 and x_2 as follows

$$\begin{aligned} bx_i &= bx_{ref} - \Delta bx_i & &= bx_{ref} - r_s Cos(\theta_i) Cos(\phi_i) \\ by_i &= by_{ref} - \Delta by_i & &= by_{ref} - r_s Cos(\theta_i) Sin(\phi_i) \\ bz_i &= bz_{ref} - \Delta bz_i g_t(\vec{x}) & &= bz_{ref} - r_s Sin(\phi_i) g_t(\vec{x}) \end{aligned} \tag{7.86}$$

where (bx_i, by_i, bz_i) are the Cartesian coordinates of the body and parametric vector trigonometric function $g_t(\vec{x})$ is evaluated based on the value of parameter

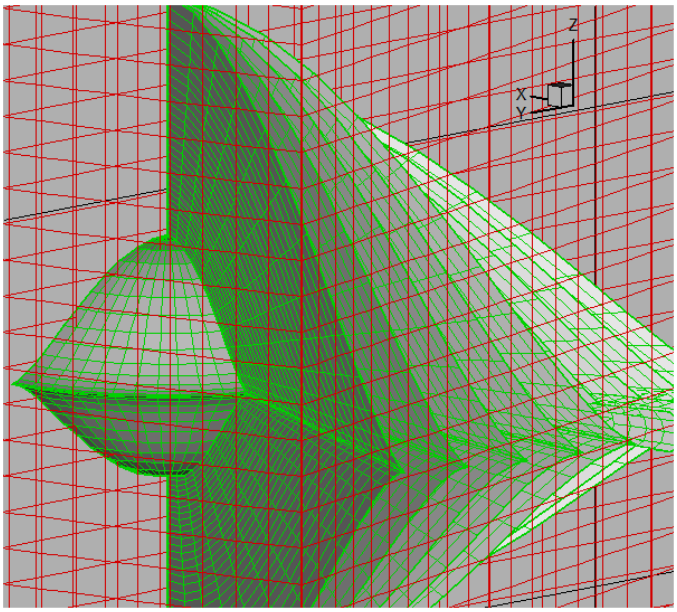

Figure 7.71: Merging of sub-clouds around the body and the background cloud.

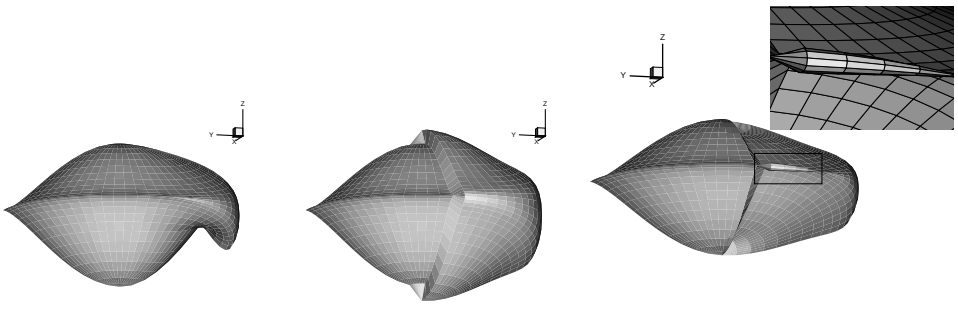

Figure 7.72: Ill-conditioned shapes due to Fourier descriptors.

Δby_i as follows

$$if\ \Delta by_i \begin{cases} < 0 & g_t = Abs\left[\frac{Sin^2(\theta_i)}{2}\right] \\ \geq 0 & g_t = \begin{array}{l} x_1 Abs\left[\frac{Sin^2(\theta_i)}{2} Cos(\phi_i)\right] \\ +x_2 Abs\left[\left(\frac{Sin^2(\theta_i)}{2} - 1\right)(Sin(\theta_i)+1)\right](1 - Cos(\phi_i)) \end{array} \end{cases} \tag{7.87}$$

The parametric space is two dimensional as $\vec{x} \equiv (x_1, x_2) \in \mathbb{R}^2$. The objective function in the present case is also two dimensional as it is based on minimization of maximum value of temperature T_{Max} on the body and minimization of baroclinic term given as follows

$$\begin{aligned} f_1 &= \bar{T}_M = \frac{T_{Max}}{T_{ref}} \\ f_2 &= \bar{\chi} = \frac{\chi_{avg}}{\chi_{ref}} \end{aligned} \tag{7.88}$$

The term $\bar{T}_M$ is made dimensionless based on reference temperature, T_{ref}.The term χ_{ref} is reference baroclinic term and χ_{avg} is baroclinic term averaged over a prescribed plane defined as

$$\chi_{avg} = \frac{1}{S} \int \left(\frac{1}{\rho^2} \nabla\rho \times \nabla p \right) dS \tag{7.89}$$

where S is the surface area of the prescribed plane. Before running the solver the parametric space was further pruned and reduced to avoid ill-conditioned shapes as shown in Fig 7.72. The concept of ϵ-dominance has been taken as the basis for the cooperative multiple objective optimizations.

7.3.12.2 Dynamic evaluation of goal vector

In the present case two non-interacting simplex are used where vertex of each simplex is defined by the vector $\vec{x}$ in the parametric space. At k^{th} iteration we get 3 vertices for simplex r as $r_1^k(\vec{x})$, $r_2^k(\vec{x})$ and $r_3^k(\vec{x})$ and similarly we get 3 vertices for simplex s as $s_1^k(\vec{x})$, $s_2^k(\vec{x})$ and $s_3^k(\vec{x})$. These two simplex are shown in the objective space in Figure 7.73(a) populated with six members given by all the vertices. Figure 7.73(b) shows the non-dominated Pareto ranking based on six members. The present case is a two-dimensional optimization problem with functions $f_1 = \bar{T}_M$ and $f_2 = \bar{\chi}$. The term $(f_i(\vec{x}))^k$ is the minimum of the i^{th}

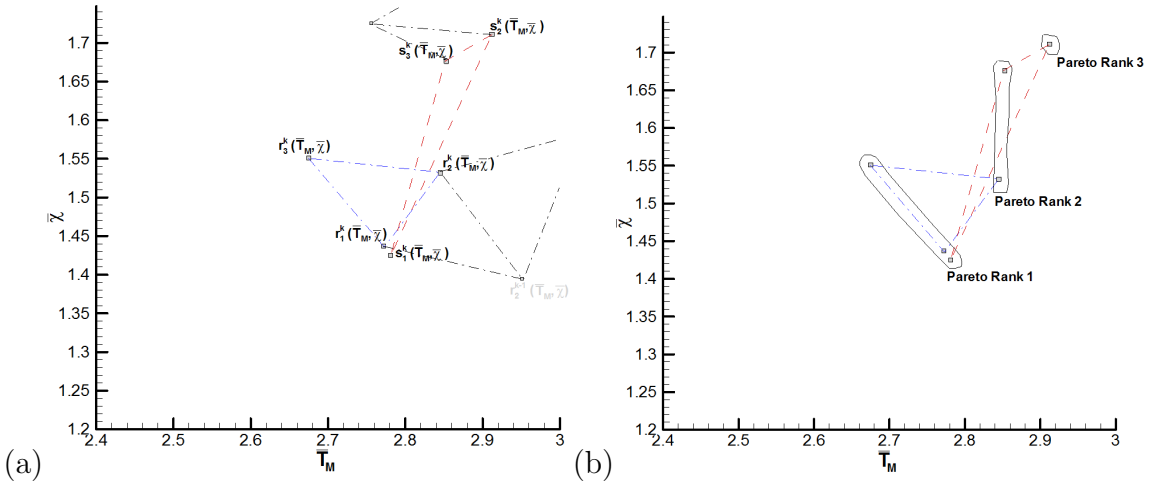

Figure 7.73: Two simplex in the objective space (a)population of 6 vertices, and (b)their non-dominated Pareto ranking.

component amongst all the population i.e. vertices of the participating simplex at k^{th} optimization iteration given as follows

$$(f_i(\vec{x}))^k = \underset{\vec{x}\in\mathbb{R}^n}{min}\{f_i(\vec{x}_{r_1}), f_i(\vec{x}_{r_2}), \cdots, f_i(\vec{x}_{s_1}), f_i(\vec{x}_{s_3})\} \tag{7.90}$$

In this problem we do not have a priori information of minimum or decision maker's definition of goal. In the absence of decision maker we define goal vector as an ideal vector $\vec{q}^*$ made up of individual minimum of each component of a vector obtained during the course of optimization after k evaluations of the problem q_i^* is obtained as follows

$$q_i^* = \underset{\vec{x}\in\mathbb{R}^n}{min}\{(f_i(\vec{x}))^1, \cdots, (f_i(\vec{x}))^k\} \tag{7.91}$$

Figure 7.74(a) shows the evaluation of goal vector q_i^* after k iteration of optimization routine. In this study scalarization step $s : Q\times Y\rightarrow\mathbb{R}^1$ is implemented by weighted L_2-problem as

$$\underset{\vec{x}\in\mathbb{R}^n}{min}\, L_2^{(\vec{f},\vec{w},\vec{q}^*)}(\vec{x}) = \left(\sum_{i=1}^{m} w_i|f_i(\vec{x}) - q_i^*|^2\right)^{1/2} \tag{7.92}$$

where $\vec{q}^*\in Q\subset\mathbb{R}^m$ is the goal vector based on decision makers' overall preferences for trade-off between different objectives. Figure 7.74(b) shows the ϵ-dominance

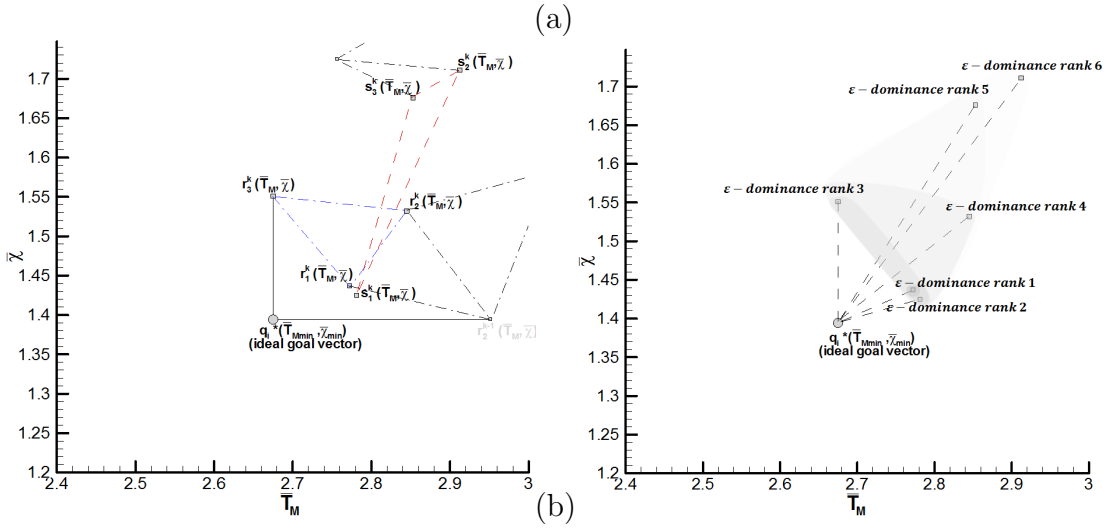

Figure 7.74: Evaluation of (a)goal vector, and (b)ϵ-dominated ranking.

based ranking as compared to non-dominated Pareto ranking based on six members shown in Figure 7.73(b). In this problem L_2 metric is used and each vertex of the simplex gives a score or a scalarized value based on its distance from the goal vector $\bar{q}^*$ evaluated after each optimization iteration. Using this method a multi-objective problem is rendered into a single value. The optimization problems runs till it reaches the maximum number of iterations defined by the user. The vertex which is nearest to the goal vector is taken as the best candidate solution. This new approach of sorting using scalarization proposed in this research is based on ϵ-dominance with L_2 metric strategy described by Figure 7.74(b) and Eq. 7.93

$$\vec{f}^* \prec \vec{f} :\Leftrightarrow \underset{i\in 1,2,\dots m}{\forall}(f_i(\vec{x}^*) \leq f_i(\vec{x}) - \epsilon_i) \wedge \underset{i\in 1,2,\cdots,m}{\exists}(f_i(\vec{x}^*) < f_i(\vec{x}) - \epsilon_i)$$
$$\exists L_2^{(\vec{f},\vec{w},\vec{q}^*)}(\vec{x}) < L_2^{(\vec{f}-\epsilon_i,\vec{w},\vec{q}^*)}(\vec{x}) \;;\; \epsilon_i = \zeta(f_i^{max} - f_i^{min});\; \zeta \in (0,1) \qquad (7.93)$$

ζ is a user defined parameter which determines the ϵ-dominance rank as shown in Figure 7.74(b).

7.3.12.3 Results of optimization

Fig 7.75 shows the evolution of the shapes and generation of cloud of points for the meshless method. In the present study the multi-objective routine with a

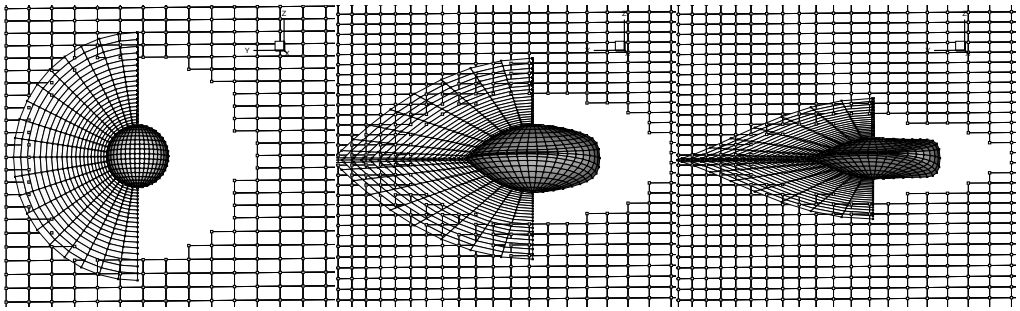

Figure 7.75: Evolving shapes and cloud of points

population of two non-interacting simplex was run for $k = 10$ iterations which required total 42 CFD runs. Fig 7.76 shows the different shapes of the stationary body and its temperature contour. Fig 7.77 and Fig 7.78 shows Mach and axial velocity contours for a typical set of optimal shapes in a strongly rotating field of air. This test case fulfills the prime motivation of the thesis towards the development of a robust meshless method based on kinetic theory that can carry out multi-objective optimization of stationary bodies under strong rotations and rarefied slip flows.

7.4 Summary

The meshless SLKNS solver was verified and validated with a variety of test cases including continuum flows and non-continuum slip flows. Validation test includes comparison with both experimental pressure drop and sets of numerical 2D/3D examples of slip flows in rarefied medium around stationary bodies. It was found that SLKNS works more efficiently for high speed supersonic flows as compared to low speed subsonic flows. The capability of meshless solver SLKNS to resolve slip flow features, supersonic flows and typical features of the strongly rotating flows characterized by steep density gradient and thin boundary layers was demonstrated for stretched distribution of points. *The developed SLKNS numerical solver avoids extremely costly multi-scale simulation as it uses a thermodynamically consistent flux splitting scheme, a unified wall boundary condition which satisfies Onsager's relationship and simulates both continuum and rarefied slip flow within Navier-Stokes equation.* Further, SLKNS was also able to carry out

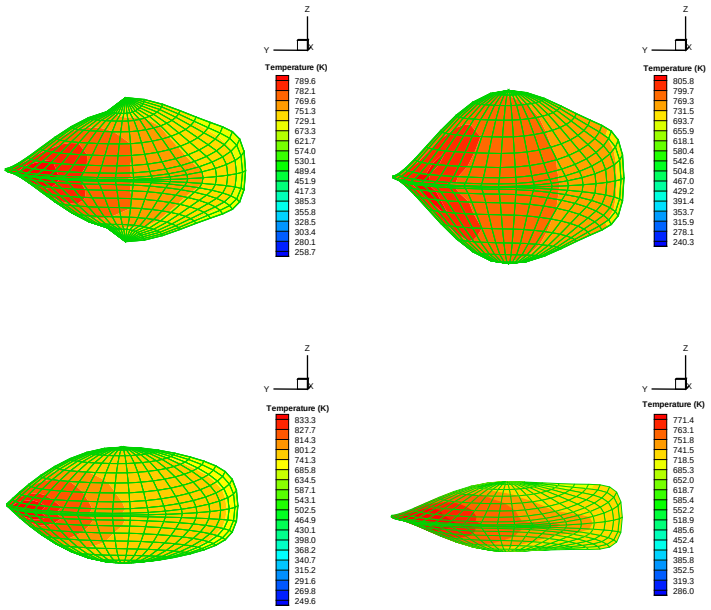

Figure 7.76: Shapes of stationary body and its temperature contour during the course of optimization.

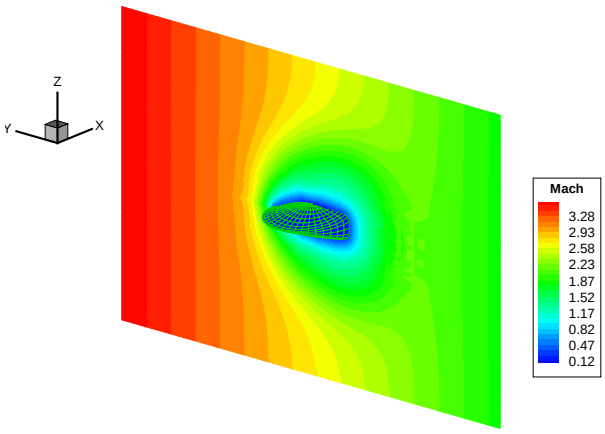

Figure 7.77: Mach contours for an optimal shape.

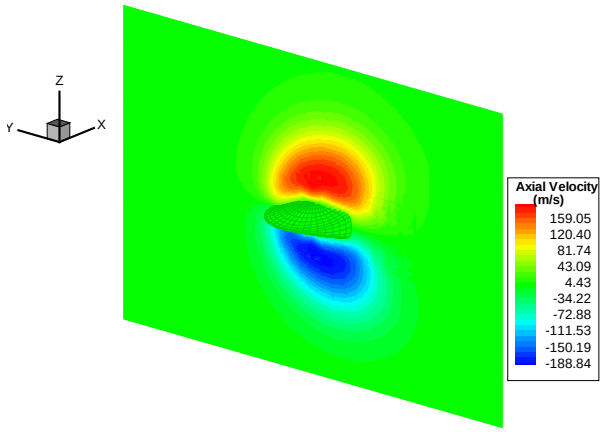

Figure 7.78: Contours of axial velocity for an optimal shape.

multi-objective optimization within meshless framework using non-linear simplex with ϵ-dominance strategy.

Chapter 8

Conclusions

8.1 Contributions and research findings

The primary objective of the thesis is met as slip flow is simulated effectively through kinetic theory route incorporating features of non-equilibrium thermodynamics using meshless method which remains well conditioned near the boundary where highly stretched distribution of points are present. The present investigation involved research in the field of kinetic theory, non-equilibrium thermodynamics, kinetic schemes, meshless methods and optimization approaches. The kinetic upwind scheme was shown to simulate the entire range from rarefied slip flow to continuum flow, and flow with shocks as it is derived using kinetic theory incorporating phenomenological theory of non-equilibrium thermodynamics. The kinetic theory based unified wall boundary condition which satisfies Onsager's relationship was able to simulate both continuum and rarefied slip flow within Navier-Stokes equation avoiding extremely costly multi-scale simulation. SLKNS was also able to resolve weak secondary flow even under strong rotation using kinetic flux vector splitting in its variance reduced form. The meshless solver was able to carry out multi-objective optimization using ϵ-dominance strategy. Research contributions are made in following three fields:

- Kinetic scheme for modelling viscous slip flows.
- Fluid mechanics of slip flow.
- Meshless method.

Salient research findings and fundamental contributions made in these fields are highlighted in the following sections.

8.1.1 Contributions made to kinetic scheme for modelling viscous slip flows

To develop a single monolithic solver which can operate from low speed to hypersonic rarefied slip flow to high speed continuum flow is a challenging task because of two unknown factors, i) the correct amount of dissipation or entropy generation, and ii) distribution of dissipation or entropy generation for each thermodynamic force. Most of the upwind scheme fail to ensure the correct distribution of the entropy generation for each thermodynamic force associated with shear stress tensor and heat flux vector. The kinetic scheme developed in the thesis follows the principle of non-equilibrium thermodynamics and ensures the correct division of entropy generation for each thermodynamic force as the state update moves from one conservation state to another following the path laid down by non-equilibrium thermodynamics. The research work gives a fresh new look to Navier-Stokes equation from the prism of non-equilibrium thermodynamics and kinetic theory. Present research for the first time adds an additional condition based on the concept of correct distribution of entropy or dissipation for any upwind scheme to remain valid across different regimes of flow.

The major contribution of the thesis is in the development of kinetic model, derivation of non-equilibrium distribution and formulation of kinetic scheme which incorporates features of non-equilibrium thermodynamics in the microscopic level and apply discretization at the Boltzmann level. The new upwind scheme for macroscopic conservation equations involves three steps : i) in the first step the Boltzmann equation is rendered into an upwind discretized form using distribution function which complies with phenomenological theory of non-equilibrium thermodynamics , ii) in the second step inviscid fluxes are obtained by taking $\mathbf{\Psi}$ moments of split Maxwellian distribution, iii) in the third step viscous fluxes are obtained by taking moments and full tensor contraction of split microscopic tensors. The research work also presents derivation of gradient based velocity slip, temperature jump and novel kinetic flux vector splitting based wall boundary

condition. Major contributions are listed as follows.

8.1.1.1 Onsager reciprocity principle based new kinetic model

The research findings have revealed that kinetic model should satisfy an additional property i.e. Onsager relation for entropy production. With this new addition, the main properties of the kinetic model can be listed as follows

1. Locality and Galilean invariance
2. Additive invariants of the collision integral
3. Uniqueness of equilibrium
4. Local entropy production inequality
5. Correct transport coefficients in the hydrodynamic limit
6. Positive distribution
7. Onsager relation for entropy production

BGK model is one of the simplest kinetic model and its extension for polyatomic gas is Morse-BGK model. Both the models give incorrect Prandtl number and and fail to comply with the principles on non-equilibrium thermodynamics. One of the fundamental contribution of the thesis is the development of a new non-equilibrium thermodynamics based kinetic model described in section 3.4. The non-equilibrium part of the distribution function is obtained as full tensor contraction of thermodynamic forces and its associated microscopic tensors. Using this Navier-Stokes equation can be derived with correct Prandtl number and kinetic schemes can be formulated which complies with the principles on non-equilibrium thermodynamics.

8.1.1.2 Microscopic tensors and novel concept of macroscopic tensors

Microscopic tensor associated with shear stress tensor and heat flux vector was identified based on derivation of first order distribution. Section 3.3.1 gives the expressions of thermodynamic forces and microscopic tensors associated with polyatomic gas. The thesis also reports a novel method of extracting viscous fluxes by

full tensor contraction of macroscopic tensors and its conjugate thermodynamic forces described in section 3.4.3. The macroscopic tensors are moments of microscopic tensors and follow Onsager's reciprocity principle. They can be used to quantify the contribution of each thermodynamic forces.

8.1.1.3 Kinetic scheme based on microscopic tensor splitting

Successful upwind scheme can be seen as a scheme which not only adds the correct dissipation or entropy but also ensures the correct division for each thermodynamic force as the state update moves from one conservation state to another so as to satisfy thermodynamics. Hence, it is more rational to incorporate features of non-equilibrium thermodynamics in the microscopic level and apply discretization at the Boltzmann level rather than the derived macroscopic variables. The present kinetic scheme proposed in section 4.2 of the thesis achieves this in two ways:

- Embeds non-equilibrium thermodynamics at the microscopic level.
  The distribution function at the microscopic level is written in terms of thermodynamic forces and its conjugate microscopic fluxes. Once the kinetic model is formulated in the Onsager's form at the microscopic level the derived distribution function also complies with the principles on non-equilibrium thermodynamics.

- Upwind discretization in the Boltzmann level.
  Upwind discretization is performed in the Boltzmann level and the upwind scheme for macroscopic conservation equations is obtained in following three steps : i) in the first step the Boltzmann equation is rendered into an upwind discretized form , ii) in the second step inviscid fluxes are obtained by taking $\mathbf{\Psi}$ moments of split Maxwellian distribution, iii) in the third step viscous fluxes are obtained by taking moments and full tensor contraction of split microscopic tensors.

The advantage of the present upwind method is that it does not require construction of the distribution function. The present method only requires split microscopic tensor and its conjugate thermodynamic forces, hence it can be easily be extended for problems with multiple thermodynamic forces i.e. species

transport problem which can be solved by splitting the microscopic tensor associated with it. The thesis presents schemes developed for three dimensional and axi-symmetric geometries and also describes a novel method based on variance reduced form of kinetic flux vector splitting. The final expression and derivations of slip macroscopic tensors and split fluxes are included in Appendix D.

8.1.1.4 Flux based kinetic wall boundary condition

Wall boundary condition is an important part in simulation of fluid flow. No-slip and slip condition at the wall provide a realistic boundary condition used for the solution of Navier-Stokes equation in the continuum and rarefied regime respectively. Another fundamental contribution is the implementation of kinetic flux vector splitting based wall boundary which uses Maxwell model, kinetic theory and incorporates features of linear non-equilibrium thermodynamics. The new boundary condition described in section 5.5 is flux based rather than gradient based boundary condition reported in literature. Present thesis gives the expressions of split wall fluxes derived using the new distribution. The boundary condition for velocity slip and temperature jump was also derived for cases with negligible tangential flow variations and compared with Maxwell velocity slip and von Smoluchowski temperature jump conditions. The flow simulation effectively captures slip flow features under combined effects of adverse pressure gradient and rarefaction. The simulation also captures high speed rotating flow with rarefied slip flow regions.

8.1.1.5 Treatment of Knudsen layer based on collision probability function

Treatment of slip flow near the transition regime requires a second order distribution. The present research work in the thesis has proposed an alternative method described in section 5.6.3 which is based on collision probability function to simulate Knudsen layer. The new proposed method can also be interpreted as an implementation of new kinetic model with varying relaxation time. This new method of simulation was validated with numerical test case described in section 7.3.9.2 and was found promising and easy to implement.

8.1.2 Contributions made to fluid mechanics of slip flow

The present research work was also able to confirm the existence of negligible slip existing in continuum regime as reported by many researchers. The investigation also reveals symmetry breaking in axi-symmetric problems induced due to slip flow. The derivations of wall boundary condition for cases with negligible fluid dynamic variations in tangential direction led to more accurate expressions of Maxwell velocity slip and von Smoluchowski temperature jump.

8.1.2.1 Existence of slip at the wall for continuum flows.

According to continuum theory no-slip condition prevails at the wall as the slip at the wall is exactly zero. On the other hand results of kinetic theory reveals that the velocity slip and temperature jump will always be present even in continuum flow regime. The thesis also explores this fundamental question of existence of no-slip for continuum flows. The numerical test conducted in section 7.3.1.3 using kinetic wall boundary condition for continuum flows confirms the observation reported in literature that temperature jump and velocity slip will be present however, with negligible magnitude for all dissipative walls even in continuum regime.

8.1.2.2 Symmetry breaking due to slip flow

Due to slip the axi-symmetric problems do not remain symmetric. Numerical results described in section 7.3.5 and 7.3.6.4 reveal that temperature contours become wavy and unsymmetrical due to slip phenomenon which produces instability mechanism due to shear rate thinning. This needs further research and investigations to establish the instability mechanism.

8.1.2.3 Improvement over gradient based Maxwell velocity slip and von Smoluchowski temperature jump

The present research work described in section 5.4.1 and 5.4.2 gives new expressions of velocity slip called Onsager-Maxwell velocity slip and new expression for temperature jump called Onsager-von Smoluchowski jump condition derived

using normal half range distribution based on new kinetic model. The new boundary conditions complies with the principles of non-equilibrium thermodynamics and were found to be more accurate than the Maxwell velocity slip and von Smoluchowski jump condition based on numerical test case described in section 7.3.2.

8.1.2.4 Quantification of cross phenomenon due to shear stress tensor and heat flux vector

A new term based on Onsager's reciprocity principle was derived using the viscous split fluxes. This term called as Reciprocity number described in section 7.3.2 gives the contribution of mass flux as well as entropy generation due to thermodynamic forces associated with shear stress tensor and heat flux vector to quantify the cross phenomenon involved in slip flow. This also brings forth the advantage of kinetic scheme over any numerical based scheme as we can have correct term by term description of the contributions made in the slip mass flow in the boundary layer due shear stress tensor and heat flux vector.

8.1.3 Contribution made to meshless method

Most of the meshless methods are either based on radial basis functions (RBFs) or they use least square based approach. Approach based on least squares is more preferred for flow problems with shock. Normal equations as well as QR approach used in least square method produces inaccurate results when applied to stretched distribution of points required to resolve boundary layers of a viscous flow problem. The present approach overcomes the limitations due to the ill-conditioning which is the weakness of normal equations by using a novel concept of stencil splitting. The thesis presents a new approach to solve least square problem by generating a non-symmetric cross-product matrix by suitable selection of sub-stencils such that the matrix is diagonally dominant and well conditioned.

8.1.3.1 Least square based meshless method

The new approach described in section 6.3 was able to solve least square problem by generating a non-symmetric cross-product matrix by suitable selection of sub-stencils such that the matrix is diagonally dominant and well conditioned. The present method like normal equations approach requires $(m + n/3)n^2$ flops and provides stable results for highly stretched distribution of points involving about half the arithmetic for larger connectivity set as compared to QR approach for a full rank least squares problem. The novel Split-stencil Least square Kinetic upwind method for Navier-Stokes (SLKNS) solver makes use of least squares and Kinetic Flux Vector Splitting (KFVS) scheme based on microscopic tensor splitting with kinetic wall boundary condition. SLKNS was found to be capable and accurate for wide range of problems of interest. SLKNS based on Variance Reduction Kinetic Flux Vector Splitting (VRKFVS) was able to resolve weak secondary flow even under strong rotation while simulating the slip flow in the rarefied core.

8.1.3.2 Parallelization of meshless code

Parallelization of SLKNS code described in section 6.5 was carried out using domain decomposition with optimal contention free communication schedule. Graph based on adjacency list built using symmetric connectivity was used to carry out domain decomposition. Cloud sequencing with coarse-medium-fine cloud was used to further accelerate the code.

8.1.3.3 Multi-objective optimization using meshless code

The present solver was able to carry out multi-objective optimization of stationary bodies under strong rotations and rarefied slip flows in a meshless framework which was one of the prime motivations of the thesis. Multi-objective optimization described in section 6.6 was accomplished using a novel approach by i) merging the sub-cloud around body undergoing optimization, ii) shape parametrization based on Fourier descriptors (trigonometric functions), iii) non-linear simplex as an optimization method, and iv) Pareto optimality, ϵ-dominance and reference point approach as a basis for the cooperative multiple objective optimizations.

8.2 Summary of Contributions

The major contributions of the research accomplished in the thesis can be summarized as follows :

- Development of Onsager reciprocity principle based new kinetic model.
- Development of kinetic viscous flux vector splitting based on microscopic tensor splitting
- Concept of macroscopic tensors, derivation of Onsager's reciprocity relationship and its relationship with kinetic flux vector splitting to bring out connection between non-equilibrium thermodynamics and kinetic theory.
- Development of kinetic slip boundary condition using first order non-equilibrium thermodynamics based distribution function and Maxwell specular-diffuse reflection model. Derivation of split macroscopic tensors and split fluxes.
- Correction over existing Maxwell velocity slip and von Smoluchowski temperature jump boundary conditions.
- Development of a new method based on collision probability function to simulate the flow in the Knudsen layer.
- Development of Variance Reduction Kinetic Flux Vector Splitting (VRK-FVS) method to capture weak secondary flow in a strong primary flow field.
- Extending kinetic scheme for axi-symmetric flows.
- Development of least square based meshless solver which gives more stable results compared to normal equations and QR approach, and is considerably faster than QR.
- Parallelization of the meshless code with optimized communication scheduling.
- Development of multi-objective optimization for meshless method based on Pareto optimality, ϵ-dominance and reference point approach.

- Experimental evaluation of tangential momentum accommodation coefficient (TMAC) which takes into account the effect of varying pressure gradient along the test section.

8.3 Future recommendations

Numerical modeling of multi-species, reacting, non-continuum, hypersonic viscous flow with many components is a challenge. The present study can be further extended in future to include coupling non-continuum regions with the DSMC or with direct numerical solution of Boltzmann equation and development of more accurate kinetic model for the Knudsen layer. In the discretization front future potential exists for the development of meshless formulation which possesses conservation properties and at the same time remains well conditioned for highly stretched distribution of points. The ultimate long term aim is to develop SLKNS based hybrid code that can solve a large scale multi-species, reacting, non-continuum, hypersonic viscous flow problem. This task of development of such industrial scale 3-D solver will require following steps :

- Improvement over SLKNS:
  - Extending 5 moments based on $\mathbf{\Psi} = \left[1, \vec{v}, \mathbb{I} + \frac{1}{2}\vec{v}^T\vec{v}\right]^T$ to 13 moment system described by $\mathbf{\Psi} = \left[1, \vec{v}, \mathbb{I} + \frac{1}{2}\vec{v}^T\vec{v}, \vec{v} \otimes \vec{v}, \left(\mathbb{I} + \frac{1}{2}\vec{v}^T\vec{v}\right)\vec{v}\right]^T$ such that evolution of shear stress tensor and heat flux vector are included.
  - Implementation of CLL gas-surface interaction model.
  - Development for more accurate collision probability function to simulate the Knudsen layer.
  - Extending the kinetic scheme for multi-component, reacting gas flows.
  - Development of meshless formulation that possess conservation properties.
  - Extending the kinetic upwind using meshless method for moving bodies.
- Validation with rotating high speed wind tunnel and application to industrial problems

  - Validation of code with ground based rotating test facility.
  - Application to wide variety of industrial problems involving slip flows.
  - Simulating a large size multi-physics problem.

- Development of Hybrid solver based on:
  - Coupling with Direct Monte Carlo Simulation (DSMC) in the non-continuum regions.
  - Coupling with Direct Numerical Solution (DNS) of Boltzmann equation in the non-continuum regions.

Appendix A

Mean free path of the gas

Consider ideal gas under standard ambient temperature and pressure (SATP) condition defined by temperature, T =298.15 K and pressure,p =$10^5 N/m^2$. Ideal gas law relates number of particles, N with pressure, p in volume, V with temperature, T as $pV = Nk_BT$, where k_B is the Boltzmann's constant. The average volume available for one molecule corresponds to cube of side length, l_d also called mean molecular distance expressed as follows

$$l_d = \left(\frac{V}{N}\right)^{\frac{1}{3}} = \left(\frac{k_BT}{P}\right)^{\frac{1}{3}} = 3.45281 \times 10^{-9} m \tag{A.1}$$

Consider a molecule of diameter d moving with velocity v. In time δt the molecule will collide with all the molecules with center in the cylinder of $\pi d^2 v \Delta t$. The mean free path or the average distance traveled by a molecule between successive collision is given by

$$\lambda = \frac{k_BT}{\sqrt{2}\pi d^2 p} \tag{A.2}$$

The effective diameter of a gas molecule depends on the type of gas and is typically between 2×10^{-10} m to 6×10^{-10} m. Thus, mean free path at SATP is therefore given as

$$\lambda = \frac{9.26524 \times 10^{-27}}{d^2} \tag{A.3}$$

For average collision diameter of the air molecule is 3.66×10^{-10} m we get a mean free path of 6.92×10^{-8} m. Table A.1 shows the collision diameters and mean free

Table A.1: Collision diameter and mean free path of common gases [57]

.

Gas	Diameter (m)	Mean free path (m)
Air	3.66×10^{-10}	6.92×10^{-8}
Ar	3.58×10^{-10}	7.23×10^{-8}
CO_2	4.53×10^{-10}	4.51×10^{-8}
H_2	2.71×10^{-10}	1.26×10^{-7}
He	2.15×10^{-10}	2.00×10^{-7}
Kr	4.08×10^{-10}	5.56×10^{-8}
N_2	3.70×10^{-10}	6.76×10^{-8}
NH_3	4.32×10^{-10}	4.96×10^{-8}
Ne	2.54×10^{-10}	1.43×10^{-7}
O_2	3.55×10^{-10}	7.35×10^{-8}
Xe	4.78×10^{-10}	4.05×10^{-8}

paths of different gases [57]. Thus, effective diameter, d of the molecule is one order magnitude less than the mean molecular distance, l_d. In turn mean free path, λ is one or two orders of magnitude larger than the mean particle distance, l_d and two to three orders of magnitude larger than the particle diameter. When λ is much larger than molecule diameter then the gas can be considered as an ideal gas. In such a case mean free path of the gas can be written as

$$\lambda = \mu\sqrt{\frac{\pi}{2\rho p}} \tag{A.4}$$

It should be noted that structure of the molecule might introduce long range electrostatic forces such that the interaction potential makes the interaction diameter, d_i much larger than actual diameter of the molecule and ratio d/λ becomes relevant. One of the example is molecule of water vapor where the dipole structure introduces long range electrostatic forces.

Appendix B

Kinetic Theory and Fluid Flow

The detailed description of the classical gas system consisting of N particles in three dimensions is the Hamiltonian representation, $\mathbb{H}(\vec{x}, \vec{v})$ with $3N$ coordinates and $3N$ momenta. The classical Hamiltonian dynamics can also described in terms of two body potential U as

$$\mathbb{H}(\vec{x}, \vec{v}) = \frac{1}{2} \sum_{i=1}^{N} |v_i|^2 + \sum_{i \neq j} U(x_i - x_j) \tag{B.1}$$

This can also be represented by Liouville equation as

$$\frac{\partial F^{(N)}(\vec{x}, \vec{v}, t)}{\partial t} + \mathbb{L} F^{(N)}(\vec{x}, \vec{v}, t) = 0 \tag{B.2}$$

where $F^{(N)}$ is density with respect to Lebesgue measure of such a system at time t and $\mathbb{L}$ is the Liouville operator given as

$$\mathbb{L} = \sum_{i=1}^{N} \left[\frac{\partial \mathbb{H}(\vec{x}, \vec{v})}{v_i} \frac{\partial}{x_i} - \frac{\partial \mathbb{H}(\vec{x}, \vec{v})}{x_i} \frac{\partial}{v_i} \right] \tag{B.3}$$

The alternative representation using the Gibbs ensemble described by Liouville equation forms the basic statistical equation for conservation of N particle distribution function, $F^{(N)}$ which can be seen as Gibbs measure $(exp(-\beta \mathbb{H}(\vec{x}, \vec{v})))$ of the Hamiltonian $\mathbb{H}(\vec{x}, \vec{v})$ in $6N$ dimensional phase space [234]. BBGKY[1] hi-

[1]BBGKY equations are named after the five authors Bogoliubov, Born, Green, Kirkwood and Yvon who first suggested these equations.

erarchy of equations are obtained after successive integration of the Liouville equation. Each chain in the hierarchy involves reduced distribution function $F^{(H)}$ and higher order distribution function $F^{(H+1)}$. Boltzmanns molecular chaos (Stosszahl Ansatz) assumption gives a closed equation for $F^{(1)}$ by introducing time irreversibility while asserting the absence of correlations between molecules entering a binary collision. In this case the gas system is described by the single particle distribution function governed by Boltzmann equation. It is this aspect of the Boltzmann equation that leads to entropy production. There are kinetic theories which are not based on the BBGKY hierarchy like Prigogine-Balescu's method[220] and Markov's method of random flight [94].

B.1 Boltzmann Equation

The Boltzmann transport equation [41, 45] describes the transient molecular distribution function, $f(\vec{x}, \vec{v}, \mathbb{I}, t) : \mathbb{R}^D \times \mathbb{R}^D \times \mathbb{R}^+ \times \mathbb{R}^+ \rightarrow \mathbb{R}^+$. For a gas in absence of external force and without internal degrees of freedom, the Boltzmann equation is as follows

$$\frac{\partial f}{\partial t} + \vec{a} \cdot \nabla_{\vec{v}} f + \nabla_{\vec{x}} \cdot (\vec{v} f) = J_B(f, f) \tag{B.4}$$

where $\vec{x}$, the position vector, $\vec{a}$ is the acceleration vector and $\vec{v}$ is the velocity vector of molecules given in $\mathbb{R}^D$. The left hand side describes the streaming operation as $\nabla \cdot \vec{v} = 0$, thus it expresses advection of molecules written in conservative form and the right hand side factor $J_B(f, f)$ corresponds to binary collision at the same position $\vec{x}$. While Bogoliubov's generalized form [56] in inertial frame being

$$\frac{\partial f}{\partial t} + \nabla_{\vec{x}} \cdot (\vec{v} f) = J(f, f) + K(f, f, f) + L(f, f, f, f) + \cdots \tag{B.5}$$

where $J(f, f)$ is binary or two particle collision, $K(f, f, f)$ being the ternary or three particle collision and $L(f, f, f, f)$ is quaternary or four particle collision. Here in J, K, L the difference in position between the colliding particles is taken into account. The binary collision integral $J(f, f)$ can be described as

$$J(f, f) = \int_0^{\pi/2} \int_0^{2\pi} \int_{\mathbb{R}^+} \int_{\mathbb{R}^D} \left(f^a f'^a - f f' \right) B(|\vec{v}_a - \vec{v}'_a|, cos(\Theta)) d\vec{v}' \, d\mathbb{I} d\varrho d\Theta \tag{B.6}$$

where $f = f(\vec{x}, \vec{v}, \mathbb{I}, t)$ and $f' = f(\vec{x}, \vec{v}', \mathbb{I}, t)$ are the distribution functions of the

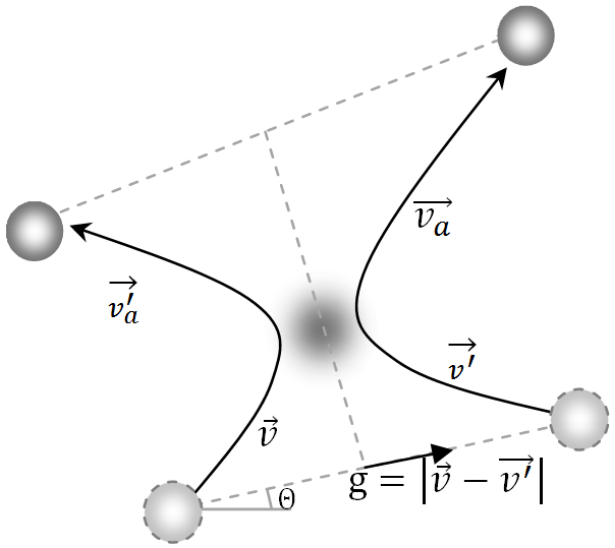

Figure B.1: Binary Collision

molecules before collision and $f^a = f(\vec{x}, \vec{v}_a, \mathbb{I}, t)$ and $f'^a = f(\vec{x}, \vec{v}'_a, \mathbb{I}, t)$ are the distribution functions of the molecules after collision. Also, $g = \left|\vec{v} - \vec{v'}\right|$ is the magnitude of the relative velocity of the particles before collision relative to path of the centre of gravity of the system consisting of two particles as illustrated in Figure B.1. Integration with respect to ϱ goes from 0 to 2π, while angle Θ varies from 0 (head-on collisions) to $\pi/2$ (grazing collisions). The term $B(|\vec{v}_a - \vec{v}'_a|, cos(\Theta))$ is the un-normalized probability density of a relative deflection equal to $\pi - 2\Theta$ for a pair of molecules having a relative speed of g. This can also be expressed as

$$B(|\vec{v}_a - \vec{v}'_a|, cos(\Theta)) = gr\frac{\partial r}{\partial \Theta} \tag{B.7}$$

where r is the impact parameter which can be interpreted as the distance of closest approach of the two molecules had they continued their motion without interaction [45]. The pre-collision velocities can be calculated using the post-collision velocities $\vec{v}_a$, $\vec{v}'_a$ and relative velocity g as follows

$$\begin{aligned} \vec{v} &= \tfrac{1}{2}(\vec{v}_a + \vec{v}'_a + |\vec{v}_a - \vec{v}'_a|g) \\ \vec{v}' &= \tfrac{1}{2}(\vec{v}_a + \vec{v}'_a - |\vec{v}_a - \vec{v}'_a|g) \end{aligned} \tag{B.8}$$

Angle Θ is the angle between $\vec{v}_a - \vec{v}_a^{'}$ and $\vec{v} - \vec{v}^{'}$ expressed as

$$\Theta = cos^{-1}\left(\frac{g(\vec{v}_a - \vec{v}_a^{'})}{|\vec{v}_a - \vec{v}_a^{'}|}\right) \tag{B.9}$$

Consider molecules as rigid sphere of radius r_h such that two body potential $U = 0$ for $r \geq r_h$ and $U = \infty$ for $r < r_h$, the factor $B(|\vec{v}_a - \vec{v}_a^{'}|, cos(\Theta))$ for this hard interaction is given as

$$B(|\vec{v}_a - \vec{v}_a^{'}|, cos(\Theta)) = gr_h^2 cos(\Theta) sin(\Theta) \tag{B.10}$$

It can be seen that even for simple two body potentials like inverse power potentials ($U(r) = kr^{-(n-1)}, n =\neq 2, 3$) the term $B(|\vec{v}_a - \vec{v}_a^{'}|, cos(\Theta))$ cannot be described in terms of elementary functions. With power-law potentials $U(r) = kr^{-(n-1)}$, $n > 3$ the un-normalized probability density of relative deflection $B(|\vec{v}_a - \vec{v}_a^{'}|, cos(\Theta))$ is proportional to fractional power of relative speed of g [45] as follows

$$B(|\vec{v}_a - \vec{v}_a^{'}|, cos(\Theta)) \propto g^{\frac{n-5}{n-1}} \tag{B.11}$$

when $n = 5$ the un-normalized probability density of relative deflection $B(|\vec{v}_a - \vec{v}_a^{'}|, cos(\Theta))$ is no longer a function of relative velocity g. This simplification was discovered by Maxwell and fictitious molecules interacting in this fashion are called Maxwell molecules. The probability density of relative deflection for different interacting molecules are

- Maxwell molecules : $B(|\vec{v}_a - \vec{v}_a^{'}|, cos(\Theta)) =$ constant.
- Hard Sphere (HS) molecules : $B(|\vec{v}_a - \vec{v}_a^{'}|, cos(\Theta)) =$ constant $|\vec{v}_a - \vec{v}_a^{'}|$.
- Variable Hard Sphere (VHS) molecules : $B(|\vec{v}_a - \vec{v}_a^{'}|, cos(\Theta)) =$ constant$|\vec{v}_a - \vec{v}_a^{'}|^{\alpha}$.

The binary collision integral $J(f, f)$ can also be described as

$$J(f,f) = \int_0^{\pi/2} \int_0^{2\pi} \int_{\mathbb{R}^+} \int_{\mathbb{R}^D} \left(f^a f'^a - f f'\right) g \, \bar{\Pi} \, d\vec{v}^{'} \, d\mathbb{I} d\varrho d\Theta \tag{B.12}$$

$\bar{\Pi}$ is the molecular collision cross section, for hard sphere $\bar{\Pi} = d^2/4$, where d is diameter of the hard sphere with $\bar{\Pi} \propto 1/g$. HS model predicts transport coefficients which are proportional to square root of temperature i.e. $T^{0.5}$ while

real gases vary as $T^{0.7}$. With better collision model like Variable Hard Sphere (VHS) model in which $\bar{\Pi} \propto g^{-\alpha}$ for a constant $\alpha > 0$ more realistic prediction of transport properties can be made. This binary collision integral vanishes in the Euler limit when the distribution becomes a Maxwellian, f_0.

B.1.1 The Grad-Boltzmann Limit

Boltzmann equation has been formulated for hard sphere molecules undergoing binary collision at same position $\vec{x}$. The mathematical condition is given by the Grad-Boltzmann limit. This is defined as a limit when number of particles $n(\vec{x}, t)$ tends to infinity, the diameter of the hard sphere d tends to zero, the volume occupied by the particles, $n(\vec{x}, t)d^3$ tends to zero while total cross-section, $n(\vec{x}, t)d^2$ remains constant. Thus the rarefied regime can be characterized by the mean free path which remains constant even though the volume occupied by the particles approaches zero.

B.1.2 Molecular Chaos

The Boltzmann's molecular chaos ("*Stosszahl Ansatz*") assumption introduces time irreversibility and asserts the absence of correlations between molecules entering a binary collision. It is this aspect of the Boltzmann equation that leads to entropy production.

B.1.3 Moments and extended thermodynamics

Levermore [149] proposed a procedure that generates hierarchy of closed systems of moment equations. The Levermore closure procedure ensures every member of the hierarchy is symmetric hyperbolic with an entropy, and formally recovers to Euler limit. Consider finite dimensional linear subspace Ξ of functions of $\vec{v}$ satisfying the following conditions :

$$\left.\begin{array}{ll} \text{(I)} & \Psi \equiv span\{1, \vec{v}, \vec{v}^T\vec{v}\} \subset \Xi \\ \text{(II)} & \Xi \quad \text{follows Galilean invariance} \\ \text{(III)} & \Xi_c \equiv \{\bar{z} \in \Xi : \langle \exp(\bar{z}(\vec{v}))\rangle < +\infty\} \end{array}\right\} \tag{B.13}$$

Examples of such admissible subspace with maximal degree two and four are

$$\left.\begin{aligned}\Xi &= span\{1, \vec{v}, \vec{v}^T\vec{v}\}\\ \Xi &= span\{1, \vec{v}, \vec{v}\otimes\vec{v}\}\end{aligned}\right\}\text{maximal degree} = 2$$
$$\left.\begin{aligned}\Xi &= span\{1, \vec{v}, \vec{v}\otimes\vec{v}, \vec{v}(\vec{v}^T\vec{v}), (\vec{v}^T\vec{v})(\vec{v}^T\vec{v})\}\\ \Xi &= span\{1, \vec{v}, \vec{v}\otimes\vec{v}, \vec{v}\otimes\vec{v}\otimes\vec{v}, (\vec{v}^T\vec{v})(\vec{v}^T\vec{v})\}\\ \Xi &= span\{1, \vec{v}, \vec{v}\otimes\vec{v}, \vec{v}\otimes\vec{v}\otimes\vec{v}, \vec{v}(\vec{v}^T\vec{v})\otimes\vec{v}\}\\ \Xi &= span\{1, \vec{v}, \vec{v}\otimes\vec{v}, \vec{v}\otimes\vec{v}\otimes\vec{v}, \vec{v}\otimes\vec{v}\otimes\vec{v}\otimes\vec{v}\}\end{aligned}\right\}\text{maximal degree} = 4 \tag{B.14}$$

Thus there can be 5, 10, 14, 21, 26 and 35 equations with entropy based closures using Levermore procedure [119, 151]. Closure based on Maxwellian (equilibrium solution) distribution will give us 13 and 20 moment equations. In the kinetic theory moments of the phase density define the macroscopic thermodynamic quantities. Using moment vector function defined as $\mathbf{\Psi}=\left[1, \vec{v}, \mathbb{I}+\frac{1}{2}\vec{v}^T\vec{v}\right]^T$ the moments of the Boltzmann equation are as follows :

$$[\rho, \rho\vec{u}, \rho E]^T = \langle \mathbf{\Psi}, f\rangle \equiv \int_{\mathbb{R}^+}\int_{\mathbb{R}^D} \Psi f(\vec{x}, \vec{v}, \mathbb{I}, t) d\vec{v} d\mathbb{I} \tag{B.15}$$

Thus we can define j^{th} component of the macroscopic thermodynamic quantity $\overline{\Psi}_{k_1k_2k_3\cdots k_j}(\vec{x}, t)$ based on the j^{th} component of the vector of collision invariant , Ψ as follows

$$\overline{\Psi}_{k_1k_2k_3\cdots k_j}(\vec{x}, t) = \int_{\mathbb{R}^+}\int_{\mathbb{R}^D} \Psi_{k_1k_2k_3\cdots k_j}(\vec{v}, I, t) f(\vec{x}, \vec{v}, \mathbb{I}, t) d\vec{v} d\mathbb{I} \tag{B.16}$$

The moments of the Boltzmann equation satisfy an infinite hierarchy of balance laws expressed as follows :

$$\begin{aligned}
&\partial_t\overline{\Psi} + \partial_i\overline{\Psi}_i = 0,\\
&\quad\swarrow\\
&\partial_t\overline{\Psi}_{k_1} + \partial_i\overline{\Psi}_{ik_1} = 0,\\
&\quad\swarrow\\
&\partial_t\overline{\Psi}_{k_1k_2} + \partial_i\overline{\Psi}_{ik_1k_2} = P_{k_1k_2},\\
&\quad\swarrow\\
&\partial_t\overline{\Psi}_{k_1k_2k_3} + \partial_i\overline{\Psi}_{ik_1k_2k_3} = P_{k_1k_2k_3},\\
&\quad\swarrow\\
&\vdots\\
&\partial_t\overline{\Psi}_{k_1k_2k_3\cdots k_n} + \partial_i\overline{\Psi}_{ik_1k_2k_3\cdots k_n} = P_{k_1k_2k_3\cdots k_n},\\
&\vdots
\end{aligned} \tag{B.17}$$

From the continuum mechanics perspective the flux in an equation becomes the density in the next one, as there can be infinite moments. Thus, there is a problem of the closure when we cut this hierarchy at the density with tensor of rank n as its flux and production term will require its balance as they become density in the next hierarchical step. According to the idea of rational extended thermodynamics Müller and Ruggeri [196] have treated this truncated system as a phenomenological system of continuum mechanics governed by universal principle of entropy, objectivity, causality and stability (convexity of entropy). The differential system is hyperbolic and classical constitutive equations are approximation of balance laws when relaxation times are negligible. (This avoids the *heat paradox*[1] observed in the classical theory.) The diffusion equation and the Navier-Stokes equation are valid only when particles have suffered many collisions and their distribution has relaxed to have weak spatial gradients and slow temporal variations. However, there are physical situations where gradients are large on the scale of a collisional mean free path or temporal changes are rapid relative to the mean collision time. Examples include radiation hydrodynamics in optically thin media (Levermore and Pomraning [150]), viscous angular momentum transport in boundary layers of accretion disks (Popham & Narayan [216]) and electron heat transport in laser produced plasma (Max [183]). It should be noted that Navier-Stokes equations do not have equations for evolution of shear stress and heat flux vectors as compared to 13-moments Grad system [102]. When relaxation time for evolution of shear stress and heat flux are negligible then 13-moments Grad system reduces to classical Navier-Stokes as illustrated by extended thermodynamics. Fig. B.2 shows various hierarchies of equations due to Knudsen number expansion and number of moments compiled from Struchtrup [264].

[1] The parabolic nature of heat equation in classical theory implies an infinite speed of propagation of disturbance in temperature. This paradox is similar to paradox of diffusion and shear waves.

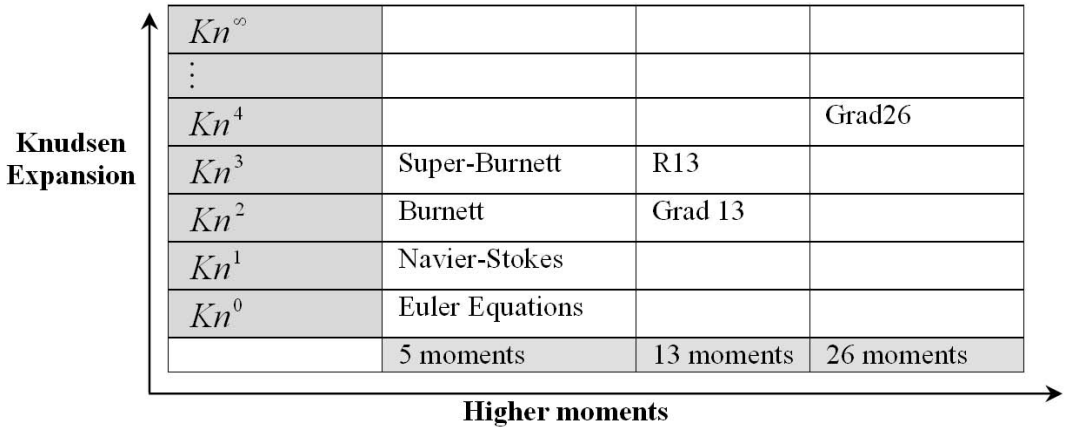

Figure B.2: Hierarchy of equations due to Knudsen number expansion and number of moments for Maxwell molecule. ([264])

B.2 Boltzmann equation and the Collision operator

The collision redistributes the particles in the space leading to a change in the local fluid dynamic field. This term contains irreversibility of the kinetic description, entropy production, etc. The collision integral preserves some of the basic properties of the Boltzmann equation.

B.2.1 Locality and Galilean invariance

The molecules considered in the Boltzmann equation are point particles whose interaction is governed by the finite range intermolecular forces. Hence collision term is local in the position space and non-local in the velocity space. Since the Boltzmann equation is invariant under Galilean transformation hence the collision term $J(f, f)$ depends only on peculiar velocity $\vec{c} = \vec{v} - \vec{u}$. This property is important from numerical simulation of the collision term.

B.2.2 Additive invariants of the collision

This property represents conservation of number of particles, the three components of particles momentum and its energy due to collision. Mathematically it can be represented as

$$\int_{\mathbb{R}^+}\int_{\mathbb{R}^D} J(f,f)\mathbf{\Psi} d\vec{v}d\mathbb{I} = 0 \tag{B.18}$$

Thus, the local fluid dynamics field redistributes as a consequence of the collision.

B.2.3 Uniqueness of equilibrium

The zero point of collision integral given as

$$J(f,f) = 0 \tag{B.19}$$

implies detailed balance condition as

$$f(\vec{x},\vec{v},\mathbb{I},t)f^{'}(\vec{x},\vec{v}^{'},\mathbb{I},t) = f_a(\vec{x},\vec{v_a},\mathbb{I},t)f_a^{'}(\vec{x},\vec{v}_a^{'},\mathbb{I},t) \tag{B.20}$$

Chapman-Enskog method like many other perturbative schemes for solving the Boltzmann equation use this condition of detailed balance as the lowest order of approximation to the distribution function.

B.2.4 Local entropy production inequality and Boltzmann H-theorem

Taking moments of the Boltzmann equation with function $\Psi_e = -Rlnf$ we obtain the density of entropy, ρ_s and its flux, $\vec{j}_s$ given as

$$\rho_s = \int_{\mathbb{R}^+}\int_{\mathbb{R}^D} (-Rflnf)d\vec{v}d\mathbb{I} = -k_B H \tag{B.21}$$

$$\vec{j}_s = \int_{\mathbb{R}^+}\int_{\mathbb{R}^D} (-Rflnf)\vec{v}d\vec{v}d\mathbb{I} \tag{B.22}$$

Thus, we get the Boltzmann H-theorem

$$\frac{\partial \rho_s}{\partial t} + \nabla_{\vec{x}}\cdot(\vec{j}_s) = \sigma(\vec{v},t) \geq 0 \tag{B.23}$$

The rate of change of entropy equals the non-negative entropy production. For certain boundary condition such as specular reflection or flow condition at infinity the flux of entropy density $\vec{j}_s$ gives no contribution. Local entropy production due to the collision term can be written as

$$\sigma(\vec{v},t) = -R\int_{\mathbb{R}^+}\int_{\mathbb{R}^D} lnfJ(f,f)d\vec{v}d\mathbb{I} \geq 0 \tag{B.24}$$

where R is the specific gas constant. It follows from the Boltzmann equation that entropy production is linked to the collision term. Collisions between the molecules in the non-equilibrium state leads to entropy production. Thus local production inequality describes the relaxation of the distribution function towards the equilibrium distribution given by local Maxwellian. It should be noted that when the distribution function f is expressed in terms of number density as $\breve{f}$, in that case the density of entropy, ρ_s and its flux, $\vec{j}_s$ are given as

$$\rho_s = \int_{\mathbb{R}^+}\int_{\mathbb{R}^D} (-k_B\breve{f}ln\breve{f})d\vec{v}d\mathbb{I} = -k_BH \tag{B.25}$$

$$\vec{j}_s = \int_{\mathbb{R}^+}\int_{\mathbb{R}^D} (-k_B\breve{f}ln\breve{f})\vec{v}d\vec{v}d\mathbb{I} \tag{B.26}$$

as moment $\Psi_e = -k_Bln\breve{f}$, local entropy production due to the collision term can be written as

$$\sigma(\vec{v},t) = -k_B\int_{\mathbb{R}^+}\int_{\mathbb{R}^D} ln\breve{f}J(\breve{f},\breve{f})d\vec{v}d\mathbb{I} \geq 0 \tag{B.27}$$

where k_B is the Boltzmann's constant.

B.2.5 Correct transport coefficients in the hydrodynamic limit

In the hydrodynamic limit the collision operator should generate correct transport coefficients such as viscosity, μ and thermal conductivity, κ and Prandtl number, Pr.

B.2.6 Positive distribution

The local H-function is independent of spatial position as it can be cast as follows

$$\frac{dH}{dt} = -\frac{\sigma(\vec{v},t)}{R} = \int_{\mathbb{R}^+}\int_{\mathbb{R}^D} lnfJ(f,f)d\vec{v}d\mathbb{I} \tag{B.28}$$

The H-function decays monotonically along the solution such that Boltzmann equation leads towards the unique global Maxwellian. The H-function of the kinetic model should decay monotonically such that Boltzmann equation gives positive distribution leading towards the unique equilibrium solution.

B.3 Quasi-Gas-Dynamics (QGD) and hydrodynamic theory of Brenner

Consider coordinate system C^* moving relative to another inertial coordinate system C with constant speed U. Then the coordinates of a material point x^* and time t^* in C^* can be expressed as *Galileo transforms* with respect to coordinate x and t in the coordinate system C as

$$x^* = x - U(t - t_0) \tag{B.29}$$

$$t^* = t \tag{B.30}$$

At an instant t_0, both systems coincide i.e. equations of motion in theses systems are invariant. Invariance of hydrodynamic equations can be ascertained by the change in the macroscopic parameters - the density ρ, the velocity u and temperature T when passing from coordinate C to C^*. The instant spatial averages can be expressed as

$$\rho_s^* = \rho_s, \quad u_s^* = u_s - U, \quad T_s^* = T_s \tag{B.31}$$

Thus invariance of Navier-Stokes equations constructed using spatial averages as shown in Equation B.31 is verified. For spatial-time averages, the volume ΔV in the fixed coordinate system differs from the volume ΔV^* in the moving coordinate system. The instant spatial-time averages can be expressed as

$$\rho_{st}^* \approx \rho_{st}, \quad u_{st}^* \approx u_{st} - U, \quad T_{st}^* \approx T_{st} \tag{B.32}$$

The invariance of instant spatial-time averages of density, velocity and temperature with respect to Galileo transform is violated in this case. Galileo transformation does not hold for the gas-dynamic equations based on spatial-time averages. For example consider continuity equation

$$\frac{\partial \rho}{\partial t} + \frac{\partial j_m}{\partial x} = \frac{\partial \rho}{\partial t} + \frac{\partial \rho u}{\partial x} = 0 \tag{B.33}$$

where j_m is the mass flux density. The Galileo transform holds for the equation of continuity as well as the spatial averages as

$$\frac{\partial \rho_s(x,t)}{\partial t} + \frac{\partial \rho_s(x,t) u_s(x,t)}{\partial x} = 0 \tag{B.34}$$

In terms of spatial-time averages, the continuity equation can be written as

$$\frac{1}{\Delta t}\int_t^{t+\Delta t} \frac{\partial \rho_s(x,t^{'})}{\partial t} = -\frac{1}{\Delta t}\int_t^{t+\Delta t} div\left(\rho_s(x,t^{'})u_s(x,t^{'})\right) dt^{'} \tag{B.35}$$

This is simplified as

$$\begin{array}{ll} \frac{\partial \rho_{st}(x,t^{'})}{\partial t} & = -div\left(\frac{1}{\Delta t}\int_t^{t+\Delta t} \rho_s(x,t^{'})u_s(x,t^{'})dt^{'}\right) \\ & \neq -div\left(\rho_{st}(x,t^{'})u_{st}(x,t^{'})\right) \end{array} \tag{B.36}$$

This inequality is due to

$$\int_t^{t+\Delta t} \rho_s(x,t^{'})u_s(x,t^{'})dt^{'} \neq \int_t^{t+\Delta t} \rho_s(x,t^{'})dt^{'}\int_t^{t+\Delta t} u_s(x,t^{'})dt^{'} \tag{B.37}$$

For spatial-time averages, the mass flux density may not be same as momentum of the volume unit as even for small time Δt, the instant value of density and momentum change. Thus Galileo transform does not hold for the gas-dynamic equations based on spatial-time averages. Quasi-gas-dynamics (QGD) [81] and Quasi-hydrodynamic [248] approach uses the time-spatial averaging procedure for the definition of the main gas dynamic quantities: density, velocity, and temperature as compared to spatial averaging used in conventional Navier-Stokes theory. For example QGD introduces of small velocity w in the expression of mass flux such that time-spatial averages are invariant under Galileo transform. In QGD the mass flux density is calculated as

$$j_m = \rho(u - w) \tag{B.38}$$

where

$$w = \frac{t_s}{\rho}\left[div(\rho u \otimes u) + \nabla p - \rho F\right] \tag{B.39}$$

where t_s is the additional parameter related to averaging (smoothing) in time and F is the mass density of exterior forces. This is similar to modification in hydrodynamic theory proposed by Brenner [38] by introducing a new mass diffusion contribution to the continuity equation. The equations were formalized by Ottinger [208] by providing thermodynamical basis. Greenshields and Reese [103] investigated monoatomic gas shocks and found that results with Brenner's modifications are significantly better than those of the standard Navier-Stokes equations.

B.4 Grad moment method

The method projects the Boltzmann equation onto Hermite basis i.e. we seek solution of mass, momentum and energy conservation equation by expanding the distribution function $f(\vec{x}, \vec{v}, t)$ in Hermite or Gram-Charlier polynomials. The unique feature of Hermite ortho-normal polynomials forming the expansion basis is that its expansion coefficients correspond to the velocity moments. The distribution function represented in terms of Hermite polynomials is

$$f(\vec{x}, \vec{v}, t) = \omega(\vec{v}) \sum_{n=0}^{\infty} \frac{1}{n!} \mathbf{a}^{(n)} \mathbb{H}^{(n)}(\vec{v}) \tag{B.40}$$

where both $\mathbf{a}^{(n)}$ and $\mathbb{H}^{(n)}$ are rank-n tensors. In a D-dimensional Cartesian coordinates the weight function associated with the Hermite polynomial is

$$\omega(\vec{v}) = \frac{1}{(2\pi)^{D/2}} exp(-\vec{v}.\vec{v}) \tag{B.41}$$

The nth order Hermite polynomial which is also nth rank symmetric tensor is defined as

$$\mathbb{H}^{(n)}(\vec{v}) = \frac{(-1)^n}{\omega(\vec{v})} \nabla^n \omega(\vec{v}) \tag{B.42}$$

The first few polynomials are

$$\begin{aligned}
\mathbb{H}^{(0)}(\vec{v}) &= 1 \\
\mathbb{H}^{(1)}_i(\vec{v}) &= v_i \\
\mathbb{H}^{(2)}_{ij}(\vec{v}) &= v_i v_j - \delta_{ij} \\
\mathbb{H}^{(3)}_{ijk}(\vec{v}) &= v_i v_j v_k - v_i\delta_{jk} - v_j\delta_{ik} - v_k\delta_{ij}
\end{aligned} \tag{B.43}$$

The expansion coefficients are linear combinations of the velocity moments of f as follows

$$\begin{aligned}
\mathbf{a}^{(0)} &= \int f d\vec{v} = \rho \\
\mathbf{a}^{(1)} &= \int f \vec{v} d\vec{v} = \rho\vec{u} \\
\mathbf{a}^{(2)} &= \int f(\vec{v}^2 - \delta) d\vec{v} = \mathbf{P} + \rho(\vec{u}^2 - \delta) \\
\mathbf{a}^{(3)} &= \int f(\vec{v}^3 - \vec{v}\delta) d\vec{v} = \vec{q} + \vec{u}\mathbf{a}^{(2)} - (D-1)\rho\vec{u}^3
\end{aligned} \tag{B.44}$$

Here the product of two tensors is sum of all possible permutations of tensor product. Thus the state variables $[\rho, \vec{u}, T]^T$, the momentum flux tensor $\mathbf{P}$ or its traceless part the stress tensor σ and the heat flux vector $\vec{q}$ can be completely determined by the first four Hermite expansion coefficients.

$$\begin{aligned}
\rho &= \mathbf{a}^{(0)} \\
\rho\vec{u} &= \mathbf{a}^{(1)} \\
\mathbf{P} &= \mathbf{a}^{(2)} - \rho(\vec{u}^2 - \delta) \\
\vec{q} &= \mathbf{a}^{(3)} - \vec{u}\mathbf{a}^{(2)} + (D-1)\rho\vec{u}^3
\end{aligned} \tag{B.45}$$

Thus, Nth order distribution function can be approximated by its projection onto a Hilbert subspace spanned by the first N Hermite polynomials

$$f(\vec{x}, \vec{v}, t) \approx f^N(\vec{x}, \vec{v}, t) = \omega(\vec{v}) \sum_{n=0}^{N} \frac{1}{n!} \mathbf{a}^{(n)} \mathbb{H}^{(n)}(\vec{v}) \tag{B.46}$$

B.5 Closure coefficients for second order Chapman-Enskog distribution

Evaluation shows that $< \mathbf{\Psi}, \mathrm{Kn}^2 \bar{f}_2 > \neq 0$ so we require additional moment closure terms thus making the determination of f_2 non-unique [22]. The complete second order can be evaluated in terms of moment closure coefficients $\vartheta_{\tau,k}$ and $\vartheta_{q,k}$ as

$$f_2 \;\; = f_0 + \mathrm{Kn}\bar{f}_1 - \mathrm{Kn}t_R \left[\tfrac{D\bar{f}_1}{Dt} + \tfrac{\partial f_0 \tilde{\xi}_1}{\partial x} \right] \tag{B.47}$$

Table B.1: Closure coefficients

$\vartheta_{\tau,1}$	$\vartheta_{\tau,2}$	$\vartheta_{\tau,3}$	$\vartheta_{q,1}$	$\vartheta_{q,2}$	$\vartheta_{q,3}$
3	3	1	1	$\frac{1}{5}\left(\frac{3\gamma-5}{\gamma-1}\right)$	$-\frac{1}{3}\left(\frac{3-\gamma}{\gamma-1}\right)$
3	3	1	$-3\left(\frac{\gamma-1}{3-\gamma}\right)$	$-\frac{3}{5}\left(\frac{3\gamma-5}{3-\gamma}\right)$	1
1	1	3	1	$\frac{1}{5}\left(\frac{3\gamma-5}{\gamma-1}\right)$	$-\frac{1}{3}\left(\frac{3-\gamma}{\gamma-1}\right)$
1	1	3	$-3\left(\frac{\gamma-1}{3-\gamma}\right)$	$-\frac{3}{5}\left(\frac{3\gamma-5}{3-\gamma}\right)$	1

$$\tilde{\xi}_1 = -\frac{1}{\mathrm{Kn}}\left(\frac{\tilde{\xi}_\tau}{p}\tau + \frac{\tilde{\xi}_q}{p}q\right) \tag{B.48}$$

$$\tilde{\xi}_\tau = \left(\frac{3\gamma-5}{2(3-\gamma)}\vartheta_{\tau,1} - \frac{\mathbb{I}}{\mathbb{I}_o^2}\frac{1}{4\beta}\vartheta_{\tau,2} + \beta c_x^2\vartheta_{\tau,3}\right) \tag{B.49}$$

$$\tilde{\xi}_q = 2\beta\left(\frac{\gamma-1}{\gamma}\right)\left(-\frac{\mathbb{I}}{\mathbb{I}_o}c_x\vartheta_{q,1} + \frac{5}{2}c_x\vartheta_{q,2} - \beta c_x^3\vartheta_{q,3}\right) \tag{B.50}$$

where closure coefficients $\vartheta_{\tau,k}$ and $\vartheta_{q,k}\forall\ \mathrm{k} = 1,2,3$ differ from the closure coefficients given by Balakrishnan [22]. Table B.1 shows the closure coefficients. It should be noted that Burnett equations are embedded within Grad's 13 moment method [102] and can easily be extracted using Chapman-Enskog theory. Another alternative to extract Burnett equations from moment systems is Maxwellian iteration of Ikenberry and Truesdell [125]. For more details on second order Chapman-Enskog expansion and Burnett equation refer Struchtrup [264].

B.6 Linearized Boltzmann equation

Boltzmann equation for binary collision is

$$\frac{\partial f}{\partial t} + \nabla_{\vec{x}}\cdot(\vec{v}f) = J(f,f) \tag{B.51}$$

where $J(f,f)$ is binary or two particle collision integral describing the collision amongst the molecules which vanishes in the Euler limit. The distribution can

be linearized about a local Maxwellian as follows

$$f(\vec{x},\vec{v},\mathbb{I},t) = f_0(\vec{x},\vec{v},\mathbb{I},t)[1+\Phi(\vec{x},\vec{v},\mathbb{I},t)] \tag{B.52}$$

Neglecting the dependence of Φ on $\vec{x}$ and t we can write

$$f(\vec{x},\vec{v},\mathbb{I},t) = f_0(\vec{x},\vec{v},\mathbb{I},t)[1+\Phi(\vec{v},\mathbb{I})] \tag{B.53}$$

With the further assumption that $|\Phi| \ll 1$ and both Maxwellian and unknown Φ vary slowly in space and time, with this assumption we can neglect the product of Φ with derivatives of Maxwellian f_0 as well as derivatives of Φ . With this the linearized Boltzmann equation in terms of linearized collision operator $\mathbb{J}\Phi$ becomes

$$\frac{1}{f_0}\left(\frac{\partial f_0}{\partial t} + \nabla_{\vec{x}}\cdot(\vec{v}f_0)\right) + \mathbb{J}\Phi = 0 \tag{B.54}$$

The linearized collision operator $\mathbb{J}\Phi$ is defined as

$$\mathbb{J}\Phi = -\frac{1}{f_0}\left(\int_0^{\pi/2}\int_0^{2\pi}\int_{\mathbb{R}^+}\int_{\mathbb{R}^D} f_0 f_0^{'}\left(\Phi^a + \Phi^{'a} - \Phi - \Phi^{'}\right) g\ \Pi\ d\vec{v}^{'} d\mathbb{I} d\varrho d\Theta\right) \tag{B.55}$$

The linearized collision operator $\mathbb{J}$ has following properties [186]

- a) The operator $\mathbb{J}$ is linear :

$$\mathbb{J}(\alpha_1\Phi_1 + \alpha_2\Phi_2) = \alpha_1\mathbb{J}\Phi_1 + \alpha_2\mathbb{J}\Phi_2 \tag{B.56}$$

- b) The operator $\mathbb{J}$ has rotational invariance:

$$\mathbb{O}^{-1}\mathbb{J}\mathbb{O} = \mathbb{J} \tag{B.57}$$

  where $\mathbb{O}$ is any three dimensional rotation operator

- c) The operator $\mathbb{J}$ is self adjoint :

$$\int_{\mathbb{R}^+}\int_{\mathbb{R}^D} \Phi_i\mathbb{J}\Phi_j d\vec{v}d\mathbb{I} = \int_{\mathbb{R}^+}\int_{\mathbb{R}^D} \Phi_j\mathbb{J}\Phi_i d\vec{v}d\mathbb{I} \tag{B.58}$$

  The symmetry indicates that operator $\mathbb{J}$ is self-adjoint, the matrix elements are hermitean symmetric giving rise to Onsager symmetry relations. This property arises from the equality of the differential cross-sections for direct and inverse collisions.

- d) The positive semi-definiteness of the collision operator $\mathbb{J}$:

$$\int_{\mathbb{R}^+}\int_{\mathbb{R}^D}\Phi_i\mathbb{J}\Phi_i d\vec{v}d\mathbb{I}\geq 0 \tag{B.59}$$

It should be noted that the perturbation terms satisfies the moment closure property, expressed as

$$\langle\boldsymbol{\psi}, f_0\Phi\rangle = \int_{\mathbb{R}^+}\int_{\mathbb{R}^D}\Psi(\vec{v},\mathbb{I},t)f_0\Phi d\vec{v}d\mathbb{I}=0 \tag{B.60}$$

where moment vector is $\boldsymbol{\Psi}=\left[1,\vec{v},\mathbb{I}+\frac{1}{2}\vec{v}^T\vec{v}\right]^T$. Taking moments of the function $\Psi_e=-Rlnf$ of the linearized Boltzmann equation

$$\frac{\partial f_0}{\partial t}+\nabla_{\vec{x}}\cdot(\vec{v}f_0)=-f_0\mathbb{J}\Phi \tag{B.61}$$

we obtain the entropy density production equation expressed as

$$\frac{\partial\rho_s}{\partial t}+\nabla_{\vec{x}}\cdot(j_s)=R\int_{\mathbb{R}^+}\int_{\mathbb{R}^D}lnf(f_0\mathbb{J})\Phi d\vec{v}d\mathbb{I} \tag{B.62}$$

Because of linearization factor lnf can be expressed as

$$lnf=lnf_0+ln(1+\Phi)=lnf_0+\Phi \tag{B.63}$$

Since lnf_0 is a collisional invariant and hence makes no contribution. Entropy density production equation can now be written as

$$\frac{\partial\rho_s}{\partial t}+\nabla_{\vec{x}}\cdot(j_s)=R\int_{\mathbb{R}^+}\int_{\mathbb{R}^D}f_0\Phi\mathbb{J}\Phi d\vec{v}d\mathbb{I}=\sigma(\vec{v},t)\geq 0 \tag{B.64}$$

B.7 Extending kinetic model for gas-mixture

Extension of the kinetic model for mixture of non-reacting gas can be accomplished in two different ways i)single fluid model, ii)multi-fluid model. For example single fluid kinetic model for binary mixture of non-reacting gas can be written as

$$J_m(f,f_0)=-\left(\frac{f-f_0}{t_{R(\tau)}}\right)_{\boldsymbol{X}_q=0,\boldsymbol{X}_d=0}-\left(\frac{f-f_0}{t_{R(q)}}\right)_{\boldsymbol{X}_\tau=0,\boldsymbol{X}_d=0}-\left(\frac{f-f_0}{t_{R(d)}}\right)_{\boldsymbol{X}_\tau=0,\boldsymbol{X}_q=0} \tag{B.65}$$

where $\boldsymbol{X}_\tau$, $\boldsymbol{X}_q$ and $\boldsymbol{X}_d$ are the thermodynamic force terms associated with shear stress tensor, heat flux vector and species diffusion flux vector. Parameters $t_{R(\tau)}$, $t_{R(q)}$ and $t_{R(d)}$ are the relaxation time due thermodynamic force associated with shear stress tensor, heat flux vector and species concentration vector. The distribution function can be derived as

$$f_1 = f_0 - \sum_j \boldsymbol{\Upsilon}_j \odot \boldsymbol{X}_j = f_0 - (\boldsymbol{\Upsilon}_\tau : \boldsymbol{X}_\tau + \boldsymbol{\Upsilon}_q \cdot \boldsymbol{X}_q + \boldsymbol{\Upsilon}_d \cdot \boldsymbol{X}_d) \tag{B.66}$$

where $\boldsymbol{\Upsilon}_\tau$, $\boldsymbol{\Upsilon}_q$ and $\boldsymbol{\Upsilon}_d$ are the thermodynamic force terms associated with shear stress tensor, heat flux vector and species diffusion flux vector. Here $\boldsymbol{X}_q$ and $\boldsymbol{X}_d$ are of same tensorial order, hence Onsager's cross coupling gives the Soret and Dufour effect.

In case of two fluid approximation we will have kinetic models for each species. The kinetic model will not only depend on relaxation time associated with self-collisions but also on relaxation time associated with cross collisions of specie i with specie j. The kinetic model $J_m(f, f_0)(i)$ for specie i and $J_m(f, f_0)(j)$ for specie j can be expressed as

$$\begin{aligned} J_m(f, f_0)(i) \;&= -\left(\tfrac{f(i)-f_0(i)}{t_{R(\tau,ii)}}\right)_{\boldsymbol{X}_q=0} - \left(\tfrac{f(i)-f_0(i)}{t_{R(q,ii)}}\right)_{\boldsymbol{X}_\tau=0} \\ &\quad - \left(\tfrac{f(i)-\tilde{f}_0(i)}{t_{R(\tau,ij)}}\right)_{\boldsymbol{X}_q=0} - \left(\tfrac{f(i)-\tilde{f}_0(i)}{t_{R(q,ij)}}\right)_{\boldsymbol{X}_\tau=0} \end{aligned} \tag{B.67}$$

$$\begin{aligned} J_m(f, f_0)(j) \;&= -\left(\tfrac{f(j)-f_0(j)}{t_{R(\tau,jj)}}\right)_{\boldsymbol{X}_q=0} - \left(\tfrac{f(j)-f_0(j)}{t_{R(q,jj)}}\right)_{\boldsymbol{X}_\tau=0} \\ &\quad - \left(\tfrac{f(j)-\tilde{f}_0(j)}{t_{R(\tau,ji)}}\right)_{\boldsymbol{X}_q=0} - \left(\tfrac{f(j)-\tilde{f}_0(j)}{t_{R(q,ji)}}\right)_{\boldsymbol{X}_\tau=0} \end{aligned} \tag{B.68}$$

where f_i and $f_0(i)$ is the non-equilibrium and equilibrium distribution for specie i. Similarly, f_j and $f_0(j)$ is the non-equilibrium and equilibrium distribution for specie j. Maxwellian distribution $\tilde{f}_0(i)$ and $\tilde{f}_0(j)$ is based on free temperature parameter as derived by Morse[193]. Parameters $t_{R(\tau,ii)}$, $t_{R(q,ii)}$ are the relaxation time due to self collisions of specie i while $t_{R(\tau,jj)}$, $t_{R(q,jj)}$ are the relaxation time due to self collisions of specie j. Parameters $t_{R(\tau,ij)}$, $t_{R(q,ij)}$ are the relaxation time due to cross collisions of specie i with specie j while $t_{R(\tau,ji)}$, $t_{R(q,ji)}$ is the relaxation time due to self collisions of specie j with specie i. The cross collision relaxation time $t_{R(\alpha,ij)}$ and $t_{R(\alpha,ji)}$ is related to number density as follows

$$\frac{t_{R(\alpha,ij)}}{t_{R(\alpha,ji)}} = \frac{n_i}{n_j} \tag{B.69}$$

where n_i and n_j is the number density of specie i and specie j.

Appendix C

Treatment of thermally and calorically imperfect gas

The definition of a perfect gas is stated in two parts: i)the gas is *thermally perfect* i.e. it obeys the thermal equation of state or ideal law $p = \rho RT$, and ii) the gas is *calorically perfect* i.e. the gas specific heats are constants.

C.1 Thermally imperfect gas

At higher pressures or lower temperatures the behaviour of gases deviates from ideal gas law relationship and follow a relationship given as

$$\frac{p}{\rho RT} = 1 + B\rho + C\rho^2 + \cdots \tag{C.1}$$

where B and C are the virial coefficients which are functions of temperature and are determined experimentally. Another commonly used formulation is van der Waals equation of state given as

$$p = \frac{RT}{v - b} - \frac{a}{v^2} \tag{C.2}$$

Another alternative method is based on compressibility factor, Z defined as

$$Z = \frac{p}{\rho RT} \tag{C.3}$$

where Z has a value of 1.0 for ideal gas and its deviation from 1.0 characterizes the non-ideality of gases.

C.2 Calorically imperfect gas

For the calorically imperfect gas the specific heat capacity at constant pressure and volume, c_p and c_v; the ratio of specific heat capacities, γ and the enthlapy are non-linear functions of temperature.
The probability, p_i to find the system in some state i with energy E_i is

$$p_i = \frac{exp(-\beta E_i)}{Z} = \frac{exp(-\beta E_i)}{\sum_i exp(-\beta E_i)} \tag{C.4}$$

where $\beta = 1/k_B T$ with k_B as the Boltzmann's constant and Z from German name *Zustandssummme* is the factor of normalization which is the sum over all micro eigenstates i which system takes. The factor Z is also called partition function for canonical ensemble for the N indistinguishable molecules. It can also be expressed as

$$Z = \frac{1}{N! h^{N D_f}} \int \cdots \int exp(-\frac{\mathbb{H}}{k_B T}) d\vec{r_1} d\vec{r_2} \cdots d\vec{r_N} d\vec{p_1} d\vec{p_2} \cdots d\vec{p_N} \tag{C.5}$$

where $\mathbb{H}$ designates the Hamiltonian molecule system, vectors $d\vec{r_1} d\vec{r_2} \cdots d\vec{r_N}$ describe the position of N molecules and $d\vec{p_1} d\vec{p_2} \cdots d\vec{p_N}$ describe the momenta of the N molecules. D_f gives the degrees of freedom of individual molecules, k is the Boltzmann's constant and h is Planck's constant.

C.2.1 Partition function and thermodynamic properties

It should be noted that Boltzmann distribution is the probability of dominant macrostate. For N molecules the probability that the system is in macro state with energy E_i is the product of N Boltzmann distributions

$$Z_N = \sum_i exp(-\beta E_i^{(1)} + \cdots + E_i^{(N)}) = \left(\sum_i exp(-\beta E_i) \right)^N \tag{C.6}$$

Thus the partition function,Z_N for a system of N calorically imperfect gas molecules can be written as

$$Z_N = Z^N \tag{C.7}$$

where Z is the single molecule partition function of calorically imperfect gas which can be written as

$$Z = Z_{trans} Z_{vib} Z_{rot} Z_{ir} Z_{el} Z_{nuc} Z_{conf} \tag{C.8}$$

The partition function Z is a product of terms of the translation (trans), the vibration (vib), the rotation (rot), the internal rotation (ir), the influence of electron excitation (el), the influence of nuclei excitation (nuc) and the influence of the intermolecular potential energy (conf). Thus canonical ensemble partition function Z_N for N independent indistinguishable molecules is given as

$$Z_N = \frac{Z_{trans}^N}{N!} Z_{vib}^N Z_{rot}^N Z_{ir}^N Z_{el}^N Z_{nuc}^N Z_{conf}^N \tag{C.9}$$

The $N!$ associated with the translational term is necessary to account for the $N!$ ways of permuting N molecules. The assumption that each modes are decoupled the thermodynamic properties of a molecule can be calculated by summing the individual contributions from each mode. For example total internal energy of a molecule U can be written as

$$U = U_{trans} + U_{rot} + U_{vib} + \cdots \tag{C.10}$$

The thermodynamic functions can be evaluated as follows

$$\begin{aligned}
&Pressure, && p = k_B T \left(\tfrac{\partial ln(Z_N)}{\partial V}\right)_T, \\
&Helmholtz\ \ free\ \ energy, && H = -k_B T\ ln(Z_N), \\
&Internal\ \ energy, && U = k_B T^2 \left(\tfrac{\partial ln(Z_N)}{\partial T}\right)_V, \\
&Entropy, && S = k_B \left[ln(Z_N) + T \left(\tfrac{\partial ln(Z_N)}{\partial T}\right)_V\right], \\
&Enthalpy, && H = k_B T \left[T \left(\tfrac{\partial ln(Z_N)}{\partial T}\right)_V + V \left(\tfrac{\partial ln(Z_N)}{\partial V}\right)_T\right], \\
&Free\ \ Enthalpy, && G = -k_B T \left[ln(Z_N) - V \left(\tfrac{\partial ln(Z_N)}{\partial V}\right)_T\right]
\end{aligned} \tag{C.11}$$

where T is the temperature and V is the volume of molecular system. As described earlier each energy mode has an associated partition function Z which is obtained from the quantitized molecular energy levels E_i of the mode. If an energy level

is degenerate the degeneracy, g_i must also be accounted. In such a case the molecular partition function for each mode is

$$Z = \sum_{i}^{\infty} g_i exp(-\beta E_i) \tag{C.12}$$

When $E_i > k_B T$ then all the energy levels are assumed to accessible to the molecule, thus integral approximation replaces the discrete summation of the partition function leading to classical representation of the system i.e. the kinetic theory of gases. Another way of determining whether the quantized or continuum representation of the partition function should be used is to calculate the characteristic temperature $\theta_i = E_i/k_B$ for each mode. In most of the cases translational, rotational and vibrational partition functions contribute to the thermodynamic properties in the temperature ranges encountered in engineering applications.

C.2.2 Translational partition function

The quantized translational energy available to a molecule confined to a cubic box of volume $V = a^3$ in three dimensions is

$$E_i = \frac{h^2(n_x^2 + n_y^2 + n_z^2)}{8ma^2} \tag{C.13}$$

where n_x,n_y, n_z are translational quantum numbers, h is Planck's constant and m is the mass of the molecule. The characteristic translational temperature per mole is

$$\theta_{trans} = \frac{h^2}{8mk_B a^2} = \frac{h^2}{8mk_B V^{2/3}} \tag{C.14}$$

With an assumption that there is no translational degeneracy and translational characteristic temperature is less than the temperature of interest, the total translational contribution to the partition function for N molecules is

$$Z_{N(trans)} = \frac{Z_{trans}^N}{N!} = \frac{V^N}{N!}\left(\frac{2\pi m k_B T}{h^2}\right)^{3N/2} \tag{C.15}$$

The translational contribution to internal energy and enthalpy can be shown to be

$$\begin{aligned} U_{trans} &= \tfrac{3Nk_BT}{2} \\ H_{trans} &= \tfrac{5Nk_BT}{2} \end{aligned} \tag{C.16}$$

C.2.3 Rotational partition function

The quantized rotational energy is given by

$$E_i = \frac{h^2 J(J+1)}{8\pi^2 I_{A,B,C}} \tag{C.17}$$

where J is the rotational quantum number and $I_{A,B,C}$ are the principal moments of inertia of the molecule. The characteristic rotational temperature of a molecule being

$$\theta_{rot} = \frac{h^3}{8k_B\pi^2 I_A} \tag{C.18}$$

With an assumption that rotational characteristic temperature is less than the temperature of interest, the total rotational contribution to the partition function for N molecules is

$$Z_{N(rot)} = Z_{rot}^N = \left(\frac{\left(\frac{k_B T}{h}\right)^{3/2} \pi^{1/2}}{\sigma(ABC)^{1/2}} \right)^N \tag{C.19}$$

where $\sigma(ABC)$ is the rotational symmetry number. The rotational contribution to internal energy and enthalpy can be shown to be

$$\begin{aligned} U_{rot} &= \tfrac{3Nk_BT}{2} \\ H_{rot} &= \tfrac{3Nk_BT}{2} \end{aligned} \tag{C.20}$$

C.2.4 Vibrational partition function

The quantized vibrational energy relative to the ground state can be written as

$$E_i = h\ vib_i \tag{C.21}$$

where vib_i is a fundamental vibrational frequency. The characteristic vibrational temperature of a molecule is

$$\theta_{vib} = \frac{h\ vib\ c}{k_B} \tag{C.22}$$

In many polyatomic molecules the vibrational characteristic temperature is sometimes near the temperature of interest. In such a case we have to use quantized model of the vibrational contribution given as

$$Z_{vib} = \sum_{i=1}^{\infty} g_i exp(-\frac{\theta_i}{T}) \tag{C.23}$$

where g_i is the degeneracy of the i^{th} vibrational mode, θ_i is the characteristic temperature. Expanding the partition function as a geometric series the partition function for nv number of vibrational mode for N molecules can be expressed as

$$Z_{N(vib)} = Z_{vib}^{N} = \Pi_{i=1}^{i=nv} \left(\frac{g_i}{1 - exp(-\frac{\theta_i}{T})} \right)^{N} \tag{C.24}$$

The vibrational contribution to internal energy and enthalpy can be shown to be

$$\begin{aligned} U_{vib} &= R \sum_{i=1}^{i=nv} \left(\frac{g_i \theta_i exp(-\frac{\theta_i}{T})}{1-exp(-\frac{\theta_i}{T})} \right) \\ H_{vib} &= R \sum_{i=1}^{i=nv} \left(\frac{g_i \theta_i exp(-\frac{\theta_i}{T})}{1-exp(-\frac{\theta_i}{T})} \right) \end{aligned} \tag{C.25}$$

C.2.5 Internal energy, Enthalpy, Specific heats and γ

Internal energy and enthalpy per unit mass for calorically imperfect polyatomic molecules can be now be written as

$$\begin{aligned} U &= U_{trans} + U_{rot} + U_{vib} = 3RT + R \sum_{i=1}^{i=nv} \left(\frac{g_i \theta_i exp(-\frac{\theta_i}{T})}{1-exp(-\frac{\theta_i}{T})} \right) \\ H &= H_{trans} + H_{rot} + H_{vib} = 4RT + R \sum_{i=1}^{i=nv} \left(\frac{g_i \theta_i exp(-\frac{\theta_i}{T})}{1-exp(-\frac{\theta_i}{T})} \right) \end{aligned} \tag{C.26}$$

The specific heat at constant volume, C_v and constant pressure, C_p can be derived as

$$\begin{aligned} C_v &= \frac{\partial U}{\partial T} = 3R + R \sum_{i=1}^{i=nv} \left(\frac{g_i \left(\frac{\theta_i}{T}\right)^2 exp(-\frac{\theta_i}{T})}{\left(1-exp(-\frac{\theta_i}{T})\right)^2} \right) \\ C_p &= \frac{\partial H}{\partial T} = 4R + R \sum_{i=1}^{i=nv} \left(\frac{g_i \left(\frac{\theta_i}{T}\right)^2 exp(-\frac{\theta_i}{T})}{\left(1-exp(-\frac{\theta_i}{T})\right)^2} \right) \end{aligned} \tag{C.27}$$

The expression for ratio of specific heats, γ can be written as

$$\gamma = 1 + \frac{1}{3 + \sum_{i=1}^{i=nv} \left(\frac{g_i \left(\frac{\theta_i}{T}\right)^2 exp(-\frac{\theta_i}{T})}{\left(1-exp(-\frac{\theta_i}{T})\right)^2} \right)} \tag{C.28}$$

Appendix D

Split macroscopic tensors and Kinetic Flux Vector Split Fluxes

D.1 Split macroscopic tensors, $\Lambda_{ij}^{\pm\cdot}$ and $\Lambda_{ij}^{\cdot\pm}$ for 2D

D.1.1 X Split macroscopic tensors, $\Lambda_{ij}^{\pm\cdot}$

$$
\begin{aligned}
\mathbf{\Lambda}_{\tau}^{+\cdot} &= \left\langle \mathbf{\Psi}, v_x \mathbf{\Upsilon}_{\tau}^{+\cdot} \right\rangle \\
&\equiv \int_0^{+\infty} \int_{-\infty}^{+\infty} \int_0^{+\infty} \mathbf{\Psi} v_x \mathbf{\Upsilon}_{\tau} dv_x dv_y d\mathbb{I} \\
\mathbf{\Lambda}_{\tau}^{-\cdot} &= \left\langle \mathbf{\Psi}, v_x \mathbf{\Upsilon}_{\tau}^{-\cdot} \right\rangle \\
&\equiv \int_0^{+\infty} \int_{-\infty}^{+\infty} \int_{-\infty}^{0} \mathbf{\Psi} v_x \mathbf{\Upsilon}_{\tau} dv_x dv_y d\mathbb{I} \\
\mathbf{\Lambda}_{q}^{+\cdot} &= \left\langle \mathbf{\Psi}, v_x \mathbf{\Upsilon}_{q}^{+\cdot} \right\rangle \\
&\equiv \int_0^{+\infty} \int_{-\infty}^{+\infty} \int_0^{+\infty} \mathbf{\Psi} v_x \mathbf{\Upsilon}_{q} dv_x dv_y d\mathbb{I} \\
\mathbf{\Lambda}_{q}^{-\cdot} &= \left\langle \mathbf{\Psi}, v_x \mathbf{\Upsilon}_{q}^{-\cdot} \right\rangle \\
&\equiv \int_0^{+\infty} \int_{-\infty}^{+\infty} \int_{-\infty}^{0} \mathbf{\Psi} v_x \mathbf{\Upsilon}_{q} dv_x dv_y d\mathbb{I}
\end{aligned}
$$

$$\Lambda_{1,\tau}^{\pm\cdot} = \left\langle \Psi_1, v_x \boldsymbol{\Upsilon}_\tau^{\pm\cdot} \right\rangle = \frac{\mu}{p} \begin{bmatrix} \frac{B_1^{\mp}(\gamma-3)\rho}{8\sqrt{\pi}\beta^{3/2}} & 0 \\ 0 & \frac{B_1^{\mp}(\gamma-1)\rho}{8\sqrt{\pi}\beta^{3/2}} \end{bmatrix}$$

$$\Lambda_{1,q}^{\pm\cdot} = \left\langle \Psi_1, v_x \boldsymbol{\Upsilon}_q^{\pm\cdot} \right\rangle = \frac{(\gamma-1)}{\gamma} \frac{\kappa}{pR} \begin{bmatrix} -\frac{B_1^{\mp} u_x \rho}{4\sqrt{\pi}\beta^{3/2}} & 0 \end{bmatrix}$$

$$\Lambda_{2,\tau}^{\pm\cdot} = \left\langle \Psi_2, v_x \boldsymbol{\Upsilon}_\tau^{\pm\cdot} \right\rangle = \frac{\mu}{p} \begin{bmatrix} -\frac{A_1^{\pm}(\gamma-3)\rho}{8\beta^2} & 0 \\ 0 & -\frac{A_1^{\pm}(\gamma-1)\rho}{8\beta^2} \end{bmatrix}$$

$$\Lambda_{2,q}^{\pm\cdot} = \left\langle \Psi_2, v_x \boldsymbol{\Upsilon}_q^{\pm\cdot} \right\rangle = \frac{(\gamma-1)}{\gamma} \frac{\kappa}{pR} \begin{bmatrix} \frac{B_1^{\mp}\rho}{4\sqrt{\pi}\beta^{5/2}} & 0 \end{bmatrix}$$

$$\Lambda_{3,\tau}^{\pm\cdot} = \left\langle \Psi_3, v_x \boldsymbol{\Upsilon}_\tau^{\pm\cdot} \right\rangle = \frac{\mu}{p} \begin{bmatrix} \frac{B_1^{\mp} u_y(\gamma-3)\rho}{8\sqrt{\pi}\beta^{3/2}} & \frac{A_1^{\pm}\rho}{8\beta^2} \\ \frac{A_1^{\pm}\rho}{8\beta^2} & \frac{B_1^{\mp} u_y(\gamma-1)\rho}{8\sqrt{\pi}\beta^{3/2}} \end{bmatrix}$$

$$\Lambda_{3,q}^{\pm\cdot} = \left\langle \Psi_3, v_x \boldsymbol{\Upsilon}_q^{\pm\cdot} \right\rangle = \frac{(\gamma-1)}{\gamma} \frac{\kappa}{pR} \begin{bmatrix} -\frac{B_1^{\mp} u_x u_y \rho}{4\sqrt{\pi}\beta^{3/2}} & \frac{B_1^{\mp}\rho}{8\sqrt{\pi}\beta^{5/2}} \end{bmatrix}$$

$$\Lambda_{4,\tau}^{\pm\cdot} = \left\langle \Psi_4, v_x \boldsymbol{\Upsilon}_\tau^{\pm\cdot} \right\rangle = \frac{\mu}{p} \begin{bmatrix} -\frac{(\gamma-3)C_1^{\pm}\rho}{32\sqrt{\pi}\beta^{5/2}(\gamma-1)} & \frac{A_1^{\pm} u_y \rho}{8\beta^2} \\ \frac{A_1^{\pm} u_y \rho}{8\beta^2} & -\frac{C_1^{\pm}\rho}{32\sqrt{\pi}\beta^{5/2}} \end{bmatrix}$$

$$\Lambda_{4,q}^{\pm\cdot} = \left\langle \Psi_4, v_x \boldsymbol{\Upsilon}_q^{\pm\cdot} \right\rangle = \frac{(\gamma-1)}{\gamma} \frac{\kappa}{pR} \begin{bmatrix} -\frac{(B_1^{\mp}\sqrt{\beta} u_x (3+2{u_y}^2\beta(\gamma-1)-\gamma)+2A_1^{\pm}\sqrt{\pi}\gamma)\rho}{16\sqrt{\pi}\beta^3(\gamma-1)} & \frac{B_1^{\mp} u_y \rho}{8\sqrt{\pi}\beta^{5/2}} \end{bmatrix}$$

D.1.2 Y Split macroscopic tensors, $\Lambda_{ij}^{\cdot\pm}$

$$\begin{aligned}
\boldsymbol{\Lambda}_\tau^{\cdot+} &= \left\langle \boldsymbol{\Psi}, v_y \boldsymbol{\Upsilon}_\tau^{\cdot+} \right\rangle \\
&\equiv \int_0^{+\infty} \int_0^{+\infty} \int_{-\infty}^{+\infty} \boldsymbol{\Psi} v_y \boldsymbol{\Upsilon}_\tau dv_x dv_y d\mathbb{I} \\
\boldsymbol{\Lambda}_\tau^{\cdot-} &= \left\langle \boldsymbol{\Psi}, v_y \boldsymbol{\Upsilon}_\tau^{\cdot-} \right\rangle \\
&\equiv \int_0^{+\infty} \int_{-\infty}^{0} \int_{-\infty}^{+\infty} \boldsymbol{\Psi} v_y \boldsymbol{\Upsilon}_\tau dv_x dv_y d\mathbb{I} \\
\boldsymbol{\Lambda}_q^{\cdot+} &= \left\langle \boldsymbol{\Psi}, v_y \boldsymbol{\Upsilon}_q^{\cdot+} \right\rangle \\
&\equiv \int_0^{+\infty} \int_0^{+\infty} \int_{-\infty}^{+\infty} \boldsymbol{\Psi} v_y \boldsymbol{\Upsilon}_q dv_x dv_y d\mathbb{I} \\
\boldsymbol{\Lambda}_q^{\cdot-} &= \left\langle \boldsymbol{\Psi}, v_y \boldsymbol{\Upsilon}_q^{\cdot-} \right\rangle \\
&\equiv \int_0^{+\infty} \int_{-\infty}^{0} \int_{-\infty}^{+\infty} \boldsymbol{\Psi} v_y \boldsymbol{\Upsilon}_q dv_x dv_y d\mathbb{I}
\end{aligned}$$

$$\Lambda_{1,\tau}^{\cdot\pm} = \left\langle \Psi_1, v_y \boldsymbol{\Upsilon}_\tau^{\cdot\pm} \right\rangle = \frac{\mu}{p} \begin{bmatrix} \frac{B_2^{\mp}(\gamma-1)\rho}{8\sqrt{\pi}\beta^{3/2}} & 0 \\ 0 & \frac{B_2^{\mp}(\gamma-3)\rho}{8\sqrt{\pi}\beta^{3/2}} \end{bmatrix}$$

$$\Lambda_{1,q}^{\cdot\pm} = \left\langle \Psi_1, v_y \boldsymbol{\Upsilon}_q^{\cdot\pm} \right\rangle = \frac{(\gamma-1)}{\gamma}\frac{\kappa}{pR} \begin{bmatrix} 0 & -\frac{B_2^{\mp}u_y\rho}{4\sqrt{\pi}\beta^{3/2}} \end{bmatrix}$$

$$\Lambda_{2,\tau}^{\cdot\pm} = \left\langle \Psi_2, v_y \boldsymbol{\Upsilon}_\tau^{\cdot\pm} \right\rangle = \frac{\mu}{p} \begin{bmatrix} \frac{B_2^{\mp}u_x(\gamma-1)\rho}{8\sqrt{\pi}\beta^{3/2}} & \frac{A_2^{\pm}\rho}{8\beta^2} \\ \frac{A_2^{\pm}\rho}{8\beta^2} & \frac{B_2^{\mp}u_x(\gamma-3)\rho}{8\sqrt{\pi}\beta^{3/2}} \end{bmatrix}$$

$$\Lambda_{2,q}^{\cdot\pm} = \left\langle \Psi_2, v_y \boldsymbol{\Upsilon}_q^{\cdot\pm} \right\rangle = \frac{(\gamma-1)}{\gamma}\frac{\kappa}{pR} \begin{bmatrix} \frac{B_2^{\mp}\rho}{8\sqrt{\pi}\beta^{5/2}} & -\frac{B_2^{\mp}u_xu_y\rho}{4\sqrt{\pi}\beta^{3/2}} \end{bmatrix}$$

$$\Lambda_{3,\tau}^{\cdot\pm} = \left\langle \Psi_3, v_y \boldsymbol{\Upsilon}_\tau^{\cdot\pm} \right\rangle = \frac{\mu}{p} \begin{bmatrix} -\frac{A_2^{\pm}(\gamma-1)\rho}{8\beta^2} & 0 \\ 0 & -\frac{A_2^{\pm}(\gamma-3)\rho}{8\beta^2} \end{bmatrix}$$

$$\Lambda_{3,q}^{\cdot\pm} = \left\langle \Psi_3, v_y \boldsymbol{\Upsilon}_q^{\cdot\pm} \right\rangle = \frac{(\gamma-1)}{\gamma}\frac{\kappa}{pR} \begin{bmatrix} 0 & \frac{B_2^{\mp}\rho}{4p\sqrt{\pi}\beta^{5/2}} \end{bmatrix}$$

$$\Lambda_{4,\tau}^{\cdot\pm} = \left\langle \Psi_4, v_y \boldsymbol{\Upsilon}_\tau^{\cdot\pm} \right\rangle = \frac{\mu}{p} \begin{bmatrix} -\frac{C_2^{\pm}\rho}{32\sqrt{\pi}\beta^{5/2}} & \frac{A_2^{\pm}u_x\rho}{8\beta^2} \\ \frac{A_2^{\pm}u_x\rho}{8\beta^2} & -\frac{(\gamma-3)C_2^{\pm}\rho}{32\sqrt{\pi}\beta^{5/2}} \end{bmatrix}$$

$$\Lambda_{4,q}^{\cdot\pm} = \left\langle \Psi_4, v_y \boldsymbol{\Upsilon}_q^{\cdot\pm} \right\rangle = \frac{(\gamma-1)}{\gamma}\frac{\kappa}{pR} \begin{bmatrix} \frac{B_2^{\mp}u_x\rho}{8p\sqrt{\pi}\beta^{5/2}} & \frac{(-B_2^{\mp}u_y\sqrt{\beta}(3+2{u_x}^2\beta(\gamma-1)-\gamma)+2A_2^{\pm}\sqrt{\pi}\gamma)\rho}{16\sqrt{\pi}\beta^3(\gamma-1)} \end{bmatrix}$$

where $A_1^{\pm} = 1 \pm Erf(u_x\sqrt{\beta})$, $A_2^{\pm} = 1 \pm Erf(u_y\sqrt{\beta})$, $B_1^{\pm} = \pm exp(-\beta u_x^2)$, $B_2^{\pm} = \pm exp(-\beta u_y^2)$ and

$C_1^{\pm} = 4A_1^{\pm}u_x\sqrt{\beta}\sqrt{\pi}(\gamma-1) + B_1^{\mp}(1-2u_y^2\beta(\gamma-1)-3\gamma)$

$C_2^{\pm} = 4A_2^{\pm}u_y\sqrt{\beta}\sqrt{\pi}(\gamma-1) + B_2^{\mp}(1-2u_x^2\beta(\gamma-1)-3\gamma)$

D.2 Split macroscopic tensors, $\Lambda_{ij}^{\pm\cdot\cdot}$,$\Lambda_{ij}^{\cdot\pm\cdot}$ and $\Lambda_{ij}^{\cdot\cdot\pm}$ for 3D

D.2.1 X macroscopic tensors, $\Lambda_{ij}^{\pm\cdot\cdot}$

$$
\begin{aligned}
\mathbf{\Lambda}_{\tau}^{+\cdot\cdot} &= \left\langle \mathbf{\Psi}, v_x \mathbf{\Upsilon}_{\tau}^{+\cdot\cdot} \right\rangle \\
&\equiv \int_0^{+\infty}\int_{-\infty}^{+\infty}\int_{-\infty}^{+\infty}\int_0^{+\infty} \mathbf{\Psi} v_x \mathbf{\Upsilon}_{\tau} dv_x dv_y dv_z d\mathbb{I} \\
\mathbf{\Lambda}_{\tau}^{-\cdot\cdot} &= \left\langle \mathbf{\Psi}, v_x \mathbf{\Upsilon}_{\tau}^{-\cdot\cdot} \right\rangle \\
&\equiv \int_0^{+\infty}\int_{-\infty}^{+\infty}\int_{-\infty}^{+\infty}\int_{-\infty}^{0} \mathbf{\Psi} v_x \mathbf{\Upsilon}_{\tau} dv_x dv_y dv_z d\mathbb{I} \\
\mathbf{\Lambda}_{q}^{+\cdot\cdot} &= \left\langle \mathbf{\Psi}, v_x \mathbf{\Upsilon}_{q}^{+\cdot\cdot} \right\rangle \\
&\equiv \int_0^{+\infty}\int_{-\infty}^{+\infty}\int_{-\infty}^{+\infty}\int_0^{+\infty} \mathbf{\Psi} v_x \mathbf{\Upsilon}_{q} dv_x dv_y dv_z d\mathbb{I} \\
\mathbf{\Lambda}_{q}^{-\cdot\cdot} &= \left\langle \mathbf{\Psi}, v_x \mathbf{\Upsilon}_{q}^{-\cdot\cdot} \right\rangle \\
&\equiv \int_0^{+\infty}\int_{-\infty}^{+\infty}\int_{-\infty}^{+\infty}\int_{-\infty}^{0} \mathbf{\Psi} v_x \mathbf{\Upsilon}_{q} dv_x dv_y dv_z d\mathbb{I}
\end{aligned}
$$

$$
\Lambda_{1,\tau}^{\pm\cdot\cdot} = \left\langle \Psi_1, v_x \mathbf{\Upsilon}_{\tau}^{\pm\cdot\cdot} \right\rangle = \frac{\mu}{p}\begin{bmatrix} \frac{B_1^{\mp}(-3+\gamma)\rho}{8\sqrt{\pi}\beta^{3/2}} & 0 & 0 \\ 0 & \frac{B_1^{\mp}(-1+\gamma)\rho}{8\sqrt{\pi}\beta^{3/2}} & 0 \\ 0 & 0 & \frac{B_1^{\mp}(-1+\gamma)\rho}{8\sqrt{\pi}\beta^{3/2}} \end{bmatrix}
$$

$$
\Lambda_{1,q}^{\pm\cdot\cdot} = \left\langle \Psi_1, v_x \mathbf{\Upsilon}_{q}^{\pm\cdot\cdot} \right\rangle = \frac{(\gamma-1)}{\gamma}\frac{\kappa}{pR}\left[-\frac{B_1^{\mp}u_x\rho}{4\sqrt{\pi}\beta^{3/2}}, 0, 0\right]
$$

$$
\Lambda_{2,\tau}^{\pm\cdot\cdot} = \left\langle \Psi_2, v_x \mathbf{\Upsilon}_{\tau}^{\pm\cdot\cdot} \right\rangle = \frac{\mu}{p}\begin{bmatrix} -\frac{A_1^{\pm}(-3+\gamma)\rho}{8\beta^2} & 0 & 0 \\ 0 & -\frac{A_1^{\pm}(-1+\gamma)\rho}{8\beta^2} & 0 \\ 0 & 0 & -\frac{A_1^{\pm}(-1+\gamma)\rho}{8\beta^2} \end{bmatrix}
$$

$$
\Lambda_{2,q}^{\pm\cdot\cdot} = \left\langle \Psi_2, v_x \mathbf{\Upsilon}_{q}^{\pm\cdot\cdot} \right\rangle = \frac{(\gamma-1)}{\gamma}\frac{\kappa}{pR}\left[\frac{B_1^{\mp}\rho}{4\sqrt{\pi}\beta^{5/2}}, 0, 0\right]
$$

$$
\Lambda_{3,\tau}^{\pm\cdot\cdot} = \left\langle \Psi_3, v_x \mathbf{\Upsilon}_{\tau}^{\pm\cdot\cdot} \right\rangle = \frac{\mu}{p}\begin{bmatrix} \frac{B_1^{\mp}u_y(-3+\gamma)\rho}{8\sqrt{\pi}\beta^{3/2}} & \frac{A_1^{\pm}\rho}{8\beta^2} & 0 \\ \frac{A_1^{\pm}\rho}{8\beta^2} & \frac{B_1^{\mp}u_y(-1+\gamma)\rho}{8\sqrt{\pi}\beta^{3/2}} & 0 \\ 0 & 0 & \frac{B_1^{\mp}u_y(-1+\gamma)\rho}{8\sqrt{\pi}\beta^{3/2}} \end{bmatrix}
$$

$$
\Lambda_{3,q}^{\pm\cdot\cdot} = \left\langle \Psi_3, v_x \mathbf{\Upsilon}_{q}^{\pm\cdot\cdot} \right\rangle = \frac{(\gamma-1)}{\gamma}\frac{\kappa}{pR}\left[\frac{-B_1^{\mp}u_x u_y\rho}{4\sqrt{\pi}\beta^{3/2}}, \frac{B_1^{\mp}\rho}{8\sqrt{\pi}\beta^{5/2}}, 0\right]
$$

$$\Lambda_{4,\tau}^{\pm\cdot\cdot} = \left\langle \Psi_4, v_x \boldsymbol{\Upsilon}_\tau^{\pm\cdot\cdot} \right\rangle = \frac{\mu}{p} \begin{bmatrix} \frac{B_1^{\mp} u_z(-3+\gamma)\rho}{8\sqrt{\pi}\beta^{3/2}} & 0 & \frac{A_1^{\pm}\rho}{8\beta^2} \\ 0 & \frac{B_1^{\mp} u_z(-1+\gamma)\rho}{8\sqrt{\pi}\beta^{3/2}} & 0 \\ \frac{A_1^{\pm}\rho}{8\beta^2} & 0 & \frac{B_1^{\mp} u_z(-1+\gamma)\rho}{8\sqrt{\pi}\beta^{3/2}} \end{bmatrix}$$

$$\Lambda_{4,q}^{\pm\cdot\cdot} = \left\langle \Psi_4, v_x \boldsymbol{\Upsilon}_q^{\pm\cdot\cdot} \right\rangle = \frac{(\gamma-1)}{\gamma} \frac{\kappa}{pR} \left[-\frac{B_1^{\mp} u_x u_z \rho}{4\sqrt{\pi}\beta^{3/2}}, 0, \frac{B_1^{\mp}\rho}{8\sqrt{\pi}\beta^{5/2}} \right]$$

$$\Lambda_{5,\tau}^{\pm\cdot\cdot} = \left\langle \Psi_5, v_x \boldsymbol{\Upsilon}_\tau^{\pm\cdot\cdot} \right\rangle = \frac{\mu}{p} \begin{bmatrix} -\frac{(-3+\gamma)C_1^{\pm}\rho}{32\sqrt{\pi}\beta^{5/2}(-1+\gamma)} & \frac{A_1^{\pm} u_y \rho}{8\beta^2} & \frac{A_1^{\pm} u_z \rho}{8\beta^2} \\ \frac{A_1^{\pm} u_y \rho}{8\beta^2} & -\frac{C_1^{\pm}\rho}{32\sqrt{\pi}\beta^{5/2}} & 0 \\ \frac{A_1^{\pm} u_z \rho}{8\beta^2} & 0 & -\frac{C_1^{\pm}\rho}{32\sqrt{\pi}\beta^{5/2}} \end{bmatrix}$$

$$\Lambda_{5,q}^{\pm\cdot\cdot} = \left\langle \Psi_5, v_x \boldsymbol{\Upsilon}_q^{\pm\cdot\cdot} \right\rangle = \frac{(\gamma-1)}{\gamma} \frac{\kappa}{pR} \left[-\frac{\rho(B_1^{\mp} u_x \sqrt{\beta}(3+byz-\gamma)+2\sqrt{\pi}\gamma A_1^{\pm})}{16\sqrt{\pi}\beta^3(-1+\gamma)}, \frac{B_1^{\mp} u_y \rho}{8\sqrt{\pi}\beta^{5/2}}, \frac{B_1^{\mp} u_z \rho}{8\sqrt{\pi}\beta^{5/2}} \right]$$

D.2.2 Y Split macroscopic tensors, $\Lambda_{ij}^{\cdot\pm\cdot}$

$$\begin{aligned}
\boldsymbol{\Lambda}_\tau^{\cdot+\cdot} &= \left\langle \boldsymbol{\Psi}, v_y \boldsymbol{\Upsilon}_\tau^{\cdot+\cdot} \right\rangle \\
&\equiv \int_0^{+\infty}\int_{-\infty}^{+\infty}\int_0^{+\infty}\int_{-\infty}^{+\infty} \boldsymbol{\Psi} v_y \boldsymbol{\Upsilon}_\tau dv_x dv_y dv_z d\mathbb{I} \\
\boldsymbol{\Lambda}_\tau^{\cdot-\cdot} &= \left\langle \boldsymbol{\Psi}, v_y \boldsymbol{\Upsilon}_\tau^{\cdot-\cdot} \right\rangle \\
&\equiv \int_0^{+\infty}\int_{-\infty}^{+\infty}\int_{-\infty}^{0}\int_{-\infty}^{+\infty} \boldsymbol{\Psi} v_y \boldsymbol{\Upsilon}_\tau dv_x dv_y dv_z d\mathbb{I} \\
\boldsymbol{\Lambda}_q^{\cdot+\cdot} &= \left\langle \boldsymbol{\Psi}, v_y \boldsymbol{\Upsilon}_q^{\cdot+\cdot} \right\rangle \\
&\equiv \int_0^{+\infty}\int_{-\infty}^{+\infty}\int_0^{+\infty}\int_{-\infty}^{+\infty} \boldsymbol{\Psi} v_y \boldsymbol{\Upsilon}_q dv_x dv_y dv_z d\mathbb{I} \\
\boldsymbol{\Lambda}_\tau^{\cdot-\cdot} &= \left\langle \boldsymbol{\Psi}, v_y \boldsymbol{\Upsilon}_q^{\cdot-\cdot} \right\rangle \\
&\equiv \int_0^{+\infty}\int_{-\infty}^{+\infty}\int_{-\infty}^{0}\int_{-\infty}^{+\infty} \boldsymbol{\Psi} v_y \boldsymbol{\Upsilon}_q dv_x dv_y dv_z d\mathbb{I}
\end{aligned}$$

$$\Lambda_{1,\tau}^{\cdot\pm\cdot} = \left\langle \Psi_1, v_y \boldsymbol{\Upsilon}_{\tau}^{\cdot\pm\cdot} \right\rangle = \frac{\mu}{p} \begin{bmatrix} \frac{B_2^{\mp}(-1+\gamma)\rho}{8\sqrt{\pi}\beta^{3/2}} & 0 & 0 \\ 0 & \frac{B_2^{\mp}(-3+\gamma)\rho}{8\sqrt{\pi}\beta^{3/2}} & 0 \\ 0 & 0 & \frac{B_2^{\mp}(-1+\gamma)\rho}{8\sqrt{\pi}\beta^{3/2}} \end{bmatrix}$$

$$\Lambda_{1,q}^{\cdot\pm\cdot} = \left\langle \Psi_1, v_y \boldsymbol{\Upsilon}_{q}^{\cdot\pm\cdot} \right\rangle = \frac{(\gamma-1)}{\gamma} \frac{\kappa}{pR} \left[0, -\frac{B_2^{\mp} u_y \rho}{4\sqrt{\pi}\beta^{3/2}}, 0 \right]$$

$$\Lambda_{2,\tau}^{\cdot\pm\cdot} = \left\langle \Psi_2, v_y \boldsymbol{\Upsilon}_{\tau}^{\cdot\pm\cdot} \right\rangle = \frac{\mu}{p} \begin{bmatrix} \frac{B_2^{\mp} u_x(-1+\gamma)\rho}{8\sqrt{\pi}\beta^{3/2}} & \frac{A_2^{\pm}\rho}{8\beta^2} & 0 \\ \frac{A_2^{\pm}\rho}{8\beta^2} & \frac{B_2^{\mp} u_x(-3+\gamma)\rho}{8\sqrt{\pi}\beta^{3/2}} & 0 \\ 0 & 0 & \frac{B_2^{\mp} u_x(-1+\gamma)\rho}{8\sqrt{\pi}\beta^{3/2}} \end{bmatrix}$$

$$\Lambda_{2,q}^{\cdot\pm\cdot} = \left\langle \Psi_2, v_y \boldsymbol{\Upsilon}_{q}^{\cdot\pm\cdot} \right\rangle = \frac{(\gamma-1)}{\gamma} \frac{\kappa}{pR} \left[\frac{B_2^{\mp}\rho}{8\sqrt{\pi}\beta^{5/2}}, -\frac{B_2^{\mp} u_x u_y \rho}{4\sqrt{\pi}\beta^{3/2}}, 0 \right]$$

$$\Lambda_{3,\tau}^{\cdot\pm\cdot} = \left\langle \Psi_3, v_y \boldsymbol{\Upsilon}_{\tau}^{\cdot\pm\cdot} \right\rangle = \frac{\mu}{p} \begin{bmatrix} -\frac{A_2^{\pm}(-1+\gamma)\rho}{8\beta^2} & 0 & 0 \\ 0 & -\frac{A_2^{\pm}(-3+\gamma)\rho}{8\beta^2} & 0 \\ 0 & 0 & -\frac{A_2^{\pm}(-1+\gamma)\rho}{8\beta^2} \end{bmatrix}$$

$$\Lambda_{3,q}^{\cdot\pm\cdot} = \left\langle \Psi_3, v_y \boldsymbol{\Upsilon}_{q}^{\cdot\pm\cdot} \right\rangle = \frac{(\gamma-1)}{\gamma} \frac{\kappa}{pR} \left[0, \frac{B_2^{\mp}\rho}{4\sqrt{\pi}\beta^{5/2}}, 0 \right]$$

$$\Lambda_{4,\tau}^{\cdot\pm\cdot} = \left\langle \Psi_4, v_y \boldsymbol{\Upsilon}_{\tau}^{\cdot\pm\cdot} \right\rangle = \frac{\mu}{p} \begin{bmatrix} \frac{B_2^{\mp} u_z(-1+\gamma)\rho}{8\sqrt{\pi}\beta^{3/2}} & 0 & 0 \\ 0 & \frac{B_2^{\mp} u_z(-3+\gamma)\rho}{8\sqrt{\pi}\beta^{3/2}} & \frac{A_2^{\pm}\rho}{8\beta^2} \\ 0 & \frac{A_2^{\pm}\rho}{8\beta^2} & \frac{B_2^{\mp} u_z(-1+\gamma)\rho}{8\sqrt{\pi}\beta^{3/2}} \end{bmatrix}$$

$$\Lambda_{4,q}^{\cdot\pm\cdot} = \left\langle \Psi_4, v_y \boldsymbol{\Upsilon}_{q}^{\cdot\pm\cdot} \right\rangle = \frac{(\gamma-1)}{\gamma} \frac{\kappa}{pR} \left[0, -\frac{B_2^{\mp} u_y u_z \rho}{4\sqrt{\pi}\beta^{3/2}}, \frac{B_2^{\mp}\rho}{8\sqrt{\pi}\beta^{5/2}} \right]$$

$$\Lambda_{5,\tau}^{\cdot\pm\cdot} = \left\langle \Psi_5, v_y \boldsymbol{\Upsilon}_{\tau}^{\cdot\pm\cdot} \right\rangle = \frac{\mu}{p} \begin{bmatrix} -\frac{C_2^{\pm}\rho}{32\sqrt{\pi}\beta^{5/2}} & \frac{A_2^{\pm} u_x \rho}{8\beta^2} & 0 \\ \frac{A_2^{\pm} u_x \rho}{8\beta^2} & -\frac{(-3+\gamma)C_2^{\pm}\rho}{32\sqrt{\pi}\beta^{5/2}(-1+\gamma)} & \frac{A_2^{\pm} u_z}{8\beta^2} \\ 0 & \frac{A_2^{\pm} u_z \rho}{8\beta^2} & -\frac{C_2^{\pm}\rho}{32\sqrt{\pi}\beta^{5/2}} \end{bmatrix}$$

$$\Lambda_{5,q}^{\cdot\pm\cdot} = \left\langle \Psi_5, v_y \boldsymbol{\Upsilon}_{q}^{\cdot\pm\cdot} \right\rangle = \frac{(\gamma-1)}{\gamma} \frac{\kappa}{pR} \left[\frac{B_2^{\mp} u_x \rho}{8\sqrt{\pi}\beta^{5/2}}, -\frac{\rho(B_2^{\mp} u_y \sqrt{\beta}(3+bxz-\gamma)+2\sqrt{\pi}\gamma A_2^{\pm})}{16\sqrt{\pi}\beta^3(-1+\gamma)}, \frac{B_2^{\mp} u_z \rho}{8\sqrt{\pi}\beta^{5/2}} \right]$$

D.2.3 Z Split macroscopic tensors, $\Lambda_{ij}^{\cdot\cdot\pm}$

$$
\begin{aligned}
\boldsymbol{\Lambda}_{\tau}^{\cdot\cdot+} &= \left\langle \boldsymbol{\Psi}, v_z \boldsymbol{\Upsilon}_{\tau}^{\cdot\cdot+} \right\rangle \\
&\equiv \int_0^{+\infty}\int_0^{+\infty}\int_{-\infty}^{+\infty}\int_{-\infty}^{+\infty} \boldsymbol{\Psi} v_y \boldsymbol{\Upsilon}_{\tau} dv_x dv_y dv_z d\mathbb{I} \\
\boldsymbol{\Lambda}_{\tau}^{\cdot\cdot-} &= \left\langle \boldsymbol{\Psi}, v_z \boldsymbol{\Upsilon}_{\tau}^{\cdot\cdot-} \right\rangle \\
&\equiv \int_0^{+\infty}\int_{-\infty}^{0}\int_{-\infty}^{+\infty}\int_{-\infty}^{+\infty} \boldsymbol{\Psi} v_y \boldsymbol{\Upsilon}_{\tau} dv_x dv_y dv_z d\mathbb{I} \\
\boldsymbol{\Lambda}_{q}^{\cdot\cdot+} &= \left\langle \boldsymbol{\Psi}, v_z \boldsymbol{\Upsilon}_{q}^{\cdot\cdot+} \right\rangle \\
&\equiv \int_0^{+\infty}\int_0^{+\infty}\int_{-\infty}^{+\infty}\int_{-\infty}^{+\infty} \boldsymbol{\Psi} v_y \boldsymbol{\Upsilon}_{q} dv_x dv_y dv_z d\mathbb{I} \\
\boldsymbol{\Lambda}_{q}^{\cdot\cdot-} &= \left\langle \boldsymbol{\Psi}, v_z \boldsymbol{\Upsilon}_{q}^{\cdot\cdot-} \right\rangle \\
&\equiv \int_0^{+\infty}\int_{-\infty}^{0}\int_{-\infty}^{+\infty}\int_{-\infty}^{+\infty} \boldsymbol{\Psi} v_y \boldsymbol{\Upsilon}_{q} dv_x dv_y dv_z d\mathbb{I}
\end{aligned}
$$

$$
\Lambda_{1,\tau}^{\cdot\cdot\pm} = \left\langle \Psi_1, v_z \boldsymbol{\Upsilon}_{\tau}^{\cdot\cdot\pm} \right\rangle = \frac{\mu}{p}\begin{bmatrix} \frac{B_3^{\mp}(-1+\gamma)\rho}{8\sqrt{\pi}\beta^{3/2}} & 0 & 0 \\ 0 & \frac{B_3^{\mp}(-1+\gamma)\rho}{8\sqrt{\pi}\beta^{3/2}} & 0 \\ 0 & 0 & \frac{B_3^{\mp}(-3+\gamma)\rho}{8\sqrt{\pi}\beta^{3/2}} \end{bmatrix}
$$

$$
\Lambda_{1,q}^{\cdot\cdot\pm} = \left\langle \Psi_1, v_z \boldsymbol{\Upsilon}_{q}^{\cdot\cdot\pm} \right\rangle = \frac{(\gamma-1)}{\gamma}\frac{\kappa}{pR}\left[0, 0, -\frac{B_3^{\mp} u_z \rho}{4\sqrt{\pi}\beta^{3/2}}\right]
$$

$$
\Lambda_{2,\tau}^{\cdot\cdot\pm} = \left\langle \Psi_2, v_z \boldsymbol{\Upsilon}_{\tau}^{\cdot\cdot\pm} \right\rangle = \frac{\mu}{p}\begin{bmatrix} \frac{B_3^{\mp} u_x(-1+\gamma)\rho}{8\sqrt{\pi}\beta^{3/2}} & 0 & \frac{A_3^{\pm}\rho}{8\beta^2} \\ 0 & \frac{B_3^{\mp} u_x(-1+\gamma)\rho}{8\sqrt{\pi}\beta^{3/2}} & 0 \\ \frac{A_3^{\pm}\rho}{8\beta^2} & 0 & \frac{B_3^{\mp} u_x(-3+\gamma)\rho}{8\sqrt{\pi}\beta^{3/2}} \end{bmatrix}
$$

$$
\Lambda_{2,q}^{\cdot\cdot\pm} = \left\langle \Psi_2, v_z \boldsymbol{\Upsilon}_{q}^{\cdot\cdot\pm} \right\rangle = \frac{(\gamma-1)}{\gamma}\frac{\kappa}{pR}\left[\frac{B_3^{\mp}\rho}{8\sqrt{\pi}\beta^{5/2}}, 0, -\frac{B_3^{\mp} u_x u_z \rho}{4\sqrt{\pi}\beta^{3/2}}\right]
$$

$$
\Lambda_{3,\tau}^{\cdot\cdot\pm} = \left\langle \Psi_3, v_z \boldsymbol{\Upsilon}_{\tau}^{\cdot\cdot\pm} \right\rangle = \frac{\mu}{p}\begin{bmatrix} \frac{B_3^{\mp} u_y(-1+\gamma)\rho}{8\sqrt{\pi}\beta^{3/2}} & 0 & 0 \\ 0 & \frac{B_3^{\mp} u_y(-1+\gamma)\rho}{8\sqrt{\pi}\beta^{3/2}} & \frac{A_3^{\pm}\rho}{8\beta^2} \\ 0 & \frac{A_3^{\pm}\rho}{8\beta^2} & \frac{B_3^{\mp} u_y(-3+\gamma)\rho}{8\sqrt{\pi}\beta^{3/2}} \end{bmatrix}
$$

$$
\Lambda_{3,q}^{\cdot\cdot\pm} = \left\langle \Psi_3, v_z \boldsymbol{\Upsilon}_{q}^{\cdot\cdot\pm} \right\rangle = \frac{(\gamma-1)}{\gamma}\frac{\kappa}{pR}\left[0, \frac{B_2^{\mp}\rho}{8\sqrt{\pi}\beta^{5/2}}, -\frac{B_2^{\mp} u_y u_z \rho}{4\sqrt{\pi}\beta^{3/2}}\right]
$$

$$
\Lambda_{4,\tau}^{\cdot\cdot\pm} = \left\langle \Psi_4, v_z \boldsymbol{\Upsilon}_{\tau}^{\cdot\cdot\pm} \right\rangle = \frac{\mu}{p}\begin{bmatrix} -\frac{A_3^{\pm}(-1+\gamma)\rho}{8\beta^2} & 0 & 0 \\ 0 & -\frac{A_3^{\pm}(-1+\gamma)\rho}{8\beta^2} & 0 \\ 0 & 0 & -\frac{A_3^{\pm}(-3+\gamma)\rho}{8\beta^2} \end{bmatrix}
$$

$$\Lambda_{4,q}^{\cdot\cdot\pm} = \left\langle \Psi_4, v_z \boldsymbol{\Upsilon}_q^{\cdot\cdot\pm} \right\rangle = \frac{(\gamma-1)}{\gamma}\frac{\kappa}{pR}\left[0, 0, \frac{B_3^{\mp}\rho}{4\sqrt{\pi}\beta^{5/2}}\right]$$

$$\Lambda_{5,\tau}^{\cdot\cdot\pm} = \left\langle \Psi_5, v_z \boldsymbol{\Upsilon}_\tau^{\cdot\cdot\pm} \right\rangle = \frac{\mu}{p}\begin{bmatrix} -\frac{C_3^{\pm}\rho}{32\sqrt{\pi}\beta^{5/2}} & 0 & \frac{A_3^{\pm}u_x\rho}{8\beta^2} \\ 0 & -\frac{C_3^{\pm}\rho}{32\sqrt{\pi}\beta^{5/2}} & \frac{u_y\rho A_3^{\pm}}{8\beta^2} \\ \frac{A_3^{\pm}u_x\rho}{8\beta^2} & \frac{u_y\rho A_3^{\pm}}{8\beta^2} & -\frac{C_3^{\pm}(-3+\gamma)\rho}{32\sqrt{\pi}\beta^{5/2}(-1+\gamma)} \end{bmatrix}$$

$$\Lambda_{5,q}^{\cdot\cdot\pm} = \left\langle \Psi_5, v_z \boldsymbol{\Upsilon}_q^{\cdot\cdot\pm} \right\rangle = \frac{(\gamma-1)}{\gamma}\frac{\kappa}{pR}\left[\frac{B_3^{\mp}u_x\rho}{8\sqrt{\pi}\beta^{5/2}}, \frac{B_3^{\mp}u_y\rho}{8\sqrt{\pi}\beta^{5/2}}, -\frac{\rho(B_3^{\mp}u_z\sqrt{\beta}(3+bxy-\gamma)+2\sqrt{\pi}\gamma A_3^{\pm})}{16\sqrt{\pi}\beta^3(-1+\gamma)}\right]$$

where
$byz = 2(u_y^2 + u_z^2)\beta(-1+\gamma)$
$C_1^{\pm} = 4A_1^{\pm}\sqrt{\pi}ux\sqrt{\beta}(-1+\gamma) + B_1^{\mp}(1-2byz-3\gamma)$
$bxz = 2(u_x^2 + u_z^2)\beta(-1+\gamma)$
$C_2^{\pm} = 4A_2^{\pm}\sqrt{\pi}uy\sqrt{\beta}(-1+\gamma) + B_2^{\mp}(1-2bxz-3\gamma)$
$bxy = 2(u_x^2 + u_y^2)\beta(-1+\gamma)$
$C_3^{\pm} = 4A_3^{\pm}\sqrt{\pi}uz\sqrt{\beta}(-1+\gamma) + B_3^{\mp}(1-2bxy-3\gamma)$

D.3 KFVS Split Fluxes

The inviscid part of the flux component, $\boldsymbol{GX}_I^{\pm}$ for 2D is defined as

$$\boldsymbol{GX}_I^{+} = \left\langle \boldsymbol{\Psi}, v_x f_0^{+\cdot} \right\rangle = \int_0^{+\infty}\int_{-\infty}^{+\infty}\int_0^{+\infty} \boldsymbol{\Psi} v_x f_0 dv_x dv_y d\mathbb{I}$$

$$\boldsymbol{GX}_I^{-} = \left\langle \boldsymbol{\Psi}, v_x f_0^{-\cdot} \right\rangle = \int_0^{+\infty}\int_{-\infty}^{+\infty}\int_{-\infty}^{0} \boldsymbol{\Psi} v_x f_0 dv_x dv_y d\mathbb{I}$$

The expression of inviscid flux $\boldsymbol{GY}_I^{\pm}$ for 2D is given as

$$\boldsymbol{GY}_I^{+} = \left\langle \boldsymbol{\Psi}, v_y f_0^{\cdot+} \right\rangle = \int_0^{+\infty}\int_0^{+\infty}\int_{-\infty}^{+\infty} \boldsymbol{\Psi} v_y f_0 dv_x dv_y d\mathbb{I}$$

$$\boldsymbol{GY}_I^{-} = \left\langle \boldsymbol{\Psi}, v_y f_0^{\cdot-} \right\rangle = \int_0^{+\infty}\int_{-\infty}^{0}\int_{-\infty}^{+\infty} \boldsymbol{\Psi} v_y f_0 dv_x dv_y d\mathbb{I}$$

The viscous part of the flux component, $\boldsymbol{GX}_V^{\pm}$ and $\boldsymbol{GY}_V^{\pm}$ are defined as

$$\begin{aligned}
\boldsymbol{GX}_V^{\pm} &= -\textstyle\sum_j \boldsymbol{\Lambda}_j^{\pm\cdot} \odot \boldsymbol{X}_j = -(\boldsymbol{\Lambda}_\tau^{\pm\cdot} : \boldsymbol{X}_\tau + \boldsymbol{\Lambda}_q^{\pm\cdot} \cdot \boldsymbol{X}_q) \\
\boldsymbol{GY}_V^{\pm} &= -\textstyle\sum_j \boldsymbol{\Lambda}_j^{\cdot\pm} \odot \boldsymbol{X}_j = -(\boldsymbol{\Lambda}_\tau^{\cdot\pm} : \boldsymbol{X}_\tau + \boldsymbol{\Lambda}_q^{\cdot\pm} \cdot \boldsymbol{X}_q)
\end{aligned}$$

Conjugate thermodynamic forces, $\boldsymbol{X_\tau}$ and $\boldsymbol{X_q}$ are

$$\boldsymbol{X}_\tau \equiv \begin{bmatrix} 2\beta\frac{\partial u_x}{\partial x} & \beta(\frac{\partial u_x}{\partial y} + \frac{\partial u_y}{\partial x}) \\ \beta(\frac{\partial u_x}{\partial y} + \frac{\partial u_y}{\partial x}) & 2\beta\frac{\partial u_y}{\partial y} \end{bmatrix}$$

$$\boldsymbol{X}_q \equiv \left[-2R\beta^2\frac{\partial T}{\partial x}, -2R\beta^2\frac{\partial T}{\partial y}\right]$$

The inviscid part of the split flux component, $\boldsymbol{GX}_I^{\pm}$ $\boldsymbol{GY}_I^{\pm}$ and $\boldsymbol{GZ}_I^{\pm}$ are evaluated as

$$\begin{aligned}
\boldsymbol{GX}_I^{+} &= \left\langle \boldsymbol{\Psi}, v_x f_0^{+\cdot\cdot} \right\rangle = \int_0^{+\infty}\int_{-\infty}^{+\infty}\int_{-\infty}^{+\infty}\int_0^{+\infty} \boldsymbol{\Psi} v_x f_0 dv_x dv_y dv_z d\mathbb{I} \\
\boldsymbol{GX}_I^{-} &= \left\langle \boldsymbol{\Psi}, v_x f_0^{-\cdot\cdot} \right\rangle = \int_0^{+\infty}\int_{-\infty}^{+\infty}\int_{-\infty}^{+\infty}\int_{-\infty}^{0} \boldsymbol{\Psi} v_x f_0 dv_x dv_y dv_z d\mathbb{I} \\
\boldsymbol{GY}_I^{+} &= \left\langle \boldsymbol{\Psi}, v_y f_0^{\cdot+\cdot} \right\rangle = \int_0^{+\infty}\int_{-\infty}^{+\infty}\int_0^{+\infty}\int_{-\infty}^{+\infty} \boldsymbol{\Psi} v_y f_0 dv_x dv_y dv_z d\mathbb{I} \\
\boldsymbol{GY}_I^{-} &= \left\langle \boldsymbol{\Psi}, v_y f_0^{\cdot-\cdot} \right\rangle = \int_0^{+\infty}\int_{-\infty}^{+\infty}\int_{-\infty}^{0}\int_{-\infty}^{+\infty} \boldsymbol{\Psi} v_y f_0 dv_x dv_y dv_z d\mathbb{I} \\
\boldsymbol{GZ}_I^{+} &= \left\langle \boldsymbol{\Psi}, v_z f_0^{\cdot\cdot+} \right\rangle = \int_0^{+\infty}\int_0^{+\infty}\int_{-\infty}^{+\infty}\int_{-\infty}^{+\infty} \boldsymbol{\Psi} v_z f_0 dv_x dv_y dv_z d\mathbb{I} \\
\boldsymbol{GZ}_I^{-} &= \left\langle \boldsymbol{\Psi}, v_z f_0^{\cdot\cdot-} \right\rangle = \int_0^{+\infty}\int_{-\infty}^{0}\int_{-\infty}^{+\infty}\int_{-\infty}^{+\infty} \boldsymbol{\Psi} v_z f_0 dv_x dv_y dv_z d\mathbb{I}
\end{aligned}$$

The viscous part of the flux component, $\boldsymbol{GX}_V^{\pm}$, $\boldsymbol{GY}_V^{\pm}$ and $\boldsymbol{GZ}_V^{\pm}$ are defined as

$$\begin{aligned}
\boldsymbol{GX}_V^{\pm} &= -\textstyle\sum_j \boldsymbol{\Lambda}_j^{\pm\cdot\cdot} \odot \boldsymbol{X}_j = -(\boldsymbol{\Lambda}_\tau^{\pm\cdot\cdot} : \boldsymbol{X}_\tau + \boldsymbol{\Lambda}_q^{\pm\cdot\cdot} \cdot \boldsymbol{X}_q) \\
\boldsymbol{GY}_V^{\pm} &= -\textstyle\sum_j \boldsymbol{\Lambda}_j^{\cdot\pm\cdot} \odot \boldsymbol{X}_j = -(\boldsymbol{\Lambda}_\tau^{\cdot\pm\cdot} : \boldsymbol{X}_\tau + \boldsymbol{\Lambda}_q^{\cdot\pm\cdot} \cdot \boldsymbol{X}_q) \\
\boldsymbol{GZ}_V^{\pm} &= -\textstyle\sum_j \boldsymbol{\Lambda}_j^{\cdot\cdot\pm} \odot \boldsymbol{X}_j = -(\boldsymbol{\Lambda}_\tau^{\cdot\cdot\pm} : \boldsymbol{X}_\tau + \boldsymbol{\Lambda}_q^{\cdot\cdot\pm} \cdot \boldsymbol{X}_q)
\end{aligned}$$

The thermodynamic force associated with shear stress tensor

$$\boldsymbol{X}_\tau \equiv \beta \begin{bmatrix} 2\frac{\partial u_x}{\partial x} & (\frac{\partial u_x}{\partial y} + \frac{\partial u_y}{\partial x}) & (\frac{\partial u_x}{\partial z} + \frac{\partial u_z}{\partial x}) \\ (\frac{\partial u_x}{\partial y} + \frac{\partial u_y}{\partial x}) & 2\frac{\partial u_y}{\partial y} & (\frac{\partial u_y}{\partial y} + \frac{\partial u_y}{\partial z}) \\ (\frac{\partial u_x}{\partial z} + \frac{\partial u_z}{\partial x}) & (\frac{\partial u_y}{\partial y} + \frac{\partial u_y}{\partial z}) & 2\frac{\partial u_y}{\partial z} \end{bmatrix}$$

The thermodynamic force associated with heat vector is

$$\boldsymbol{X}_q \equiv -2R\beta^2 \begin{bmatrix} \frac{\partial T}{\partial x} & \frac{\partial T}{\partial y} & \frac{\partial T}{\partial z} \end{bmatrix}$$

D.3.1 Expressions for the 2-D KFVS Split Fluxes

The x-component of the inviscid and viscous split fluxes in 2-D are given by

$$GX_I(1)^{\pm} = \frac{\rho}{2\sqrt{\beta}}\left(\frac{B_1^{\pm}}{\sqrt{\pi}} + s_x A_1^{\pm}\right)$$
$$GX_V(1)^{\pm} = -\frac{\rho}{4p\sqrt{\beta}}\frac{B_1^{\pm}}{\sqrt{\pi}}\left(2\sqrt{\beta}\eta q_x s_x + \tau_{xx}\right)$$

$$GX_I(2)^{\pm} = \frac{\rho}{2\beta}\left(\frac{B_1^{\pm}}{\sqrt{\pi}} s_x + \frac{(1+2s_x^2)}{2} A_1^{\pm}\right)$$
$$GX_V(2)^{\pm} = \frac{\rho}{4p\beta}\left(\frac{B_1^{\pm}}{\sqrt{\pi}} 2\sqrt{\beta}\eta q_x - A_1^{\pm}\tau_{xx}\right)$$

$$GX_I(3)^{\pm} = \frac{\rho}{2\beta} s_y \left(\frac{B_1^{\pm}}{\sqrt{\pi}} + s_x A_1^{\pm}\right)$$
$$GX_V(3)^{\pm} = \frac{\rho}{4p\beta}\left(\frac{B_1^{\pm}}{\sqrt{\pi}}\left(\sqrt{\beta}\eta(q_y - 2q_x s_x s_y) - s_y\tau_{xx}\right) - A_1^{\pm}\tau_{xy}\right)$$
$$GX_I(4)^{\pm} = \frac{\rho}{8\beta^{3/2}}\left(\frac{B_1^{\pm}}{\sqrt{\pi}}\frac{(1+\gamma+ds)}{(-1+\gamma)} + s_x\frac{(2\gamma+ds)}{(-1+\gamma)} A_1^{\pm}\right)$$
$$GX_V(4)^{\pm} = \frac{\rho}{16p\beta^{3/2}}\begin{pmatrix} \frac{B_1^{\pm}}{\sqrt{\pi}}\left(4\sqrt{\beta}\eta q_y s_y + 2\sqrt{\beta} q_x s_x \frac{(-3+\gamma-dy)}{\gamma} + \frac{(1-3\gamma-dy)}{-1+\gamma}\tau_{xx}\right) \\ +4(\sqrt{\beta}q_x - s_x\tau_{xx} - s_y\tau_{xy})A_1^{\pm} \end{pmatrix}$$

The y-component of the inviscid and viscous split fluxes in 2-D are given by

$$GY_I(1)^{\pm} = \frac{\rho}{2\sqrt{\beta}}\left(\frac{B_2^{\pm}}{\sqrt{\pi}} + s_y A_2^{\pm}\right)$$
$$GY_V(1)^{\pm} = -\frac{\rho}{4p\sqrt{\beta}}\frac{B_2^{\pm}}{\sqrt{\pi}}\left(2\sqrt{\beta}\eta q_y s_y + \tau_{yy}\right)$$

$$GY_I(2)^{\pm} = \frac{\rho}{2\beta} s_x \left(\frac{B_2^{\pm}}{\sqrt{\pi}} + s_y A_2^{\pm}\right)$$
$$GY_V(2)^{\pm} = \frac{\rho}{4p\beta}\left(\frac{B_2^{\pm}}{\sqrt{\pi}}\left(\sqrt{\beta}\eta(q_x - 2q_y s_x s_y) - s_x\tau_{yy}\right) - A_2^{\pm}\tau_{xy}\right)$$
$$GY_I(3)^{\pm} = \frac{\rho}{2\beta}\left(\frac{B_2^{\pm}}{\sqrt{\pi}} s_y + \frac{(1+2s_y^2)}{2} A_2^{\pm}\right)$$
$$GY_V(3)^{\pm} = \frac{\rho}{4p\beta}\left(\frac{B_2^{\pm}}{\sqrt{\pi}} 2\sqrt{\beta}\eta q_y - A_2^{\pm}\tau_{yy}\right)$$

$$GY_I(4)^{\pm} = \frac{\rho}{8\beta^{3/2}}\left(\frac{B_2^{\pm}}{\sqrt{\pi}}\frac{(1+\gamma+ds)}{(-1+\gamma)} + s_y\frac{(2\gamma+ds)}{(-1+\gamma)} A_2^{\pm}\right)$$
$$GY_V(4)^{\pm} = \frac{\rho}{16p\beta^{3/2}}\begin{pmatrix} \frac{B_2^{\pm}}{\sqrt{\pi}}\left(4\sqrt{\beta}\eta q_x s_x + 2\sqrt{\beta} q_y s_y \frac{(-3+\gamma-dx)}{\gamma} + \frac{(1-3\gamma-dx)}{-1+\gamma}\tau_{yy}\right) \\ +4(\sqrt{\beta}q_y - s_x\tau_{xy} - s_y\tau_{yy})A_2^{\pm} \end{pmatrix}$$

where

$$s_x = \sqrt{\beta}u_x$$
$$s_y = \sqrt{\beta}u_y$$
$$dx = 2(\gamma - 1)s_x^2$$
$$dy = 2(\gamma - 1)s_y^2$$

$ds = 2(\gamma - 1)(s_x^2 + s_y^2)$
$\eta = (\gamma - 1)/\gamma$
$B_1^{\pm} = \pm Exp[-s_x^2]$
$B_2^{\pm} = \pm Exp[-s_y^2]$
$A_1^{\pm} = 1 \pm Erf[s_x]$
$A_2^{\pm} = 1 \pm Erf[s_y]$

D.3.2 Expressions for the 2-D KFVS Wall Split Fluxes

The x-component of the wall split fluxes in 2-D are given by
$GX_I(1)^{\pm -} = \frac{\rho}{4\sqrt{\beta}} A_2^- \left(\frac{B_1^{\pm}}{\sqrt{\pi}} + \sqrt{\beta} u_x A_1^{\pm} \right)$

$$GX_V(1)^{\pm -} = \frac{\rho}{8p\sqrt{\beta}} \begin{pmatrix} \frac{B_1^{\pm}}{\sqrt{\pi}} \begin{pmatrix} -2\sqrt{\beta}\frac{B_2^{\pm}}{\sqrt{\pi}} u_y (2\beta\eta q_y u_y + \tau_{yy}) \\ -(2\beta\eta q_x u_x + \tau_{xx}) A_2^- \end{pmatrix} \\ +2\frac{B_2^{\pm}}{\sqrt{\pi}} \begin{pmatrix} \beta\eta q_y u_x (1 - 2\beta u_y^2) + \tau_{xy} \\ +\beta u_y (\eta q_x - u_x \tau_{yy}) \end{pmatrix} A_1^{\pm} \end{pmatrix}$$

$GX_I(2)^{\pm -} = \frac{\rho}{8\beta} A_2^- \left(\frac{B_1^{\pm}}{\sqrt{\pi}} 2\sqrt{\beta} u_x + (1 + 2\beta u_x^2) A_1^{\pm} \right)$

$$GX_V(2)^{\pm -} = \frac{\rho}{8p\beta} \begin{pmatrix} 2\frac{B_1^{\pm}}{\sqrt{\pi}} \begin{pmatrix} \frac{B_2^{\pm}}{\sqrt{\pi}} (\beta\eta q_y u_x (1 - 2\beta u_y^2) + 2\tau_{xy} + \beta u_y (2\eta q_x - u_x \tau_{yy})) \\ +\sqrt{\beta}\eta q_x A_2^- \end{pmatrix} \\ + \begin{pmatrix} -\sqrt{\beta}\frac{B_2^{\pm}}{\sqrt{\pi}} \begin{pmatrix} \eta q_y (1 + 2\beta(u_y^2 + u_x^2(-1 + 2\beta u_y^2))) \\ -4u_x(\beta\eta q_x u_y + \tau_{xy}) + (1 + 2\beta u_x^2) u_y \tau_{yy} \end{pmatrix} \\ -\tau_{xx} A_2^- \end{pmatrix} A_1^{\pm} \end{pmatrix}$$

$GX_I(3)^{\pm -} = \frac{\rho}{4\beta} \left(\frac{B_2}{\sqrt{\pi}} - \sqrt{\beta} u_y A_2^- \right) \left(-\frac{B_1^{\pm}}{\sqrt{\pi}} - \sqrt{\beta} u_x A_1^{\pm} \right)$

$$GX_V(3)^{\pm -} = \frac{\rho}{8p\beta} \begin{pmatrix} \frac{B_1^{\pm}}{\sqrt{\pi}} \begin{pmatrix} \frac{B_2^{\pm}}{\sqrt{\pi}} (2\beta\eta(q_x u_x + q_y u_y) + \tau_{xx} + \tau_{yy}) \\ +\sqrt{\beta}(\eta q_y - u_y(2\beta\eta q_x u_x + \tau_{xx})) A_2^- \end{pmatrix} \\ -\left(\sqrt{\beta}\frac{B_2^{\pm}}{\sqrt{\pi}} (\eta q_x - u_x(2\beta\eta q_y u_y + \tau_{yy})) + \tau_{xy} A_2^- \right) A_1^{\pm} \end{pmatrix}$$

$$GX_I(4)^{\pm -} = \frac{\rho}{16\beta^{3/2}} \begin{pmatrix} \frac{B_1^\pm}{\sqrt{\pi}} \left(-\frac{2\sqrt{\beta} B_2 u_y}{\sqrt{\pi}} + \frac{(1+du+\gamma)A_2^-}{-1+\gamma} \right) \\ + \left(-\frac{2\beta B_2 u_x u_y}{\sqrt{\pi}} + \frac{\sqrt{\beta}(du+2\gamma)u_x A_2^-}{-1+\gamma} \right) A_1^\pm \end{pmatrix}$$

$$GX_V(4)^{\pm -} = \frac{\rho}{32p\beta^{3/2}} \begin{pmatrix} \frac{B_1^\pm}{\sqrt{\pi}} \begin{pmatrix} 2\sqrt{\beta}\frac{B_2^\pm}{\sqrt{\pi}} \begin{pmatrix} \frac{q_y(-4\gamma+dx+2\beta(-2-dx)u_y^2)}{\gamma} \\ +(u_y(8\beta\eta q_x u_x + \tau_{xx}) + 6u_x\tau_{xy}) \\ -\frac{(2+dx)u_y\tau_{yy}}{-1+\gamma} \end{pmatrix} \\ + \begin{pmatrix} 4\beta\eta q_y u_y + \frac{2\beta q_x u_x(-3+\gamma-dy)}{\gamma} \\ +\frac{(1-3\gamma-dy)\tau_{xx}}{-1+\gamma} \end{pmatrix} A_2^- \end{pmatrix} \\ +2 \begin{pmatrix} -\frac{B_2^\pm}{\sqrt{\pi}} \begin{pmatrix} -\frac{\beta q_x(1+\gamma+3dx)u_y}{\gamma} \\ +\frac{\beta q_y u_x(-1+3\gamma-dx+(2\beta(1+\gamma)+2\beta dx)u_y^2)}{\gamma} \\ +\frac{(1-3\gamma-3dx)\tau_{xy}+\beta u_x(1+\gamma+dx)u_y\tau_{yy}}{-1+\gamma} \end{pmatrix} \\ +2\sqrt{\beta}(q_x - (u_x\tau_{xx} + u_y\tau_{xy}))A_2^- \end{pmatrix} A_1^\pm \end{pmatrix}$$

where
$dx = 2\beta(\gamma-1)u_x^2$
$dy = 2\beta(\gamma-1)u_y^2$
$du = 2u^2\beta(\gamma-1)$
$\eta = (\gamma-1)/\gamma$

D.3.3 Expressions for the 3-D KFVS Split Fluxes

The x-component of the inviscid and viscous split fluxes in 3-D are given by

$GX_I(1)^\pm = \frac{\rho}{2\sqrt{\beta}}(\frac{B_1^\pm}{\sqrt{\pi}} + s_x A_1^\pm)$
$GX_V(1)^\pm = -\frac{\rho}{4p\sqrt{\beta}}\frac{B_1^\pm}{\sqrt{\pi}}(2\sqrt{\beta}\eta q_x s_x + \tau_{xx})$

$GX_I(2)^\pm = \frac{\rho}{2\beta}(\frac{B_1^\pm}{\sqrt{\pi}} s_x + \frac{(1+2s_x^2)}{2} A_1^\pm)$
$GX_V(2)^\pm = -\frac{\rho}{4p\beta}(-2\sqrt{\beta}\eta q_x \frac{B_1^\pm}{\sqrt{\pi}} + \tau_{xx} A_1^\pm)$

$GX_I(3)^\pm = \frac{\rho}{2\beta}(\frac{B_1^\pm}{\sqrt{\pi}} s_y + s_x s_y A_1^\pm)$
$GX_V(3)^\pm = \frac{\rho}{4p\beta}(\frac{B_1^\pm}{\sqrt{\pi}}(\sqrt{\beta}\eta q_y - s_y(2\sqrt{\beta}\eta q_x s_x + \tau_{xx})) - \tau_{xy} A_1^\pm)$

$GX_I(4)^\pm = \frac{\rho}{2\beta}(\frac{B_1^\pm}{\sqrt{\pi}} s_z + s_x s_z A_1^\pm)$
$GX_V(4)^\pm 4 = \frac{\rho}{4p\beta}(\frac{B_1^\pm}{\sqrt{\pi}}(\sqrt{\beta}\eta q_z - s_z(2\sqrt{\beta}\eta q_x s_x + \tau_{xx})) - \tau_{xz} A_1^\pm)$

$$GX_I(5)^{\pm} = \frac{\rho}{8\beta^{3/2}}\left(\frac{(1+\gamma+du)}{(-1+\gamma)}\frac{B_1^{\pm}}{\sqrt{\pi}} + \frac{(2\gamma+du)}{(-1+\gamma)}s_x A_1^{\pm}\right)$$

$$GX_V(5)^{\pm}5 = \frac{\rho}{16p\beta^{3/2}}\left(\begin{array}{l} \frac{B_1^{\pm}}{\sqrt{\pi}}\left(\begin{array}{l} 4(\sqrt{\beta}\eta q_y s_y + \sqrt{\beta}\eta q_z s_z) \\ -2\sqrt{\beta}\eta q_x s_x\frac{(3-\gamma+dy+dz)}{(-1+\gamma)} - \frac{(-1+3\gamma+dy+dz)}{(-1+\gamma)}\tau_{xx}\end{array}\right) \\ +4(\sqrt{\beta}q_x - (s_x\tau_{xx} + s_y\tau_{xy} + s_z\tau_{xz}))A_1^{\pm}\end{array}\right)$$

The y-component of the inviscid and viscous split fluxes in 3-D are given by

$$GY_I(1)^{\pm} = \frac{\rho}{2\sqrt{\beta}}\left(\frac{B_2^{\pm}}{\sqrt{\pi}} + s_y A_2^{\pm}\right)$$

$$GY_V(1)^{\pm} = -\frac{\rho}{4p\sqrt{\beta}}\frac{B_2^{\pm}}{\sqrt{\pi}}(2\sqrt{\beta}\eta q_y s_y + \tau_{yy})$$

$$GY_I(2)^{\pm} = \frac{\rho}{2\beta}\left(\frac{B_2^{\pm}}{\sqrt{\pi}}s_x + s_x s_y A_2^{\pm}\right)$$

$$GY_V(2)^{\pm} = -\frac{\rho}{4p\beta}(\sqrt{\beta}\frac{B_2^{\pm}}{\sqrt{\pi}}(-\eta q_x + u_x(2\sqrt{\beta}\eta q_y s_y + \tau_{yy})) + \tau_{xy}A_2^{\pm})$$

$$GY_I(3)^{\pm} = \frac{\rho}{2\beta}\left(\frac{B_2^{\pm}}{\sqrt{\pi}}s_y + \frac{(1+2s_y^2)}{2}A_2^{\pm}\right)$$

$$GY_V(3)^{\pm} = \frac{\rho}{4p\beta}(2\sqrt{\beta}\eta q_y\frac{B_2^{\pm}}{\sqrt{\pi}} - \tau_{yy}A_2^{\pm})$$

$$GY_I(4)^{\pm} = \frac{\rho}{2\beta}\left(\frac{B_2^{\pm}}{\sqrt{\pi}}s_z + s_z s_y A_2^{\pm}\right)$$

$$GY_V(4)^{\pm} = -\frac{\rho}{4p\beta}(\frac{B_2^{\pm}}{\sqrt{\pi}}(-\sqrt{\beta}\eta q_z + s_z(2\sqrt{\beta}\eta q_y s_y + \tau_{yy})) + \tau_{yz}A_2^{\pm})$$

$$GY_I(5)^{\pm} = \frac{\rho}{8\beta^{3/2}}\left(\frac{(1+\gamma+du)}{(-1+\gamma)}\frac{B_2^{\pm}}{\sqrt{\pi}} + \frac{(2\gamma+du)}{(-1+\gamma)}s_y A_2^{\pm}\right)$$

$$GY_V(5)^{\pm} = \frac{\rho}{16p\beta^{3/2}}\left(\begin{array}{l} \frac{B_2^{\pm}}{\sqrt{\pi}}\left(\begin{array}{l} 4(\sqrt{\beta}\eta q_x s_x + \sqrt{\beta}\eta q_z s_z) \\ -2\sqrt{\beta}\eta q_y s_y\frac{(3-\gamma+dx+dz)}{(-1+\gamma)} - \frac{(-1+3\gamma+dx+dz)}{(-1+\gamma)}\tau_{yy}\end{array}\right) \\ +4(\sqrt{\beta}q_y - (s_x\tau_{xy} + s_y\tau_{yy} + s_z\tau_{yz}))A_2^{\pm}\end{array}\right)$$

The z-component of the inviscid and viscous split fluxes in 3-D are given by

$$GZ_I(1)^{\pm} = \frac{\rho}{2\sqrt{\beta}}\left(\frac{B_3^{\pm}}{\sqrt{\pi}} + s_z A_3^{\pm}\right)$$

$$GZ_V(1)^{\pm} = -\frac{\rho}{4p\sqrt{\beta}}\frac{B_3^{\pm}}{\sqrt{\pi}}(2\sqrt{\beta}\eta q_z s_z + \tau_{zz})$$

$$GZ_I(2)^{\pm} = \frac{\rho}{2\beta}\left(\frac{B_3^{\pm}}{\sqrt{\pi}}s_x + s_x s_z A_3^{\pm}\right)$$

$$GZ_V(2)^{\pm} = -\frac{\rho}{4p\beta}(\frac{B_3^{\pm}}{\sqrt{\pi}}(-\sqrt{\beta}\eta q_x + s_x(2\sqrt{\beta}\eta q_z s_z + \tau_{zz})) + \tau_{xz}A_3^{\pm})$$

$$GZ_I(3)^{\pm} = \frac{\rho}{2\beta}\left(\frac{B_3^{\pm}}{\sqrt{\pi}}s_y + s_y s_z A_3^{\pm}\right)$$

$$GZ_V(3)^{\pm} = -\frac{\rho}{4p\beta}(\frac{B_3^{\pm}}{\sqrt{\pi}}(-\sqrt{\beta}\eta q_y + s_y(2\sqrt{\beta}\eta q_z s_z + \tau_{zz})) + \tau_{yz}A_3^{\pm})$$

$$GZ_I(4)^{\pm} = \frac{\rho}{2\beta}(\frac{B_3^{\pm}}{\sqrt{\pi}}s_z + \frac{(1+2s_z^2)}{2}A_3^{\pm})$$
$$GZ_V(4)^{\pm} = \frac{\rho}{4p\beta}(2\sqrt{\beta}\eta q_z\frac{B_3^{\pm}}{\sqrt{\pi}} - \tau_{zz}A_3^{\pm})$$

$$GZ_I(5)^{\pm} = \frac{\rho}{8\beta^{3/2}}(\frac{(1+\gamma+du)}{(-1+\gamma)}\frac{B_3^{\pm}}{\sqrt{\pi}} + \frac{(2\gamma+du)}{(-1+\gamma)}s_zA_3^{\pm})$$
$$GZ_V(5)^{\pm} = \frac{\rho}{16p\beta^{3/2}}\begin{pmatrix} \frac{B_3^{\pm}}{\sqrt{\pi}}\begin{pmatrix} 4(\sqrt{\beta}\eta q_x s_x + \sqrt{\beta}\eta q_y s_y) \\ -2\sqrt{\beta}\eta q_z s_z\frac{(3-\gamma+dx+dy)}{(-1+\gamma)} - \frac{(-1+3\gamma+dx+dy)}{(-1+\gamma)}\tau_{zz}\end{pmatrix} \\ +4(\sqrt{\beta}q_z - (s_x\tau_{xz} + s_y\tau_{yz} + s_z\tau_{zz}))A_3^{\pm}\end{pmatrix}$$

where
$\eta = (\gamma - 1)/\gamma$
$s_x = \sqrt{\beta}u_x$
$s_y = \sqrt{\beta}u_y$
$s_z = \sqrt{\beta}u_z$
$u^2 = u_x^2 + u_y^2 + u_z^2$
$ss = \sqrt{\beta}u$
$dyz = 2\beta(\gamma - 1)u_yu_z$
$dxz = 2\beta(\gamma - 1)u_xu_z$
$dx = 2\beta(\gamma - 1)u_x^2$
$dy = 2\beta(\gamma - 1)u_y^2$
$dz = 2\beta(\gamma - 1)u_z^2$
$du = 2\beta(\gamma - 1)u^2$
$B_1^{\pm} = \pm Exp[-s_x^2]$
$B_2^{\pm} = \pm Exp[-s_y^2]$
$B_3^{\pm} = \pm Exp[-s_z^2]$
$A_1^{\pm} = 1 \pm Erf[s_x]$
$A_2^{\pm} = 1 \pm Erf[s_y]$
$A_3^{\pm} = 1 \pm Erf[s_z]$

D.3.4 Expressions for the 3-D KFVS Wall Split Fluxes

The x-component of the inviscid and viscous wall split fluxes in 3-D are given by
$GX_I^{\pm\cdot-}(1) = \frac{\rho}{4\sqrt{\beta}}A_3^{-}\left(\frac{B_1^{\pm}}{\sqrt{\pi}} + u_x\sqrt{\beta}A_1^{\pm}\right)$

$$GX_V^{\pm\cdot-}(1) = \frac{\rho}{8p\sqrt{\beta}} \begin{pmatrix} -\frac{B_1^\pm}{\sqrt{\pi}} \begin{pmatrix} 2\sqrt{\beta}\frac{B_3}{\sqrt{\pi}} u_z(2\beta\eta q_z u_z + \tau_{zz}) \\ +(2\beta\eta q_x u_x + \tau_{xx})A_3^- \end{pmatrix} \\ +2\frac{B_3}{\sqrt{\pi}} \left(\tau_{xz} + \beta \begin{pmatrix} \eta q_z u_x + \eta q_x u_z \\ -2\beta\eta q_z u_x u_z^2 - u_x u_z \tau_{zz} \end{pmatrix} \right) A_1^\pm \end{pmatrix}$$

$$GX_I^{\pm\cdot-}(2) = \frac{\rho}{8\beta} A_3^- \left(\frac{B_1^\pm}{\sqrt{\pi}} 2\sqrt{\beta} u_x + A_1^\pm + 2\beta u_x^2 A_1^\pm \right)$$

$$GX_V^{\pm\cdot-}(2) = \frac{\rho}{8p\beta} \begin{pmatrix} \frac{B_1^\pm}{\sqrt{\pi}} \begin{pmatrix} 2\frac{B_3}{\sqrt{\pi}}(2\tau_{xz} + \beta(\eta q_z u_x + 2\eta q_x u_z - 2\beta\eta q_z u_x u_z^2 - u_x u_z \tau_{zz})) \\ +2\sqrt{\beta}\eta q_x A_3^- \end{pmatrix} \\ + \begin{pmatrix} \sqrt{\beta}\frac{B_3}{\sqrt{\pi}} \begin{pmatrix} \eta \begin{pmatrix} 4\beta q_x u_x u_z \\ +q_z(-1 + 2\beta u_x^2 - 2\beta(1 + 2\beta u_x^2)u_z^2) \end{pmatrix} \\ +4u_x\tau_{xz} - (1 + 2\beta u_x^2)u_z\tau_{zz} \end{pmatrix} \\ -\tau_{xx}A_3^- \end{pmatrix} A_1^\pm \end{pmatrix}$$

$$GX_I^{\pm\cdot-}(3) = \frac{\rho}{4\sqrt{\beta}} u_y A_3^- \left(\frac{B_1^\pm}{\sqrt{\pi}} + u_x\sqrt{\beta} A_1^\pm \right)$$

$$GX_V^{\pm\cdot-}(3) = \frac{\rho}{8p\beta} \begin{pmatrix} \frac{B_1^\pm}{\sqrt{\pi}} \begin{pmatrix} 2\frac{B_3}{\sqrt{\pi}}(\tau_{yz} + \beta u_z(\eta q_y - 2\beta\eta q_z u_y u_z - u_y\tau_{zz})) \\ +\sqrt{\beta}(\eta q_y - u_y(2\beta\eta q_x u_x + \tau_{xx}))A_3^- \end{pmatrix} \\ + \begin{pmatrix} 2\sqrt{\beta}\frac{B_3}{\sqrt{\pi}} \begin{pmatrix} u_y\tau_{xz} + u_x\tau_{yz} \\ +\beta \begin{pmatrix} \eta \begin{pmatrix} q_z u_x u_y + q_y u_x u_z \\ +q_x u_y u_z - 2\beta q_z u_x u_y u_z^2 \end{pmatrix} \\ -u_x u_y u_z \tau_{zz} \end{pmatrix} \end{pmatrix} \\ -\tau_{xy}A_3^- \end{pmatrix} A_1^\pm \end{pmatrix}$$

$$GX_I^{\pm\cdot-}(4) = \frac{\rho}{4\beta} \left(-\frac{B_3}{\sqrt{\pi}} + \sqrt{\beta} u_z A_3^- \right) \left(\frac{B_1^\pm}{\sqrt{\pi}} + \sqrt{\beta} u_x A_1^\pm \right)$$

$$GX_V^{\pm\cdot-}(4) = \frac{\rho}{8p\beta} \begin{pmatrix} \frac{B_1^\pm}{\sqrt{\pi}} \begin{pmatrix} \frac{B_3}{\sqrt{\pi}}(2\beta\eta(q_x u_x + q_z u_z) + \tau_{xx} + \tau_{zz}) \\ +\sqrt{\beta}(\eta q_z - u_z(2\beta\eta q_x u_x + \tau_{xx}))A_3^- \end{pmatrix} \\ + \left(\sqrt{\beta}\frac{B_3}{\sqrt{\pi}}(-\eta q_x + 2\beta\eta q_z u_x u_z + u_x\tau_{zz}) - \tau_{xz}A_3^- \right) A_1^\pm \end{pmatrix}$$

$$GX_I^{\pm\cdot-}(5) = \frac{\rho}{16\beta^{3/2}} \begin{pmatrix} (\frac{(1+\gamma)}{(-1+\gamma)} + 2u^2\beta)\frac{B_1^\pm}{\sqrt{\pi}} A_3^- \\ +2\sqrt{\beta}(u^2\beta + \frac{\gamma}{(-1+\gamma)})u_x A_3^- A_1^\pm \\ -2\sqrt{\beta}\frac{B_3}{\sqrt{\pi}} u_z (\frac{B_1^\pm}{\sqrt{\pi}} + \sqrt{\beta}u_x A_1^\pm) \end{pmatrix}$$

$$GX_V^{\pm\cdot-}(5) = \frac{\rho}{32p\beta^{3/2}} \begin{pmatrix} \frac{B_1^\pm}{\sqrt{\pi}} \begin{pmatrix} -2\sqrt{\beta}\frac{B_3}{\sqrt{\pi}} \begin{pmatrix} -8\beta\eta q_x u_x u_z + \frac{q_z(4\gamma - dx + 2\beta(2+dx+dy)u_z^2)}{\gamma} \\ -u_z(\frac{4\beta(-1+\gamma)q_y u_y}{\gamma} + \tau_{xx}) \\ -6u_x\tau_{xz} - 4u_y\tau_{yz} + \frac{(2+dx+dy)u_z\tau_{zz}}{-1+\gamma} \end{pmatrix} \\ - \begin{pmatrix} -\frac{4\beta(-1+\gamma)(q_y u_y + q_z u_z)}{\gamma} + \frac{2\beta q_x u_x(3-\gamma+dy+dz)}{\gamma} \\ +\frac{(-1+3\gamma+dy+dz)\tau_{xx}}{-1+\gamma} \end{pmatrix} A_3^- \end{pmatrix} \\ +2 \begin{pmatrix} -\frac{B_3}{\sqrt{\pi}} \begin{pmatrix} -4\beta^2\eta q_y u_x u_y u_z - \frac{\beta q_x(1+\gamma+3dx+dy)u_z}{\gamma} \\ +\frac{\beta q_z u_x(-1+3\gamma-dx-dy+2\beta(1+\gamma+dx+dy)u_z^2)}{\gamma} \\ +\frac{(1-3\gamma-3dx-dy)\tau_{xz}}{\gamma-1} \\ +\frac{\beta u_x(-4(-1+\gamma)u_y\tau_{yz} + (1+\gamma+dx+dy)u_z\tau_{zz})}{\gamma-1} \end{pmatrix} \\ +2\sqrt{\beta}(q_x - (u_x\tau_{xx} + u_y\tau_{xy} + u_z\tau_{xz}))A_3^- \end{pmatrix} A_1^\pm \end{pmatrix}$$

The y-component of the inviscid and viscous wall split fluxes in 3-D are given by

$$GY_I^{\cdot\pm-}(1) = \frac{\rho}{4\sqrt{\beta}} A_3^- (\frac{B_2^\pm}{\sqrt{\pi}} + u_y\sqrt{\beta}A_2^\pm)$$

$$GY_V^{\cdot\pm-}(1) = \frac{\rho}{8p\sqrt{\beta}} \begin{pmatrix} -\frac{B_2^\pm}{\sqrt{\pi}} \begin{pmatrix} 2\sqrt{\beta}\frac{B_3}{\sqrt{\pi}} u_z(2\beta\eta q_z u_z + \tau_{zz}) \\ +(2\beta\eta q_y u_y + \tau_{yy})A_3^- \end{pmatrix} \\ +2\frac{B_3}{\sqrt{\pi}} \begin{pmatrix} \tau_{yz} + \beta \begin{pmatrix} \eta q_z u_y + \eta q_y u_z \\ -2\beta\eta q_z u_y u_z^2 - u_y u_z \tau_{zz} \end{pmatrix} \end{pmatrix} A_2^\pm \end{pmatrix}$$

$$GY_I^{\cdot\pm-}(2) = \frac{\rho}{4\sqrt{\beta}} u_x A_3^- (\frac{B_2^\pm}{\sqrt{\pi}} + u_y\sqrt{\beta}A_2^\pm)$$

$$GY_V^{\cdot\pm-}(2) = \frac{\rho}{8p\beta} \begin{pmatrix} \frac{B_2^\pm}{\sqrt{\pi}} \begin{pmatrix} 2\frac{B_3}{\sqrt{\pi}}(\tau_{xz} + \beta u_z(\eta(q_x - 2\beta q_z u_x u_z) - u_x\tau_{zz})) \\ +\sqrt{\beta}(\eta(q_x - 2\beta q_y u_x u_y) - u_x\tau_{yy})A_3^- \end{pmatrix} \\ + \begin{pmatrix} -2\sqrt{\beta}\frac{B_3}{\sqrt{\pi}} \begin{pmatrix} -u_y\tau_{xz} - u_x\tau_{yz} \\ +\beta \begin{pmatrix} -\eta \begin{pmatrix} (q_y u_x + q_x u_y)u_z \\ +q_z u_x u_y(1 - 2\beta u_z^2) \end{pmatrix} \\ +u_x u_y u_z \tau_{zz} \end{pmatrix} \end{pmatrix} \\ -\tau_{xy}A_3^- \end{pmatrix} A_2^\pm \end{pmatrix}$$

$$GY_I^{\cdot\pm-}(3) = \tfrac{\rho}{8\beta} A_3^- (\tfrac{B_2^\pm}{\sqrt{\pi}} 2\sqrt{\beta} u_y + (1 + 2\beta u_y^2) A_2^\pm)$$

$$GY_V^{\cdot\pm-}(3) = \tfrac{\rho}{8p\beta} \begin{pmatrix} 2\frac{B_2^\pm}{\sqrt{\pi}} \begin{pmatrix} \frac{B_3}{\sqrt{\pi}} (\beta\eta q_z u_y (1 - 2\beta u_z^2) + 2\tau_{yz} + \beta u_z (2\eta q_y - u_y \tau_{zz})) \\ +\sqrt{\beta}\eta q_y A_3^- \end{pmatrix} \\ - \begin{pmatrix} \sqrt{\beta}\frac{B_3}{\sqrt{\pi}} \begin{pmatrix} \eta q_z (1 + 2\beta(u_z^2 + u_y^2(-1 + 2\beta u_z^2))) \\ -4u_y(\beta\eta q_y u_z + \tau_{yz}) + (1 + 2\beta u_y^2) u_z \tau_{zz} \end{pmatrix} \\ +\tau_{yy} A_3^- \end{pmatrix} A_2^\pm \end{pmatrix}$$

$$GY_I^{\cdot\pm-}(4) = \tfrac{\rho}{4\beta} (-\tfrac{B_3}{\sqrt{\pi}} + \sqrt{\beta} u_z A_3^-)(\tfrac{B_2^\pm}{\sqrt{\pi}} + \sqrt{\beta} u_y A_2^\pm)$$

$$GY_V^{\cdot\pm-}(4) = \tfrac{\rho}{8p\beta} \begin{pmatrix} \frac{B_2^\pm}{\sqrt{\pi}} \begin{pmatrix} \frac{B_3}{\sqrt{\pi}} (2\beta\eta(q_y u_y + q_z u_z) + \tau_{yy} + \tau_{zz}) \\ +\sqrt{\beta}(\eta q_z - u_z(2\beta\eta q_y u_y + \tau_{yy})) A_3^- \end{pmatrix} \\ +(\sqrt{\beta}\frac{B_3}{\sqrt{\pi}}(-\eta q_y + u_y(2\beta\eta q_z u_z + \tau_{zz})) - \tau_{yz} A_3^-) A_2^\pm \end{pmatrix}$$

$$GY_I^{\cdot\pm-}(5) = \tfrac{\rho}{16\beta^{3/2}} \begin{pmatrix} (\frac{(1+\gamma)}{(-1+\gamma)} + 2u^2\beta)\frac{B_2^\pm}{\sqrt{\pi}} A_3^- \\ +2\sqrt{\beta}(u^2\beta + \frac{\gamma}{(-1+\gamma)}) u_y A_3^- A_2^\pm \\ -2\sqrt{\beta}\frac{B_3}{\sqrt{\pi}} u_z (\frac{B_2^\pm}{\sqrt{\pi}} + \sqrt{\beta} u_y A_2^\pm) \end{pmatrix}$$

$$GY_V^{\cdot\pm-}(5) = \tfrac{\rho}{32p\beta^{3/2}} \begin{pmatrix} \frac{B_2^\pm}{\sqrt{\pi}} \begin{pmatrix} -2\sqrt{\beta}\frac{B_3}{\sqrt{\pi}} \begin{pmatrix} -4\beta\eta q_x u_x u_z - 8\beta\eta q_y u_y u_z \\ +\frac{q_z(-dy+4\gamma+2(2+dx+dy)\beta u_z^2)}{\gamma} \\ -4u_x\tau_{xz} - u_z\tau_{yy} - 6u_y\tau_{yz} \\ +\frac{(2+dx+dy)u_z\tau_{zz}}{-1+\gamma} \end{pmatrix} \\ + \begin{pmatrix} \frac{4\beta(-1+\gamma)(q_x u_x + q_z u_z)}{\gamma} \\ +\frac{2\beta(-3-dx-dz+\gamma)q_y u_y}{\gamma} \\ -\frac{(-1+dx+dz+3\gamma)\tau_{yy}}{-1+\gamma} \end{pmatrix} A_3^- \end{pmatrix} \\ +2 \begin{pmatrix} \frac{B_3}{\sqrt{\pi}} \begin{pmatrix} \frac{\beta(1+dx+3dy+\gamma)q_y u_z}{\gamma} + \frac{4\beta^2(-1+\gamma)q_x u_x u_y u_z}{\gamma} \\ +\frac{\beta q_z u_y (1+dx+dy-3\gamma-2\beta(1+dx+dy+\gamma)u_z^2)}{\gamma} \\ +4\beta u_x u_y \tau_{xz} + \frac{(-1+dx+3dy+3\gamma)\tau_{yz}}{-1+\gamma} \\ -\frac{\beta(1+dx+dy+\gamma)u_y u_z \tau_{zz}}{-1+\gamma} \end{pmatrix} \\ +2\sqrt{\beta}(q_y - u_x\tau_{xy} - u_y\tau_{yy} - u_z\tau_{yz}) A_3^- \end{pmatrix} A_2^\pm \end{pmatrix}$$

where
$\eta = (\gamma - 1)/\gamma$
$s_x = \sqrt{\beta} u_x$
$s_y = \sqrt{\beta} u_y$
$s_z = \sqrt{\beta} u_z$
$dx = 2\beta(\gamma - 1)u_x^2$
$dy = 2\beta(\gamma - 1)u_y^2$
$dz = 2\beta(\gamma - 1)u_z^2$

$B_1^{\pm} = \pm Exp[-s_x^2]$
$B_2^{\pm} = \pm Exp[-s_y^2]$
$B_3^{\pm} = \pm Exp[-s_z^2]$
$B_3 = Exp[-s_z^2]$
$A_1^{\pm} = 1 \pm Erf[s_x]$
$A_2^{\pm} = 1 \pm Erf[s_y]$
$A_3^{\pm} = 1 \pm Erf[s_z]$

D.4 Axi-symmetric polar KFVS Split Fluxes

Kinetic upwind 3-D axi-symmetric formulation of Navier-Stokes equations is given as

$$\frac{\partial \boldsymbol{U}}{\partial t} + \frac{\partial \boldsymbol{GZ}^{\pm}}{\partial z} + \frac{1}{r}\frac{\partial r \boldsymbol{GR}^{\pm}}{\partial r} + \boldsymbol{S} = 0$$

where $\boldsymbol{GZ}^{\pm}$ and $\boldsymbol{GR}^{\pm}$ represents axial and radial split fluxes. This formulation is 3-D axi-symmetric as azimuthal velocity component u_θ is updated, the state update vector $\boldsymbol{U}$ is given as

$$\boldsymbol{U} = [\rho, \rho u_z, \rho u_r, \rho u_\theta, \rho E]^T$$

where $E = RT/(\gamma - 1) + \frac{1}{2}(u_z^2 + u_r^2 + u_\theta^2)$, u_z, u_r and u_θ are the z, r and θ components of macroscopic fluid velocity and γ is the specific heat ratio. Unsplit source term $\boldsymbol{S}$ is expressed as

$$\boldsymbol{S} = \left[0, 0, -\frac{p}{r} - \frac{\rho u_\theta^2}{r} - \frac{\tau_{\theta\theta}}{r}, \frac{\rho u_r u_\theta}{r} + \frac{\tau_{r\theta}}{r}, 0\right]^T$$

where p is the pressure, $\tau_{\theta\theta}$ and $\tau_{r\theta}$ are the components of shear stress tensor. The z-component of the inviscid and viscous split fluxes in 3-D axi-symmetric polar form are given by

$GZ_I(1)^\pm = \frac{\rho}{2\sqrt{\beta}}(\frac{B_z^\pm}{\sqrt{\pi}} + s_z A_z^\pm)$
$GZ_V(1)^\pm = -\frac{\rho}{4p\sqrt{\beta}}\frac{B_z^\pm}{\sqrt{\pi}}(2\sqrt{\beta}\eta q_z s_z + \tau_{zz})$

$GZ_I(2)^\pm = \frac{\rho}{2\beta}(\frac{B_z^\pm}{\sqrt{\pi}} s_z + \frac{(1+2s_z^2)}{2} A_z^\pm)$
$GZ_V(2)^\pm = -\frac{\rho}{4p\beta}(-2\sqrt{\beta}\eta q_z \frac{B_z^\pm}{\sqrt{\pi}} + \tau_{zz} A_z^\pm)$

$GZ_I(3)^\pm = \frac{\rho}{2\beta}(\frac{B_z^\pm}{\sqrt{\pi}} s_r + s_z s_r A_z^\pm)$
$GZ_V(3)^\pm = \frac{\rho}{4p\beta}(\frac{B_z^\pm}{\sqrt{\pi}}(\sqrt{\beta}\eta q_r - s_r(2\sqrt{\beta}\eta q_z s_z + \tau_{zz})) - \tau_{zr} A_z^\pm)$

$GZ_I(4)^\pm = \frac{\rho}{2\beta}(\frac{B_z^\pm}{\sqrt{\pi}} s_\theta + s_z s_\theta A_z^\pm)$
$GZ_V(4)^\pm = \frac{\rho}{4p\beta}(\frac{B_z^\pm}{\sqrt{\pi}}(-s_\theta(2\sqrt{\beta}\eta q_z s_z + \tau_{zz})) - \tau_{z\theta} A_z^\pm)$

$GZ_I(5)^\pm = \frac{\rho}{8\beta^{3/2}}(\frac{(1+\gamma+du)}{(-1+\gamma)}\frac{B_z^\pm}{\sqrt{\pi}} + \frac{(2\gamma+du)}{(-1+\gamma)} s_z A_z^\pm)$

$$GZ_V(5)^\pm = \frac{\rho}{16p\beta^{3/2}}\left(\begin{array}{l} \frac{B_z^\pm}{\sqrt{\pi}}\left(\begin{array}{l} 4(\sqrt{\beta}\eta q_r s_r) \\ -2\sqrt{\beta}\eta q_z s_z \frac{(3-\gamma+dr+d\theta)}{(-1+\gamma)} - \frac{(-1+3\gamma+dr+d\theta)}{(-1+\gamma)}\tau_{zz} \end{array}\right) \\ +4(\sqrt{\beta}q_z - (s_z\tau_{zz} + s_r\tau_{zr} + s_\theta\tau_{z\theta}))A_z^\pm \end{array}\right)$$

The r-component of the inviscid and viscous split fluxes in 3-D axi-symmetric polar form are given by

$GR_I(1)^\pm = \frac{\rho}{2\sqrt{\beta}}(\frac{B_r^\pm}{\sqrt{\pi}} + s_r A_r^\pm)$
$GR_V(1)^\pm = -\frac{\rho}{4p\sqrt{\beta}}\frac{B_r^\pm}{\sqrt{\pi}}(2\sqrt{\beta}\eta q_r s_r + \tau_{rr})$

$GR_I(2)^\pm = \frac{\rho}{2\beta}(\frac{B_r^\pm}{\sqrt{\pi}} s_z + s_z s_r A_r^\pm)$
$GR_V(2)^\pm = -\frac{\rho}{4p\beta}(\sqrt{\beta}\frac{B_r^\pm}{\sqrt{\pi}}(-\eta q_z + u_z(2\sqrt{\beta}\eta q_r s_r + \tau_{rr})) + \tau_{zr} A_r^\pm)$

$GR_I(3)^\pm = \frac{\rho}{2\beta}(\frac{B_r^\pm}{\sqrt{\pi}} s_r + \frac{(1+2s_r^2)}{2} A_r^\pm)$
$GR_V(3)^\pm = \frac{\rho}{4p\beta}(2\sqrt{\beta}\eta q_r \frac{B_r^\pm}{\sqrt{\pi}} - \tau_{rr} A_r^\pm)$

$$GR_I(4)^{\pm} = \frac{\rho}{2\beta}(\frac{B_r^{\pm}}{\sqrt{\pi}}s_\theta + s_\theta s_r A_r^{\pm})$$
$$GR_V(4)^{\pm} = -\frac{\rho}{4p\beta}(\frac{B_r^{\pm}}{\sqrt{\pi}}(s_\theta(2\sqrt{\beta}\eta q_r s_r + \tau_{rr})) + \tau_{r\theta}A_r^{\pm})$$

$$GR_I(5)^{\pm} = \frac{\rho}{8\beta^{3/2}}(\frac{(1+\gamma+du)}{(-1+\gamma)}\frac{B_z^{\pm}}{\sqrt{\pi}} + \frac{(2\gamma+du)}{(-1+\gamma)}s_r A_r^{\pm})$$
$$GR_V(5)^{\pm} = \frac{\rho}{16p\beta^{3/2}}\left(\begin{array}{l} \frac{B_r^{\pm}}{\sqrt{\pi}}\left(\begin{array}{l} 4(\sqrt{\beta}\eta q_z s_z) \\ -2\sqrt{\beta}\eta q_r s_r\frac{(3-\gamma+dz+d\theta)}{(-1+\gamma)} - \frac{(-1+3\gamma+dz+d\theta)}{(-1+\gamma)}\tau_{rr} \end{array}\right) \\ +4(\sqrt{\beta}q_r - (s_z\tau_{zr} + s_r\tau_{rr} + s_\theta\tau_{r\theta}))A_r^{\pm} \end{array}\right)$$

where

$\eta = (\gamma - 1)/\gamma$
$s_z = \sqrt{\beta}u_z$
$s_r = \sqrt{\beta}u_r$
$s_\theta = \sqrt{\beta}u_\theta$
$u^2 = u_z^2 + u_r^2 + u_\theta^2$
$dz = 2\beta(\gamma - 1)u_z^2$
$dr = 2\beta(\gamma - 1)u_r^2$
$d\theta = 2\beta(\gamma - 1)u_\theta^2$
$du = 2\beta(\gamma - 1)u^2$
$B_z^{\pm} = \pm Exp[-s_z^2]$
$B_r^{\pm} = \pm Exp[-s_r^2]$
$A_z^{\pm} = 1 \pm Erf[s_z]$
$A_r^{\pm} = 1 \pm Erf[s_r]$
$\tau_{zz} = 2\mu\left(\frac{\partial u_z}{\partial z}\right) + (1-\gamma)\mu\nabla\cdot\vec{u}$
$\tau_{rr} = 2\mu\left(\frac{\partial u_r}{\partial r}\right) + (1-\gamma)\mu\nabla\cdot\vec{u}$
$\tau_{\theta\theta} = 2\mu\left(\frac{u_r}{r}\right) + (1-\gamma)\mu\nabla\cdot\vec{u}$
$\tau_{zr} = \tau_{rz} = \mu\left(\frac{\partial u_z}{\partial r} + \frac{\partial u_r}{\partial z}\right)$
$\tau_{\theta z} = \tau_{z\theta} = \mu\left(\frac{\partial u_\theta}{\partial z}\right)$
$\tau_{r\theta} = \tau_{\theta r} = \mu\left(r\frac{\partial(u_\theta/r)}{\partial r}\right)$
$\nabla\cdot\vec{u} = \frac{1}{r}\frac{\partial(ru_r)}{\partial r} + \frac{\partial u_z}{\partial z}$
$q_z = -\kappa\frac{\partial T}{\partial z}$
$q_r = -\kappa\frac{\partial T}{\partial r}$

Appendix E

Experimental determination of tangential momentum accommodation coefficient (TMAC)

Existing methods available in current literature use microchannels to evaluate TMAC and assume pressure gradient to be constant along the test section [14, 85]. The tangential momentum accommodation coefficient (TMAC), σ can be determined by conducting a simple pressure drop experiment. Thus an investigation is required to account for the effect of varying pressure gradient along the test-section. Experiments were conducted for two different tubes : i) 0.25 inch OD of inner diameter 0.475 cm and length 54 cm, and ii) 0.50 inch OD of inner diameter 1.205 cm and length 100.8 cm. This section presents methodology for determination of tangential momentum accommodation coefficient (TMAC) when pressure gradient variation along the pipe is significant. Table E.1 and table E.2 gives the flow and pressure experimental data for 0.25 OD and 0.50 OD pipe

Fig. E.1 and fig. E.2 depicts the flow and conductance variation with respect

Table E.1: Mass flow rate versus inlet and outlet pressure experimental data for 0.25 inch OD pipe.

Mass flowrate (mbar liter/s)	Inlet Pressure (mbar)	Outlet Pressure (mbar)
4.543	10.49	6.77
3.786	9.46	6.01
3.596	9.16	5.80
3.407	8.90	5.60
3.218	8.58	5.38
3.028	8.30	5.18
2.839	8.01	4.98
2.650	7.70	4.76
2.460	7.40	4.55
2.271	7.07	4.32
2.082	6.73	4.10
1.892	6.39	3.87
1.703	6.04	3.63
1.514	5.66	3.38
1.325	5.26	3.12
1.135	4.84	2.85
0.946	4.38	2.56
0.757	3.88	2.24
0.567	3.31	1.89
0.378	2.66	1.50
0.189	1.85	1.01

Table E.2: Mass flow rate versus inlet and outlet pressure experimental data for 0.50 inch OD pipe.

Mass flowrate (mbar liter/s)	Inlet Pressure (mbar)	Outlet Pressure (mbar)
9.389	10.33	10.02
8.518	9.53	9.22
7.572	8.67	8.36
6.625	7.81	7.52
5.679	6.90	6.62
4.732	6.04	5.77
3.786	5.17	4.92
2.839	4.22	3.99
1.892	3.22	3.01
1.703	3.01	2.82
1.514	2.79	2.61
1.325	2.55	2.37
1.135	2.28	2.12
0.946	2.07	1.92
0.757	1.79	1.65
0.567	1.49	1.37
0.378	1.09	0.99
0.189	0.73	0.66

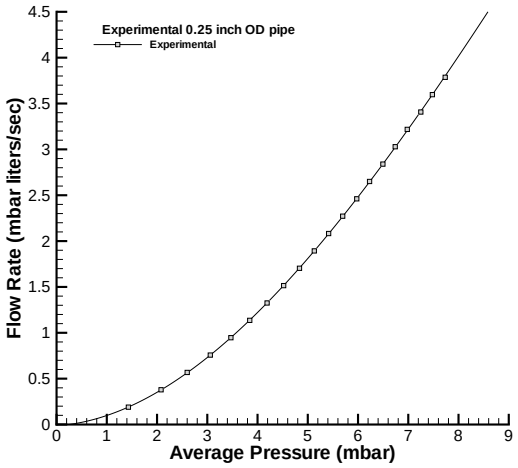

Figure E.1: Experimental flow versus average pressure for 0.25 inch OD pipe.

to average pressure for 0.25 inch OD. Similarly fig. E.3 and fig. E.4 depicts the flow and conductance variation with respect to average pressure for 0.50 inch OD pipe.

E.0.1 Determination of tangential momentum accommodation coefficient (TMAC)

Most of the methods which determine the tangential momentum accommodation coefficient (TMAC) assume that pressure gradient $\frac{\partial p}{\partial z}$ along the length of the pipe is constant with a value $\frac{\Delta p}{L}$. The mass flow rate for a short pipe in terms of average pressure and its gradient derived in the thesis is expressed as

$$\begin{aligned} M &= -\frac{\pi a^4}{8\mu}\bar{p}\frac{d\bar{p}}{dz}\left(1+f_{slip}\right) \\ &= \frac{\pi a^4}{8\mu}\bar{p}\frac{\Delta p}{L}\bar{\phi_p}\left(1+f_{slip}\right) \end{aligned} \tag{E.1}$$

where

$$\bar{p}\frac{\Delta p}{L} = \left(\frac{p_i+p_o}{2}\right)\frac{(p_i-p_o)}{L} \tag{E.2}$$

and $\bar{\phi_p}$ is

$$\bar{\phi_p} = \frac{(p_i+p_o+2f_{slip}\bar{p})^2}{4(p_i+f_{slip}\bar{p})(p_o+f_{slip}\bar{p})} \tag{E.3}$$

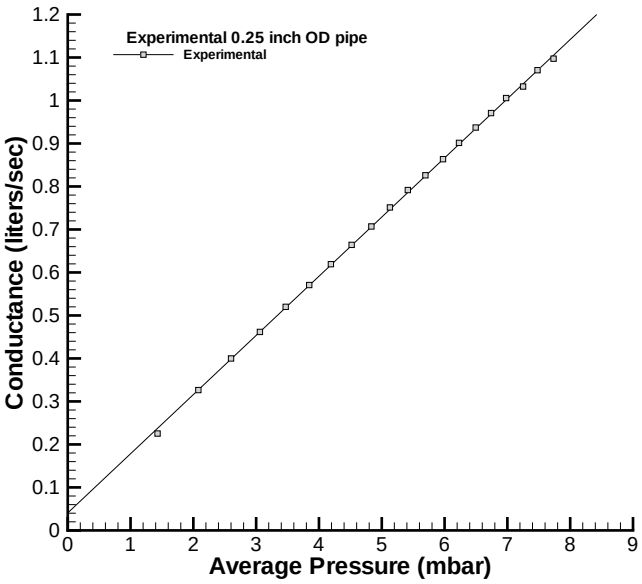

Figure E.2: Experimental conductance versus average pressure for 0.25 inch OD pipe.

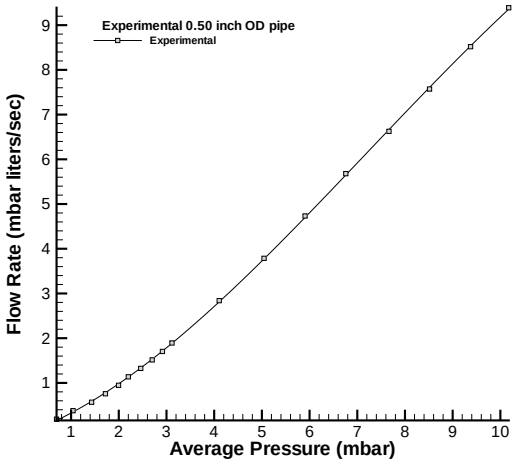

Figure E.3: Experimental flow versus average pressure for 0.50 inch OD pipe.

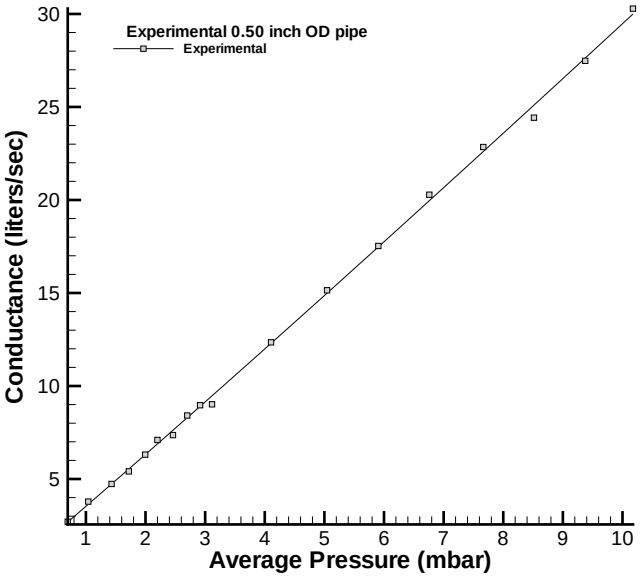

Figure E.4: Experimental conductance versus average pressure for 0.50 inch OD pipe.

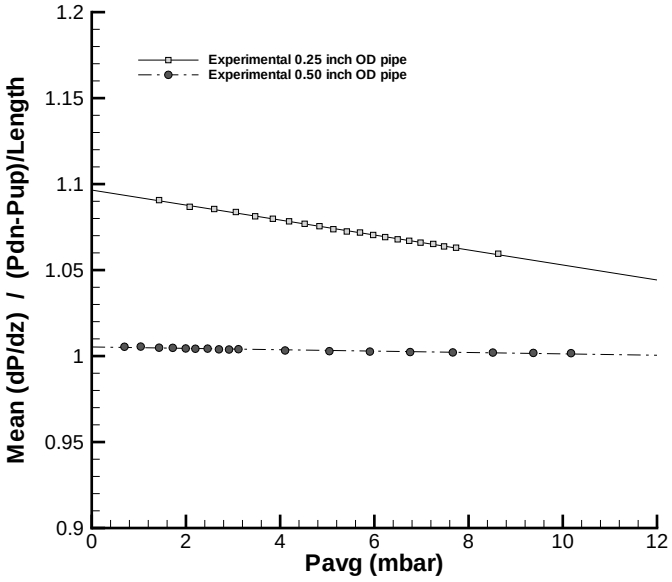

Figure E.5: Ratio of the analytical mean pressure gradient $\frac{\partial p}{\partial z}$ with respect to pressure gradient $\frac{\Delta p}{L}$ based on experimental data for 0.25 and 0.50 inch OD pipe.

Thus analytical derivations reveals that for pipes of smaller diameter the pressure gradient varies linearly as compared to the larger diameter pipe. Fig. E.5 shows the ratio of the analytical obtained mean pressure gradient $\frac{\partial p}{\partial z}$ with respect to pressure gradient $\frac{\Delta p}{L}$. The method of TMAC determination can either use graphical methods like i) Method-I based on the ratio of mass flow rate with respect to pressure drop plotted with respect to average pressure, or ii) Method-II based on the ratio of mass flow rate with respect to product of pressure and pressure drop plotted with respect to reciprocal of average pressure. Alternatively, Method-III uses least error minimization between the experimental flow values and analytical flow values to get the TMAC.

$$\begin{aligned} \frac{M}{\Delta p}\left(\frac{8\mu L}{\pi a^4}\right) &= \bar{p}\bar{\phi}\left(1+8\overline{Kn}\left(\frac{2-\sigma}{\sigma}\right)\right) \\ &= \bar{p}\bar{\phi}\left(1+8\frac{\mu}{2a\bar{p}}\sqrt{\frac{\pi RT}{2}}\left(\frac{2-\sigma}{\sigma}\right)\right) \\ &= \frac{4\mu}{a}\sqrt{\frac{\pi RT}{2}}\left(\frac{2-\sigma}{\sigma}\right)\bar{\phi}+\bar{\phi}\bar{p} \end{aligned} \tag{E.4}$$

Table E.3: TMAC evaluation for 0.25 and 0.50 inch OD pipe.

Experiment	Method-I	Method-II	Method-III
0.25 inch OD	0.550	0.675	0.641
0.50 inch OD	0.372	0.292	0.452

Method-II can be written as

$$\begin{aligned} \frac{M}{\bar{p}\Delta p}\left(\frac{8\mu L}{\pi a^4}\right) &= \bar{\phi}\left(1+8\overline{Kn}\frac{2-\sigma}{\sigma}\right) \\ &= \bar{\phi}\left(1+8\frac{\mu}{2a\bar{p}}\sqrt{\frac{\pi RT}{2}}\left(\frac{2-\sigma}{\sigma}\right)\right) \\ &= \bar{\phi}+\frac{4\mu}{a}\sqrt{\frac{\pi RT}{2}}\left(\frac{2-\sigma}{\sigma}\right)\bar{\phi}\left(\frac{1}{\bar{p}}\right) \end{aligned} \tag{E.5}$$

In Method-I the factor on the right hand side $\frac{M}{\Delta p}\left(\frac{8\mu L}{\pi a^4}\right)$ when plotted with respect to average pressure, $\bar{p}$ will have y-intercept by slope ratio of

$$\frac{y-intercept}{slope} = \frac{4\mu}{a}\sqrt{\frac{\pi RT}{2}}\left(\frac{2-\sigma}{\sigma}\right) \tag{E.6}$$

Method-II is similar to method of Arkilic [13], the factor on the right hand side $\frac{M}{\bar{p}\Delta p}\left(\frac{8\mu L}{\pi a^4}\right)$ when plotted with respect to reciprocal of average pressure, $\frac{1}{\bar{p}}$ will have slope by y-intercept ratio of

$$\frac{slope}{y-intercept} = \frac{4\mu}{2a}\sqrt{\frac{\pi RT}{2}}\left(\frac{2-\sigma}{\sigma}\right) \tag{E.7}$$

Method-III uses least square error minimization of E with respect to TMAC, σ where sum of square of error, E is expressed as

$$E = \sum(F_{exp} - F_{num}(\sigma))^2 \tag{E.8}$$

where F_{exp} is the value of the experimental flow rate, and $F_{num}(\sigma)$ is the numerically obtained value of the flow for a particular assumed value of TMAC, σ.

Using Method-I as shown in Fig. E.6 and Fig. E.8 the TMAC, $\sigma = 0.550$ and TMAC, $\sigma = 0.3724$ is obtained for 0.25 OD and 0.50 OD pipe. Using Method-II as shown in Fig. E.7 and Fig. E.9 the TMAC, $\sigma = 0.675$ and TMAC, $\sigma = 0.292$ is obtained for 0.25 OD and 0.50 OD pipe. After least square error minimization

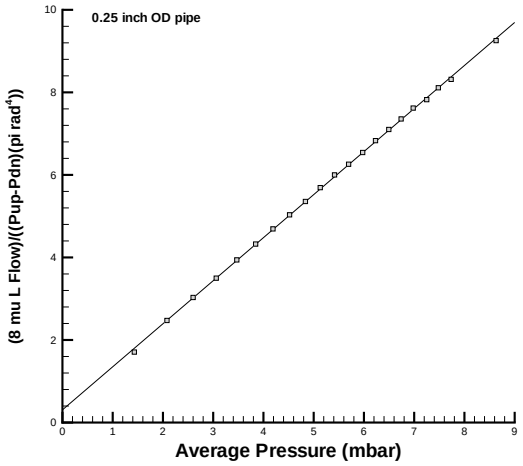

Figure E.6: Plot of $\frac{M}{\Delta p}(\frac{8\mu L}{\pi a^4})$ with respect to average pressure, $\bar{p}$ for 0.25 inch OD pipe.

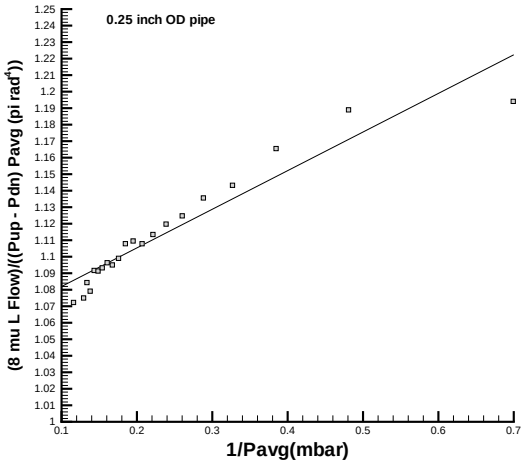

Figure E.7: Plot of $\frac{M}{\bar{p}\Delta p}(\frac{8\mu L}{\pi a^4})$ with respect to reciprocal of average pressure, $\frac{1}{\bar{p}}$ for 0.25 inch OD pipe.

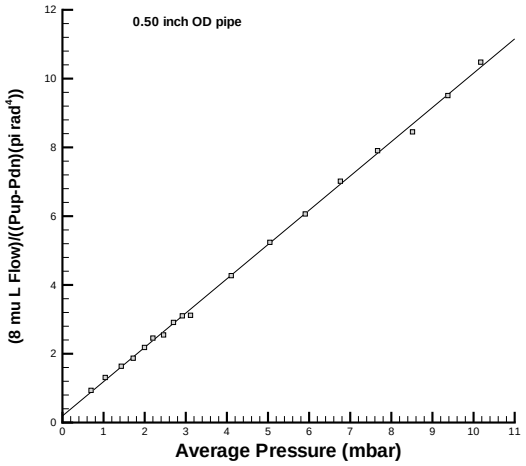

Figure E.8: Plot of $\frac{M}{\Delta p}(\frac{8\mu L}{\pi a^4})$ with respect to average pressure, $\bar{p}$ for 0.50 inch OD pipe.

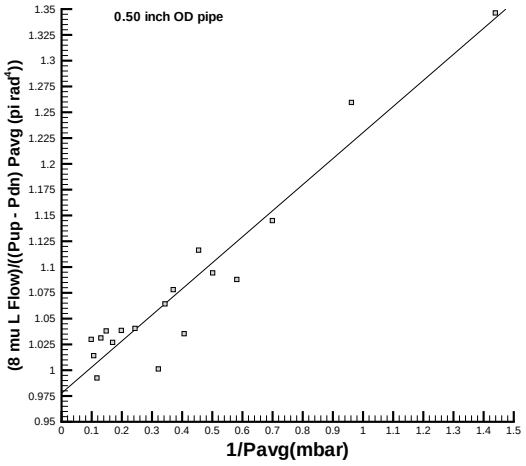

Figure E.9: Plot of $\frac{M}{\bar{p}\Delta p}(\frac{8\mu L}{\pi a^4})$ with respect to reciprocal of average pressure, $\frac{1}{\bar{p}}$ for 0.50 inch OD pipe.

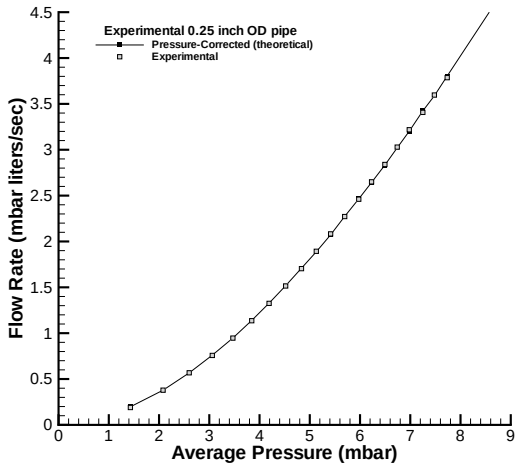

Figure E.10: Theoretical flow and experimental flow versus average pressure for 0.25 inch OD pipe.

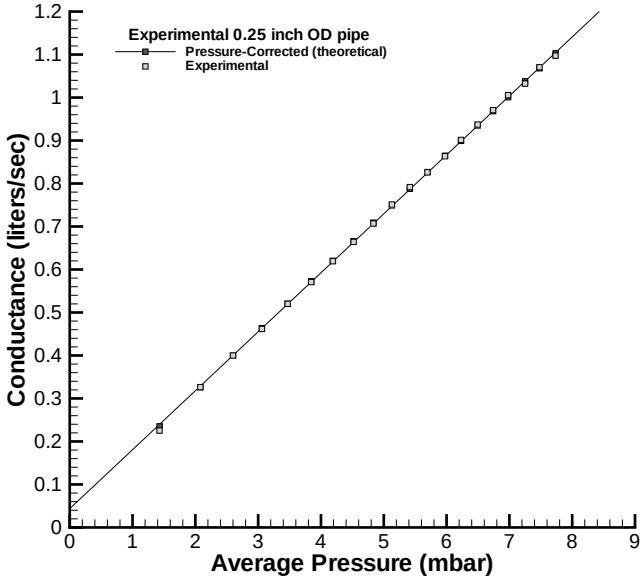

Figure E.11: Theoretical conductance and experimental conductance versus average pressure for 0.25 inch OD pipe.

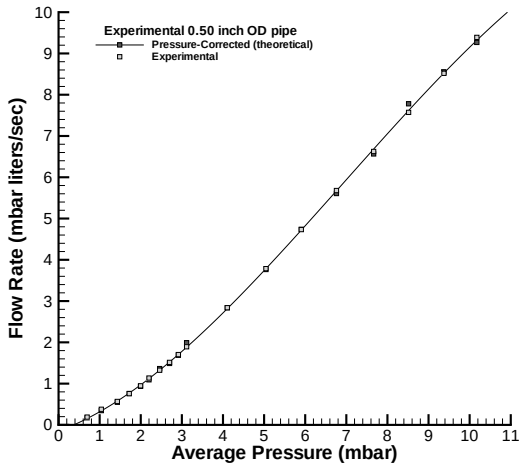

Figure E.12: Theoretical flow and experimental flow versus average pressure for 0.50 inch OD pipe.

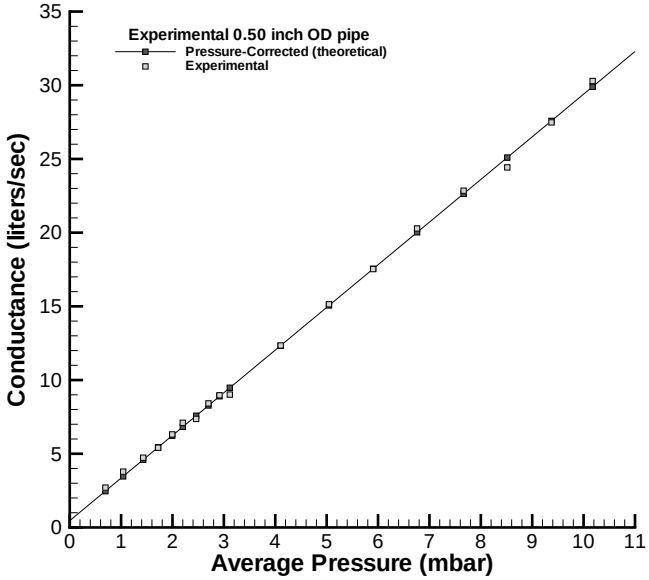

Figure E.13: Theoretical conductance and experimental conductance versus average pressure for 0.50 inch OD pipe.

Method-III gives the TMAC as $\sigma = 0.641$. Fig. E.10 show the comparison of theoretical and experimental flow and Fig. E.11 shows the comparison of theoretical and experimental conductance for 0.25 OD pipe. Similarly, Method-III for 0.50 OD pipe gives the TMAC, $\sigma = 0.452$. Fig. E.12 show the comparison of theoretical and experimental flow and Fig. E.13 shows the comparison of theoretical and experimental conductance for 0.50 OD pipe. Table E.3 gives the values of TMAC evaluated using Method-I, Method-II and Method-III for 0.25 OD and 0.50 OD pipe.

References

[1] Agarwal, R., Yun, K.Y. & Balakrishnan, R. (2001). Beyond Navier-Stokes: Burnett equations for flows in the continuum-transition regime. *Physics of Fluids*, **13**, 3061–3085. 40

[2] Agrawal, A., Djenidi, L. & Antonia, R. (2005). Simulation of gas flow in microchannels with a sudden expansion or contraction. *Journal of Fluid Mechanics*, **530**, 135–144. 33

[3] Albertoni, S., Cercignani, C. & Gotusso, L. (1963). Numerical evaluation of the slip coefficient. *Physics of Fluid*, **6(7)**, 993–996. 33, 36

[4] Anandhanarayanan, K. (2004). *Development and applications of a grid-free kinetic upwind solver to multibody configurations.*. Ph.D. thesis, Indian Institute of Science, Bangalore. 83

[5] Anders, A.S. & Szeri, A. (1984). Flow between eccentric rotating cylinders. *ASME Journal of Applied Mechanics*, **51**, 869–878. 301

[6] Andries, P. & Perthame, B. (2001). *The ES-BGK model equation with correct Prandtl number. In:Rarefied Gas Dynamics: 22nd International Symposium, ed. T.J. Bartel and A.A. Gallis*, 30–36. AIP. 48, 49, 50

[7] Anil, N., Rajan, N. & Deshpande, S. (2005). *Mathematical analysis of dissipation in m-KFVS Method., Fluid Mechanics Report 2005 FM 1*. Indian Institute of Science. 70, 72

[8] Ansumali, S. & Karlin, I. (2002). Kinetic boundary conditions in the lattice Boltzmann method. *Physical Review E*, **66**, 026311(1)–026311(6). 38

[9] Aoki, K., Yoshida, H., Nakanishi, T. & Garcia, A. (2003). Inverted velocity profile in the cylindrical couette flow of a rarefied gas. *Physical Review E*, **68**, 016302(1)–016302(11). 277, 278

[10] Araujo, J., Ruas, V. & Vargas, A. (1990). Finite element solution of flow between eccentric cylinders with viscous dissipation. *International Journal of Numerical Methods in Fluids*, **11**, 849–865. 301

[11] Aristov, V. (2001). *Direct methods for solving the Boltzmann equations and study of non equilibrium flows.*. Plenum, Kluwer. 24, 25

[12] Arkilic, E., Breuer, K. & Schmidt, M. (1994). Gaseous flow in microchannels. *ASME FED - Application of Microfabrication to Fluid Mechanics*, **197**, 57–66. 31

[13] Arkilic, E., Schmidt, M. & Breuer, K. (1997). Gaseous slip flow in long microchannels. *Journal of Microelectromechanical systems*, **6(2)**, 167–178. 5, 31, 252, 394

[14] Arkilic, E., Breuer, K. & Schmidt, M. (2001). Mass flow and tangential momentum accommodation in silicon micromachined channels. *Journal of Fluid Mechanics*, **437**, 29–43. 387

[15] Athanasiadis, A.N. & Deconinck, H. (2003). Object-oriented three-dimensional hybrid grid generation. *International Journal for Numerical Methods in Engineering*, **58(2)**, 301–318. 81

[16] Atluri, S. & Zhu, T. (1998). New meshless local petrov-galerkin (mlpg) approach in computational mechanics. *Comput. Mech.*, **22(2)**, 117–127. 82

[17] Aubert, C. & Colin, S. (2001). High-order boundary conditions for gaseous flows in rectangular microducts. *Microscale Thermophys.*, **5**, 41–54. 36

[18] Avci, M. & Aydin, O. (2008). Laminar forced convection slip-flow in a micro-annulus between two concentric cylinders. *International Journal of Heat and Mass Transfer*, **51**, 3460–3467. 273, 276

[19] Babarsky, R., Herbst, I. & Wood III, H. (2002). A new variational approach to gas flow in a rotating system. *Physics of Fluids*, **14(10)**, 3624–3640. 77, 291

[20] Babuska, I. (1997). The partition of unity. *Int. J. Numer. Methods Engg.*, **40**, 727–758. 82

[21] Baker, L. & Hadjiconstantinou, N. (2005). Variance reduction for Monte Carlo solutions of the Boltzmann equation. *Physics of Fluid*, **17**, 051703(1)–051703(4). 153

[22] Balakrishnan, R. (2004). An approach to entropy consistency in second-order hydrodynamic equations. *Journal of Fluid Mechanics*, **503**, 201–245. 31, 54, 355, 356

[23] Ballal, B. & Rivlin, R. (1977). Flow of a Newtonian fluid between eccentric rotating cylinders: inertial effects. *Archive of Rational Mechanics and Analysis*, **62**, 237–294. 301

[24] Bao, F.B. & Lin, J.Z. (2008). Burnett simulations of gas flow in microchannels. *Fluid Dynamics Research*, **40**, 679–694. 40

[25] Barba, L., Leonard, A. & Allen, C. (2005). Advances in viscous vortex methods–meshless spatial adaption based on radial basis function interpolation. *International Journal for Numerical Methods in Fluids*, **47**, 387–421. 83

[26] Bark, F. & Bark, T. (1976). On vertical boundary layers in a rapidly rotating gas. *Journal of Fluid Mechanics*, **78**, 815–825. 77

[27] Batina, J. (1976). A gridless Euler/Navier-Stokes solution algorithm for complex aircraft applications. *Journal of Fluid Mechanics*, **78**, 815–825. 83

[28] Belystchko, T., Lu, Y. & Gu, L. (1994). Element free galerkin methods. *Int. J. Numerical Methods Engg.*, **37(2)**, 229–256. 82

[29] Benek, J., Donegan, T. & Suhs, N. (1987). Extended chimera grid embedding scheme with application to viscous flows. *AIAA paper 87-1126, AIAA 8th Computational Fluid Dynamics Conference*. 80

[30] Beretta, G. (2006). Nonlinear model dynamics for closed-system, constrained, maximal-entropy-generation relaxation by energy redistribution. *Physical Review E*, **73**, 026113(1)–026113(11). 103

[31] Bergera, M., Aftosmisb, M., Marshallc, D. & Murmand, S. (2005). Performance of a new cfd flowsolver using a hybrid programming paradigm. *Journal of Parallel and Distributed Computing*, **65**, 414–423. 90

[32] Beskok, A. (2001). Validation of a new velocity-slip model for separated gas microflows. *Numerical heat transfer, Part B*, **40**, 451–471. 33, 34, 36, 37, 40

[33] Beskok, A. & Karniadakis, G. (1993). Simulation of heat and momentum transfer in micro-geometries. *AIAA Paper 93-3269*. 31

[34] Beylich, A. (2000). Solving the kinetic equation for all knudsen numbers. *Physics of Fluids*, **12**, 444–465. 29

[35] Bhatnagar, P., Gross, E. & Krook, M. (1954). A model for collision processes in gases. i. small amplitude processes in charged and neutral one-component systems. *Physical Review*, **94**, 511–525. 46

[36] Bird, G. (1994). *Molecular Gas Dynamics and the Direct Simulation of Gas Flows*. Oxford Science, Oxford. 24, 135, 136, 268, 278

[37] Boman, E., Devine, K., Fisk, L., Heaphy, R., Hendrickson, B., Vaughan, C., Catalyurek, U., Bozdag, D., Mitchell, W. & Teresco, J. (2007). *Zoltan 3.0 : Parallel Partitioning, Load-balancing, and Data Management Services; User's Guide,Tech. Report SAND2007-4748W*. Sandia National Laboratories, Albuquerque, NM. 91

[38] Brenner, H. (2005). Navier-Stokes revisited. *Physica A*, **349**, 60–132. 39, 151, 354

[39] Bristeau, M., Glowinski, R., Periaux, J. & (Eds), H.V. (1987). *Numerical Simulation of Compressible Navier-Stokes Flows.*. Vieweg and Sonh Braunschweigh, Wiesbaden. 258

[40] Brouwers, J. (1978). On compressible flow in a rotating cylinder. *Journal of Engineering Mathematics*, **12**, 265–285. 77

[41] Brush, S. (1972). *Kinetic Theory*. Peragamon Press, New York. 343

[42] Burt, J. & Boyd, I. (2009). A hybrid particle approach for continuum and rarefied flow simulation. *Journal of Computational Physics*, **228**, 460–475. 25, 28, 29

[43] Catalano, L., Palma, P.D., Naplitano, M. & Pascazio, G. (1997). *Genuinely multidimensional upwind methods for accurate and efficient solutions of compressible flows. In:Notes on Numerical Fluid Mechanism*, 221–250. Vieweg-Verlag, Braunschweig. 258, 264

[44] Cercignani, C. (1964). *Higher order slip according to the linearized Boltzmann equation.*. Institute of Engineering Research Report AS-64-19, University of California,, Berkeley. 33, 36

[45] Cercignani, C. (1990). *Mathematical Methods in Kinetic Theory*. Plenum, New York. 31, 52, 343, 344, 345

[46] Cercignani, C. & Lampis, M. (1971). Kinetic models for gas-surface interactions. *Transport Theory and Statistical Physics*, **1**, 101–114. 23

[47] Cercignani, C. & Lorenzani, S. (2010). Variational derivation of second-order slip coefficients on the basis of the Boltzmann equation for hard-sphere molecules. *Physics of Fluids*, **22**, 062004(1)–062004(8). 35, 36

[48] Cercignani, C., Lampis, M. & Lorenzani, S. (2004). Variational approach to gas flows in microchannels. *Physics of Fluids*, **16**, 3426–3437. 27, 36

[49] Chae, D., Kim, C. & Rho, O. (2000). Development of an improved gas-kinetic BGK scheme for inviscid and viscous flows. *Journal of Computational Physics*, **158**, 1. 48

[50] Chang, C.W. (1948). *On the theory of the thickness of weak shock waves, Technical report no. APL/JHU, CM-503*. Dept. of Eng. Research, University of Michigan. 30, 31, 54

[51] Chang, C.W. & Uhlenbeck, G. (1952). *On the propagation of sound in monatomic gases, Project M999*. Engg. Research Institute, University of Michigan, Ann Arbor. 61

[52] Chapman, S. & Cowling, T.G. (1970). *The Mathematical Theory of Non-Uniform Gases*. Cambridge University Press, Cambridge. 30, 31, 52, 53

[53] Chiu, E.K., Wang, Q. & Jameson, A. (2011). A conservative meshless scheme: General order formulation and application to Euler equations. *AIAA 2011-651,49th AIAA Aerospace Sciences Meeting including the New Horizons Forum and Aerospace Exposition*. 84

[54] Chou, S. & Baganoff, D. (1996). Kinetic flux-vector splitting for the Navier-Stokes equations. *Journal of Computational Physics*, **130**, 217–230. 67, 129, 131, 161

[55] Cliff, S., Thomas, S., Baker, T. & Jameson, A. (2002). Aerodynamic shape optimization using unstructured grid methods. *AIAA paper 2002-5550, 9th AIAA/ISSMO Symposium on Multidisciplinary Analysis and Optimization*. 95

[56] Cohen, E. (1993). Fifty years of kinetic theory. *Physica A*, **194**, 229–257. 343

[57] CRC (1999-2000). *Handbook of Chemistry and Physics*. 80^{th} Ed., CRC Press. xlv, 340, 341

[58] Crouseilles, N., Degond, P. & Lemou, M. (2004). A hybrid kinetic/fluid models for solving the gas dynamics Boltzmann-BGK equation. *Journal of Computational Physics*, **199**, 776. 29

[59] Danielson, K., Hao, S., Liu, W., Uras, R. & Li, S. (2000). Parallel computation of meshless methods for explicit dynamic analysis. *Int. J. Numer. Meth. Engng.*, **47**, 1323–1341. 92

[60] De, S. & Bathe, K.J. (2000). The method of finite spheres. *Comput. Mech.*, **25**, 329–345. 82

[61] de Groot, S. & Mazur, P. (1962). *Non-Equilibrium Thermodynamics*. North-Holland, Amsterdam. 56

[62] de Socio, L. & Marino, L. (2000). Numerical experiments on the gas flow between eccentric rotating cylinders. *International Journal for Numerical Methods in Fluids*, **34**, 229–240. 301, 304

[63] de Socio, L. & Marino, L. (2003). Flow separation between rotating eccentric cylinders. *European Journal of Mechanics B/Fluids*, **22**, 85–97. 301, 302, 304

[64] Deconinck(Ed.), H. (1998). *Algorithms and data structures for structured and unstructured grid generation: selected special topics from previous VKI lectures.*. Von Karman Institute for Fluid Dynamics, Rhode-St-Gense. 81

[65] Deconinck(Ed.), H. (2002). *Multi-Objective Optimization Using Evolutionary Algorithms.*. Chichester, New York. 98

[66] Degond, P., Pareschi, L. & (Eds.), G.R. (2004). *Modeling and Computational methods for Kinetic Equations.*. Birkhauser, Boston. 28

[67] Deissler, R. (1964). An analysis of second-order slip flow and temperature jump boundary conditions for rarefied gases. *Int. J. Heat Mass Transfer*, **7**, 681–694. 33, 36

[68] Dellar, P. (2007). Macroscopic description of rarefied gases from the elimination of fast variables. *Physics of Fluids*, **19**, 107101(1)–107101(14). 53

[69] Deshpande, S. (1986). On the Maxwellian distribution, symmetric form, and entropy conservation for the Euler equations. *NASA Technical Paper No. 2583*. 42

[70] Deshpande, S. (1986). A second order accurate, kinetic-theory based method for inviscid compressible flows. *NASA Technical Paper No. 2613*. 66, 67, 129

[71] Deshpande, S., Balakrishnan, N. & Rao, S.R. (1994). Pvu and wave-particle splitting schemes for Euler equations of gas dynamics. *Sadhana*, **19(6)**, 1027–1054. 73

[72] Deshpande, S., Kumar, G.S. & Mahendra, A. (2005). *Shape Optimization using grid free solver and evolutionary algorithm. In:Workshop on Optimization in Aerodynamics*. Humboldt-University Berlin. 95

[73] DeZeeuw, D. & Powell, K. (1993). An adaptively refined Cartesian mesh solver for the Euler equations. *Journal of Computational Physics*, **104(1)**, 56–68. 81

[74] d'Humierés, D. (1992). Generalized lattice Boltzmann equations. in rarefied gas dynamics: theory and simulations (ed. b. d. shizgal & d. p.weaver). *Prog. Astronaut. Aeronaut.*, **159**, 450–458. 49

[75] d'Humierés, D., Ginzburg, I., Krafczyk, M., Lallemend, P. & Luo, L.S. (2002). Multiple-relaxation-time lattice Boltzmann models in three dimensions. *Phil. Trans. R. Soc. Lond. A*, **360**, 437–451. 49

[76] Dickinson, G. & Jones, I. (1981). Numerical solutions for the compressible flow in a rapidly rotating cylinder. *Journal of Fluid Mechanics*, **107**, 89–107. 77

[77] Dongari, N., Agrawal, A. & Agrawal, A. (2007). Analytical solution of gaseous slip flow in long microchannels. *International Journal of Heat and Mass Transfer*, **50**, 3411–3412. 36

[78] Dorigo, M. (1992). *Optimization, learning and natural algorithms*. Ph.D. thesis, Politecnico di Milano, Milano. 94

[79] Duarte, C. & Oden, J. (1996). H-p clouds - and h-p meshless method. *Numer. Methods Partial Differ. Equations*, **12(6)**, 673–705. 82

[80] Einzel, D., Panzer, P. & Liu, M. (1990). Boundary condition for fluid flow : Curved or rough surfaces. *Phys. Rev. Lett.*, **64**, 2269–2272. 277

[81] Elizarova, T. (2009). *Quasi-Gas Dynamic Equations*. Springer-Verlag, Berlin. 39, 151, 353

[82] Elizarova, T. (2009). *Quasi-gas dynamic equations and possibilities in rarefied gas flow simulations. In: Rarefied Gas Dynamics:26th International Symposium ed. T. Abe*, vol. CP1084, 129–134. AIP. 39

[83] Eu, B. (1986). On the modified moment method and irreversible thermodynamics. *J. Chem. Phys.*, **85**, 1592–1602. 62, 116

[84] Eu, B. (1992). *Kinetic Theory and Irreversible Thermodynamics*. Wiley, New York. 31

[85] Ewart, T., Perrier, P., Graur, I. & Meolans, J. (2007). Mass flow rate measurements in a microchannel, from hydrodynamic to near free molecular regimes. *Journal of Fluid Mechanics*, **584**, 337–356. 33, 36, 387

[86] Fan, J. & Shen, C. (1999). *Statistical simulation of low-speed unidirectional flows in transition regime. In: Rarefied Gas Dynamics, edited by R. Brun et al.*, vol. 2, 245. Cepadus-Editions, Toulouse. 27

[87] Fan, J. & Shen, C. (2001). Statistical simulation of low-speed rarefied gas flows. *Journal of Computational Physics*, **167**, 393. 27

[88] Fichman, M. & Hetsroni, G. (2005). Viscosity and slip velocity in gas flow in microchannels. *Physics of Fluids*, **17**, 123102(1)–123102(5). 37

[89] Fortunato, B. & Magi, V. (1995). *An implicit Lambda Method for 2-D Viscous Compressible Flows. In: Fourteenth International Conference on Numerical Methods in Fluid Dynamics*, 259–264. Springer. 258

[90] Fried, E. & Gurtin, M. (2007). Thermomechanics of the interface between a body and its environment. *Continuum Mechanics and Thermodynamics*, **19**, 253–271. 39, 260

[91] Garey, M. & Johnson, D. (1979). *Computers and Intractability, A guide to the theory of N-completeness.*. W.H. Freeman and company, New York. 92

[92] Ghosh, A. (1996). *Robust Least Squares Kinetic Upwind Method for Inviscid Compressible Flows.*. Ph.D. thesis, Indian Institute of Science, Bangalore. 200, 205

[93] Ghosh, A. & Deshpande, S. (1995). Least squares kinetic upwind method for inviscid compressible flows. *AIAA paper 95-1735, AIAA 12th Computational Fluid Dynamics Conference*. 83

[94] Gibberd, R. & Hoffman, D. (1973). On an algebraic approach to the derivation of markovian kinetic equations. *Physica*, **68**, 23–42. 343

[95] Gingold, R.A. & Monaghan, J.J. (1977). Smoothed particle hydrodynamics: theory and application to non-spherical stars. *Mon. Notices Royal Astro. Soc.,*, **181**, 375–389. 82

[96] Goldberg, D. (1989). *Genetic Algorithms in Search, Optimization and Machine Learning*. Addison-Wesley, Reading. 98

[97] Goldstein, D., Sturtevant, B. & Broadwell, J. (1989). *Investigation of the motion of the discrete velocity gases,). In:16th International Symposium on Rarefied Gas Dynamics: Progress in Astronautics and Aeronautics: E.P. Muntz et al. (Eds.)*, vol. 118, 100. AIP. 28

[98] Golub, G. & Loan, C.V. (1996). *Matrix Computations 3rd Edition*. The John Hopkins University Press, Baltimore and London. 187, 189

[99] Golub, G. & M.A.Saunders (1969). *Linear least squares and quadratic programming, Technical report no. CS 134*. Stanford University. 188

[100] Gorban, A. & Karlin, I. (1994). General approach to constructing models of the Boltzmann equation. *Physics A*, **206**, 401–420. 46

[101] Gorban, A., Karlin, I. & Zinovyev, A. (2004). Constructive methods of invariant manifolds for kinetic problems. *Physics Reports*, **396**, 197–403. 52

[102] Grad, H. (1949). On the kinetic theory of rarefied gases. *Comm. Pure Appl. Math*, **2**, 331–407. 30, 31, 52, 61, 150, 304, 348, 356

[103] Greenshields, C. & Reese, J. (2007). The structure of shock waves as a test of brenners modifications to the NavierStokes equations. *Journal of Fluid Mechanics*, **580**, 407–429. 354

[104] Greenshields, C. & Reese, J. (doi:10.1016/j.paerosci.2011.08.001). Rarefied hypersonic flow simulations using the Navier-Stokes equations with non-equilibrium boundary conditions. *Progress in Aerospace Sciences*. 40, 266, 271

[105] Greenspan, H. (1980). *The theory of rotating fluids*. Cambridge university press, Cambridge. 283

[106] Griebel, M. & Schweitzer, M. (2000). A particle-partition of unity method for the solution of elliptic, parabolic, and hyperbolic pdes. *SIAM Journal on Scientific Computing*, **22(3)**, 853–890. 82

[107] Gross, E. & Jackson, E. (1959). Kinetic models and the linearized Boltzmann equation. *The physics of fluids*, **2**, 432–441. 61

[108] Guo, Z. & Xu, K. (2009). Numerical validation of brenner's hydrodynamic model by force driven poiseuille flow. *Adv. Appl. Math. Mech.*, **1(3)**, 391–401. 39

[109] Guo, Z., Zheng, C. & Shi, B. (2008). Lattice Boltzmann equation with multiple effective relaxation times for gaseous microscale flow. *Physical Review E*, **77**, 036707(1)–036707(12). 38, 39

[110] Gyarmati, I. (1970). *Non-Equilibrium Thermodynamics: Field Theory and Variational Principle*. Springer, New York. 57

[111] Hadjiconstantinou, N. (2003). Comment on cercignani's second-order slip coefficient. *Physics of Fluids*, **15**, 2352–2354. 33, 36

[112] Hadjiconstantinou, N. (2006). The limits of Navier-Stokes theory and kinetic extensions for describing small-scale gaseous hydrodynamics. *Physics of Fluids*, **18**, 111301(1)–111301(19). 30

[113] Hadjiconstantinou, N. & Al-Mohssen, H. (2005). A linearized kinetic formulation including a second-order slip model for an impulsive start problem at arbitrary knudsen numbers. *Journal of Fluid Mechanics*, **533**, 47–56. 36

[114] Hak, M.G.E. (1999). The fluid mechanics of microdevices - the freeman scholar lecture. *ASME Journal of Fluids Engineering*, **121**, 5–33. 4, 25

[115] Harley, J., Huang, Y., Bau, H. & Zemel, J. (1995). Gas flow in microchannels. *Journal of Fluid Mechanics*, **284**, 257–274. 31

[116] Harten, A. (1983). On the symmetric form of systems of conservation laws with entropy. *Journal of Computational Physics*, **49**, 151–164. 64

[117] Harten, A., Lax, P. & Leer, B.V. (1983). On upstream differencing and godunov type schemes for hyperbolic conservation laws. *SIAM Review*, **25**, 35–61. 62, 64, 65

[118] Hash, D. & H.A.Hassan (1997). Two-dimensional coupling issues of hybrid dsmc/Navier–Stokes solvers. *AIAA paper 97-2507*. 29

[119] Hauck, C., Levermore, C. & Tits, A. (2008). Convex duality an entropy-based moment closures: Characterizing degenerate densities. *SIAM J. Control Optimization*, **47(4)**, 1977–2015. 347

[120] Hendrickson, B. & Leland, R. (1995). *The Chaco user's guide: version 2.0., Technical Report SAND94-2692*. Sandia National Labs, Alburquerque, NM. 91

[121] Holland, J. (1975). *Adaptation in natural and artificial systems.*. The university of Michigan Press, Ann Arbor. 94

[122] Holway, H. (1966). *Kinetic theory of shock structure using an ellipsoidal distribution function. In: Rarefied Gas Dynamics, Vol. I (Proc. Fourth International Symposium University of Toronto, 1964)*, 193–215. Academic Press, New York. 48, 49

[123] Homolle, T. & Hadjiconstantinou, N. (2007). Low-variance deviational simulation Monte Carlo. *Physics of Fluids*, **19**, 041701(1)–041701(4). 153

[124] Hsia, Y. & Domoto, G. (1983). An experimental investigation of molecular rarefaction effects in gas lubricated bearings at ultra low clearances. *Journal of Lubrication Technology*, **105**, 120–130. 36

[125] Ikenberry, E. & Truesdell, C. (1956). On the pressures and the flux of energy in a gas according to Maxwell's kinetic theory i. *J. of Rat. Mech. Anal.*, **5**, 1–54. 61, 356

[126] Jameson, A. (1993). Artificial diffusion, upwind biasing, limiters and their effect on accuracy and multigrid convergence in transonic and hypersonic flows. *AIAA paper 93-3359, AIAA 11th Computational Fluid Dynamics Conference*. 75

[127] Jin, S. & Slemrod, M. (2001). Regularization of the Burnett equations via relaxation. *Journal of Statistical Physics*, **103 (5/6)**, 1009–1033. 31, 54

[128] Johnson, E. & Stopford, P. (1983). Shear flow in the presence of 'strong rotation': Ii. approximations for continuum-plus-rarefied flow. *J. Phys. D: Appl. Phys*, **16**, 1207–1215. 77

[129] Jones, M. & Plassmann, P. (1994). Computational results for parallel unstructured mesh computations. *Computing Systems in Engineering*, **5(4)**, 297–309. 91

[130] Kallinderis, Y. (1996-06). Domain partitioning and load balancing for parallel computation in:vki lecture series. 91

[131] Kamal, M. (1966). Separation in the flow between eccentric rotating cylinders. *ASME Journal of Basic Engineering*, **88**, 717–724. 301

[132] Kansa, E. (1990). Multiquadricsa scattered data approximation scheme with applications to computational fluid-dynamicsi. *Computers Math. Applic.*, **19(6/8)**, 127–145. 83

[133] Kansa, E. (1990). Multiquadricsa scattered data approximation scheme with applications to computational fluid-dynamicsii. *Computers Math. Applic.*, **19(6/8)**, 147–161. 83

[134] Karlin, I., Asinari, P. & Succi, S. (2011). Matrix lattice Boltzmann reloaded. *Phil. Trans. R. Soc. A*, **369**, 2202–2210. 49

[135] Karniadakis, G., Beskok, A. & Aluru, N. (2005). *Microflows and Nanoflows: Fundamentals and Simulation*. Springer-Verlag, New York. 37

[136] Karypis, G. & Kumar, V. (1995). *A fast and high quality multilevel scheme for partitioning irregular graphs, Technical Report TR95-035*. Department of Computer Science, University of Minnesota. 91

[137] Katz, A. & Jameson, A. (2008). Edge-based meshless methods for compressible viscous flow with applications to overset grids. *AIAA paper 2008-3989, AIAA 38th Fluid Dynamics Conference*. 83, 84, 86, 89

[138] Katz, A. & Jameson, A. (2009). A comparison of various meshless schemes within a unified algorithm. *AIAA paper 2009-596, AIAA 47th AIAA Aerospace Sciences Meeting Including The New Horizons Forum and Aerospace Exposition*. 83

[139] Kennard, E. (1938). *Kinetic Theory of Gases*. McGraw-Hill, New York. 32, 173

[140] Kennedy, J. & Eberhart, R. (1995). *Particle swarm optimization. In:Proceedings of the 1995 IEEE International Conference on Neural Networks, Perth*, 1942–1948. IEEE Service Center, Piscataway. 94

[141] Kim, S., Pitsch, H. & Boyd, I. (2008). Slip velocity and knudsen layer in the lattice Boltzmann method for microscale flows. *Physical Review E*, **77**, 026704(1) –026704(12). 38

[142] Knight, D. (2006). *Elements of Numerical Methods for compressible flows*. Cambridge university press, New York. 68

[143] Kolobov, V., Arslanbekov, R., Aristov, V., Frolova, A. & Zabelok, S. (2007). Unified solver for rarefied and continuum flows

with adaptive mesh and algorithm refinement. *Journal of Computational Physics*, **223**, 589–608. 22, 25, 28

[144] Kullback, S. & Leibler, R. (1951). On information and sufficiency. *The annals of mathematical statistics*, **22**, 79–86. 118

[145] Kumar, G.S., Mahendra, A. & Rao, S.R. (2007). Shape optimization using hybrid ga-aco method and grid-free cfd solver. *AIAA paper 2007-3830, 18th AIAA Computational Fluid Dynamics Conference*. 95

[146] Kumar, G.S., Mahendra, A. & Deshpande, S. (2008). Optimization using genetic algorithm and grid free solver. *Computational Fluid Dynamics Journal*, **41**, 426–433. 95

[147] Lang, H. (1976). Second order slip effects in poiseuille flow. *Physics of Fluid*, **19**, 366–371. 36, 61

[148] Lebowitz, J., Frisch, H. & Helfand, E. (1960). Nonequilibrium distribution functions in a fluid. *Physics of Fluid*, **3(3)**, 325–338. 46

[149] Levermore, C. (1996). Moment closure hierarchies for kinetic theories. *Journal of statistical Physics*, **83(5/6)**, 1021–1065. 151, 346

[150] Levermore, C. & Pomraning, G. (1981). A flux-limited diffusion theory. *Astrophysics Journal*, **248**, 321–334. 348

[151] Levermore, C., Morokoff, W. & B.T., N. (1998). Moment realizability and the validity of the Navier-Stokes equations for rarefied gas dynamics. *Physics of Fluids*, **10(12)**, 3214–3226. 22, 347

[152] Li, Q., Fu, S. & Xu, K. (2005). Application of gas-kinetic scheme with kinetic boundary conditions in hypersonic flow. *AIAA Journal*, **43**, 2170–2176. 40

[153] Li, Z. & Zhang, H. (2004). Gas kinetic algorithm using Boltzmann model equation. *Computers & Fluids*, **33**, 967–991. 40

[154] Lilley, C. & Sader, J. (2008). Velocity profile in the knudsen layer according to the Boltzmann equation. *Proc. of the Royal Society A*, **464**, 2015–2035. 38, 182

[155] Liou, M. & Steffen, J. (1991). *A new flux splitting scheme*. NASA TM-104404, NASA Lewis Research Center. 75

[156] Liszka, T. & Orkisz, J. (1980). The finite difference method at arbitrary irregular grids and its applications in applied mechanics. *Computers and Structures*, **11(1/2)**, 83–95. 83

[157] Liu, G. (1990). A method for constructing a model form for the Boltzmann equation. *Physics of Fluid A*, **2**, 277. 49

[158] Liu, G. (2002). *Mesh Free Methods: Moving beyond the finite element Method.*. CRC Press. 82

[159] Liu, W., Jun, S. & Zhang, Y. (1995). Reproducing kernel particle methods. *Int. J. Numerical Methods Fluids*, **20(8)**, 1081–1106. 82

[160] Liu, W., Li, S. & Belytschko, T. (1997). Moving least square reproducing kernel methods part i: Methodology and convergence. *Comput. Methods Appl. Mech. Engg.*, **143(1-2)**, 113–154. 82

[161] Lockerby, D. & Reese, J. (2003). Microchannel flow in the slip regime: gas-kinetic BGK-Burnett solutions. *Journal of Computational Physics*, **188**, 333–347. 40

[162] Lockerby, D., Reese, J., Emerson, D. & Barber, R. (2004). Velocity boundary condition at solid walls in rarefied gas calculations. *Physical Review E*, **70**, 017303–1–017303–4. 31, 32, 34, 35, 36, 180, 277

[163] Lockerby, D., Reese, J. & Gallis, M. (2005). The usefulness of higher-order constitutive relations for describing the knudsen layer. *Physics of Fluids*, **17**, 100609(1)–100609(9). xlv, 29, 30, 31, 40, 167, 268

[164] Lockerby, D., Struchtrup, H. & Reese, J. (2009). *Switching criteria for hybrid rarefied gas flow solvers. In: Rarefied Gas Dynamics:26th International Symposium ed. T. Abe*, vol. CP1084, 434–440. AIP. 22

[165] Löhner, R. & Parikh, P. (1988). Generation of three-dimensional unstructured grids by the advancing front method. *AIAA Paper 88-0515, AIAA 26th Aerospace Sciences Meeting*. 80

[166] Löhner, R., Sacco, C., Onate, E. & Idelsohn, S. (2002). A finite point method for compressible flow. *Int. J. Numerical Method Engg.*, **53**, 1765–1779. 83

[167] Lord, R. (1991). Some extension to the c- l gas surface scattering kernel. *Physics of Fluids A*, **3**, 706–710. 23

[168] Loyalka, S. (1971). Kinetic theory of thermal transpiration and mechanocaloric effect i. *The journal of chemical physics*, **55**, 4497–4503. 61

[169] Loyalka, S. (1975). Velocity profile in the knudsen layer for the kramer's problem. *Physics of Fluids*, **18**, 1666–1669. 30

[170] Loyalka, S. & Hickey, K. (1989). Plane poiseuille flow: Near continuum results for a rigid sphere gas. *Physica A*, **160**, 395. 33, 36

[171] Loyalka, S. & Tompson, R. (2009). The velocity slip problem: Accurate solutions of the BGK model integral equation. *European Journal of Mechanics B/Fluids*, **28**, 211–213. 33

[172] Loyalka, S., Petrellis, N. & Storvick, T. (1975). Some numerical results for the BGK model: Thermal creep and viscous slip problems with arbitrary accommodation at the surface. *Physics of Fluids*, **18**, 1094–1099. 31, 33, 36

[173] Lucy, L. (1977). A numerical approach to testing the fission hypothesis. *Astronomy Journal*, **82(12)**, 1013–1024. 82

[174] LumpkinIII, F. (1990). *Development and evaluation of continuum models for translational-rotational nonequilibrium*. Ph.D. thesis, Stanford University. 31

[175] Macrossan, M. (2001). *A particle simulation method for the BGK equation. In: Rarefied Gas Dynamics: 22nd International Symposium, Sydney. Eds. T.J. Bartel and M.A. Gallis*, 426–433. AIP. 66, 79

[176] Mahalanobis, P. (1936). On the generalized distance in statistics. *Proc. Nat. Inst. of Sciences of India*, **2**, 49–55. 118

[177] Mahendra, A. (2003). *Application of least squares kinetic upwind method to strongly rotating viscous flows*. Master's thesis, Indian Institute of Science, Bangalore. 67

[178] Mahendra, A. (2010). Adaptive ϵ-dominance coupled lp metric strategy for multiobjective - multicomponent problems. *MDD Internal report, BARC, Trombay, Mumbai*. 240, 242

[179] Mandal, J. & Deshpande, S. (1994). Kinetic flux vector splitting for Euler equations. *Computers & Fluids*, **23(2)**, 447–478. 66, 67

[180] Martyushev, L. & Seleznev, V. (2006). Maximum entropy production principle in physics,chemistry and biology. *Physics Reports*, **426**, 1–45. 57, 58, 60, 61, 103

[181] Maurer, J., Tabeling, P., Joseph, P. & Willaime, H. (2003). Second-order slip laws in microchannels for helium and nitrogen. *Physics of Fluids*, **15**, 2613–2621. 33, 36

[182] Mavriplis, D. (1990). Adaptive mesh generation for viscous flows using triangulation. *Journal of Computational Physics*, **90(2)**, 271–291. 81

[183] Max, C. (1981). *Theory of the Coronal Plasma in Laser Fusion targets, Physics of Laser Fusion*. LLNL report No. UCRL-53107. 348

[184] Maxwell, J. (1879). On stresses in rarefied gases arising from inequalities of temperature. *Philosophical Transactions Royal Society of London*, **170**, 231–256. 31, 36, 172

[185] May, G., Srinivasan, B. & Jameson, A. (2007). An improved gas-kinetic BGK finite-volume method for three-dimensional transonic flow. *Journal of Computational Physics*, **220**, 856–878. 48, 66

[186] McCourt, F., Beenakker, J., Köhler, W. & Kuščer, I. (1990). *Nonequilibrium Phenomenon in Polyatomic Gases*. Clarendon Press, Oxford. 61, 357

[187] McLeod, R. & Baart, M. (1998). *Geometry and Interpolation of Curves and Surfaces*. Cambridge University Press, Cambridge. 88

[188] Meng, J. & Zhang, Y. (2010). Analytical solution for the lattice Boltzmann model beyond Navier-Stokes. *Advances in Applied Mathematics and Mechanics*, **2(5)**, 670–676. 38

[189] Mieussens, L. (2000). Discrete-velocity models and numerical schemes for the Boltzmann-BGK equation in plane and axisymmetric geometries. *Journal of Computational Physics*, **162**, 429–466. 40, 79

[190] Mieussens, L. & Struchtrup, H. (2003). *Numerical solutions for the BGK-Model with velocity-dependent collision frequency. In: Rarefied Gas Dynamics: 23rd International Symposium, eds. A. D. Ketsdever and E. P. Muntz*, vol. CP 663. AIP. 49

[191] Mitsuya, Y. (1983). Modified Reynolds equation for ultra-thin film gas lubrication using 1.5-order slip-flow model and considering surface accommodation coefficient. *Journal of Tribology*, **115**, 289–294. 36

[192] Morse, T. (1964). Kinetic model for gases with internal degrees of freedom. *The physics of fluids*, **7**, 159–169. 42, 47

[193] Morse, T. (1964). Kinetic model for gases with internal degrees of freedom. *The physics of fluids*, **7**, 2012–2013. 359

[194] Mukherjee, Y.X. & Mukherjee, S. (1997). The boundary node method for potential problems. *Int. J. Numer. Methods Engg.*, **40**, 797–815. 82

[195] Müller, I. (1972). On the frame dependence of stress and heat flux. *Arch. Rational Mech. Anal.*, **45**, 241–250. 77, 78

[196] Müller, I. & Ruggeri, T. (1998). *Springer Tracts in Natural Philosophy 37 2nd ed.– Rational Extended Thermodynamics*. Springer Verlag, Berlin. 149, 150, 348

[197] Narayan, R., Loeb, A. & Kumar, P. (1994). Causality in strong shear flows. *The Astrophysical Journal Part 1*, **431(1)**, 279–359. 78

[198] Nayroles, B., Touzol, G. & Villon, P. (1992). Generating the finite element method: diffuse approximation and diffuse elements. *Comput. Mech.*, **10(5)**, 307–318. 82

[199] Nelder, J. & Mead, R. (1965). A simplex method for function minimization. *The Computer Journal*, **7**, 308–313. 94

[200] Nemec, M., Zingg, D. & Pulliam, T. (2004). Multipoint and multi-objective aerodynamic shape optimization. *AIAA Journal*, **42(6)**, 1057–1065. 95

[201] Ohwada, T., Sone, Y. & Aoki, K. (1989). Numerical analysis of the poiseuille and thermal transpiration flows between two parallel plates on the basis of the Boltzmann equation for hard-sphere molecules. *Physics of Fluid A*, **1**, 2042–2049. 24, 33

[202] Onate, E. & Idelsohn, S. (1998). A mesh-free finite point method for advective-diffusive transport and fluid flow problems. *Computational Mechanics*, **21**, 283–292. 83

[203] Onate, E., Idelsohn, S., Zienkiewicz, O., Taylor, R. & Sacco, C. (1996). A stabilized finite point method for analysis of fluid mechanics problems. *Computer Methods in Applied Mechanics and Engineering*, **139**, 315–346. 83

[204] Onsager, L. (1931). Reciprocal relations in irreversible processes i. *Phys. Rev.*, **37**, 405–426. 55

[205] Onsager, L. (1931). Reciprocal relations in irreversible processes ii. *Phys. Rev.*, **38**, 2265–2279. 55, 57

[206] Oran, E., Oh, C. & Cybyk, B. (1998). Direct simulation Monte Carlo: recent advances and applications. *Annu. Rev. Fluid Mech.*, **30**, 403–441. 28

[207] Osher, S. (1981). Numerical solution of singular perturbation problems and hyperbolic system of conservation laws. *North-Holland Mathematical Studies*, **47**, 179. 63, 64, 65

[208] Ottinger, H. (2005). *Beyond Equilibrium Thermodynamics*. Wiley, Hoboken. 354

[209] Pan, L., Liu, G. & Lam, K. (1999). Determination of slip coefficient for rarefied gas flows using direct simulation Monte Carlo. *J .Micromech. Microeng.*, **9**, 89–96. 36

[210] Park, J. & Hyun, J. (2004). Flow of a compressible fluid in a rapidly rotating pipe with azimuthally varying wall thermal condition. *Journal of Fluid Mechanics*, **518**, 125–145. 77

[211] Patterson, G. (1956). *Molecular flow of Gases*. John Wiley and Sons, New York. 40

[212] Pearce, D., Stanley, S., Martin, F., Gomez, R., Beau, G., Buning, P., Chan, W., Chui, T., Wulf, A. & Akdag, V. (1993). Development of a large scale chimera grid system for the space shuttle launch vehicle. *AIAA paper no. 93-0533*. 80

[213] Pellegrini, F. (2006). *Scotch 4.0 User Guide, Technical Report ENSEIRB & LaBRI, UMR CNRS 5800*. Université Bordeaux I. 91

[214] Perthame, B. (1991). Boltzmann-type scheme for gas dynamic and the entropy property. *SIAM journal of numerical analysis*, **27**, 1405–1421. 66

[215] Pironneau, O. (1984). *Optimal Shape Design for Elliptic Systems.*. Springer-Verlag, New York. 93

[216] Popham, R. & Narayan, R. (1992). Supersonic infall and causality in accretion disk boundary layers. *The Astrophysical Journal*, **394**, 255–260. 348

[217] Praveen, C. (2004). *Development and application of kinetic meshless methods for Euler Equations*. Ph.D. thesis, Indian Institute of Science, Bangalore. 83, 86, 89

[218] Praveen, C., Ghosh, A. & Deshpande, S. (2009). Positivity preservation, stencil selection and applications of lskum to 3-d inviscid flows. *Computers & Fluids*, **38(8)**, 1481–1494. 83, 86, 89

[219] Prendergast, K. & Xu, K. (1993). Numerical hydrodynamics from gas-kinetic theory. *Journal of Computational Physics*, **109**, 53–66. 66

[220] Prigogine, I. & Balescu, R. (1959). Irreversible processes in gases ii. the equations of evolution. *Physica*, **25**, 302–323. 343

[221] Pullin, D. (1980). Direct simulation methods for compressible inviscid gas flow. *Journal of Computational Physics*, **34**, 231–244. 65

[222] Pullin, D. & Harvey, J. (1976). A numerical simulation of the rarefied hypersonic flat-plate problem. *Journal of Fluid Mechanics*, **78**, 689–707. xxxix, 266

[223] Ramesh, P. & Lean, M. (1991). A boundary integral equation method for NavierStokes equations. application to flow in annulus of eccentric cylinders. *International Journal of Numerical Methods in Fluids*, **13**, 355–369. 301

[224] Ramesh, V. (2001). *Least squares grid free kinetic upwind method*. Ph.D. thesis, Indian Institute of Science, Bangalore. 83

[225] Rao, S.R. (1994). *New upwind methods based on kinetic theory for inviscid compressible flows*. Ph.D. thesis, Indian Institute of Science, Bangalore. 76

[226] Rao, S.R. & Deshpande, S. (1995). Peculiar velocity based upwind method for inviscid compressible flows. *Lecture Notes in Physics*, **No.453**, 112–116. 66, 75

[227] Reitz, R. (1981). One-dimensional compressible gas dynamic calculations using the Boltzmann equation. *Journal of Computational Physics*, **42**, 108–123. 65

[228] Rendall, T. & Allen, C. (2010). Reduced surface point selection options for efficient mesh deformation using radial basis functions. *Journal of Computational Physics*, **229**, 2810–2820. 95

[229] Roe, P. (1981). Approximate riemann solvers, parameter vectors and difference schemes. *Journal of Computational Physics*, **43**, 357–372. 63, 64, 65

[230] Rogier, F. & Schneider, J. (1994). A direct method for solving Boltzmann equation. *Trans. Theo. Stat. Phys.*, **23(1-3)**, 313–338. 28

[231] Roldughin, V. (1996). Non-equilibrium thermodynamics of boundary conditions for rarefied gases and related phenomenon. *Advances in Colloid and Interface Science*, **65**, 1–35. 40

[232] Roohi, E. & Darbandi, M. (2009). Extending the Navier-Stokes solutions to transition regime in two-dimensional micro- and nanochannel flows using information preservation scheme. *Physics of Fluids*, **21**, 082001(1)–082001(12). 37

[233] Sagan, H. (1994). *Space filling curves.*. Springer, Berlin. 91

[234] Saint-Raymond, L. (2009). *Hydrodynamic Limits of the Boltzmann Equation. (Lecture Notes in Mathematics 1971)*. Springer-Verlag, Heidelberg. 53, 342

[235] Samareh, J. (1999). *A survey of shape parametrization techniques. In: CEAS/AIAA/ICASE/NASA Langley International Forum on Aeroelasticity and Structural Dynamics*, vol. CP-1999-209136, 333–343. NASA. 95

[236] Sanders, R. & Pendergast, K. (1974). On the origin of the 3-kiloparsec arm. *Astrophysics Journal*, **88**, 489–500. 63, 65

[237] Sbragaglia, M. & Succi, S. (2005). Analytical calculation of slip flow in lattice Boltzmann models with kinetic boundary conditions. *Physics of Fluids*, **17**, 093602(1)–093602(8). 38

[238] Schamberg, R. (1947). *The Fundamental Differential Equations and the Boundary Conditions for High Speed Slip-Flow, and Their Application to Several Specific Problems.*. Ph.D. thesis, California Institute of Technology, Pasadena, CA. 36

[239] Schroeder, W. & Shephard, M. (1990). A combined octree/delaunay method for fully automatic 3-d mesh generation. *International Journal for Numerical Methods in Engineering*, **29(1)**, 37–55. 81

[240] Schwartzentruber, T. & Boyd, I. (2006). A hybrid particle-continuum method applied to shock waves. *Journal of Computational Physics*, **215**, 402–416. 22, 28

[241] Shakhov, E. (1968). Generalization of the krook kinetic relaxation equation. *Fluid Dynamics*, **3**, 95–96. 48, 50

[242] Shan, X. & He, X. (1998). Discretization of the velocity space in solution of Boltzmann equation. *Physics Review Letters*, **80**, 65. 52

[243] Sharipov, F. & Kremer, G. (1999). Non-isothermal couette flow of a rarefied gas between two rotating cylinders. *Eur. J. Mech. B/Fluids*, **18(1)**, 121–130. 77, 79

[244] Sharipov, F., Cumin, L. & Kremer, G. (2001). Transport phenomena in rotating rarefied gases. *Physics of Fluid*, **13(1)**, 335–346. 77, 79

[245] Shen, C. (2005). *Rarefied Gas Dynamics : Fundamentals, Simulations and Micro Flows*. Springer, Berlin. 24, 27

[246] Shen, S., Chen, G., Crone, R. & Ananya-Dufresne, M. (2007). A kinetic-theory based first order slip boundary condition for gas flow. *Physics of Fluids*, **19**, 086101(1)–086101(6). 40

[247] Shephard, M. & Georges, M. (1991). Automatic three-dimensional mesh generation by the finite octree technique. *International Journal for Numerical Methods in Engineering*, **32(4)**, 709–749. 81

[248] Sheretov, Y. (1997). *Quasi-hydrodynamic equations as a model of flows of compressible viscous, heat-conducting medium. In: Applications of Functional Analysis in Approximation Theory [in Russian]*, 127–155. Tver, Moscow. 39, 353

[249] Shu, C. & Osher, S. (1988). Efficient implementation of essentially non-oscillatory schemes. *Journal of Computational Physics*, **77**, 439–471. 206, 249, 258, 291

[250] Shu, C., Ding, H. & Yeo, K. (2003). Local radial basis function-based differential quadrature method and its application to solve two-dimensional

incompressible Navier-Stokes equations. *Comput. Methods Appl. Mech. Engg*, **192**, 941–954. 83

[251] Shu, C., Ding, H., Chen, H. & Wang, T. (2005). An upwind local rbf-dq method for simulation of inviscid compressible flows. *Computer Methods in Applied Mechanics and Engineering*, **194**, 2001–2017. 83

[252] Shu, C., Ding, H. & Zhao, N. (2006). Numerical comparison of least square-based finite-difference (lsfd) and radial basis function-based finite-difference (rbffd) methods. *Computers and Mathematics with Applications*, **51**, 1297–1310. 83, 87, 88, 89

[253] Sreekanth, A. (1969). *Flow through long circular tubes. In: Proceedings of the sixth international symposium on Rarefied Gas Dynamics ed. L. Trilling, H.Y. Wachman*, 667–680. Academic Press. 33, 36

[254] Sridar, D. & Balakrishnan, N. (2003). An upwind finite difference scheme for meshless solvers. *Journal of Computational Physics*, **189**, 1–29. 83

[255] Sridar, D. & Balakrishnan, N. (2006). Convergence acceleration of an upwind least squares finite difference based meshless solver. *AIAA Journal*, **44**, 2189–2196. 83

[256] Steger, J. & Warming, R. (1981). Flux vector splitting of the inviscid gas dynamics equations with application to finite difference methods. *Journal of Computational Physics*, **40**, 263–293. 63

[257] Steinbrenner, J., Chawner, J. & Fouts, C. (1990). Multiple block grid generation in the interactive environment. *AIAA paper no. 90-1602, AIAA 21st Fluid Dynamics Conference*. 80

[258] S.Tiwari & Klar, A. (2011). *Coupling of the Navier-Stokes and the Boltzmann equations with a meshfree particle and kinetic particle methods for a micro cavity . In: Meshfree Methods for Partial Differential Equations V : eds. M. Griebel, M.A. Schweitzer*, vol. Lecture Notes in Computational Science and Engineering vol. 79, 155–171. Springer-Verlag, Berlin Heidelberg. 28

[259] S.Tiwari & Kuhnert, J. (2002). *Finite pointset method based on the projection method for simulations of the incompressible Navier-Stokes equations. In: Meshfree Methods for Partial Differential Equations*, vol. Lecture Notes in Computational Science and Engineering vol. 26. Springer-Verlag, Berlin Heidelberg. 82

[260] S.Tiwari & Kuhnert, J. (2005). *A numerical scheme for solving incompressible and low Mach number flows by Finite Pointset Method . In: Meshfree Methods for Partial Differential Equations II*, vol. Lecture Notes in Computational Science and Engineering vol. 43. Springer-Verlag, Berlin Heidelberg. 82

[261] S.Tiwari, Klar, A. & Hardt, S. (2009). A particle-particle hybrid method for kinetic and continuum equations. *Journal of Computational Physics*, **228**, 7109–7124. 28

[262] Storvick, T., Park, H. & Loyalka, S. (1978). Thermal transpiration: A comparison of experiment and theory. *Journal of Vacuum Science and Technology*, **15(6)**, 1844–1852. 56

[263] Struchtrup, H. (2001). Positivity of entropy production and phase density in the Chapman-Enskog expansion. *Technical Notes :Journal of Thermophysics*, **15(3)**, 372–373. 126

[264] Struchtrup, H. (2005). *Macroscopic transport equations for rarefied gas flows-approximation methods in kinetic theory. Interaction of Mechanics and Mathematics Series.*. Springer, Berlin. xliii, 348, 349, 356

[265] Struchtrup, H. (2008). What does an ideal wall look like? *Continuum Mechanics and Thermodynamics*, **19**, 493–498. 39, 77, 260, 265

[266] Struchtrup, H. & Torrilhon, M. (2003). Regularization of Grad's 13 moment equations: derivation and linear analysis. *Physics of Fluids*, **15**, 2668–2680. 31, 34, 40

[267] Struchtrup, H. & Torrilhon, M. (2008). Higher-order effects in rarefied channel flows. *Physical Review E*, **78**, 046301(1)–046301(11). 2, 34, 36

[268] Succi, S. (2001). *The lattice Boltzmann equation for fluid dynamics and beyond.*. Oxford University Press, Oxford. 38

[269] Sugimoto, H. & Soni, Y. (1992). Numerical analysis of steady flows of a gas evaporating from its cylindrical condensed phase on the basis of kinetic theory. *Physics of Fluid A*, **4(2)**, 419–440. 79

[270] Sun, Q. & Boyd, I. (2002). A direct simulation method for subsonic, microscale gas flows. *Journal of Computational Physics*, **179**, 400–425. 24, 27, 272

[271] Sun, Y., Barber, R. & Emerson, D. (2005). *The Impact Of Accommodation Coefficient On Concentric Couette Flow. In:Rarefied Gas Dynamics: 24th International Symposium, ed. M. Capitelli*, vol. CP762, 707–712. AIP. xl, 279, 280

[272] Surma, D., Tongsima, S. & Sha, E. (1996). Optimal communication scheduling based on collision graph model. *Speech and Signal processing*, **VI**, 3319–3322. 92

[273] Tan, Z. (1994). The δ-e method for the Boltzmann equation. *Journal of Computational Physics*, **110**, 327. 28

[274] Tcheremissine, F. (2006). Solution to the Boltzmann kinetic equation for high-speed flows. *Comput. Math. Phys.*, **46**, 315. 28

[275] Tibbs, K., Baras, F. & Garcia, A. (1997). Anomalous flow profile due to the curvature effect on slip length. *Physical Review E*, **56(2)**, 2282–2283. 277

[276] Tota, P. & Wang, Z. (2007). Meshfree Euler solver using local radial basis functions for inviscid compressible flows. *AIAA Paper 2007-4581, 18th AIAA Computational Fluid Dynamics Conference*. 83

[277] Tretheway, D. & Meinhart, C.D. (2002). Apparent fluid slip at hydrophobic microchannel walls. *Physics of Fluids*, **14**, L9–L12. 260

[278] VAN KAMPEN, N. (1987). Chapman-Enskog as an application of the method for eliminating fast variables. *Journal of Statistical Physics*, **46(3/4)**, 709–727. 52

[279] VAN LEER, B. (1982). *Flux vector splitting for Euler equations*. ICASE Report 82-30, NASA Langley Research Center, Hampton. 62, 64

[280] VAN LEER, B. (1991). *Flux Vector Splitting for the 1990's*. NASA CP-3078, NASA Lewis Research Center. 64, 65

[281] VAN LEER, B., J.L.THOMAS, ROE, P. & NEWSOME, R. (1987). *A comparison of numerical flux formulas for the Euler and Navier-Stokes equations. In: AIAA 8th Computational Fluid Dynamics Conference*. 63

[282] ŽUPANOVIĆ , P., KUIĆ, D., Ž.B. LOŠIĆ, PETROV, D., JURETIĆ, D. & BRUMEN, M. (2010). The maximum entropy production principle and linear irreversible processes. *Entropy*, **12**, 996–1005. 57

[283] WALDMANN, L. (1967). Non-equilibrium thermodynamics of boundary conditions. *Z. Naturforsch*, **22a**, 1269–1280. 40

[284] WALSHAW, C., CROSS, M. & EVERETT, M. (1995). A localized algorithm of optimizing unstructured mesh partitions. *International Journal of Supercomputer Applications*, **9(4)**, 280–295. 91

[285] WANG, M., MACROSSAN, M. & LI, Z. (2007). Relaxation time simulation method with internal energy exchange for perfect gas flow at near-continuum conditions. *Communications in Nonlinear Science and Numerical Simulation.*, **12**, 1277–1282. 66

[286] WANG, W.L. & BOYD, I. (2003). Predicting continuum breakdown in hypersonic viscous flows. *Physics of Fluids*, **15**, 91–100. 22

[287] WANNIER, G. (1950). A contribution to the hydrodynamics of lubrication. *Quarterly Journal of Applied Mathematics*, **8**, 1–32. 301

[288] WATANABE, K., UDAGAWA, Y. & UDAGAWA, H. (1999). Drag reduction of Newtonian fluid in a circular pipe with a highly water-repellent wall. *Journal of Fluid Mechanics*, **381**, 225–238. 260

[289] Weatherill, N. (1992). Delaunay triangulation in computational fluid dynamics. *Computers & Mathematics with Applications*, **24(5/6)**, 129–150. 80

[290] Wierzbicki, A. (1999). *Reference point approaches In: Multicriteria Decision Making: Advances in MCDM Models, Algorithms, Theory, and Applications. Gal T, Stewart T, Hanne T.(eds).*, 9.1–9.39. Kluwer Academic Publishers. 238

[291] Wood, L. (1983). Frame-indifferent kinetic theory. *Journal of Fluid Mechanics*, **136**, 423–433. 31, 48, 54, 178

[292] Wood, W. (1957). The asymptotic expansions at large Reynolds numbers for steady motion between non-coaxial rotating cylinders. *Journal of Fluid Mechanics*, **8**, 159–175. 301

[293] Xu, K. (2001). A gas-kinetic BGK scheme for the Navier–Stokes equations and its connection with artificial dissipation and godunov method. *Journal of Computational Physics*, **171**, 289–335. 48, 66, 79

[294] Xu, K. & Huang, J.C. (2010). A unified gas-kinetic scheme for continuum and rarefied flow. *Journal of Computational Physics*, **229**, 7747–7764. 66

[295] Xu, K. & Li, Z. (2004). Microchannel flow in the slip regime: gas-kinetic BGK-Burnett solutions. *Journal of Fluid Mechanics*, **513**, 87–110. 40

[296] Yang, J.Y., Hsieh, T.Y., Shi, Y.H. & Xu, K. (2007). High-order kinetic flux vector splitting schemes in general coordinates for ideal quantum gas dynamics. *Journal of Computational Physics*, **227**, 967–982. 67

[297] Ye, T., Mittal, R. & H.S. Udaykumar and, W.S. (1999). An accurate Cartesian grid method for viscous incompressible flows with complex immersed boundaries. *Journal of Computational Physics*, **156(2)**, 209–240. 81

[298] Yong, W.A. (2009). An Onsager-like relation for the lattice Boltzmann method. *Journal Computers & Mathematics with Applications*, **58**, 862–866. 49

[299] Zahn, C. & Roskies, R. (1972). Fourier descriptors for plane closed curves. *IEEE Transactions on computers*, **c-21**, 269–281. 293, 320

[300] Zhdanov, V. & Roldughin, V. (1998). Non-equilibrium thermodynamics and kinetic theory of rarefied gases. *Physics-Uspekhi*, **41(4)**, 349–378. 40, 55, 61

[301] Zheng, Y. & Struchtrup, H. (2005). Ellipsoidal statistical Bhatnagar-Gross-Krook model with velocity-dependent collision frequency. *Physics of fluids*, **17**, 127103(1)–127103(17). 49

[302] Zhong, X., MacCormack, R.W. & Chapman, D.R. (1993). Stabilization of the Burnett equations and application to hypersonic flows. *AIAA Journal*, **31**. 31

[303] Zhu, T. & Atluri, S. (1998). A modified collocation method and a penalty formulation for enforcing the essential boundary conditions in the element free galerkin method. *Comput. Mech.*, **21(3)**, 211–222. 82

[304] Zhu, T., Zhang, J.D. & Atluri, S. (1998). A local boundary integral equation (lbie) method in computational mechanics and meshless discretization approach. *Comput. Mech.*, **21(3)**, 223–235. 82

[305] Ziegler, H. (1983). *An Introduction to Thermomechanics*. North-Holland, Amsterdam. 57